PERFORMANCE EVALUATION AND OPTIMISATION OF VANELESS DIFFUSER OF VARIOUS SHAPES FOR A CENTRIFUGAL COMPRESSOR

NOUKHEZ AHMED

A thesis submitted to the University of Huddersfield in partial fulfilment of the requirements for the degree of the doctor of philosophy

The University of Huddersfield in collaboration with the Cummins Turbo Technologies Ltd. Huddersfield

November 2017

ABSTRACT

In recent years, diesel engines with reduced emissions and low fuel consumption have been developed worldwide for the purpose of environmental protection and energy conservation. Turbochargers are playing an important role in these modern engines by providing power boost to the engine. A turbocharger comprises of three major parts i.e. the turbine stage, the bearing housing and the compressor stage. Turbocharger designers are continuously seeking for compact stage designs, while maintaining the stage performance. A turbocharger's compressor stage comprises of various parts i.e. inlet, impeller, diffuser and volute. The diffuser is an important section of the turbocharger compressor stage that plays a key role in increasing the isentropic efficiency of the stage. The diffuser converts the kinetic energy imparted to the flow by the impeller, into static pressure rise, which in-turn increases the isentropic efficiency of the stage. The shape of a diffuser is conventionally simple in design. Modifications to the diffuser geometry can lead to higher efficiencies and compact designs of the compressor stage.

The present study focuses on the use of advanced computational techniques, such as Computational Fluid Dynamics (CFD), to analyse the effects of diffuser modifications on the local flow features, and the global performance parameters. A baseline diffuser configuration, consisting of a parallel wall diffuser, is numerically analysed to establish the accuracy of CFD based predictions. Various diffusers' geometrical configurations have been analysed in the present study, both qualitatively and quantitatively. These geometrical configurations cover a wide range, such as diverging, tilting and curving of the diffuser walls. These parametric investigations aid to improve the compressor stage performance and make it more compact.

The first aim of the study is to quantify the increase in the stage performance by diverging the straight wall vaneless diffuser passage. This is carried out by diverging the shroud wall (i.e. increasing the outlet-to-inlet width ratio) and varying the location of the divergence point on the shroud wall. The results obtained depict that the effect of increasing the diffuser's outlet-to-inlet width ratio is dominant in comparison with the location of the wall divergence point. Moreover, increase in diffuser's outlet-to-inlet width ratio increases the downstream area ratio of the diffuser, causing the flow to separate and creating flow recirculation near the hub wall. This creates restriction to the flow and causes air blockage. Furthermore, shifting the wall divergence point towards the outlet of the diffuser relocates the flow separation point closer to the diffuser exit.

The second aim of this study is to analyse the effects of tilted diffuser walls on the flow variables within the compressor stage of the turbocharger. Tilting diffuser walls provides an increased streamwise length to the flow. Furthermore, divergence is applied to the diffuser hub wall in order to increase the outlet-to-inlet width ratio. This makes the turbocharger compressor stage compact in design, while maintaining the stage performance, which is the current requirement of the automotive sector. Design of Experiments, using Taguchi method, has been incorporated in this study to define the scope of the numerical work. The results obtained show that the diffuser with both titled and diverged walls together, performs optimally as compared to the other configurations considered.

The third aim of this study is to use curved diffuser walls in order to make the design more compact. Divergence to the hub wall is also applied to enhance the performance of the compressor stage. Various configurations of curvilinear diffuser walls have been considered for numerical analysis. The local flow field analysis has been carried out, quantifying the effects of the geometrical parameters on the stage performance. The results depict that a curved diffuser model reduces the losses within the diffuser passage, but there is negligible effect on the stage efficiency. However, when the divergence is applied to the hub wall of the curved diffuser, there is significant increase in the stage efficiency. Based on these investigations, a turbocharger's compressor stage can be designed for a compact design and optimal efficiency.

DECLARATION

1. The author of this thesis (including any appendices and/or schedules to this thesis) owns any copyright in it (the "Copyright") and he has given The University of Huddersfield the right to use such Copyright for any administrative, promotional, educational and/or teaching purposes.

2. Copies of this thesis, either in full or in extracts, may be made only in accordance with the regulations of the University Library. Details of these regulations may be obtained from the Librarian. This page must form part of any such copies made.

3. The ownership of any patents, designs, trademarks and any and all other intellectual property rights except for the Copyright (the "Intellectual Property Rights") and any reproductions of copyright works, for example graphs and tables ("Reproductions"), which may be described in this thesis, may not be owned by the author and may be owned by third parties. Such Intellectual Property Rights and Reproductions cannot and must not be made available for use without the prior written permission of the owner(s) of the relevant Intellectual Property Rights and/or Reproductions.

ACKNOWLEDGEMENTS

First and foremost, I would like to thank Allah Almighty for giving me the strength, knowledge, ability and opportunity to undertake this research study, and to pursue and complete it satisfactorily. Without His blessings, this achievement would not have been possible.

I would like to express my gratitude to Prof. Rakesh Mishra for offering the possibility to this research, supervising and guiding the process. His great influence on this work should be recognised. His insights, ideas and general guidance were magnificent throughout the process.

Secondly, I should mention my special gratitude to my better half Adeeba Rani for her patience and encouragement and to our son Rehaan Ahmed, who kept our life happy during this period at University of Huddersfield. Without their help I would not be able to achieve this.

I would like to acknowledge made by my parents Mr and Mrs Lt Col (retd.) Mohabbat Ali, and my wife's parents Mr and Mrs Mohammed Javed in terms of moral, emotional and financial support throughout the growing years.

I would like to acknowledge Dr. Subenuka Sivagnanasundaram for her supervision and support. I also acknowledge support of my colleagues in EEERG at University of Huddersfield, especially my co-supervisor Dr. Taimoor Asim for his considerable help in analysing the flow field within the centrifugal compressor stage. Furthermore, I would also like to thank my Turbocharger group colleagues Sree Nirjhor Kaysthagir and Karina Zala for their help during PhD journey.

I gratefully acknowledge the financial contributions of Prof. Rakesh Mishra and Cummins Turbo Technologies Huddersfield.

Noukhez Ahmed
November 2017
Huddersfield, UK

CONTENTS

LIST OF FIGURES

LIST OF TABLES

NOMENCLATURE

A	m^2	Area, Total blade passage area
a	m/s	Acoustic velocity
b	m/s	Passage depth (normal mean meridional velocity component)
C	m/s	Absolute velocity
c_{slip}	m/s	Slip velocity
C_p	J/kgK	Specific heat at constant pressure
c_f	-	Friction coefficient
C_r	-	Contraction ratio
h	J	Enthalpy
Δh	J	Change in enthalpy
$\dot{m}$	kg/s	Mass flow rate
M	-	Mach number
n	-	Frequency of experiment or numerical simulation in each group (Taguchi method)
N	rev/s	Shaft speed
p	Pa	Absolute pressure
PR	-	Pressure ratio
$P_{o,out}$	Pa	Outlet absolute total pressure
$P_{o,in}$	Pa	Inlet absolute total pressure
R	M	radius
R	J/kgK	Gas constant
dS	-	Entropy change
T	K	Absolute temperature
$T_{o,out,is}$	K	Isentropic outlet absolute total temperature
$T_{o,in}$	K	Inlet absolute total temperature
$T_{o,out}$	K	Outlet absolute total temperature
U	m/s	Blade speed (ωr)
V	m/s	Velocity

W	m/s	Relative velocity
W_x	J	Total shaft work per unit mass of the fluid
$W_{ideal\ comp}$	J	Work that would be required to compress the gas isentropically through the pressure ratio across the compressor
$W_{actual\ comp}$	J	Work done on the gas flowing through the compressor
y_i	-	Value of the *i* experiment in each group (Taguchi method)
z	-	Number of blades or vanes
A	˚ (deg)	Flow angle with respect to tangent
β	˚ (deg)	Relative flow angle, Blade angle with respect to tangent
ϒ	˚ (deg)	Specific heat ratio
η	-	Isentropic efficiency
η_{A1}	-	Response value of *S/N* ratio of 1 level of factor A
η_1, η_2, η_3, η_4, η_5	-	Response value of *S/N* ratio of No. 1, 2, 3, 4 and 5 respectively
μ	Ns/m^2	Dynamic viscosity coefficient
ρ	kg/m^3	density
ω	rpm	Rotational speed

SUBSCRIPTS

B	Blade
FB	Full blades
h	hub
m	Meridional velocity component
ref	Reference value
SB	Splitter blades
s	shroud
TT	Total-to-total ratio
t	Total thermodynamic condition
th	Throat
0,1,2,3,..	Stations in the stage
0	Stagnation (total) state
θ	Tangential component

Auxiliary Symbols

`	Value relative to rotating frame of reference

CHAPTER 1
INTRODUCTION

International legislation demands lowering the emissions and the fuel consumption in the internal combustion engines. Reducing the fuel consumption without sacrificing the level of performance delivered by the current vehicles has become a challenge for automotive industries. Turbocharging is one of the solutions to reduce emission levels. The turbocharger's performance is explicitly dependent upon the compressor stage efficiency. The compressor stage efficiency is further dependent upon the flow characteristics within the different components of the compressor, especially the diffuser passage. This chapter provides an introductory discussion regarding the flow characteristics within the centrifugal compressor stage of the turbocharger. The various components of the compressor stage are discussed in detailed, focusing on the diffuser. The compressor map, along with the modifications to the diffuser that can help enhance the stage performance, have been included in this chapter. Last but not the least, the motivation of the work, and the research aims are the highlight of this chapter.

1.1. Turbochargers

Naturally aspirated engines breathe fresh air within the cylinders as the piston moves down. Normally 80% of the cylinder volume is filled with air, while 20% is filled with fuel. In order to increase the engine power, while maintaining the air-fuel ratio, more dense air needs to be injected into the cylinders. This is achieved through the use of Turbochargers with internal combustion engines. Turbochargers increase air pressure entering the engine cylinders (above atmospheric pressure). This results in higher power generated from the combustion engine.

Turbocharger is a device used to increase the power output of the internal combustion engine by increasing the pressure and the density of air. It extracts energy from the engine exhaust gases and employs it to compress ambient air into the engine cylinders. A turbocharger consists of a turbine, an impeller and the shaft and bearing system. Turbine expands hot exhaust gas and recuperates part of the gas energy. Compressor utilises the energy extracted by the turbine via shaft and bearing system to compress the ambient air. Shaft and bearing system mechanically connect the turbine and compressor impellers, so that energy can be transferred from the engine exhaust to the intake flow. A typical turbocharging system is shown in figure 1.1.

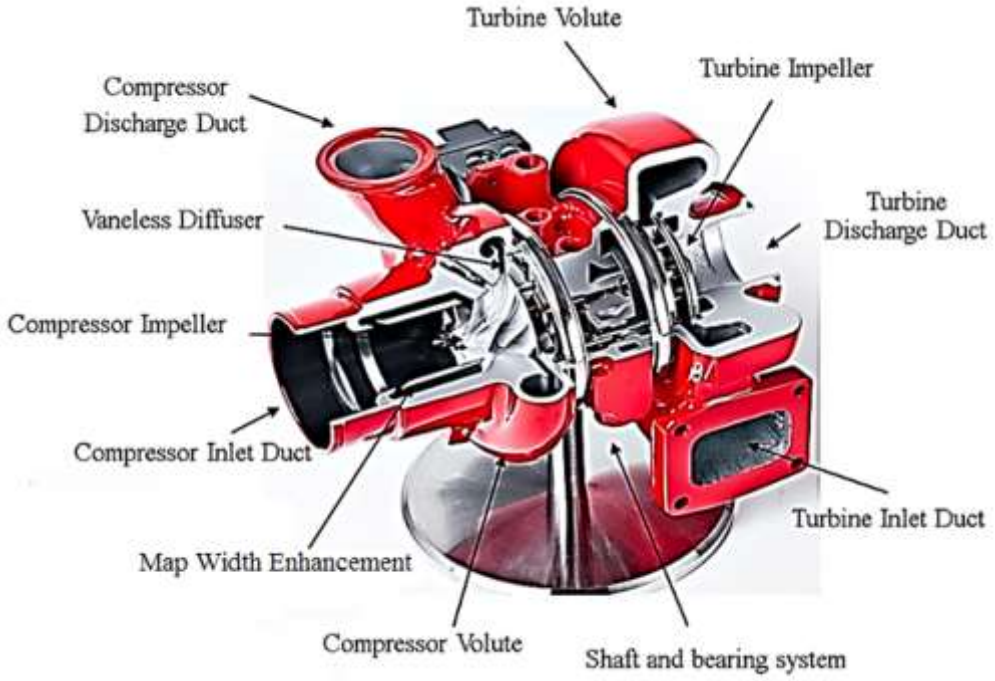

Figure 1.1: A typical turbocharger [1]

A Swiss Engineer, Alfred Buchi, developed the first turbocharger between 1909AD and 1912AD, which was patented in 1927AD (named Exhaust Driven Turbo-Supercharging). General Electrics built turbochargers to be used in aircrafts in World War II. Cummins, Volvo and Scania developed turbochargers for trucks. Garrett (now called Honeywell) and Schwitzer (now called BorgWarner) started manufacturing turbochargers for Caterpillar and Mach Truck in 1952AD. General Motors introduced the first passenger car (named Corvair) with turbocharged engine, in 1962AD.

1.1.1. Turbine Stage

The turbocharger turbine stage consists of an inlet duct, a volute, an impeller and an outlet duct, as depicted in figure 1.1. The exhaust gases form the engine enters the turbine via the inlet duct at high velocity and temperature. These gases flow through the turbine volute that distributes these gases around the turbine impeller blades. A ring of nozzle guide vanes shrouds the turbine impeller. The flow area is varied by changing the width of the flow passage. [1] The turbine volute can be single-entry volute or twin-entry volute. The twin entry volute is used to separate the front side of the engine from the backside. It captures the pulsating effects and uses them to enhance the stage performance. Single entry volute is suitable for higher engine speeds, but has worse transient response in comparison with the twin-entry turbine volute. The function of the turbine impeller is to convert radial flow into axial flow. It also extracts energy from the exhaust gases and converts it into mechanical power to rotate the shaft connecting the two stages.

1.1.2. Shaft and Bearing System

The shaft and bearing system, shown in figure 1.2, comprises of the bearing housing, which holds the shaft and bearing together. The shaft is connected to the turbine impeller at one end, and it is connected to the compressor impeller at the other end. The thrust bearing helps to manage the axial moment of the rotor system generated by the net gas loading on the turbine and compressor wheels. The highest loads are mostly towards the compressor stage due to its larger back face area and higher-pressure ratio. The net load varies across the compressor map. [1] Axial loads being exerted on the shaft are inclined towards the compressor stage at near-surge design points, while they are inclined towards the turbine stage at near-choke design points.

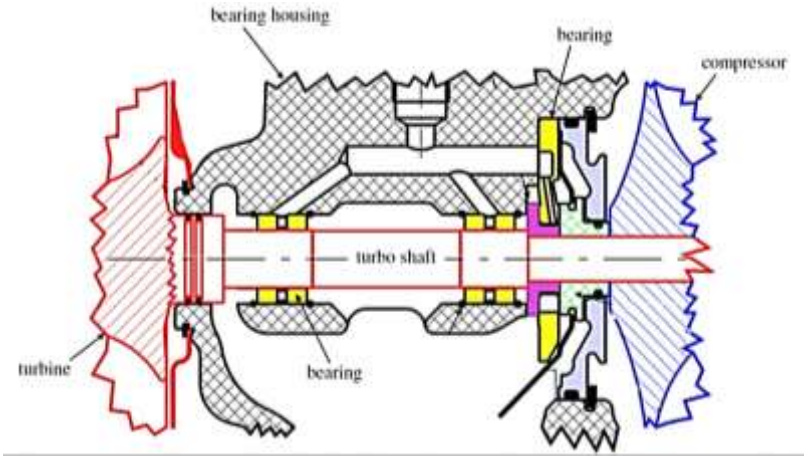

Figure 1.2: Cross-sectional view of the shaft and bearing system [1]

1.1.3. Compressor Stage

The turbocharger compressor stage consists of an inlet duct, a Map Width Enhancement (MWE), an impeller, a diffuser and a volute, as shown in figure 1.1. The ambient air enters the compressor stage axially via an inlet duct. The rotating impeller creates suction and draws the air from the inlet duct. The impeller consists of blades used to guide the air. Upon exiting the impeller, the flow is three-dimensional, consisting of velocity components in circumferential, radial and axial directions. The air exits from the impeller blades' trailing edges and enters into the diffuser. The diffuser is a radial annular passage that converts the kinetic energy of air into static pressure, decreasing the flow velocity. The air, after leaving the diffuser, enters the volute. The volute, also known as the compressor housing, resembles a conical diffuser in shape. The flow velocity further decreases within the volute passage. Finally, the fluid exits the discharge duct at high pressure, temperature and density.

The Compressor Maps

The performance characteristics of a compressor are usually shown in the form of compressor maps, as shown in figure 1.3. These maps depict the variations in the total-to-total isentropic efficiency and pressure ratio against the corrected mass flow rate of air passing through the compressor at various compressor speeds, where these parameters are defined as:

$$\eta_t = \frac{T_{o,in} \times \left[PR_C^{\frac{\gamma-1}{\gamma}} - 1 \right]}{T_{o,out} - T_{o,in}} \tag{1.1}$$

$$PR_C = \frac{P_{o,out}}{P_{o,in}} \tag{1.2}$$

where η_t is the total stage efficiency, T_o is the total temperature, PR_C is the compressor stage pressure ratio, P_o is the total pressure and γ is the ratio of specific heats. The corrected mass flow rate is explained using equation 1.3. Similarly, the pressure ratio and the stage efficiency are shown at different rotational speeds. The rotational speeds are presented, using the equation 1.4.

$$\text{Corrected mass flow rate} = \left[\frac{\dot{m}_{\text{physical}}\left(\frac{\text{kg}}{\text{sec}}\right)\times\sqrt{T_{o,in}(\text{K})}}{P_{o,in}(\text{MPa})}\right] \tag{1.3}$$

$$\text{Rotational Speed} = \left[\frac{N(rpm)}{\sqrt{T_{o,in}(\text{K})}}\right] \tag{1.4}$$

It can be seen that at a constant compressor speed, as the mass flow rate of air passing through the compressor stage of the turbocharger increases, the isentropic efficiency of the stage first increases, up to the Best Efficiency Point (BEP), and then decreases. Moreover, as the compressor speed increases, the efficiency curves shift towards high mass flow rate regions. It can be further noticed that as the compressor speed increases, the pressure ratio increases. Furthermore, as the mass flow rate of air increases, the pressure ratio decreases.

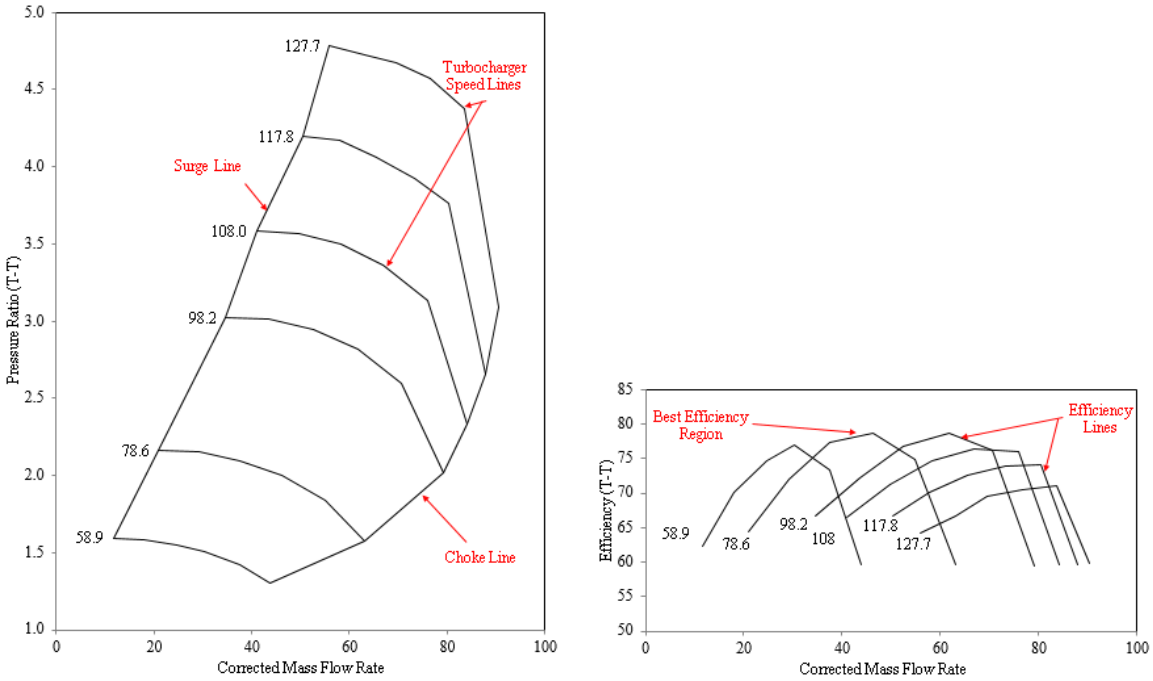

Figure 1.3: The compressor maps

Either ends of the compressor maps' curves are marked by off-design conditions. The extreme condition corresponding to the lower mass flow rate is known as surge, while the other one (at higher mass flow rates) is called choke. Under surge conditions, the backpressure within the

impeller blade passages increases, which causes flow reversals. The choke is characterised by the upper limit of the mass flow rate passing through the compressor stage. Under choke conditions, further increase in the differential pressure across the compressor stage does not increase the mass flow rate passing through the system.

Components of the Compressor Stage

This section describes the various components of the turbocharger compressor stage in detail, with a focus on the diffuser section.

Map Width Enhancement (MWE) Duct

Map Width Enhancement (MWE) duct is a cavity on the circumference of the inducer with two bleed slots on either ends of the cavity, as shown in figure 1.4. It is normally used to widen the range of the compressor map i.e. increasing both the surge and the choke margins/boundaries. Under surge condition, the backpressure is channelled through the MWE duct to the entrance of the inducer, from where, the flow then resumes in its normal direction. Under choke condition, excessive air from the inducer entrance is channelled through the MWE duct towards the MWE exit bleed slot.

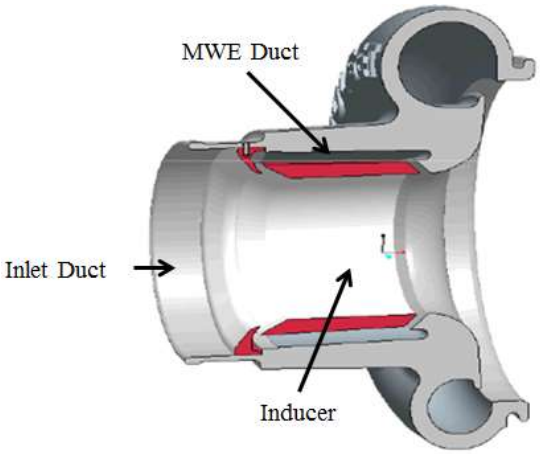

Figure 1.4: The MWE duct [1]

Impeller

The impeller is one of the most important components of the centrifugal compressor stage. The primary function of the impeller is to impart energy (kinetic) to the flow. A compressor's impeller consists of a number of backswept blades, which guides the flow towards the diffuser. The impeller blades are structurally supported by the hub wall, which is the back plate of the impeller wheel. Moreover, a part of the impeller's front section is covered by the shroud wall,

which is the compressor cover. There is a small gap between the shroud wall and the impeller blades, known as impeller tip gap. A typical radial impeller is shown in figure 1.5.

[2] Rodgers reports that the cross-sectional area of the flow passage across the impeller blade passages increases in the streamwise direction. The minimum flow area within the compressor stage is located near the impeller inlet, where choking takes place. To reduce blade blockage at the impeller inlet, some blades are cut from the inlet portion of the impeller. These partial-length blades, known as the splitter blades, allow the designers to achieve a wider choke margin, while maintaining the number of blades necessary to guide the flow at the outlet.

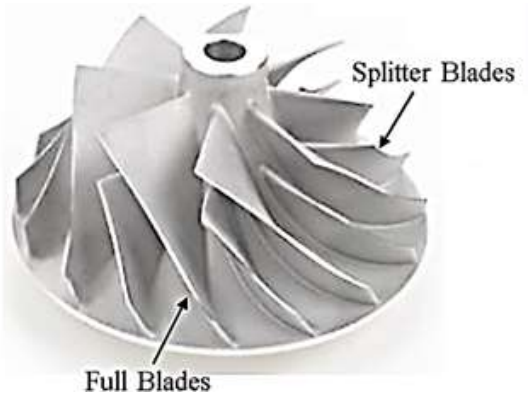

Figure 1.5: An impeller from a turbocharger compressor stage

A similar impeller to the one shown in figure 1.5, has been used in the present study, with seven full and seven splitter blades. [3] Harada found that when a constant inlet blade angle is used, excessive incidence loss at the impeller inlet occurs, because of mismatching between the inlet flow angle and the blade angle. To achieve a smooth inlet flow into the impeller passages, it is necessary to incorporate leading edge twist and vary the blade angles from the hub wall to the shroud wall. It has been noticed that a three-dimensional blade angle distribution improves the stage efficiency, as well as increases both the head coefficient and the choke mass flow rate. Hence, impeller (both full and splitter) are normally preferred.

Diffuser

The diffuser is another important section of the compressor stage where the diffusion of the flow (pressure rise associated with reduced flow velocities) takes place. The airflow having high kinetic energy leaving the impeller when enters the diffuser, the kinetic energy of the flow in converted into internal energy of air, increasing its static pressure. Diffusers can be categorised into two classes i.e. the vaned diffusers and the vaneless diffusers. The vaned diffuser (figure 1.6(a)) consists of vanes to guide the flow. The vaned diffusers are further

categorised based on their geometry, the design principle or the change in the mean flow path radius. They are used in applications where the operational range requirements are not a limitation. Furthermore, they are also used in applications where an increase in the stage efficiency is required; however, in this particular instance, they restrict the operational range considerably by reducing the choke and surge margin. On the other hand, the vaneless diffusers do not have vanes (figure 1.6(b)). The vaneless diffusers are the simplest in design, consisting of two parallel plates. The flow area increases as the radius of the vaneless diffuser increases. They are also cheaper to manufacture and are used where large operational range is required. The present work is carried out on the design improvement of the vaneless diffusers, which helps in improving the total-to-total compressor stage performance.

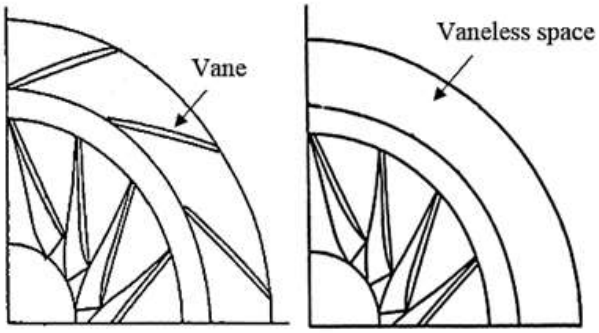

Figure 1.6: Diffuser (a) Vaned (b) Vaneless

The diffuser is a non-rotating component of the compressor stage, which typically has a simple geometry. Figure 1.7 depicts a schematic diagram of a vaneless diffuser. It can be seen that the diffuser consists of two parallel plates, or walls, known as the hub and the shroud walls. The diffuser forms a radial annular passage from the impeller tip to some limiting outer radius. The diffusion occurs due to the increase in area along the radial direction of the diffuser. The effective area of the diffuser passage is proportional to the radius ratio (r_2/r_1) and the width ratio (b_2/b_1) from the outlet to the inlet of the diffuser. The flow within the diffuser passage is dependent on the flow characteristics leaving the impeller blades. The flow within the diffuser passage is also dependent on the volute tongue. The geometry of a diffuser can be modified in order to i) enhance the performance of the compressor stage and ii) make the compressor stage design more compact, which is the primary research objective of the present study.

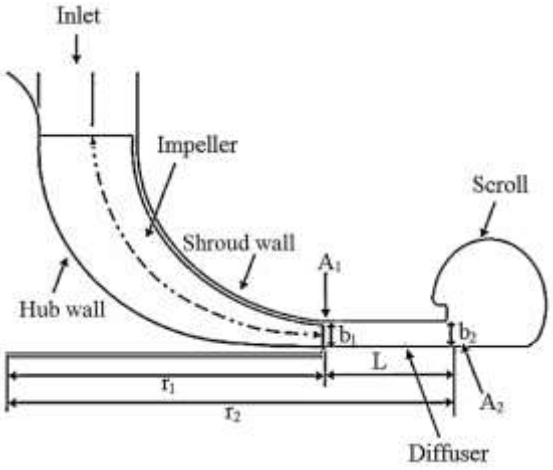

Figure 1.7: Schematic diagram of a diffuser

Volute

The volute collects the flow from the diffuser and guides it towards the outlet. A volute is composed of two parts; the scroll and the outlet duct. The volute of compressor is shown in figure 1.8. The location where the scroll meets the outlet duct is known is known as the volute-tongue region. Its shape and size have a significant effect on the performance of the centrifugal compressors. A larger volute-tongue area increases the isentropic efficiency at low pressure ratios, while smaller volute-tongue areas increase the efficiency at high pressure ratios. If the inclination of the volute-tongue does not conform to the airflow direction, shock losses and distributed flow conditions in this area arises [1]. [4] According to Khalflah, the tongue acts as a single vane where the flow is split and directed downstream to the vaneless diffuser and/or forced to re-circulate around the scroll. Furthermore, at surge condition (with lower mass flow rates), the large incidence angles at the volute-tongue lead to excessive flow separation, causing flow reversals. However, if the incidence angles are small, the volute-tongue directs most of the flow towards the outlet duct.

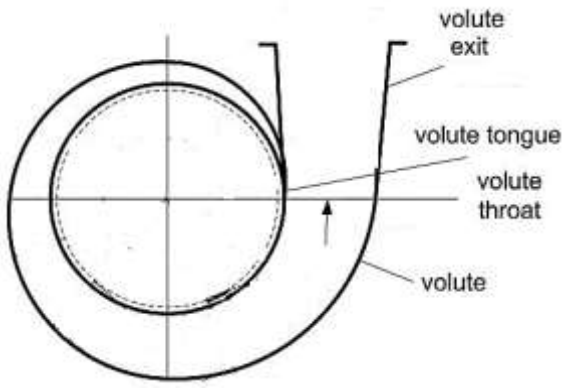

Figure 1.8: Volute

1.2. Design modifications of a Diffuser

There are several ways of modifying the design of the diffuser passage in order to make the compressor stage more compact, and to increase the isentropic efficiency of the stage. A number of these design modifications are discussed in this section.

1.2.1. Diffuser Wall Divergence

[5] Robinson, [6] Paris and [7] Shaaban have carried out investigations on diffuser wall divergence. Figure 1.9 shows different design configurations of a diffuser passage based on wall divergence. The two parameters that control the amount of divergence are i) wall divergence angle and ii) the location where the wall divergence starts. The result of wall divergence is reduction in the effective flow area. Research has shown that divergence on the diffuser wall/s helps in improving the diffuser performance.

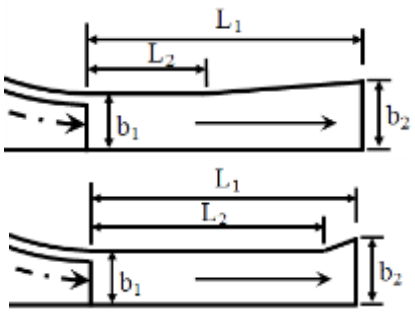

Figure 1.9: Diffuser wall divergence

1.2.2. Tilted Diffuser Walls

[8] Sweetland and [9] Boehm have investigated the effects of the diffuser walls tilting on the compressor stage performance. Figure 1.10 depicts different configurations of a tilted wall diffuser. The parameters that control the wall tilting are i) the tilt angle and ii) the direction of tilt. It can be seen in the figure that the diffuser walls can be either tilted inwards or outwards, depending upon the tilt direction. Research has shown that diffuser wall tilting has a significant effect on the compressor stage performance output. Increase in the streamwise length, due to tilting, results in higher diffusion rates, increasing the stage's isentropic efficiency. Furthermore, tilting also helps in decreasing the diffuser's flow losses that originate due to the interaction of the flow with the diffuser inlet.

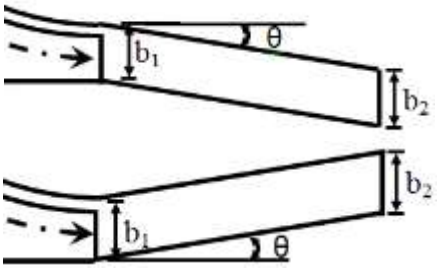

Figure 1.10: Tilted wall diffusers

1.2.3. Curved Diffuser Walls

[8] Sweetland and [10] Thenambika have investigated the effects of curving the diffuser walls. The curvature of the diffuser walls is controlled by the radius of curvature, as shown in figure 1.11. Research has shown that curving the diffuser walls has a significant effect on the compressor stage's performance. Increase in the streamwise length, due to curved walls, results in higher diffusion rates, increasing the stage's isentropic efficiency. Curved diffuser also tends to decrease the flow instabilities within the compressor stage.

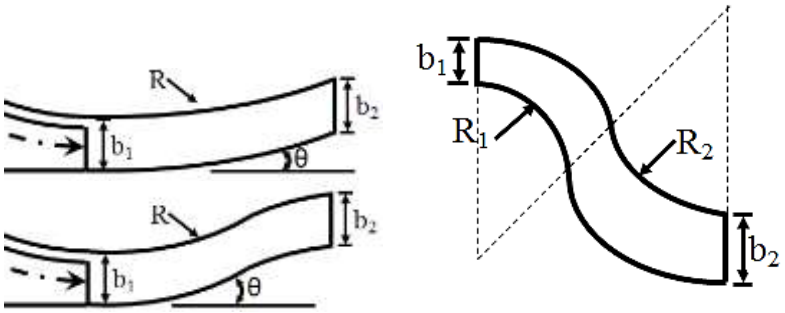

Figure 1.11: Curved wall diffusers

1.3. Motivation

It is the requirement of automotive industries to reduce the size-to-weight ratio of the vehicle parts, so as to reduce the fuel consumption. Therefore, higher efficiencies and compact design of turbochargers are the primary requirements of the automotive industry. Much of the current research is being carried out on the improvements in the stage efficiencies. The primary reason for not making the turbocharger design more compact is due to the findings, which show that compactness reduces the stage performance. Reducing the turbocharger size, along with maintaining/improving the performance of the compressor stage, is a challenging task. As very limited work has been carried out in this field of research, it has motivated the author to investigate the effects of design modifications to a turbocharger compressor diffuser, on the stage's isentropic efficiency. For this purpose, divergence to the walls of the diffuser has been specified in order to better understand the complex flow phenomena within the diffuser.

Furthermore, novel diffuser configurations have been developed for tilted and curved wall diffusers. This research has been carried out with the aim to enhance the diffuser performance, while making it more compact in design.

In the present study, numerical techniques have been extensively used in order to quantify the effects of diffuser walls divergence, tilting and curving, on the stage performance. This has been carried out separately, as well as in combination of configurations (such as divergence and tilting together etc.). For the sake of numerical analysis, this study employs advanced Computational Fluid Dynamics (CFD) based solvers. Detailed qualitative and quantitative analysis has shown that CFD predicted results can be used to identify the appropriate combination of diffuser wall modifications for optimal stage efficiency.

1.4. Organisation of the Thesis

Based on the discussions presented in the previous sections, this thesis presents the body of work, which has been carried out for the current research study.

Chapter 1 provides an overview of the turbocharger components. The working principle of a compressor stage has been presented, along with the preliminary design and analysis of the compressor stage. From this overview, the motivation for carrying out the current research has been described, which has led to the formulation of the research aims, identifying the key areas to be reviewed in Chapter 2.

Chapter 2 comprises of a detailed review of the published literature on the modifications of vaneless diffuser geometries. It includes the review of state-of-the-art research regarding the performance of the compressor stage at design and off-design conditions. Details of the scope of research are provided in the form of specific research objectives.

Chapter 3 documents the fundamental principles of Computational Fluid Dynamics. It includes the CFD modelling of the compressor stage of a turbocharger, including the solver settings and appropriate boundary conditions that have been specified to numerically solve the fluid flow governing equations in the flow domain. The meshing techniques used to spatially discretise the flow domain have also been discussed. Furthermore, a detailed discussion on the turbulence modelling and the interface specification is the highlight of the chapter.

Chapter 4 includes verification of the turbocharger compressor stage with the experimental data. It comprises of local flow field analysis inside the compressor stage. Finally, the flow

phenomena inside every stage (inlet duct, map-width enhancement duct, impeller, diffuser and volute) of the baseline model of centrifugal compressor has also been analysed in a great depth. It also covers comparison between parallel wall diffusers and diverged wall diffusers. Furthermore, it also covers the comparison of parallel wall diffusers without inserts and parallel wall diffusers with inserts. It explains the flow structure inside the straight and diverged wall diffusers and describes how the flow structure gets affected by apply wall divergence on the diffuser walls of the compressor stage. It also quantifies the effect of inserts on the overall compressor stage. The local flow analysis has been carried out inside the vaneless diffuser to formulate the effects of the wall divergence location, width ratio, number of inserts and inserts height inside the diffuser passage on the isentropic compression efficiency of the compressor stage. Furthermore, an analytical equation has been derived to obtain the local isentropic equation inside the compressor stage.

Chapter 5 sheds light on the flow phenomena inside the tilted wall diffusers. Design of Experiments, DoE using Taguchi method is presented in this chapter to reduce the number of simulations. It also covers comparison between parallel wall diffusers and tilted wall diffusers along with wall divergence. Furthermore, it also covers the comparison of tilted wall diffusers without inserts and tilted wall diffusers with inserts. It explains the flow structure inside the tilted and diverged wall diffusers and describes how the flow structure gets affected by apply wall divergence on the diffuser walls of the compressor stage. It also quantifies the effect of inserts on the overall compressor stage. The local flow analysis has been carried out inside the vaneless diffuser to formulate the effects of the wall tilt angle, divergence location, width ratio, number of inserts and inserts height inside the diffuser passage on the isentropic compression efficiency of the compressor stage.

Chapter 6 includes flow phenomena inside the curved wall diffusers. It also covers comparison between parallel wall diffusers and curved wall diffusers along with wall divergence. Furthermore, it also covers the comparison of curved wall diffusers without inserts and curved wall diffusers with inserts. It explains the flow structure inside the curved and diverged wall diffusers and describes how the flow structure gets affected by apply wall divergence on the diffuser walls of the compressor stage. It also quantifies the effect of inserts on the overall compressor stage. The local flow analysis has been carried out inside the vaneless diffuser to formulate the effects of the wall curvature radius; angle of curvature, divergence location,

width ratio, number of inserts and inserts height inside the diffuser passage on the isentropic compression efficiency of the compressor stage.

Chapter 7 concludes the findings of this study, clearly mentioning the goals achieved, and the novel contributions to the existing knowledge regarding the diffuser design process. Recommendations for future work have also been included.

CHAPTER 2
LITERATURE REVIEW

After describing the detailed information regarding the parameter affecting the design of a turbocharger compressor diffuser in the previous chapter, a detailed literature review has been presented in this chapter that will highlight the knowledge gaps in the existing literature. A wide range of resources have been thoroughly examined in an attempt to gain a better understanding of the flow behaviour within a diffuser, and the effects of its design modifications on the stage performance. The existing literature includes the published works on the diffuser walls divergence, tilting and curving. This has assisted in formulating the scope of the current work.

2.1. Flow Investigations within Diffusers of Centrifugal Compressors

The flow field analysis was primarily carried out using One Dimensional (1D) analysis. 1D analysis is means obtaining the flow field variables across the meanline of the compressor stage. The empirical equations for the losses within the compressor stage are formulated, which are used in the 1D analysis to predict the flow characteristics within the compressor stage. [1, 11, 12] Various methods have been developed to carry out 1D analysis, such as by Whitfield, Baines and Aungier. [13] Louis de Wet carried out 1D analysis on a centrifugal compressor using Aungier's fundamentals of 1D equation. It has been found out that 1D equation based predictions work well at best efficiency points of the compressor map. Aungier theory deteriorates however at off-design conditions. This is due to inability of capturing the loss coefficients at off-design conditions.

[14] Yuri and Peter determined the meanline geometric parameters of a centrifugal compressor stage. An algorithm and computer code has been used, which implements the inverse design approach. This approach has been configured to compute the loss coefficients for rotating impellers, in order to improve the losses for the compressor model. The conservation equations for each component of the compressor stage have been used, which have been solved iteratively. This results in the required 1D geometry of the impeller. The pressure losses within the impeller have been calculated by estimating the loss coefficient. Various formulae have been used to determine the new loss coefficient, enabling a distinct comparison to be made between the two values. This method has been repeated to determine the loss coefficient, until the estimated and calculated values became equal. Similarly, same procedure has been further carried out on the diffuser and the volute. The aim of this study was to determine the diameter and width of the diffuser outlet. This approach has enabled the design engineers to determine the global and local flow fields within the compressor stage components.

[15] Rotating stall, as shown in figure 2.1, consists of zones of stall passages covering a small area within the blades passages, rotating with a specific rotational speed. The rotating stall occurs in both rotating and stationary blade rows, and occurs in axial as well as centrifugal compressors. The impeller and the diffuser, either vaned or vaneless, can have rotating and non-rotating stall, but it is not necessary that the stall within the diffuser passage is the cause of initiation of the rotating stall within the impeller. Experimental evidences have shown that there is a local non-rotating stall at the inducer, but it converts to rotating stall when it is in the blade passages.

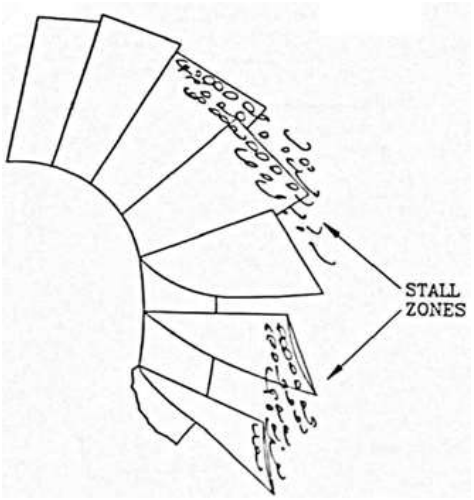

Figure 2.1: Illustration of Rotating Stall on an Axial Compressor Rotor [36]

[16] The distinction between different types of stalls within the centrifugal compressor stage has been studied experimentally. The tests have been conducted with a vaneless diffuser passage. The stall generation within the centrifugal compressor stage has been noticed to be rotor-induced only. It has been found that inducer stall begins at the tip of the leading edge of the blade, progressing down the blade spin. It was further observed that the stalled area covered the entire annulus of the blade tip, and consisted of reversed flow from the impeller. Therefore, the reversed flow has been reduced from the inducer with a tangential velocity that provided positive pre-whirl to the flow outside the stall region, as it mixed with the incoming flow. The zone of reversed flow increases with the reduction in the mass flow rate, and hence, the amount of incoming mass flow rate is affected by the pre-whirl. The combinations of these flow phenomena have eventually driven the impeller into the surge condition. Moreover, it has also been noticed that the entire blade channel has been affected by the stall cell during the impeller stall. Flow oscillations have been recorded in the measurements obtained from the upstream of the inducer to the rotor exit. The maximum pulsations occurred at 80% of the meridional distance along the shroud. Furthermore, these tests depicted the impeller-induced oscillations and interactions with the vaneless diffuser. The stall cell numbers, ranging from 2 to 7, have been identified, and cell rotation has been observed. The generation of multiple stall cells have been identified at the vaneless and vaned diffuser passages. The stall within the vaneless diffuser passage has been associated with the reversal of the radial component of velocity and the three-dimensional (3D) separations (figure 2.2). The stall within the vaned diffuser is initiated in the semi-vaneless space at the diffuser inlet.

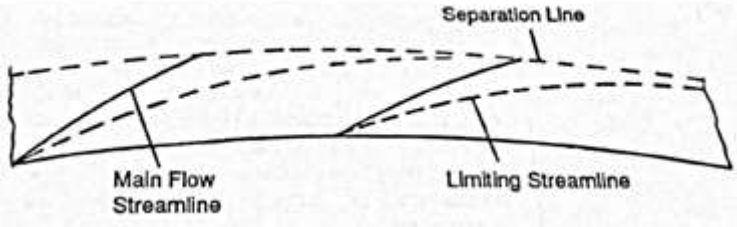

Figure 2.2: Limiting streamlines on the wall of constant area vaneless radial diffuser [17]

[18] Studies focussed on the diffuser were carried out by Japikse. The aim of these studies was to optimise the performance of the centrifugal compressor stage by diverging the diffuser walls. Eight design points from the compressor map were chosen to obtain the performance output of the compressor stage. Various design characteristics have been taken into account to investigate at different pressure ratios. Diffusion process has been noticed at the inlet section of the diffuser passage, which causes pressure drop upstream of the diffuser passage. It has been noticed that an increase in the radial length of the diffuser passage increases the overall performance output of the compressor stage. Furthermore, the studies have also established that the flow within the diffuser passage is strongly affected by the impeller blades. Henceforth, it has been suggested that the blades of the impeller can be modified to match the requirements of the diffuser passage. This matching has been found to assist in the performance output enhancements of the compressor stage.

2.2. One Dimensional Analysis of Diffusers

[19] Aungier has formulated the design of the crossover bend, and the return channel, for a compressor stage to incorporate the computerised interactive design system. The study has been carried out on the techniques used in the aerodynamic performance analysis for general vaneless annular passages and return channels. The study compares the numerical results with the experimental data. Detailed analysis has been carried out to formulate an accurate meanline performance analysis for the computation of loss mechanisms within the vaneless diffuser passages. The governing equations presented in the paper by Aungier [20] are as follows:

$$\frac{2\pi r b C_m K_B}{v} = w \tag{2.1}$$

$$bC_m \frac{d(rC_u)}{dm} = -rc_f C C_u \tag{2.2}$$

$$\frac{vdp}{dm} = \frac{C_u^2 \sin\varphi}{r} - C_m \frac{dC_m}{dm} - \frac{c_f C C_m}{b} - \frac{dI_D}{dm} - I_C \tag{2.3}$$

$$h_t = h + \frac{c^2}{2} \tag{2.4}$$

The left-hand side term, and first three terms on the right-hand side, of the equation (2.3) are conventional for meanline analysis. The last two terms address the loss contributions due to flow diffusion and passage curvature. Flow diffusion losses are modelled by a classical diffuser analogy, which is explained in detail by Reneau et al. [21]. Hence, flow diffusion term in equation (2.3) can be expressed as a second estimate of the diffusion term, as:

$$I_D = 0.65v(P_t - P)\left(1 - \frac{r_m b_m}{rb}\right) \tag{2.5}$$

If the value of I_D exceeds the local value obtained by integrating equation (2.3), it replaces the lower value. The passage curvature term in equation (2.3) can be expressed as:

$$I_C = v(P_t - P)C_m/(13RC) \tag{2.6}$$

Equation (2.6) has been developed empirically from comparisons of predictions against the test data for 35 different vaneless diffusers (or return system combinations). I_C has been found to have negligible effect on the performance of vaneless diffusers, but is always significant, and sometimes dominant, for crossover bends.

The area blockage factor and the skin friction coefficient of a vaneless diffuser are computed using a simple boundary layer growth model, based on a $1/7^{th}$ power law for boundary layer velocity profiles. Boundary layer growth is estimated from the change in angular momentum predicted by integration of the flow governing equations. The boundary layer thickness is used to compute the blockage factor. Moreover, skin friction is computed from an empirical correlation for the friction factor in case of fully developed pipe flows. This includes laminar, transitional and turbulent flows. It also incorporates the surface roughness effects, as described by Schlichting [22]. This approach of quantifying the amount of blockage is used for vaneless diffuser passages, crossover bends and other vaneless annular passages. The radial vaneless diffuser passage is modelled with a constant width parallel wall style, with a width adjustment in the first 15-20% of the passage to blend it to the impeller tip width. During the design process, a second-order polynomial variation of width is used at the entrance to match the two specified widths and the zero-gradient condition at the blend radius. However, it is believed that the use of a radial hub wall, with all width adjustments imposed on the shroud wall, needs to be applied in order to obtain more effective impeller-tip velocity profiles, which often tend

to deteriorate towards the shroud wall. It is thus concluded from the verification of the results and analysis carried out that the optimisation of vaneless diffuser design normally leads to diffuser-outlet flow angles in the range of 30˚ to 35˚, where component loss coefficients tend to reduce to minimum and a stable operating range is obtained.

2.3. Flow Investigations within Modified Straight Wall Diffusers

Many researchers have tried to improve the performance of the compressor stage by modifying the diffuser geometry. [23] Japikse and Goebel have carried out experimental studies to develop techniques in order to estimate the flow behaviour within the compressor stage, focusing on the diffuser passage. The primary aim of the study was to identify the various errors in the recorded measurements, and to use better calibrating techniques to fix them. It has been found that most of these errors occur when the tip clearance is not controlled. Further errors were generated by the inappropriate techniques used to quantify the flow fields within the diffuser passage. The reason behind most of these measurement errors was due to the fact that when the flow enters a straight diffuser, it follows the hub wall of the passage (due to the shape of the diffuser). Recirculation appears near the shroud wall of the diffuser passage. This flow behaviour reverses midway the diffuser passage. Traverses were found to be invaluable in deducing the flow field structure. Therefore, the requirement of back-to-back testing of the diffuser flow field traverses within the compressor stage becomes essential.

[24] Adachi and Otsuki have carried out experiments to improve the performance of the vaneless diffuser passage of a compressor stage. This study focused on the optimisation methods for annular vaneless diffusers for improving the overall compressor stage performance. The aim of this investigation was to improve both the surge margin and isentropic efficiency at high flow rates. This has been carried out by pinching the shroud wall of the diffuser passage, and adding a tapered passage at the vaneless diffuser outlet. Four different types of vaneless diffuser passages have been considered in this experimental study. Pinching and tapering to the shroud wall has been applied to all four different types of diffuser passages. The measurements of the flow characteristics within the compressor stage have been recorded using total pressure probes along the width of the diffuser passage. The results show that reducing the diffuser outlet width (by tapering the passage) increases the surge margin. However, if the outlet section of the diffuser passage becomes too small, the mass flow rate increases, which decreases the isentropic efficiency.

[25] Lee et al. invented new diffuser geometry to improve the performance of the compressor stage. The shroud wall of the diffuser passage is converged. This approach increases the stage isentropic efficiency by 3%. [26] Turunen-Saaresti et al. conducted experimental and numerical investigations on the vaneless diffuser of a centrifugal compressor, consisting of an unshrouded impeller and volute. Six different configurations of diffuser, with various pinch height and location, have been numerically investigated. Among these six numerical models, two further models have been verified against the experimental data. Compressor stage performance has been analysed, for each diffuser configuration, for the overall efficiency, circumferential static and total pressure and span wise total pressure distribution (before and after the diffuser). The numerical models show reasonable capability in predicting the pressure ratio, however, it over-predicts the isentropic efficiency. Both experimental and numerical results show that the pinched diffuser increases the compressor efficiency. Furthermore, the pinch on the shroud wall depicts higher efficiency as compared to the pinch on the hub wall. Pinching both the walls together show optimal compressor and diffuser performance.

[27] Jaatinen et al. studied the effect of the diffuser width variations on the performance of the compressor and the diffuser. The performance of the compressor, in terms of efficiency and total-to-total pressure ratio, has been calculated for six different diffuser configurations, having varying width. For the first three configurations, the width has been reduced from the shroud wall, while for the other three configurations; the width had been reduced from both hub and the shroud walls. Measurements show that reducing the width improves the efficiency of the compressor over a wide operating range. The pressure ratio tends to increase at low operating range; however, it decreases at high rotating speed. It has been found that pinching the shroud wall yields higher efficiency, by reducing the tip clearance flow losses. It is further concluded from this investigation that the shroud pinch should be greater than the tip clearance for narrow diffusers.

[28] Mohtar et al. conducted a series of experimental investigations aiming to study the effect of the MWE design on the compressor performance and surge extension. Different configurations of the turbocharger compressor stage have been considered in these investigations. One of the approaches used in this study is pinching the shroud wall of the diffuser, while the other approach increases the diffuser area. The total-to-total compressor stage efficiency, and surge margin, have investigated in both the cases. Results show that at low rotational speeds, the pinch on the shroud wall increase the surge margin, but at high

rotational speeds, the pinch has less effect on the surge margin. The stage efficiency has been found to decrease as the mass flow rate increases. At higher mass flow rates, the flow velocity within the diffuser increases, which leads to higher fiction loss and results in lower efficiency. Furthermore, at low mass flow rates, the efficiency decreases due to flow recirculation, which increases the inlet temperature. The second approach however show increase in the surge margin. Hence, the increased diffuser area helps in enhancing the volute diffusion by reducing the radial velocity, improving the compression ability of the diffuser.

[29] Robinson et al. conducted numerical investigations on a single stage centrifugal compressor having a vaned diffuser. In this investigation, the impeller-diffuser spacing was reduced from 15% to 7% of the impeller tip radius. The overall efficiency, pressure fluctuation in the impeller, blade surface pressure at the impeller exit, and the pressure recovery (C_p) have been quantified using the transient approach. The results of the reduced diffuser area model have been compared against the baseline model. According to the findings, the compressor with reduced diffuser width improves the stage efficiency by 1%.

[30] Jaatinen et al. conducted experimental investigations on three vaneless diffusers with different width, along with four different tip clearances. The overall stage performance and the flow field within the diffuser have been investigated by analysing the radial velocity and flow angle for each case. The results show that a moderate pinch enhances the compressor overall efficiency, reducing the losses in the diffuser. However, excessive pinch has negative effects on the efficiency due to the flow separation. The flow separation is caused by the flow acceleration and the increased opening angle of the diffuser. Moreover, reducing the diffuser area increases the flow velocity, reducing the boundary layer thickness, which in-turn reduces the boundary layer losses. A 2% increase in the efficiency has been recorded at the design point, and approximately 3% efficiency increase is recorded at higher mass flow rates.

[31] Sheng et al. studied the effects of unparalleled diffuser walls on the generation of rotating wave in a centrifugal compressor. Five diffuser configurations (convergent, convergent and divergent, and tapered shroud wall) have been investigated and compared against a parallel wall diffuser (i.e. baseline model). The critical inlet flow angle and the rotating wave speed have been analysed at various diffuser inlet Mach numbers and diffuser outlet-to-inlet radius ratios. The tapered shroud wall contraction increases the suppression effect on the rotating stall in the diffuser. The suppression effect has been found to be dependent on various parameters, such as diffuser inlet Mach number, diffuser width-to-inlet ratio, diffuser inlet-to-outlet ratio

and contraction shape. It has been noticed that the unparalleled wall diffuser maintains the flow stability at high Mach numbers. Moreover, while the convergent and divergent wall diffusers provide higher stability at low inlet Mach numbers, the convergent wall configuration seems to provide stability at higher Mach numbers. The Bezier curved shroud wall improves the diffuser stability, and its effects depend on the inlet Mach number.

[32] Schiff developed a computer program to design a radial compressor, and analyse the flow field within the impeller and the diffuser. The author has considered one impeller configuration, three vaneless diffuser configurations, and a vaned diffuser configuration to analyse the performance of the compressor stage. The velocity profile has been analysed along the diffuser. It has been noticed that the converging diffuser model yields improved diffuser stability and higher efficiency.

[33] Jaatinen et al. carried out numerical investigations on a centrifugal compressor with vaneless diffuser to investigate the effect of variation of diffuser width on the compressor performance. Seven vaneless diffusers have been investigated, with diffuser width ratio of 0.5 to 1.0 entropy change in the impeller, and the velocity profile, have been analysed to predict the compressor stage performance. The results show that for the given compressor stage, a moderate pinch on the shroud wall (ranging b/b_2= 0.85–0.91) is beneficial. The pinch reduces the tip clearance flow losses, making the flow uniform, and hence reducing the entropy and enhancing the performance. However, excessive pinching increases the velocity, making the flow field unstable. This causes flow separation near the shroud wall, which increase the entropy. The amount of flow separation depends on the shape of the pinch and the way it is implemented.

[6] Achilleos performed numerical investigations on a centrifugal compressor to optimise the diffuser geometry for optimal compressor stage performance. The shroud of the diffuser wall has been diverged at the diffuser outlet. Various configurations have been analysed by changing the divergence angle and its location. The results show that a diverged shroud wall causes an increase in the diffuser outlet width, which improves the stage efficiency, and total-to-total pressure ratio, at low mass flow rates. However, at higher mass flow rates, both efficiency and pressure ratio decreases.

[7] Shaaban conducted numerical investigations aiming to improve the performance of a radial compressor by reducing the diffuser loss coefficient, and increasing the pressure coefficient.

The author has proposed two diffuser models with convergent and divergent shroud walls. The 3D numerical simulations show that the optimised model enhances the compressor performance by reducing the loss coefficient (by 4.7%). This increases the pressure coefficient by 6.6% under wake and swirl flow conditions.

2.4. Flow Investigations within Modified Tilted and Curved Wall Diffusers

[8] Sweetland et al. invented an S-shaped diffuser that improves the performance of the compressor stage of a turbocharger. The main purpose of this study was to improve the diffusion in a turbocharger for higher air delivery rates to the internal combustion engines. The author has considered ten different diffuser models. The study also evaluates the interaction of impeller flow domain with the diffuser geometries by modifying the diffuser walls. Figure 2.3 depicts the diffuser models considered. The first model (shown in figure 2.3(a)) is considered as the baseline parallel wall diffuser model. The diffuser is then tilted at an angle α, which allows the flow to cover more radial distance without the need to increase the geometric envelope. The increased length of the diffuser yields higher diffusion, which increases the isentropic compression efficiency. Furthermore, in order to decrease friction by the straight walls, the diffuser is further modified using curved walls. This modification to the diffuser walls has shown to reduce the losses.

The author has considered three more models, as depicted in figure 2.3(d), (e) and (f). In these models, the diffuser outlet is farther away from the turbine stage of the turbocharger, which means that these are occupying more space in comparison to the previous tilted configurations. These models have been designed in order to have low momentum flow from the compressor impeller. This results in lower radial velocities, and hence, lower flow along the bend, providing stability to the fluid flow.

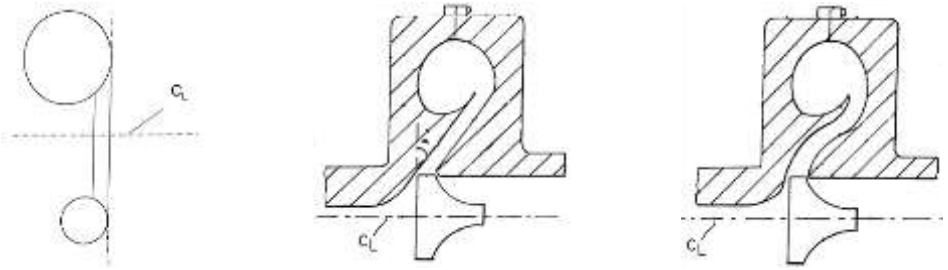

(a) (b) (c)

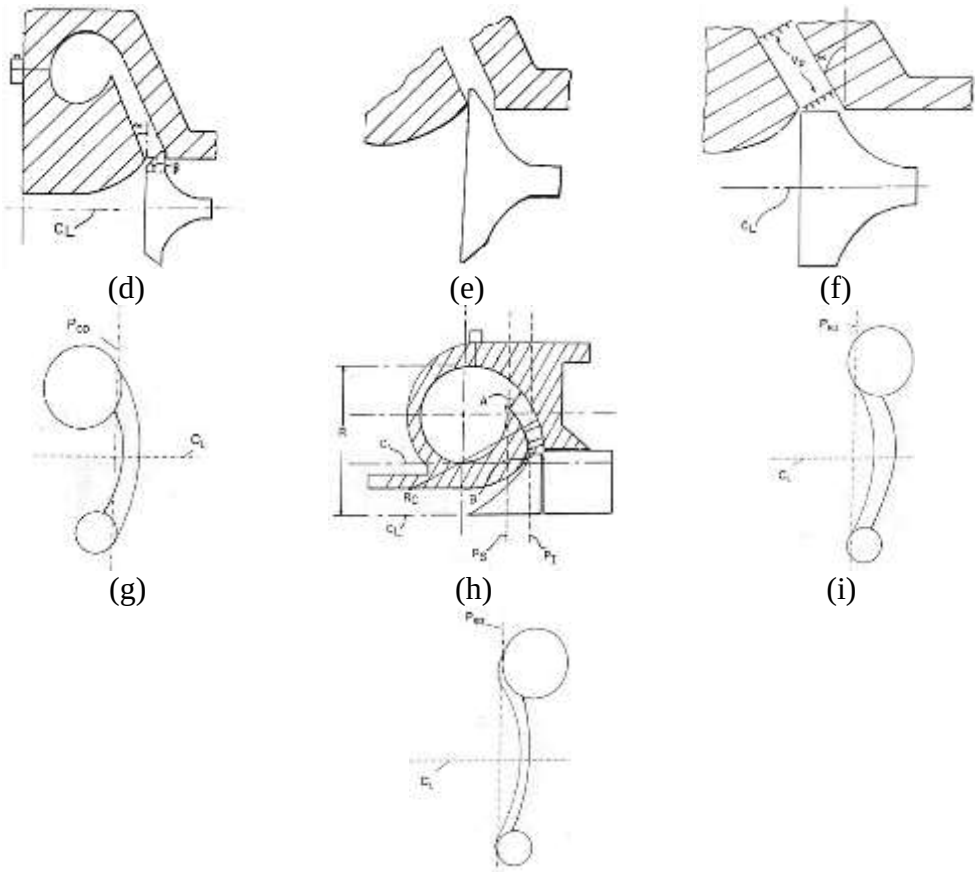

Figure 2.3: Diffuser Models [8]

It has been found that from the Sweetland et al. study that the S-shaped diffuser yields higher isentropic compression efficiency as compared to the other models. The author has investigated this particular model at different design conditions and found that the efficiency increases consistently. On the other hand, this model maintains the pressure ratio. However, the off-design margins of the compressor map have been reduced, which will result in early stall and surge conditions.

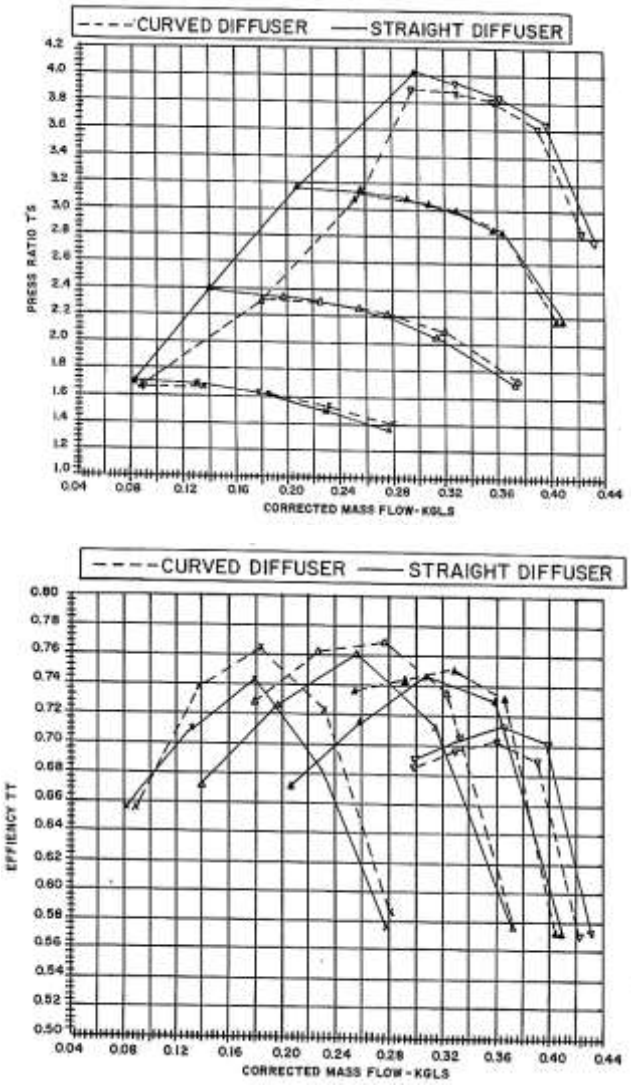

Figure 2.4: Compressor map for parallel and S-shaped diffusers (a) Pressure ratio (b) Efficiency [8]

[34] Anna et al. has carried out research on optimisation of aeration tank design and operation using computational fluid dynamics as a tool. The aeration tank consists of diffuser, which helps in dispersing the airflow. Two optimisation scenarios based on the modification of either operating parameters or diffuser density were evaluated taking into consideration mixing and oxygen mass transfer in the tank. Increase of diffuser density results in moderate oxygenation rates. Therefore, CFD tool has been used to analyse the mixing of fluid and local mixing regions has been captured.

2.5. Summary

The literature review presented focuses on the optimized diffuser designs developed by various researchers, by modifying the walls of parallel wall diffusers. It has been found that the stage performance enhances by modifying the diffuser wall geometry. However, the amount of

increase in the stage performance is dependent on the shape of the modified wall, and the way it is has been modified. It has been noticed that pinching both the diffuser walls increases the stage performance, by reducing the tip clearance losses. Similarly, a converged diffuser reduces the flow separation, which in-turn reduces the boundary layer losses. Furthermore, diffuser wall divergence increases the cross-sectional area of the diffuser, which increases the stage efficiency and pressure ratio.

The literature also has focused on the tilted and curved diffuser models for higher stage efficiencies and compact designs. Based on the literature review presented, it can be summarized that very limited research has been carried out on the tilted and curved wall diffusers. The author, to the best of his knowledge, is not aware of any published study that focuses on the application of diffuser wall divergence on tilted and curved wall diffusers. It is expected that this combination will help in higher diffusion and stage efficiency.

2.6. Research Aims

The specific research aims formulated for this research study are described in this section, whereas the detailed objectives are discussed after carrying out the literature review in the next chapter. The research aims of the current study are to:

1. An improved understanding of the flow behaviour within diverged wall vaneless diffusers.
2. Development of novel diffuser configurations having tilted and diverged walls.
3. Development of novel diffuser configurations having curved and diverged walls.

These aims cover a wide range of operation of the turbocharger compressor stage, and hence, are considered satisfactory for this study. Detailed literature review is presented in the next chapter, focusing on the aforementioned research aims, in order to fill any gaps in the existing literature.

2.7. Research Objectives

Based on the literature review and the research aims, following research objectives have been identified:

- To determine the effect of diffuser wall on the flow variations within the diffuser and on the compressor stage performance.
- To determine the effect of diffuser wall divergence on the flow variations within the diffuser and on the compressor stage performance.
- To formulate the effect of tilted diffuser wall on the flow variations within the diffuser and on the compressor stage performance.
- To formulate the effect of tilted diffuser wall divergence on the flow variations within the diffuser and on the compressor stage performance.
- To analyse the effect of curved diffuser wall on the flow variations within the diffuser and on the compressor stage performance.
- To analyse the effect of curved diffuser wall divergence on the flow variations within the diffuser and on the compressor stage performance.
- Development of semi-empirical relations for the isentropic efficiency and the geometrical configurations.
- Development of a compact diffuser used within the compressor stage based on the isentropic efficiency to volume ratio.

The next chapter presents the details of the numerical solver used in the present study in order to achieve the above objectives.

CHAPTER 3
NUMERICAL MODELLING APPLIED TO THE TURBOCHARGER COMPRESSOR STAGE

This chapter presents the advanced Computational Fluid Dynamics (CFD) based techniques necessary to carry out the investigations based on the research objectives of this study outlined in the previous chapter. CFD based techniques are used in the present study to numerically simulate the steady flow of air within the turbocharger compressor stage. The use of CFD enables to predict the flow phenomenon occurring within the turbocharger compressor stage, with a certain degree of numerical errors. The appropriate solver settings and the boundary conditions are discussed in this chapter.

3.1. Geometric Modelling of the Turbocharger Compressor Stage

A three-dimensional turbocharger compressor stage has been numerically created, as shown in the figure 3.1. The turbocharger compressor stage comprises of an inlet duct, MWE, impeller, vaneless diffuser, an overhung volute and a discharge duct. The impeller of the turbocharger compressor stage consists of seven full and seven splitters backward swept blades.

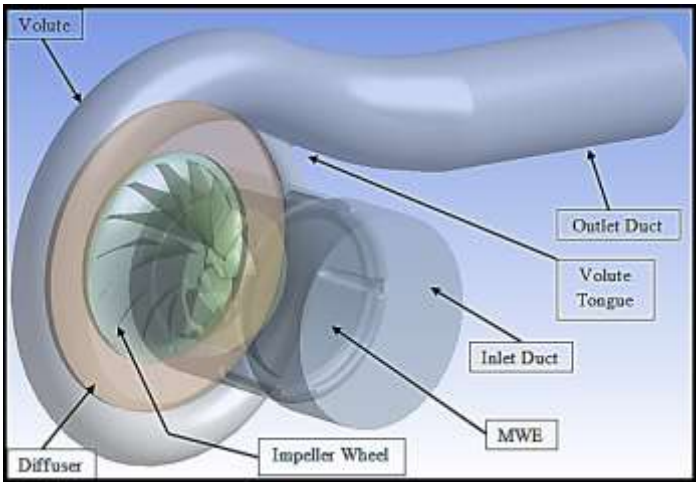

Figure 3.1: Geometry of the turbocharger compressor stage

In order to maintain fully developed flow conditions, a pipe section has been attached to the inlet duct. The entrance length is the distance, from the inlet, where the change in the wall shear stress reaches within about 2%. The entrance length is much shorter in turbulent flows and its dependence on the Reynolds number is weak. [35] In many practical engineering applications, the entrance effects become insignificant beyond a pipe length of 10 diameters. The same has been considered in the present study as well.

3.2. Mesh Generation within the Turbocharger Compressor Stage

A mesh can be characterised into sub groups, i.e. structured and unstructured. [36] Graham Cox has applied the structured and the unstructured meshes in the gas path of turbomachines. The results show that the structured mesh supports high aspect ratio elements, whereas the unstructured mesh results in unsatisfactory elements due to small skew angles. Therefore, a larger number of elements are required to achieve similar results to the structured meshing. The drawback of structural meshing is that it is very time consuming. [37] Graham Cox et al. have performed numerical analysis on the flow around the scallops of mixed flow turbines, and their effects on the stage efficiency. A hybrid mesh has been used within the turbine stage; structured mesh around the vanes within the rotor and unstructured mesh around the scroll and the back-face region. Mesh inflation layers have been

employed, in unstructured mesh region, near the walls to obtain sufficiently accurate near-wall solutions. It has been concluded that the structured mesh within the turbomachinery gas-path components gives computational efficiency and accuracy in predicted results. An, unstructured mesh can predict almost similar results but for that, more number of elements need to be specified within the flow domain. [38] Sbardella et al. have carried out numerical analysis on turbomachines, analysing the effects of semi-structured meshes on the numerical solutions. Structured mesh has been specified in the radial direction of the blades, while unstructured mesh has been specified in axial and tangential directions of the blades. Results have shown that the unstructured mesh solutions are smoother in comparison to the structured mesh. Furthermore, the convergence of corrected mass flow rate has high fluctuations for structured mesh. However, the solution has converged faster in case of semi-structured mesh. It has been concluded that unstructured mesh in the axial and tangential directions offers more flexibility than standard structured meshes, both in terms of skewness and smoothness. The solution obtained using semi-unstructured mesh seems to be superior to the structured mesh in terms of convergence rate.

Based on the literature, hybrid mesh has been employed within the compressor stage, in the present study. The structured mesh has been specified in the near-wall region and around the impeller blades. An unstructured mesh has been generated in the remaining flow domain. ICEM software has been used to generate the hybrid mesh within the compressor stage components for flow discretization. A mesh smoothing procedure has been used for each of the mapped radial layers, to minimize grid skewness. [39] The smoothing procedure includes the movement of the points around the leading and the trailing edges to preserve high resolution mesh on the blade curvatures. The steps to generate the hybrid mesh are described in the figure 3.2. The volume mesh within the flow domain has been created, followed by the hexahedral mesh near the walls. The mesh quality has been checked after the generation of the mesh.

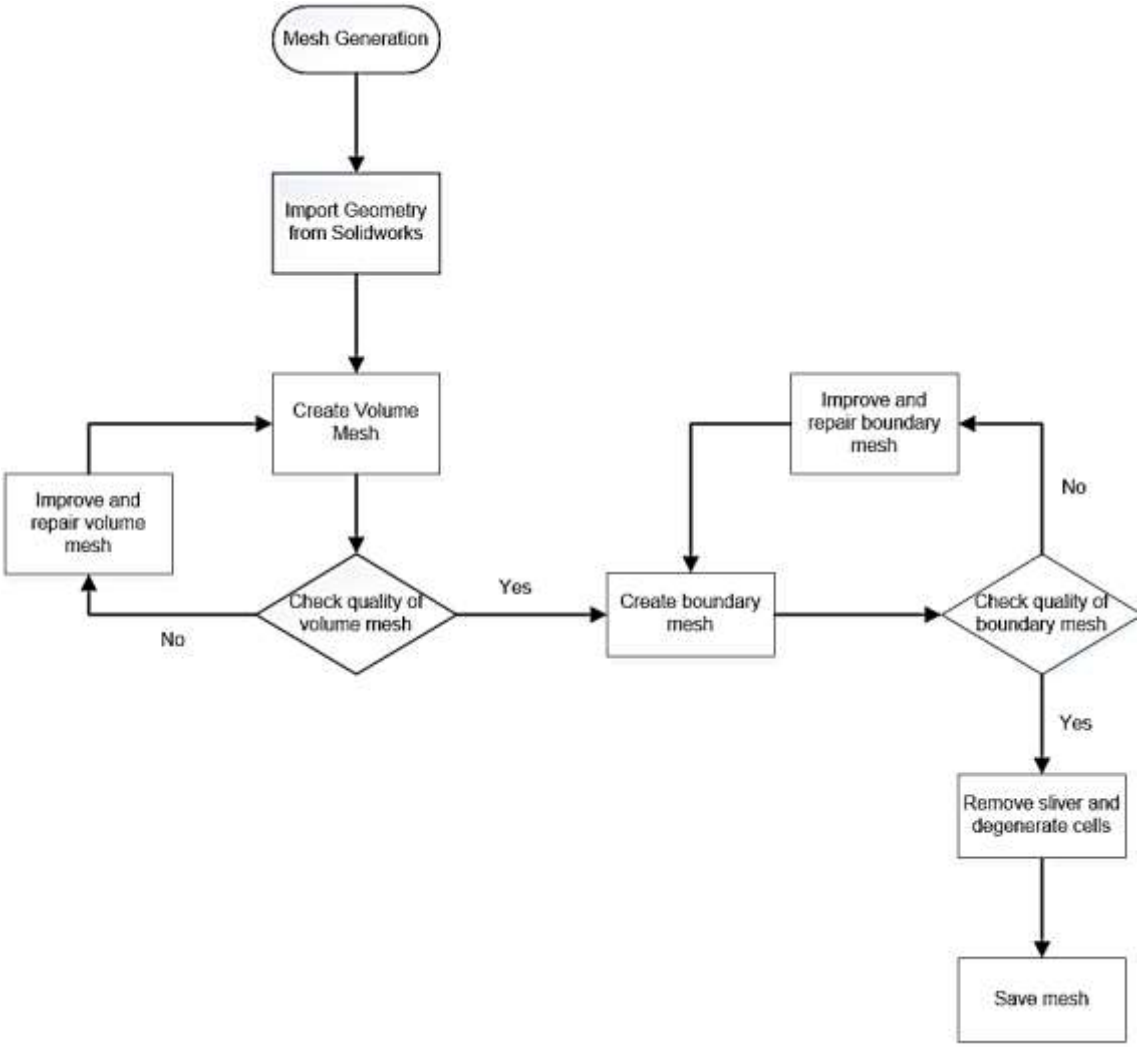

Figure 3.2: Flow chart describing the generic steps to generate the hybrid meshes in ICEM software [40]

Tetrahedral elements have been used within the compressor stage. A large number of elements have been specified on the interfaces, and the MWE slots, to obtain accurate flow predictions at the surge and choke conditions. Furthermore, more than five elements have been specified within the tip-gap of the impeller to accurately predict the effect of tip leakage losses [41].

Table 3.1 provides the details of the number of elements in each component of the turbocharger compressor stage. The specified mesh has been selected based on the mesh sensitivity testing, which has been discussed in the post processing section, later in this chapter. The flow near the walls has been captured by implementing inflation layers near the wall of the compressor stage components.

Table 3.1: Details of the Mesh Elements in each component of turbocharger compressor stage

Zones	Number of Mesh Elements
Inlet pipe	1,243,802
MWE slots and inducer	1,720,995
Impeller wheel	5,050,245
Diffuser	871,280
Volute	1,768,749
Full Compressor Stage (Total)	10,655,071 (10.6 Million)

[22] In the turbulent flow conditions, the velocity profile can be split into three distinguished regions, i.e. the viscous sublayer, the buffer layer and the inertial sublayer (log-law region). The design models where the wall bounded effects (adverse pressure gradients, pressure drop, heat transfer etc.) are dominant, full resolution of the boundary layer is required. Therefore, inflation mesh layers have been specified at the near-wall regions of the compressor stage components. [39] According to the law of the wall, y^+ is a non-dimensional parameter which is a function of first grid cell height (Δy), friction velocity (u_t), density (ρ) and the dynamic viscosity (μ). This parameter can be used to generate mesh within the boundary layer accurately. y^+ can be expressed as:

$$y^+ = \frac{\Delta y \cdot \rho \cdot u_t}{\mu} \qquad 3.3$$

Table 3.2 shows the different set of data for y^+ values and the corresponding cell numbers, at a growth rate of 1.45. It has been identified that at y^+ = 1.5, with a growth rate of 1.45, adequate number of layers can be specified to model the boundary layer. Hence, 10 layers of mesh have been considered in the present study.

Table 3.2: Specification of y^+ value at a cell growth rate of 1.45

Target y^+ values / Cells Number	1.0	1.5	2.0	2.5	3.0	3.5	4.0	4.5	5.0
1	1.0	1.5	2.0	2.5	3.0	3.5	4.0	4.5	5.0
2	1.5	2.2	2.9	3.6	4.4	5.1	5.8	6.5	7.3
3	2.1	3.2	4.2	5.3	6.3	7.4	8.4	9.5	10.5
4	3.0	4.6	6.1	7.6	9.1	10.7	12.2	13.7	15.2
5	4.4	6.6	8.8	11.1	13.3	15.5	17.7	19.9	22.1
6	6.4	9.6	12.8	16.0	19.2	22.4	25.6	28.8	32.0
7	9.3	13.9	18.6	23.2	27.9	32.5	37.2	41.8	46.5
8	13.5	20.2	27.0	33.7	40.4	47.2	53.9	60.6	67.4
9	19.5	29.3	39.1	48.9	58.6	68.4	78.2	87.9	97.7
10	28.3	42.5	56.7	70.8	85.0	99.2	113.3	127.5	141.7

Viscous sublayer

Buffer layer

Inertial sublayer

3.2.1. Grid Sensitivity Tests

Grid sensitivity study has been carried out to ascertain that the numerical predictions are independent of mesh size used. This has been carried out by systematically increasing the number of elements used within the compressor stage, and monitoring the stage efficiency. A list of cases used to investigate the mesh independency effects are presented in table 3.3.

Table 3.3: Grid sensitivity testing for the turbocharger compressor stage

Number of Cells	Efficiency (T-T)	Ratio of Efficiency (T-T) to Design Efficiency
Millions	(%)	(-)
4.6	63.9	0.89
5.6	69.7	0.97
6.6	70.4	0.98
8.6	66.0	0.92
10.6	70.9	1.00
12.6	70.8	1.00

These results show that the flow parameters are independent of mesh density after 10.6 million elements, and hence, 10.6 million mesh elements are used to carry out further analysis in the present study.

3.3. Solver Execution

Ansys CFX has been used to numerically simulate the flow of air within the compressor stage by iteratively solving the flow governing equations of mass, momentum and energy (as discussed in the appendices). Ideal gas equation for the flow of air within the compressor stage has been used to analyse the compressibility effects. A steady state solver has been employed, along with the appropriate boundary conditions and the interface models, discussed in the following sections.

3.3.1. Material Properties and Boundary Conditions

In the present study, the fluid medium within the centrifugal compressor stage is compressible. The boundary types, and their corresponding values, have been summarised in table 3.4. The inlet pressure remains constant at 1atm throughout this study, mimicking the normal atmospheric pressure. A total temperature of 288K is specified at the inlet air the is assumed to be entering the compressor stage at

room temperature. Furthermore, the walls of the flow domain have been modelled as no-slip boundaries (as observed in real world conditions).

Table 3.4: Boundary conditions applied to the turbocharger compressor stage

Boundary Name	Domain / Boundary Type	Boundary Condition
Inlet	Pressure Inlet	1 atm
	Temperature Inlet	288 K
	Operating (Reference) Pressure	0 atm
Outlet	Pressure Outlet	Variable
Impeller	Rotating	No-Slip
MWE	Stationary	No-Slip
Diffuser	Stationary	No-Slip
Volute	Stationary	No-Slip

Table 3.5 summarises the outlet boundary conditions at different design points of the compressor map.

Table 3.5: Outlet boundary conditions

Rotating Speed $rpsK^{-1/2}$	Pressure Ratio (T-T) -
58.9	1.31
58.9	1.51
58.9	1.55
58.9	1.60
78.6	1.57
78.6	2.00
78.6	2.10
78.6	2.16

Interfaces have been specified between the boundaries of the two domains that separates the rotating components from the non-rotating components of the compressor stage. A detailed discussion of the types and specification of interfaces is presented in the next section.

3.3.2. Interface Modelling

Grid General Interface (GGI) has been used to join the two domains by connecting meshes. This mesh can be conformal or non-conformal. Different types of interface models have been used to connect the components of the compressor stage for the numerical analysis. [42] Z Liu has carried out research on the appropriate selection of interface in Multiple Reference Frame (MRF). The results show that

both stage/mixing plane or frozen rotor interfaces can be used at the inlet of the impeller eye, if no Inlet Guide Vanes (IGVs) are present in the inlet duct. If IGVs are used, then only stage/mixing plane has to be specified. Furthermore, the results also show that stage/mixing plane has to be used at the interface between the impeller outlet and the vaned diffuser inlet. It is because stage/mixing plane computes the average flow parameters over the circumference of the upstream domain, and passes it to the next domain. Therefore, the effects of jets and wakes from the impeller blades cannot be obtained. On the other hand, in case of the interface between the impeller outlet and the vaneless diffuser inlet, both stage/mixing plane or frozen rotor approaches are applicable. Frozen rotor interface modelling computes the flow variable values at each node and passes it on to the next domain. Hence, the effects of jets and wakes from the trailing edges of the impeller blades are well pronounced. However, it over-predicts the performance parameters of the compressor stage. Therefore, an investigation has been carried out in the present study on this, which is discussed later in this section. A general connection interface has been specified between the inlet pipe and the MWE duct. The inducer is connected with the impeller eye via frozen rotor approach. Similarly, another frozen rotor interface model is used to connect the MWE slots to the impeller throat region from the shroud, as no IGV's are present in the compressor stage. The specification of the interface between the impeller outlet and the vaneless diffuser inlet, and between vaneless diffuser outlet and the scroll inlet, has been investigated to obtain the best approach applicable, resulting in realistic numerical predictions.

Two different types of approaches namely frozen rotor and stage/mixing plane interface models, have been implemented on the interface between the impeller outlet and the vaneless diffuser inlet. The analysis has been carried out at Best Efficiency Point (BEP) at a rotational speed of 58.9rpsK$^{-1/2}$. The total-to-total pressure change data is shown in table 3.6. Furthermore, two different types of interface models i.e. stage/mixing plane and general connection; have been specified between vaneless diffuser outlet and the scroll inlet, in order to identify the best model. The data for this is also presented in the table 3.6.

It can be seen that the frozen rotor approach between the impeller and the diffuser shows 1.31% difference in total-to-total pressure ratio, which is lower than for stage/mixing plane interface (3.05% difference). On the other hand, frozen rotor approach over-predicts the total-to-total isentropic efficiency by 11.87%, while the stage/mixing plane shows 3.93% difference. Moreover, interface modelling between the diffuser and the volute shows 2.67% difference in total-to-total pressure ratio

using the stage/mixing plane interface. However, general connection interface shows 0.46% difference. The stage interface shows 9.5% difference in the total-to-total isentropic efficiency, while general connection interface shows 2.18% difference. Based on these results, stage/mixing plane interface has been selected as the interface between the impeller outlet and the vaneless diffuser inlet, while general connection interface has been selected as the interface between the vaneless diffuser outlet and the scroll inlet.

Table 3.6: Specification of Interface type and its effect on global flow and performance parameter

Interfaces	Interface Models	Total-to-total pressure ratio (-)	Total-to-total isentropic efficiency (-)	Percentage difference in total-to-total pressure ratio (%)	Percentage difference in total-to-total isentropic efficiency (%)
Experimental	-	1.551	74.747	-	-
Impeller and diffuser	Frozen Rotor	1.572	65.872	1.31	11.87
	Stage/Mixing plane	1.600	71.809	3.05	3.93
Diffuser and Scroll	Stage	1.593	67.646	2.67	9.50
	General Connection	1.544	73.120	0.46	2.18

3.3.4. Turbulence Modelling

The theory regarding different turbulence models has been included in the appendices. However, the most appropriate turbulence model for centrifugal compressors has been identified by various researchers as the k-ω SST (Shear Stress Transport) model. [43] Jaatinen has carried out research on the performance improvement of the centrifugal stage with pinched geometry vaned diffuser. Two different turbulence models i.e. Chien's k-ε and k-ω SST models, have been used to investigate the flow characteristics locally within the diffuser passage of the compressor stage. It has been observed that the k-ω SST turbulence model predicts the performance and the flow field across the impeller and diffuser passages with higher accuracy as compared to the standard k-ε model. Hence, k-ω SST turbulence model has been used in the study for the flow field analysis within the centrifugal compressor stage.

3.4. Convergence Criteria

Getting to a converged solution is necessary in numerical simulations. A converged solution indicates that the solution has reached a stable state and the variations in the flow parameters, w.r.t. the iterative

process of the solver, have died out. [44] Hence, only a converged solution can be treated as the one which predicts the solution of the flow problem with reasonable accuracy.

The default convergence criterion for the continuity equation, velocities in three dimensions and the turbulence parameters is 0.001. This means that when the change in the continuity equation, velocities and turbulence parameters drops below the fifth place after the decimal, the solution is treated as a converged solution. However, in many practical applications, the default criterion does not necessarily indicate that the changes in the solution parameters have died out. Hence, it is advisable to monitor the convergence rather than relying on the default convergence criteria.

In the present study, the total-to-total pressure ratio (outlet-to-inlet) and the mass flow rate (at both the outlet and the inlet) have been monitored across the iterative process. The solution has been considered converged once the total-to-total pressure ratio and the mass flow rate have become stable/constant.

3.5. Scope of the Numerical Investigations

There are a large number of geometrical and flow related variables associated with the flow within the diffuser passage of the centrifugal compressor stage. A list of numerical simulations, for each chapter, is shown in tables 3.7 to 3.11. Table 3.7 lists the initial number of simulation required to carry out the verification of the numerical results against the experimental data. Table 3.8 summarises the configurations obtained by considering the wall divergence location and outlet-to-inlet width ratio. This work has been carried out in chapter 4. Table 3.9 summarises the configurations obtained by considering the wall divergence location, outlet-to-inlet width ratio and tilting of the diffuser passage. This work has been carried out in chapter 5. Table 3.10 lists the configurations obtained by considering the diffuser wall curvature. Furthermore, table 3.11 summarises the configurations obtained by diverging the wall of curved diffuser geometry. This work has been carried out in chapter 6.

Table 3.7: Models for verification of CFD results

Rotating Speed	Corrected Mass Flow Rate	Pressure Ratio (T-T)	Diffuser outlet-to-inlet width ratio, b_2/b_1
$rpsK^{-1/2}$	$kgK^{1/2}s^{-1}MPa^{-1}$	-	-
58.9	-	1.31	1.0
	-	1.51	1.0
	24.67	-	1.0
	11.64	-	1.0
78.6	-	1.57	1.0
	-	2.00	1.0
	37.59	-	1.0
	20.85	-	1.0

Table 3.8: Models for diverged wall vaneless diffuser passage analysis

Parameters	Pinch distance from the inlet of the diffuser, L/L_{max}	Diffuser outlet-to-inlet width ratio, b_2/b_1
Row No.	(-)	(-)
1	0.0	1.1
2		1.2
3		1.3
4		1.4
5	0.1	1.1
6		1.2
7		1.3
8		1.4
9	0.2	1.1
10		1.2
11		1.3
12		1.4
13	0.3	1.1
14		1.2

15		1.3
16		1.4
17	0.4	1.1
18		1.2
19		1.3
20		1.4
21	0.5	1.1
22		1.2
23		1.3
24		1.4

Table 3.9: Models for diverged tilted wall vaneless diffuser passage analysis

Parameters	Diffuser outlet-to-inlet width ratio, b_2/b_1	Diffuser passage angle from axil direction, θ/θ_{max}	Pinch distance from the inlet of the diffuser, L/L_{max}
Row No.	(-)	(-)	(-)
1	1.08	0.00	0.0
2		0.25	0.2
3		0.50	0.4
4		0.75	0.6
5		1.00	0.8
6	1.15	0.00	0.2
7		0.25	0.4
8		0.50	0.6
9		0.75	0.8
10		1.00	0.0
11	1.23	0.00	0.4
12		0.25	0.6
13		0.50	0.8
14		0.75	0.0
15		1.00	0.2
16	1.31	0.00	0.6
17		0.25	0.8
18		0.50	0.0
19		0.75	0.2
20		1.00	0.4
21	1.38	0.00	0.8
22		0.25	0.0
23		0.50	0.2
24		0.75	0.4
25		1.00	0.6

Table 3.10: Models for curved vaneless diffuser passage analysis

Parameters	Ratio of axial distance from inlet-to-outlet to diffuser inlet width, x/b_1	Ratio of angle of curvature to the maximum angle of curvature, θ/θ_{max}	Ratio of Radius of curvature to maximum radius, r/r_{max}
Row No.	(-)	(-)	(-)
1	1.71	0.0	0.6
2			0.7
3			0.8
4			0.9
5			1
6		0.5	0.6
7			0.7
8			0.8
9			0.9
10			1
11		1.0	0.6
12			0.7
13			0.8
14			0.9
15			1
16	2.37	0	0.6
17			0.7
18			0.8
19			0.9
20			1
21		0.5	0.6
22			0.7
23			0.8
24			0.9
25			1
26		1	0.6
27			0.7
28			0.8

29			0.9
30			1
31	3.03	0	0.6
32			0.7
33			0.8
34			0.9
35			1
36		0.5	0.6
37			0.7
38			0.8
39			0.9
40			1
41		1	0.6
42			0.7
43			0.8
44			0.9
45			1
46	3.69	0	0.6
47			0.7
48			0.8
49			0.9
50			1
51		0.5	0.6
52			0.7
53			0.8
54			0.9
55			1
56		1	0.6
57			0.7
58			0.8
59			0.9
60			1
61	4.35	0	0.6
62			0.7

63			0.8
64			0.9
65			1
66			0.6
67			0.7
68		0.5	0.8
69			0.9
70			1
71			0.6
72			0.7
73		1	0.8
74			0.9
75			1

Table 3.11: Models for diverged curved vaneless diffuser passage analysis

Parameters	Pinch distance from the inlet of the diffuser, L/L_{max}	Diffuser outlet-to-inlet width ratio, b_2/b_1
Row No.	(-)	(-)
1	0.0	1.1
2		1.2
3		1.3
4		1.4
5	0.1	1.1
6		1.2
7		1.3
8		1.4
9	0.2	1.1
10		1.2
11		1.3
12		1.4
13	0.3	1.1
14		1.2
15		1.3
16		1.4
17	0.4	1.1
18		1.2
19		1.3
20		1.4
21	0.5	1.1
22		1.2
23		1.3
24		1.4

3.6. Summary

Advanced numerical methods have been used to carry out the analysis. This chapter has explained the numerical model of turbocharger compressor stage. Hybrid mesh has been incorporated for the full compressor stage model that helps to solve the sophisticated numerical equations iteratively. 10.6million grid cells have been incorporated, which has been verified by grid sensitivity testing. Stage interface modelling has been used for interfaces between the domains. k-ω SST turbulence model has been used for the numerical analysis. The steady state solver has been used for all the simulations. The boundary conditions used for the compressor stage have also been described in this chapter. After numerically simulating the flow within the various geometrical configurations of the centrifugal compressor stage listed in the previous section, results have been gathered using an in-built post-processing module. Detailed discussions on these results are presented in the proceeding chapters, where the next chapter deals with the flow within the parallel and diverged wall diffusers.

CHAPTER 4
NOVEL DESIGN OF THE DIVERGED WALL STRAIGHT DIFFUSER

This chapter comprises of the results obtained after performing CFD simulations for the cases discussed in the previous chapter, regarding the parallel and diverged wall diffusers. Parametric investigations have been carried out to increase the compressor stage performance by modifying the shroud wall of the diffuser. A detailed qualitative and quantitative analysis of the results has been carried out in order to understand the complex flow structure in parallel and diverged wall diffusers. The effect of geometrical parameters and flow-related parameters on the stage performance has been investigated. Furthermore, semi-empirical relationships, of the flow within the diffuser with the stage performance have been developed.

4.1. Verification of Numerical Results

In the preliminary stage of the numerical modelling, the numerical results of the turbocharger compressor stage have been verified with the experimental data. Figure 4.1 depicts the comparison of the CFD results and the experimental data, using plot of variation of pressure ratio against mass flow rate variation (from choke line to surge line) at two operational speeds of 58.9rpsK$^{-1/2}$ and 78.6rpsK$^{-1/2}$. The results are obtained at lower operational speeds for the compressor stage because high efficiencies are obtained at these conditions. It can be seen that at the speed of 58.9rpsK$^{-1/2}$, the differences in the mass flow rate and the pressure ratio are 0.0% and 0.74% near surge condition respectively. Similarly, the differences in the mass flow rate and pressure ratio are less than 3.85% and 2.30% at BEP. Moreover, the differences in the mass flow rate and pressure ratio are 8.8% and 4.32% at near choke condition. Furthermore, it can also be seen that at the speed of 78.6rpsK$^{-1/2}$, the differences in the mass flow rate and pressure ratio are 0.0% and 0.11% near surge condition. Similarly, differences in the mass flow rate and pressure ratio are less than 5.46% and 7.55% at BEP. Moreover, the differences in the mass flow rate and pressure ratio are 10.35% and 6.46% at near choke condition. It can be seen that the numerical results match reasonably well with the experimental data.

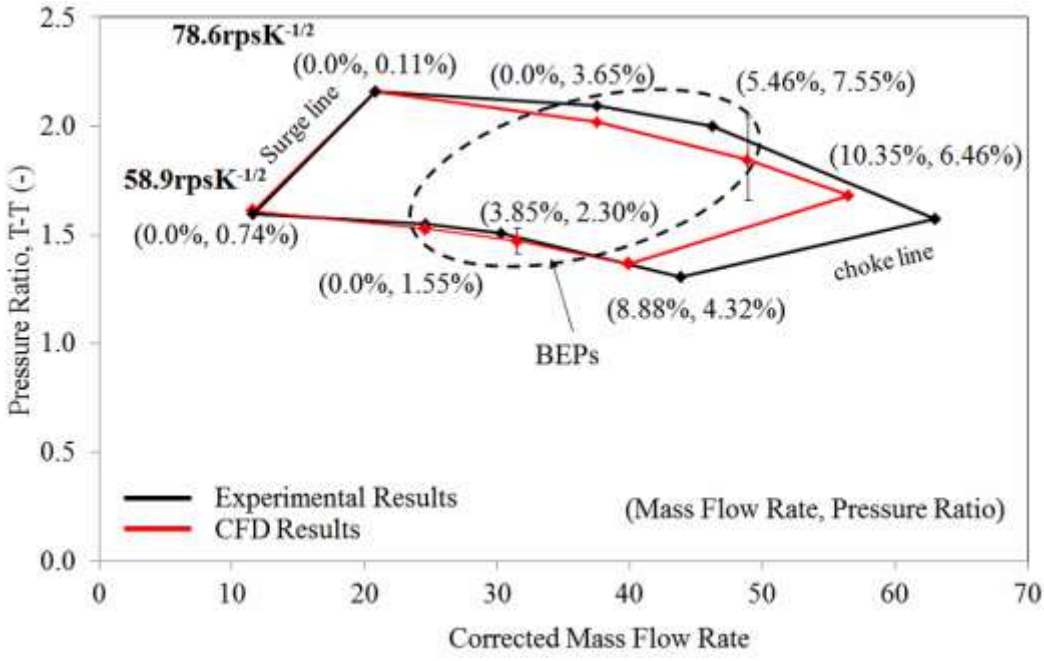

Figure 4.1: Verification of the CFD results with the experimental data using pressure ratio and mass flow rate at operational speeds of 58.9rpsK$^{-1/2}$ and 78.6rpsK$^{-1/2}$

Figure 4.2 depicts the comparison of CFD results and the experimental data, using plot of variation of efficiency - efficiency against mass flow rate variations (from choke line to surge line) at operational speeds of 58.9rpsK$^{-1/2}$ and 78.6rpsK$^{-1/2}$. It can be seen that at operational speed of 58.9rpsK$^{-1/2}$, the differences in the mass flow rate and efficiency are 0.0% and 0.82% at near surge condition. Similarly, differences in the mass flow rate and efficiency are less than 3.85% and 6.30% at BEP. Moreover, the differences in the mass flow rate and efficiency are 8.8% and 8.19% at near choke condition. Furthermore, it can also be seen that at operational speeds of 78.6rpsK$^{-1/2}$, the differences in the mass flow rate and efficiency are 0.0% and 1.57% at near surge condition. Similarly, the differences in the mass flow rate and efficiency are less than 5.46% and 7.42% at BEP. Moreover, the differences in the mass flow rate and efficiency are 10.35% and 4.97% at near choke condition.

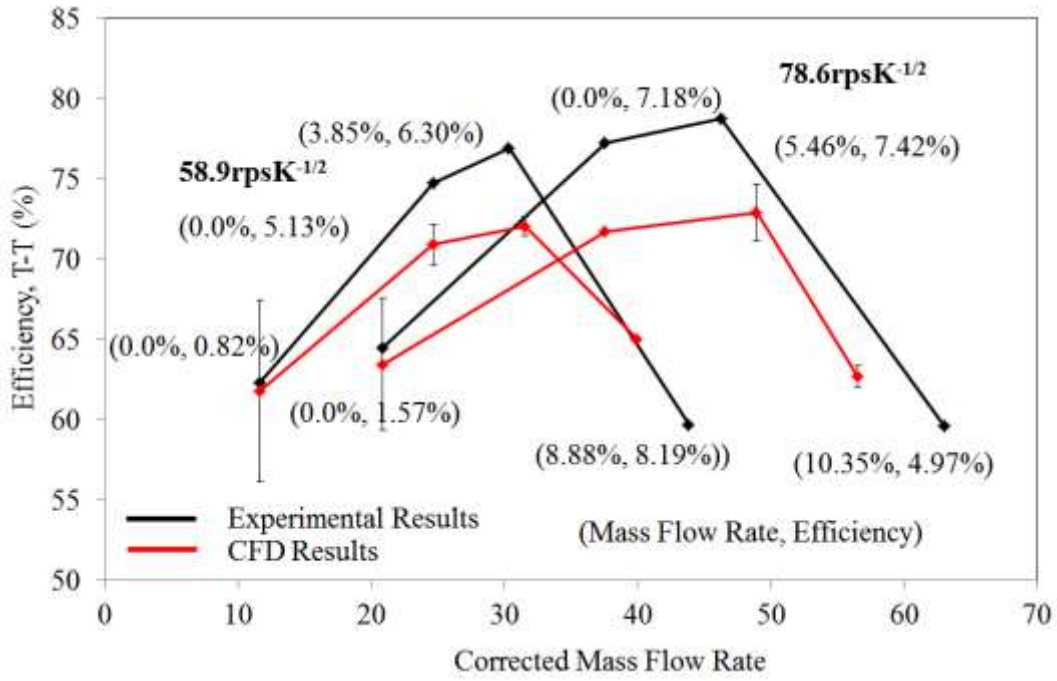

Figure 4.2: Verification of the CFD results with the experimental data using plot of variation of efficiency - efficiency against mass flow rate variations (from choke line to surge line) at operational speeds of 58.9rpsK$^{-1/2}$ and 78.6rpsK$^{-1/2}$

4.2. Flow Field Characteristics within the Centrifugal Compressor Stage

This section of the chapter comprises of the general analysis of the flow structure within the centrifugal compressor stage having straight parallel wall diffuser. This is baseline diffuser configuration normally used. The discussion presented in this section corresponds to design and near off-design conditions of the compressor stage. Figure 4.3 depicts different points considered at various locations inside the turbocharger compressor stage, represented by a range of points from P1

to P8. These points are chosen to explain the flow distribution within the compressor stage and quantify non-uniformity in the flow field.

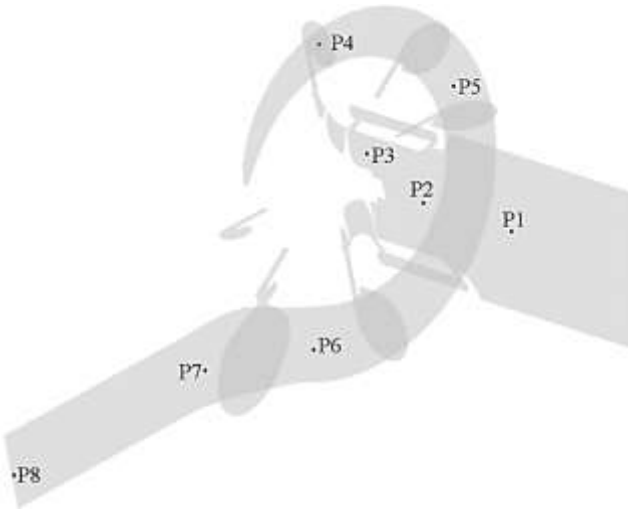

Figure 4.3: Geometry of the turbocharger compressor stage

Figure 4.4 depicts the local static pressure variations within the turbocharger compressor stage at three conditions, (a) BEP, (b) near choke and (c) near surge at an operational speed of 58.9rpsK$^{-1/2}$. The compressor stage produces maximum efficiency at BEP, with minimum losses inside the compressor stage (shown in Figure 4.4(a)). Ambient air is drawn towards the compressor's impeller due to the impeller rotation, which creates suction at the impeller inlet. The figure shows the static pressure variations within the compressor stage at different points. It can be seen that at P1, the static pressure is 0.997atm and then it is reduced by 1.2% at P2. The static pressure decreases further at the P3 (impeller eye) by 2.4% from P1 (inlet). The flow structure within the impeller is known to be three-dimensional. The impeller of the centrifugal compressor adds energy to the air, which increases its kinetic energy. The air than leaves the impeller with high kinetic energy and enters into the diffuser, where the kinetic energy of the air converts into a static pressure rise. Moreover, it can also be seen that the flow then enters into the volute region where the static pressure further rises. It can be seen that the static pressure at P4 has increased by 31.8% as compared to P1 (inlet). The static pressure rises within the volute due to constant increase in cross-sectional area of the volute. Therefore, the static pressure is increased at point P5, P6 and P7 by 32.4%, 32.6% and 34% respectively as compared to P1 (inlet). It can be seen that the static pressure increases gradually within the volute. Finally, the static pressure has increased at the outlet by 34.3% as compared to that at the P1 (inlet).

Figure 4.4(b) depicts the static pressure variations at near choke condition. The trend of the flow behaviour within the compressor stage is similar to that seen at BEP. However, at near choke condition, the mass flow rate increases with the decrease in the total pressure. The comparison of the static pressure at BEP and at near choke condition is depicted in Figure 4.5 at the same points as shown in Figure 4.3. It can be seen that the static pressure at P1 (inlet) is reduced by 0.4% as compared to the static pressure at BEP. The static pressure at P2, P3, P4, P5 P6, P7 and P8 (outlet) is further reduced by 0.9%, 2.2% 12%, 13.9%, 17.7%, 16.5% and 14% respectively as compared to the static pressure at BEP.

Figure 4.4(c) depicts the static pressure variations at near surge condition. The trend of the flow behaviour within the compressor stage is similar to that seen at BEP. However, at near surge condition, the mass flow rate decreases with the increase in the total pressure. The comparison of the static pressure at BEP and at near surge condition is depicted in Figure 4.5 at the same points as shown in Figure 4.3. It can be seen that the static pressure at P1 is increased by 0.2% as compared to the static pressure at BEP. The static pressure at P2, P3, P4, P5 P6, P7 and P8 (outlet) is further increased by 1.3%, 23% 6.9%, 6.6%, 7.2%, 5.9% and 5.5% respectively as compared to the static pressure at BEP.

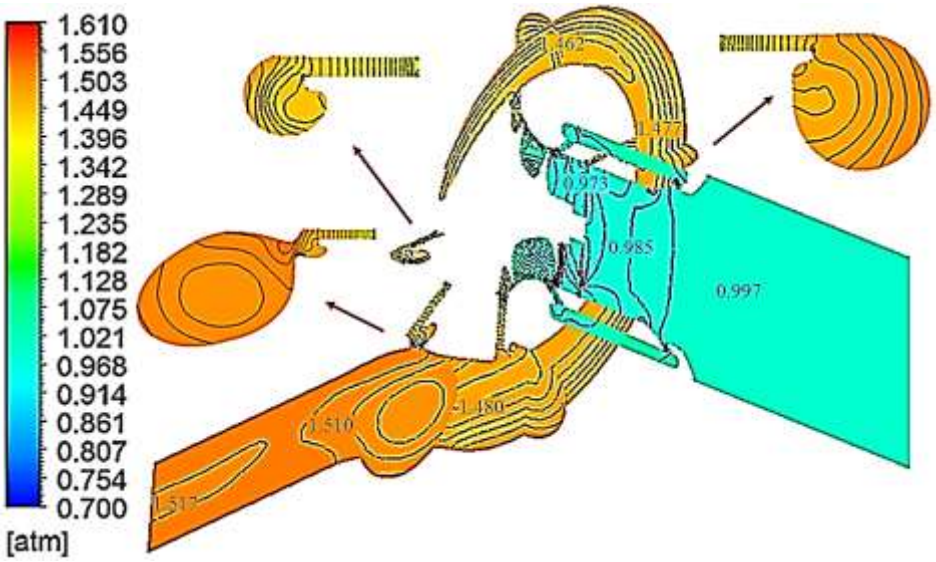

(a)

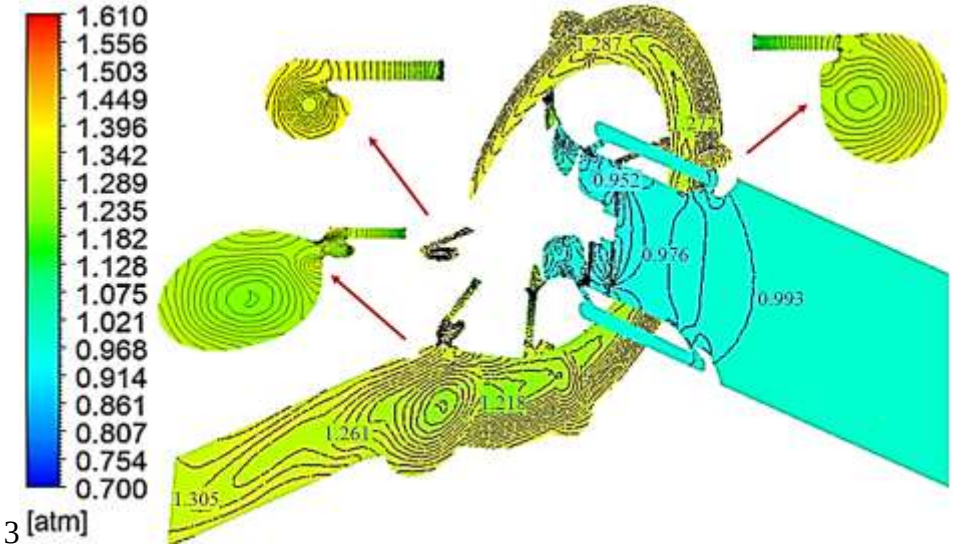

(b)

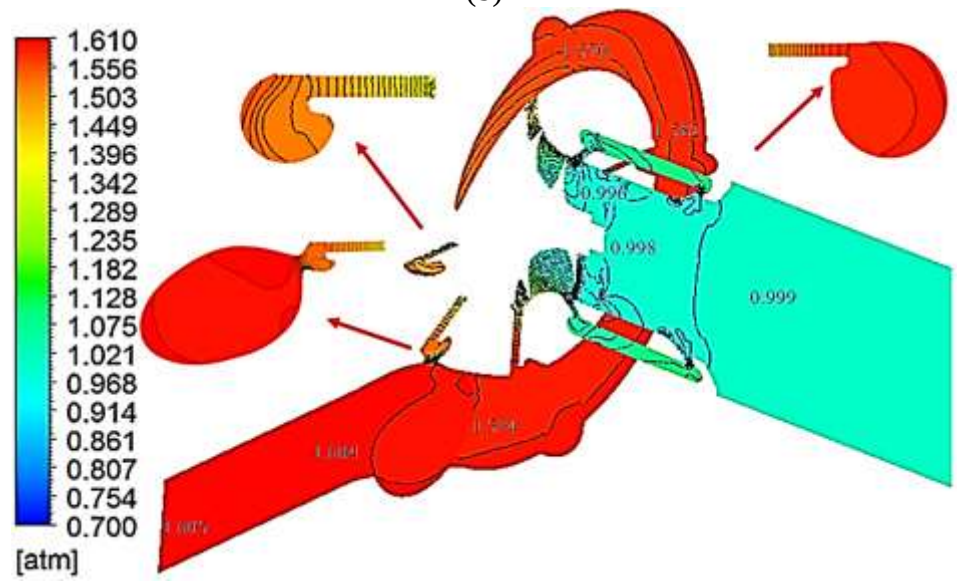

(c)

Figure 4.4: Static pressure (atm) variations within the compressor stage at an operational speed of 58.9rpsK$^{-1/2}$ for three conditions; (a) BEP, (b) near choke and (c) near surge

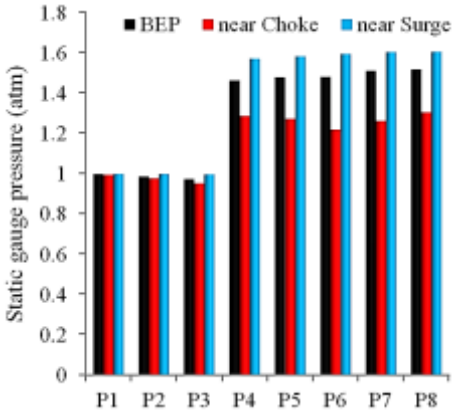

Figure 4.5: Difference in static pressure (atm) at the points shown in Figure 4.3 at design and near off-design conditions

Figure 4.6 depicts the local velocity magnitude distribution within the turbocharger compressor stage at three conditions, (a) BEP, (b) near choke and (c) near surge at an operational speed of 58.9rpsK$^{-1/2}$. Ambient air is drawn towards the compressor's impeller due to the impeller rotation, which creates suction at the impeller inlet. This increases the flow speed approaching the impeller. The figure shows the velocity magnitude distributions within the compressor stage at different points. It can be seen that at P1 (inlet), the velocity magnitude is 24m/s and then it is increased by 51% at P2. The velocity magnitude increases further at the P3 (impeller eye) by 79% from P1 (inlet). The flow structure within the impeller is known to be three-dimensional. The impeller of the centrifugal compressor adds energy to the air, which increases its kinetic energy. The velocity magnitude is maximum at the trailing edges of the impeller blades with a velocity magnitude of 206m/s, which is an increase of 88% from the velocity magnitude value at P1 (inlet). The air than leaves the impeller with high kinetic energy and enters into the diffuser, where the kinetic energy decrease, which decreased the velocity magnitude. Moreover, it can also be seen that the flow then enters into the volute region where the velocity magnitude further decreases. It can be seen that the velocity magnitude at P4 (inside the volute) has increased by 76% as compared to P1 (inlet). The velocity magnitude decreases within the volute due to constant increase in cross-sectional area of the volute. Therefore, the velocity magnitude is 74%, 72% and 64% higher at P5, P6 and P7 respectively as compared to P1, which have negative gradient. Finally, the velocity magnitude is 58% higher at P8 (outlet) as compared to that at the P1 (inlet).

Figure 4.6(b) depicts the velocity magnitude distribution at near choke condition. The trend of the flow behaviour within the compressor stage is similar to that seen at BEP. However, at near choke condition, the mass flow rate increases with the decrease in the total pressure. The comparison of the velocity magnitude at BEP and at near choke condition is depicted in Figure 4.7 at the same points as shown in Figure 4.3. It can be seen that the velocity magnitude at P1 (inlet) is increased by 32% as compared to the velocity magnitude at BEP. The velocity magnitude at P2, P3, P4, P5 P6, P7 and P8 (outlet) is further increased by 22%, 16% 10%, 29%, 44%, 45% and 38% respectively as compared to the velocity magnitude at BEP.

Figure 4.6(c) depicts the velocity magnitude distribution at near surge condition. The trend of the flow behaviour within the compressor stage is similar to that seen at BEP. However, at near surge condition, the mass flow rate decreases with the increase in the total pressure. The comparison of the velocity magnitude at BEP and at near surge condition is depicted in Figure 4.7 at the same points as

shown in Figure 4.3. It can be seen that the velocity magnitude at P1 is reduced by 49% as compared to the velocity magnitude at BEP. The static pressure at P2, P3, P4, P5 P6, P7 and P8 (outlet) is further increased by 63%, 9.3% 46%, 45%, 53%, 52% and 69% respectively as compared to the velocity magnitude at BEP.

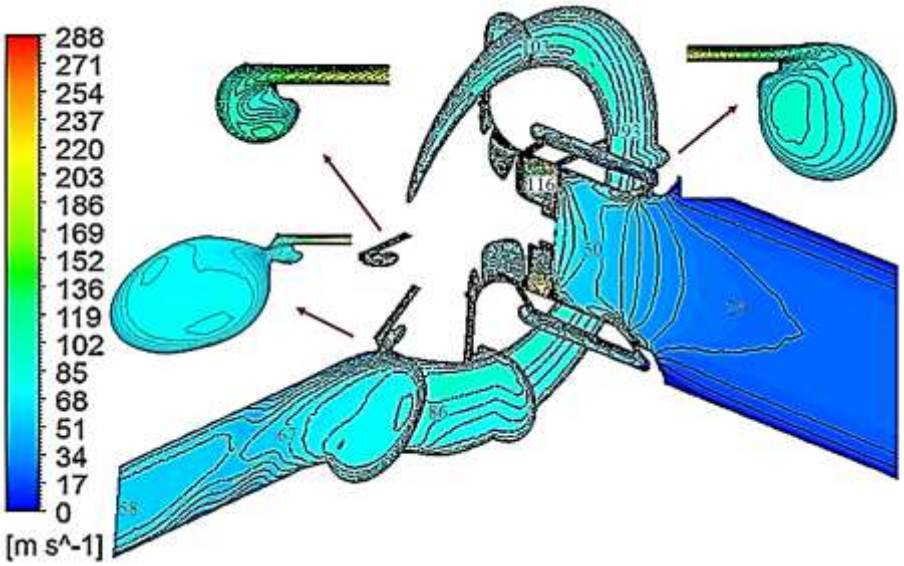

(a)

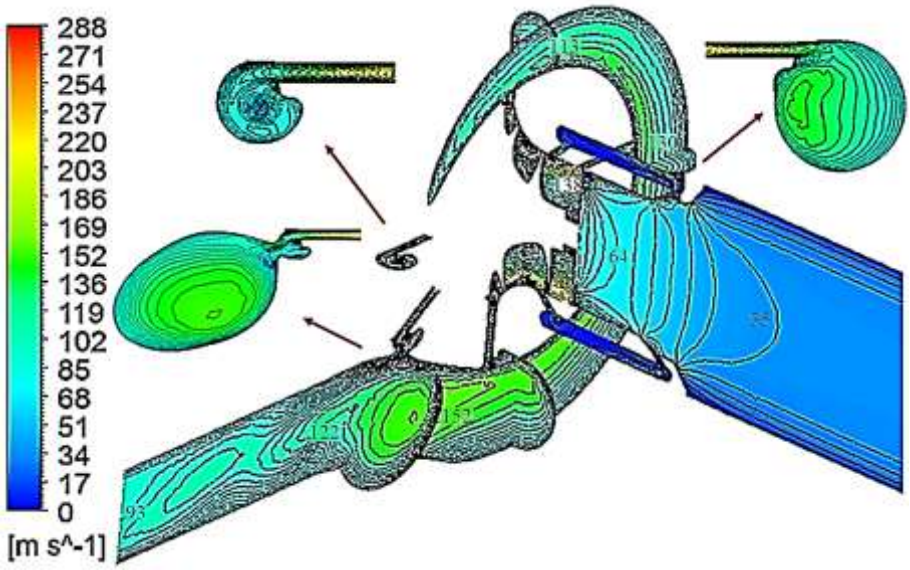

(b)

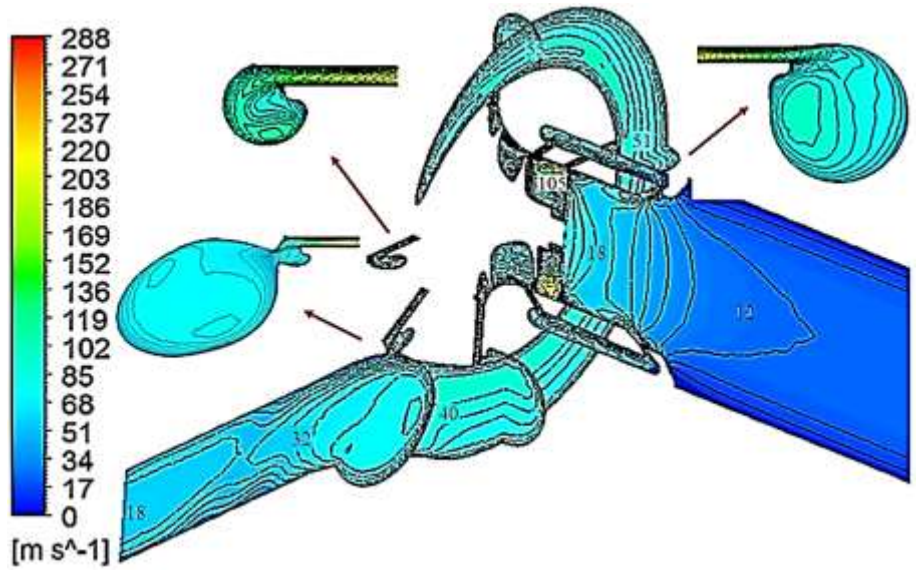

(c)

Figure 4.6: Velocity magnitude (m/s) distribution within the compressor stage at an operational speed of 58.9rpsK$^{-1/2}$ for three conditions; (a) BEP, (b) near choke and (c) near surge

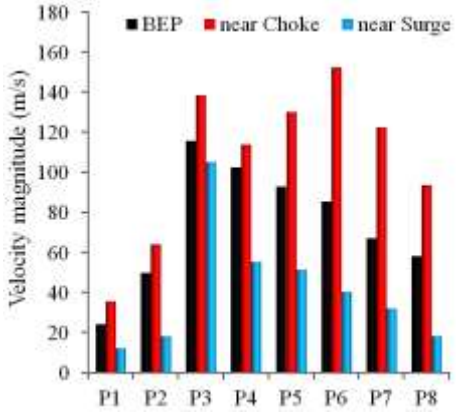

Figure 4.7: Difference in velocity magnitude (m/s) at the points shown in Figure 4.3 at design and near off-design conditions

Figure 4.8 depicts the local static temperature variations within the turbocharger compressor stage at three conditions, (a) BEP, (b) near choke and (c) near surge at an operational speed of 58.9rpsK$^{-1/2}$. The figure shows the static temperature variations within the compressor stage at different points. It can be seen that at P1, the static temperature is 287.7K and then it is reduced by 0.3% at P2. The static temperature decreases further at P3 (impeller eye) by 0.08% from P1 (inlet). The static temperature increases within the impeller. The high temperature flow recirculates via MWE from impeller throat to the inlet causing the static temperature near the walls of the inlet to rise. The high static temperature air enters the diffuser, where further static temperature increases. Similarly, the static temperature also rises inside the volute. It can be seen that the static temperature at P4 has increased by 14.3% as compared to P1 (inlet). The static temperature rises within the volute due to constant increase in cross-

sectional area of the volute. Therefore, the static temperature is increased at point P5, P6 and P7 by 14.5%, 14.6% and 14.9% respectively as compared to P1 (inlet). It can be seen that the static temperature increases gradually within the volute. Finally, the static temperature has increased at the outlet by 15.1% as compared to that at the P1 (inlet).

Figure 4.8(b) depicts the static temperature variations at near choke condition. The trend of the flow behaviour within the compressor stage is similar to that seen at BEP. However, at near choke condition, the mass flow rate increases with the decrease in the total pressure. The comparison of the static temperature at BEP and at near choke condition is depicted in Figure 4.9 at the same points as shown in Figure 4.3. It can be seen that the static temperature at P1 (inlet) is reduced by 0.1% as compared to the static temperature at BEP. The static temperature at P2, P3, P4, P5 P6, P7 and P8 (outlet) is further reduced by 0.2%, 1.1% 3.9%, 4.7%, 5.8%, 5% and 4.2% respectively as compared to the static temperature at BEP.

Figure 4.8(c) depicts the static temperature variations at near surge condition. The trend of the flow behaviour within the compressor stage is similar to that seen at BEP. However, at near surge condition, the mass flow rate decreases with the increase in the total pressure. The comparison of the static temperature at BEP and at near surge condition is depicted in Figure 4.5 at the same points as shown in Figure 4.3. It can be seen that the static temperature at P1 is increased by 0.08% as compared to the static temperature at BEP. The static temperature at P2, P3, P4, P5 P6, P7 and P8 (outlet) is further increased by 0.4%, 8.4% 7.0%, 6.93%, 6.91%, 6.62% and 6.60% respectively as compared to the static temperature at BEP.

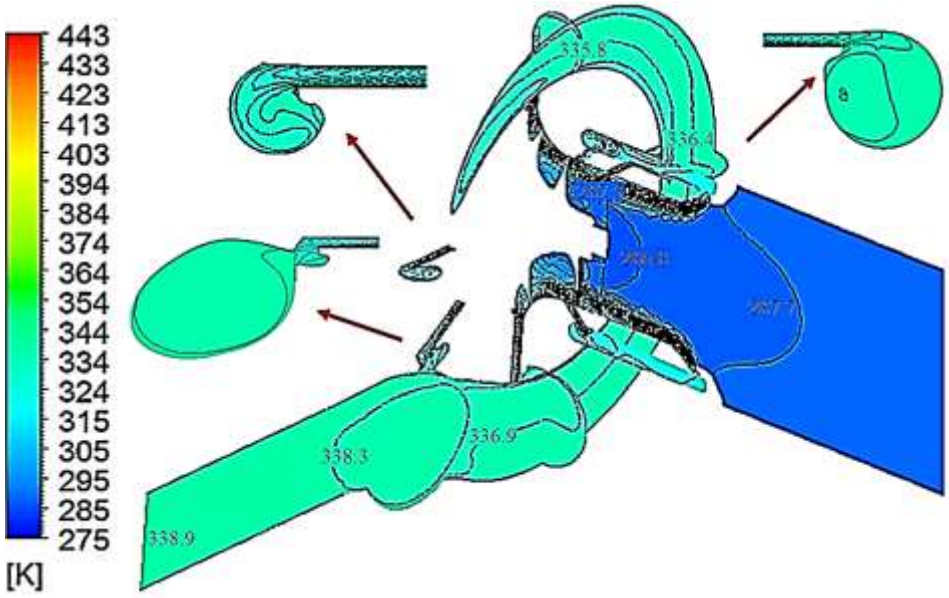

(a)

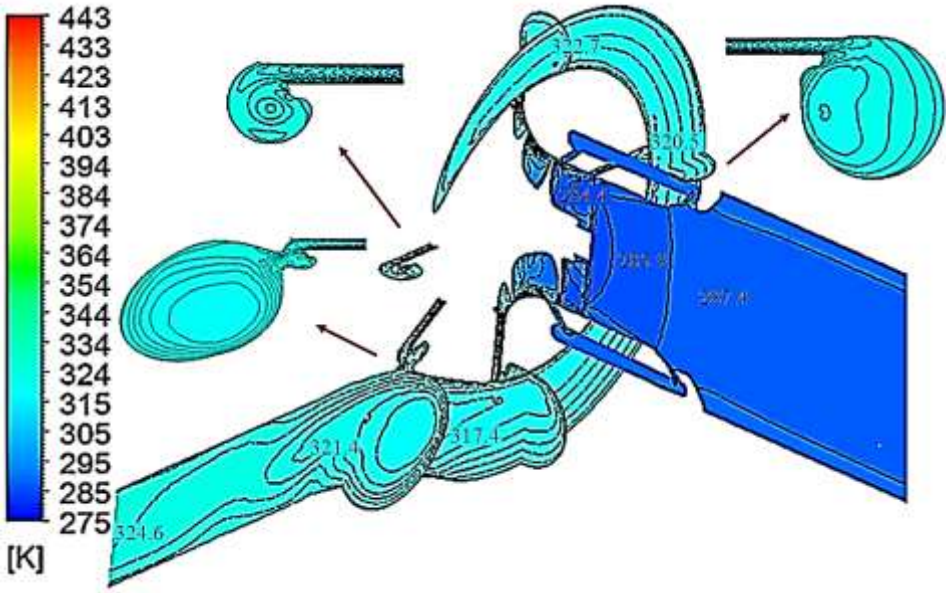

(b)

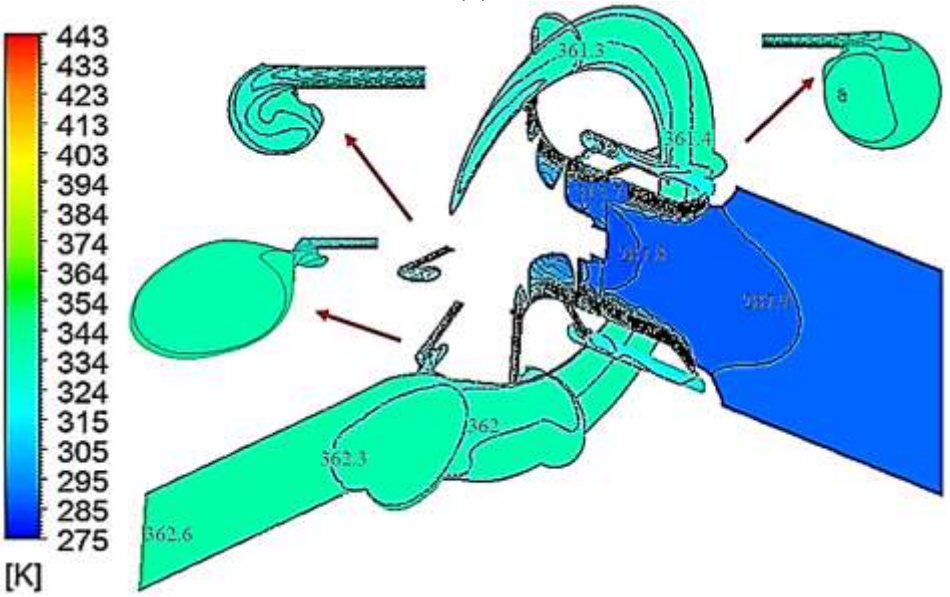

(c)

Figure 4.8: Static temperature (K) variations within the compressor stage at an operational speed of 58.9rpsK$^{-1/2}$ for three conditions; (a) BEP, (b) near choke and (c) near surge

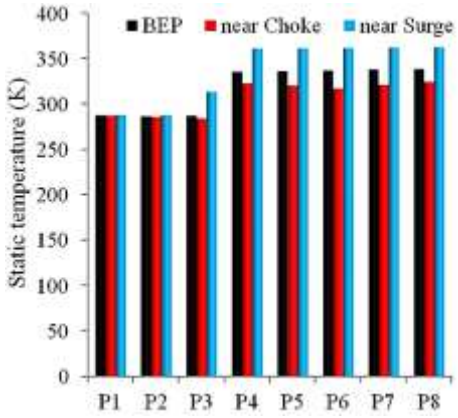

Figure 4.9: Difference in static pressure (atm) at the points shown in Figure 4.3 at design and near off-design conditions

From this analysis, it is found that every component of the compressor stage helps to improve its performance Since, the diffuser is the only component that can be easily modified to improve the compressor stage efficiency or the total pressure. Moreover, it can also be easily modified to make the compressor stage more compact. Therefore, vaneless diffuser is considered in this investigation and attempts have been made to modify its geometry to manage the stage performance as well as make the compressor stage more compact. The upcoming section provides the qualitative and quantitative analyses within the baseline diffuser. In next two chapters, geometry modifications will be attempted to manage the performance of the stage.

4.3. Flow Field Characteristics within the Straight diffuser

The flow field characteristics within the diffuser from the shroud wall to the hub wall and circumferentially across the diffuser have been investigated. Furthermore, the effect of mass flow rate change on the flow behaviour inside the compressor stage is also investigated.

Figure 4.10 depicts the static pressure variations across the centreline of the diffuser at BEP at an operational speed of 58.9rpsK$^{-1/2}$. It can be seen that the minimum static pressure of 1.33atm is obtained at the diffuser inlet after the volute-tongue region. The static pressure increases radially across the diffuser that causes reduction in the velocity magnitude. Furthermore, the static pressure also increases circumferentially in the direction of impeller rotation (ω). It has a maximum value of 1.49atm at the diffuser outlet near the volute-tongue region.

Figure 4.11(a) depicts the static pressure (atm) variations across the centreline of the diffuser at near choke condition at an operational speed of 58.9rpsK$^{-1/2}$. The overall static pressure is lower within the diffuser at near choke condition in comparison to that at BEP. It can be seen that the minimum static pressure of 1.11atm is obtained at the diffuser inlet before the volute-tongue region. The static

pressure increases radially across the diffuser similar to that seen at BEP. Furthermore, the static pressure increases circumferentially in the direction of impeller rotation having a maximum value of 1.33atm at the diffuser outlet after the volute-tongue region. Figure 4.11(b) depicts the static pressure (atm) variations across the centreline of the diffuser at near surge condition at an operational speed of 58.9rpsK$^{-1/2}$. The trend of static pressure variations is similar to that seen at BEP. However, the overall static pressure is higher within the diffuser at near surge condition in comparison to that at BEP. The minimum static pressure is seen to be 1.37atm at the diffuser inlet after volute-tongue region and the maximum static pressure is 1.58atm at the diffuser outlet near the volute-tongue region.

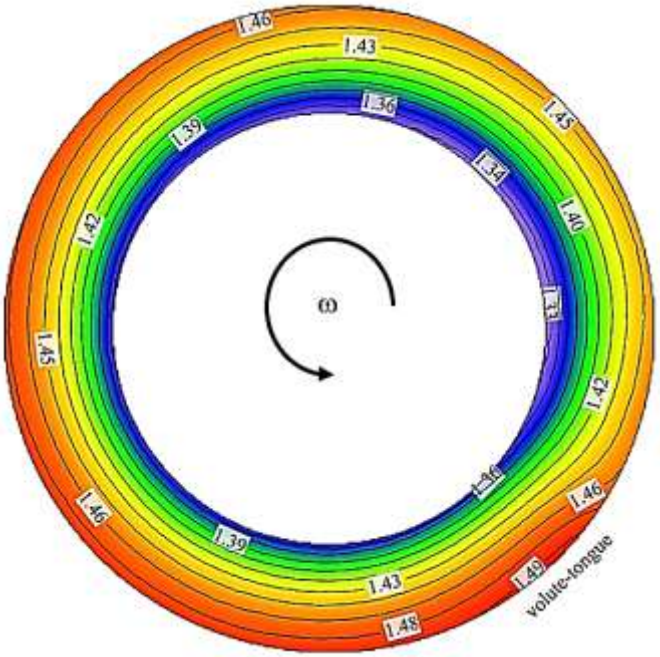

Figure 4.10: Static pressure (atm) variations across the centreline of the diffuser at BEP at an operational speed of 58.9rpsK$^{-1/2}$

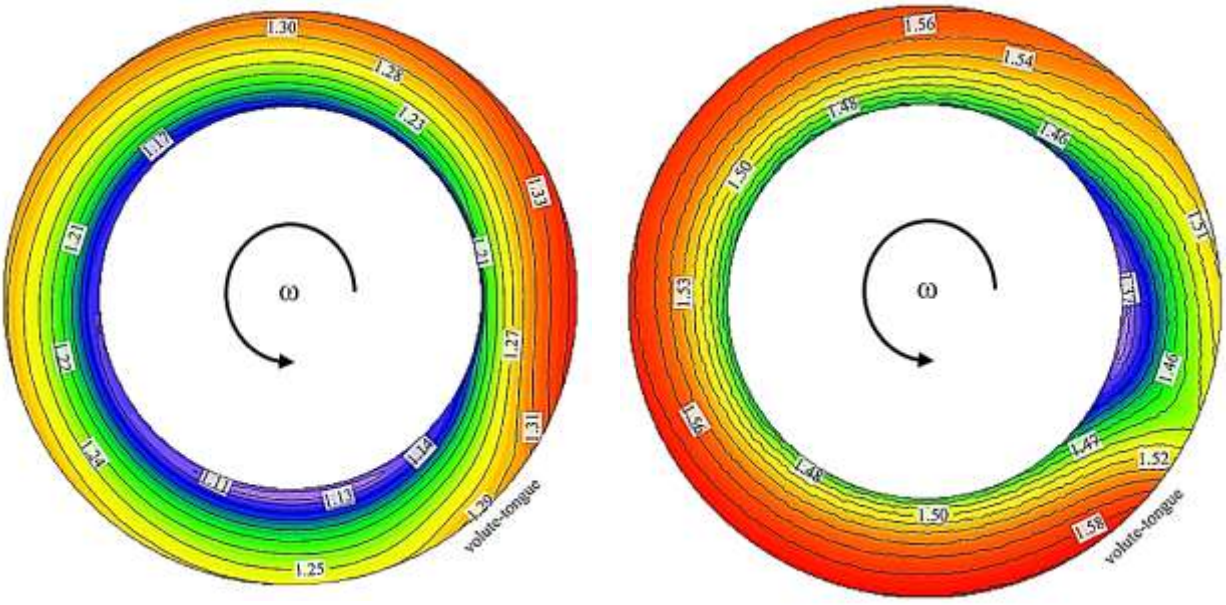

(a) (b)

Figure 4.11: Static pressure (atm) variations across the centreline of the diffuser at an operational speed of 58.9rpsK$^{-1/2}$ for off-design conditions (a) near choke and (b) near surge

Figure 4.12 depicts the static pressure variations across the centreline of the diffuser at BEP at an operational speed of 78.6rpsK$^{-1/2}$. The trend in the static pressure variations within the diffuser is similar to that at BEP at an operational speed of 58.9rpsK$^{-1/2}$. It can be seen that the minimum static pressure is obtained at the diffuser inlet after the volute-tongue region, which is 15% higher in comparison to that at BEP at an operational speed of 58.9rpsK$^{-1/2}$. Furthermore, static pressure is found to be higher near the volute-tongue region, which is 21% more than that at BEP at operational speed of 58.9rpsK$^{-1/2}$.

Figure 4.13(a) depicts the static pressure variations across the centreline of the diffuser at near choke condition at an operational speed of 78.6rpsK$^{-1/2}$. The overall static pressure is higher within the diffuser in comparison to that at near choke condition at an operational speed of 58.9rpsK$^{-1/2}$. However, the trend of the static pressure variations is similar to that at near choke condition at an operational speed of 58.9rpsK$^{-1/2}$. It can be seen that the minimum static pressure is obtained at the diffuser inlet before the volute-tongue region, which is 5% higher in comparison to that at near choke condition at an operational speed of 58.9rpsK$^{-1/2}$. Furthermore, maximum static pressure is obtained at the diffuser outlet after the volute-tongue region, which is 16% more than that at near choke condition at operational speed of 58.9rpsK$^{-1/2}$. Figure 4.13(b) depicts the static pressure variations across the centreline of the diffuser at near surge condition at an operational speed of 78.6rpsK$^{-1/2}$.

The overall static pressure is higher within the diffuser in comparison to that at near surge condition at an operational speed of 58.9rpsK$^{-1/2}$. However, the trend of the static pressure variations is similar to that at near surge condition at an operational speed of 58.9rpsK$^{-1/2}$. It can be seen that the minimum static pressure is obtained at the diffuser inlet after volute-tongue region, which 17% higher in comparison to that at near surge condition at an operational speed of 58.9rpsK$^{-1/2}$. Furthermore, the maximum static pressure is obtained at the diffuser outlet near the volute-tongue region, which is 24% more than that at near surge condition at an operational speed of 58.9rpsK$^{-1/2}$.

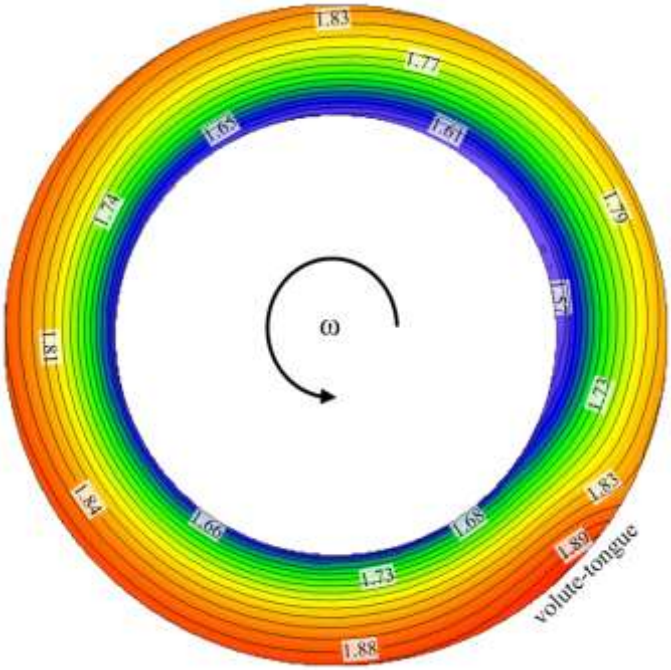

Figure 4.12: Static pressure (atm) variations across the centreline of the diffuser at BEP at an operational speed of 78.6rpsK$^{-1/2}$

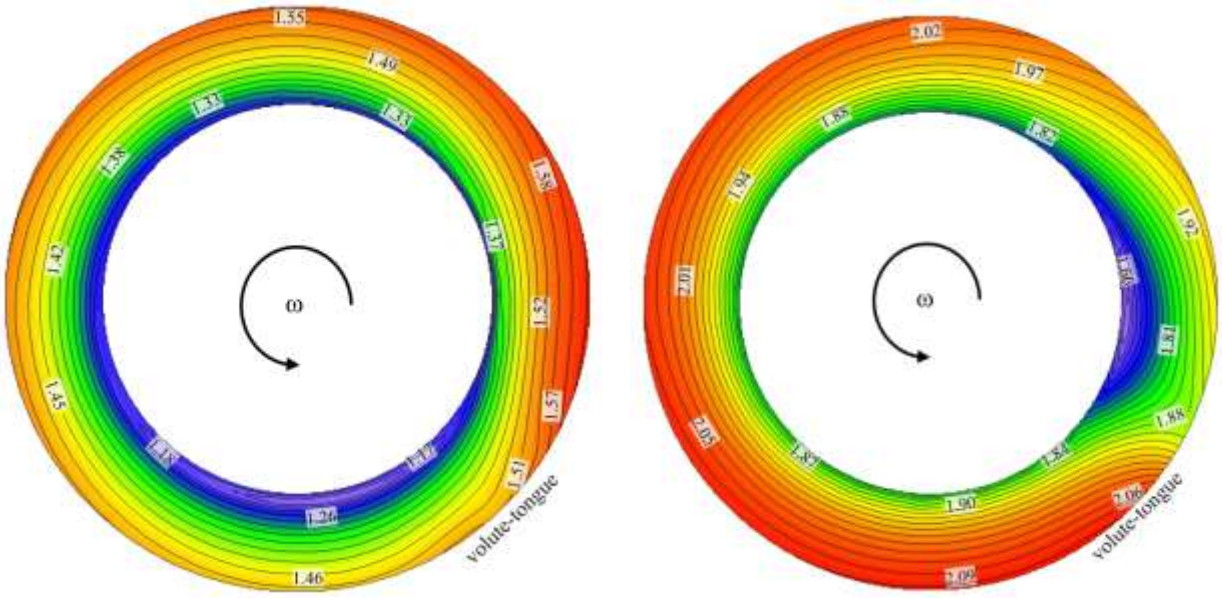

(a) (b)

Figure 4.13: Static pressure (atm) variations across the centreline of the diffuser at an operational speed of 78.6rpsK$^{-1/2}$ for off-design conditions (a) near choke and (b) near surge

Figure 4.14 depicts the cylindrical planes created from the hub wall to the shroud wall inside the diffuser (shown only 1/3rd section of the diffuser). Eleven cylindrical planes, ranging from P1 to P11, are created from the diffuser inlet to the diffuser outlet with 10% increase of each cylindrical plane from the previous plane. These planes are created to explain the performance of the diffuser and quantify non-uniformity in the flow field across the diffuser.

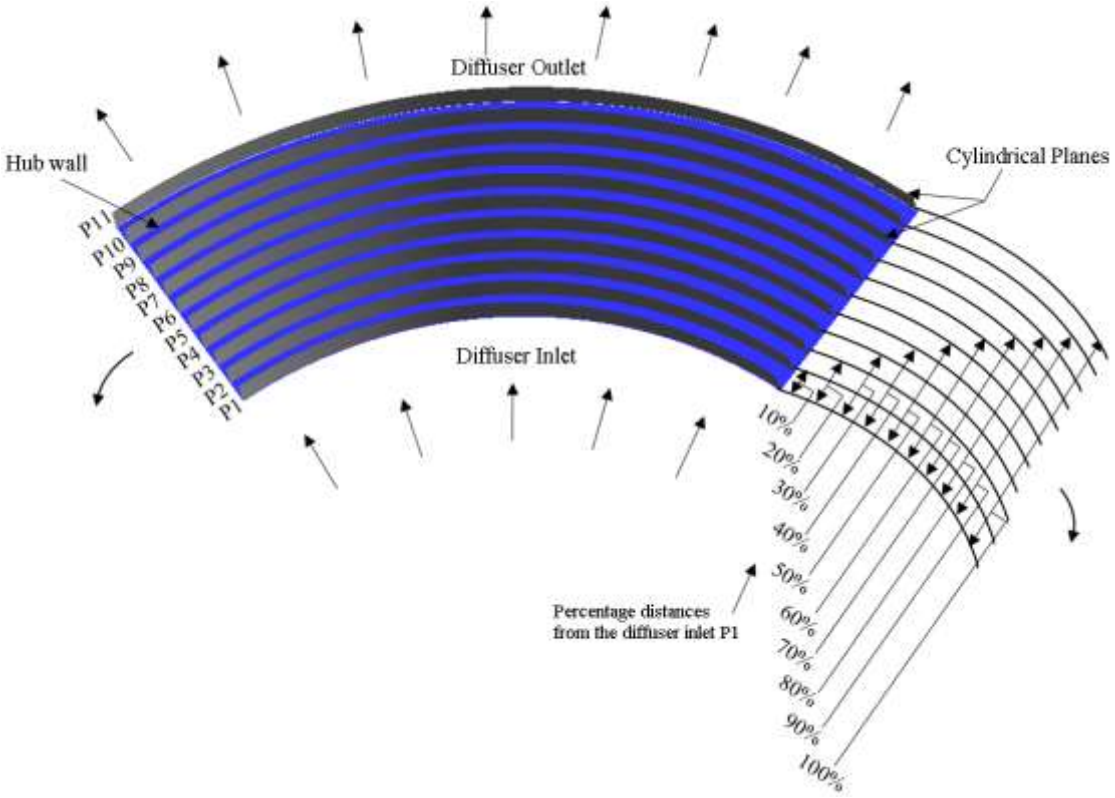

Figure 4.14: Cylindrical planes shown in 1/3rd of the diffuser section

Figure 4.15 depicts the circumferential pressure recovery with respect to area ratio, A_i/A_{in} radially across the diffuser at design and near off-design conditions at the operational speeds of 58.9rpsK$^{-1/2}$ and 78.6rpsK$^{-1/2}$. Thereby A_{in} is the area at the diffuser inlet cylindrical plane and A_i is the area at the respective diffuser cylindrical planes. This pressure recovery is calculated at each cylindrical plane shown in Figure 4.14. The circumferential pressure recovery is defined as;

$$\text{Circumferential pressure recovery} = \frac{P_i - P_1}{\frac{1}{2}\rho v_\infty^2},$$

where P_i is the average static pressure at the respective diffuser cylindrical planes, P_1 is the average static pressure at the diffuser inlet cylindrical plane, ρ is the average density at the diffuser inlet cylindrical plane and v_∞ is the maximum velocity magnitude at the diffuser inlet cylindrical plane. It can be seen in Figure 4.15(a) that the gradient of circumferential pressure recovery at the diffuser inlet is high and it reduces towards downstream. The circumferential pressure recovery across the diffuser at near choke condition is obtained as 0.45. However, the circumferential pressure recovery across the diffuser at near surge condition is higher as 0.6 and at BEP the circumferential pressure recovery across the diffuser is 0.52. Furthermore, the increase of circumferential pressure recovery

between the two cylindrical planes is similar. However, the increase of circumferential pressure recovery between the outlet cylindrical plane and 90% from the inlet cylindrical plane is more. This is because the diffuser hub wall is diverged in proximity to the diffuser outlet and that causes increase in circumferential pressure recovery. This implies that the diffuser wall divergence increases the area ratio, which in-turn increases the static pressure recovery across the diffuser.

Figure 4.15(b) depicts the circumferential pressure recovery across the straight diffuser for design and near off-design conditions at an operational speed of 78.6rpsK$^{-1/2}$. The trend for circumferential pressure recovery shown is similar to that at an operational speed of 58.9rpsK$^{-1/2}$ for all conditions. The comparison of the results for design and near off-design conditions at the operational speeds of 58.9rpsK$^{-1/2}$ and 78.6rpsK$^{-1/2}$ is shown in Figure 4.16. It can be seen that at P1 (Diffuser inlet), the circumferential pressure recovery is 100% less at near choke condition in comparison to that at an operational speed of 58.9rpsK$^{-1/2}$. On the other hand, the circumferential pressure recovery at P1 (Diffuser inlet) is same at BEP and at near surge condition in comparison to that at an operational speed of 58.9rpsK$^{-1/2}$. Furthermore, the circumferential pressure recovery at P2 is 4.7% less at near choke condition in comparison to that at an operational speed of 58.9rpsK$^{-1/2}$. Thereafter, the circumferential pressure recovery is higher at cylindrical planes P3, P4, P5, P6, P7, P8, P9, P10 and P11 having difference of 3.4%, 2.8%, 2.9%, 2.5%, 2%, 1.6%, 1.3%, 1% and 0.6% respectively at near choke condition in comparison to that at an operational speed of 58.9rpsK$^{-1/2}$. Moreover, the circumferential pressure recovery at P2, P3, P4 and P5 is 3.3%, 1.2%, 0.4% and 0.4% less at BEP in comparison to that at an operational speed of 58.9rpsK$^{-1/2}$. Thereafter, the circumferential pressure recovery is same at cylindrical planes P6, P7 and P9 in comparison to that at an operational speed of 58.9rpsK$^{-1/2}$. However, the circumferential pressure recovery at P8 is 0.2% higher at BEP in comparison to that at an operational speed of 58.9rpsK$^{-1/2}$. Thereafter, the circumferential pressure recovery at P10 and P11is 0.2% and 0.6% less at BEP in comparison to that at an operational speed of 58.9rpsK$^{-1/2}$. Furthermore, the circumferential pressure recovery at P2, P3, P4, P5, P6, P7 and P8 is 6.3%, 3.4%, 2.5%, 1.6%, 1.4% 0.9% and 0.6% less at near surge condition in comparison to that at an operational speed of 58.9rpsK$^{-1/2}$. The circumferential pressure recovery is same at P9 and it is higher at P10 and P11 having a difference of 0.5% and 0.9% at near surge condition in comparison to that at an operational speed of 58.9rpsK$^{-1/2}$.

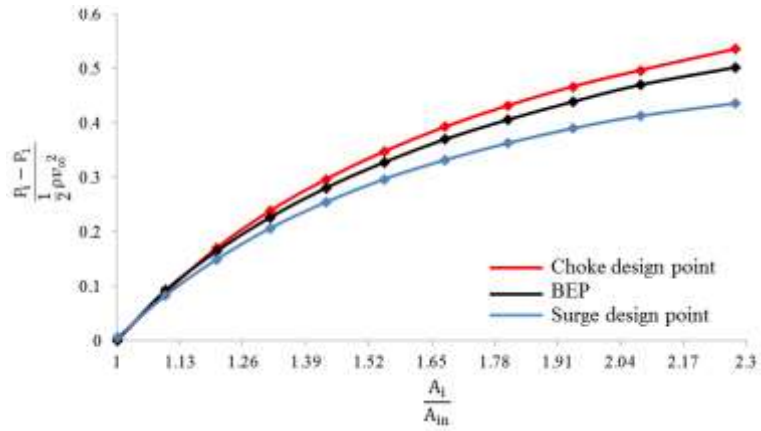

(a)

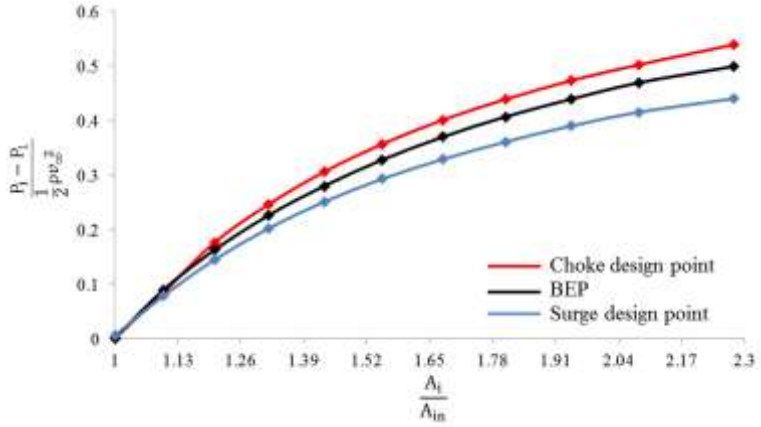

(b)

Figure 4.15: Circumferential pressure recovery radially across the vaneless diffuser for design and near off-design conditions at operational speeds of (a) 58.9rpsK$^{-1/2}$ and (b) 78.6rpsK$^{-1/2}$

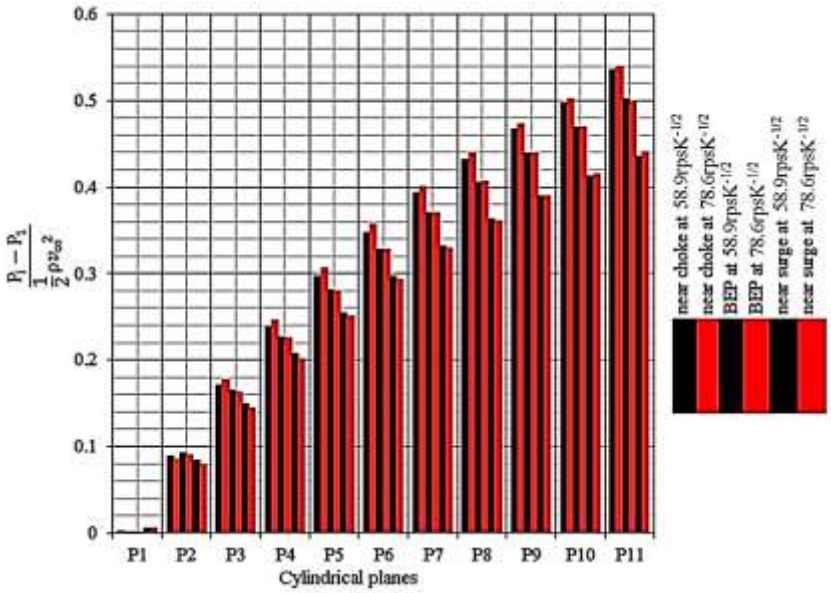

Figure 4.16: Difference in Circumferential pressure recovery at the planes shown in Figure 4.14 at design and near off-design conditions

Figure 4.17 depicts the vaneless diffuser showing five locations, ranging from L_1 to L_5, where 100 points are created from the hub wall to the shroud wall on each location. These points are placed at the distance of 0% (diffuser inlet), 25%, 50%, 75% and 100% (diffuser outlet) from the diffuser inlet, to capture the flow velocity profiles across the diffuser. This helps in explaining the effect of asymmetric ratio on the performance of the diffuser at design and near off-design conditions and quantify non-uniformity in the flow field across the diffuser.

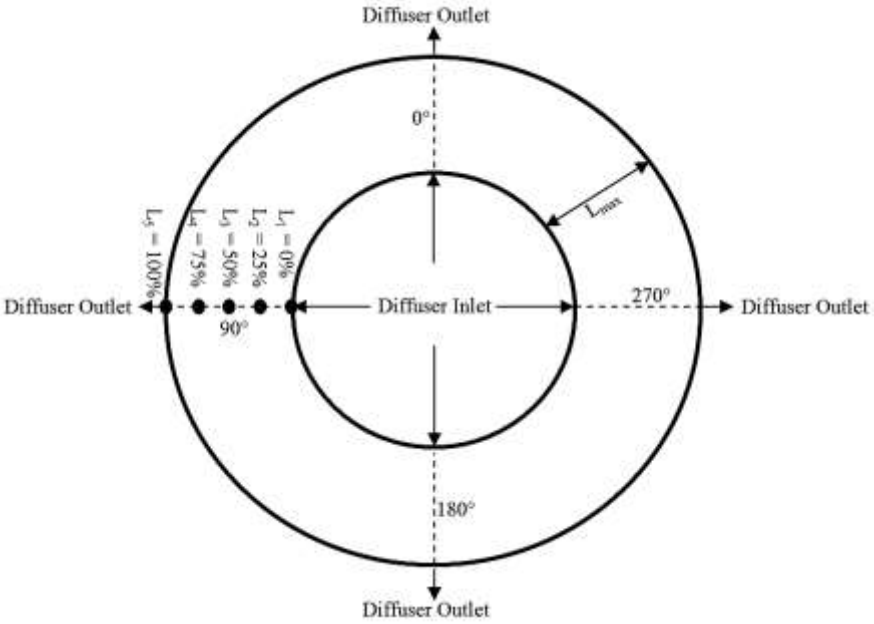

Figure 4.17: Points locations across the vaneless diffuser

Figure 4.18 depicts the velocity magnitude distribution across the diffuser from the hub wall to the shroud wall at BEP at an operational speed of 58.9rpsK$^{-1/2}$. In the figure, $b_2/b_1 = 0$ represents the hub wall of the diffuser and $b_2/b_1 = 1$ represents the shroud wall of the diffuser. It can be seen that the velocity magnitude is reduced radially across the diffuser having a maximum velocity of 206m/s at the diffuser inlet and 149m/s at the diffuser outlet. The velocity at the hub and the shroud walls is 0m/s because of no-slip wall boundary condition. Furthermore, it can also be seen that the velocity magnitude is higher near the shroud wall and lower near the hub wall because of having bigger boundary layer near the shroud wall. The reason of having bigger boundary layer near shroud wall is due to tip leakage loss, mixing and diffusion loss from impeller blades, which aids to this phenomenon [45]. Moreover, it can also be seen that as the flow moves across the diffuser, the velocity magnitude profile becomes symmetric. However, the detailed analysis has been carried out by quantifying the asymmetric ratio for the velocity magnitude profile across the diffuser.

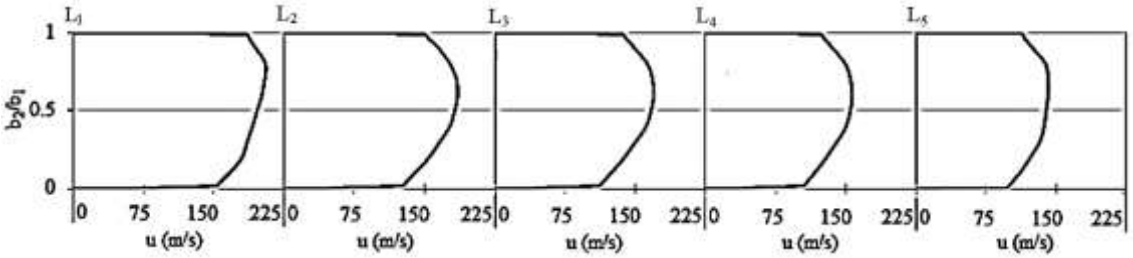

Figure 4.18: Velocity magnitude (m/s) distribution across the diffuser from the hub wall to the shroud wall at BEP at an operational speed of 58.9rpsK$^{-1/2}$

A set of data has been obtained from the velocity profiles at 10%, 20%, 30% and 40% distance from the centreline towards the hub and the shroud walls (shown Figure 4.19). These values aid to obtain the local asymmetric ratio, α from the centreline towards the walls and from the diffuser inlet to the diffuser outlet, which is explained as follows

$$\alpha = \frac{\text{Velocity at the top}}{\text{Velocity at the bottom}}$$

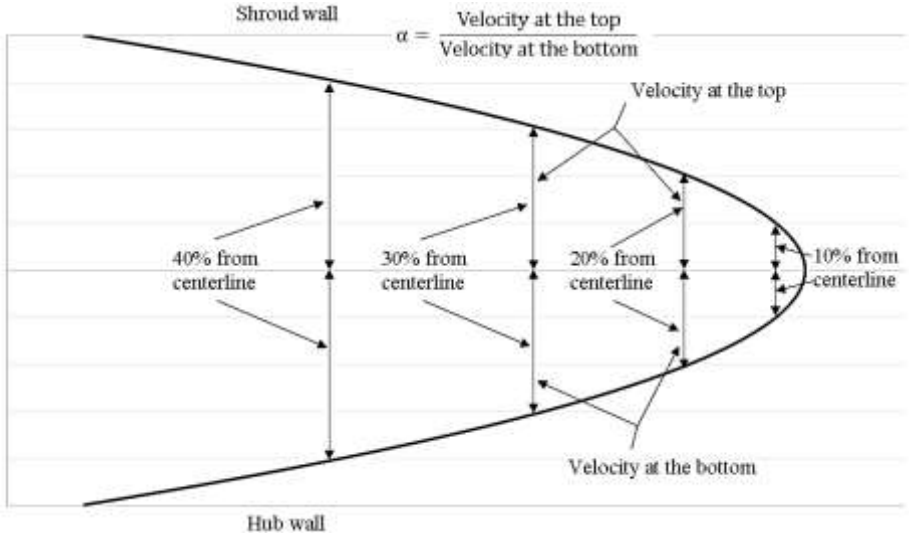

Figure 4.19: Velocity profile

The behaviour of velocity magnitude across the diffuser is explained using symmetric and asymmetric behaviour of the velocity field profiles. A ratio of the velocity magnitude values is obtained at 10%, 20%, 30% and 40% distance from the centreline of the diffuser to the walls and 0% (diffuser inlet), 25%, 50%, 75% and 100% (diffuser outlet) distance from the diffuser inlet to the diffuser outlet. Figure 4.20 depicts the local asymmetric ratio for the velocity magnitudes, α_{vm} across the diffuser at BEP at an operational speed of 58.9rpsK$^{-1/2}$. α_{vm} values of 1.0 shows the flow is symmetric, α_{vm} values below 1.0 shows asymmetric flow towards the hub wall and α_{vm} values above 1.0 shows asymmetric

flow towards the shroud wall. It can be seen that the flow is asymmetric towards the shroud wall across the straight diffuser. The asymmetric ratio for the velocity magnitude increases from the centreline of the straight diffuser towards the wall and from the diffuser inlet to the diffuser outlet.

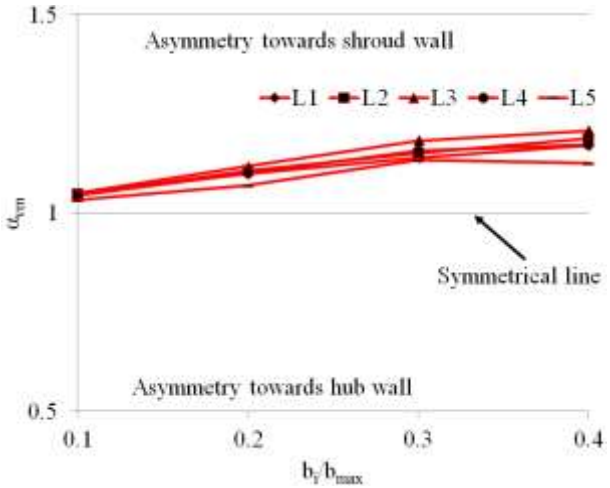

Figure 4.20: Local asymmetric ratio for the velocity magnitude, α_{vm} across the diffuser at BEP at an operational speed of 58.9rpsK$^{-1/2}$

Figure 4.21 depicts the comparison of velocity magnitude distribution across the centreline of the diffuser at the design condition and near off-design conditions at an operational speed of 58.9rpsK$^{-1/2}$. It can be seen that the velocity magnitude at the diffuser inlet is similar at near choke condition in comparison to that at BEP, whereas the velocity magnitude is higher at near surge condition in comparison to that at BEP. Furthermore, the velocity magnitude is almost similar at L2 at both near choke condition and surge condition in comparison to that at BEP. Thereafter, the velocity magnitude is decreased at L4 and L5 (diffuser outlet) at near choke condition in comparison to that at BEP. However, the velocity magnitude is increased at L4 and L5 (diffuser outlet) at near surge condition in comparison to that at BEP. The detailed analysis has been carried out by quantifying the asymmetric ratio for the velocity magnitude profile across the diffuser at design and near off-design conditions.

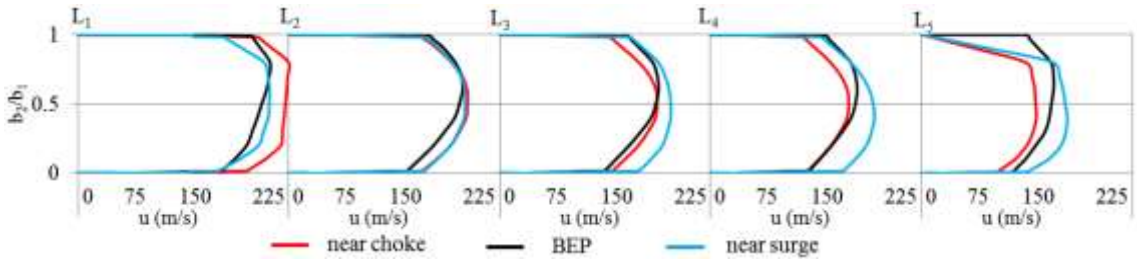

Figure 4.21: Comparison of velocity magnitude (m/s) distribution across the centreline of the diffuser at an operational speed of 58.9rpsK$^{-1/2}$ between design condition (BEP) and off-design conditions (at near choke and at near surge conditions)

Figure 4.22 depicts the local asymmetric ratio for the velocity magnitudes, α_{vm} across the diffuser at near off-design conditions at an operational speed of 58.9rpsK$^{-1/2}$. It can be seen that the flow is near symmetric line, showing less asymmetric ratio for the velocity magnitude at near choke condition in comparison to that BEP. Furthermore, it can be seen in Figure 4.22(b) that the flow is asymmetric at near surge condition across the diffuser. However, the asymmetric ratio is higher than 1.0 at L1 (diffuser inlet) and L2, showing asymmetry towards the shroud wall and the asymmetric ratio is lower than 1.0 at L3, L4 and L5 (diffuser outlet), showing asymmetry towards the hub wall. Moreover, it can be seen that at L5 (diffuser outlet) and 40% away from the centreline of the diffuser, the asymmetric ratio is nearly 0.5 at near choke condition and at near surge condition. This is because the diffuser wall is diverged near the diffuser outlet, which causes increase in the area ratio and hence has a significant effect on the asymmetric ratio.

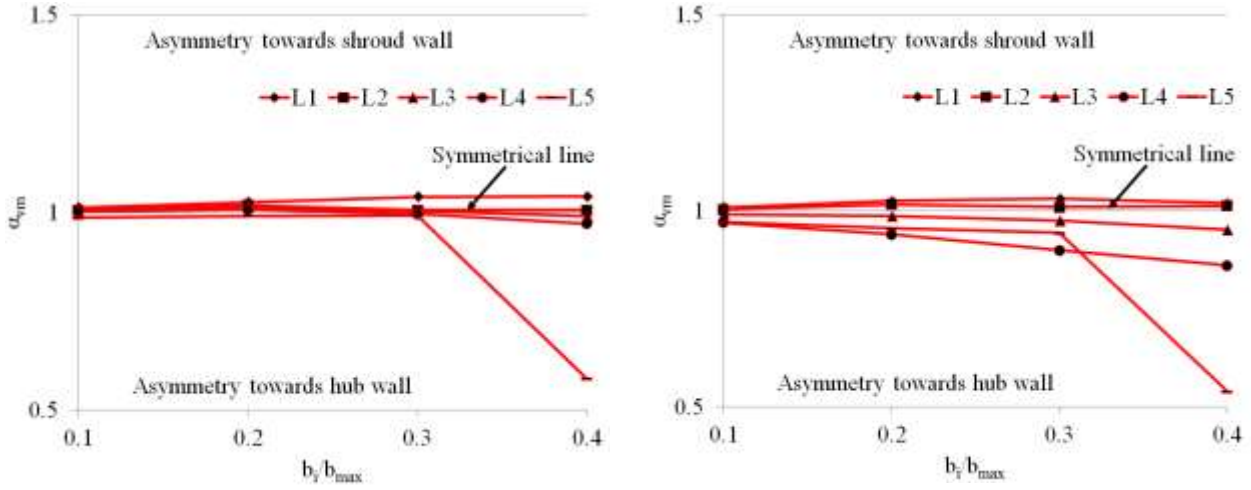

Figure 4.22: Local asymmetric ratio for the velocity magnitude, α_{vm} across the diffuser at design condition and at near off-design conditions at an operational speed of 58.9rpsK$^{-1/2}$

Figure 4.23 depicts the velocity magnitude distribution across the diffuser from the hub wall to the shroud wall at BEP at an operational speed of 78.6rpsK$^{-1/2}$. It can be seen that the velocity magnitude is reduced radially across the diffuser having a maximum velocity of 264m/s at the diffuser inlet and 195m/s at the diffuser outlet. The velocity at the hub and the shroud walls is 0m/s because of no-slip wall boundary condition. Furthermore, it can be seen that the velocity magnitude is higher near the

shroud wall and lower near the hub wall. Moreover, it can also be seen that the flow across the diffuser asymmetric. However, the detailed analysis has been carried out by quantifying the asymmetric ratio for the velocity magnitude profile across the diffuser.

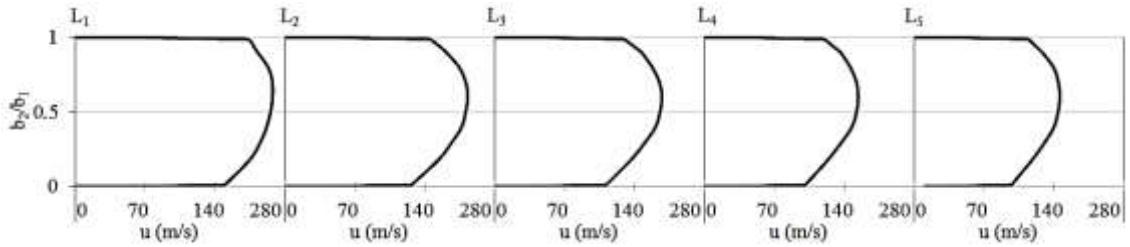

Figure 4.23: Velocity magnitude (m/s) distribution across the diffuser from the hub wall to the shroud wall at BEP at an operational speed of 78.6rpsK$^{-1/2}$

The behaviour of velocity magnitude across the diffuser is explained using symmetric and asymmetric behaviour of the velocity field profiles. Figure 4.24 depicts the local asymmetric ratio for the velocity magnitudes, α_{vm} across the diffuser at BEP at the operational speeds of 58.9rpsK$^{-1/2}$ and 78.6rpsK$^{-1/2}$. It can be seen that the flow is asymmetric towards the shroud wall across the straight diffuser. The asymmetric ratio is increasing from the centreline to the wall at BEP at an operational speed of 78.6rpsK$^{-1/2}$ similar to that at an operational speed of 58.9rpsK$^{-1/2}$. Same trend is found across the straight diffuser from P1 (diffuser inlet) to P5 (diffuser outlet) at an operational speed of 78.6rpsK$^{-1/2}$ in comparison to that at an operational speed of 58.9rpsK$^{-1/2}$.

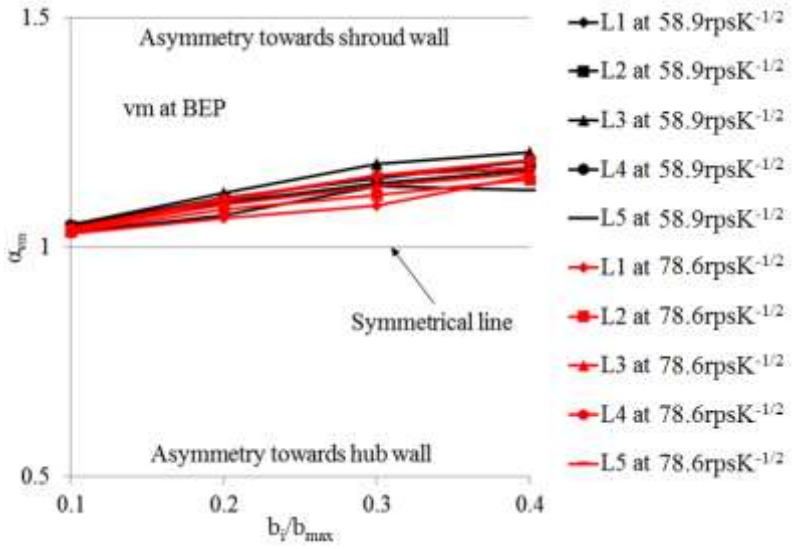

Figure 4.24: Local asymmetric ratio for the velocity magnitude, α_{vm} across the diffuser at BEP at the operational speeds of 58.9rpsK$^{-1/2}$ and 78.6rpsK$^{-1/2}$

Figure 4.25 depicts the comparison of velocity magnitude distribution across the centreline of the diffuser at the design condition and near off-design conditions at an operational speed of 78.6rpsK$^{-1/2}$. It can be seen that the velocity magnitude at the diffuser inlet is higher at near off-design conditions in comparison to that at BEP. Furthermore, the velocity magnitude is almost similar at L2 at both near choke condition and surge condition in comparison to that at BEP. Thereafter, the velocity magnitude is decreased at L4 and L5 (diffuser outlet) at near choke condition in comparison to that at BEP. However, the velocity magnitude is increased at L4 and L5 (diffuser outlet) at near surge condition in comparison to that at BEP. The detailed analysis has been carried out by quantifying the asymmetric ratio for the velocity magnitude profile across the diffuser at design and near off-design conditions. This will help to obtain the effect of asymmetric ratio for the velocity magnitude on the design and off-design conditions.

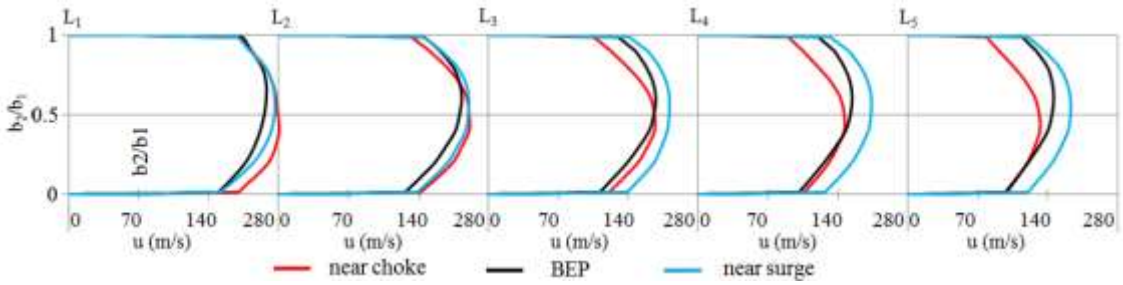

Figure 4.25: Comparison of velocity magnitude (m/s) distribution across the centreline of the diffuser at an operational speed of 78.6rpsK$^{-1/2}$ between design condition (BEP) and off-design conditions (at near choke and at near surge conditions)

Figure 4.26 depicts the comparison of local asymmetric ratio for the velocity magnitudes, α_{vm} across the diffuser at near off-design conditions between the operational speeds of 58.9rpsK$^{-1/2}$ and 78.6rpsK$^{-1/2}$. It can be seen that the flow is highly asymmetric having asymmetric ratio less than 1.0 in comparison to that at 58.9rpsK$^{-1/2}$. The asymmetric ratio is decreasing from the centreline to the wall at near choke condition (Figure 4.26(a)) in comparison to that at an operational speed of 58.9rpsK$^{-1/2}$. The flow is asymmetric towards the hub wall and it is increasing across the diffuser from L1 (diffuser inlet) to L5 (diffuser outlet). Furthermore, it can be seen in Figure 4.26(b) that the flow is asymmetric at near surge condition across the diffuser. However, the asymmetric ratio is higher than 1.0 across the width of the diffuser, which shows asymmetry towards the shroud wall. However, the asymmetric ratio is decreasing from L1 (diffuser inlet) to L5 (diffuser outlet) in comparison to that at an operational speed of 58.9rpsK$^{-1/2}$.

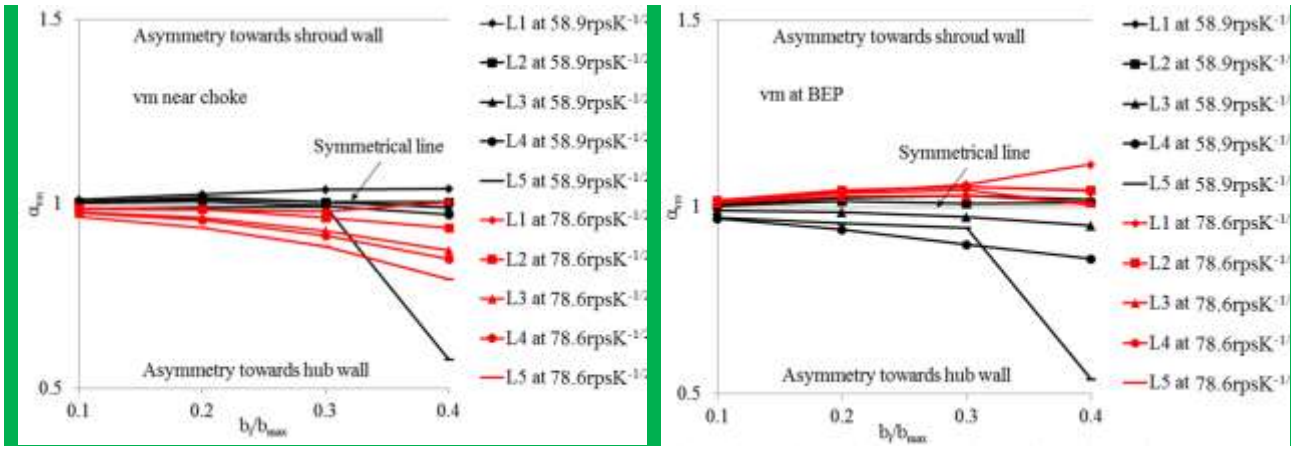

(a) (b)

Figure 4.26: Local asymmetric ratio for the velocity magnitude, α_{vm} across the diffuser at design condition and at near off-design conditions at the operational speeds of 58.9rpsK$^{-1/2}$ and 78.6rpsK$^{-1/2}$

Figure 4.27 depicts the radial velocity distribution across the centreline of the diffuser at BEP at an operational speed of 58.9rpsK$^{-1/2}$. It can be seen that the radial velocity is high at the diffuser inlet and it is reducing radially towards diffuser outlet. Furthermore, it can also be seen that radial velocity is maximum after the volute-tongue region having a magnitude of 103m/s and reduces circumferentially in the direction of impeller rotation. The radial velocity is minimum at the diffuser outlet near the volute-tongue region having a magnitude of 57m/s. However, the reduction of radial velocity in the radial direction is higher in comparison to the reduction in the circumferential direction.

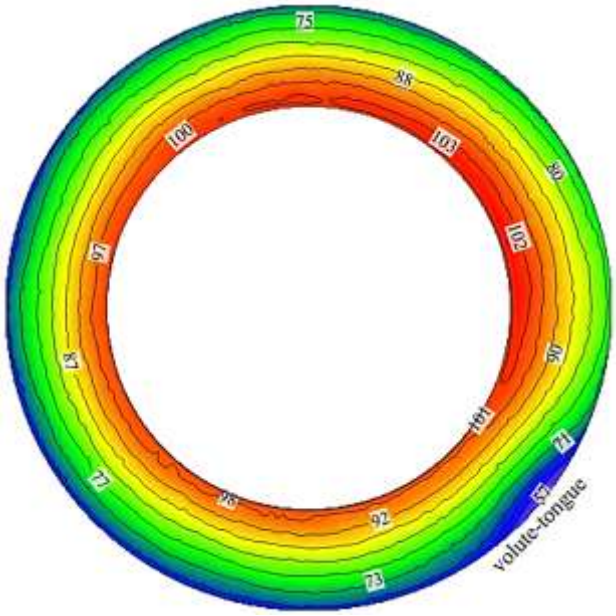

Figure 4.27: Radial velocity (m/s) distribution across the centreline of the diffuser at BEP at an operational speed of 58.9rpsK$^{-1/2}$

Figure 4.28 depicts the radial velocity distribution across the centreline of the diffuser at BEP at an operational speed of 78.6rpsK$^{-1/2}$. The trend in the radial velocity distribution within the diffuser is similar to that BEP at an operational speed of 58.9rpsK$^{-1/2}$. The radial velocity is maximum at the diffuser inlet after the volute-tongue region, which is 29% higher in comparison to that at BEP at an operational speed of 58.9rpsK$^{-1/2}$. Furthermore, the radial velocity is minimum at the diffuser outlet near the volute-tongue region, which is 24% higher in comparison to that at BEP at an operational speed of 58.9rpsK$^{-1/2}$.

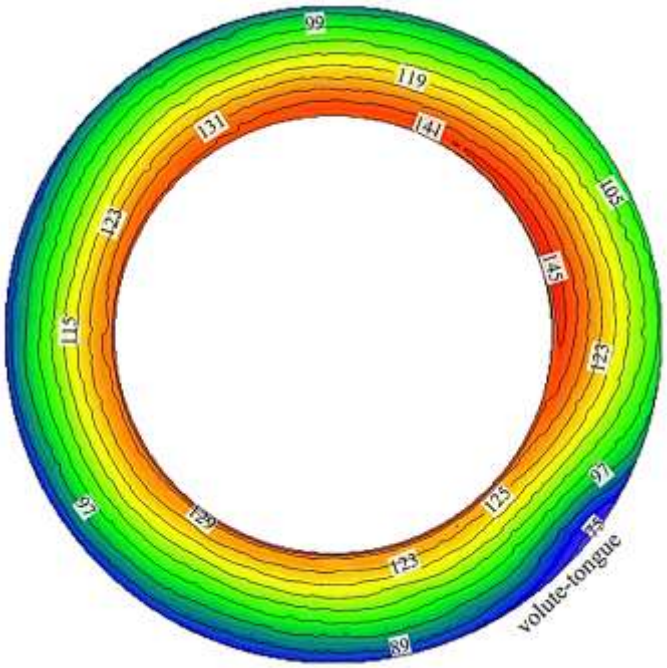

Figure 4.28: Radial velocity (m/s) distribution across the centreline of the diffuser at BEP at an operational speed of 78.6rpsK$^{-1/2}$

Figure 4.29(a) depicts the radial velocity distribution across the centreline of the diffuser at near choke condition at an operational speed of 58.9rpsK$^{-1/2}$. The overall radial velocity is higher within the diffuser at near choke condition in comparison to that at BEP. It can be seen that maximum radial velocity of 182m/s is obtained at the diffuser inlet before the volute-tongue region. The radial velocity decreases radially across the diffuser similar to that at BEP. Furthermore, the radial velocity also decreases circumferentially in the direction of rotation having the maximum radial velocity at the diffuser inlet before volute-tongue region and minimum radial velocity of 108m/s at the diffuser outlet after the volute-tongue region. Figure 4.29(b) depicts the radial velocity distribution across the

centreline of the diffuser at near surge condition at an operational speed of 58.9rpsK$^{-1/2}$. The trend of radial velocity is similar to that at BEP. However, the overall radial velocity is lower within the diffuser near surge condition in comparison to that at BEP. The minimum radial velocity is 15m/s at the diffuser outlet near volute-tongue region and the maximum radial velocity is 71m/s at the diffuser inlet after the volute-tongue region.

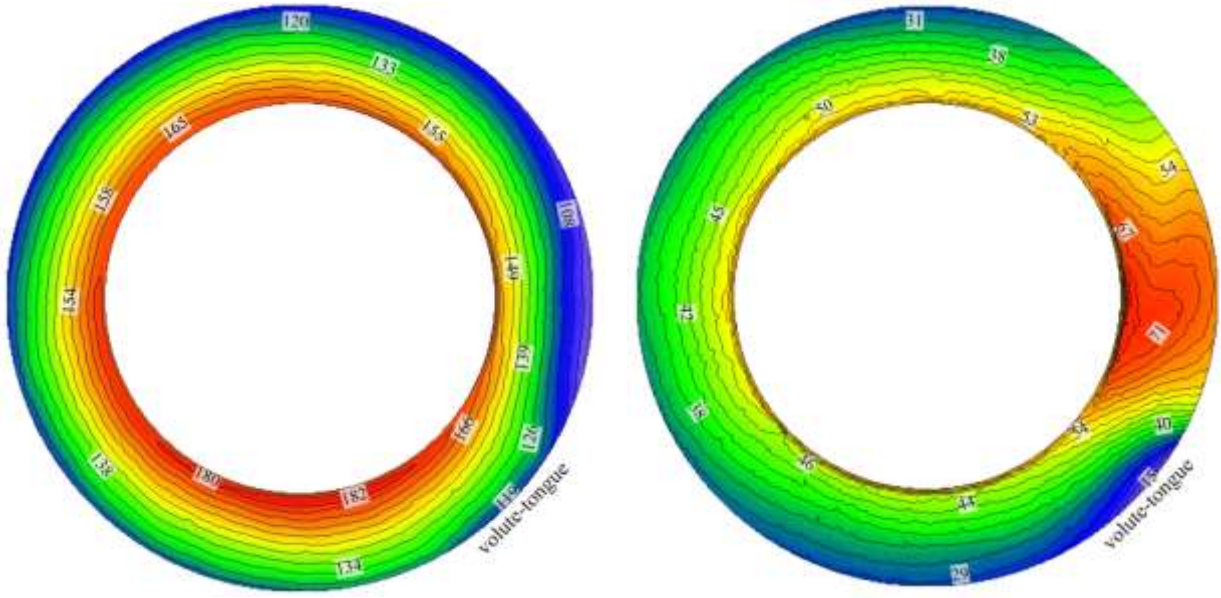

(a) (b)

Figure 4.29: Radial velocity (m/s) distribution across the centreline of the diffuser at an operational speed of 58.9rpsK$^{-1/2}$ at near off-design conditions (a) near choke and (b) near surge

Figure 4.30(a) depicts the radial velocity distribution across the centreline of the diffuser at near choke condition at an operational speed of 78.6rpsK$^{-1/2}$. The overall radial velocity is higher within the diffuser at near choke condition in comparison to that at near choke condition at an operational speed of 58.9rpsK$^{-1/2}$. However, the trend of radial velocity distribution is similar in comparison to that at near choke condition at an operational speed of 58.9rpsK$^{-1/2}$. It can be seen that maximum radial velocity is obtained at the diffuser inlet before the volute-tongue region, which is 27% higher in comparison to that at an operational speed of 58.9rpsK$^{-1/2}$. The minimum radial velocity is obtained at the diffuser outlet after the volute-tongue region, which is 26% higher in comparison to that at an operational speed of 58.9rpsK$^{-1/2}$. Figure 4.30(b) depicts the radial velocity distribution across the centreline of the diffuser at near surge condition at an operational speed of 78.6rpsK$^{-1/2}$. The overall radial velocity is higher within the diffuser at near surge condition in comparison that at near surge condition at an operational speed of 58.9rpsK$^{-1/2}$. However, the trend of radial velocity distribution is similar to that at an operational speed of 58.9rpsK$^{-1/2}$. It can be seen that maximum radial velocity is

obtained at the diffuser inlet after the volute-tongue region, which is 33% higher in comparison to near surge condition at an operational speed of 58.9rpsK$^{-1/2}$. The minimum radial velocity is obtained at the diffuser outlet near volute-tongue region, which is 53% higher in comparison to that at near surge condition at an operational speed of 58.9rpsK$^{-1/2}$.

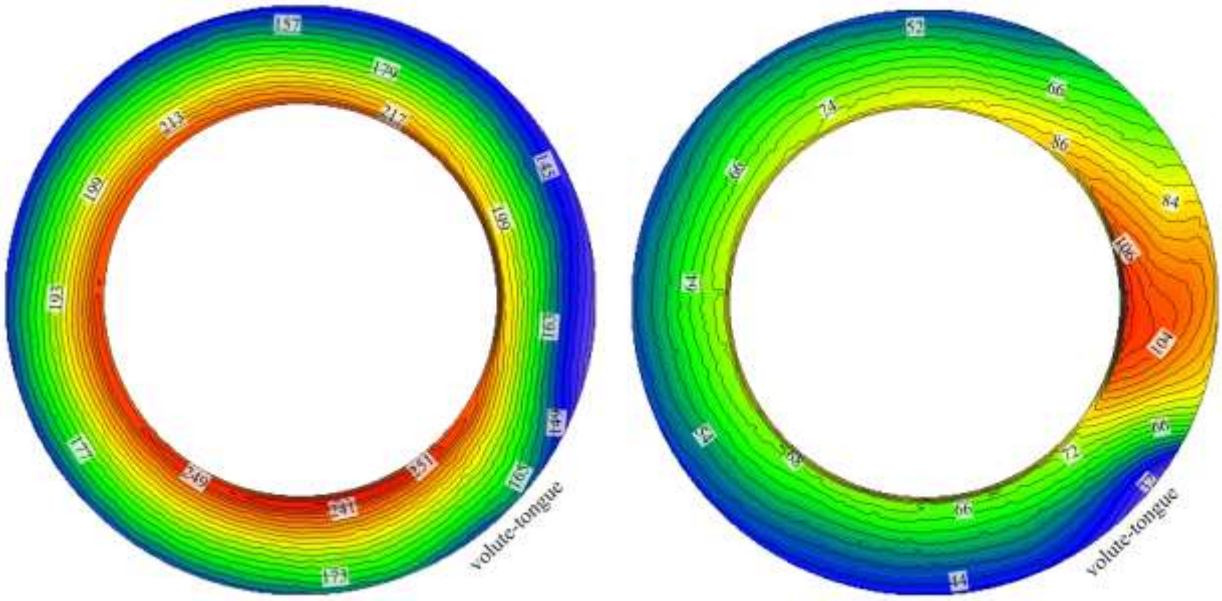

(a) (b)

Figure 4.30: Radial velocity (m/s) distribution across the centreline of the diffuser at an operational speed of 78.6rpsK$^{-1/2}$ at near off-design conditions (a) near choke and (b) near surge

Figure 4.31 depicts the radial velocity distribution across the diffuser from the hub wall to the shroud wall at BEP at an operational speed of 58.9rpsK$^{-1/2}$. It can be seen that radial velocity is reduced radially across the diffuser having a maximum radial velocity of 104m/s at the diffuser inlet and 80m/s at the diffuser outlet. Furthermore, it can also be seen that radial velocity is higher close to the shroud wall and lower close to the hub wall of the diffuser. However, the detailed analysis has been carried out by quantifying the asymmetric ratio for the radial velocity profile across the diffuser.

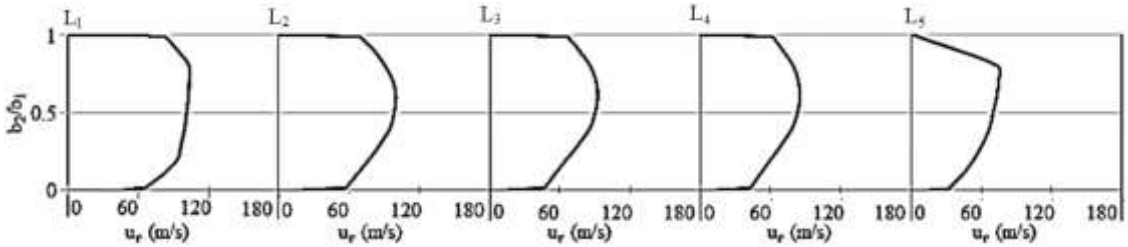

Figure 4.31: Radial velocity (m/s) distribution across the diffuser from the hub wall to the shroud wall at an operational speed of 58.9rpsK$^{-1/2}$ and BEP

Figure 4.32 depicts the local asymmetric ratio for the radial velocity, α_{vr} across the diffuser at BEP at an operational speed of 58.9rpsK$^{-1/2}$. α_{vr} values of 1.0 shows the flow is symmetric, α_{vr} values below 1.0 shows asymmetric flow towards the hub wall and α_{vr} values above 1.0 shows asymmetric flow towards the shroud wall. It can be seen that the flow is asymmetric towards the shroud wall across the straight diffuser. The asymmetric ratio for the radial velocity increases from the centreline of the straight diffuser towards the wall and from the L1 (diffuser inlet) to the L5 (diffuser outlet). Moreover, it can be seen that at L5 (diffuser outlet) and 40% away from the centreline of the diffuser, the asymmetric ratio is nearly 0.2. This is because the diffuser wall is diverged near the diffuser outlet, which causes increase in the area ratio and hence has a significant effect on the asymmetric ratio for the radial velocity.

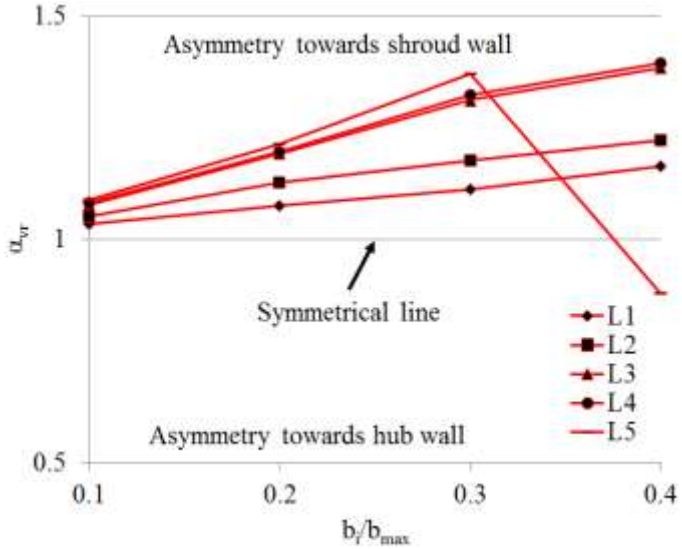

Figure 4.32: Local radial velocity ratio, α_{vr} across the diffuser at BEP at an operational speed of 58.9rpsK$^{-1/2}$

Figure 4.33 depicts the comparison of radial velocity distribution across the diffuser from the hub wall to the shroud wall between the design condition and near off-design conditions at an operational speed of 58.9rpsK$^{-1/2}$. It can be seen that the radial velocity distribution at near choke condition is higher in comparison to that at BEP, whereas radial velocity is lower at near surge condition in comparison to that at BEP. The detailed analysis has been carried out by quantifying the asymmetric ratio for the radial velocity profile across the diffuser at design and near off-design conditions. This will help to obtain the effect of asymmetric ratio for the radial velocity on the design and off-design conditions.

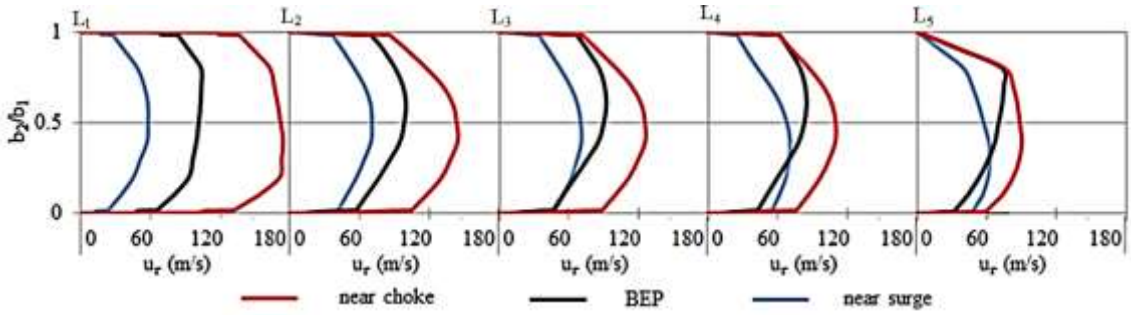

Figure 4.33: Comparison of radial velocity (m/s) distribution across the diffuser from the hub wall to the shroud wall at an operational speed of 58.9rpsK$^{-1/2}$ between the design condition (BEP) and near off-design conditions (near choke condition and near surge condition)

Figure 4.34 depicts the local asymmetric ratio for the radial velocity, α_{vr} across the diffuser at near off-design conditions at an operational speed of 58.9rpsK$^{-1/2}$. It can be seen that the flow is highly asymmetric having asymmetric ratio less than 1.0 at near choke condition in comparison to that at BEP. The asymmetric ratio is decreasing from the centreline to the wall at near choke condition at in comparison to that at BEP. The flow is asymmetric towards the hub wall and it is increasing across the diffuser from L1 (diffuser inlet) to L5 (diffuser outlet). Furthermore, it can be seen in Figure 4.34(b) that the flow is asymmetric at near surge condition across the diffuser. However, the asymmetric ratio is higher than 1.0 across the width of the diffuser, which shows asymmetry towards the shroud wall. Moreover, the asymmetric ratio is increasing from L1 (diffuser inlet) to L5 (diffuser outlet) in comparison to that at BEP.

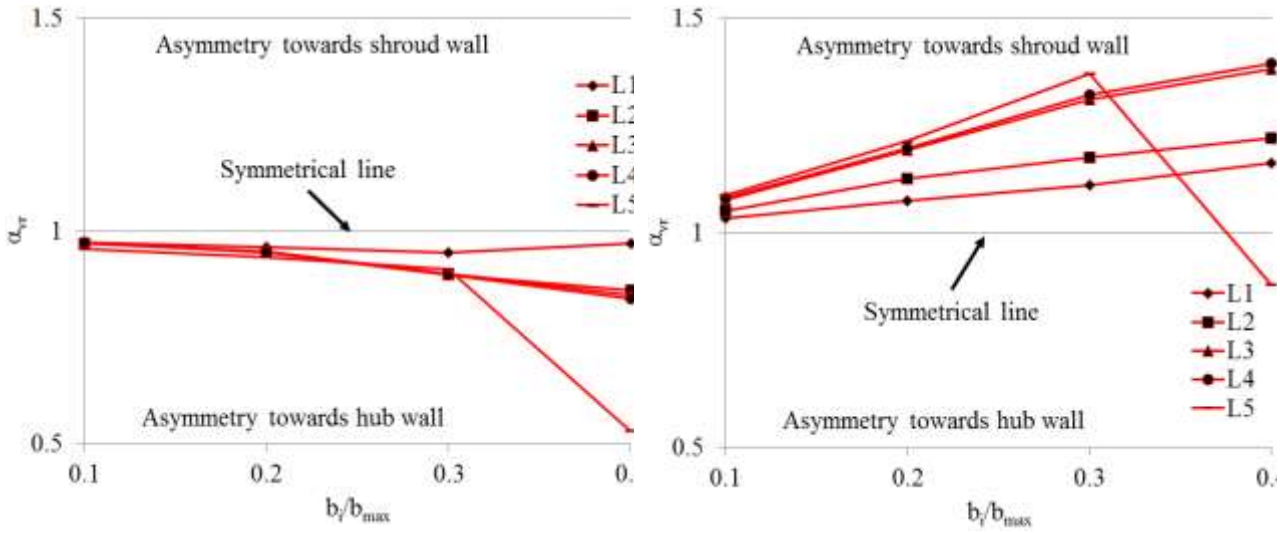

(a) (b)

Figure 4.34: Local radial velocity ratio, α_{vr} across the diffuser near off-design conditions at an operational speed of 58.9rpsK$^{-1/2}$

Figure 4.35 depicts the radial velocity distribution across the diffuser from the hub wall to the shroud wall at BEP at an operational speed of 78.6rpsK$^{-1/2}$. It can be seen that the radial velocity is reduced radially across the diffuser having a maximum velocity of 145m/s at the diffuser inlet and 112m/s at the diffuser outlet. The radial velocity at the hub and the shroud walls is 0m/s because of no-slip wall boundary condition. Furthermore, it can be seen that the flow is symmetric from L1 (diffuser inlet) to L2 and then it becomes asymmetric up to L5 (diffuser outlet). However, the detailed analysis has been carried out by quantifying the asymmetric ratio for the radial velocity profile across the diffuser.

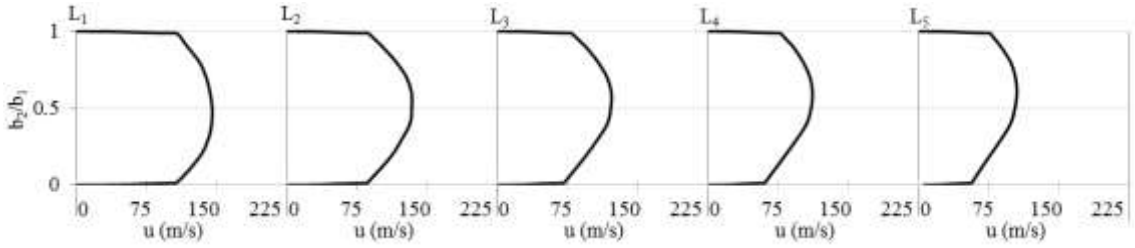

Figure 4.35: Radial velocity (m/s) distribution across the diffuser from the hub wall to the shroud wall at BEP at an operational speed of 78.6rpsK$^{-1/2}$

The behaviour of radial velocity across the diffuser is explained using symmetric and asymmetric behaviour of the radial velocity field profiles. Figure 4.36 depicts the local asymmetric ratio for the radial velocity, α_{vr} across the diffuser at BEP at the operational speeds of 58.9rpsK$^{-1/2}$ and 78.6rpsK$^{-1/2}$. It can be seen that the asymmetric ratio is below 1.0 at L1, showing flow asymmetry towards hub wall in comparison to that at an operational speed of 58.9rpsK$^{-1/2}$. Furthermore, the asymmetric ratio for the radial velocity is higher than 1.0 from L2 to L5 (diffuser outlet), showing flow asymmetry towards shroud wall. However, the overall asymmetric ratio is lower across the diffuser in comparison to that at an operational speed of 58.9rpsK$^{-1/2}$.

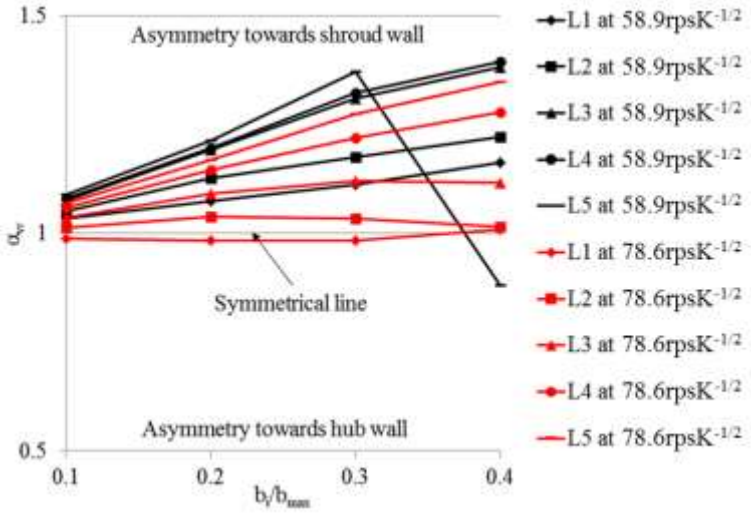

Figure 4.36: Local asymmetric ratio for the radial velocity, α_{vr} across the diffuser at BEP at the operational speeds of 58.9rpsK$^{-1/2}$ and 78.6rpsK$^{-1/2}$

Figure 4.37 depicts the comparison of radial velocity distribution across the centreline of the diffuser at the design condition and at near off-design conditions at an operational speed of 78.6rpsK$^{-1/2}$. It can be seen that the radial velocity at the diffuser inlet is higher at near choke condition and lower at near surge condition in comparison to that at BEP. This trend persists from L1 (diffuser inlet) to L2. The radial velocity reduces near shroud wall at near surge condition in comparison to that at BEP. The detailed analysis has been carried out by quantifying the asymmetric ratio for the radial velocity profile across the diffuser at design and near off-design conditions.

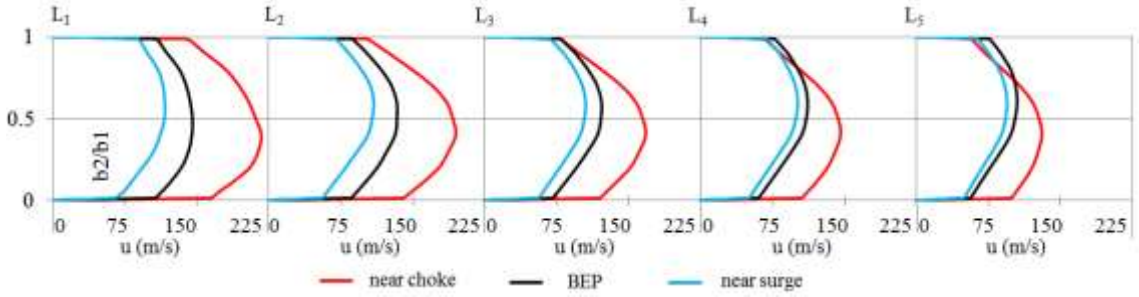

Figure 4.37: Comparison of radial velocity (m/s) distribution across the centreline of the diffuser at an operational speed of 78.6rpsK$^{-1/2}$ between design condition (BEP) and off-design conditions (at near choke and at near surge conditions)

Figure 4.38 depicts the comparison of local asymmetric ratio for the radial velocities, α_{vr} across the diffuser at near off-design conditions between the operational speeds of 58.9rpsK$^{-1/2}$ and 78.6rpsK$^{-1/2}$. It can be seen that the flow is highly asymmetric having asymmetric ratio less than 1.0 in comparison to that at 58.9rpsK$^{-1/2}$. The asymmetric ratio is decreasing from the centreline to the wall

at near choke condition (Figure 4.38(a)) in comparison to that at an operational speed of 58.9rpsK$^{-1/2}$. The radial flow velocity is asymmetric towards the hub wall and it is increasing across the diffuser from L1 (diffuser inlet) to L5 (diffuser outlet). Furthermore, it can be seen in Figure 4.38(b) that the flow is asymmetric at near surge condition across the diffuser. However, the asymmetric ratio is higher than 1.0 across the width of the diffuser, which shows asymmetry towards the shroud wall. However, the asymmetric ratio for the radial velocity is decreasing from L1 (diffuser inlet) to L5 (diffuser outlet) in comparison to that at an operational speed of 58.9rpsK$^{-1/2}$.

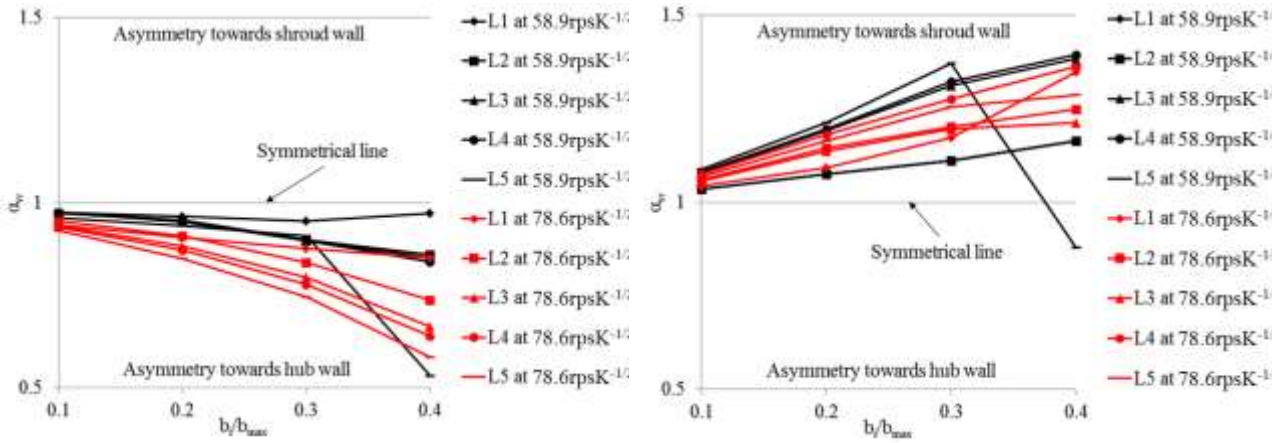

(a) (b)

Figure 4.38: Local asymmetric ratio for the radial velocity, α_{vr} across the diffuser at design condition and at near off-design conditions at the operational speeds of 58.9rpsK$^{-1/2}$ and 78.6rpsK$^{-1/2}$

Figure 4.39 depicts the circumferential velocity distribution across the centreline of the diffuser at BEP at an operational speed of 58.9rpsK$^{-1/2}$. It can be seen that the circumferential velocity is higher at the diffuser inlet and is reducing radially towards diffuser outlet. Furthermore, it can also be seen that circumferential velocity is higher after the volute-tongue region and reduces circumferentially in the direction of rotation. The circumferential velocity is maximum at the diffuser inlet after the volute-tongue region having a magnitude of 167m/s. Similarly, the circumferential velocity is minimum at the diffuser outlet near volute-tongue region having a magnitude of 103m/s. However, the rate of reduction of circumferential velocity in the radial direction is higher in comparison to the reduction in the circumferential direction.

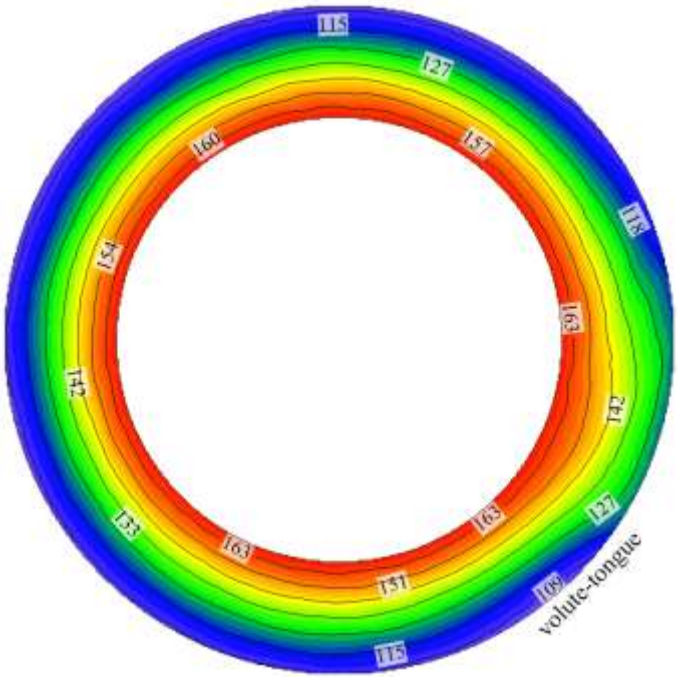

Figure 4.39: Circumferential velocity (m/s) distribution across the centreline of the diffuser at BEP at an operational speed of 58.9rpsK$^{-1/2}$

Figure 4.40 depicts the circumferential velocity distribution across the centreline of the diffuser at BEP and an operational speed of 78.6rpsK$^{-1/2}$. The trend in the circumferential velocity distribution within the diffuser is similar in comparison to that at an operational speed of 58.9rpsK$^{-1/2}$. The circumferential velocity is minimum at the diffuser outlet near the volute-tongue region, which is 29% higher in comparison to that at an operational speed of 58.9rpsK$^{-1/2}$. The circumferential velocity is maximum at the diffuser inlet after the volute-tongue region, which is 24% higher in comparison to that at an operational speed of 58.9rpsK$^{-1/2}$.

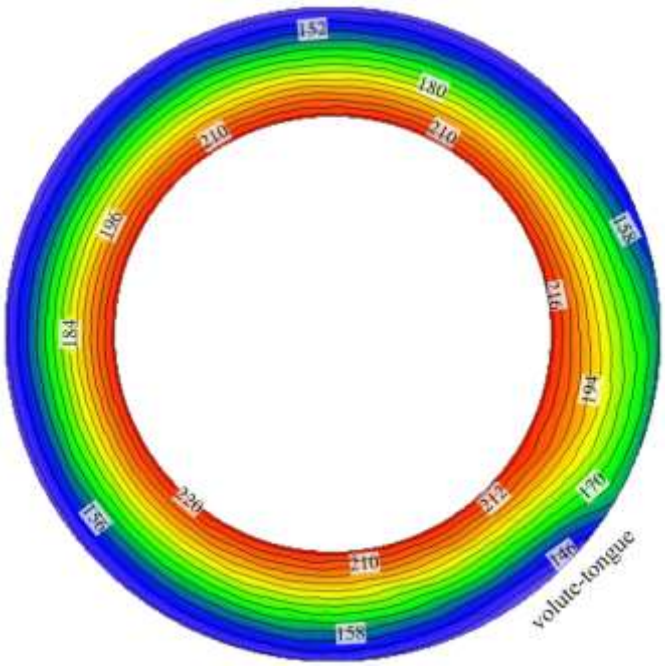

Figure 4.40: Circumferential velocity (m/s) distribution across the centreline of the diffuser at BEP at an operational speed of 78.6rpsK$^{-1/2}$

Figure 4.41 depicts the circumferential velocity distribution across the diffuser from the hub wall to the shroud wall at BEP at an operational speed of 58.9rpsK$^{-1/2}$. It can be seen that the circumferential velocity is reducing radially across the diffuser having a maximum circumferential velocity of 178m/s at the diffuser inlet and 125m/s at the diffuser outlet. Furthermore, it can also be seen that the circumferential velocity is higher near the shroud wall and lower near the hub wall and shows asymmetric flow behaviour. However, the detailed analysis has been carried out by quantifying the asymmetric ratio for the circumferential velocity profile across the diffuser.

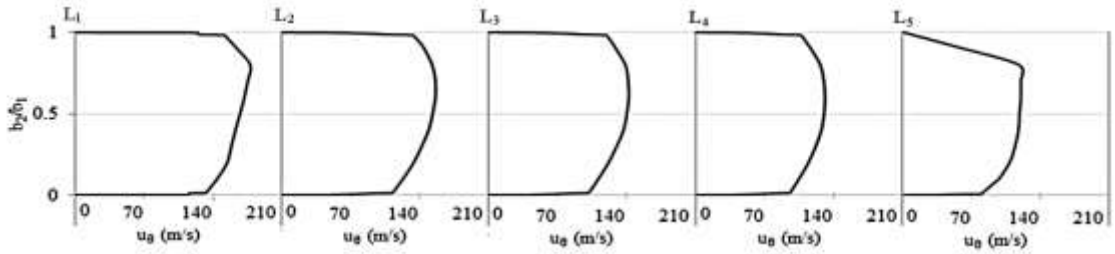

Figure 4.41: Circumferential velocity (m/s) distribution across the diffuser from the hub wall to the shroud wall at BEP at an operational speed of 58.9rpsK$^{-1/2}$

Figure 4.42 depicts the local asymmetric ratio for the circumferential velocity, α_{vc} across the diffuser at BEP at an operational speed of 58.9rpsK$^{-1/2}$. α_{vc} values of 1.0 shows the flow is symmetric, α_{vc} values below 1.0 shows asymmetric flow towards the hub wall and α_{vc} values above 1.0 shows

asymmetric flow towards the shroud wall. It can be seen that the flow is asymmetric towards the shroud wall across the straight diffuser. The asymmetric ratio for the circumferential velocity increases from the centreline of the straight diffuser towards the wall and decreases from the L1 (diffuser inlet) to the L5 (diffuser outlet). Moreover, it can be seen that at L5 (diffuser outlet) and 40% away from the centreline of the diffuser, the asymmetric ratio is nearly 0.4. This is because the diffuser wall is diverged near the diffuser outlet, which causes increase in the area ratio and hence has a significant effect on the asymmetric ratio for the circumferential velocity.

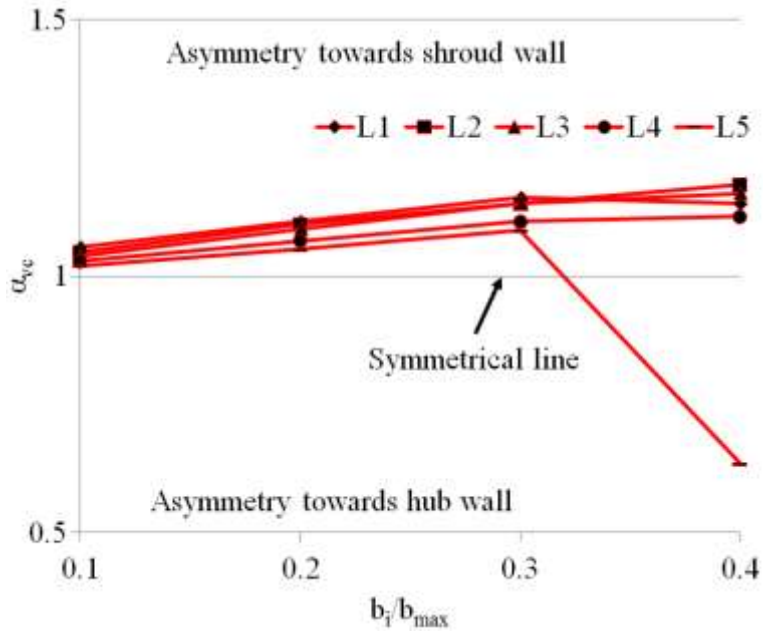

Figure 4.42: Local asymmetric ratio for the circumferential velocity, α_{vc} across the diffuser at BEP at an operational speed of 58.9rpsK$^{-1/2}$

Figure 4.43(a) depicts the circumferential velocity distribution across the centreline of the diffuser at near choke condition at an operational speed of 58.9rpsK$^{-1/2}$. The overall circumferential velocity is higher within the diffuser at near choke condition in comparison to that at BEP. It can be seen that maximum circumferential velocity of 186m/s is obtained at the diffuser inlet before the volute-tongue region. The circumferential velocity decreases radially across the diffuser similar to that at BEP. Furthermore, the circumferential velocity also decreases circumferentially in the direction of rotation having the maximum circumferential velocity at the diffuser inlet before volute-tongue region and minimum circumferential velocity of 100m/s at the diffuser outlet near the volute-tongue region. Figure 4.43(b) depicts the circumferential velocity distribution across the centreline of the diffuser at near surge condition at an operational speed of 58.9rpsK$^{-1/2}$. The trend of circumferential velocity is similar to that at BEP. The minimum circumferential velocity is 102m/s at the diffuser outlet at 110˚

from the volute-tongue region, in the direction of rotation. The maximum circumferential velocity is 198m/s at the diffuser inlet after the volute-tongue region.

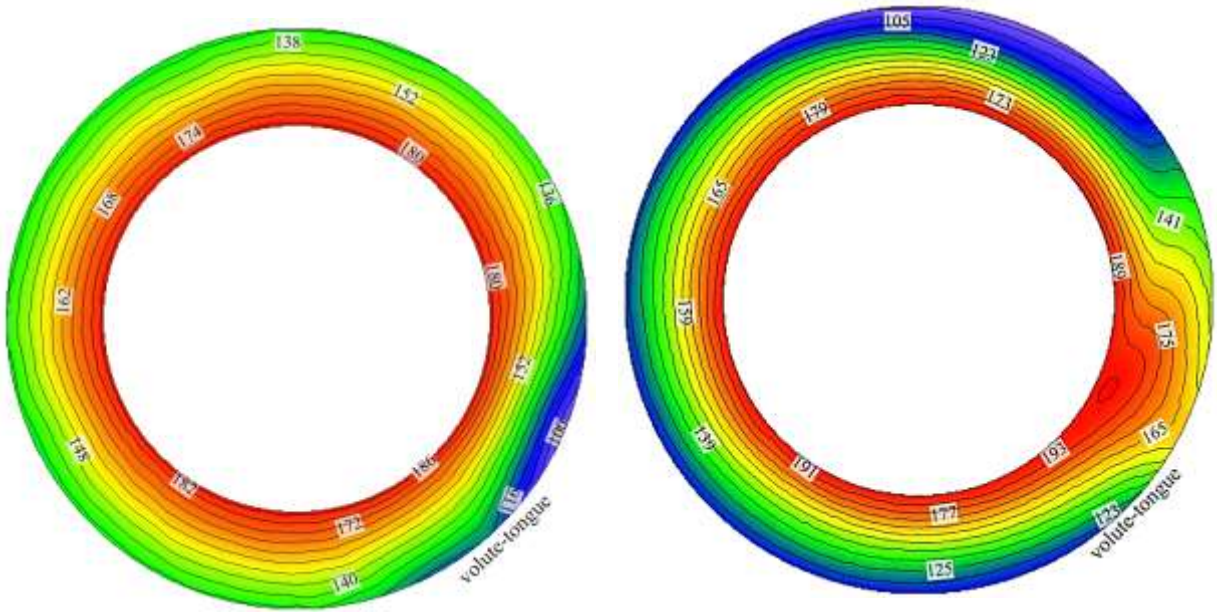

(a) (b)

Figure 4.43. Circumferential velocity (m/s) distribution across the centreline of the diffuser at an operational speed of 58.9rpsK$^{-1/2}$ at near off-design conditions (a) near choke and (b) near surge

Figure 4.44(a) depicts the circumferential velocity distribution across the centreline of the diffuser at near choke condition at an operational speed of 78.6rpsK$^{-1/2}$. The overall circumferential velocity is higher within the diffuser at near choke condition in comparison to that at an operational speed of 58.9rpsK$^{-1/2}$. However, the trend circumferential velocity distribution is similar to that at an operational speed of 58.9rpsK$^{-1/2}$. It can be seen that maximum circumferential velocity is obtained at the diffuser inlet before the volute-tongue region, which is 24% higher in comparison to that at an operational speed of 58.9rpsK$^{-1/2}$. The minimum circumferential velocity is obtained at the diffuser outlet after the volute-tongue region, which is 32% higher in comparison to that at an operational speed of 58.9rpsK$^{-1/2}$. Figure 4.44(b) depicts the circumferential velocity distribution across the centreline of the diffuser at near surge condition at an operational speed of 78.6rpsK$^{-1/2}$. The overall circumferential velocity is higher within the diffuser at near surge condition in comparison to that at an operational speed of 58.9rpsK$^{-1/2}$. However, the trend of circumferential velocity distribution is similar to that at an operational speed of 58.9rpsK$^{-1/2}$. It can be seen that maximum circumferential velocity is obtained at the diffuser outlet after the volute-tongue region, which is 22% higher in comparison that at an operational speed of 58.9rpsK$^{-1/2}$. The minimum circumferential velocity is

obtained at the diffuser outlet, around 110˚ from the volute-tongue region, in the direction of rotation, which is 42% higher in comparison that at an operational speed of 58.9rpsK$^{-1/2}$

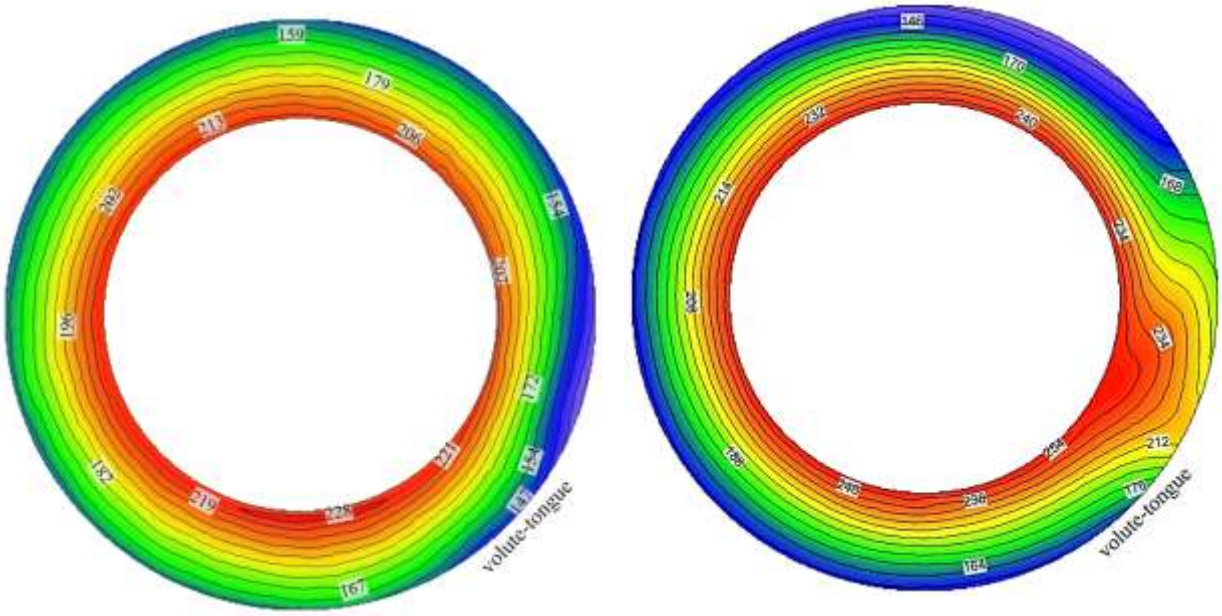

(a) (b)

Figure 4.44: Circumferential velocity (m/s) distribution across the centreline of the diffuser at an operational speed of 78.6rpsK$^{-1/2}$ at near off-design conditions (a) near choke and (b) near surge

Figure 4.45 depicts the comparison of circumferential velocity distribution across the diffuser from the hub wall to the shroud wall between the design condition and near off-design conditions at an operational speed of 58.9rpsK$^{-1/2}$. It can be seen that the circumferential velocity distribution at near choke condition is lower in comparison to that at BEP, whereas circumferential velocity is higher at near surge condition in comparison to that at BEP. Moreover, the detailed analysis has been carried out by quantifying the asymmetric ratio for the circumferential velocity profile across the diffuser at design and near off-design conditions. This will help to obtain the effect of asymmetric ratio for the circumferential velocity on the design and off-design conditions.

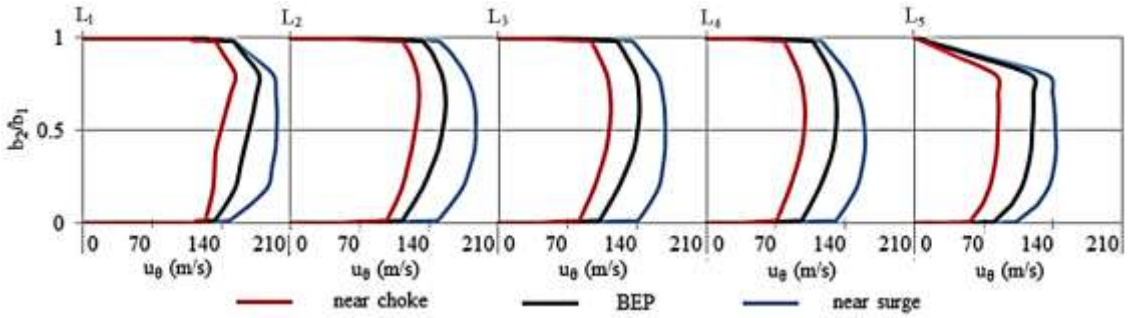

Figure 4.45: Comparison of circumferential velocity (m/s) distribution across the diffuser from the hub wall to the shroud wall at an operational speed of 58.9rpsK$^{-1/2}$ between the design condition (BEP) and near off-design conditions (near choke and near surge)

Figure 4.46 depicts the local asymmetric ratio for the circumferential velocity, α_{vc} across the diffuser at near off-design conditions at an operational speed of 58.9rpsK$^{-1/2}$. It can be seen that the flow is highly asymmetric having asymmetric ratio more than 1.0 at near off-design conditions in comparison to that at BEP. The asymmetric ratio is increasing from the centreline towards the wall at near off-design conditions in comparison to that at BEP. The flow is asymmetric towards the shroud wall and it is decreasing across the diffuser from L1 (diffuser inlet) to L5 (diffuser outlet) in both off-design conditions.

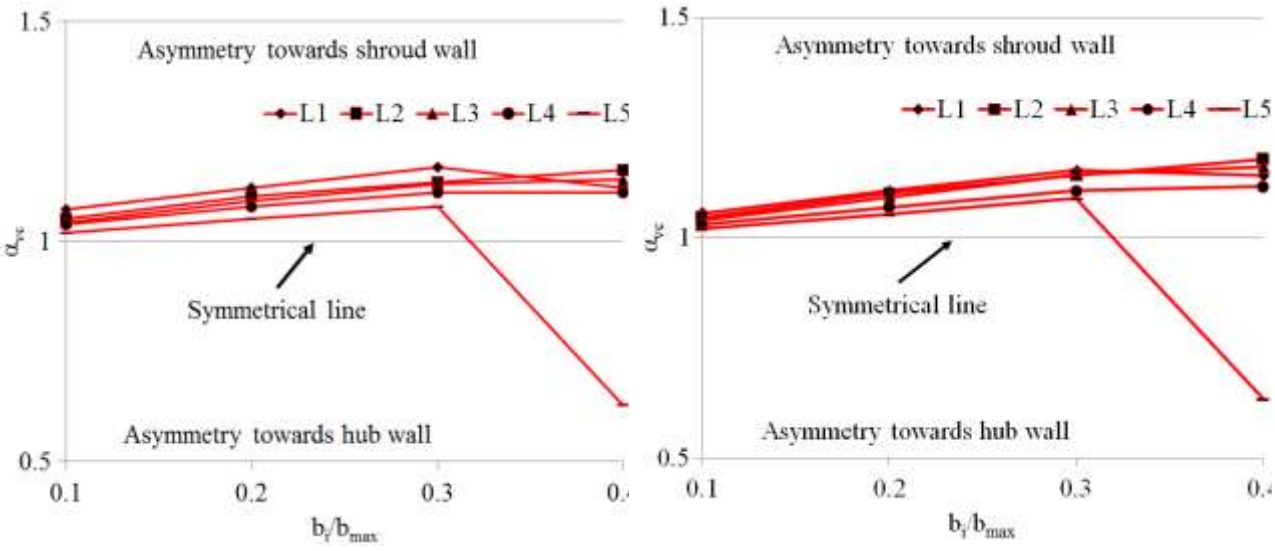

Figure 4.46: Local circumferential velocity ratio, α_{vc} across the diffuser near off-design conditions at an operational speed of 58.9rpsK$^{-1/2}$

Figure 4.47 depicts the circumferential velocity distribution across the diffuser from the hub wall to the shroud wall at BEP at an operational speed of 78.6rpsK$^{-1/2}$. It can be seen that the circumferential

velocity is reduced radially across the diffuser having a maximum circumferential velocity of 224m/s at the diffuser inlet and 164m/s at the diffuser outlet. The circumferential velocity at the hub and the shroud walls is 0m/s because of no-slip wall boundary condition. Furthermore, it can be seen that the flow is asymmetric from L1 (diffuser inlet) to L5 (diffuser outlet). However, the detailed analysis has been carried out by quantifying the asymmetric ratio for the circumferential velocity profile across the diffuser.

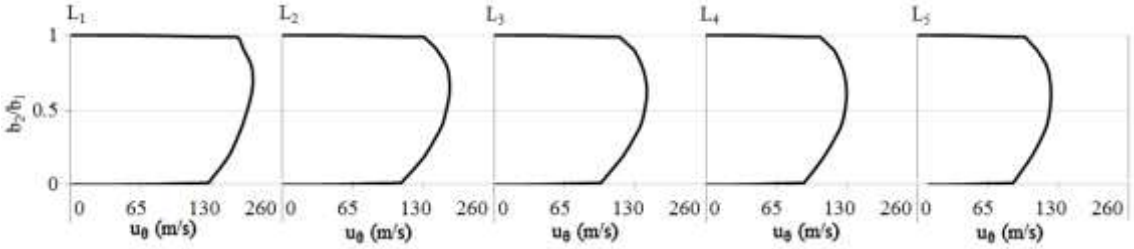

Figure 4.47: Circumferential velocity (m/s) distribution across the diffuser from the hub wall to the shroud wall at BEP at an operational speed of 78.6rpsK$^{-1/2}$

The behaviour of circumferential velocity across the diffuser is explained using symmetric and asymmetric behaviour of the circumferential velocity field profiles. Figure 4.48 depicts the local asymmetric ratio for the radial velocity, α_{vc} across the diffuser at BEP at the operational speeds of 58.9rpsK$^{-1/2}$ and 78.6rpsK$^{-1/2}$. It can be seen that the asymmetric ratio is above 1.0 at L1, showing flow asymmetry towards the shroud wall similar to that at an operational speed of 58.9rpsK$^{-1/2}$. The overall asymmetric ratio is higher across the diffuser in comparison to that at an operational speed of 58.9rpsK$^{-1/2}$.

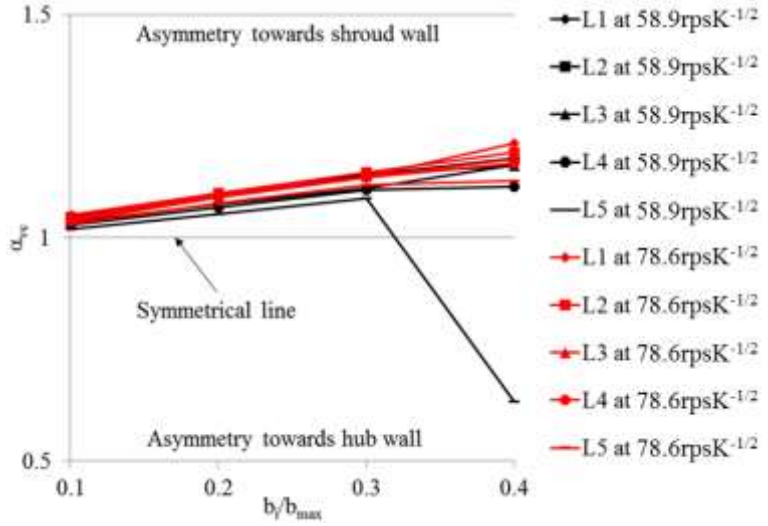

Figure 4.48: Local asymmetric ratio for the circumferential velocity, α_{vc} across the diffuser at BEP at the operational speeds of 58.9rpsK$^{-1/2}$ and 78.6rpsK$^{-1/2}$

Figure 4.49 depicts the comparison of circumferential velocity distribution across the centreline of the diffuser at the design condition and at near off-design conditions at an operational speed of 78.6rpsK$^{-1/2}$. It can be seen that the circumferential velocity at the diffuser inlet is lower at near choke condition and higher at near surge condition in comparison to that at BEP. This trend persists from L1 (diffuser inlet) to L5 (diffuser outlet). The detailed analysis has been carried out by quantifying the asymmetric ratio for the circumferential velocity profile across the diffuser at design and near off-design conditions. This will help to obtain the effect of asymmetric ratio for the circumferential velocity on the design and off-design conditions.

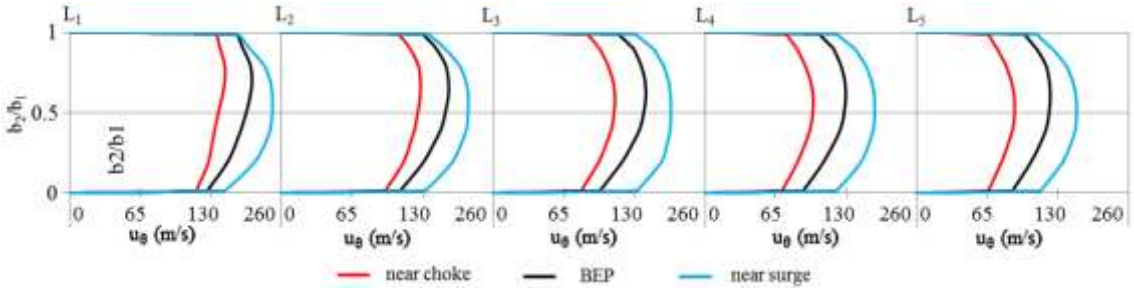

Figure 4.49: Comparison of circumferential velocity (m/s) distribution across the centreline of the diffuser at an operational speed of 78.6rpsK$^{-1/2}$ between design condition (BEP) and off-design conditions (at near choke and at near surge conditions)

Figure 4.50 depicts the comparison of local asymmetric ratio for the circumferential velocities, α_{vc} across the diffuser at near off-design conditions between the operational speeds of 58.9rpsK$^{-1/2}$ and 78.6rpsK$^{-1/2}$. It can be seen that the flow is highly asymmetric having asymmetric ratio more than 1.0 similar to that at 58.9rpsK$^{-1/2}$. The asymmetric ratio is increasing from the centreline to the wall at near choke condition (Figure 4.51(a)) in comparison to that at an operational speed of 58.9rpsK$^{-1/2}$. The circumferential flow velocity is asymmetric towards the shroud wall and it is decreasing across the diffuser from L1 (diffuser inlet) to L5 (diffuser outlet). Furthermore, it can be seen in Figure 4.50(b) that the flow is asymmetric at near surge condition across the diffuser. However, the asymmetric ratio is higher than 1.0 across the width of the diffuser, which shows asymmetry towards the shroud wall. However, the overall asymmetric ratio for the circumferential velocity across the diffuser is lower in comparison to that at an operational speed of 58.9rpsK$^{-1/2}$. Moreover, the asymmetric ratio for the circumferential velocity is decreasing from L1 (diffuser inlet) to L5 (diffuser outlet) similar to that at an operational speed of 58.9rpsK$^{-1/2}$.

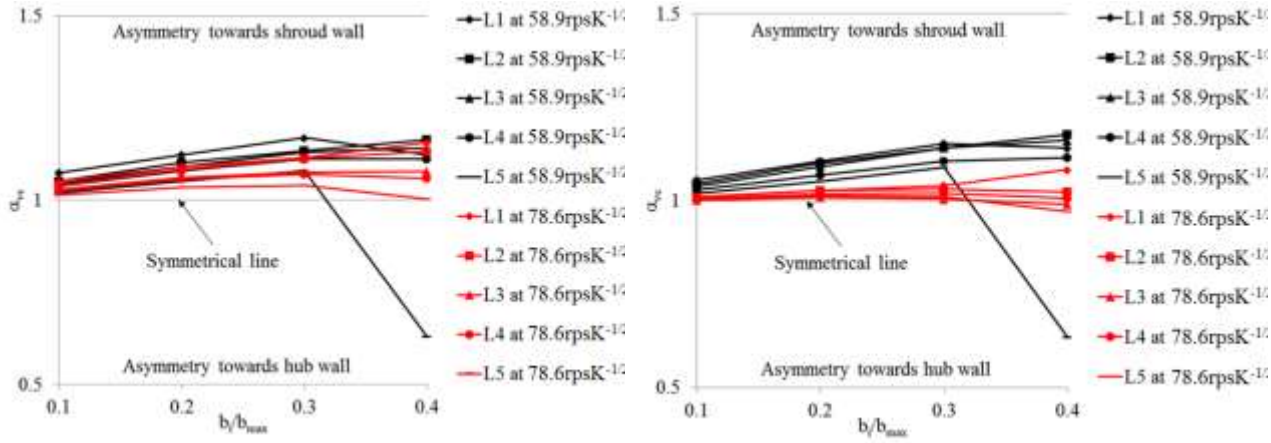

(a) (b)

Figure 4.50: Local asymmetric ratio for the circumferential velocity, α_{vc} across the diffuser at design condition and at near off-design conditions at the operational speeds of 58.9rpsK$^{-1/2}$ and 78.6rpsK$^{-1/2}$

Figure 4.51 depicts the static temperature variations across the centreline of the diffuser at BEP at an operational speed of 58.9rpsK$^{-1/2}$. It can be seen that the static temperature is lower at the diffuser inlet and it is increasing radially across the diffuser outlet. Furthermore, the static temperature also increases circumferentially in the direction of rotation having a minimum static temperature at the diffuser inlet after the volute-tongue region and maximum at the diffuser outlet near the volute-tongue region. The minimum static temperature is seen to be as 320K and maximum static temperature is seen to be as 334K. However, the rate of increase of the static temperature in the radial direction is higher in comparison to the reduction in the circumferential direction.

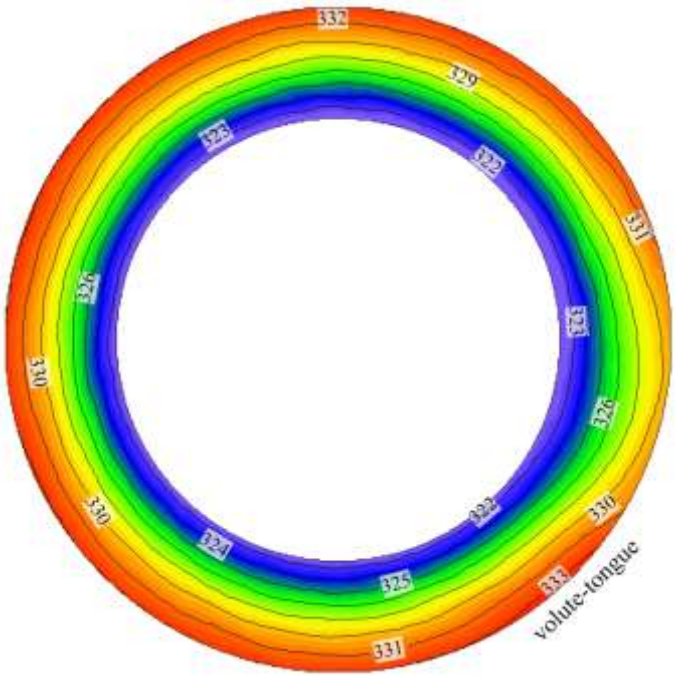

Figure 4.51: Static temperature (K) variations across the centreline of the diffuser at BEP at an operational speed of 58.9rpsK$^{-1/2}$

Figure 4.52 depicts the static temperature variations across the centreline of the diffuser at BEP at an operational speed of 78.6rpsK$^{-1/2}$. The trend in the static temperature variations within the diffuser is similar to that at an operational speed of 58.9rpsK$^{-1/2}$. It can be seen that minimum static temperature is obtained at the diffuser inlet after the volute-tongue region, which is 7% higher in comparison to that at an operational speed of 58.9rpsK$^{-1/2}$. Furthermore, static temperature is found to be higher at the diffuser outlet near volute-tongue region, which is again 7% higher in comparison to that at an operational speed of 58.9rpsK$^{-1/2}$.

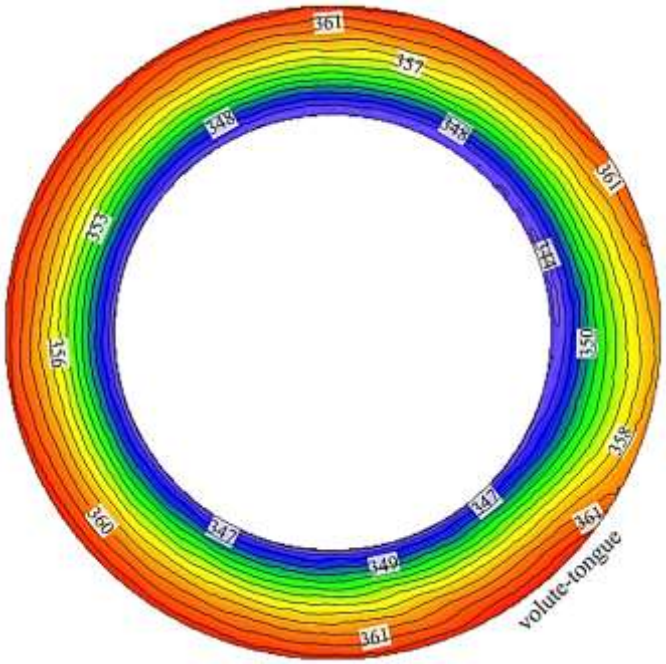

Figure 4.52: Static temperature (K) variations across the centreline of the diffuser at BEP at an operational speed of 78.6rpsK$^{-1/2}$

Figure 4.53(a) depicts the static temperature variations across the centreline of the diffuser at near choke condition at an operational speed of 58.9rpsK$^{-1/2}$. The overall static temperature is lower within the diffuser at near choke condition in comparison to that at BEP. It can be seen that the minimum static temperature of 301K is obtained at the diffuser inlet before the volute-tongue region. The static temperature increases radially across the diffuser similar to that seen at BEP. Furthermore, the static temperature increases circumferentially in the direction of impeller rotation having a maximum value of 322K at the diffuser outlet after the volute-tongue region. Figure 4.53(b) depicts the static temperature variations across the centreline of the diffuser at near surge condition at an operational speed of 58.9rpsK$^{-1/2}$. The trend of static temperature variations is similar to that seen at BEP. However, the overall static temperature is higher within the diffuser at near surge condition in comparison to that at BEP. The minimum static temperature is seen to be 341K at the diffuser inlet after volute-tongue region and the maximum static temperature is 359K at the diffuser outlet near the volute-tongue region.

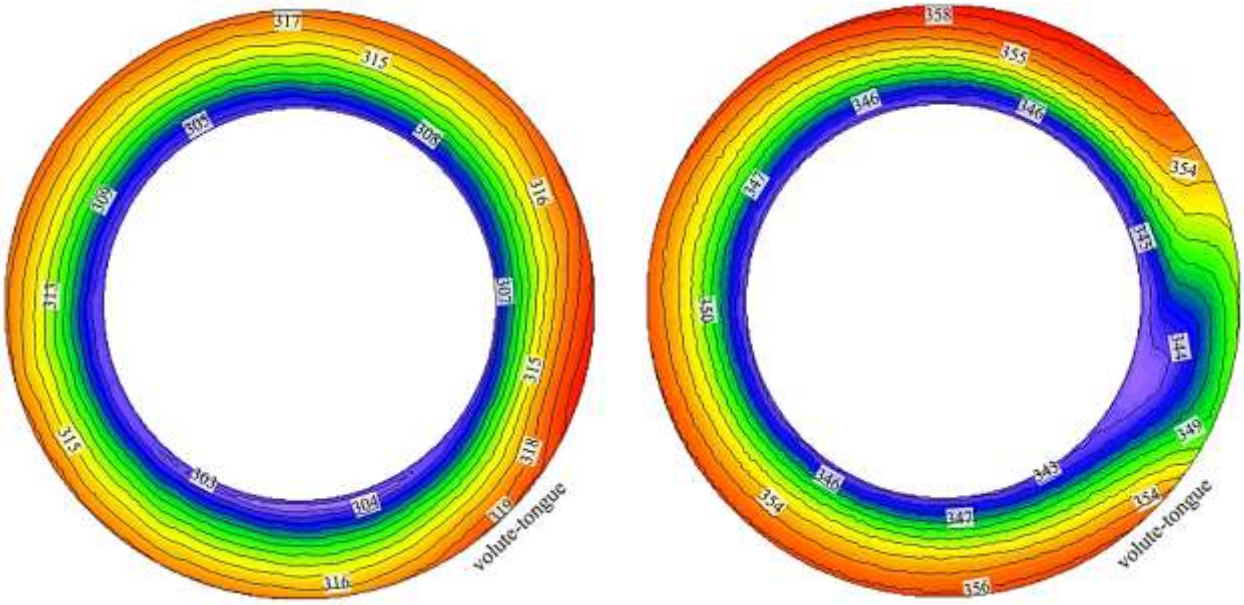

(a) (b)

Figure 4.53: Static temperature (K) variations across the centreline of the diffuser at an operational speed of 58.9rpsK$^{-1/2}$ at near off-design conditions (a) near choke and (b) near surge

Figure 4.54(a) depicts the static temperature variations across the centreline of the diffuser at near choke condition at an operational speed of 78.6rpsK$^{-1/2}$. The overall static temperature is higher within the diffuser in comparison to that at an operational speed of 58.9rpsK$^{-1/2}$. However, the trend of the static temperature variations is similar to that at near choke condition at an operational speed of 58.9rpsK$^{-1/2}$. It can be seen that the minimum static temperature is obtained at the diffuser inlet before the volute-tongue region, which is 4% higher in comparison to that at near choke condition at an operational speed of 58.9rpsK$^{-1/2}$. Furthermore, maximum static temperature is obtained at the diffuser outlet after the volute-tongue region, which is 6% more than that at operational speed of 58.9rpsK$^{-1/2}$. Figure 4.54(b) depicts the static temperature variations across the centreline of the diffuser at near surge condition at an operational speed of 78.6rpsK$^{-1/2}$. The overall static temperature is higher within the diffuser in comparison to that at near surge condition at an operational speed of 58.9rpsK$^{-1/2}$. However, the trend of the static temperature variations is similar to that at near surge condition at an operational speed of 58.9rpsK$^{-1/2}$. It can be seen that the minimum static temperature is obtained at the diffuser inlet after volute-tongue region, which 9% higher in comparison to that at near surge condition at an operational speed of 58.9rpsK$^{-1/2}$. Furthermore, the maximum static temperature is obtained at the diffuser outlet near the volute-tongue region, which is again 9% higher in comparison to that at near surge condition at an operational speed of 58.9rpsK$^{-1/2}$.

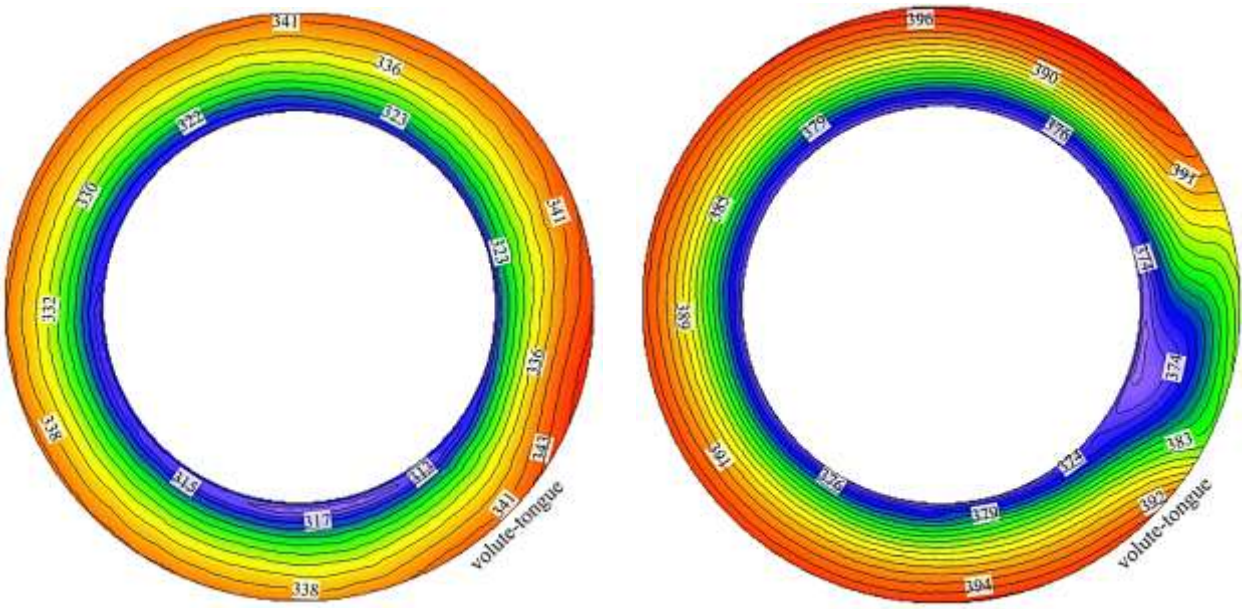

(a) (b)

Figure 4.54: Static temperature (K) variations across the centreline of the diffuser at an operational speed of 78.6rpsK$^{-1/2}$ at near off-design conditions (a) near choke and (b) near surge

4.3.1. Effect of Asymmetric Ratio on the Design and Off-Design Conditions

The behaviour of the flow within the diffuser is highly dependent upon the mass flow rate the compressor stage is working on. It has been noticed last section of this chapter that at near choke condition the flow is asymmetrical towards diffuser hub wall. Furthermore, the asymmetrical behaviour of the flow shifts from asymmetry towards diffuser hub wall to the diffuser shroud wall as the compressor working point changes from near choke condition to near surge condition. Therefore, a new term is introduced that shows the change in behaviour of the flow across the diffuser for different mass flow rates. The asymmetric ratio of the flow is defined as α, which is the ratio between the flow velocity near the shroud wall and the flow velocity near the hub wall. This ratio defines the gradient of asymmetric flow behaviour across the diffuser. The average value of asymmetric ratio at one cross sectional area of the diffuser is defined as global asymmetric ratio, ξ, written as follows;

$$\xi = \frac{1}{2}\left[\frac{\alpha_1 b_1+\alpha_2 b_2+\alpha_3 b_3+\alpha_4 b_4}{b_t}\right] \tag{4.1}$$

where, n is the number of diffuser widths considered (shown in Figure 4.19) from the walls and b is the diffuser width. Furthermore, the subscripts 1, 2, 3 and 4 are width locations from the wall, which are explained earlier in the previous section. Moreover, subscript t stands for total/maximum and ave stands for average. The global asymmetric ratio for different velocity vectors across the diffuser are

described in the following section. Furthermore, the major effects of velocity vectors on the design and off-design conditions are described in detail.

Figure 4.55 depicts the global asymmetric ratio for the velocity magnitude at the design and off-design conditions at an operational speed of 58.9rpsK$^{-1/2}$. It can be seen that the global asymmetric ratio for the velocity magnitudes at the design and near off-design conditions is towards the shroud wall of the diffuser. The global asymmetric ratio for the velocity magnitudes is higher at L1 (diffuser inlet) and it is decreasing towards L5 (diffuser outlet) at BEP. Furthermore, the global asymmetric ratio for the velocity magnitudes is higher at L1 (diffuser inlet) and it is decreasing towards L4 at off-design conditions similar to BEP. However, asymmetric ratio increases at L5 (diffuser outlet) at near off-design conditions. The asymmetric ratio values are almost similar for BEP and near surge condition, which means flow is highly asymmetric. On the other hand, the asymmetric ratio values are lower at near choke condition, which means flow is close to symmetric.

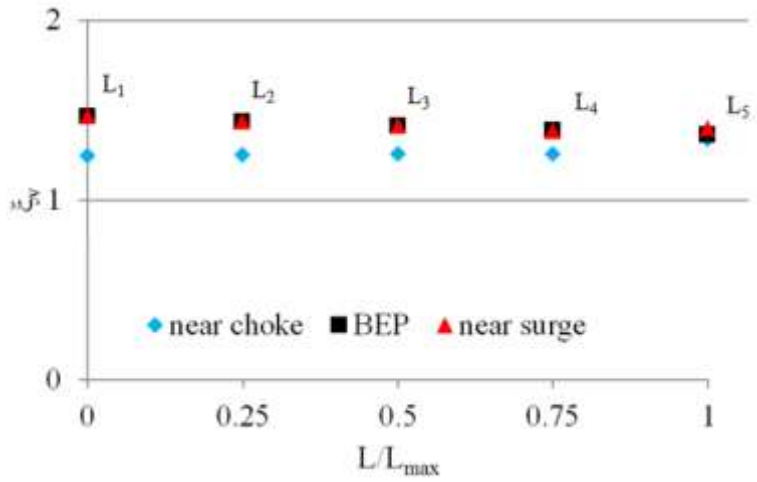

Figure 4.55: Global asymmetric ratio for the velocity magnitude at the design and off-design conditions at an operational speed of 58.9rpsK$^{-1/2}$

Figure 4.56 depicts the global asymmetric ratio for the velocity magnitude at the design and off-design conditions at an operational speed of 78.6rpsK$^{-1/2}$. It shows the same trend in comparison to that at an operational speed of 58.9rpsK$^{-1/2}$. It can be seen that the global asymmetric ratio for design and off-design conditions is towards the shroud wall of the diffuser. The global asymmetric ratio for the velocity magnitudes is higher at L_1 (diffuser inlet) and it is decreasing towards L_5 (diffuser outlet) at BEP and at near surge condition. However, the global asymmetric ratio for the velocity magnitudes is lower at L_1 (diffuser inlet) and it is increasing towards L_5 (diffuser outlet) at near choke condition. Furthermore, the asymmetric ratio values are almost similar for BEP and near surge condition, which

means flow is highly asymmetric. On the other hand, the asymmetric ratio values are lower at near choke condition, which means flow is close to symmetric.

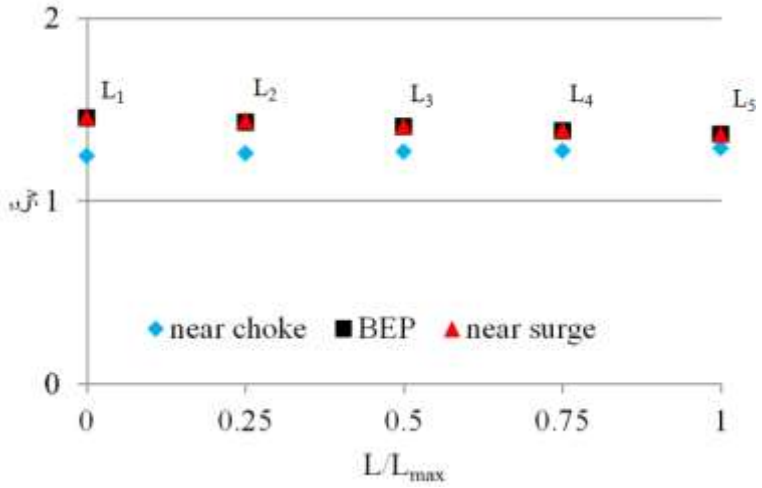

Figure 4.56: Global asymmetric ratio for velocity magnitude at the design and near off-design conditions at an operational speed of 78.6rpsK$^{-1/2}$

Figure 4.57 depicts the global asymmetric ratio for the radial velocity at the design and off-design conditions at an operational speed of 58.9rpsK$^{-1/2}$. It can be seen that the global asymmetric ratio for radial velocity at the design and near off-design conditions is towards the shroud wall of the diffuser. The global asymmetric ratio for the radial velocity is higher at L_1 (diffuser inlet) and it is decreasing towards L_5 (diffuser outlet) at BEP and at near surge condition. However, the global asymmetric ratio for the radial velocity is lower at L_1 (diffuser inlet) and it is increasing towards L_5 (diffuser outlet) at near choke condition. However, asymmetric ratio increases at L_5 (diffuser outlet) at near off-design conditions. The asymmetric ratio values are almost similar for BEP and near surge condition, which means flow is highly asymmetric. On the other hand, the asymmetric ratio values are lower at near choke condition, which means flow is close to symmetric.

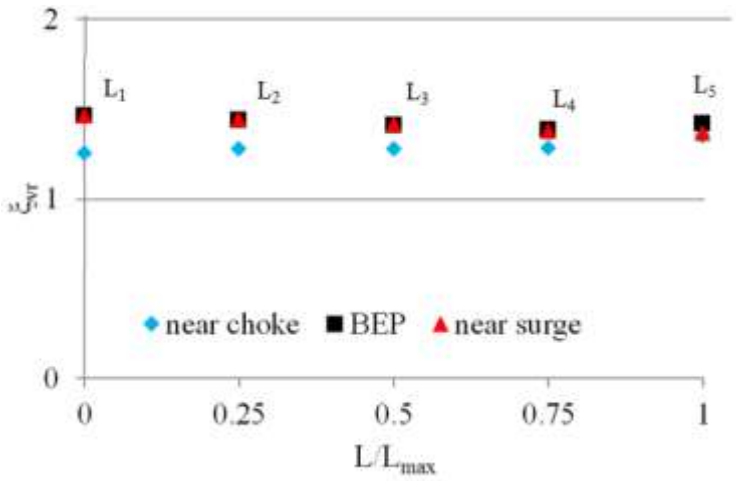

Figure 4.57: Global asymmetric ratio for radial velocity at the design and off-design conditions at an operational speed of 58.9rpsK$^{-1/2}$

Figure 4.58 depicts the global asymmetric ratio for the radial velocity at the design and off-design conditions at an operational speed of 78.6rpsK$^{-1/2}$. It shows the same trend in comparison to that at an operational speed of 58.9rpsK$^{-1/2}$. It can be seen that the global asymmetric ratio for radial velocity at the design and near off-design conditions is towards the shroud wall of the diffuser. The global asymmetric ratio for the radial velocity is higher at L_1 (diffuser inlet) and it is decreasing towards L_5 (diffuser outlet) at BEP and at near surge condition. However, the global asymmetric ratio for the radial velocity is lower at L_1 (diffuser inlet) and it is increasing towards L_5 (diffuser outlet) at near choke condition. However, asymmetric ratio increases at L_5 (diffuser outlet) at near off-design conditions. The asymmetric ratio values are almost similar for BEP and near surge condition, which means flow is highly asymmetric. On the other hand, the asymmetric ratio values are lower at near choke condition, which means flow is close to symmetric.

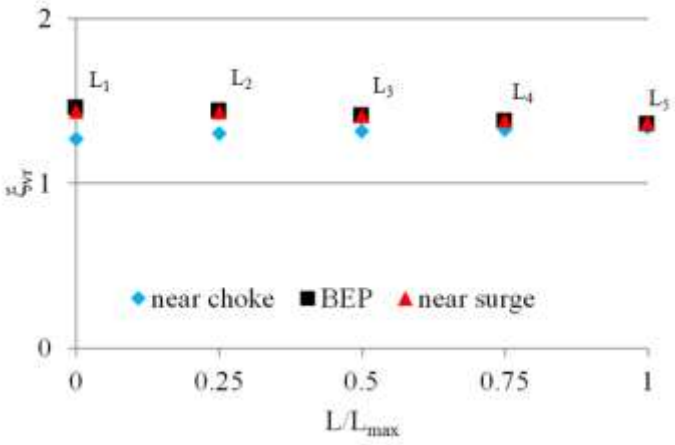

Figure 4.58: Global asymmetric ratio for radial velocity at the design and near off-design conditions at an operational speed of 78.6rpsK$^{-1/2}$

Figure 4.59 depicts the global asymmetric ratio for the circumferential velocity at the design and off-design conditions at an operational speed of 58.9rpsK$^{-1/2}$. It can be seen that the global asymmetric ratio for circumferential velocity at the design and near off-design conditions is towards the shroud wall of the diffuser. The global asymmetric ratio for the circumferential velocity is higher at L_1 (diffuser inlet) and it is decreasing towards L_5 (diffuser outlet) at BEP and at near surge condition. However, the global asymmetric ratio for the circumferential velocity is lower at L_1 (diffuser inlet) and it is increasing towards L_5 (diffuser outlet) at near choke condition. However, asymmetric ratio increases at L_5 (diffuser outlet) at near off-design conditions. The asymmetric ratio values are almost similar for BEP and near surge condition, which means flow is highly asymmetric. On the other hand, the asymmetric ratio values are lower at near choke condition, which means flow is close to symmetric.

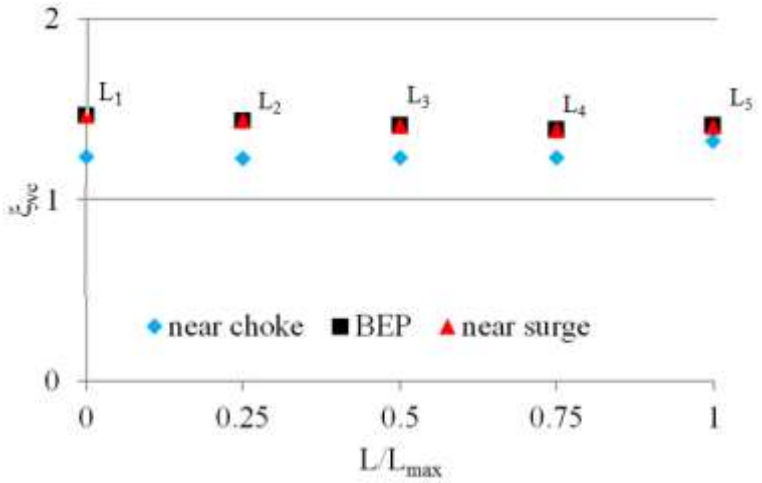

Figure 4.59: Global asymmetric ratio for circumferential velocity at the design and off-design conditions at an operational speed of 58.9rpsK$^{-1/2}$

Figure 4.60 depicts the global asymmetric ratio for the circumferential velocity at the design and off-design conditions at an operational speed of 78.6rpsK$^{-1/2}$. It shows the same trend in comparison to that at an operational speed of 58.9rpsK$^{-1/2}$. It can be seen that the global asymmetric ratio for circumferential velocity at the design and near off-design conditions is towards the shroud wall of the diffuser. The global asymmetric ratio for the circumferential velocity is higher at L_1 (diffuser inlet) and it is decreasing towards L_5 (diffuser outlet) at BEP and at near surge condition. However, the global asymmetric ratio for the circumferential velocity is lower at L_1 (diffuser inlet) and it is increasing towards L_5 (diffuser outlet) at near choke condition. However, asymmetric ratio increases at L_5 (diffuser outlet) at near off-design conditions. The asymmetric ratio values are almost similar

for BEP and near surge condition, which means flow is highly asymmetric. On the other hand, the asymmetric ratio values are lower at near choke condition, which means flow is close to symmetric.

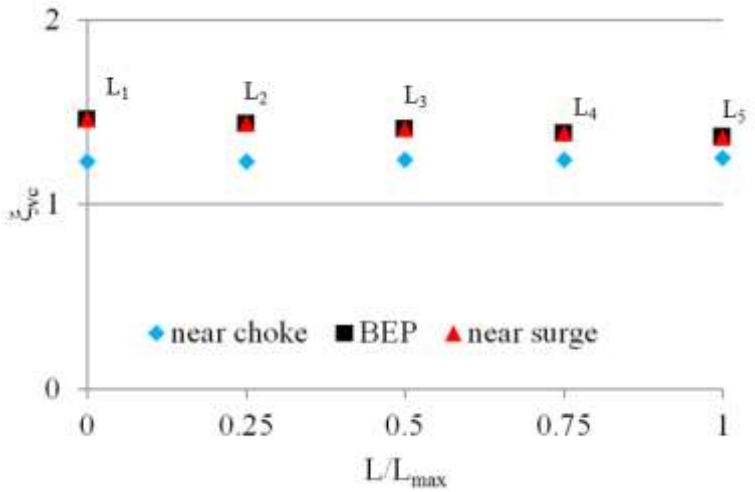

Figure 4.60: Global asymmetric ratio for circumferential velocity at the design and off-design conditions at an operational speed of 78.6rpsK$^{-1/2}$

It is concluded from the above results the flow across the straight diffuser is asymmetrical at design and off-design conditions. It has been noticed that the asymmetry increases at near choke condition from the diffuser inlet to the diffuser outlet. However, the asymmetry decreases at BEP and at near surge condition from the diffuser inlet to the diffuser outlet. Furthermore, it has also been noticed that the flow tends to be more asymmetrical at the diffuser outlet at off-design conditions in comparison to BEP. This is because the diffuser has divergence on the hub wall near the outlet, which increases the area ratio of the diffuser and hence reduces the velocity. This causes the airflow to deviate towards the shroud wall of the straight diffuser. In order to understand the overall effect of the diffuser flow field on the design and off-design conditions, the equation 4.1 has been reconsidered and manipulated to obtain the entire effect. Henceforth, a new term has been defined, which is called asymmetric effect, ζ is shown as follows;

$$\zeta = \frac{1}{n}\left[\frac{\xi_1 r_1 + \xi_2 r_2 + \xi_3 r_3 + \xi_4 r_4 + \xi_5 r_5}{r_t}\right] \tag{4.2}$$

where, n is the number of diffuser radii locations considered from the diffuser inlet and r is the diffuser radius. Furthermore, the subscripts 1, 2, 3 and 4 are radii locations from the diffuser inlet, which are 0% of distance from the diffuser inlet, 25% of distance from the diffuser inlet, 50% of distance from the diffuser inlet, 75% of distance from the diffuser inlet and 100% of distance from the diffuser inlet

respectively. Moreover, subscript t stands for total. Figure 4.61 depicts the comparison of diffuser asymmetric effect for velocity magnitude at the design and near off-design conditions at the operational speeds of 58.9rpsK$^{-1/2}$ and 78.6rpsK$^{-1/2}$. Asymmetric effect above 1.0 shows the flow to be asymmetric towards the shroud wall within the diffuser and asymmetric effect below 1.0 shows the flow to be asymmetric towards the hub wall within the diffuser. Moreover, asymmetric effect of 1.0 shows the flow to be symmetric within the diffuser. It can be seen that the asymmetric effect is higher than 1.0 at design and near off-design conditions at the operational speeds of 58.9rpsK$^{-1/2}$ and 78.6rpsK$^{-1/2}$. Furthermore, the asymmetric effect is less at near off-design conditions in comparison to that at BEP at an operational speed of 58.9rpsK$^{-1/2}$. Moreover, the asymmetric effect is less at near choke condition in comparison to that at BEP and at near surge condition at an operational speed of 78.6rpsK$^{-1/2}$. However, it has been noticed that the velocity flow field is highly asymmetric towards the shroud wall at BEP at the operational speeds of 58.9rpsK$^{-1/2}$ and 78.6rpsK$^{-1/2}$ in comparison to that at near off-design conditions.

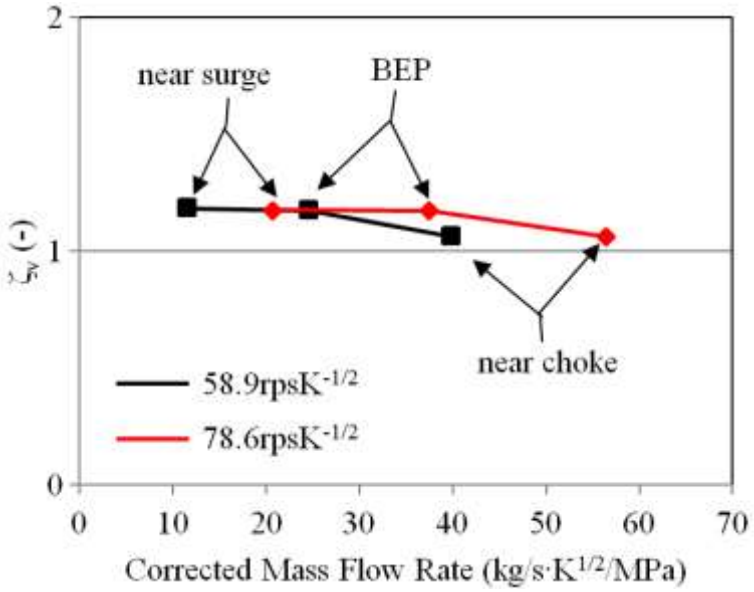

Figure 4.61: Comparison of diffuser asymmetric effect for velocity magnitude at the design and near off-design conditions at the operational speeds of 58.9rpsK$^{-1/2}$ and 78.6rpsK$^{-1/2}$

Figure 4.62 depicts the comparison of diffuser asymmetric effect for radial velocity at the design and near off-design conditions at the operational speeds of 58.9rpsK$^{-1/2}$ and 78.6rpsK$^{-1/2}$. It can be seen that the asymmetric effect is higher than 1.0 at design and off-design conditions at the operational speeds of 58.9rpsK$^{-1/2}$ and 78.6rpsK$^{-1/2}$. Furthermore, the asymmetric effect is higher at near surge condition and at BEP in comparison to that at near choke condition at the operational speeds of 58.9rpsK$^{-1/2}$ and 78.6rpsK$^{-1/2}$. However, it has been noticed that the radial flow field is highly

asymmetric towards the shroud wall at BEP and at near surge condition at the operational speeds of 58.9rpsK$^{-1/2}$ and 78.6rpsK$^{-1/2}$ in comparison to that at near choke conditions.

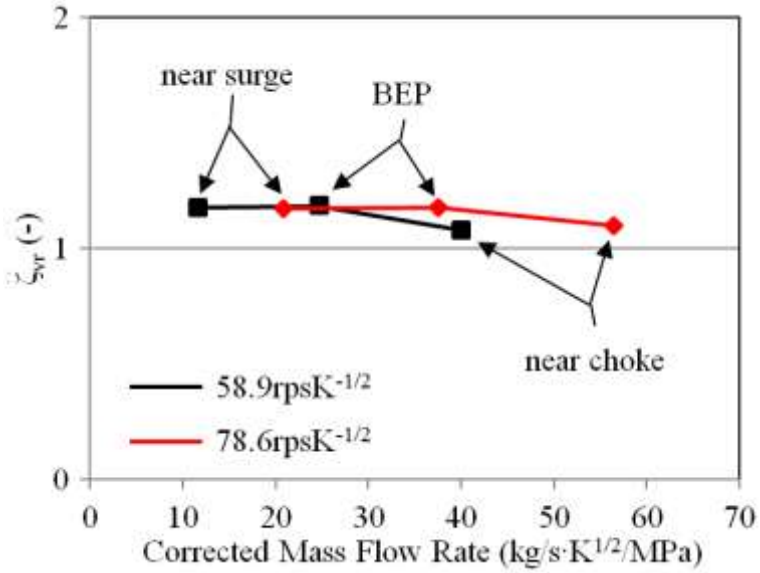

Figure 4.62: Comparison of diffuser asymmetric effect for radial velocity at the design and near off-design conditions at the operational speeds of 58.9rpsK$^{-1/2}$ and 78.6rpsK$^{-1/2}$

Figure 4.63 depicts the comparison of diffuser asymmetric effect for circumferential velocity at the design and near off-design conditions at the operational speeds of 58.9rpsK$^{-1/2}$ and 78.6rpsK$^{-1/2}$. It can be seen that the asymmetric effect is higher than 1.0 at design and off-design conditions at the operational speeds of 58.9rpsK$^{-1/2}$ and 78.6rpsK$^{-1/2}$. Furthermore, the asymmetric effect is higher at near surge condition and at BEP in comparison to that at near choke condition at the operational speeds of 58.9rpsK$^{-1/2}$ and 78.6rpsK$^{-1/2}$. However, it has been noticed that the circumferential flow field is highly asymmetric towards the shroud wall at BEP and at near surge condition at the operational speeds of 58.9rpsK$^{-1/2}$ and 78.6rpsK$^{-1/2}$ in comparison to that at near choke conditions.

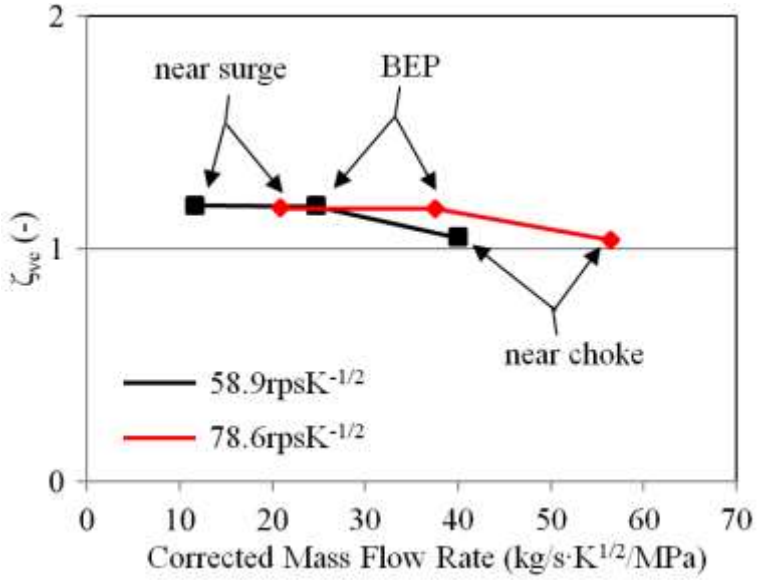

Figure 4.63: Comparison of diffuser asymmetric effect for circumferential velocity at the design and near off-design conditions at the operational speeds of 58.9rpsK$^{-1/2}$ and 78.6rpsK$^{-1/2}$

It has been concluded from the aforementioned analysis that the flow is asymmetric across the straight diffuser at the design and off-design conditions at the operational speeds of 58.9rpsK$^{-1/2}$ and 78.6rpsK$^{-1/2}$. Furthermore, the flow high asymmetric effect at BEP and less effect at off-design conditions.

4.3.2. Isentropic Efficiency within the Parallel Wall Vaneless Diffuser

Isentropic efficiency is a non-dimensional parameter to compute the performance of the compressor stage. It is a function of the total-to-total pressure ratio and total-to-total temperature ratio of the centrifugal compressor stage, which is as follows;

$$\eta_C = \frac{T_{o,in} \times \left[PR_C^{\frac{k-1}{k}} - 1 \right]}{T_{o,out} - T_{o,in}} \tag{4.3}$$

The isentropic efficiency has been analysed locally within the diffuser at three conditions (near choke, BEP and near surge). The isentropic efficiency within the diffuser has been calculated at the locations mentioned in Figure 4.14. Figure 4.64 depicts the isentropic efficiency locally within the diffuser by the method described earlier. It can be seen that 80.3% of isentropic efficiency is obtained at the diffuser inlet and it has reduced to 77.5% in the downstream of the diffuser at BEP. Furthermore, it can be seen that the trend of the isentropic efficiency is similar at near choke condition and at near surge condition. However, there are variations in the magnitude of isentropic efficiency. The isentropic efficiency values are a bit higher at the diffuser inlet at near choke condition in comparison

to that at BEP and however, have same values at the diffuser outlet. This shows very less losses within the diffuser at near choke condition in comparison to that at BEP. Moreover, the isentropic efficiency values are lower across the diffuser at near surge condition in comparison to that at BEP. This shows that increased amount of losses generated while the compressor stage was working at near surge condition. These losses are due to skin friction loss, high static temperature loss and the recirculation within the diffuser.

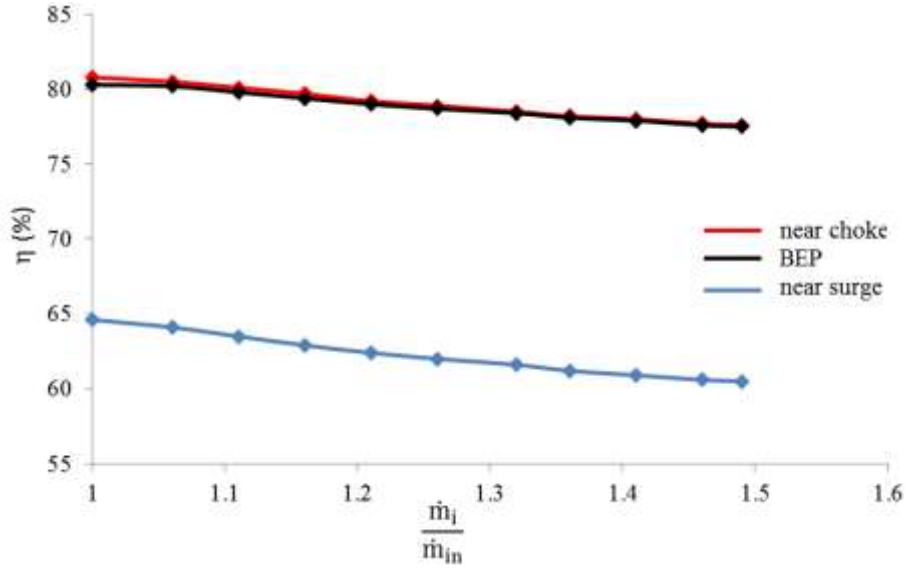

Figure 4.64: Isentropic efficiency locally within the diffuser at design and off-design conditions

Furthermore, a regression analysis approach is used to quantify the effects of geometrical parameters and the flow parameters on the isentropic efficiency. The flow within the diffuser is dependent on numerous factors, which could affect the isentropic efficiency locally within the diffuser of the compressor stage. The important parameters include the flow velocity components; circumferential velocity, v_θ, radial velocity, v_r and axial velocity v_a. However, axial velocity has negligible effect on the flow within the diffuser hence axial velocity component is neglected. Moreover, the diffuser is like a circular disc whereby the flow velocity is directed radially outward. Therefore, the isentropic efficiency is also the function of the geometrical parameters including inner and outer radii of the diffuser, inner and outer widths of the diffuser and azimuthal angle of the diffuser. A regression analysis has been carried out to develop an equation by which isentropic efficiency can be calculated at any location within the diffuser.

$$\eta = f(N, \theta, r, b_2, z, \omega, T_\circ, |v|, v_\theta, v_r) \tag{4.4}$$

Using the regression analysis approach following equation has been developed. This expression is only valid for straight diffuser.

$$\eta = 1.82 \cdot \left(\frac{N\theta}{r}\right)^{k_1} \cdot \left(\frac{b_2 - z}{b_2}\right)^{k_2} \cdot \left(\frac{\omega r}{\sqrt{\gamma R T_\circ}}\right)^{k_3} \cdot \left(\frac{|v| - v_\theta}{|v| - v_r}\right)^{k_4} \quad (4.5)$$

where

$$k_1 = 0.0023$$
$$k_2 = 0.038$$
$$k_3 = 2.26$$
$$k_4 = 0.0319$$

These coefficients' values are only valid for the respective initial and boundary conditions. Furthermore, these coefficients represent the mean change in the response variable at one unit of change in the predictor variable while holding the other predictor variable in the model constant. The response variables are $\frac{N\theta}{r}$, $\frac{b_2 - z}{b_2}$, $\frac{\omega r}{\sqrt{\gamma R T_\circ}}$ and $\frac{|v| - v_\theta}{|v| - v_r}$, whereas the predictor variable is the isentropic efficiency, η. The first term in the equation 1.82 is the y-intercept value. Furthermore, the exponent values of k_1, k_2, k_3 and k_4 are given, which shows that which term has maximum effect on the isentropic efficiency value. Henceforth, it can be seen that the maximum effect is dependent upon $\frac{\omega r}{\sqrt{\gamma R T_\circ}}$ term. This term identifies the rotational speed of the impeller and the Mach number obtained at the impeller trailing edge tip.

The data obtained via Eq. 4.5 has been verified with the calculated numerical results of the isentropic efficiency, as depicted in the Figure 4.65, which has shown the maximum percentage difference of 7.01% and having R^2 value of 0.60. Based upon this, it can be concluded that the aforementioned semi-empirical equation can be used to compute the isentropic efficiency within the diffuser.

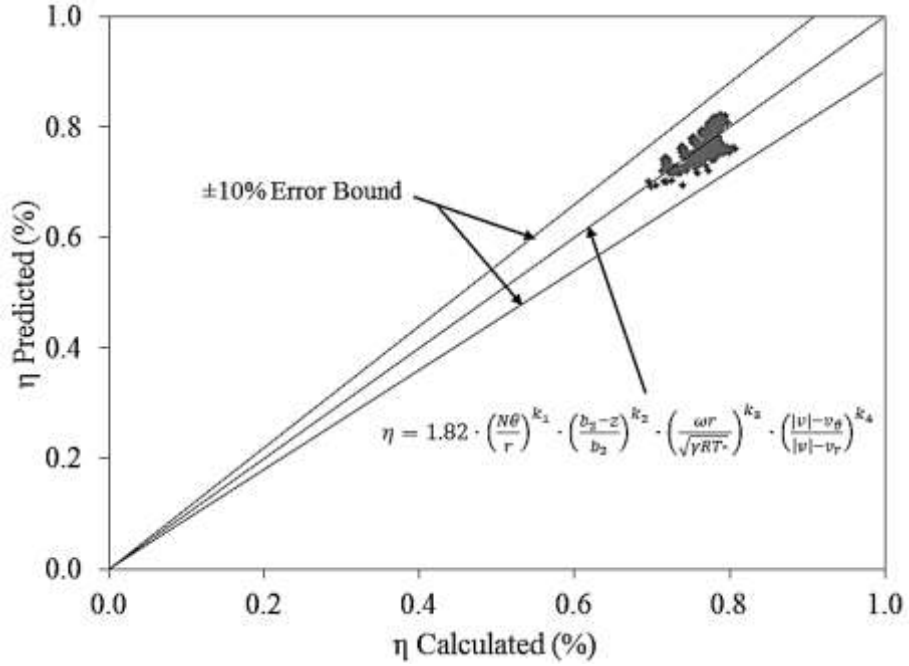

Figure 4.65: Comparison between numerically calculated, obtained via regression analysis, isentropic efficiency and predicted, using CFD, isentropic efficiency within the diffuser

4.4. Flow Field Characteristics within the Diverged Wall Vaneless Diffuser

Many researchers have carried out various investigations to improve the compressor stage performance either by pinching, converging or diverging the diffuser walls as described in Chapter 2 of the thesis. Similar approach is used in this section as well to identify the effects of the wall divergence on the performance of the compressor stage. Furthermore, in this study the effect of wall divergence on the local flow variations are also investigated. This methodology will help in the later sections to either maintain the compressor stage performance or enhance the compressor stage performance while compacting the compressor by modifying the diffuser using various approaches. Parametric investigations have been carried out to analyse the flow field characteristics within the diverged wall vaneless diffuser. To carry out the parametric investigations a Full Factorial based Design of Experiments (DoE) technique has been employed in the present study to determine the possible practical combinations of the geometrical parameters. Minitab 17 Statistical Software has been used in the present study to carry out Full Factorial based DoE studies, where a practical range of different parameters has been specified. The factors/parameters considered for the diffuser configurations, along with their levels, have been summarised in the Table 4.1. Furthermore, a sample design of diverged wall straight diffuser has also been presented in Figure 4.66. It can be seen that the shroud wall is diverged from the diffuser inlet to one-fifth of the diffuser and is applied on the circumference of the diffuser. Furthermore, the diffuser outlet width has increased up to 1.4 of the diffuser inlet width. The diffuser outlet width cannot be extended more than 1.4 because of the limitation on the volute inlet section. The results obtained from the diverged wall diffuser have been compared with the straight diffuser to investigate the performance improvement within the compressor stage. Based upon the Full Factorial based DoE 24 number of numerical simulations has been required to carry out this parametric investigation. The total-to-total pressure ratio and isentropic efficiency have been recorded for each simulation. Best design model has been chosen based upon the highest localised isentropic efficiency within the compressor stage, which is the function of various geometrical and flow parameters.

Table 4.1: Factors and levels for full factorial design of diffuser configurations

Factors	Level 1	Level 2	Level 3	Level 4	Level 5	Level 6
L/L_{max}	0.0	0.1	0.2	0.3	0.4	0.5
b_2/b_1	1.1	1.2	1.3	1.4	-	-

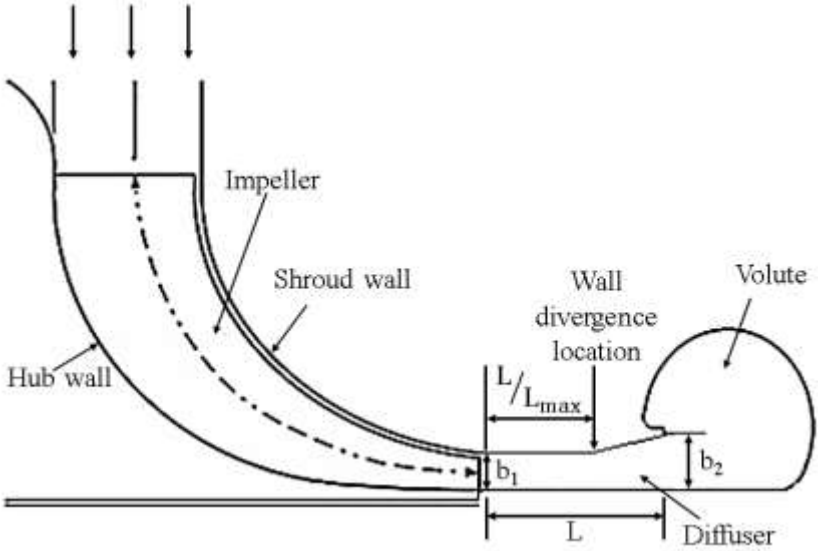

Figure 4.66: Sample configuration of the diverged wall vaneless diffuser

4.4.1. Performance Characteristics of Compressor Stage using Diverged Wall Straight Diffuser

Numerical analysis has been carried out to obtain the total-to-total stage performance and flow field characteristics across various configurations of the diverged wall straight diffuser have been analysed. Table 4.2 shows the results obtained from numerical simulations of CFD for the global parameters of all 24 configurations. Two geometrical parameters are considered, divergence location from the inlet on the shroud wall and the diffuser outlet-to-inlet width ratio to analyse the effect on the local flow field and on the total-to-total stage performance. It can be seen from the Table 4.2 that a small increase of outlet-to-inlet width ratio causes increase in the pressure ratio and the isentropic efficiency. However, with a further increase of outlet-to-inlet width ratio causes reduction in the stage performance. Furthermore, change in the location of wall divergence has a very small effect on the global performance parameters. However, local flow fields within the diffuser do change, which are explained in the later sections. Furthermore, it can be seen that the pressure ratio and isentropic efficiency is maximum at three diverged wall diffuser configurations; Configuration 9 (L/L_{max} = 0.2 & b_2/b_1 = 1.1), Configuration 13 (L/L_{max} = 0.3 & b_2/b_1 = 1.1) and Configuration 17 (L/L_{max} = 0.4 & b_2/b_1 = 1.1).

Table 4.2: CFD results of centrifugal compressor stage using different configurations of diverged wall vaneless diffuser

Parameters	Divergence location from the inlet on the shroud wall, L/L_{max}	Diffuser outlet-to-inlet width ratio, b_2/b_1	Pressure Ratio, PR_C	Isentropic efficiency, η
Configuration No.	(-)	(-)	(-)	(%)
Straight diffuser	0.0	1.0	1.527	70.9
1	0.0	1.1	1.542	72.3
2		1.2	1.536	71.6
3		1.3	1.531	71.0
4		1.4	1.522	69.9
5	0.1	1.1	1.542	72.3
6		1.2	1.536	71.6
7		1.3	1.531	71.0
8		1.4	1.521	69.9
9	0.2	1.1	1.543	72.3
10		1.2	1.536	71.6
11		1.3	1.532	71.1
12		1.4	1.522	69.9
13	0.3	1.1	1.543	72.3
14		1.2	1.537	71.7
15		1.3	1.533	71.2
16		1.4	1.523	70.1
17	0.4	1.1	1.543	72.3
18		1.2	1.537	71.6
19		1.3	1.534	71.2
20		1.4	1.525	70.2
21	0.5	1.1	1.534	71.3
22		1.2	1.537	71.6
23		1.3	1.529	70.7
24		1.4	1.522	69.8

4.4.2. Flow Field Characteristics within the Diverged Wall Straight Diffuser

This section demonstrates the flow field analyses within the diverged wall straight diffuser based upon static pressure, velocity magnitude, circumferential velocity, radial velocity and static temperature variations. The analyses have been carried out in such a way that firstly the effect of outlet-to-inlet diffuser width ratio has been investigated by considering configurations having same wall divergence from the diffuser inlet. Thereafter, the effect of the wall divergence at different locations on the shroud wall from the diffuser inlet has been investigated by considering those configurations maximum diffuser outlet-to-inlet width ratio. Finally, the combined effects of the wall

divergence at different locations on the shroud wall from the diffuser inlet and the diffuser outlet-to-inlet width ratio have been investigated. These investigations have helped the author to quantify the effects of geometrical parameters on the local flow field within the diverged wall vaneless diffuser. Furthermore, the effect of wall divergence on the flow asymmetry within the diffuser has been quantified to establish a relationship of wall divergence with asymmetric effect and isentropic efficiency.

Figure 4.67 depicts the static pressure variations across the centreline of the diverged wall diffuser configurations ((a) L/L_{max} = 0.0 & b_2/b_1 = 1.1 and (b) L/L_{max} = 0.0 & b_2/b_1 = 1.4) at BEP at an operational speed of 58.9rps$K^{-1/2}$. The trend of the static pressure across the diverged wall straight diffusers is similar to that across the straight diffuser. It can be seen that the minimum static pressure is obtained at the diffuser inlet after the volute-tongue region. The static pressure increases radially across the diffuser. Furthermore, the static pressure also increases circumferentially in the direction of impeller rotation (ω). The maximum static pressure is obtained at the diffuser outlet at near the volute-tongue region. It can be seen that the static pressure values are same across the parallel wall diffuser and diverged wall diffuser configuration (L/L_{max} = 0.0 & b_2/b_1 = 1.1). Furthermore, it can be seen that the static pressure is increased at the diffuser inlet by 0.75% and decreased at the diffuser outlet by 2.68% across diffuser configuration of L/L_{max} = 0.0 & b_2/b_1 = 1.4 in comparison to that across diffuser configuration of L/L_{max} = 0.0 & b_2/b_1 = 1.1. This trend explains that the static pressure decreases when outlet-to-inlet width ratio of the diffuser is increased by keeping the divergence location at the diffuser inlet.

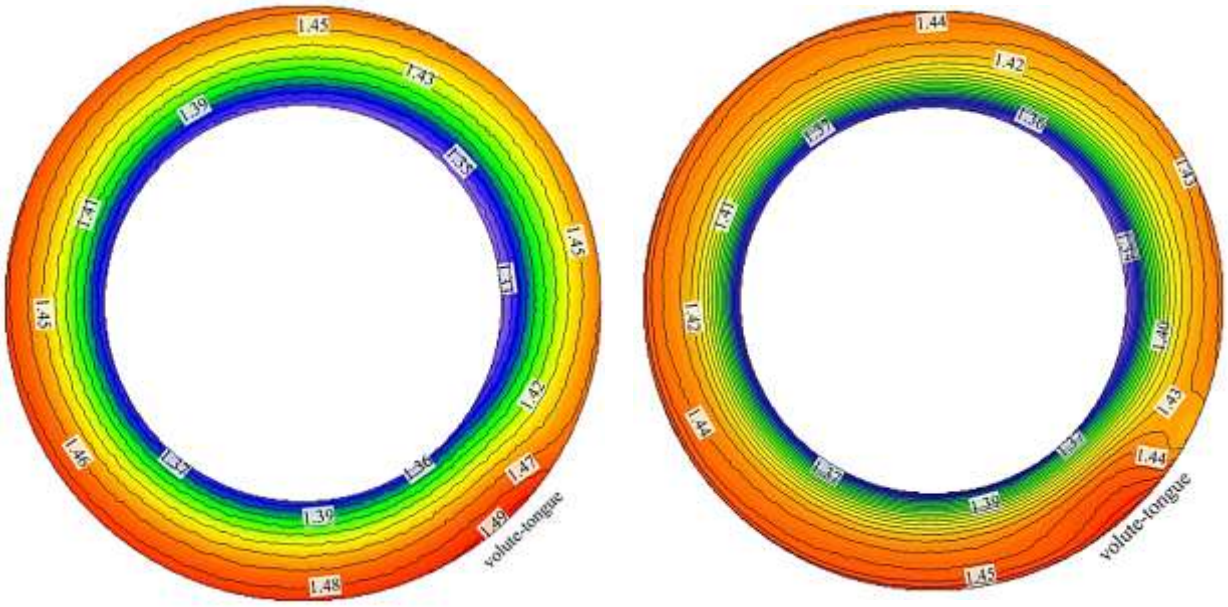

(a) (b)

Figure 4.67: Static pressure (atm) variations across the centreline of the diverged wall straight diffuser (a) L/L_{max} = 0.0 & b_2/b_1 = 1.1 and (b) L/L_{max} = 0 & b_2/b_1 = 1.4 at BEP at an operational speed of 58.9rpsK$^{-1/2}$

Figure 4.68 depicts the static pressure variations across the centreline of the diverged wall diffuser configurations ((a) L/L_{max} = 0.0 & b_2/b_1 = 1.4 and (b) L/L_{max} = 0.3 & b_2/b_1 = 1.4) at BEP at an operational speed of 58.9rpsK$^{-1/2}$. The trend of the static pressure across the diverged wall straight diffusers is similar to that across the straight diffuser. It can be seen that the minimum static pressure is obtained at the diffuser inlet after the volute-tongue region. The static pressure increases radially across the diffuser. Furthermore, the static pressure also increases circumferentially in the direction of impeller rotation (ω). The maximum static pressure is obtained at the diffuser outlet at near the volute-tongue region. It can be seen that the static pressure values are decreased across the diverged wall diffuser configuration (L/L_{max} = 0.0 & b_2/b_1 = 1.4) in comparison to that across the parallel wall diffuser. The static pressure is increased at the diffuser inlet by 0.75% and decreased at the diffuser outlet by 2.68% in comparison to that at parallel wall diffuser. Furthermore, it can also be seen that the static pressure is same across both diverged wall diffuser configurations. This trend explains that the static pressure remains same when the distance between the divergence location and the diffuser inlet is increased by considering the divergence location at the diffuser inlet.

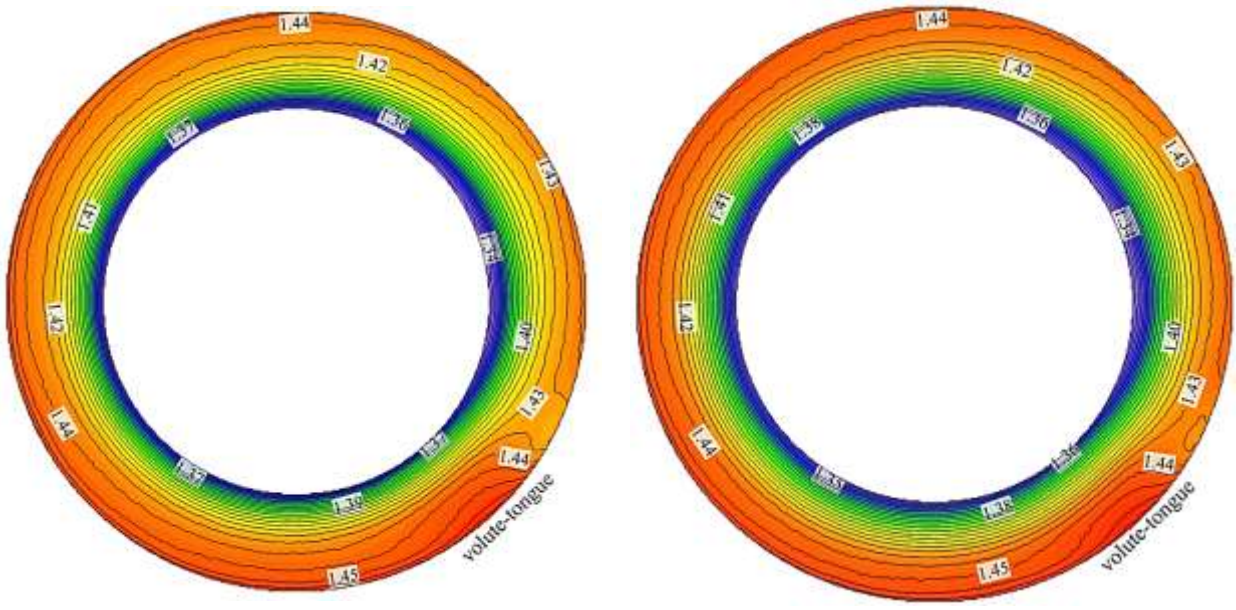

(a) (b)

Figure 4.68: Static pressure (atm) variations across the centreline of the diverged wall straight diffuser (a) L/L_{max} = 0.0 & b_2/b_1 = 1.4 and (b) L/L_{max} = 0.3 & b_2/b_1 = 1.4 at BEP at an operational speed of 58.9rpsK$^{-1/2}$

Figure 4.69 depicts the static pressure variations across the centreline of the diverged wall diffuser configurations (a) L/L_{max} = 0.0 & b_2/b_1 = 1.1, (b) L/L_{max} = 0.1 & b_2/b_1 = 1.2, (c) L/L_{max} = 0.2 & b_2/b_1 = 1.3 and (d) L/L_{max} = 0.3 & b_2/b_1 = 1.4) at BEP at an operational speed of 58.9rpsK$^{-1/2}$. The trend of the static pressure across the diverged wall straight diffusers is similar to that across the straight diffuser. It can be seen that the minimum static pressure is obtained at the diffuser inlet after the volute-tongue region. The static pressure increases radially across the diffuser. Furthermore, the static pressure also increases circumferentially in the direction of impeller rotation (ω). The maximum static pressure is obtained at the diffuser outlet at near the volute-tongue region. It can be seen that the static pressure values are same across the parallel wall diffuser and diverged wall diffuser configuration (L/L_{max} = 0.0 & b_2/b_1 = 1.1). Furthermore, the static pressure is increased at the diffuser inlet by 1.50% and decreased at the diffuser outlet by 0.67% across diffuser configuration of L/L_{max} = 0.1 & b_2/b_1 = 1.2 in comparison to that across diffuser configuration of L/L_{max} = 0.0 & b_2/b_1 = 1.1. Similar trend is obtained for the rest of the diverged wall diffuser configurations. The static pressure is increased by 0.75% and 0.75% at the diffuser inlet across the diverged wall diffuser configurations of L/L_{max} = 0.2 & b_2/b_1 = 1.3 and L/L_{max} = 0.3 & b_2/b_1 = 1.4 in comparison to that across diffuser configuration of L/L_{max} = 0.0 & b_2/b_1 = 1.1. Moreover, the static pressure is decreased by 1.34% and 2.68% at the diffuser outlet across the diverged wall diffuser configurations of L/L_{max} = 0.2 & b_2/b_1 = 1.3 and L/L_{max} = 0.3 & b_2/b_1 = 1.4 in comparison to that across diffuser configuration of L/L_{max} =

0.0 & b_2/b_1 = 1.1. This trend explains that the static pressure remains same when both the distance between the divergence location and the diffuser inlet and outlet-to-inlet width ratio of the diffuser are increased by one point. Thereafter, the static pressure decreases with the further increase of both the distance between the divergence location and the diffuser inlet and outlet-to-inlet width ratio of the diffuser.

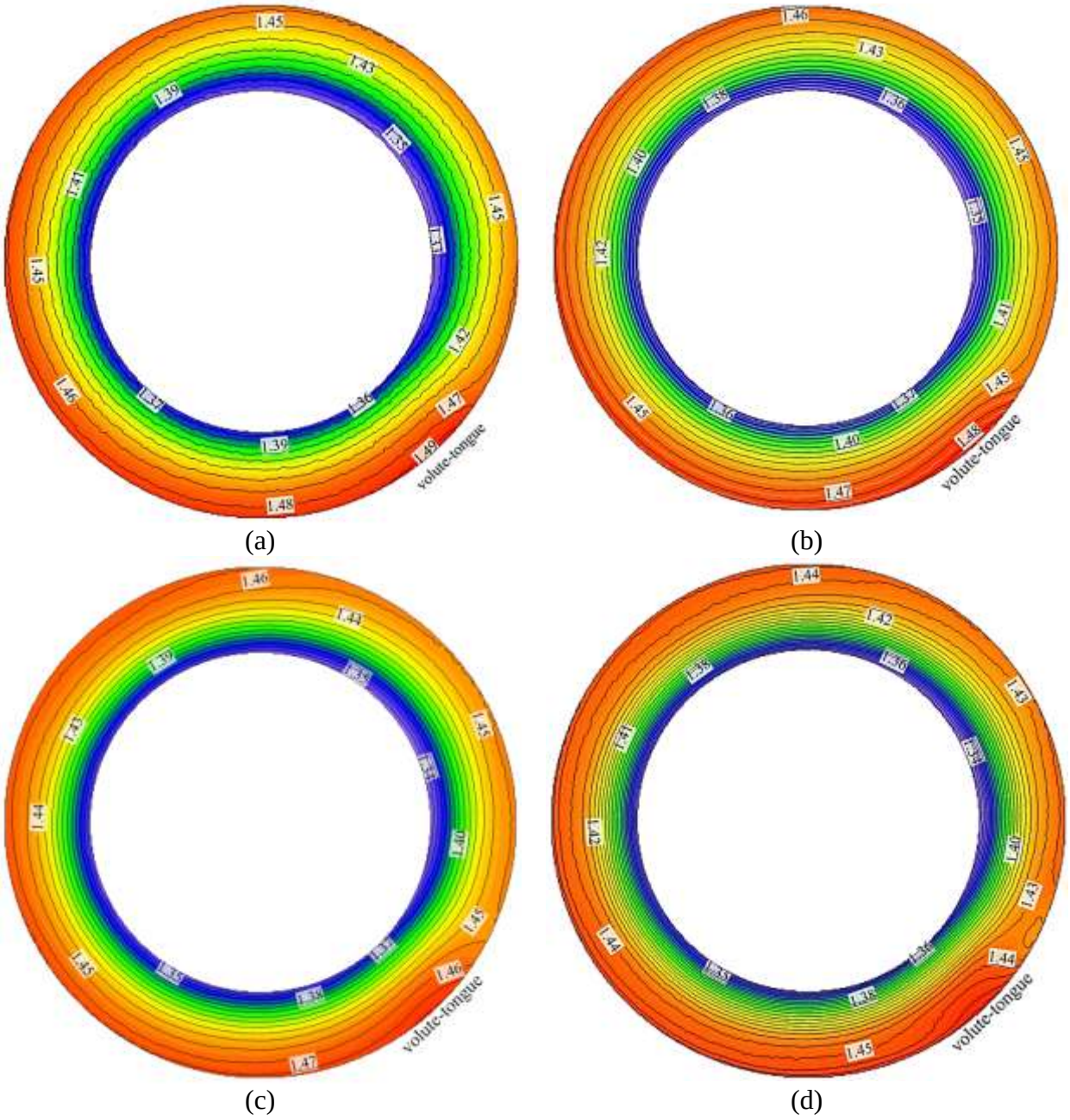

Figure 4.69: Static pressure (atm) variations across the centreline of the diverged wall straight diffuser (a) L/L_{max} = 0.0 & b_2/b_1 = 1.1, (b) L/L_{max} = 0.1 & b_2/b_1 = 1.2, (c) L/L_{max} = 0.2 & b_2/b_1 = 1.3 and (d) L/L_{max} = 0.3 & b_2/b_1 = 1.4 at BEP at an operational speed of 58.9rpsK$^{-1/2}$

Figure 4.70 depicts the flow streamlines radially across (a) parallel wall diffuser and diverged wall straight diffuser configurations ((b) L/L_{max} = 0.0 & b_2/b_1 = 1.1, (c) L/L_{max} = 0.1 & b_2/b_1 = 1.2, (d) L/L_{max} = 0.2 & b_2/b_1 = 1.3 and (e) L/L_{max} = 0.3 & b_2/b_1 = 1.4) at BEP at an operational speed of 58.9rpsK$^{-1/2}$. It can be seen from the Figure 4.70(a) that the flow stream within the parallel wall diffuser is uniform, with no flow reversals. Similar flow behaviour is obtained in diverged wall straight diffuser of L/L_{max} = 0.0 & b_2/b_1 = 1.1. Furthermore, it can be seen a further increase of outlet-to-inlet width ratio along with an increase in the distance between the divergence location and the diffuser inlet has caused flow reversals within the diffuser near the diffuser outlet and in the volute. Same flow behaviour has been obtained in the diverged wall diffuser configuration of L/L_{max} = 0.1 & b_2/b_1 = 1.2, L/L_{max} = 0.2 & b_2/b_1 = 1.3 and L/L_{max} = 0.3 & b_2/b_1 = 1.4. It can be seen from the figures that increase in the outlet-to-inlet width ratio has increased cross sectional area, which in-turn increases the flow reversals area. Furthermore, it can also be seen that increase in the distance between the divergence location and the diffuser inlet has shifted the flow separation point on the hub wall. It has been analysed from these flow behaviours within diverged wall diffuser configurations that increased area ratio causes increase in the adverse pressure gradient on the hub wall. The adverse pressure gradient values away from zero causes the flow separation. Furthermore, the location of separation point is dependent upon the velocity gradient normal to the hub wall. When the velocity gradient is equal to zero (dw/dx = 0), it causes wall shear stress to be zero. Furthermore, the location where the velocity gradient normal to the surface is zero is known as flow separation point. This thickens the boundary layer along with flow separation region [22] and hence causes blockage, which can be captured at the flow separation point [1]. However, after separation of the boundary layer, the assumptions used for boundary layer theory does not work and hence calculated experimentally [22].

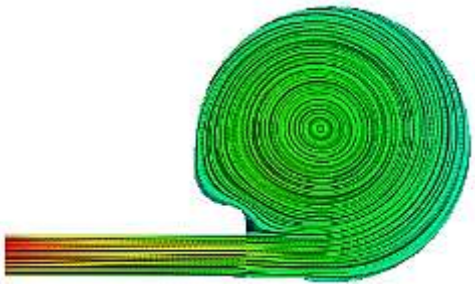

(a)

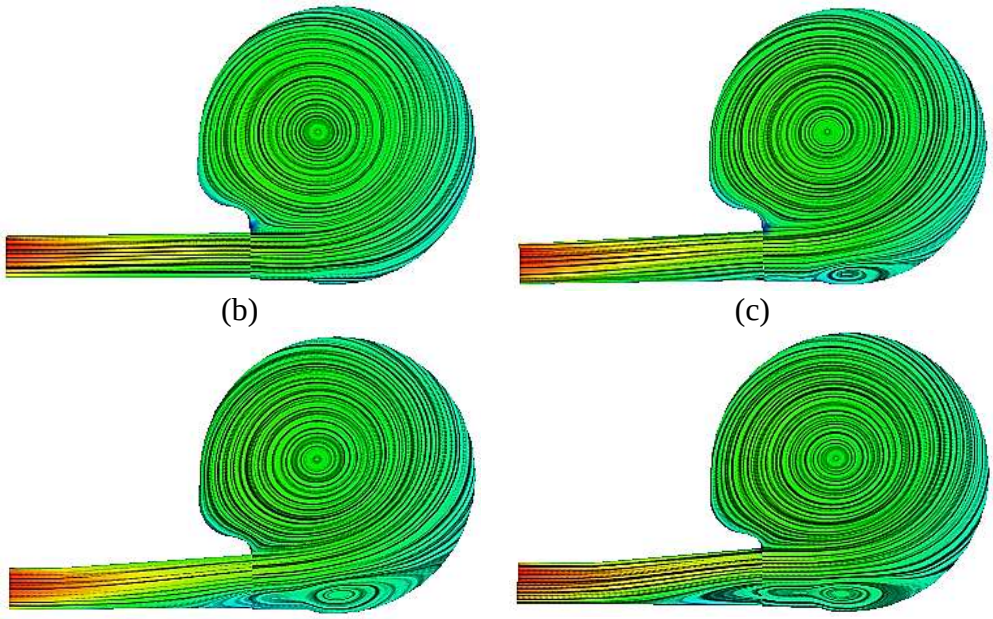

(b) (c)

(d) (e)

Figure 4.70: Flow streamlines radially across the (a) parallel wall diffuser and diverged wall straight diffuser configurations ((b) L/L_{max} = 0.0 & b_2/b_1 = 1.1 (c) L/L_{max} = 0.1 & b_2/b_1 = 1.2, (d) L/L_{max} = 0.2 & b_2/b_1 = 1.3 and (e) L/L_{max} = 0.3 & b_2/b_1 = 1.4) and volute at BEP an operational speed of 58.9rpsK$^{-1/2}$

The analysis has also been carried out in order to observe the flow characteristics circumferentially within the diverged wall straight diffuser and volute. In order to qualitatively analyse the flow characteristics many planes have been created at every 45˚ within the diffuser and volute for the design configuration of L/L_{max} = 0.3 and b_2/b_1 = 1.4. Streamlines have been shown on each plane of the diffuser and the volute (shown in Figure 4.71). It can be seen from the figures that the size of the flow reversals and location of flow separation changes based upon the cross-sectional area of the volute. If the volute cross-sectional area is small, the size of the flow reversals is large and vice versa.

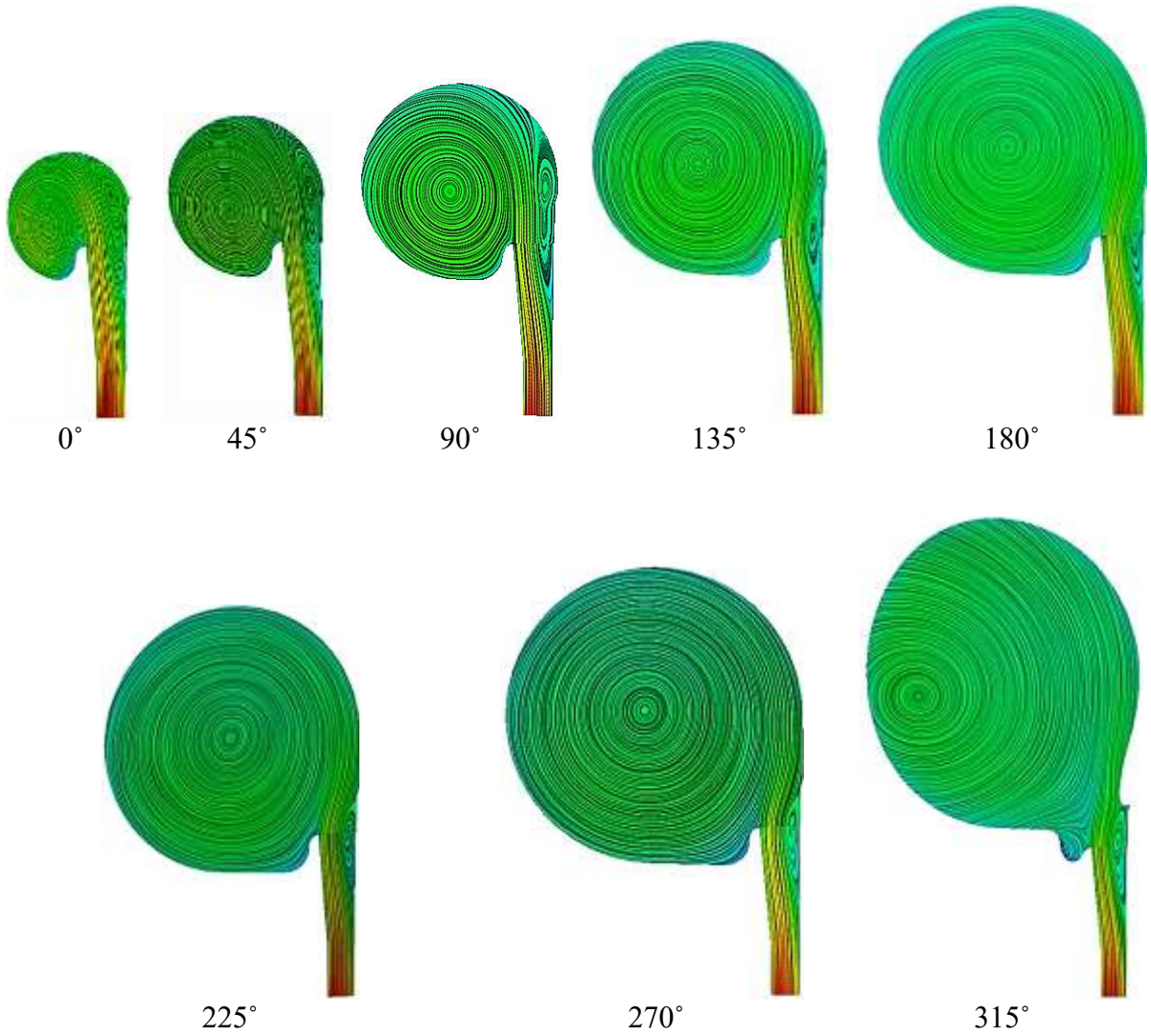

Figure 4.71: Flow streamlines radially across the diverged wall straight diffuser configuration of L/L_{max} = 0.3 & b_2/b_1 = 1.4 and volute for every 45˚ at BEP at an operational speed of 58.9rpsK$^{-1/2}$

Figure 4.72 depicts the comparison of velocity magnitude distribution across parallel wall and diverged wall straight diffuser configurations (L/L_{max} = 0.0 & b_2/b_1 = 1.1 and L/L_{max} = 0.0 & b_2/b_1 = 1.4) from the hub wall to the shroud wall at BEP at an operational speed of 58.9rpsK$^{-1/2}$. It can be seen that the velocity magnitude is reduced radially across the diffuser. It can be seen that the velocity magnitude at L1 (diffuser inlet) is similar at parallel and diverged wall straight diffusers, whereas the velocity magnitude is lower at L5 (diffuser outlet) for diverged wall diffuser configurations in comparison to parallel wall diffuser. Furthermore, it has been observed that the velocity magnitude is asymmetric across the parallel and diverged wall straight diffuser. Moreover, it can be seen from the figure that the velocity magnitude becomes highly asymmetric across the diverged wall diffuser configuration of L/L_{max} = 0.0 & b_2/b_1 = 1.4. This is due to flow reversals at the outlet of diverged wall

straight diffuser. However, the detailed analysis has been carried out by quantifying the asymmetric ratio for the velocity magnitude profile across the diverged wall diffusers.

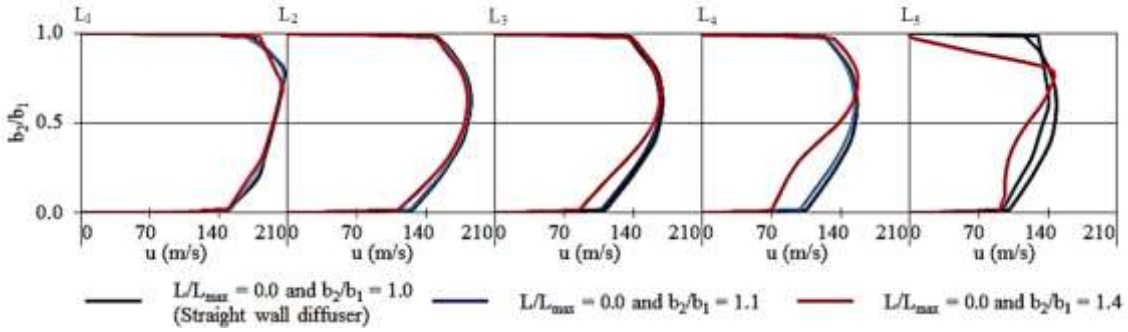

Figure 4.72: Comparison of velocity magnitude (m/s) distribution across parallel wall and diverged wall straight diffuser configurations from the hub wall to the shroud wall at BEP at an operational speed of 58.9rpsK$^{-1/2}$

The behaviour of velocity magnitude across the diverged wall straight diffuser is explained using symmetric and asymmetric behaviour of the velocity field profiles. Figure 4.73 depicts the local asymmetric ratio for the velocity magnitudes, α_{vm} across the diverged wall diffusers (L/L_{max} = 0.0 & b_2/b_1 = 1.1 and L/L_{max} = 0.0 & b_2/b_1 = 1.4) at BEP at an operational speed of 58.9rpsK$^{-1/2}$. α_{vm} values of 1.0 shows the flow is symmetric, α_{vm} values below 1.0 shows asymmetric flow towards the hub wall and α_{vm} values above 1.0 shows asymmetric flow towards the shroud wall. It can be seen that the flow is asymmetric towards the shroud wall across the diverged wall diffuser. The asymmetric ratio for the velocity magnitude increases from the centreline of the diffuser towards the wall and from the diffuser inlet to the diffuser outlet in both diverged wall diffusers. However, it has been noticed that increase of outlet-to-inlet width ratio by considering same wall diverged location from the inlet makes the flow highly asymmetrical.

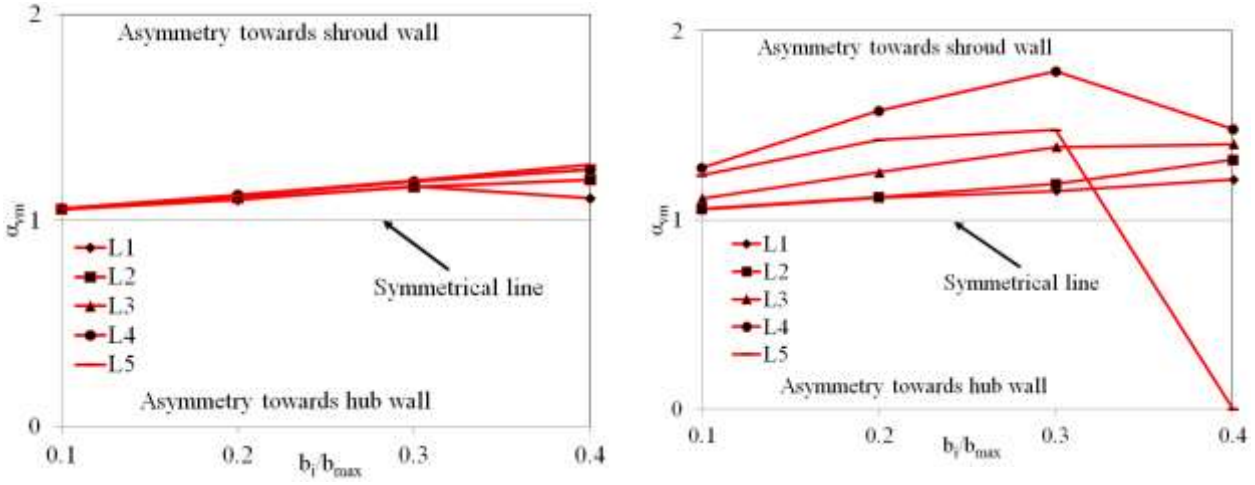

(a) (b)

Figure 4.73: Local asymmetric ratio for the velocity magnitude, α_{vm} across the diverged wall diffusers ((a) L/L_{max} = 0.0 & b_2/b_1 = 1.1 and (b) L/L_{max} = 0.0 & b_2/b_1 = 1.4) at BEP at an operational speed of 58.9rpsK$^{-1/2}$

Figure 4.74 depicts the comparison of velocity magnitude distribution across parallel wall and diverged wall straight diffuser configurations (L/L_{max} = 0.0 & b_2/b_1 = 1.4 and L/L_{max} = 0.3 & b_2/b_1 = 1.4) from the hub wall to the shroud wall at BEP at an operational speed of 58.9rpsK$^{-1/2}$. It can be seen that the velocity magnitude is reduced radially across the diffuser. It can be seen that the velocity magnitude at L1 (diffuser inlet) is similar at parallel and diverged wall straight diffusers, whereas the velocity magnitude is lower at L5 (diffuser outlet) for diverged wall diffuser configurations in comparison to parallel wall diffuser. Furthermore, it has been observed that the velocity magnitude is asymmetric across the parallel and diverged wall straight diffuser. Moreover, it can be seen from the figure that the velocity magnitude becomes highly asymmetric across both diverged wall diffuser configurations analysed. This is due to flow reversals at the outlet of diverged wall straight diffuser. However, the detailed analysis has been carried out by quantifying the asymmetric ratio for the velocity magnitude profile across the diverged wall diffusers.

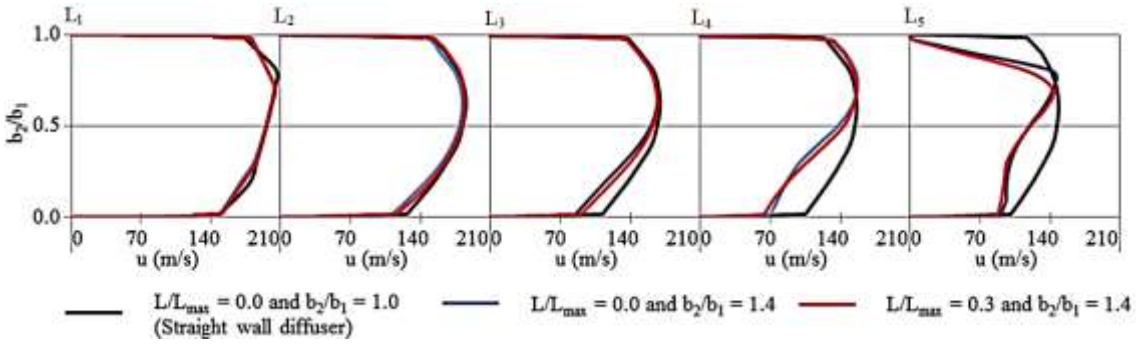

Figure 4.74: Comparison of velocity magnitude (m/s) distribution across parallel wall and diverged wall straight diffuser configurations from the hub wall to the shroud wall at BEP at an operational speed of 58.9rpsK$^{-1/2}$

Figure 4.75 depicts the local asymmetric ratio for the velocity magnitudes, α_{vm} across the diverged wall diffusers (L/L_{max} = 0.0 & b_2/b_1 = 1.4 and L/L_{max} = 0.3 & b_2/b_1 = 1.4) at BEP at an operational speed of 58.9rpsK$^{-1/2}$. It can be seen that the flow is asymmetric towards the shroud wall across the diverged wall diffusers. The asymmetric ratio for the velocity magnitude remains similar from the centreline of the diffuser towards the wall and from the diffuser inlet to the diffuser outlet in both diverged wall diffusers. However, it has been noticed that by increasing wall diverged location from

the inlet and considering same increase of outlet-to-inlet width ratio do not have considerable effect on the asymmetry of the flow within the diffuser.

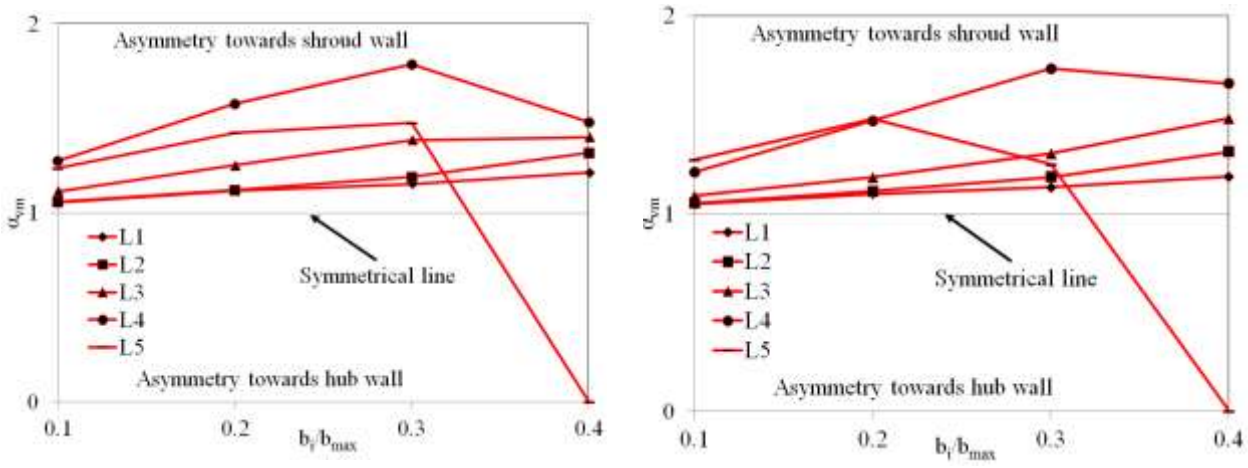

Figure 4.75: Local asymmetric ratio for the velocity magnitude, α_{vm} across the diverged wall diffusers ((a) L/L_{max} = 0.0 & b_2/b_1 = 1.4 and (b) L/L_{max} = 0.3 & b_2/b_1 = 1.4) at BEP at an operational speed of 58.9rpsK$^{-1/2}$

Figure 4.76 depicts the comparison of velocity magnitude distribution across parallel wall and diverged wall straight diffuser configurations (L/L_{max} = 0.0 & b_2/b_1 = 1.1, L/L_{max} = 0.1 & b_2/b_1 = 1.2, L/L_{max} = 0.2 & b_2/b_1 = 1.3 and L/L_{max} = 0.3 & b_2/b_1 = 1.4) from the hub wall to the shroud wall at BEP at an operational speed of 58.9rpsK$^{-1/2}$. It can be seen that the velocity magnitude is reduced radially across the diffuser. It can be seen that the velocity magnitude at L1 (diffuser inlet) is similar at parallel and diverged wall straight diffusers, whereas the velocity magnitude is lower at L5 (diffuser outlet) for diverged wall diffuser configurations in comparison to parallel wall diffuser. Furthermore, it has been observed that the velocity magnitude is asymmetric across the parallel and diverged wall straight diffuser. Moreover, it can be seen that the flow asymmetry for velocity magnitude is increasing with the combined increase of diffuser outlet-to inlet width ratio and wall divergence location from the inlet. However, the detailed analysis has been carried out by quantifying the asymmetric ratio for the velocity magnitude profile across the diverged wall diffusers, which has been explained in the next sections.

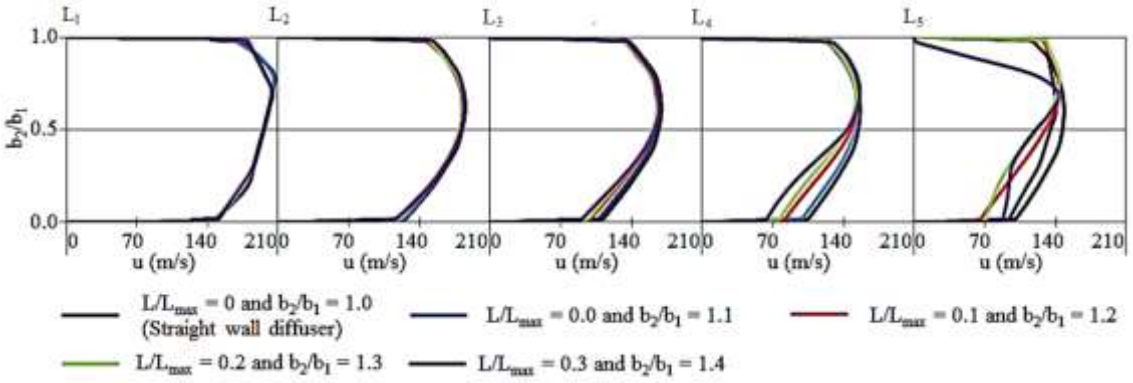

Figure 4.76: Comparison of velocity magnitude (m/s) distribution across parallel wall and diverged wall straight diffuser configurations from the hub wall to the shroud wall at BEP at an operational speed of 58.9rpsK$^{-1/2}$

Figure 4.77 depicts the local asymmetric ratio for the velocity magnitudes, α_{vm} across the diverged wall diffusers (L/L_{max} = 0.0 & b_2/b_1 = 1.1, L/L_{max} = 0.1 & b_2/b_1 = 1.2, L/L_{max} = 0.2 & b_2/b_1 = 1.3 and L/L_{max} = 0.3 & b_2/b_1 = 1.4) at BEP at an operational speed of 58.9rpsK$^{-1/2}$. It can be seen that the flow is asymmetric towards the shroud wall across the diverged wall diffusers. The asymmetric ratio for the velocity magnitude constantly increases from the centreline of the diffuser towards the wall and from the diffuser inlet to the diffuser outlet in both diverged wall diffusers. However, it has been noticed that increasing both wall diverged location from the inlet and outlet-to-inlet width ratio increases local asymmetric ratio of the flow within the diffuser. It can also be observed that at diverged wall diffuser of L/L_{max} = 0.3 & b_2/b_1 = 1.4, the flow near the wall has asymmetry towards the hub wall.

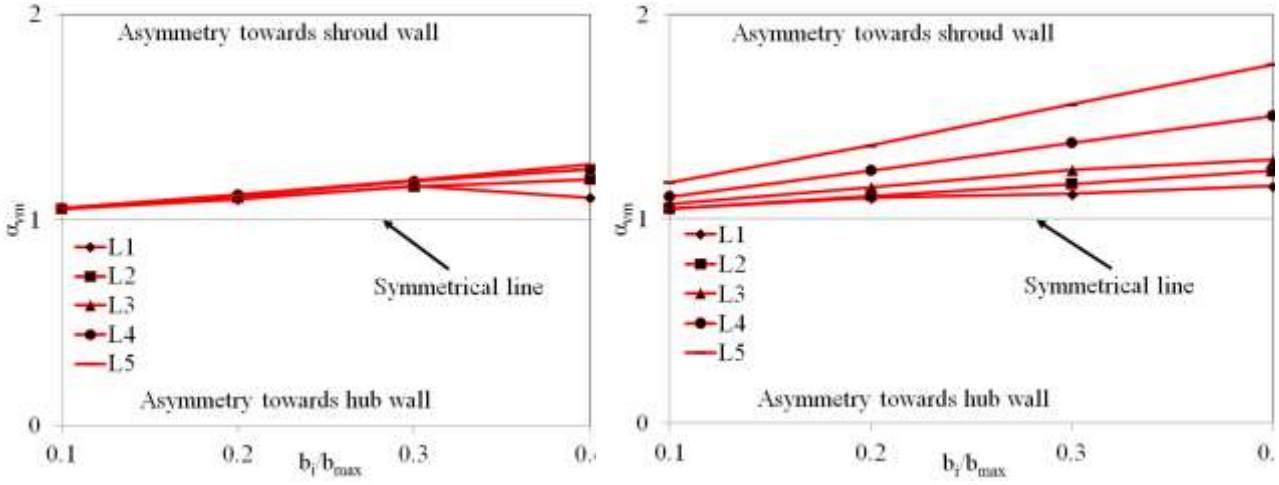

(a) (b)

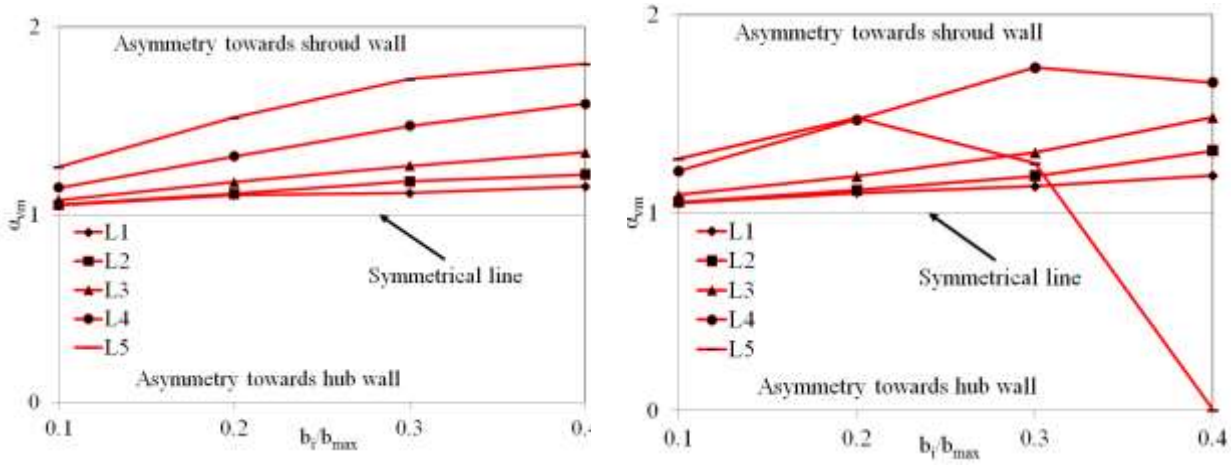

Figure 4.77: Local asymmetric ratio for the velocity magnitude, α_{vm} across the diverged wall diffusers ((a) L/L_{max} = 0.0 & b_2/b_1 = 1.1, (b) L/L_{max} = 0.1 & b_2/b_1 = 1.2, (c) L/L_{max} = 0.2 & b_2/b_1 = 1.3 and (d) L/L_{max} = 0.3 & b_2/b_1 = 1.4) at BEP at an operational speed of 58.9rpsK$^{-1/2}$

Figure 4.78 depicts the radial velocity distribution across the centreline of the diverged wall diffuser configurations ((a) L/L_{max} = 0.0 & b_2/b_1 = 1.1 and (b) L/L_{max} = 0.0 & b_2/b_1 = 1.4) at BEP at an operational speed of 58.9rpsK$^{-1/2}$. The trend of the radial velocity across the diverged wall straight diffusers is similar to that across the straight diffuser. It can be seen that the maximum radial velocity is obtained at the diffuser inlet after the volute-tongue region. The radial velocity decreases radially across the diffuser. Furthermore, the radial velocity also decreases circumferentially in the direction of impeller rotation (ω). The minimum radial velocity is obtained at the diffuser outlet at near the volute-tongue region. It can be seen that the radial velocity values are increased by 3.5% and 1.0% at the diffuser inlet and diffuser outlet across diverged wall diffuser configuration (L/L_{max} = 0.0 & b_2/b_1 = 1.1) in comparison to that across the parallel wall diffuser. Furthermore, it can be seen that the radial velocity is further increased at the diffuser inlet by 27% and decreased at diffuser outlet by 1.9% across diffuser configuration of L/L_{max} = 0.0 & b_2/b_1 = 1.4 in comparison to that across diffuser configuration of L/L_{max} = 0.0 & b_2/b_1 = 1.1. This trend explains that the radial velocity increases when outlet-to-inlet width ratio of the diffuser is increased up to 1.1 and it is decreased when b_2/b_1 is 1.4 whilst keeping the divergence location at the diffuser inlet.

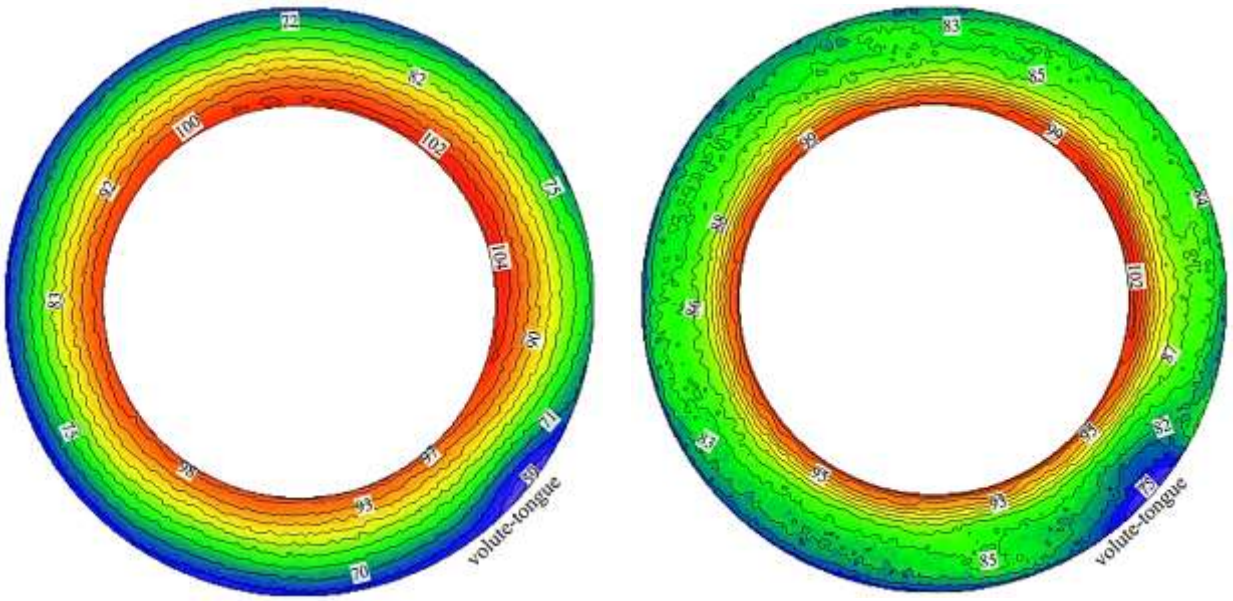

(a) (b)

Figure 4.78: Radial velocity (m/s) distributions across the centreline of the diverged wall straight diffuser (a) L/L_{max} = 0.0 & b_2/b_1 = 1.1 and (b) L/L_{max} = 0 & b_2/b_1 = 1.4 at BEP at an operational speed of 58.9rpsK$^{-1/2}$

Figure 4.79 depicts the radial velocity distribution across the centreline of the diverged wall diffuser configurations ((a) L/L_{max} = 0.0 & b_2/b_1 = 1.4 and (b) L/L_{max} = 0.3 & b_2/b_1 = 1.4) at BEP at an operational speed of 58.9rpsK$^{-1/2}$. The trend of the radial velocity across the diverged wall straight diffusers is similar to that across the straight diffuser. It can be seen that the maximum radial velocity is obtained at the diffuser inlet after the volute-tongue region. The radial velocity decreases radially across the diffuser. Furthermore, the radial velocity also decreases circumferentially in the direction of impeller rotation (ω). The minimum radial velocity is obtained at the diffuser outlet at near the volute-tongue region. It can be seen that the radial velocity values are increased across the diverged wall diffuser configuration (L/L_{max} = 0.0 & b_2/b_1 = 1.4) in comparison to that across the parallel wall diffuser. The radial velocity is increased at the diffuser inlet by 32% and decreased at the diffuser outlet by 1.0% in comparison to that at parallel wall diffuser. Furthermore, it can also be seen that the radial velocity is same across both diverged wall diffuser configurations. This trend explains that the radial velocity remains same when the distance between the divergence location and the diffuser inlet is increased by considering the divergence location at the diffuser inlet.

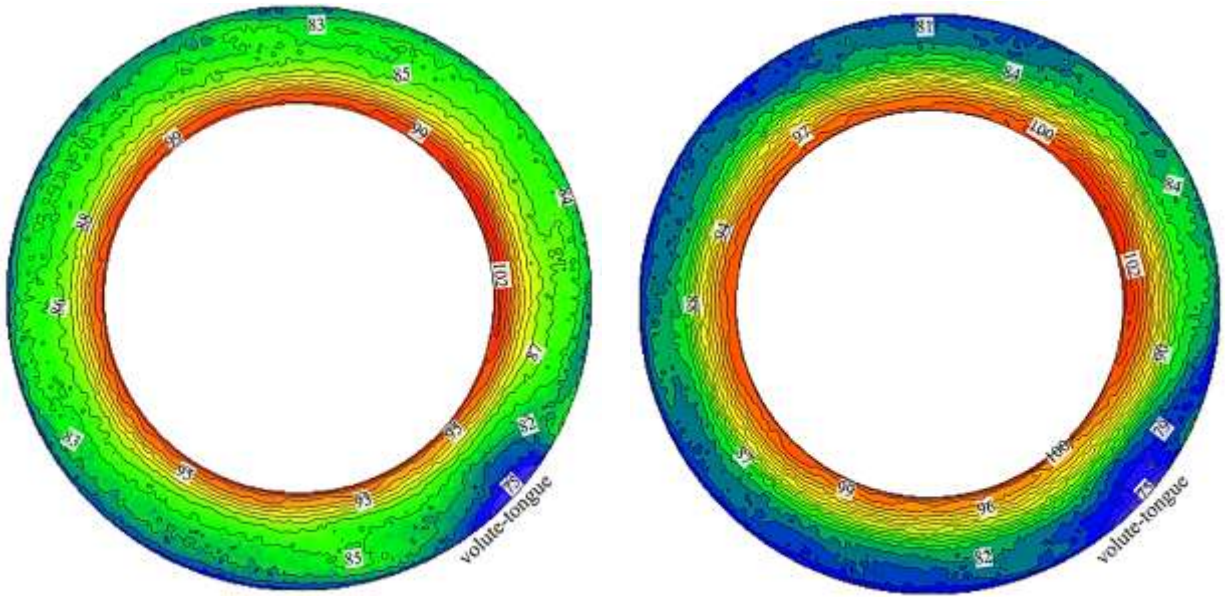

(a) (b)

Figure 4.79: Radial velocity (m/s) distributions across the centreline of the diverged wall straight diffuser (a) L/L_{max} = 0.0 & b_2/b_1 = 1.4 and (b) L/L_{max} = 0.3 & b_2/b_1 = 1.4 at BEP at an operational speed of 58.9rpsK$^{-1/2}$

Figure 4.80 depicts the radial velocity distribution across the centreline of the diverged wall diffuser configurations (a) L/L_{max} = 0.0 & b_2/b_1 = 1.1, (b) L/L_{max} = 0.1 & b_2/b_1 = 1.2, (c) L/L_{max} = 0.2 & b_2/b_1 = 1.3 and (d) L/L_{max} = 0.3 & b_2/b_1 = 1.4) at BEP at an operational speed of 58.9rpsK$^{-1/2}$. The trend of the radial velocity across the diverged wall straight diffusers is similar to that across the straight diffuser. It can be seen that the maximum radial velocity is obtained at the diffuser inlet after the volute-tongue region. The radial velocity decreases radially across the diffuser. Furthermore, the radial velocity also decreases circumferentially in the direction of impeller rotation (ω). The minimum radial velocity is obtained at the diffuser outlet at near the volute-tongue region. It can be seen that the radial velocity is higher at the diffuser inlet and diffuser outlet by 3.5% and 1.0% respectively across the diverged wall diffuser configuration (L/L_{max} = 0.0 & b_2/b_1 = 1.1) in comparison to that at parallel wall diffuser. Furthermore, the radial velocity is increased at the diffuser inlet by 12% and decreased at the diffuser outlet by 1.0% across diffuser configuration of L/L_{max} = 0.1 & b_2/b_1 = 1.2 in comparison to that across diffuser configuration of L/L_{max} = 0.0 & b_2/b_1 = 1.1. Similar trend is obtained for the rest of the diverged wall diffuser configurations. The radial velocity is increased by 15% and 27% at the diffuser inlet across the diverged wall diffuser configurations of L/L_{max} = 0.2 & b_2/b_1 = 1.3 and L/L_{max} = 0.3 & b_2/b_1 = 1.4 in comparison to that across diffuser configuration of L/L_{max} = 0.0 & b_2/b_1 = 1.1. Moreover, the radial velocity is decreased by 1.9% each at the diffuser outlet across the diverged wall diffuser configurations of L/L_{max} = 0.2 & b_2/b_1 = 1.3 and L/L_{max} = 0.3 &

b_2/b_1 = 1.4 in comparison to that across diffuser configuration of L/L_{max} = 0.0 & b_2/b_1 = 1.1. This trend explains that the radial decreases with the increase of both the distance between the divergence location and the diffuser inlet and outlet-to-inlet width ratio of the diffuser.

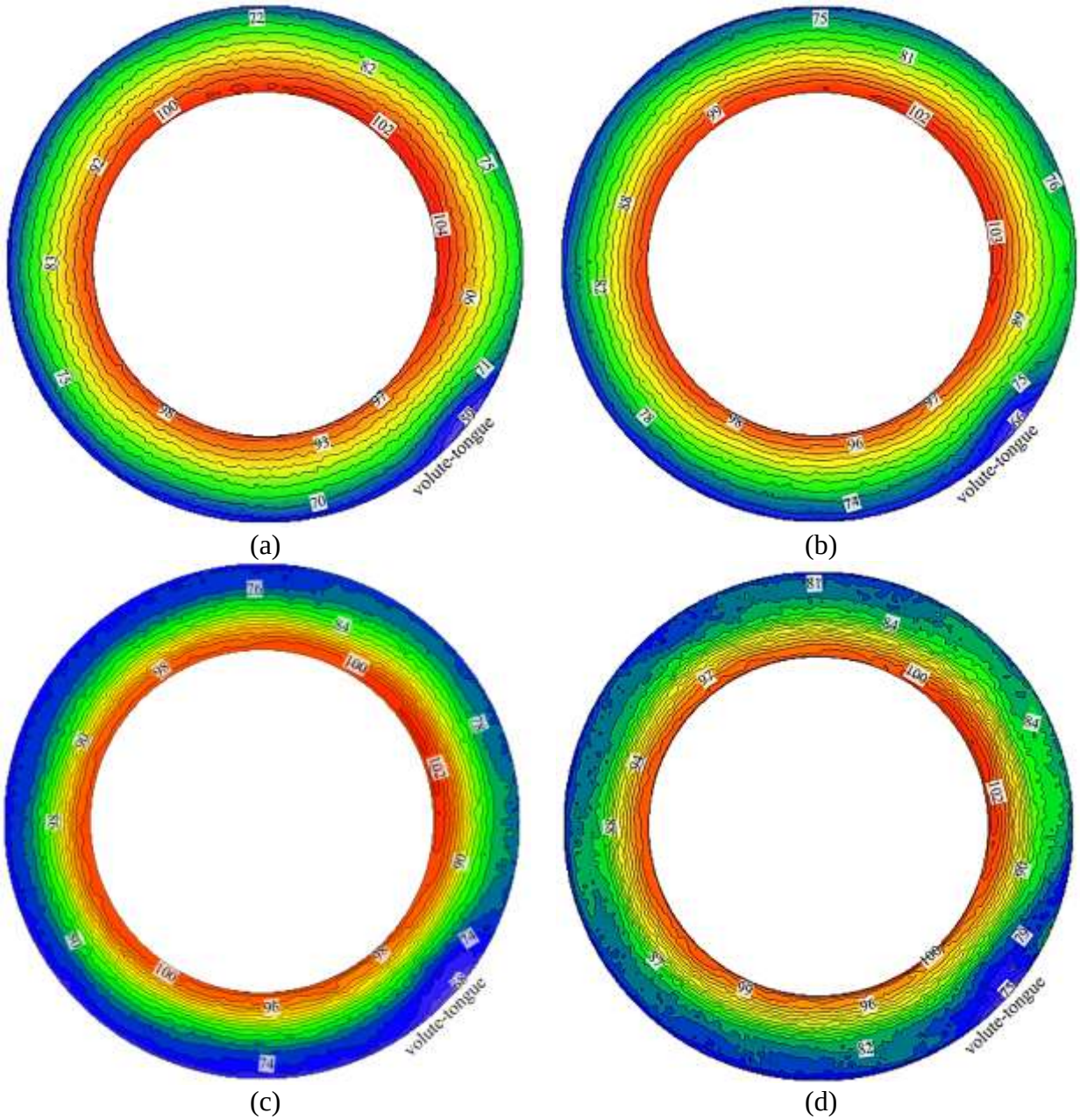

(a) (b)

(c) (d)

Figure 4.80: Radial velocity (m/s) distributions across the centreline of the diverged wall straight diffuser (a) L/L_{max} = 0.0 & b_2/b_1 = 1.1, (b) L/L_{max} = 0.1 & b_2/b_1 = 1.2, (c) L/L_{max} = 0.2 & b_2/b_1 = 1.3 and (d) L/L_{max} = 0.3 & b_2/b_1 = 1.4 at BEP at an operational speed of 58.9rpsK$^{-1/2}$

Figure 4.81 depicts the comparison of radial velocity distribution across parallel wall and diverged wall straight diffuser configurations (L/L_{max} = 0.0 & b_2/b_1 = 1.1 and L/L_{max} = 0.0 & b_2/b_1 = 1.4) from

the hub wall to the shroud wall at BEP at an operational speed of 58.9rpsK$^{-1/2}$. It can be seen that the radial velocity is reduced radially across the diffuser. It can be seen that the radial velocity at L1 (diffuser inlet) is similar at parallel and diverged wall straight diffusers, whereas the radial velocity is lower at L5 (diffuser outlet) for diverged wall diffuser configurations in comparison to parallel wall diffuser. Furthermore, it has been observed that the radial velocity is asymmetric across the parallel and diverged wall straight diffuser. Moreover, it can be seen from the figure that the radial velocity becomes highly asymmetric across the diverged wall diffuser configuration of L/L_{max} = 0.0 & b_2/b_1 = 1.4. This is due to flow reversals near the hub wall at the outlet of diverged wall straight diffuser. However, the detailed analysis has been carried out by quantifying the asymmetric ratio for the radial velocity profile across the diverged wall diffusers.

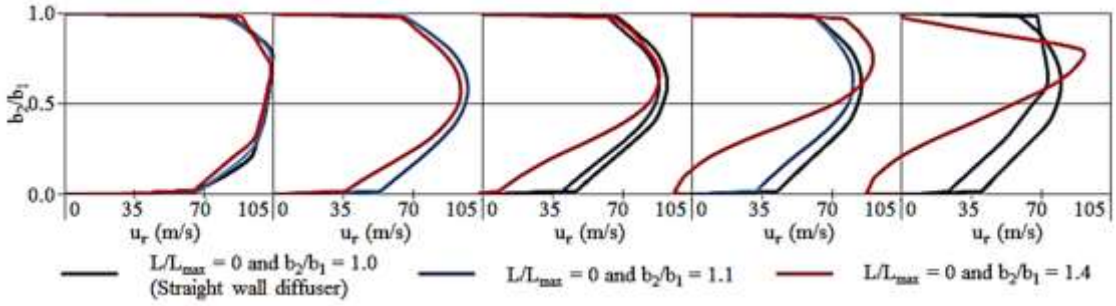

Figure 4.81: Comparison of radial velocity (m/s) distribution across parallel wall and diverged wall straight diffuser configurations from the hub wall to the shroud wall at BEP at an operational speed of 58.9rpsK$^{-1/2}$

The behaviour of radial velocity across the diverged wall straight diffuser is explained using symmetric and asymmetric behaviour of the velocity field profiles. Figure 4.82 depicts the local asymmetric ratio for the radial velocity, α_{vr} across the diverged wall diffusers (L/L_{max} = 0.0 & b_2/b_1 = 1.1 and L/L_{max} = 0.0 & b_2/b_1 = 1.4) at BEP at an operational speed of 58.9rpsK$^{-1/2}$. α_{vr} values of 1.0 shows the flow is symmetric, α_{vr} values below 1.0 shows asymmetric flow towards the hub wall and α_{vr} values above 1.0 shows asymmetric flow towards the shroud wall. It can be seen that the flow is asymmetric towards the shroud wall across the diverged wall diffuser. The asymmetric ratio for the radial velocity increases from the centreline of the diffuser towards the wall and from the diffuser inlet to the diffuser outlet in both diverged wall diffusers. However, it has been noticed that increase of outlet-to-inlet width ratio by considering same wall diverged location from the inlet makes the flow highly asymmetrical. This causes flow reversal near the hub wall of the diverged wall diffuser.

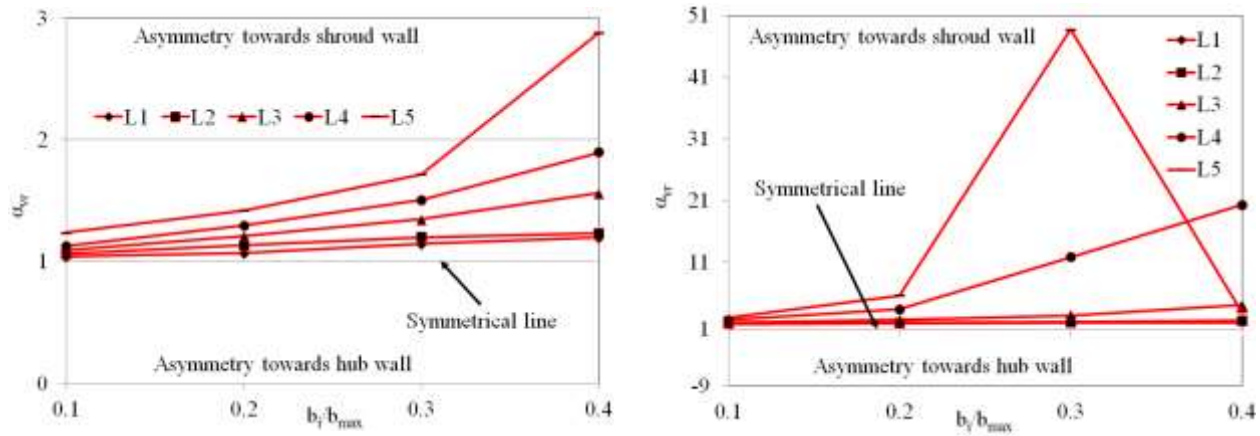

Figure 4.82: Local asymmetric ratio for the radial velocity, α_{vr} across the diverged wall diffusers ((a) L/L_{max} = 0.0 & b_2/b_1 = 1.4 and (b) L/L_{max} = 0.3 & b_2/b_1 = 1.4) at BEP at an operational speed of 58.9rpsK$^{-1/2}$

Figure 4.83 depicts the comparison of radial velocity distribution across parallel wall and diverged wall straight diffuser configurations (L/L_{max} = 0.0 & b_2/b_1 = 1.4 and L/L_{max} = 0.3 & b_2/b_1 = 1.4) from the hub wall to the shroud wall at BEP at an operational speed of 58.9rpsK$^{-1/2}$. It can be seen that the radial velocity is reduced radially across the diffuser. It can be seen that the radial velocity at L1 (diffuser inlet) is similar at parallel and diverged wall straight diffusers, decreasing across the diffuser at from L2 to L5 (diffuser outlet) for diverged wall diffuser configurations in comparison to parallel wall diffuser. Furthermore, it has been observed that the radial velocity is asymmetric across the parallel and diverged wall straight diffuser. It can also be seen from the figure that the radial velocity becomes highly asymmetric across both diverged wall diffuser configurations analysed. This is due to flow reversals near the hub wall at the outlet of diverged wall straight diffuser. However, the detailed analysis has been carried out by quantifying the asymmetric ratio for the radial velocity profile across the diverged wall diffusers.

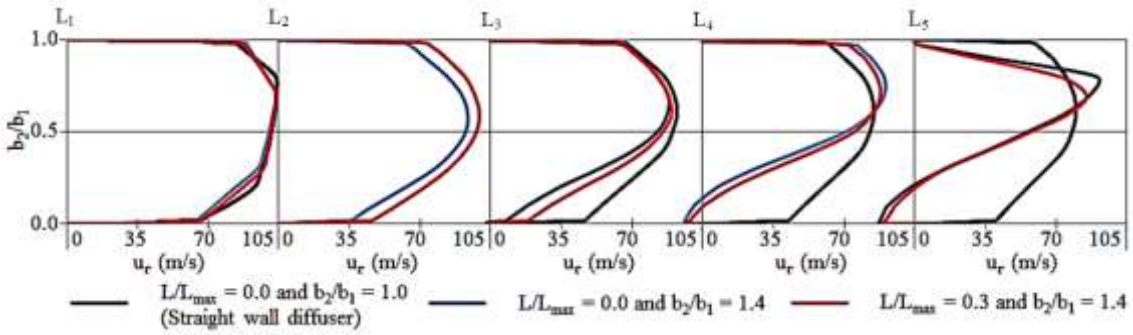

Figure 4.83: Comparison of radial velocity (m/s) distribution across parallel wall and diverged wall straight diffuser configurations from the hub wall to the shroud wall at BEP at an operational speed of 58.9rpsK$^{-1/2}$

Figure 4.84 depicts the local asymmetric ratio for the radial velocity, α_{vr} across the diverged wall diffusers (L/L_{max} = 0.0 & b_2/b_1 = 1.4 and L/L_{max} = 0.3 & b_2/b_1 = 1.4) at BEP at an operational speed of 58.9rpsK$^{-1/2}$. It can be seen that the flow is asymmetric towards the shroud wall across the diverged wall diffusers. The asymmetric ratio for the radial velocity remains similar from the centreline of the diffuser towards the wall and from the diffuser inlet to the diffuser outlet in both diverged wall diffusers. It has been noticed that by increasing wall diverged location from the inlet and considering same increase of outlet-to-inlet width ratio increases the asymmetry of the flow at L5. However, flow field at L4 changes its asymmetry from the shroud wall to the hub wall.

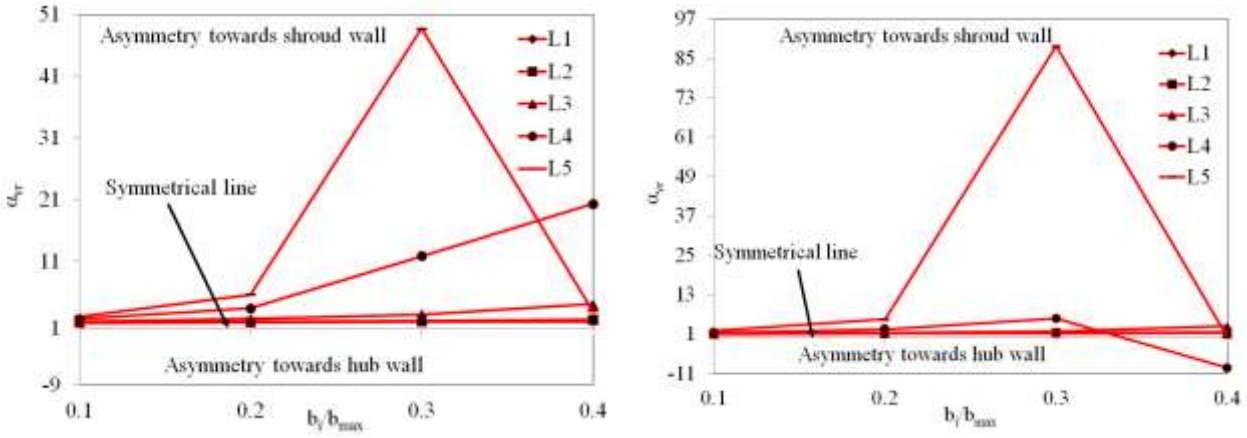

(a) (b)

Figure 4.84: Local asymmetric ratio for the radial velocity, α_{vr} across the diverged wall diffusers ((a) L/L_{max} = 0.0 & b_2/b_1 = 1.4 and (b) L/L_{max} = 0.3 & b_2/b_1 = 1.4) at BEP at an operational speed of 58.9rpsK$^{-1/2}$

Figure 4.85 depicts the comparison of radial velocity distribution across parallel wall and diverged wall straight diffuser configurations (L/L_{max} = 0.0 & b_2/b_1 = 1.1, L/L_{max} = 0.1 & b_2/b_1 = 1.2, L/L_{max} = 0.2 & b_2/b_1 = 1.3 and L/L_{max} = 0.3 & b_2/b_1 = 1.4) from the hub wall to the shroud wall at BEP at an operational speed of 58.9rpsK$^{-1/2}$. It can be seen that the radial velocity is reduced radially across the diffuser. It can be seen that the radial velocity at L1 (diffuser inlet) is similar at parallel and diverged wall straight diffusers, whereas the radial velocity is decreasing towards L5 (diffuser outlet) for diverged wall diffuser configurations in comparison to parallel wall diffuser. Furthermore, it has been observed that the radial velocity is asymmetric across the parallel and diverged wall straight diffuser.

However, it has been noticed that the radial flow velocity has no flow reversal in L/L_{max} = 0.0 & b_2/b_1 = 1.1, which is similar to parallel wall diffuser. On the other hand, as the outlet to inlet width ratio increases along with the increase of wall divergence location from the inlet, flow reversals have been found. This behaviour makes the flow highly asymmetric for those diverged wall diffuser configurations. However, the detailed analysis has been carried out by quantifying the asymmetric ratio for the radial velocity profile across the diverged wall diffusers.

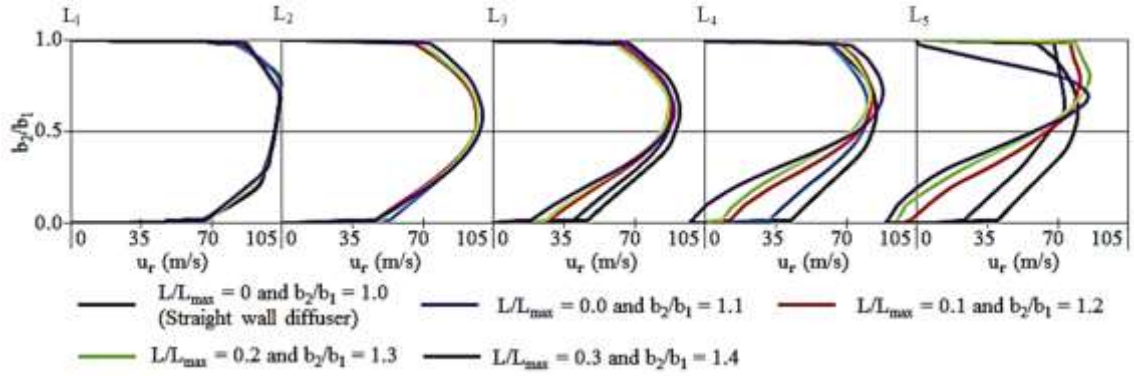

Figure 4.85: Comparison of radial velocity (m/s) distribution across parallel wall and diverged wall straight diffuser configurations from the hub wall to the shroud wall at BEP at an operational speed of 58.9rpsK$^{-1/2}$

Figure 4.86 depicts the local asymmetric ratio for the radial velocity, α_{vr} across the diverged wall diffusers (L/L_{max} = 0.0 & b_2/b_1 = 1.1, L/L_{max} = 0.1 & b_2/b_1 = 1.2, L/L_{max} = 0.2 & b_2/b_1 = 1.3 and L/L_{max} = 0.3 & b_2/b_1 = 1.4) at BEP at an operational speed of 58.9rpsK$^{-1/2}$. It can be seen that the flow is asymmetric towards the shroud wall across the diverged wall diffusers. The asymmetric ratio for the radial velocity constantly increases from the centreline of the diffuser towards the wall and from the diffuser inlet to the diffuser outlet in both diverged wall diffusers. This causes the flow reversal within the diverged wall diffusers. It can also be observed that at diverged wall diffuser of L/L_{max} = 0.3 & b_2/b_1 = 1.4, the flow near the wall has asymmetry towards the hub wall.

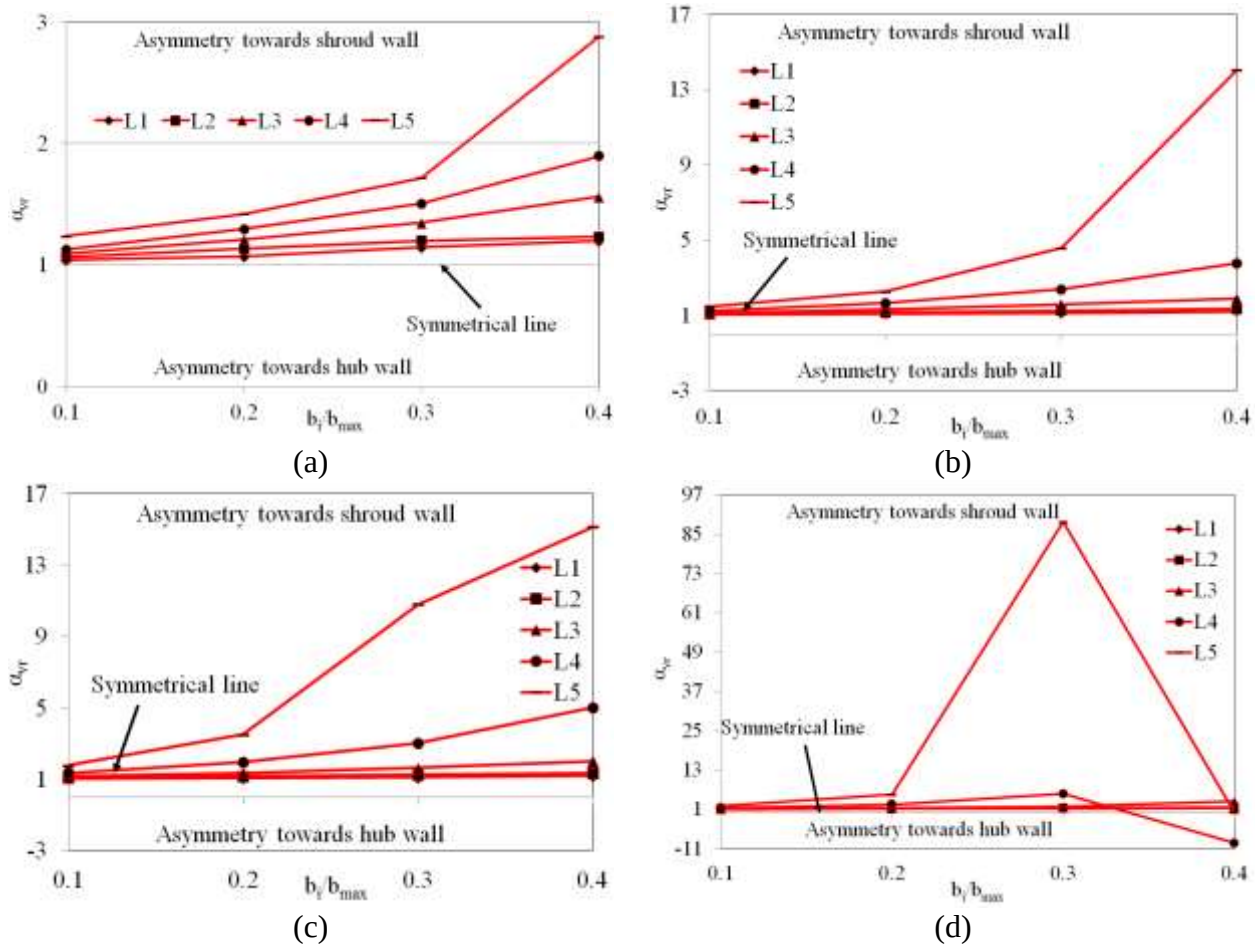

Figure 4.86: Local asymmetric ratio for the radial velocity, α_{vr} across the diverged wall diffusers ((a) L/L_{max} = 0.0 & b_2/b_1 = 1.1, (b) L/L_{max} = 0.1 & b_2/b_1 = 1.2, (c) L/L_{max} = 0.2 & b_2/b_1 = 1.3 and (d) L/L_{max} = 0.3 & b_2/b_1 = 1.4) at BEP at an operational speed of 58.9rpsK$^{-1/2}$

Figure 4.87 depicts the circumferential velocity distribution across the centreline of the diverged wall diffuser configurations ((a) L/L_{max} = 0.0 & b_2/b_1 = 1.1 and (b) L/L_{max} = 0.0 & b_2/b_1 = 1.4) at BEP at an operational speed of 58.9rpsK$^{-1/2}$. The trend of the circumferential velocity across the diverged wall straight diffusers is similar to that across the straight diffuser. It can be seen that the maximum circumferential velocity is obtained at the diffuser inlet after the volute-tongue region. The circumferential velocity decreases radially across the diffuser. Furthermore, the circumferential velocity also decreases circumferentially in the direction of impeller rotation (ω). The minimum circumferential velocity is obtained at the diffuser outlet at near the volute-tongue region. It can be seen that the circumferential velocity is increased by 9.7% at the diffuser inlet and decreased by 0.6% at diffuser outlet across diverged wall diffuser configuration (L/L_{max} = 0.0 & b_2/b_1 = 1.1) in comparison to that across the parallel wall diffuser. Furthermore, it can be seen that the

circumferential velocity is decreased at the diffuser inlet by 3.5% and increased at diffuser outlet by 0.6% across diffuser configuration of L/L_{max} = 0.0 & b_2/b_1 = 1.4 in comparison to that across diffuser configuration of L/L_{max} = 0.0 & b_2/b_1 = 1.1. This trend explains that the circumferential velocity increases when outlet-to-inlet width ratio of the diffuser is increased up to 1.1 and it is decreased when b_2/b_1 is 1.4 whilst keeping the divergence location at the diffuser inlet.

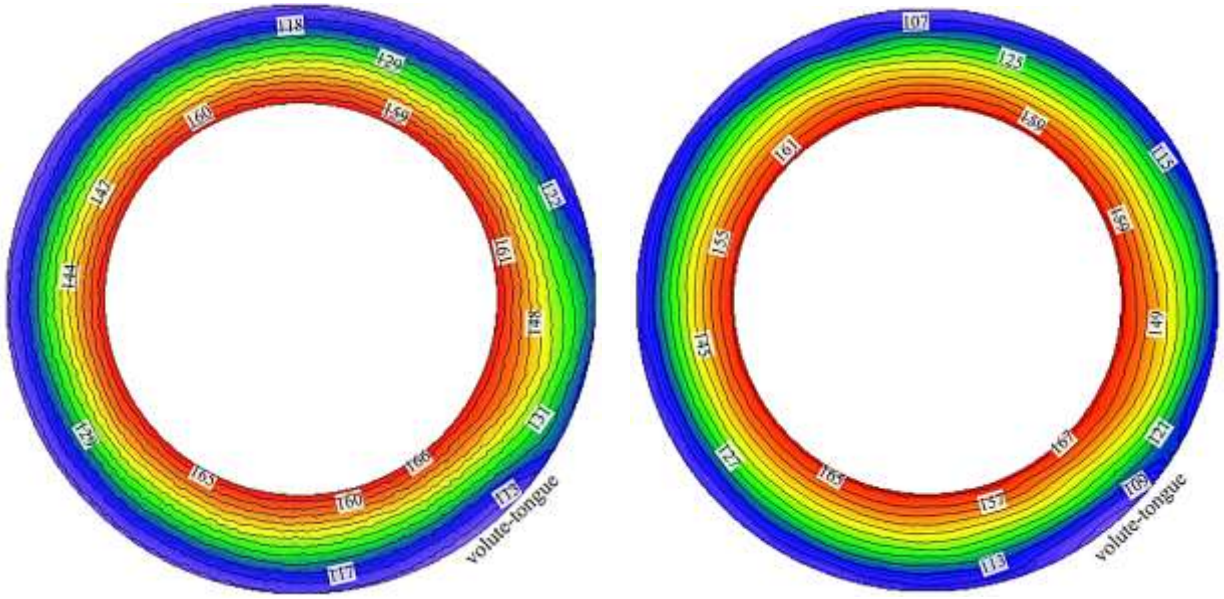

(a) (b)

Figure 4.87: Circumferential velocity (m/s) distributions across the centreline of the diverged wall straight diffuser (a) L/L_{max} = 0.0 & b_2/b_1 = 1.1 and (b) L/L_{max} = 0 & b_2/b_1 = 1.4 at BEP at an operational speed of 58.9rpsK$^{-1/2}$

Figure 4.88 depicts the circumferential velocity distribution across the centreline of the diverged wall diffuser configurations ((a) L/L_{max} = 0.0 & b_2/b_1 = 1.4 and (b) L/L_{max} = 0.3 & b_2/b_1 = 1.4) at BEP at an operational speed of 58.9rpsK$^{-1/2}$. The trend of the circumferential velocity across the diverged wall straight diffusers is similar to that across the straight diffuser. It can be seen that the maximum circumferential velocity is obtained at the diffuser inlet after the volute-tongue region. The circumferential velocity decreases radially across the diffuser. Furthermore, the circumferential velocity also decreases circumferentially in the direction of impeller rotation (ω). The minimum circumferential velocity is obtained at the diffuser outlet at near the volute-tongue region. It can be seen that the circumferential velocity values are increased across the diverged wall diffuser configuration (L/L_{max} = 0.0 & b_2/b_1 = 1.4) in comparison to that across the parallel wall diffuser. The circumferential velocity is increased at the diffuser inlet by 5.8% and remains same at the diffuser outlet in comparison to that at parallel wall diffuser. Furthermore, it can also be seen that the

circumferential velocity is same across both diverged wall diffuser configurations. This trend explains that the circumferential velocity remains same when the distance between the divergence location and the diffuser inlet is increased by considering the divergence location at the diffuser inlet.

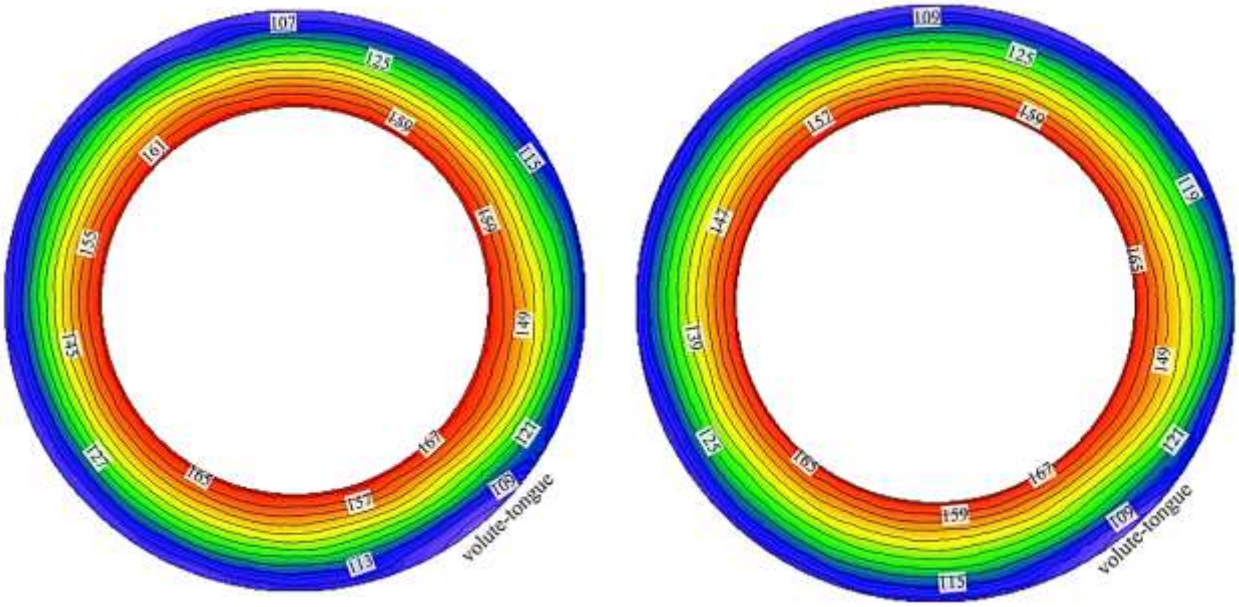

(a) (b)

Figure 4.88: Circumferential velocity (m/s) distributions across the centreline of the diverged wall straight diffuser (a) L/L_{max} = 0.0 & b_2/b_1 = 1.4 and (b) L/L_{max} = 0.3 & b_2/b_1 = 1.4 at BEP at an operational speed of 58.9rpsK$^{-1/2}$

Figure 4.89 depicts the circumferential velocity distribution across the centreline of the diverged wall diffuser configurations (a) L/L_{max} = 0.0 & b_2/b_1 = 1.1, (b) L/L_{max} = 0.1 & b_2/b_1 = 1.2, (c) L/L_{max} = 0.2 & b_2/b_1 = 1.3 and (d) L/L_{max} = 0.3 & b_2/b_1 = 1.4) at BEP at an operational speed of 58.9rpsK$^{-1/2}$. The trend of the circumferential velocity across the diverged wall straight diffusers is similar to that across the straight diffuser. It can be seen that the maximum circumferential velocity is obtained at the diffuser inlet after the volute-tongue region. The circumferential velocity decreases radially across the diffuser. Furthermore, the circumferential velocity also decreases circumferentially in the direction of impeller rotation (ω). The minimum circumferential velocity is obtained at the diffuser outlet at near the volute-tongue region. It can be seen that the circumferential velocity is higher at the diffuser inlet by 10% and lower at the diffuser outlet by 0.6% and 1.0% respectively across the diverged wall diffuser configuration (L/L_{max} = 0.0 & b_2/b_1 = 1.1) in comparison to that at parallel wall diffuser. Furthermore, the circumferential velocity is decreased at the diffuser inlet and diffuser outlet by 2.7% and 1.2% respectively across diffuser configuration of L/L_{max} = 0.1 & b_2/b_1 = 1.2 in

comparison to that across diffuser configuration of L/L_{max} = 0.0 & b_2/b_1 = 1.1. Similar trend is obtained for the rest of the diverged wall diffuser configurations. The circumferential velocity is decreased by 4.4% and 3.5% at the diffuser inlet across the diverged wall diffuser configurations of L/L_{max} = 0.2 & b_2/b_1 = 1.3 and L/L_{max} = 0.3 & b_2/b_1 = 1.4 in comparison to that across diffuser configuration of L/L_{max} = 0.0 & b_2/b_1 = 1.1. Moreover, the circumferential velocity is remains same at the diffuser outlet across the diverged wall diffuser configuration of L/L_{max} = 0.2 & b_2/b_1 = 1.3 in comparison to that across diffuser configuration of L/L_{max} = 0.0 & b_2/b_1 = 1.1. Furthermore, the circumferential velocity is increased at the diffuser outlet across the diverged wall diffuser configuration of L/L_{max} = 0.3 & b_2/b_1 = 1.4 in comparison to that across diffuser configuration of L/L_{max} = 0.0 & b_2/b_1 = 1.1. This trend explains that the circumferential decreases with the increase of both the distance between the divergence location and the diffuser inlet and outlet-to-inlet width ratio of the diffuser.

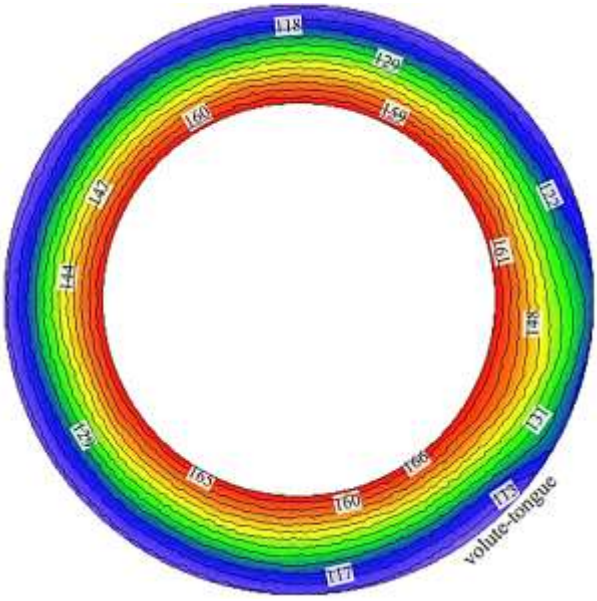

(a)

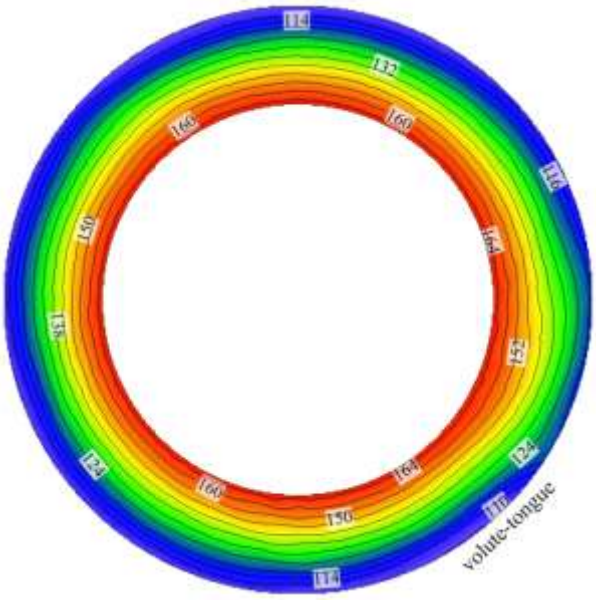

(b)

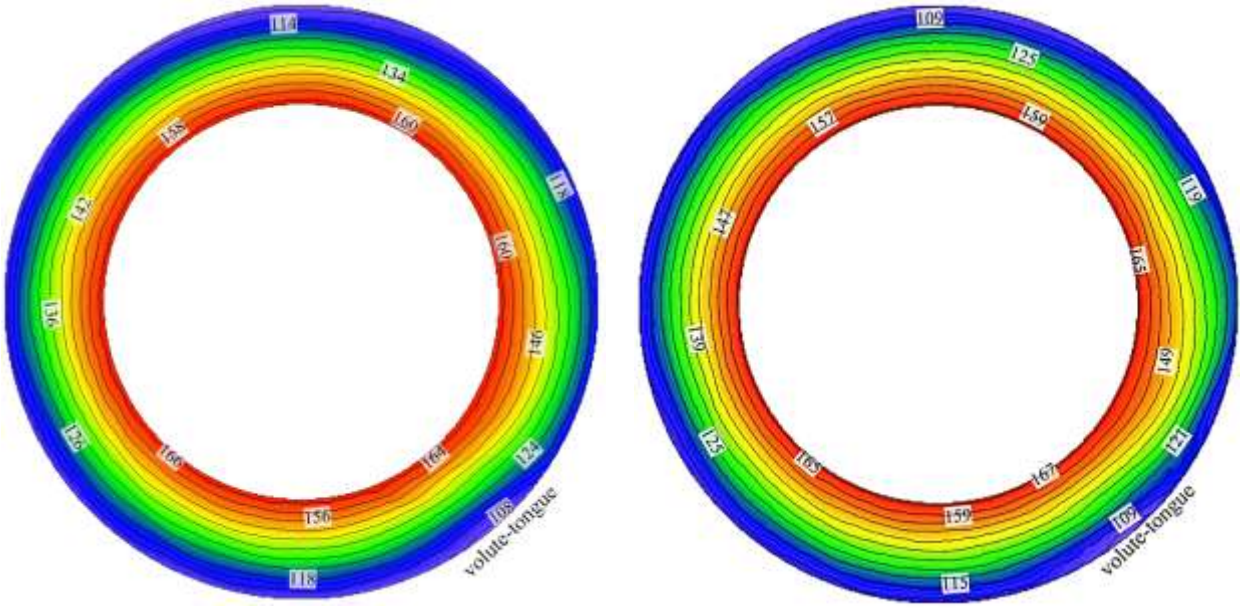

(c) (d)

Figure 4.89: Circumferential velocity (m/s) distributions across the centreline of the diverged wall straight diffuser (a) L/L_{max} = 0.0 & b_2/b_1 = 1.1, (b) L/L_{max} = 0.1 & b_2/b_1 = 1.2, (c) L/L_{max} = 0.2 & b_2/b_1 = 1.3 and (d) L/L_{max} = 0.3 & b_2/b_1 = 1.4 at BEP at an operational speed of 58.9rpsK$^{-1/2}$

Figure 4.90 depicts the comparison of circumferential velocity distribution across parallel wall and diverged wall straight diffuser configurations (L/L_{max} = 0.0 & b_2/b_1 = 1.1 and L/L_{max} = 0.0 & b_2/b_1 = 1.4) from the hub wall to the shroud wall at BEP at an operational speed of 58.9rpsK$^{-1/2}$. It can be seen that the circumferential velocity is reduced radially across the diffuser. It can be seen that the circumferential velocity at L1 (diffuser inlet) is similar at parallel and diverged wall straight diffusers, whereas the circumferential velocity is decreased towards at L5 (diffuser outlet) for diverged wall diffuser configurations in comparison to parallel wall diffuser. Furthermore, it has been observed that the circumferential velocity is asymmetric across the parallel and diverged wall straight diffuser. However, the detailed analysis has been carried out by quantifying the asymmetric ratio for the circumferential velocity profile across the diverged wall diffusers.

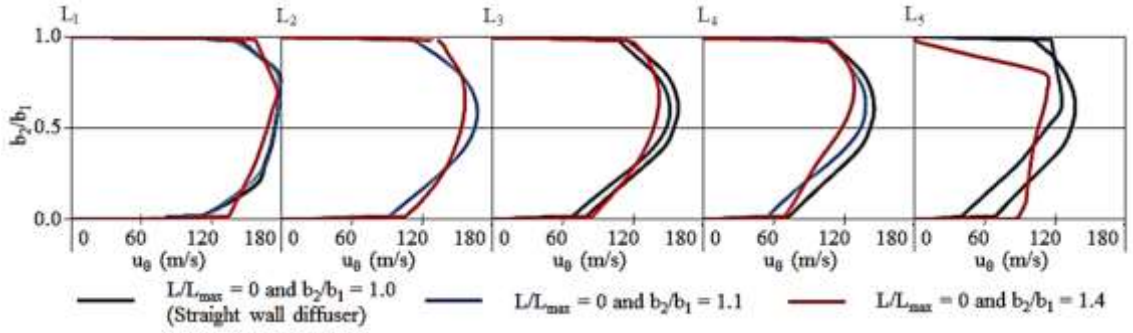

Figure 4.90: Comparison of circumferential velocity (m/s) distribution across parallel wall and diverged wall straight diffuser configurations from the hub wall to the shroud wall at BEP at an operational speed of 58.9rpsK$^{-1/2}$

The behaviour of circumferential velocity across the diverged wall straight diffuser is explained using symmetric and asymmetric behaviour of the velocity field profiles. Figure 4.91 depicts the local asymmetric ratio for the circumferential velocity, α_{vc} across the diverged wall diffusers (L/L_{max} = 0.0 & b_2/b_1 = 1.1 and L/L_{max} = 0.0 & b_2/b_1 = 1.4) at BEP at an operational speed of 58.9rpsK$^{-1/2}$. α_{vc} values of 1.0 shows the flow is symmetric, α_{vc} values below 1.0 shows asymmetric flow towards the hub wall and α_{vc} values above 1.0 shows asymmetric flow towards the shroud wall. It can be seen that the flow is asymmetric towards the shroud wall across the diverged wall diffuser. The asymmetric ratio for the circumferential velocity increases from the centreline of the diffuser towards the wall and from the diffuser inlet to the diffuser outlet in both diverged wall diffusers. However, it has been noticed that increase of outlet-to-inlet width ratio by considering same wall diverged location from the inlet does not have much effect on the circumferential velocity.

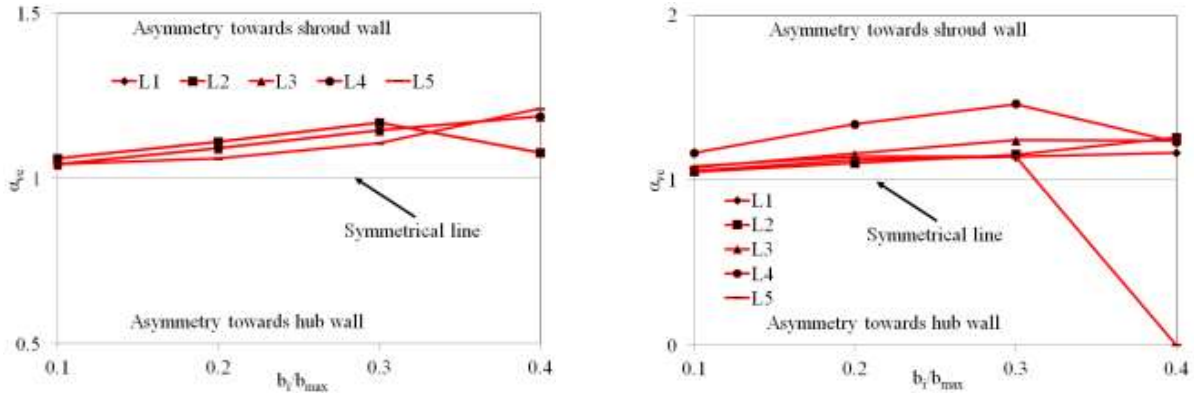

Figure 4.91: Local asymmetric ratio for the circumferential velocity, α_{vc} across the diverged wall diffusers ((a) L/L_{max} = 0.0 & b_2/b_1 = 1.4 and (b) L/L_{max} = 0.3 & b_2/b_1 = 1.4) at BEP at an operational speed of 58.9rpsK$^{-1/2}$

Figure 4.92 depicts the comparison of circumferential velocity distribution across parallel wall and diverged wall straight diffuser configurations (L/L_{max} = 0.0 & b_2/b_1 = 1.4 and L/L_{max} = 0.3 & b_2/b_1 = 1.4) from the hub wall to the shroud wall at BEP at an operational speed of 58.9rpsK$^{-1/2}$. It can be seen that the circumferential velocity is reduced radially across the diffuser. It can be seen that the circumferential velocity at L1 (diffuser inlet) and L2 is similar at parallel and diverged wall straight diffusers, decreasing across the diffuser at from L3 to L5 (diffuser outlet) for diverged wall diffuser configurations in comparison to parallel wall diffuser. Furthermore, it has been observed that the circumferential velocity is asymmetric across the parallel and diverged wall straight diffuser. However, the detailed analysis has been carried out by quantifying the asymmetric ratio for the circumferential velocity profile across the diverged wall diffusers.

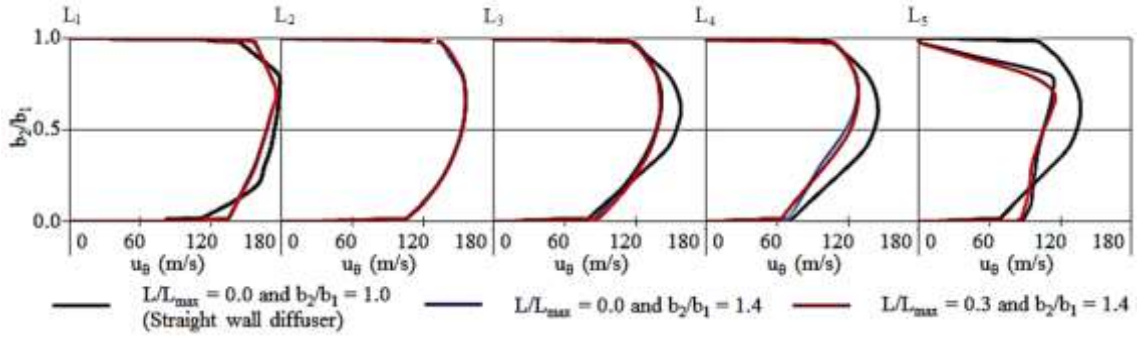

Figure 4.92: Comparison of circumferential velocity (m/s) distribution across parallel wall and diverged wall straight diffuser configurations from the hub wall to the shroud wall at BEP at an operational speed of 58.9rpsK$^{-1/2}$

Figure 4.93 depicts the local asymmetric ratio for the circumferential velocity, α_{vc} across the diverged wall diffusers (L/L_{max} = 0.0 & b_2/b_1 = 1.4 and L/L_{max} = 0.3 & b_2/b_1 = 1.4) at BEP at an operational speed of 58.9rpsK$^{-1/2}$. It can be seen that the flow is asymmetric towards the shroud wall across the diverged wall diffusers. The asymmetric ratio for the circumferential velocity remains similar from the centreline of the diffuser towards the wall and from the diffuser inlet to the diffuser outlet in both diverged wall diffusers. It has been noticed that by increasing wall diverged location from the inlet and considering same increase of outlet-to-inlet width ratio decreases asymmetric ratio of L4 to 0.0, which changes the asymmetric flow behaviour from the shroud wall to the hub wall.

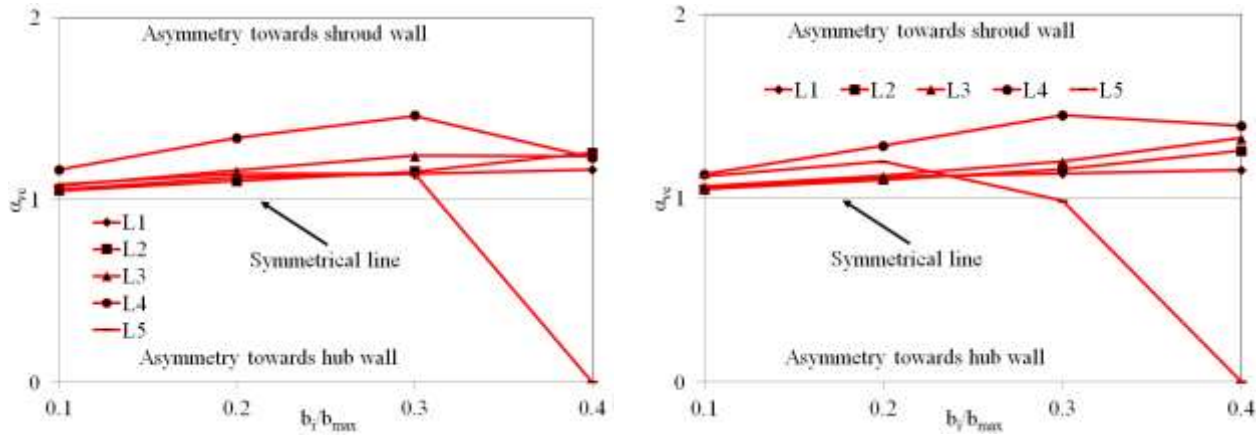

Figure 4.93: Local asymmetric ratio for the circumferential velocity, α_{vc} across the diverged wall diffusers ((a) L/L_{max} = 0.0 & b_2/b_1 = 1.4 and (b) L/L_{max} = 0.3 & b_2/b_1 = 1.4) at BEP at an operational speed of 58.9rpsK$^{-1/2}$

Figure 4.94 depicts the comparison of circumferential velocity distribution across parallel wall and diverged wall straight diffuser configurations (L/L_{max} = 0.0 & b_2/b_1 = 1.1, L/L_{max} = 0.1 & b_2/b_1 = 1.2, L/L_{max} = 0.2 & b_2/b_1 = 1.3 and L/L_{max} = 0.3 & b_2/b_1 = 1.4) from the hub wall to the shroud wall at BEP at an operational speed of 58.9rpsK$^{-1/2}$. It can be seen that the circumferential velocity is reduced radially across the diffuser. It can be seen that the circumferential velocity at L1 (diffuser inlet) and L2 is similar at parallel and diverged wall straight diffusers, whereas the circumferential velocity is decreasing from L3 to L5 (diffuser outlet) for diverged wall diffuser configurations in comparison to parallel wall diffuser. Furthermore, it has been observed that the circumferential velocity is asymmetric across the parallel and diverged wall straight diffuser. However, the detailed analysis has been carried out by quantifying the asymmetric ratio for the circumferential velocity profile across the diverged wall diffusers.

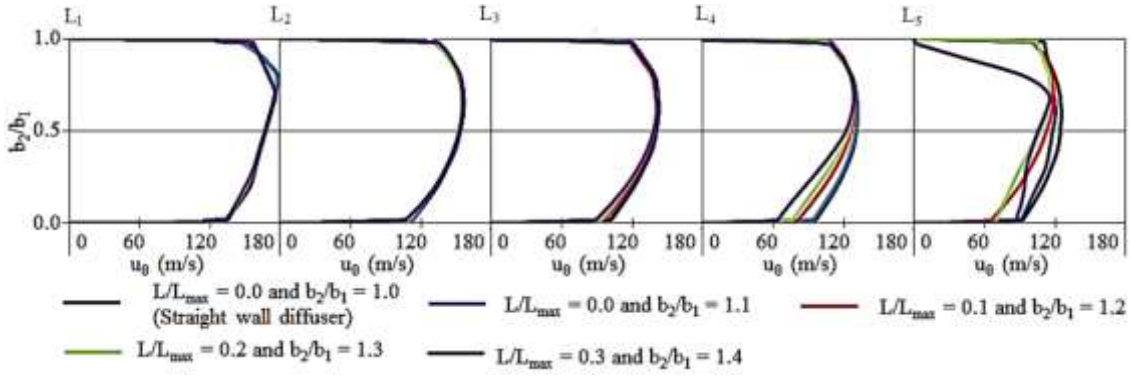

Figure 4.94: Comparison of circumferential velocity (m/s) distribution across parallel wall and diverged wall straight diffuser configurations from the hub wall to the shroud wall at BEP at an operational speed of 58.9rpsK$^{-1/2}$

Figure 4.95 depicts the local asymmetric ratio for the circumferential velocity, α_{vc} across the diverged wall diffusers (L/L_{max} = 0.0 & b_2/b_1 = 1.1, L/L_{max} = 0.1 & b_2/b_1 = 1.2, L/L_{max} = 0.2 & b_2/b_1 = 1.3 and L/L_{max} = 0.3 & b_2/b_1 = 1.4) at BEP at an operational speed of 58.9rpsK$^{-1/2}$. It can be seen that the flow is asymmetric towards the shroud wall across the diverged wall diffusers. The asymmetric ratio for the circumferential velocity constantly increases from the centreline of the diffuser towards the wall and from the diffuser inlet to the diffuser outlet in both diverged wall diffusers. It can also be observed that at diverged wall diffuser of L/L_{max} = 0.3 & b_2/b_1 = 1.4, the flow near the wall has asymmetry towards the hub wall.

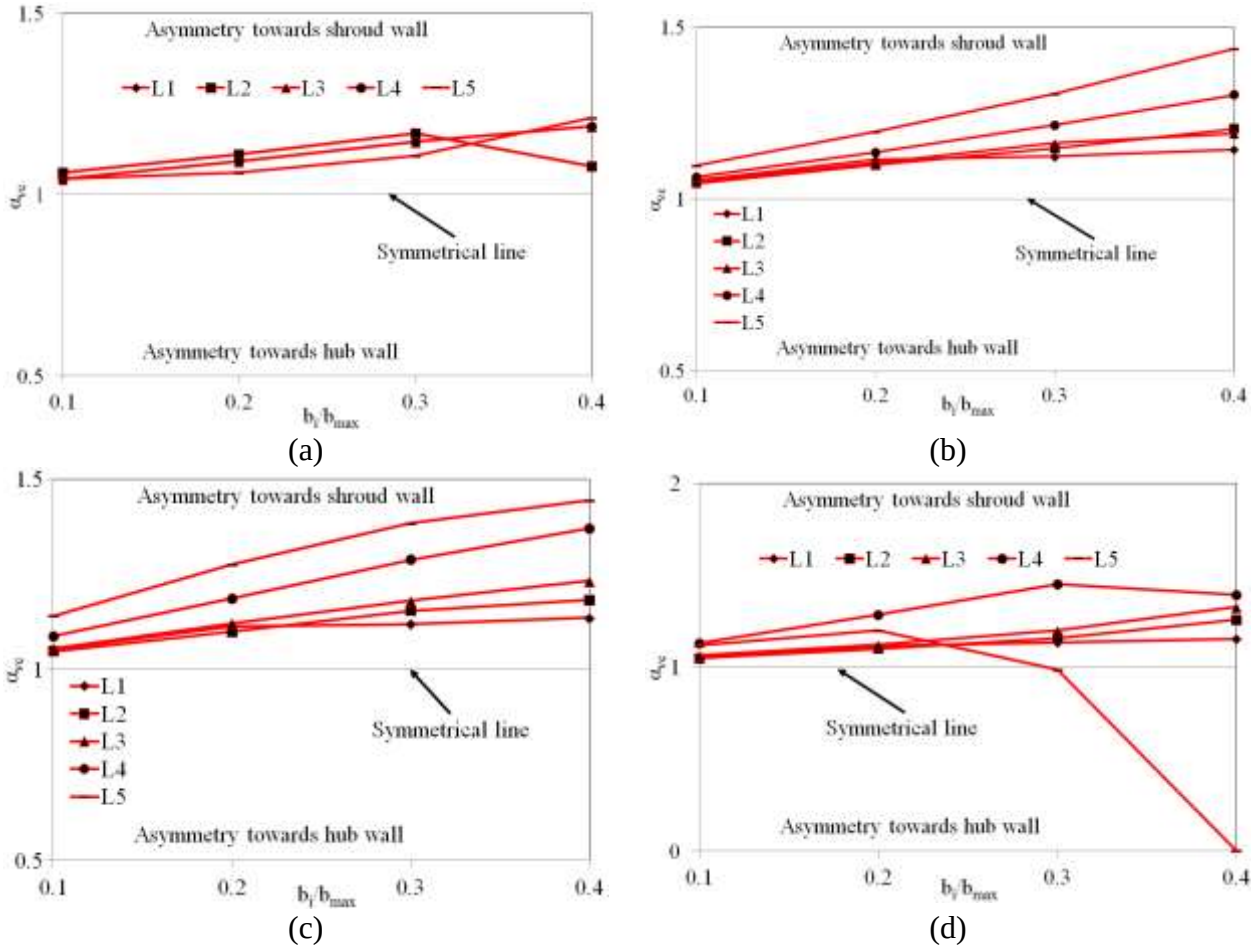

Figure 4.95: Local asymmetric ratio for the circumferential velocity, α_{vc} across the diverged wall diffusers ((a) L/L_{max} = 0.0 & b_2/b_1 = 1.1, (b) L/L_{max} = 0.1 & b_2/b_1 = 1.2, (c) L/L_{max} = 0.2 & b_2/b_1 = 1.3 and (d) L/L_{max} = 0.3 & b_2/b_1 = 1.4) at BEP at an operational speed of 58.9rpsK$^{-1/2}$

Figure 4.96 depicts the static temperature variations across the centreline of the diverged wall diffuser configurations ((a) L/L_{max} = 0.0 & b_2/b_1 = 1.1 and (b) L/L_{max} = 0.0 & b_2/b_1 = 1.4) at BEP at an operational speed of 58.9rpsK$^{-1/2}$. The trend of the static temperature across the diverged wall straight diffusers is similar to that across the straight diffuser. It can be seen that the minimum static temperature is obtained at the diffuser inlet after the volute-tongue region. The static temperature increases radially across the diffuser. Furthermore, the static temperature also increases circumferentially in the direction of impeller rotation (ω). The maximum static temperature is obtained at the diffuser outlet at near the volute-tongue region. It can be seen that the static temperature values are same across the parallel wall diffuser and diverged wall diffuser configuration (L/L_{max} = 0.0 & b_2/b_1 = 1.1). Furthermore, it can be seen that the static temperature is same at the diffuser inlet and decreased at the diffuser outlet by 0.6% across diffuser configuration of L/L_{max} = 0.0 & b_2/b_1 = 1.4 in comparison to that across diffuser configuration of L/L_{max} = 0.0 & b_2/b_1 = 1.1. This trend explains that the static temperature decreases when outlet-to-inlet width ratio of the diffuser is increased by keeping the divergence location at the diffuser inlet.

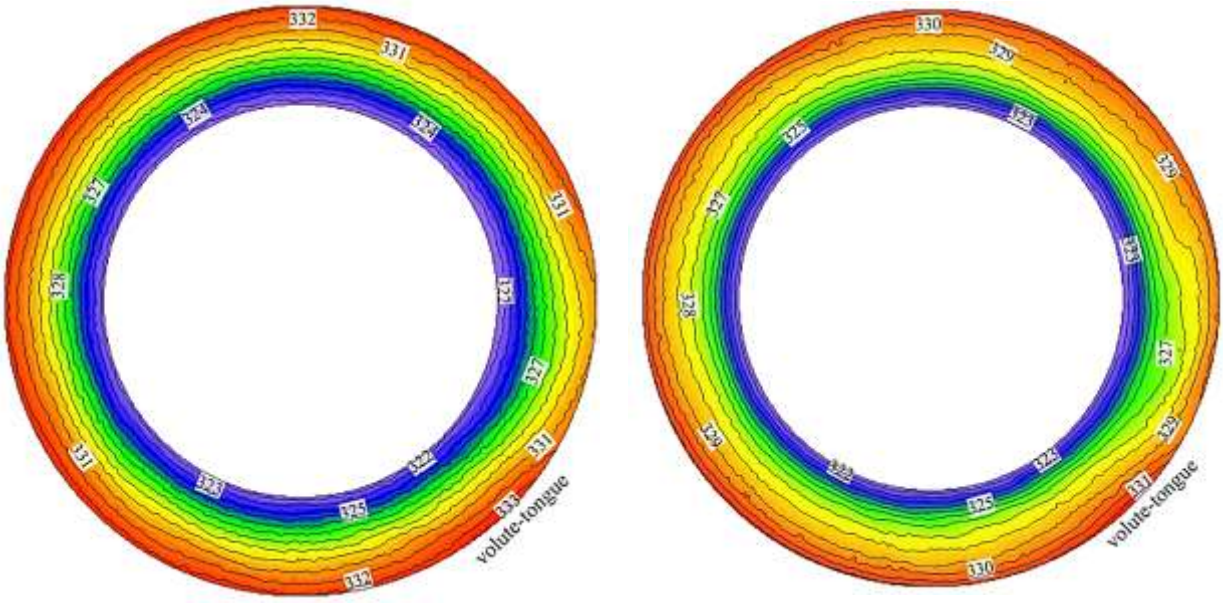

(b) (c)

Figure 4.96: Static temperature (K) variations across the centreline of the diverged wall straight diffuser (a) L/L_{max} = 0.0 & b_2/b_1 = 1.1 and (b) L/L_{max} = 0 & b_2/b_1 = 1.4 at BEP at an operational speed of 58.9rpsK$^{-1/2}$

Figure 4.97 depicts the static temperature variations across the centreline of the diverged wall diffuser configurations ((a) L/L_{max} = 0.0 & b_2/b_1 = 1.4 and (b) L/L_{max} = 0.3 & b_2/b_1 = 1.4) at BEP at an operational speed of 58.9rpsK$^{-1/2}$. The trend of the static temperature across the diverged wall straight

diffusers is similar to that across the straight diffuser. It can be seen that the minimum static temperature is obtained at the diffuser inlet after the volute-tongue region. The static temperature increases radially across the diffuser. Furthermore, the static temperature also increases circumferentially in the direction of impeller rotation (ω). The maximum static temperature is obtained at the diffuser outlet at near the volute-tongue region. It can be seen that the static temperature values are decreased across diverged wall diffuser configuration (L/L_{max} = 0.0 & b_2/b_1 = 1.4) in comparison to that across the parallel wall diffuser. The static temperature is same at the diffuser inlet and decreased at the diffuser outlet by 0.6% in comparison to that at parallel wall diffuser. Furthermore, it can also be seen that the static temperature is decreased at the diffuser inlet and diffuser outlet by 0.3% each respectively in comparison to that across diverged wall diffuser configuration of L/L_{max} = 0.3 & b_2/b_1 = 1.4. This trend explains that the static temperature decreases when the distance between the divergence location and the diffuser inlet is increased by considering the divergence location at the diffuser inlet.

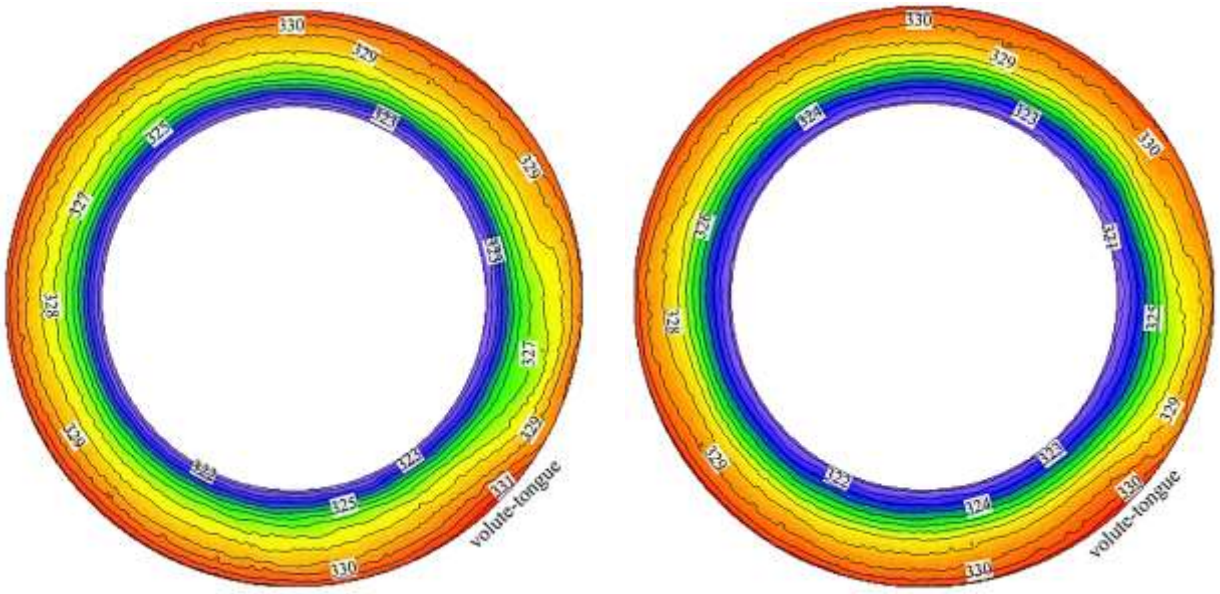

(b) (c)

Figure 4.97: Static temperature (K) variations across the centreline of the diverged wall straight diffuser (a) L/L_{max} = 0 & b_2/b_1 = 1.4 and (b) L/L_{max} = 0.3 & b_2/b_1 = 1.4 at BEP at an operational speed of 58.9rpsK$^{-1/2}$

Figure 4.98 depicts the static temperature variations across the centreline of the diverged wall diffuser configurations (a) L/L_{max} = 0.0 & b_2/b_1 = 1.1, (b) L/L_{max} = 0.1 & b_2/b_1 = 1.2, (c) L/L_{max} = 0.2 & b_2/b_1 = 1.3 and (d) L/L_{max} = 0.3 & b_2/b_1 = 1.4) at BEP at an operational speed of 58.9rpsK$^{-1/2}$. The trend of the static temperature across the diverged wall straight diffusers is similar to that across the straight

diffuser. It can be seen that the minimum static temperature is obtained at the diffuser inlet after the volute-tongue region. The static temperature increases radially across the diffuser. Furthermore, the static temperature also increases circumferentially in the direction of impeller rotation (ω). The maximum static temperature is obtained at the diffuser outlet at near the volute-tongue region. It can be seen that the static temperature values are same across the parallel wall diffuser and diverged wall diffuser configuration (L/L_{max} = 0.0 & b_2/b_1 = 1.1). Furthermore, the static temperature is same at the diffuser inlet and decreased at the diffuser outlet by 0.3% across diffuser configuration of L/L_{max} = 0.1 & b_2/b_1 = 1.2 in comparison to that across diffuser configuration of L/L_{max} = 0.0 & b_2/b_1 = 1.1. Similar trend is obtained for the rest of the diverged wall diffuser configurations. The static temperature is decreased by 0.0% and 0.3% at the diffuser inlet across the diverged wall diffuser configurations of L/L_{max} = 0.2 & b_2/b_1 = 1.3 and (d) L/L_{max} = 0.3 & b_2/b_1 = 1.4. Moreover, the static temperature is decreased by 0.3% and 0.9% at the diffuser outlet across the diverged wall diffuser configurations of L/L_{max} = 0.2 & b_2/b_1 = 1.3 and (d) L/L_{max} = 0.3 & b_2/b_1 = 1.4. This trend explains that the static temperature remains same at the diffuser inlet and decreases at the diffuser outlet when both the distance between the divergence location and the diffuser inlet and outlet-to-inlet width ratio of the diffuser are increased. Since isentropic efficiency is inversely proportional to temperature ratio. Therefore, it can be analysed from this investigations that isentropic efficiency increases with the decrease in the static temperature across the diverged wall straight diffuser.

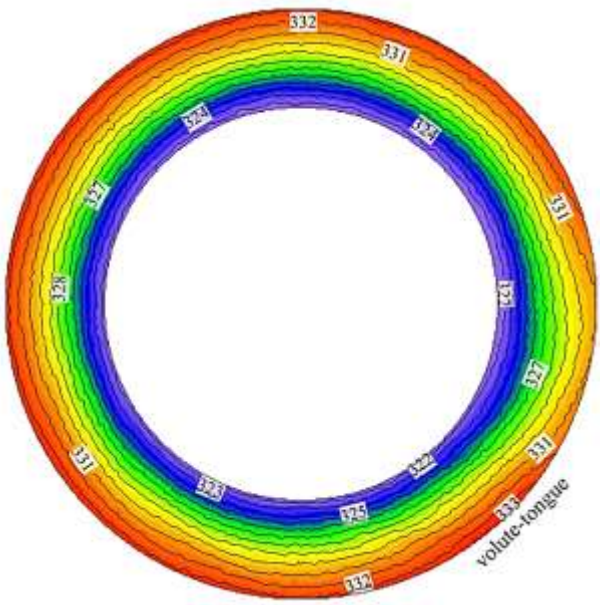

(b)

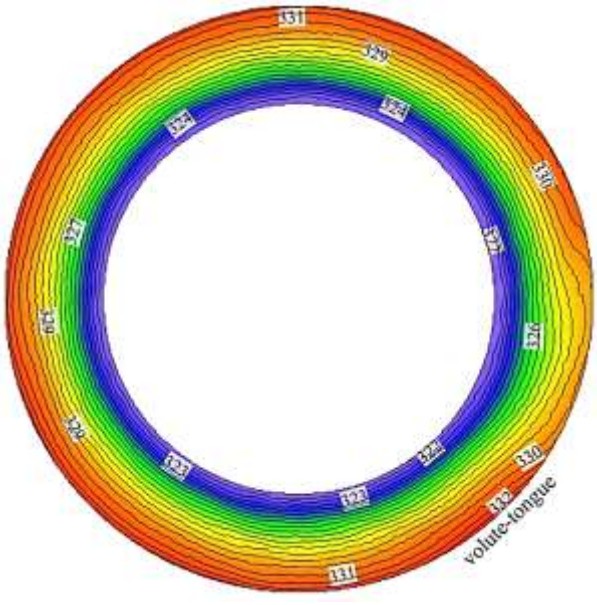

(c)

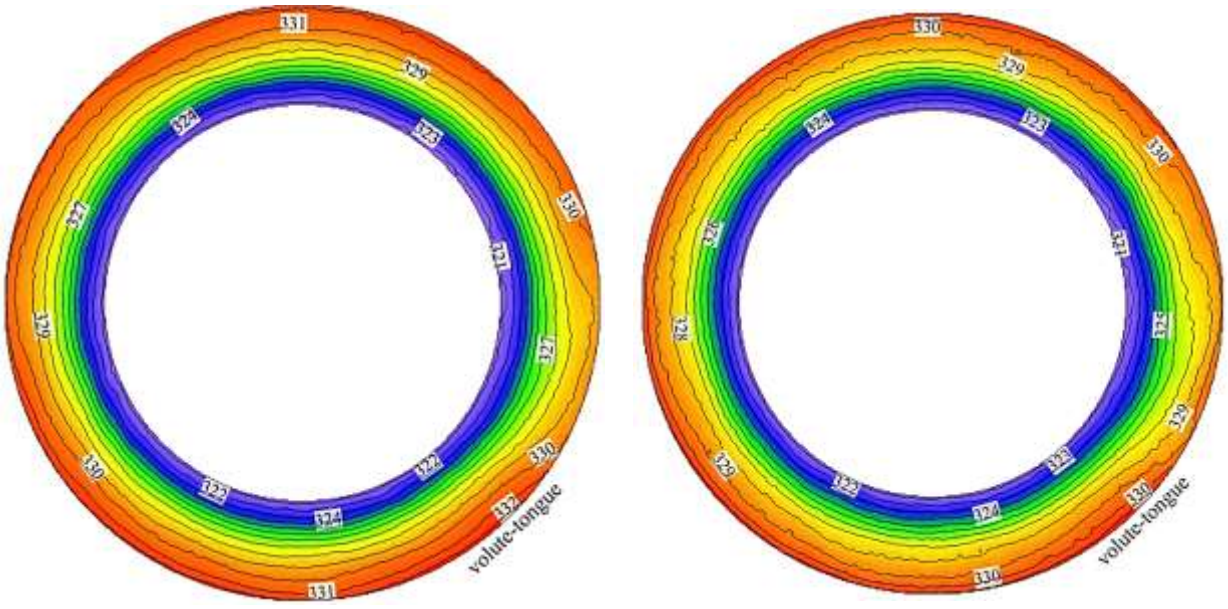

(d) (e)

Figure 4.98: Static temperature (K) variations across the centreline of the diverged wall straight diffuser (a) L/L_{max} = 0 and b_2/b_1 = 1.1, (b) L/L_{max} = 0.1 and b_2/b_1 = 1.2, (c) L/L_{max} = 0.2 b_2/b_1 = 1.3 and (d) L/L_{max} = 0.3 b_2/b_1 = 1.4 at BEP at an operational speed of 58.9rpsK$^{-1/2}$

4.4.3. Effect of Asymmetric Ratio across the Diverged Wall Straight Diffuser

The behaviour of the flow within the diverged wall straight diffuser is highly dependent upon the geometrical parameter considered. It has been noticed in the previous section that increase of diffuser width ratio increases the asymmetry of the flow towards the shroud wall of the diverged wall diffuser. Furthermore, increase of divergence location on the shroud wall of the diffuser from the diffuser inlet does not affect the asymmetric behaviour of the flow. A new term is introduced that shows the change in behaviour of the flow across the diverged wall diffusers. The asymmetric ratio of the flow is defined as α, which is the ratio between the flow velocity near the shroud wall and the flow velocity near the hub wall. Equation 4.1 is used again used to obtain the global effect of diverged wall diffuser. The major effect of geometrical parameters on the asymmetric flow behaviour and stage performance is described in detail.

Figure 4.99 depicts the global asymmetric ratio for the velocity magnitude across the diverged wall straight diffuser at BEP at an operational speed of 58.9rpsK$^{-1/2}$. It can be seen that the global asymmetric ratio across the diverged wall diffusers is towards the shroud wall of the diffuser. The global asymmetric ratio for the velocity magnitudes is same from L1 (diffuser inlet) to L5 (diffuser

outlet) across diverged wall diffuser of L/L_{max} = 0.0 & b_2/b_1 = 1.1 and it is decreasing from L1 (diffuser inlet) to L5 (diffuser outlet) across diverged wall diffuser of L/L_{max} = 0.0 & b_2/b_1 = 1.4.

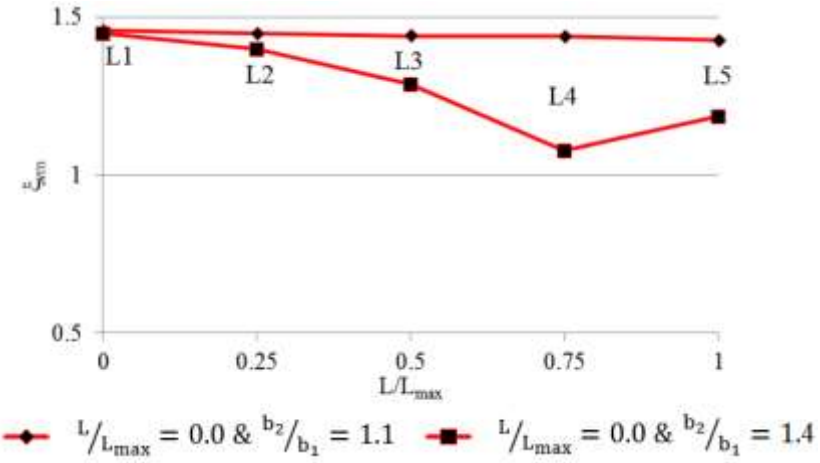

Figure 4.99: Global asymmetric ratio for the velocity magnitude of the diverged wall straight diffuser at BEP at an operational speed of 58.9rpsK$^{-1/2}$

Figure 4.100 depicts the global asymmetric ratio for the velocity magnitude across the diverged wall straight diffuser at BEP at an operational speed of 58.9rpsK$^{-1/2}$. It can be seen that the global asymmetric ratio across the diverged wall diffusers is towards the shroud wall of the diffuser. The global asymmetric ratio for the velocity magnitudes is decreasing from L1 (diffuser inlet) to L5 (diffuser outlet) across both diverged wall diffusers. However, it shows that diverged wall diffuser L/L_{max} = 0.3 & b_2/b_1 = 0.4 has higher global asymmetric ratio in comparison to diverged wall diffuser L/L_{max} = 0.0 & b_2/b_1 = 1.4.

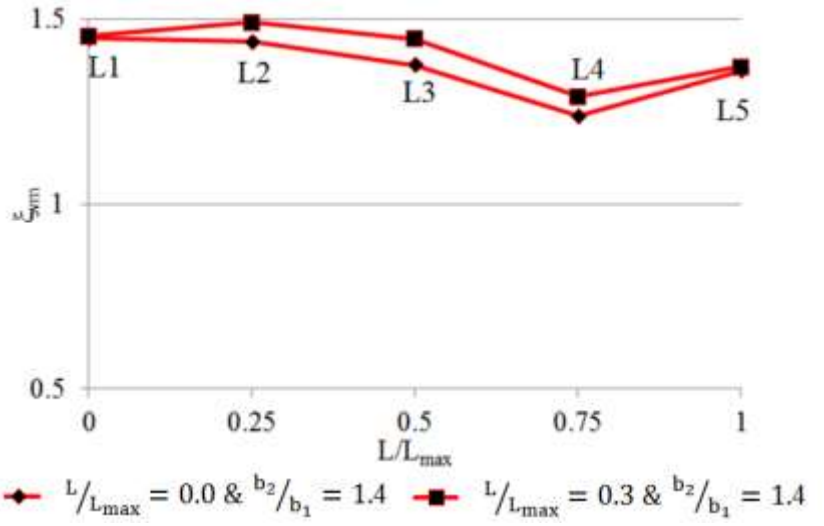

Figure 4.100: Global asymmetric ratio for the velocity magnitude of the diverged wall straight diffuser at BEP at an operational speed of 58.9rpsK$^{-1/2}$

Figure 4.101 depicts the global asymmetric ratio for the velocity magnitude across the diverged wall straight diffuser at BEP at an operational speed of 58.9rpsK$^{-1/2}$. It can be seen that the global asymmetric ratio across the diverged wall diffusers is towards the shroud wall of the diffuser. The global asymmetric ratio for the velocity magnitudes is constantly decreasing from L1 (diffuser inlet) to L5 (diffuser outlet) across diverged wall diffusers of L/L_{max} = 0.1 & b_2/b_1 = 1.2, L/L_{max} = 0.2 & b_2/b_1 = 1.3 and L/L_{max} = 0.3 & b_2/b_1 = 1.4. It can be analysed form this behaviour that diffusers having global asymmetric ratio decrease introduces the flow reversals within the diverged wall straight diffusers.

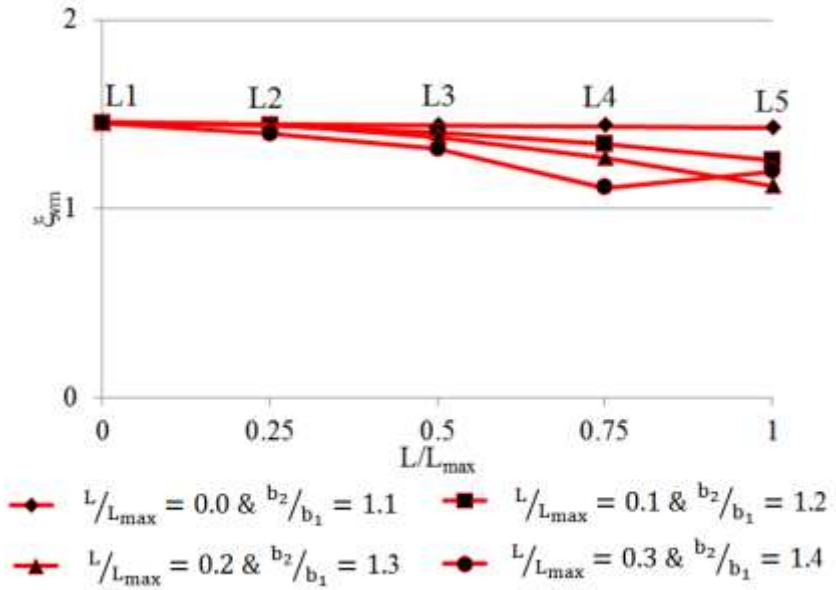

Figure 4.101: Global asymmetric ratio for the velocity magnitude of the diverged wall straight diffuser at BEP at an operational speed of 58.9rpsK$^{-1/2}$

Figure 4.102 depicts the global asymmetric ratio for the radial velocity across the diverged wall straight at BEP at an operational speed of 58.9rpsK$^{-1/2}$. It can be seen that the global asymmetric ratio across the diverged wall diffusers is towards the shroud wall of the diffuser. The global asymmetric ratio for the radial velocity is same from L1 (diffuser inlet) to L5 (diffuser outlet) across diverged wall diffuser of L/L_{max} = 0.0 & b_2/b_1 = 1.1 and it is decreasing from L1 (diffuser inlet) to L5 (diffuser outlet) across diverged wall diffuser of L/L_{max} = 0.0 & b_2/b_1 = 1.4. The global asymmetric ratio value reduces 1.0 introduces the flow reversal within the diverged wall diffuser.

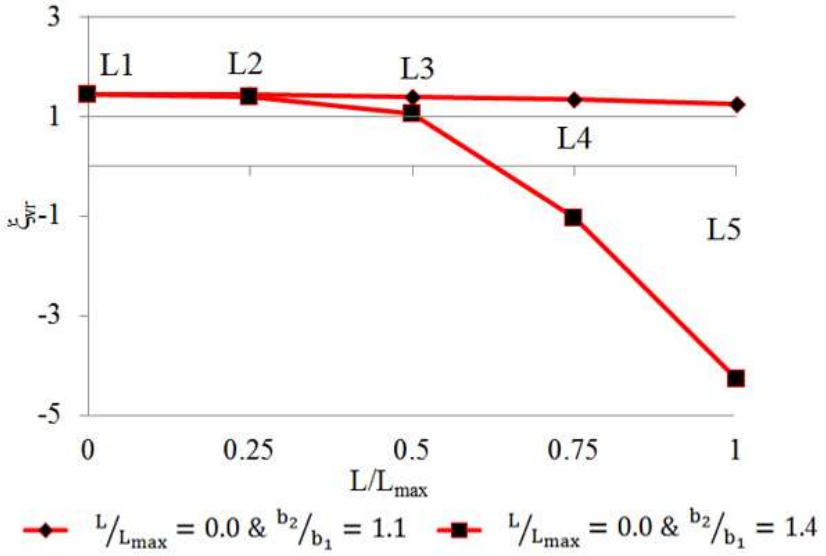

Figure 4.102: Global asymmetric ratio for the radial velocity of the diverged wall straight diffuser at BEP at an operational speed of 58.9rpsK$^{-1/2}$

Figure 4.103 depicts the global asymmetric ratio for the radial velocity across the diverged wall straight at BEP at an operational speed of 58.9rpsK$^{-1/2}$. It can be seen that the global asymmetric ratio across the diverged wall diffusers is towards the shroud wall of the diffuser. The global asymmetric ratio for the radial velocity is decreasing from L1 (diffuser inlet) to L5 (diffuser outlet) across both diverged wall diffusers. However, it shows that diverged wall diffuser $L/L_{max} = 0.3$ & $b_2/b_1 = 0.4$ has higher global asymmetric ratio in comparison to diverged wall diffuser $L/L_{max} = 0.0$ & $b_2/b_1 = 1.4$. It can be seen that the global asymmetric ratio values for both the diffusers is below 1.0, which represents flow reversals within the diverged wall diffusers.

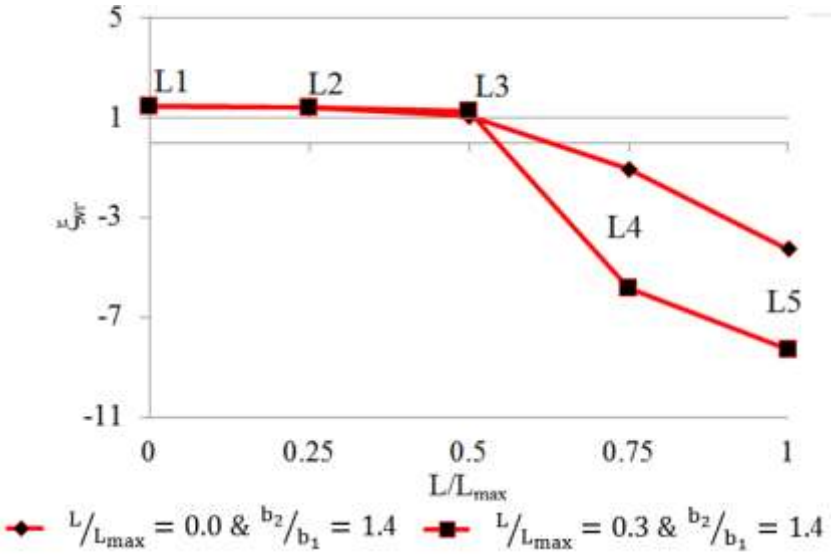

Figure 4.103: Global asymmetric ratio for the radial velocity of the diverged wall straight diffuser at BEP at an operational speed of 58.9rpsK$^{-1/2}$

Figure 4.104 depicts the global asymmetric ratio for the radial velocity across the diverged wall straight at BEP at an operational speed of 58.9rpsK$^{-1/2}$. It can be seen that the global asymmetric ratio across the diverged wall diffusers is towards the shroud wall of the diffuser. The global asymmetric ratio for the radial velocity is constantly decreasing from L1 (diffuser inlet) to L5 (diffuser outlet) across diverged wall diffusers of L/L_{max} = 0.1 & b_2/b_1 = 1.2, L/L_{max} = 0.2 & b_2/b_1 = 1.3 and L/L_{max} = 0.3 & b_2/b_1 = 1.4. It can be analysed form this behaviour that diffusers having global asymmetric ratio below 1.0 represents the flow reversals within the diverged wall straight diffusers.

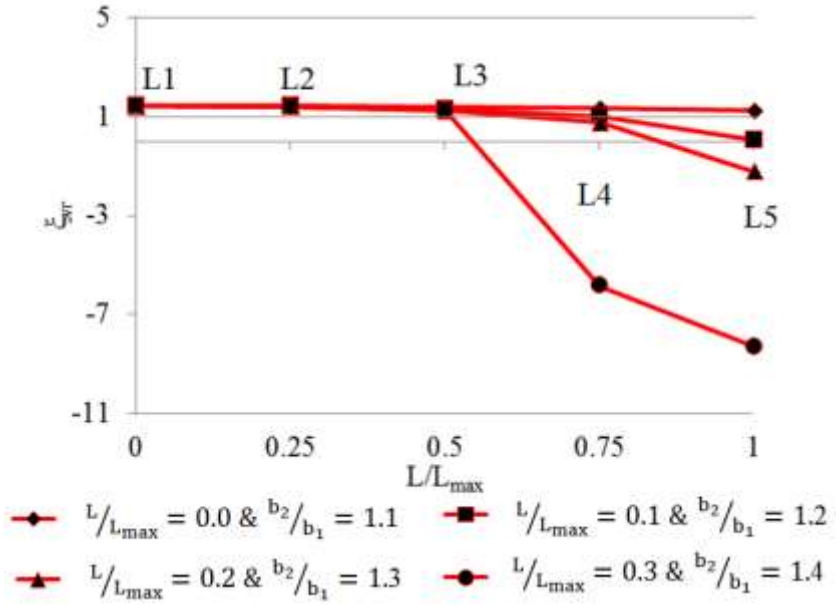

Figure 4.104: Global asymmetric ratio for the radial velocity of the diverged wall straight at BEP at an operational speed of 58.9rpsK$^{-1/2}$

Figure 4.105 depicts the global asymmetric ratio for the circumferential velocity across the diverged wall straight at BEP at an operational speed of 58.9rpsK$^{-1/2}$. It can be seen that the global asymmetric ratio across the diverged wall diffusers is towards the shroud wall of the diffuser. The global asymmetric ratio for the circumferential velocity is same from L1 (diffuser inlet) to L5 (diffuser outlet) across diverged wall diffuser of L/L_{max} = 0.0 & b_2/b_1 = 1.1 and it is decreasing from L1 (diffuser inlet) to L5 (diffuser outlet) across diverged wall diffuser of L/L_{max} = 0.0 & b_2/b_1 = 1.4.

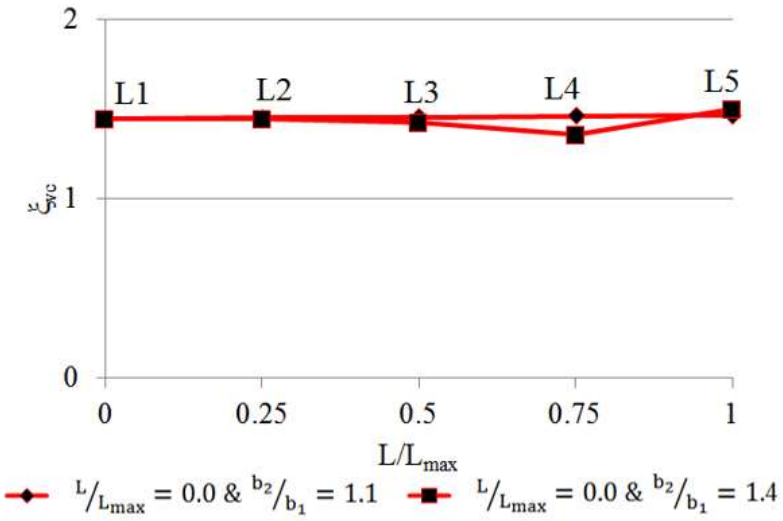

Figure 4.105: Global asymmetric ratio for the radial velocity of the diverged wall straight diffuser at BEP at an operational speed of 58.9rpsK$^{-1/2}$

Figure 4.106 depicts the global asymmetric ratio for the circumferential velocity across the diverged wall straight at BEP at an operational speed of 58.9rpsK$^{-1/2}$. It can be seen that the global asymmetric ratio across the diverged wall diffusers is towards the shroud wall of the diffuser. The global asymmetric ratio for the circumferential velocity is decreasing from L1 (diffuser inlet) to L5 (diffuser outlet) across both diverged wall diffusers. However, it shows that diverged wall diffuser L/L_{max} = 0.3 & b_2/b_1 = 0.4 has similar asymmetric ratio in comparison to diverged wall diffuser L/L_{max} = 0.0 & b_2/b_1 = 1.4.

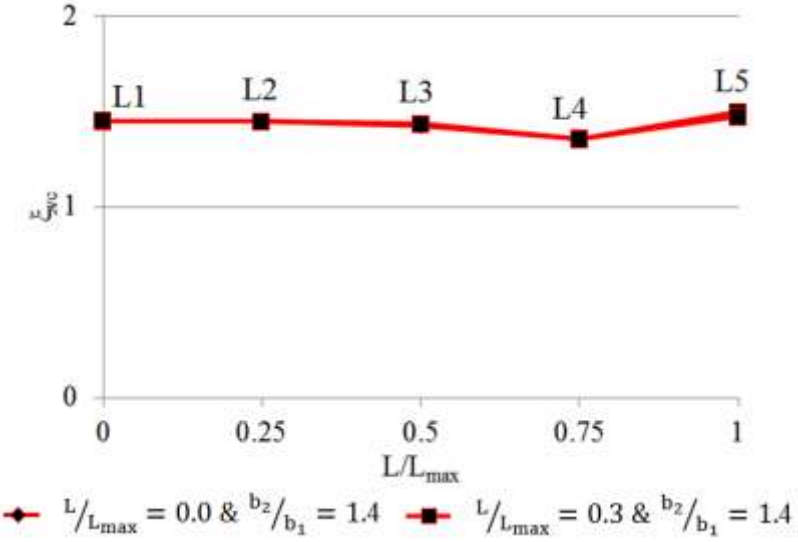

Figure 4.106: Global asymmetric ratio for the circumferential velocity of the diverged wall straight diffuser at BEP at an operational speed of 58.9rpsK$^{-1/2}$

Figure 4.107 depicts the global asymmetric ratio for the circumferential velocity across the diverged wall straight at BEP at an operational speed of 58.9rpsK$^{-1/2}$. It can be seen that the global asymmetric ratio across the diverged wall diffusers is towards the shroud wall of the diffuser. The global asymmetric ratio for the circumferential velocity is constantly decreasing from L1 (diffuser inlet) to L5 (diffuser outlet) across diverged wall diffusers of L/L_{max} = 0.1 & b_2/b_1 = 1.2, L/L_{max} = 0.2 & b_2/b_1 = 1.3 and L/L_{max} = 0.3 & b_2/b_1 = 1.4.

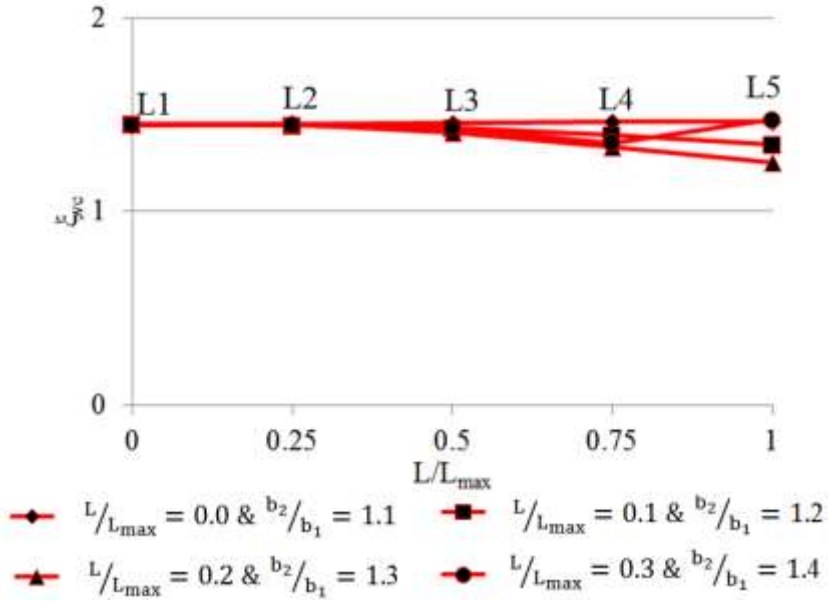

Figure 4.107: Global asymmetric ratio for the circumferential velocity of the diverged wall straight diffuser at BEP at an operational speed of 58.9rpsK$^{-1/2}$

It is concluded from the above results the flow is asymmetrical across the diverged wall straight diffusers. It has been noticed that the asymmetry increases are the outlet-to-inlet width. However, there is not much effect on the flow behaviour if the wall divergence location from the inlet is increased. In order to understand the overall effect of the geometrical effect on the diffuser flow field and stage performance, the equation 4.2 is used.

Figure 4.108 depicts the comparison of diffuser asymmetric effect for velocity magnitude across the diverged wall straight diffusers and parallel wall diffuser at BEP at the operational speeds of 58.9rpsK$^{-1/2}$. It can be seen the diffuser asymmetric effect is reduced with the increase of outlet-to-inlet width ratio and wall divergence location form the inlet. Similar effect is obtained for the isentropic efficiency across the diverged wall diffusers.

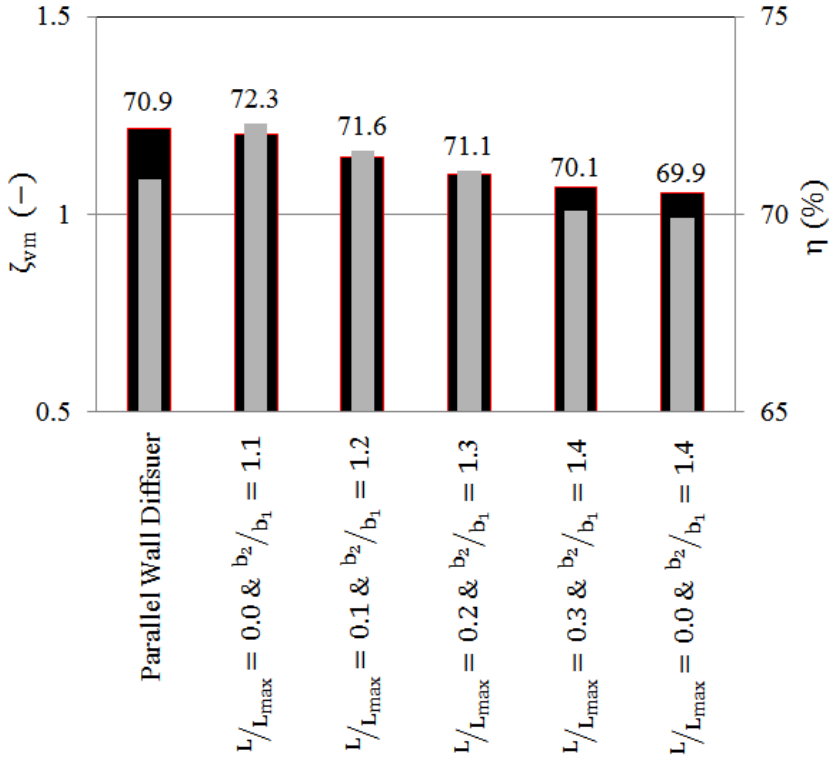

Figure 4.108: Comparison of diffuser asymmetric effect for velocity magnitude at the of the diverged wall straight diffusers at BEP at the operational speeds of 58.9rpsK$^{-1/2}$

Figure 4.109 depicts the comparison of diffuser asymmetric effect for radial velocity across the diverged wall straight diffusers and parallel wall diffuser at BEP at the operational speeds of 58.9rpsK$^{-1/2}$. It can be seen the diffuser asymmetric effect is reduced with the increase of outlet-to-inlet width ratio and wall divergence location form the inlet. Furthermore, diffuser asymmetric effect below 1.0 represents the radial flow reversals with the diverged wall diffusers. Further decrease of the diffuser asymmetric effect increases the flow reversal are within the diffusers. This causes blockage within the diffusers. Similar effect is obtained for the isentropic efficiency across the diverged wall diffusers.

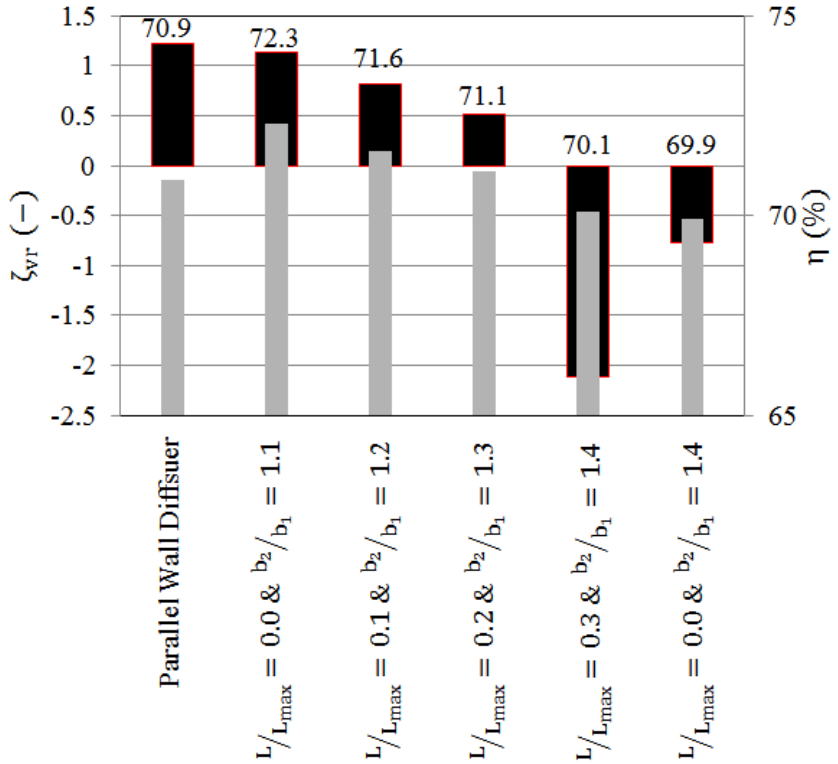

Figure 4.109: Comparison of diffuser asymmetric effect for radial velocity at the of the diverged wall straight diffusers at BEP at the operational speeds of 58.9rpsK$^{-1/2}$

Figure 4.110 depicts the comparison of diffuser asymmetric effect for circumferential velocity across the diverged wall straight diffusers and parallel wall diffuser at BEP at the operational speeds of 58.9rpsK$^{-1/2}$. It can be seen the diffuser asymmetric effect is reduced with the increase of outlet-to-inlet width ratio and wall divergence location form the inlet. Similar effect is obtained for the isentropic efficiency across the diverged wall diffusers.

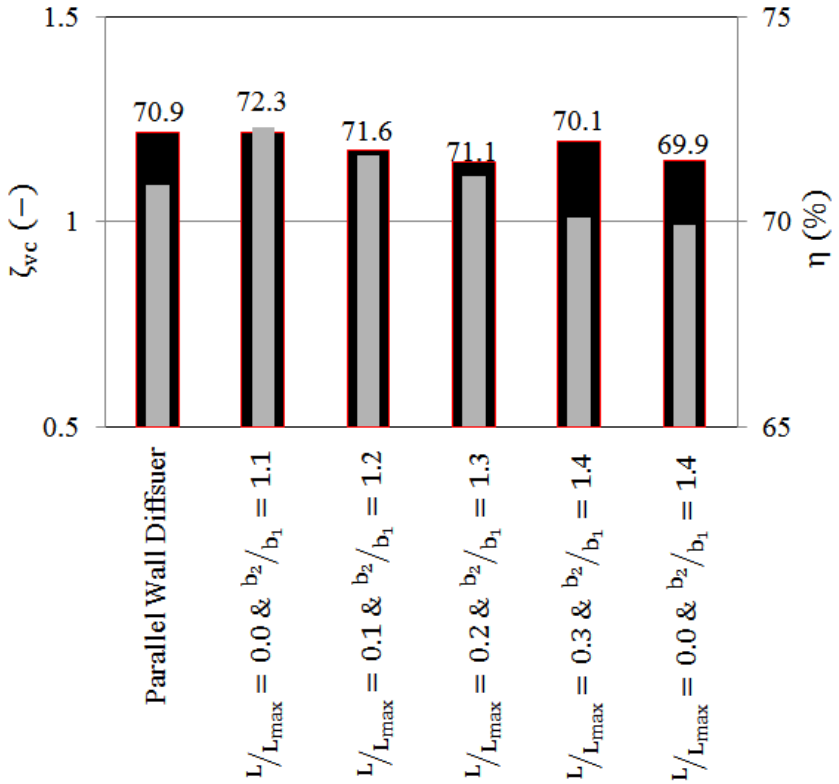

Figure 4.110: Comparison of diffuser asymmetric effect for circumferential velocity at the of the diverged wall straight diffusers at BEP at the operational speeds of 58.9rpsK$^{-1/2}$

It has been concluded from the aforementioned analysis that the flow is asymmetric across the diffuser and it is increasing with the increase of outlet-to-inlet width ratio for the diverged wall straight diffusers.

4.4.4. Isentropic Efficiency within the Diverged Wall Vaneless Diffuser

This section comprised of the diverged wall straight diffuser performance parameters of the compressor stage. Furthermore, local isentropic efficiency is calculated within the diverged wall diffuser using regression analysis.

The analytical expression used earlier for the parallel wall diffuser has been modified by inputting one more variable of wall divergence location from the diffuser inlet with changing outlet-to-inlet width ratio. The equation is shown below. Moreover, this equation is only valid for the respective initial and boundary conditions. As the boundary conditions or initial conditions change, the coefficient values will change as well.

$$\eta = 3.182 \cdot \left(\frac{N\theta}{r}\right)^{k_1} \cdot \left(\frac{b_2 - z}{b_2} \cdot \frac{N-L}{L}\right)^{k_2} \cdot \left(\frac{\omega r}{\sqrt{\gamma R T_\circ}}\right)^{k_3} \cdot \left(\frac{|v| - v_\theta}{|v| - v_r}\right)^{k_4} \quad (4.6)$$

Where

$$k_1 = 0.004$$
$$k_2 = 0.029$$
$$k_3 = 3.988$$
$$k_4 = 0.023$$

Furthermore, these coefficients represent the mean change in the response variable at one unit of change in the predictor variable while holding the other predictor variable in the model constant. The response variables are $\frac{N\theta}{r}$, $\left(\frac{b_2 - z}{b_2} \cdot \frac{N-L}{L}\right)$, $\frac{\omega r}{\sqrt{\gamma R T_\circ}}$ and $\frac{|v| - v\theta}{|v| - vr}$, whereas the predictor variable is efficiency, η. The first term in the equation 3.182 is known as the y-intercept value. Furthermore, $\frac{N-L}{L}$ is an addiditonal term used in this equation. This term gives the value of one, when isentropic compression efficiency is analysed in parallel wall diffuser. Otherwise, it varies as the divergence is implemented on the shroud wall of the vaneless diffuser. Furthermore, the exponent values of k_1, k_2, k_3 and k_4 are given, which shows that which term has maximum effect on the isentropic efficiency value. Henceforth, it can be seen that the maximum effect is dependent upon $\frac{\omega r}{\sqrt{\gamma R T_\circ}}$ term. This term identifies the rotation speed of the impeller and the Mach number obtained at the impeller trailing edge tip

The data obtained via Eq. 4.111 has been verified with the CFD results as depicted in the Figure 4.70, which has shown maximum percentage difference of 44.9% and having R^2 value of 0.64. Based upon this, it can be concluded that the aforementioned semi-empirical equation can be used to compute the isentropic efficiency within the diffuser. This high percentage difference is occurred only due to few values obtained that are far away from the actual values obtained via CFD.

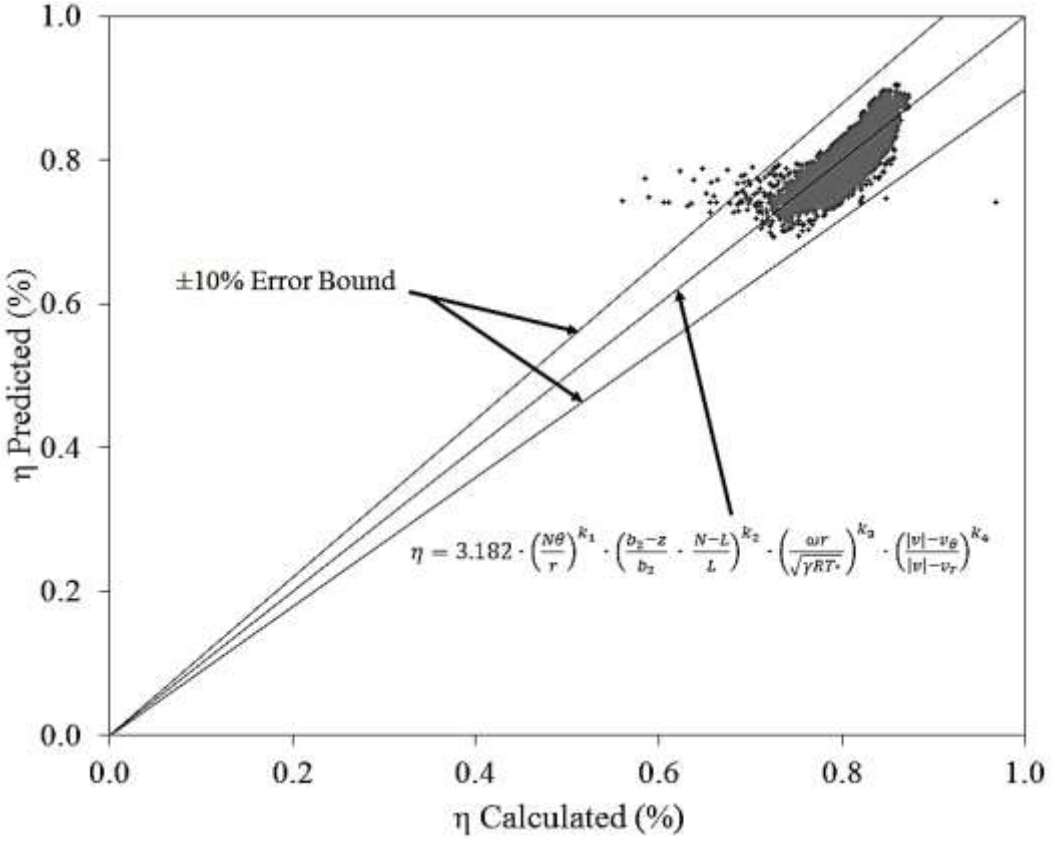

Figure 4.111: Comparison between numerically calculated, obtained via regression analysis, isentropic compression efficiency and predicted, using CFD, isentropic compression efficiency within the diffuser

4.5. Effects of Geometrical Parameters

This section investigates the effects of the divergence on the shroud wall of the diffuser and diffuser outlet-to-inlet width ratio on the diffuser local performance. The diffuser performance is dependent upon the recovery of static pressure across the diffuser.

4.5.1. Effects of Geometrical Parameters on Pressure Recovery across the different Diffusers

Two geometrical parameters, the divergence on the shroud wall of the diffuser and the diffuser outlet-to-inlet width ratio have used to modify the vaneless diffuser geometry. These configurations have affected the diffuser performance. Figure 4.112 depicts the variation in the coefficient of pressure C_p while changing the diffuser outlet-to-inlet area ratio across the radii of the straight diffuser and diverged wall diffuser configurations (L/L_{max} = 0 and b_2/b_1 = 1.1, and L/L_{max} = 0 and b_2/b_1 = 1.4). It can be seen that increase of the diffuser outlet-to-inlet area ratio increases the pressure recovery within the diffuser in comparison to straight diffuser. The area ratio is a function of the divergence location

on the shroud wall of the diffuser and outlet-to-inlet width ratio. However, increasing large number of the diffuser outlet-to-inlet area ratio decreases the pressure recovery.

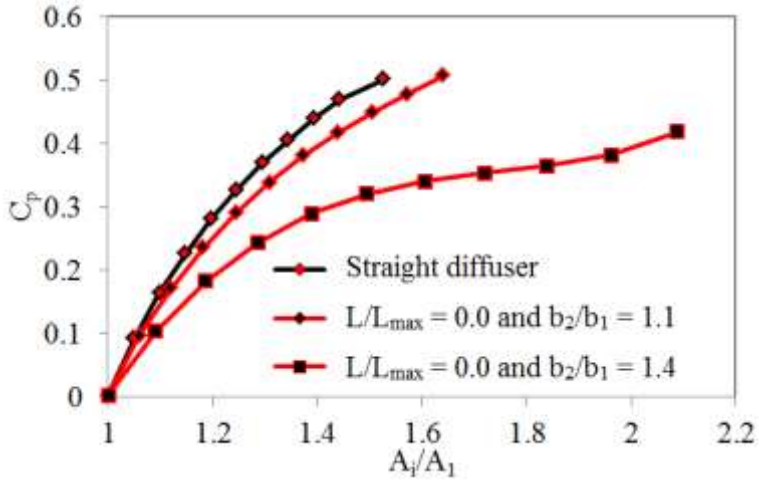

Figure 4.112: Variation in the coefficient of pressure C_p while changing the diffuser outlet-to-inlet area ratio across the radii of the straight diffuser and diverged wall diffuser configurations

Figure 4.113 depicts the variation in the coefficient of pressure C_p while changing the diffuser outlet-to-inlet area ratio across the radii of the straight diffuser and diverged wall diffuser configurations (L/L_{max} = 0.0 and b_2/b_1 = 1.4, and L/L_{max} = 0.3 and b_2/b_1 = 1.4). It can be seen that increase of the wall divergence location from the diffuser inlet, decreases the coefficient of pressure while changing the area ratio.

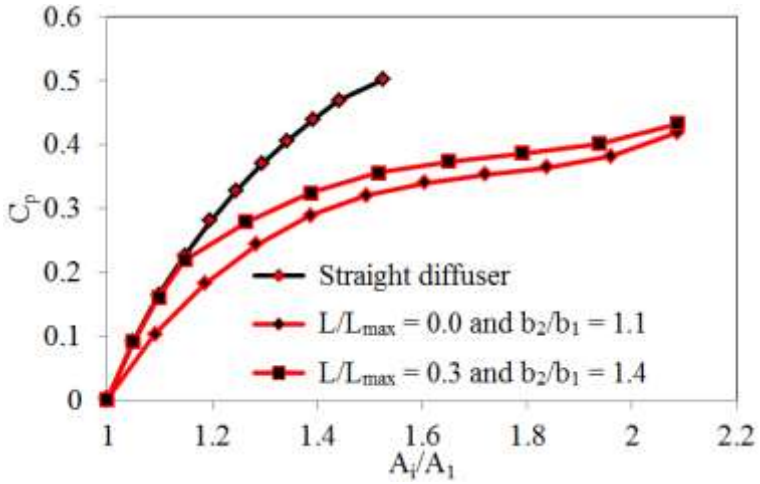

Figure 4.113: Variation in the coefficient of pressure C_p while changing the diffuser outlet-to-inlet area ratio across the radii of the straight diffuser and diverged wall diffuser configurations

Figure 4.114 depicts the variation in the coefficient of pressure C_p while changing the diffuser outlet-to-inlet area ratio across the radii of the straight diffuser and diverged wall diffuser configurations (L/L_{max} = 0.0 and b_2/b_1 = 1.1, L/L_{max} = 0.1 and b_2/b_1 = 1.2, L/L_{max} = 0.2 and b_2/b_1 = 1.3 and L/L_{max} = 0.3 and b_2/b_1 = 1.4). It can be seen that increase of the wall divergence location from the diffuser inlet, decreases the coefficient of pressure while changing the area ratio.

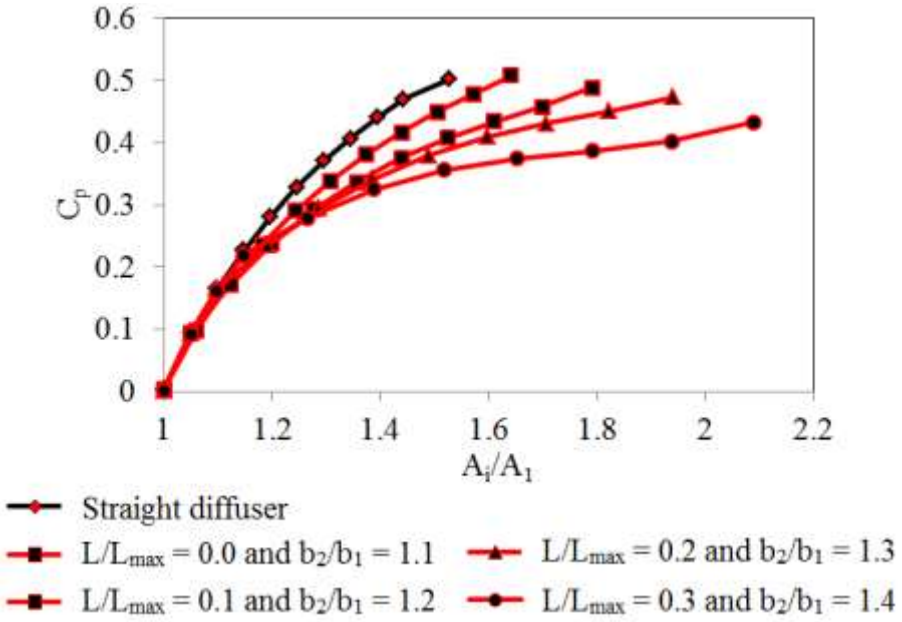

Figure 4.114: Variation in the coefficient of pressure C_p while changing the diffuser outlet-to-inlet area ratio across the radii of the straight diffuser and diverged wall diffuser configurations

4.6. Summary

It has been concluded that the maximum static pressure is recovered from the straight diffuser of the compressor stage. The analysis has been carried out where static pressure fields, velocity magnitudes, radial velocity, circumferential velocity and static temperature field results have been obtained. These results have been obtained to analyse the flow phenomena whilst compressor is working at design and off-design conditions. The results for the straight diffuser have been summarised as follows;

1. The flow within the straight diffuser is asymmetric and asymmetry is towards the shroud wall at design and off-design conditions, and at the operational speeds of 58.9rpsK$^{-1/2}$ and 78.6rpsK$^{-1/2}$.
2. The local asymmetric ratio is less symmetric near the centreline of the straight diffuser and it is increasing near the wall at design and off-design conditions, and at the operational speeds of 58.9rpsK$^{-1/2}$ and 78.6rpsK$^{-1/2}$.

3. The local asymmetric ratio increases for the velocities from the diffuser inlet to the diffuser outlet at design and off-design conditions, and at the operational speeds of 58.9rpsK$^{-1/2}$ and 78.6rpsK$^{-1/2}$.
4. It has also been noticed that the asymmetric effect is higher at BEP and lower at the off-design conditions, and at the operational speeds of 58.9rpsK$^{-1/2}$ and 78.6rpsK$^{-1/2}$.
5. Semi-empirical equation has been developed using regression analysis, which is used to calculate the isentropic efficiency at any point across the straight diffuser.
6. It is found that the maximum effect is obtained on the isentropic efficiency is due to Mach number at the inlet of the diffuser.

Once the analysis for the straight wall diffuser has been completed, the diffuser wall from the shroud wall has been diverged to obtain the diverged wall effect on the compressor performance. It has been concluded from the analysis that the alteration of diffuser wall causes a small increase in static pressure. It is important to obtain high isentropic compression efficiency within the compressor stage to decrease losses during operation. The diffuser is one of the most important components of the turbocharger compressor stage and has a key purpose of partially recovering the static pressure. The local isentropic efficiency has been investigated and a semi-empirical equation has also been developed by which the isentropic efficiency can be calculated at any location within the diverged wall diffuser. Various flow behaviours have been noticed during this investigation.

1. Increase in b_2/b_1 causes increase in the static pressure when b_2/b_1 is 1.1 and then the static pressure is reduced by increasing b_2/b_1. It is caused due to flow reversals within the diffuser.
2. Increase in b_2/b_1 causes decrease in the static temperature, which results in increased isentropic efficiency.
3. Increase of L/L_{max} does not have much effect on the stage performance.

Furthermore, diffuser asymmetric effect for the diverged wall diffusers has been investigated. It has been noticed that increase b_2/b_1 and L/L_{max} decreases the diffuser asymmetric effect. The diffuser asymmetric effect below 1.0 represents the radial flow reversals with the diverged wall diffusers. Further decrease of the diffuser asymmetric effect increases the flow reversal within the diverged wall diffusers. This causes blockage within the diverged wall diffusers. This behaviour decreases the area for the flow in the downstream direction, which increase the velocity and reduces the static pressure.

An analytical expression is developed for the local isentropic efficiency within the diffuser. This expression is valid for the diverged wall diffuser. A term $\frac{N-L}{L}$ is added that helps to calculate the isentropic efficiency based upon wall divergence location from the diffuser inlet. If the term $\frac{N-L}{L}$ gives the value equals to 1, than this equation becomes valid for the straight wall diffuser.

CHAPTER 5
NOVEL DESIGN OF THE DIVERGED WALL TILTED DIFFUSER

This chapter comprises of the results obtained after performing CFD simulations for the cases discussed in chapter 3, regarding the tilted and diverged wall diffusers. Parametric investigations have been carried out using Taguchi's method based DoE technique to make the compressor stage more compact and increase the compressor stage performance by modifying the hub wall of the diffuser. A detailed qualitative and quantitative analysis of the results has been carried out in order to understand the complex flow structure in tilted and diverged wall diffusers. The effect of geometrical parameters and flow-related parameters on the stage performance has been investigated.

5.1. Description of Compressor Model

Many researchers have carried out various investigations to make the compressor stage more compact by tilting the diffuser as described in Chapter 2 of the thesis. Similar, approach is used in this chapter to make the compressor stage more compact. However, this causes reduction in the stage performance. Wall divergence technique, which is applied in the previous chapter on parallel wall diffuser, is applied on tilted wall diffuser. This technique aids to improve the stage performance. Diffuser is tilted towards inlet of the compressor stage as shown in Figure 5.1. Tilting the diffuser causes flow reversals within the volute, which is explained in later section. To reduce flow reversals volute geometry is inverted. This provides a smooth flow across the compressor stage with minimum losses. Furthermore, wall divergence is applied to recover the losses generated within the tilted diffuser. Wall divergence increases the outlet-to-inlet width ratio of the tilted diffuser. Therefore, these techniques are used in this chapter to identify the effects of tilting the diffuser as well as increasing the outlet-to-inlet diffuser width on the stage performance. Furthermore, the effect of diffuser tilting and hub wall divergence on the local flow variations is also investigated in this chapter. Parametric investigations have been carried out to analyse the flow field characteristics within the diverged wall tilted diffuser. To carry out the parametric investigations a Taguchi's method based Design of Experiments (DoE) technique has been employed in the present study to determine the possible practical combinations of the geometrical parameters. Taguchi's method is incorporated to reduce the number of practical combinations of the geometrical parameters obtained via Full Factorial method. Taguchi's method uses orthogonal arrays to obtain the practical combinations and uses optimisation technique to design the best model based upon the signal-to-noise (S/N) ratio. A detailed step-by-step procedure of obtaining the optimised model has been explained in this chapter.

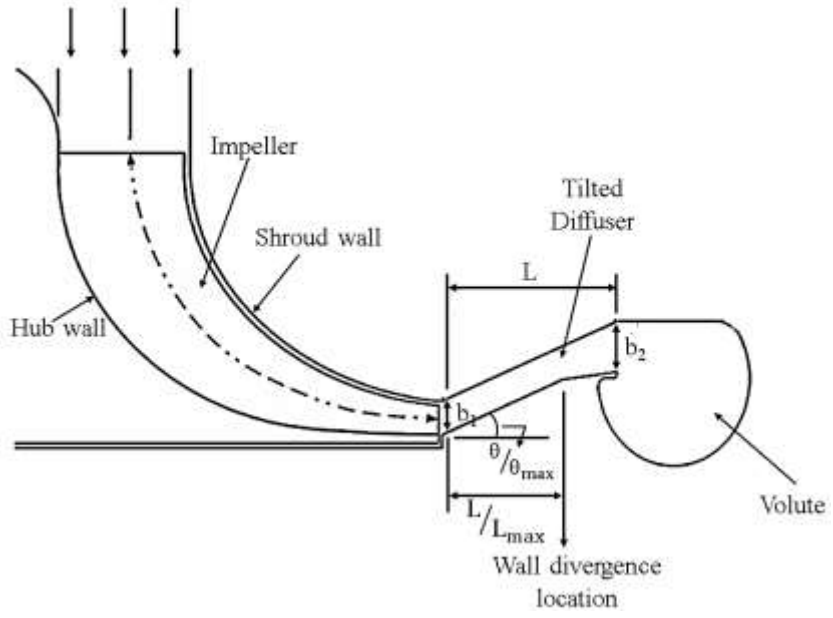

Figure 5.1: Sample configuration of the diverged wall tilted diffuser

5.2. Taguchi's Method based Design of Experiment (DoE)

[46] Design of Experiment (DoE) is a technique that is developed to investigate all possible conditions in an experiment or numerical analysis, which involves multiple factors. This technique is very costly and time consuming, henceforth a new set of approaches have been considered and an algorithm has been developed to incorporate those approaches to optimise the model. The approaches are as follows:

i. A term quality has been introduced, which defines the consistency of the performance. Consistency is achieved when the performance is close to the target with least variations. The quality can be improved either by finding the factor-level combination that reduces performance variability or adjusting the factor levels that bring performance closer to the target.

ii. A special set of tables, called orthogonal arrays (OAs), are used in the obtaining the practical combinations, which represent the smallest fractional factorials.

iii. The noise factors are included in the numerical simulation layout. This facilitates the use of numerical simulations of smaller size to study the effects of a larger number of noise factors, which leads to a favourable performance with the mean close to the target and reduces the variations around the mean.

iv. The mathematical formula associated with the concept of the loss function proposed has been incorporated, which allows a simple way to quantify the improvements. The concepts can be easily used to express predicted improvement from DoE results.

v. Signal-to-noise ratio has been used instead of the results to analyse the data obtained from numerical simulations. The logarithmic transformation of the results in terms of S/N ratios empowers the prediction of improvement in the performance of results.

The algorithm is used to optimise the diverged wall tilted diffuser as shown in Figure 5.2. A set of numerical simulations data have been generated, which is called as Generation. This data set defines the optimised model dependent upon the diffuser local efficiency. The population of numerical simulations are obtained from the orthogonal arrays, which are explained in the Appendix A-8. The orthogonal arrays provide a set of geometrical parameters to choose and diverged wall tilted diffuser models are designed. The models are designed in Solidworks (SW). Thereafter a generic script file has been written, which generates the mesh in all models using ICEM. Furthermore, a generic Communication Command Language (CCL) script has been written in Ansys CFX to specify the boundary conditions to the compressor stage. A set of data is extracted using Command Editor in CFD Post and pressure recovery across the diverged wall tilted diffuser. Once the simulations are completed a statistical analysis has been carried out, which is explained step-by-step in the later section, using S/N ratio and Analysis of Variances (ANOVA). These analyses provide the local efficiency of diverged wall tilted diffuser and stage performance. This procedure is repeatedly until the optimal geometrical parameters are obtained. Thereafter, final investigation has been carried out to obtain the stage performance optimal diffuser and it is compared with parallel wall diffuser. The geometrical parameters considered are tilted angle θ/θ_{max}, wall divergence location from the diffuser inlet L/L_{max} and outlet-to-inlet width ratio b_2/b_1.

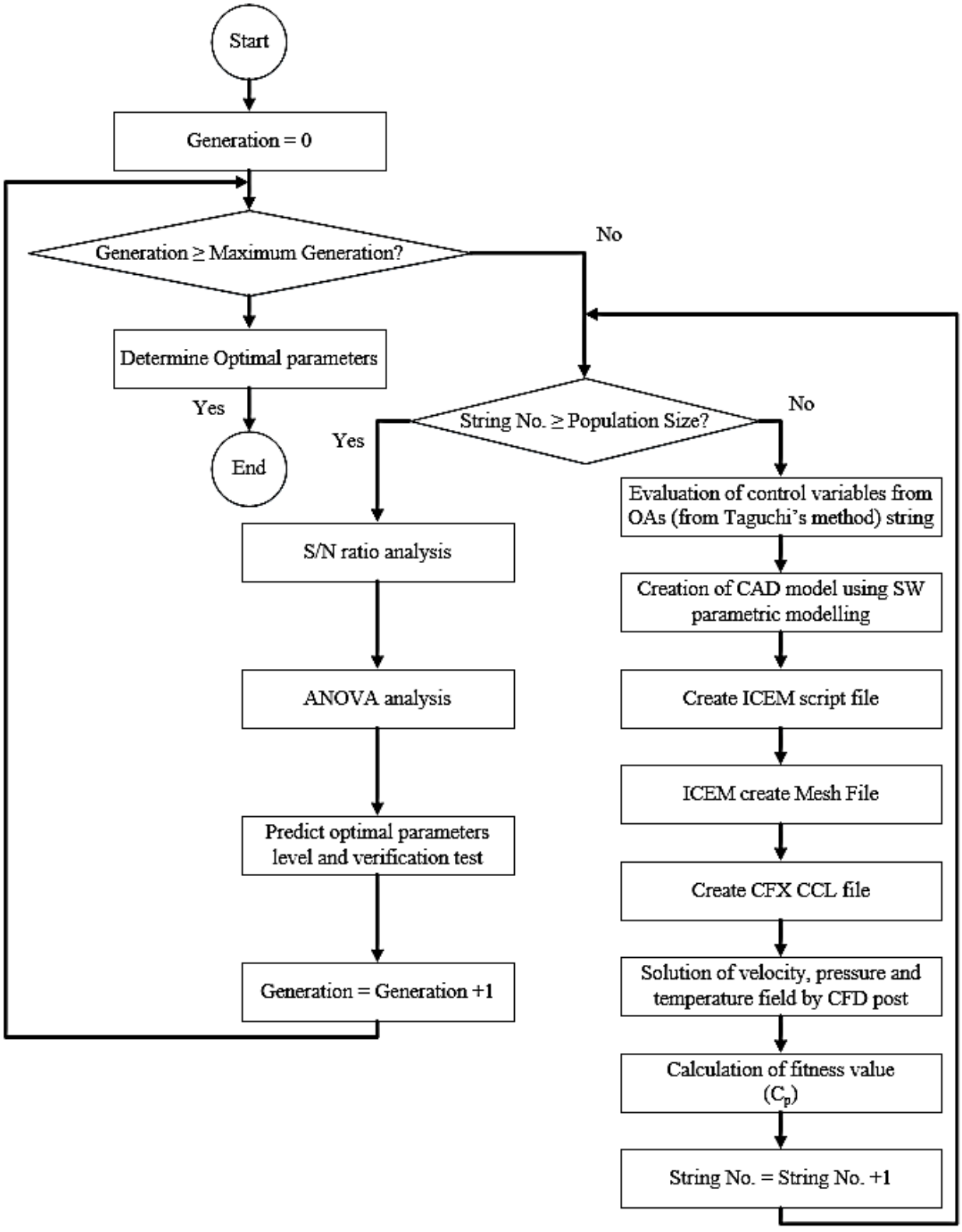

Figure 5.2: A schematic showing the proposed methodology to solve the problem

The desirability of results is dependent upon the criterion of bigger-the-better. In this study, a compressor stage has been investigated to determine the optimal design parameters that maximize the performance characteristics, whereby isentropic efficiency is used as primary performance characteristic. Henceforth, bigger-the-better approach has been used to obtain the highest isentropic efficiency. The S/N ratio for bigger-the-better criterion is defined as follows:

$$\mathrm{S/N} = -10\log\left(\frac{1}{n}\sum_{i=1}^{n}\left(\frac{1}{y_i^2}\right)\right) \tag{5.1}$$

where, n is frequency of numerical simulation in each group and y is value of i^{th} experiment in each group. The subscript i is the numerical simulation.

Figure 5.3 depicts the relational diagram of quality characteristics, whereby three factors known as control factor, source factor and interference factor are shown, which have a direct impact on the system's response and hence, the quality characteristics. The source factor and the response value of the system have input and output relations. Therefore, the source factor here is represented as the mass flow rate entering and leaving the compressor stage. The control factor is an important factor of quality characteristics' optimization. The control factor comprises of the tilted angle θ/θ_{max}, wall divergence location from the diffuser inlet L/L_{max} and outlet-to-inlet width ratio b_2/b_1. The interference factor is an uncontrolled parameter, which cannot be determined and is represented by the losses generated within the diverged wall tilted diffuser. The parameter levels of the control factors in this study are as shown in Table 5.1. The maximum and minimum specification of these levels is based upon the limitation of diverged wall tilted diffuser of the compressor stage. Five levels for each control factor have been specified in order to quantify the effect of each parameter on the local diffuser efficiency and hence the compressor stage performance.

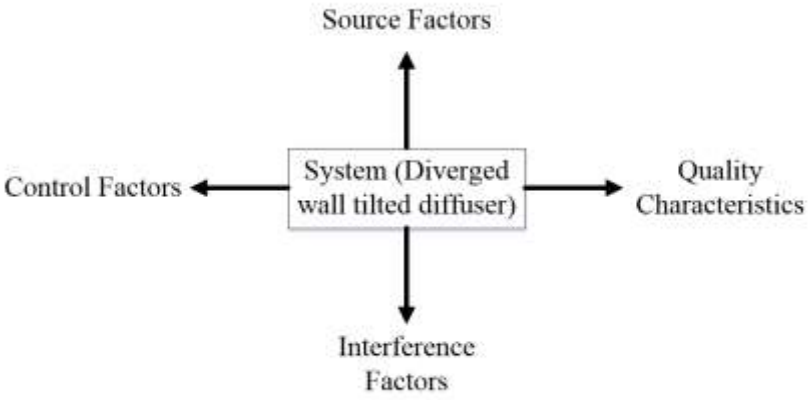

Figure 5.3: State diagram of diverged wall tilted diffuser of centrifugal compressor stage

Table 5.1: Levels of control factor parameters

Description	Level 1	Level 2	Level 3	Level 4	Level 5
Tilted angle, θ/θ_{max}	0	0.25	0.50	0.75	1.00
Outlet-to-inlet width ratio, b_2/b_1	1.10	1.20	1.30	1.40	1.50
Wall divergence location from the diffuser inlet, L/L_{max}	0.0	0.19	0.38	0.57	0.76

Symbolically, the level for each factor is represented by α, β and γ as shown in Table 5.2. The subscripts 1, 2, 3, 4 and 5 are the number of levels for each factor.

Table 5.2: Levels of control factor parameters

Description	Level 1	Level 2	Level 3	Level 4	Level 5
Tilted angle, θ/θ_{max}	α_1	α_2	α_3	α_4	α_5
Outlet-to-inlet width ratio, b_2/b_1	β_1	β_2	β_3	β_4	β_5
Wall divergence location from the diffuser inlet, L/L_{max}	γ_1	γ_2	γ_3	γ_4	γ_5

Since, the numerical analysis carried out by this study has three control factors with five-elements (five-levels), henceforth the orthogonal arrays derived from these combinations are based upon $OA_{25}(5^3)$. Based upon this orthogonal array, a set of practical combinations have been obtained which are shown in Table 5.3. There are 25 number of numerical simulations have been required to carry out this parametric investigation.

Table 5.3: Orthogonal array $OA_{25}(5^3)$ for diverged wall tilted diffuser

Parameters	Outlet-to-inlet width ratio, b_2/b_1	Tilted angle, θ/θ_{max}	Wall divergence location from the diffuser inlet, L/L_{max}
Row No.	(-)	(-)	(-)
1	1.10	0.00	0.00
2	1.10	0.25	0.19
3	1.10	0.50	0.38
4	1.10	0.75	0.57
5	1.10	1.00	0.76
6	1.20	0.00	0.19
7	1.20	0.25	0.38
8	1.20	0.50	0.57
9	1.20	0.75	0.76
10	1.20	1.00	0.00
11	1.30	0.00	0.38
12	1.30	0.25	0.57
13	1.30	0.50	0.76
14	1.30	0.75	0.00
15	1.30	1.00	0.19
16	1.40	0.00	0.57
17	1.40	0.25	0.76
18	1.40	0.50	0.00
19	1.40	0.75	0.19
20	1.40	1.00	0.38
21	1.50	0.00	0.76
22	1.50	0.25	0.00
23	1.50	0.50	0.19
24	1.50	0.75	0.38
25	1.50	1.00	0.57
Generator	x_1	x_2	$x_2+ x_1$

5.3. Selection of Volute Design for the Newly desing Diverged Wall Tilted Diffuser

A new compressor model has been designed that comprises of tilted diffuser geometry with specific parameters obtained using Taguchi's method. The volute could be connected in two different ways as depicted in the Figure 5.4(a) and Figure 5.4(b), which are the same overhung volute models oppositely interfaced with the tilted diffuser. The baseline model has a straight wall diffuser interfaced at the impeller outlet, and volute is connected with the diffuser at the diffuser outlet as shown in Figure 5.4(a). The new compressor is designed with inversely positioned volute as depicted in Figure 5.4(b). . The drawback of using this is that it increases compressor area while being used in straight wall diffuser. Figure 5.4(c) and Figure 5.4(d) depicts the diffuser and the volute configurations. The

tilted wall diffuser model is used as a compressor component instead of straight wall diffuser, flow reversals are pronounced inside the volute when baseline volute (Figure 5.4(c)), which are depicted in Figure 5.5. This reduces the stage performance. Therefore, in order to eliminate these flow reversals, oppositely interfaced volute model has been used which guides the flow smoothly across the diffuser and the volute with minimum losses as shown in Figure 5.4(d).

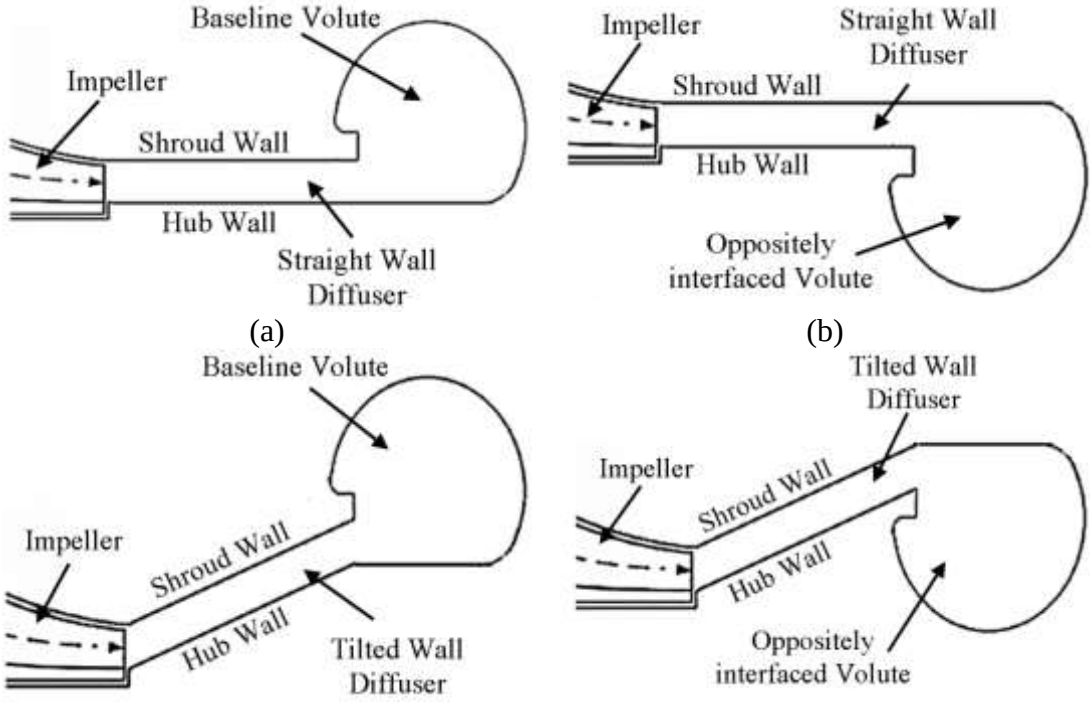

Figure 5.4: Diffuser and volute configurations of compressor stage (a) straight wall diffuser and baseline volute, (b) straight wall diffuser and oppositely interfaced volute, (c) tilted wall diffuser and baseline volute and (d) tilted wall diffuser and oppositely interfaced volute

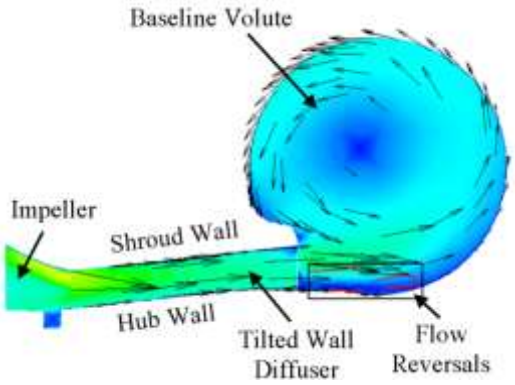

Figure 5.5: Flow reversal within the volute using tilted wall diffuser

Moreover, the new compressor model having straight wall radial diffuser with oppositely interfaced volute model has been compared with the baseline compressor model and the experimental data. The comparison between these has been shown in the Table 5.4. The model has been numerically simulated at only one design point at an operational speed of 58.9rpsK$^{-1/2}$. It can be seen that the percentage difference of pressure ratio and stage efficiency between the numerical results and the experimental results are 1.31% and 5.43%. Furthermore, the percentage difference of pressure ratio and stage efficiency between the numerical results of the baseline volute model and oppositely interfaced volute model results are 1.32% and 1.58%. It can be noticed that using the oppositely interface volute model decreases the stage performance as well as increasing the compressor stage envelope size.

Table 5.4: Comparison of new compressor model

Compressor Models		Pressure Ratio	Isentropic Efficiency	Percentage Difference in Pressure Ratio	Percentage Difference in Isentropic Efficiency
		(-)	(%)	(%)	(%)
Baseline volute model	Experimental data	1.55	74.75	(-)	(-)
	Numerical data	1.53	70.90	-1.31	-5.43
Oppositely interfaced volute model	Numerical data	1.51	69.80	-1.32	-1.58

The aim of this chapter is to design the compact compressor stage while increasing the stage performance. Therefore, diffuser model is tilted to make the compressor stage more compact. Furthermore, wall divergence is implemented on the hub wall to increase the stage performance. An

optimisation technique has been carried out in this chapter. The algorithm of pursuing this set of analysis has been mentioned earlier. The next section demonstrates the simulated data obtained from the numerical simulations carried out using Ansys CFX.

5.4. Performance Characterisitcs of the Compressor Stage using Diverged Wall Tilted Diffuser

Numerical analysis has been carried out to obtain the total-to-total stage performance and flow field characteristics across various configurations of the diverged wall tilted diffuser have been analysed. Table 5.5 shows the results obtained from the numerical simulations of CFD for the global parameters of all 25 configurations. Three geometrical parameters are considered, the diffuser outlet-to-inlet width ratio, the tilt angle and the divergence location from the inlet on the shroud wall to analyse the effect on the local flow field and on the total-to-total stage performance. It can be seen from the Table 5.4 that increase of outlet-to-inlet width ratio causes increase in the stage performance. Furthermore, decrease in the tilt angle and increase in diverge location causes increase stage performance. Since the data has been obtained using Taguchi's method whereby less numerical data have been simulated. Henceforth, it is difficult to quantify the effect of each parameter on the stage performance. Therefore, Taguchi based analysis has been carried out in next section of the chapter, which will help in quantifying the geometrical effect on the stage performance

Table 5.5: CFD results of centrifugal compressor stage using different configurations of diverged wall tilted diffuser

Parameters	Outlet-to-inlet width ratio, b_2/b_1	Tilted angle, θ/θ_{max}	Wall divergence location from the diffuser inlet, L/L_{max}	Isentropic efficiency, η	S/N ratio
Row No.	(-)	(-)	(-)	(%)	dB
1		0.00	0.00	71.56	37.09
2		0.25	0.19	71.96	37.14
3	1.10	0.50	0.38	71.57	37.09
4		0.75	0.57	71.10	37.04
5		1.00	0.76	69.99	36.90
6		0.00	0.19	72.15	37.16
7		0.25	0.38	72.26	37.18
8	1.20	0.50	0.57	71.81	37.12
9		0.75	0.76	71.14	37.04
10		1.00	0.00	70.57	36.97
11		0.00	0.38	71.99	37.15
12	1.30	0.25	0.57	72.04	37.15
13		0.50	0.76	71.39	37.07

14		0.75	0.00	71.26	37.06
15		1.00	0.19	70.69	36.99
16		0.00	0.57	72.40	37.20
17		0.25	0.76	72.25	37.18
18	1.40	0.50	0.00	72.14	37.16
19		0.75	0.19	72.02	37.15
20		1.00	0.38	71.16	37.04
21		0.00	0.76	71.93	37.14
22		0.25	0.00	72.32	37.18
23	1.50	0.50	0.19	72.21	37.17
24		0.75	0.38	71.80	37.12
25		1.00	0.57	70.89	37.01

5.5. Optimal Designing of Diverged Wall Tilted Diffsuer using Statistical Analysis

This section of the chapter investigates the optimal design of the diverged wall diffuser using statistical analysis. The statistical analysis comprises of mean value analysis and analysis of variances, which will help in obtaining the predicted results outside the simulated number of orthogonal arrays. Furthermore, it also helps in obtaining the relationship between the geometrical parameters on the basis of stage performance.

5.5.1. Mean Value Analysis

The S/N ratio in the experiment has been calculated in the last section, which has been used to create a response table and plot a response diagram. The response value of the S/N ratio of each factor has been calculated by obtaining the average value of each set of levels by using the equation 5.2 and hence, the calculated data has been presented in the Table 5.6.

$$\eta_{A1} = \frac{1}{5}(\eta_1 + \eta_2 + \eta_3 + \eta_4 + \eta_5) \tag{5.2}$$

Table 5.6: Integration results of response in Taguchi numerical analysis

Parameters	Outlet-to-inlet width ratio, b_2/b_1	Tilted angle, θ/θ_{max}	Wall divergence location from the diffuser inlet, L/L_{max}
Level of factor	A	B	C
1	37.05	37.15	37.09
2	37.10	37.17	37.12
3	37.08	37.13	37.12
4	37.15	37.08	37.10
5	37.13	36.98	37.07

Effect	0.09	0.18	0.06
Rank	2	1	3

Bigger-the-better criterion has been chosen, as obtaining highest isentropic efficiency is the demand for the compressor stage. Therefore, in this study, the optimal diffuser has the ability to maximize the isentropic efficiency for the centrifugal compressor stage. Henceforth, when bigger-the-better criterion is selected than higher value of S/N ratio needs to be designated because S/N ratio are proportional to each other from equation 5.1. The results obtained from Table 5.6 and Figure 5.6 it can be seen that the optimal geometrical parameter level has been predicted as the diffuser outlet-to-inlet width ratio of 1.31, diffuser tilt angle of 0.25and wall divergence location from the diffuser inlet of 0.19. Moreover, response in the Table 5.6 has calculated the degree of contribution of the parameters to the system. Degree of contribution is a statistical approach that has helped to identify the magnitude of effect of parameters on the performance characteristics. The effect in statistics is the different between the highest average for each factor and the lowest average of each factor. Furthermore, the effect has also been ranked based upon the effect size as B > A > C. it can be noticed that the maximum effect obtained is by the Factor B, which is the tilt angle. Thereafter, the outlet-to-inlet width ratio and wall divergence location form the inlet has second and third degree of effect respectively.

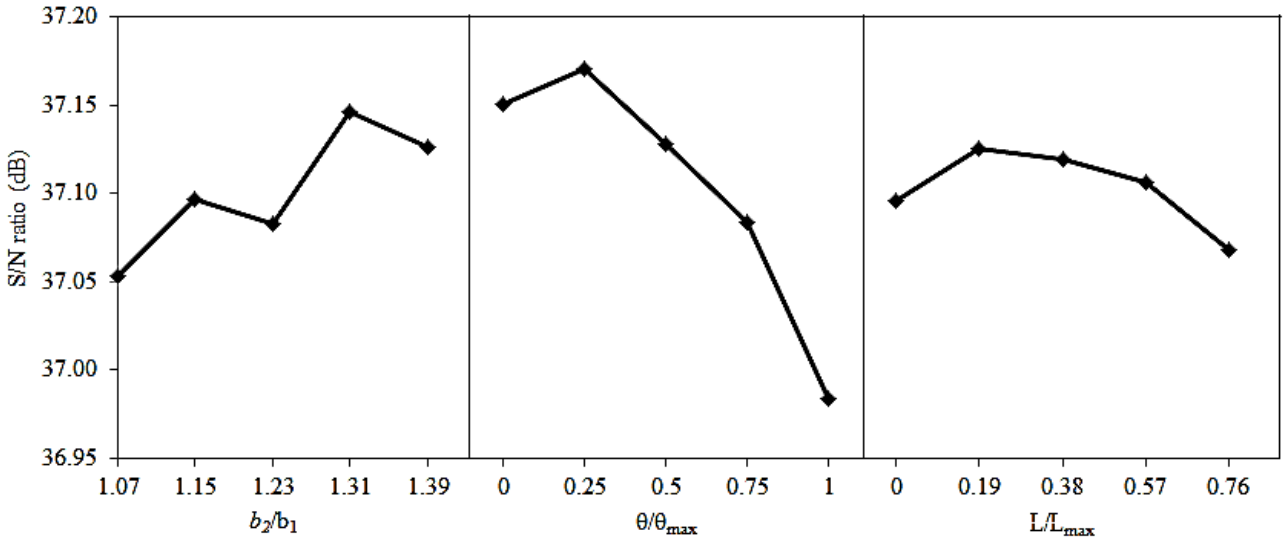

Figure 5.6: Response diagram of Taguchi numerical analysis

5.5.2. Analysis of Variance (ANOVA)

Taguchi method cannot judge and determine effect of individual parameters on the entire process while percentage contribution of individual parameters can be well determined using ANOVA. Minitab 2017 software of ANOVA module has been employed to investigate the effects of process parameters (b_2/b_1, θ/θ_{max} and L/L_{max}). [47] Analysis of variances (ANOVA) aims to evaluate the numerical errors, and F-ratio method and P-ratio methods are used to identify the influential degree of each factor. ANOVA can be useful for determining influence of any given input parameter from a series of numerical results obtained by Taguchi based DoE. It can also be used to interpret numerical data. P-value of 0.001 (shown in Table 5.7) of parameters indicates that b_2/b_1 is significantly contributing towards the compressor stage performance.

Table 5.7: Integration results of response in Taguchi numerical analysis

Source	DF	Seq SS	Adj SS	Adj MS	F	P
b_2/b_1	4	0.026348	0.026348	0.006587	4.49	0.019
θ/θ_{max}	4	0.106574	0.106574	0.026643	18.15	0.001
L/L_{max}	4	0.009989	0.009989	0.002497	1.7	0.118
Residual Error		12	0.017619	0.017619	0.001468	
Total	24	0.16053				

Based upon the ANOVA analysis carried out in the earlier section, new compressor model with optimised diverged wall tilted diffuser model has been designed and investigated. It has been found that the pressure ratio has been increased by 0.01atm but on the other hand, the isentropic efficiency has been significantly increased by 4.1% due to the temperature decrement. The in-depth analysis in the tilted diffuser has been illustrated in the next sections.

Table 5.8: Comparison of numerical results for straight wall diffuser model with diverged wall diffuser model

Compressor Models		Pressure Ratio	Efficiency	Percentage Difference in Pressure Ratio	Percentage Difference in Efficiency
		(-)	(%)	(%)	(%)
Straight wall diffuser model	Experimental data	1.55	74.75	(-)	(-)
	Numerical data	1.53	70.90	-1.31	-5.43
Diverged wall diffuser model	Numerical data	1.54	72.93	0.65	2.78

The numerical data has also been verified with the statistical results. It has been shown that the percentage difference between the numerical data and statistical results in only 1.58%, which shows very good agreement (shown in Table 5.9). A semi-empirical equation (Equation 5.3) has also been developed using linear regression approach. This equation is based upon the actual and predicted data. The equation provides the stage efficiency, which is dependent upon the levels for the geometrical factors considered.

$$\eta = 71.62 - 0.389(\alpha_1) - 0.38(\alpha_2) - 0.149(\alpha_3) - 0.371(\alpha_4) + 0.205(\alpha_5) + 0.381(\beta_1) + 0.542(\beta_2) + 0.2(\beta_3) - 0.158(\beta_4) - 0.965(\beta_5) - 0.055(\gamma_1) + 0.178(\gamma_2) + 0.134(\gamma_3) + 0.025(\gamma_4) - 0.282(\gamma_5) \quad (5.3)$$

Table 5.9: Comparison between numerical data and statistical results for straight wall diffuser model

Value	Isentropic Efficiency	Percentage Difference in Isentropic Efficiency (%)
Predicted value	72.72	-
Actual value	73.93	1.58

5.6. Flow Field Characteristics within the Diverged Wall Tilted Diffusers

This section demonstrates the flow field analyses within the diverged wall tilted diffuser based upon static pressure, velocity magnitude, circumferential velocity, radial velocity and static temperature variations. The analyses have been carried out in such a way that certain combinations of simulated data have been compared to obtain the effect of geometrical parameter on the stage performance. The geometrical parameters considered are θ/θ_{max}, L/L_{max} and b_2/b_1. The combinations considered are mentioned in Table 5.10 with their names. These names are used in the analysis. Since Taguchi method has been used, therefore number of simulations is not in linear order. They are obtained via orthogonal arrays. Therefore, these shown in Table 5.10 are chosen, which explains the geometrical effect on the flow parameter. Furthermore, the effect of wall divergence on the flow asymmetry within the diffuser has been quantified to establish a relationship of wall divergence with asymmetric effect and isentropic efficiency.

Table 5.10: Practical combinations selected for flow field analysis

Name	θ/θ_{max}	L/L_{max}	b_2/b_1
DC_1	0	0	1.10
DC_2	0	0.57	1.40
DC_3	0.5	0	1.40
DC_4	0.5	0.57	1.20
DC_5	1.0	0	1.20
DC_6	1.0	0.57	1.50

Figure 5.7 depicts the static pressure variations across the centreline of the diverged wall tilted diffuser configurations ((a) DC_1, (b) DC_2, (c) DC_3, (d) DC_4, (e) DC_5 and (f) DC_6) at BEP at an operational speed of 58.9rpsK$^{-1/2}$. The trend of the static pressure across the diverged wall tilted diffusers is similar to that across the straight diffuser. It can be seen that the minimum static pressure is obtained at the diffuser inlet after the volute-tongue region. The static pressure increases radially across the diffuser. Furthermore, the static pressure also increases circumferentially in the direction of impeller rotation (ω). The maximum static pressure is obtained at the diffuser outlet near the volute-tongue region. It can be seen that the static pressure is decreased by 0.75% and 0.67% at the diffuser inlet and diffuser outlet respectively across the diffuser configuration of DC_1 in comparison to parallel wall straight diffuser. Furthermore, it can also be seen that the static pressure is same at the diffuser inlet across DC_2, DC_3 and DC_6 and at the diffuser outlet across DC3 in comparison to that across diffuser configuration of DC_1. It can also be seen that the static pressure is increased at the diffuser inlet across DC_4 and at the diffuser outlet of diffuser across DC_2, DC_4 and DC_5 in comparison to that across DC_1. Moreover, the static pressure in decreased at the diffuser inlet of diffuser configurations of DC_5 and the diffuser outlet of DC_6 in comparison to that across DC_1. It can be concluded from the results that the static pressure increases up to the tilt angle of 0.5, L/L_{max} of 0.57 and outlet-to-inlet width ratio of 1.15, and then the static pressure decreases up to the diffuser outlet.

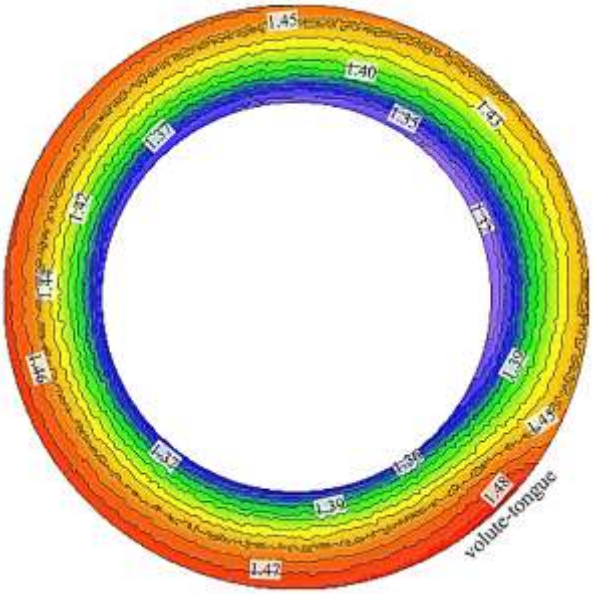

(a)

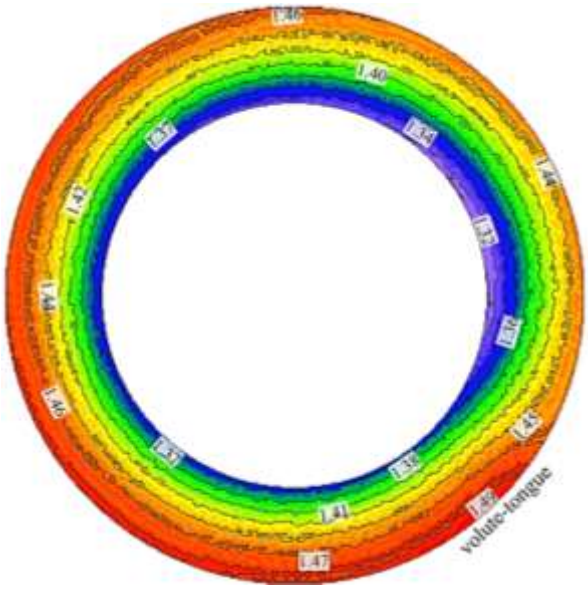

(b)

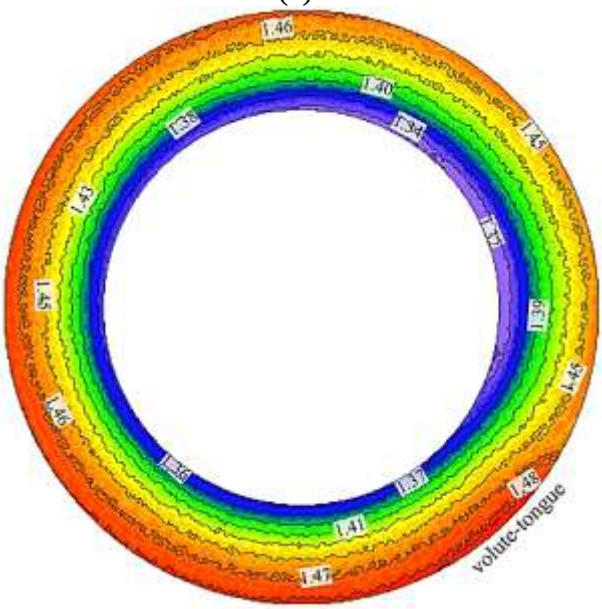

(c)

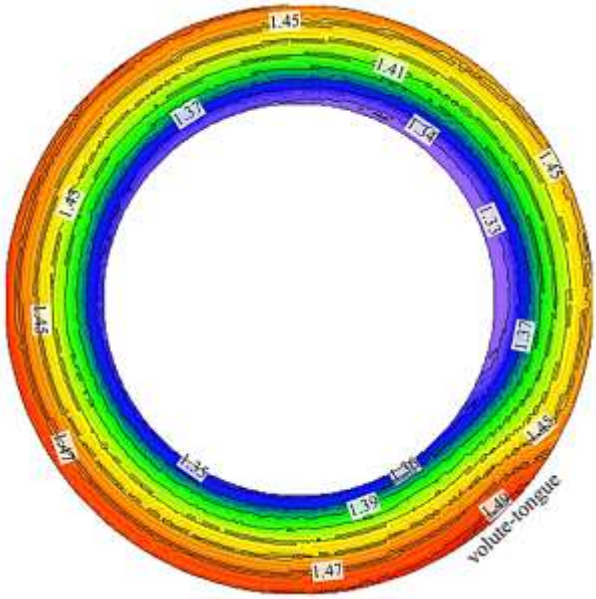

(d)

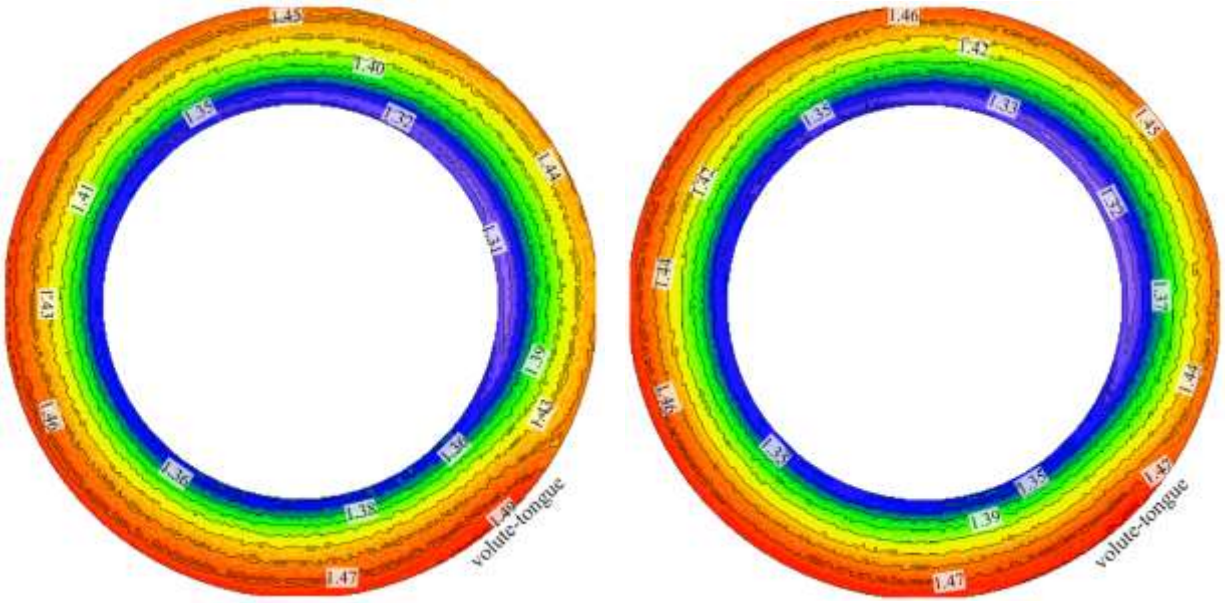

(e) (f)

Figure 5.7: Static pressure (atm) variations across the centreline of the diverged wall tilted diffuser (a) DC_1, (b) DC_2, (c) DC_3, (d) DC_4, (e) DC_5 and (f) DC_6 at BEP at an operational speed of 58.9rpsK$^{-1/2}$

Figure 5.8 depicts the flow streamlines radially across (a) parallel wall diffuser and diverged wall tilted diffuser configurations ((a) DC_1, (b) DC_2, (c) DC_3, (d) DC_4, (e) DC_5 and (f) $DC_{6)}$ at BEP at an operational speed of 58.9rpsK$^{-1/2}$. It can be seen from the figures that increasing the wall divergence do not increases the flow separation with the diffuser and volute in comparison to that across the diverged wall straight diffuser. Therefore, less losses are generated within the diffuser and helps in increasing the stage performance. The detailed analysis across the diffusers is explained in the later sections.

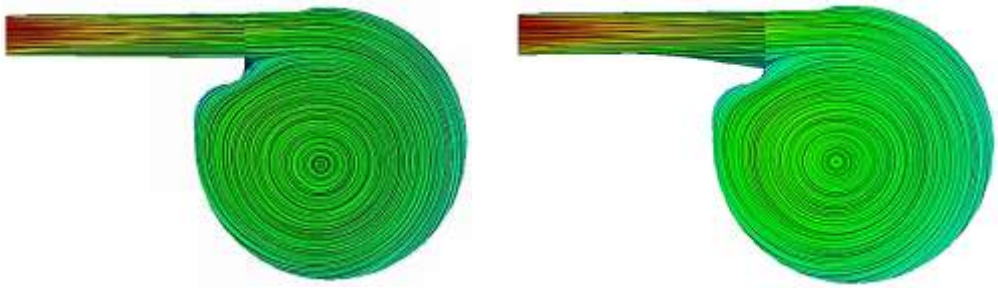

(a)

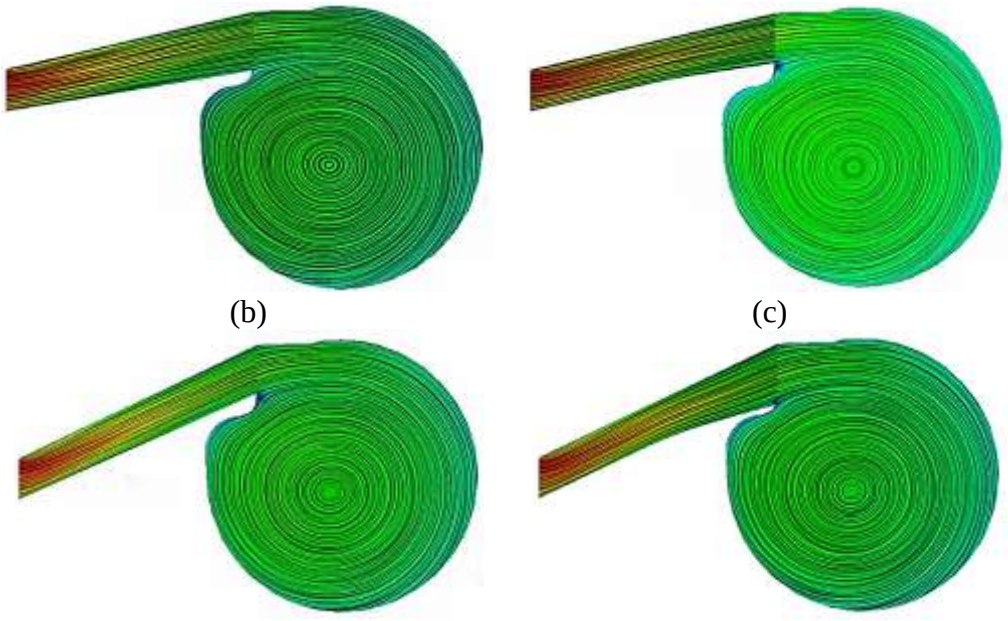

(b) (c)

(d) (e)

Figure 5.8: Flow streamlines radially the diverged wall tilted diffuser (a) DC_1, (b) DC_2, (c) DC_3, (d) DC_4, (e) DC_5 and (f) DC_6 at BEP at an operational speed of 58.9rpsK$^{-1/2}$

Figure 5.9 depicts the comparison of velocity magnitude distribution across parallel wall and diverged wall tilted diffuser configurations (DC_1, DC_2, DC_3, DC_4, DC_5 and DC_6) from the hub wall to the shroud wall at BEP at an operational speed of 58.9rpsK$^{-1/2}$. It can be seen that the velocity magnitude is reduced radially across the diffuser. It can be seen that the velocity magnitude across diverged wall tilted diffusers is decreased in comparison to parallel wall straight diffuser. Furthermore, it has been observed that the velocity magnitude is asymmetric towards hub wall across diverged wall tilted wall diffusers in comparison to parallel wall diffuser. Moreover, it can be seen that the flow asymmetry for velocity magnitude is decreasing with the combined increase of diffuser outlet-to inlet width ratio, wall divergence location from the inlet and tilt angle. However, the detailed analysis has been carried out by quantifying the asymmetric ratio for the velocity magnitude profile across the diverged wall diffusers.

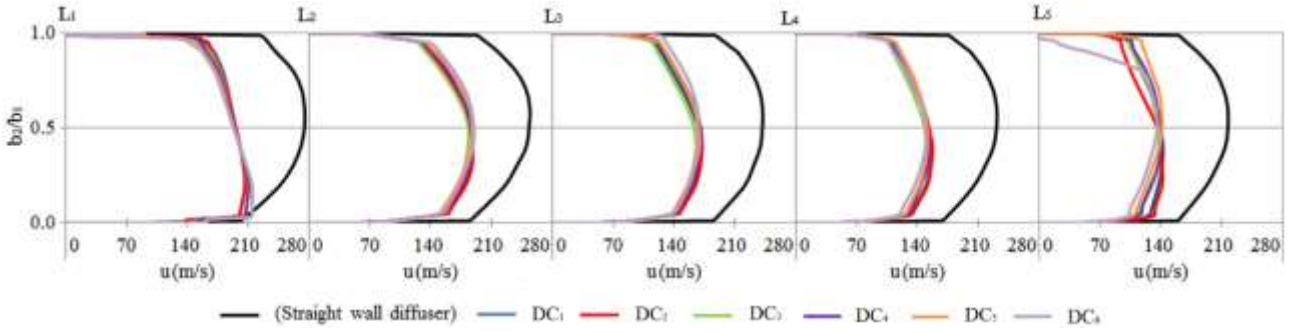

Figure 5.9: Comparison of velocity magnitude (m/s) distribution across parallel wall and diverged wall tilted diffuser configurations from the hub wall to the shroud wall at BEP at an operational speed of 58.9rpsK$^{-1/2}$

Figure 5.10 depicts the local asymmetric ratio for the velocity magnitudes, α_{vm} across the diverged wall diffusers (DC_1, DC_2, DC_3, DC_4, DC_5 and DC_6) at BEP at an operational speed of 58.9rpsK$^{-1/2}$. It can be seen that the flow is asymmetric towards the hub wall across the diverged wall diffusers. The asymmetric ratio for the velocity magnitude constantly increases from the centreline of the diffuser towards the wall and from the diffuser inlet to the diffuser outlet across diffuser configurations of DC_1, DC_2, DC_3 and DC_4. It has been noticed that the asymmetric ratio for the velocity magnitude constantly decreases from the centreline of the diffuser towards the wall and increases from the diffuser inlet to the diffuser outlet across diffuser configurations of DC_5 and DC_6.

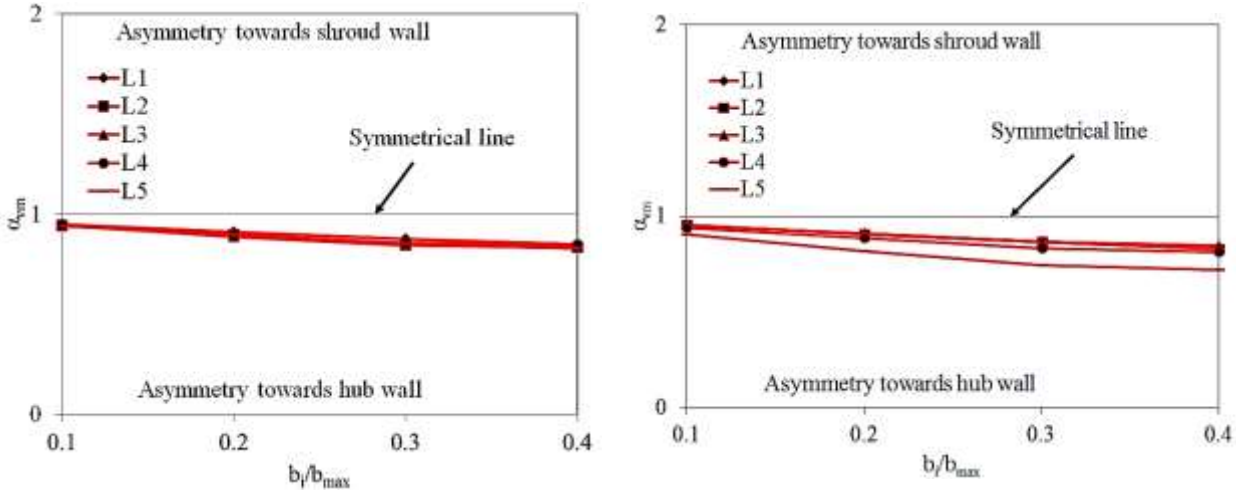

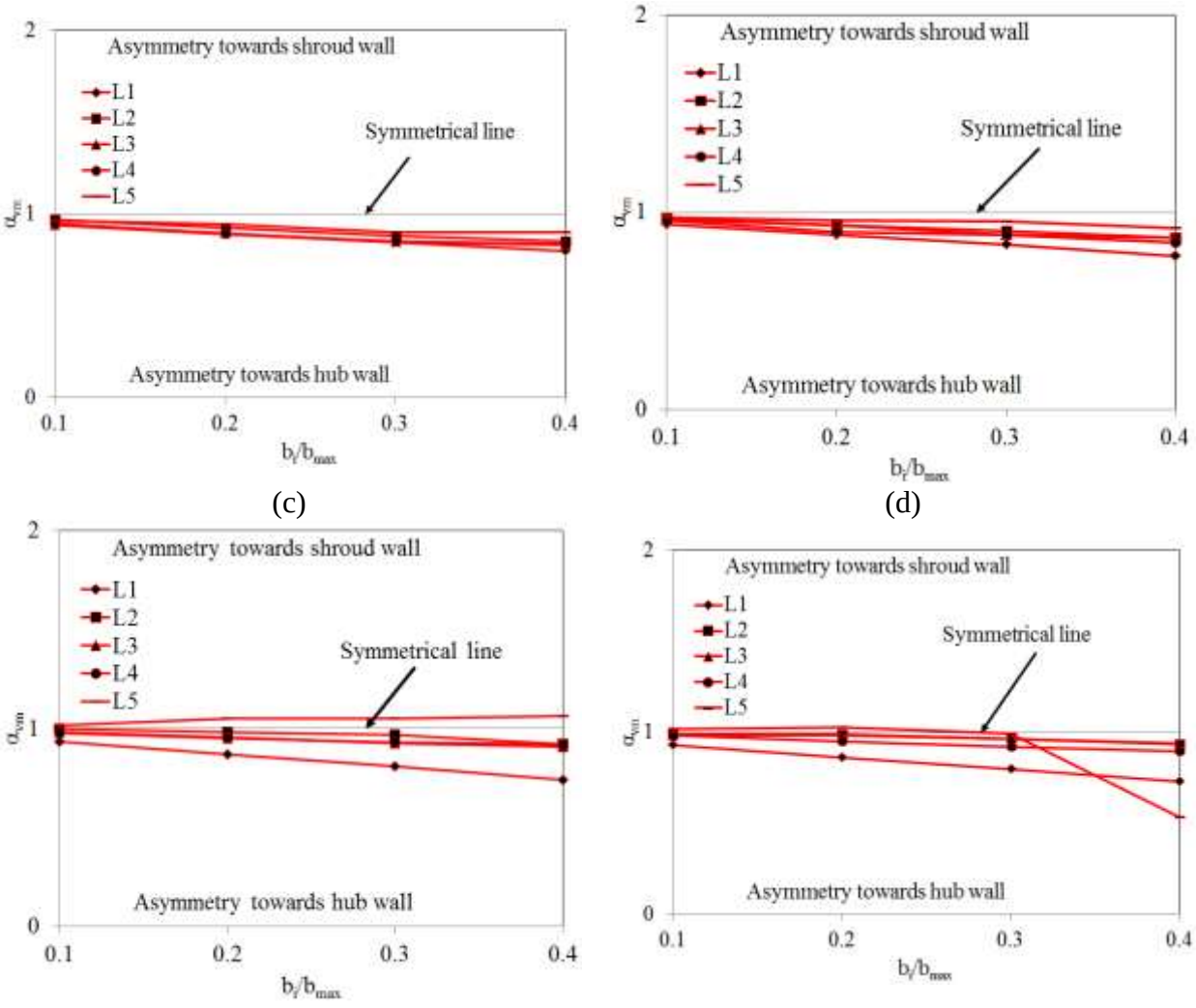

Figure 5.10: Local asymmetric ratio for the velocity magnitude, α_{vm} across the diverged wall diffusers ((a) DC_1, (b) DC_2, (c) DC_3, (d) DC_4, (e) DC_5 and (f) DC_6) at BEP at an operational speed of 58.9rpsK$^{-1/2}$

Figure 5.11 depicts the radial velocity distribution across the centreline of the diverged wall tilted diffuser configurations (DC_1, DC_2, DC_3, DC_4, DC_5 and DC_6) at BEP at an operational speed of 58.9rpsK$^{-1/2}$. The trend of the radial velocity across the diverged wall tilted diffusers is similar to that across the straight diffuser. It can be seen that the maximum radial velocity is obtained at the diffuser inlet after the volute-tongue region. The radial velocity decreases radially across the diffuser. Furthermore, the radial velocity also decreases circumferentially in the direction of impeller rotation (ω). The minimum radial velocity is obtained at the diffuser outlet at near the volute-tongue region. It can be seen that the radial velocity value is decreased at the diffuser inlet by 12.3% and increased at the diffuser outlet by 1.9% across DC_1 in comparison to that across the parallel wall diffuser.

Furthermore, it can be seen that the radial velocity is further decreased at the diffuser inlet by 46%, 28%, 2% and 2% at the diffuser inlet across DC_2, DC_3, DC_4 and DC_6 respectively in comparison to that across DC_1. Similarly, the radial velocity is also decreased at the diffuser outlet by 0.0% and 1.0% across DC_2 and DC_3 in comparison to that across DC_1. Thereafter, it can be seen that the radial velocity is increased at the diffuser inlet by 4% across DC_5 and it at the diffuser outlet by 3.8%, 2.9% and 9.5% across DC_4 DC_5 and DC_6 in comparison to that across DC_1. It can be concluded from the results that the radial velocity decreases up to increase the tilt angle of 0.5, L/L_{max} of 0.0 and outlet-to-inlet width ratio of 1.31, and then the radial velocity increases.

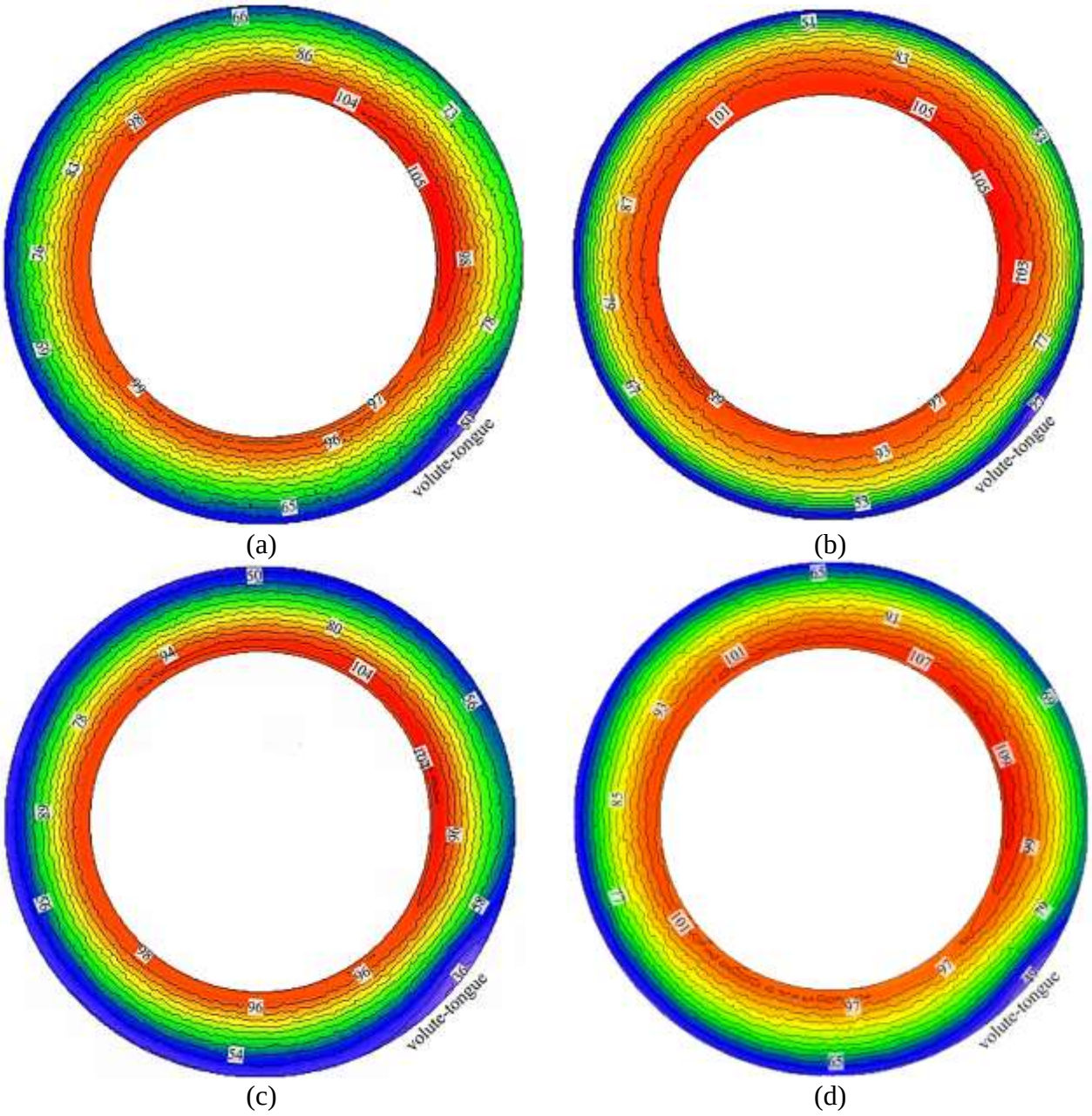

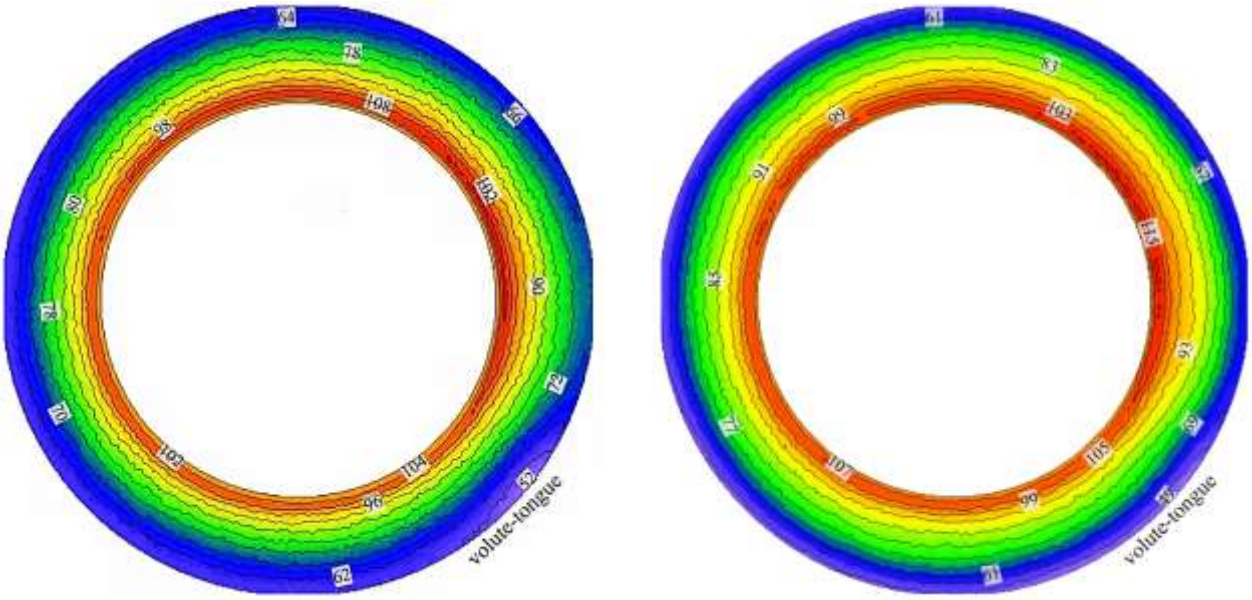

(e) (f)

Figure 5.11: Radial velocity (m/s) distributions across the centreline of the diverged wall tilted diffuser (a) DC_1, (b) DC_2, (c) DC_3, (d) DC_4, (e) DC_5 and (f) DC_6 at BEP at an operational speed of $58.9rpsK^{-1/2}$

5.12 depicts the comparison of radial velocity distribution across parallel wall and diverged wall tilted diffuser configurations (DC_1, DC_2, DC_3, DC_4, DC_5 and DC_6) at BEP at an operational speed of $58.9rpsK^{-1/2}$. It can be seen that the radial velocity is reduced radially across the diffuser. It can be seen that the radial velocity at L1 (diffuser inlet) is similar across parallel and diverged wall tilted diffusers, whereas the radial velocity is decreasing towards L5 (diffuser outlet) for diverged wall tilted diffuser configurations in comparison to parallel wall diffuser. Furthermore, it has been observed that the radial velocity is asymmetric across the parallel and diverged wall straight diffuser. However, it has been noticed that the diverged wall tilted diffuser have asymmetry towards hub wall in comparison to that across parallel wall diffuser having asymmetry towards shroud wall. Furthermore, it has also been noticed that diverged wall tilted diffuser having tilt angle above 1.0 have similar asymmetry in comparison to parallel wall diffuser. However, the detailed analysis has been carried out by quantifying the asymmetric ratio for the radial velocity profile across the diverged wall diffusers.

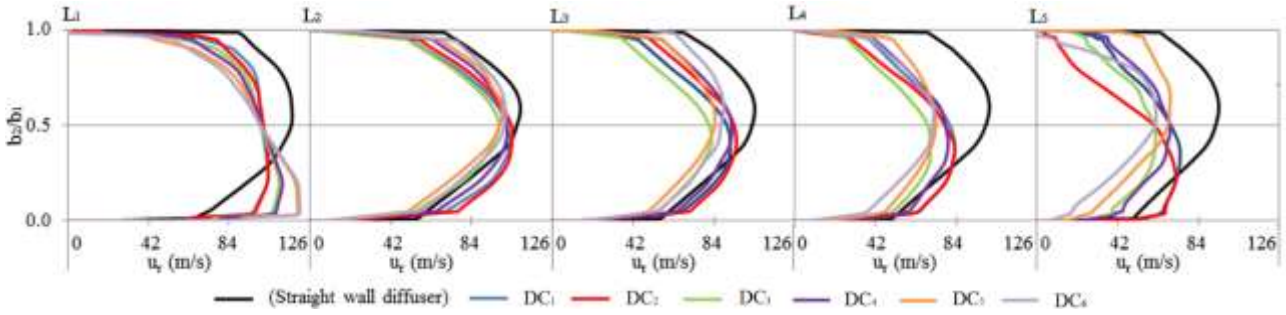

Figure 5.12: Comparison of radial velocity (m/s) distribution across parallel wall and diverged wall tilted diffuser configurations from the hub wall to the shroud wall at BEP at an operational speed of 58.9rpsK$^{-1/2}$

Figure 5.13 depicts the local asymmetric ratio for the radial velocity, α_{vr} across the diverged wall diffusers (DC_1, DC_2, DC_3, DC_4, DC_5 and DC_6) at BEP at an operational speed of 58.9rpsK$^{-1/2}$. It can be seen that the flow is asymmetric towards the hub wall across the diverged wall diffusers. The asymmetric ratio for the radial velocity constantly increases from the centreline of the diffuser towards the wall and from the diffuser inlet to the diffuser outlet across diffuser configurations of DC_1, DC_2, DC_3 and DC_4. It has also been noticed that the asymmetric ratio for the radial velocity decreases towards hub wall and increases towards shroud wall across diffuser configurations of DC_5 and DC_6. However, asymmetric ratio increases from diffuser inlet to outlet across diffuser configurations of DC_5 and DC_6.

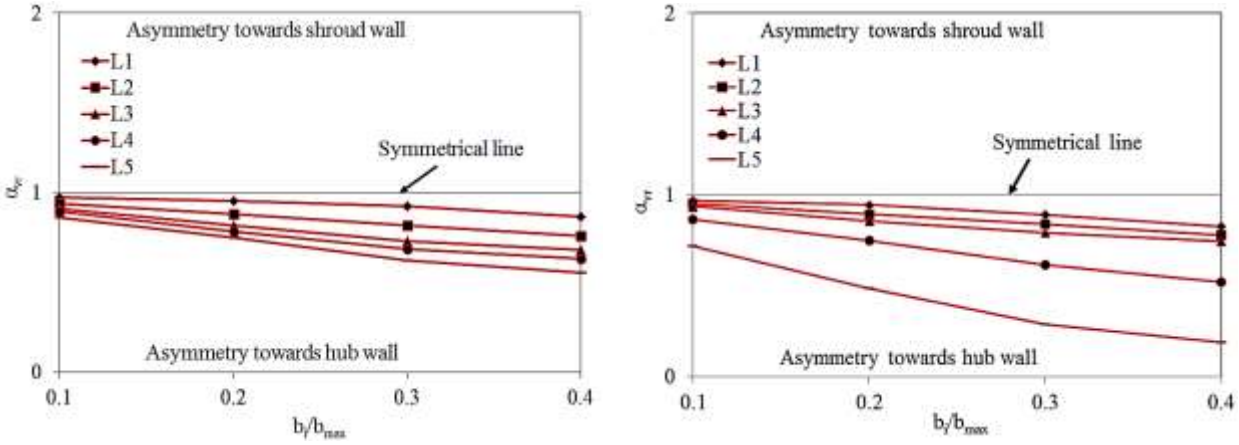

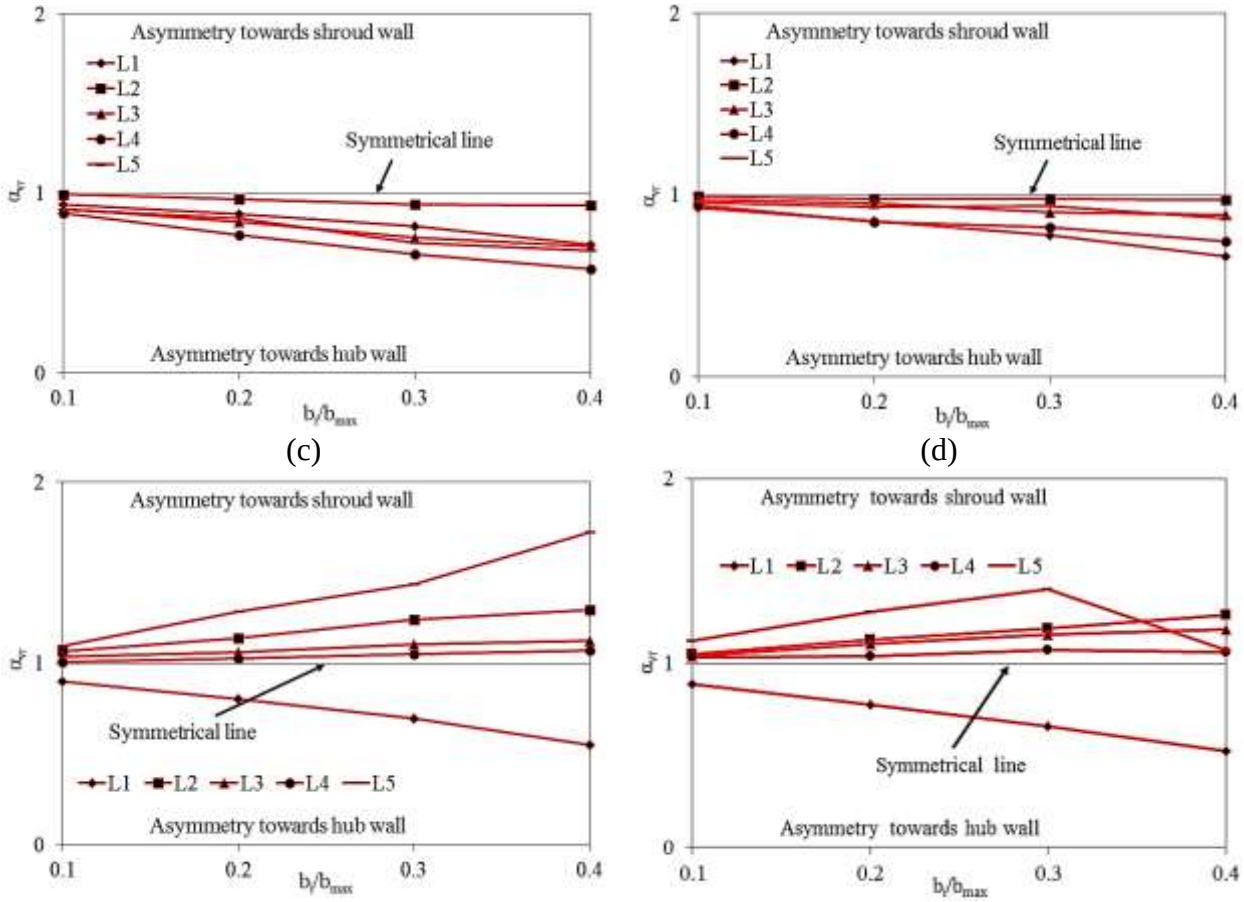

Figure 5.13: Local asymmetric ratio for the radial velocity, α_{vr} across the diverged wall diffusers (a) DC_1, (b) DC_2, (c) DC_3, (d) DC_4, (e) DC_5 and (f) DC_6) at BEP at an operational speed of $58.9rpsK^{-1/2}$

Figure 5.14 depicts the circumferential velocity distribution across the centreline of the diverged wall tilted diffuser configurations ((a) DC_1, (b) DC_2, (c) DC_3, (d) DC_4, (e) DC_5 and (f) DC_6) at BEP at an operational speed of $58.9rpsK^{-1/2}$. The trend of the circumferential velocity across the diverged wall tilted diffusers is similar to that across the straight diffuser. It can be seen that the maximum circumferential velocity is obtained at the diffuser inlet after the volute-tongue region. The circumferential velocity decreases radially across the diffuser. Furthermore, the circumferential velocity also decreases circumferentially in the direction of impeller rotation (ω). The minimum circumferential velocity is obtained at the diffuser outlet at near the volute-tongue region. It can be seen that the circumferential velocity value is increased at the diffuser inlet by 10.7% and decreased at the diffuser outlet by 0.6% across DC_1 in comparison to that across the parallel wall diffuser. Furthermore, it can be seen that the circumferential velocity is decreased at the diffuser inlet by 15%, 9.6%, 7%, 5.3% and 7% at the diffuser inlet across DC_2, DC_3, DC_4, DC_5 and DC_6 respectively in

comparison to that across DC_1. Moreover, the circumferential velocity is increased at the diffuser outlet by 0.6% across DC_2 and then decreased by 0.6%, 36% across DC_3 and DC_4 in comparison to that across DC_1. Thereafter, it can be seen that the circumferential velocity remains same at the diffuser outlet across DC_5 and DC_6 in comparison to that across DC_1. It can be concluded from the results that the circumferential velocity decreases up to increase the tilt angle of 0.5, L/L_{max} of 0.57 and outlet-to-inlet width ratio of 1.15, and then the circumferential velocity increases.

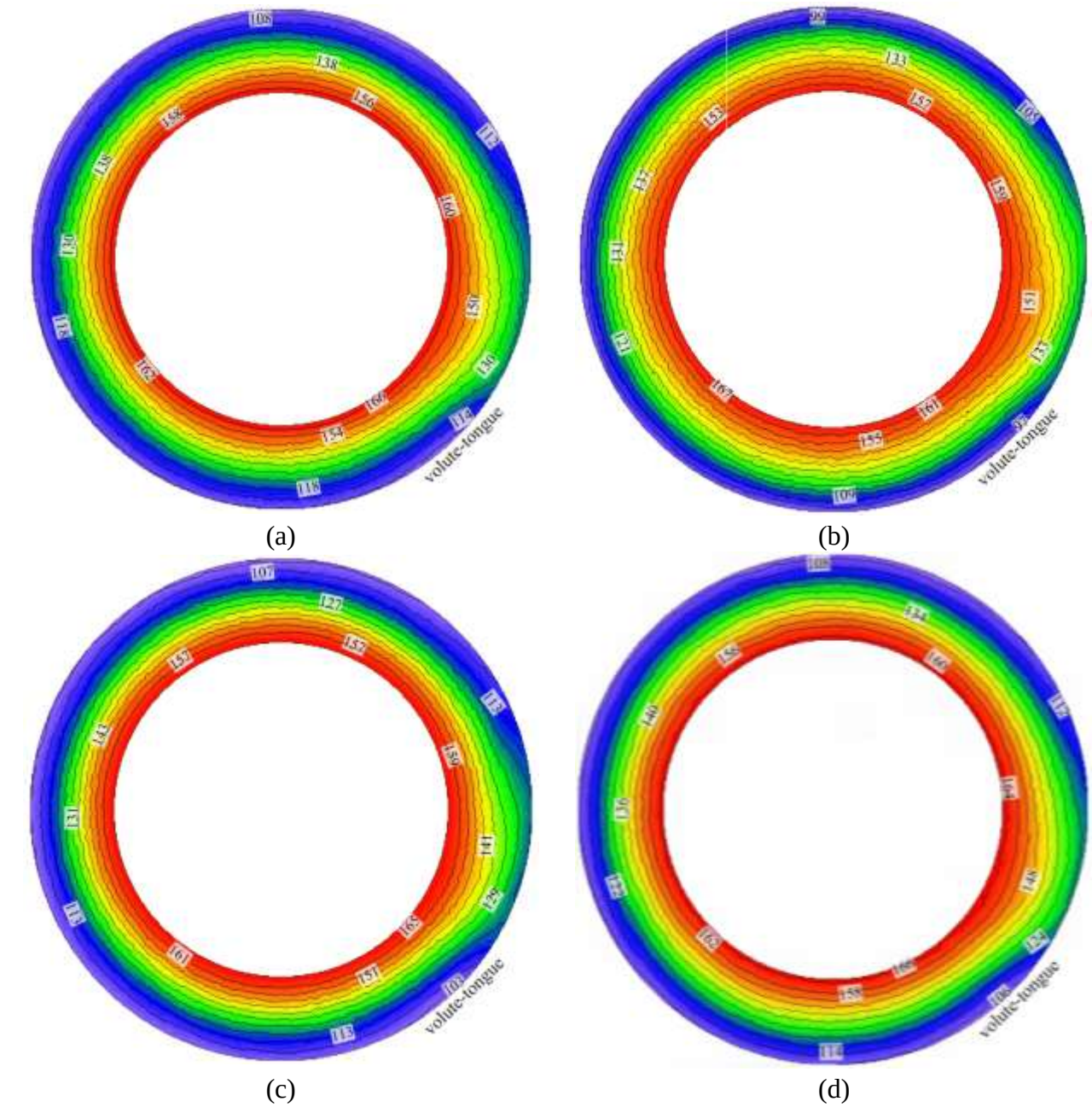

(a) (b)

(c) (d)

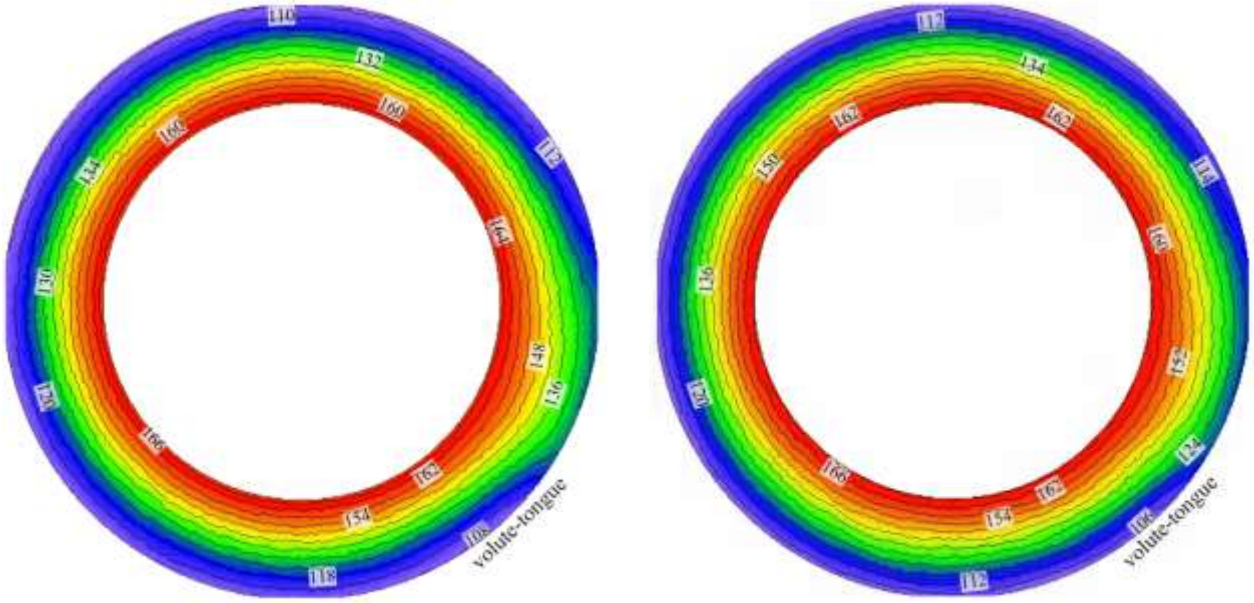

(e) (f)

Figure 5.14: Circumferential velocity (m/s) distributions across the centreline of the diverged wall tilted diffuser (a) DC_1, (b) DC_2, (c) DC_3, (d) DC_4, (e) DC_5 and (f) DC_6 at BEP at an operational speed of 58.9rpsK$^{-1/2}$

Figure 5.15 depicts the comparison of circumferential velocity distribution across parallel wall and diverged wall tilted diffuser configurations (DC_1, DC_2, DC_3, DC_4, DC_5 and DC_6) at BEP at an operational speed of 58.9rpsK$^{-1/2}$. It can be seen that the circumferential velocity is reduced radially across the diffuser. It can be seen that the circumferential is lower across the diverged wall tilted diffuser in comparison to parallel wall diffuser. Furthermore, it has been observed that the circumferential velocity is asymmetric towards hub wall at L_1, L_2 and L_3 and that becomes symmetric in comparison to that across parallel wall diffuser. However, the detailed analysis has been carried out by quantifying the asymmetric ratio for the circumferential velocity profile across the diverged wall tilted diffusers.

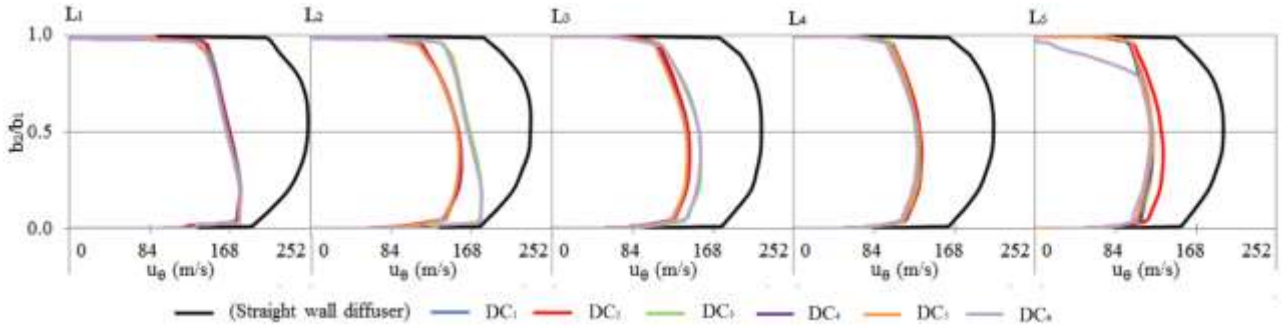

Figure 5.15: Comparison of circumferential velocity (m/s) distribution across parallel wall and diverged wall tilted diffuser configurations from the hub wall to the shroud wall at BEP at an operational speed of 58.9rpsK$^{-1/2}$

Figure 5.16 depicts the local asymmetric ratio for the circumferential velocity, α_{vc} across the diverged wall diffusers (DC_1, DC_2, DC_3, DC_4, DC_5 and DC_6) at BEP at an operational speed of 58.9rpsK$^{-1/2}$. It can be seen that the flow is asymmetric towards the hub wall across the diverged wall diffusers. The asymmetric ratio for the circumferential velocity constantly decreases from the centreline of the diffuser towards the wall and increases from the diffuser inlet to the diffuser outlet across diffuser configurations of DC_1, DC_2, DC_3, DC_4, DC_5 and DC_6.

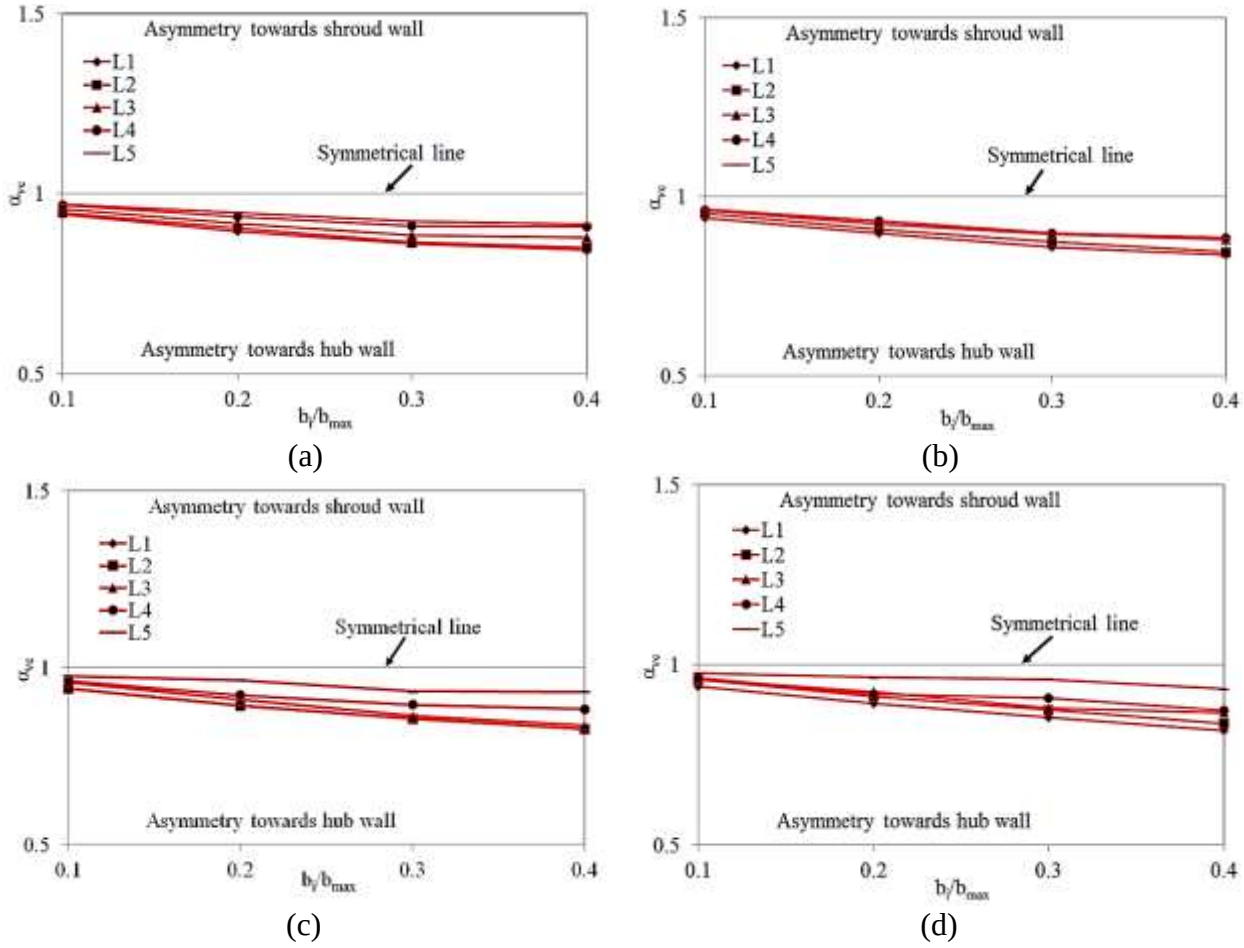

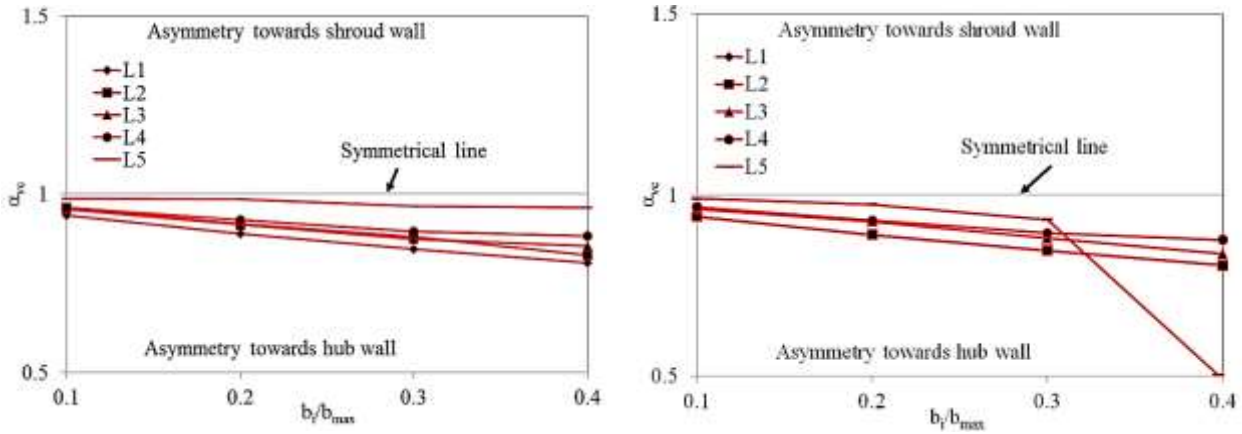

Figure 5.16: Local asymmetric ratio for the radial velocity, α_{vr} across the diverged wall diffusers (a) DC_1, (b) DC_2, (c) DC_3, (d) DC_4, (e) DC_5 and (f) DC_6) at BEP at an operational speed of $58.9 rpsK^{-1/2}$

Figure 5.17 depicts the static temperature variations across the centreline of the diverged wall tilted diffuser configurations ((a) DC_1, (b) DC_2, (c) DC_3, (d) DC_4, (e) DC_5 and (f) DC_6) at BEP at an operational speed of $58.9 rpsK^{-1/2}$. The trend of the static temperature across the diverged wall tilted diffusers is similar to that across the straight diffuser. It can be seen that the minimum static temperature is obtained at the diffuser inlet after the volute-tongue region. The static temperature increases radially across the diffuser. Furthermore, the static temperature also increases circumferentially in the direction of impeller rotation (ω). The maximum static temperature is obtained at the diffuser outlet at near the volute-tongue region. It can be seen that the static temperature is same at the diffuser inlet and decreased by 0.3% at the diffuser outlet across DC_1 in comparison to parallel wall straight diffuser. Furthermore, it can also be seen that the static temperature is further decreased at the diffuser inlet by 0.3% each across DC_2, DC_3, DC_4, DC_5 and DC_6 respectively, in comparison to that across DC_1. Moreover, it can also be seen that the static temperature is increased at the diffuser outlet by 0.3 each across DC_2, DC_3, DC_4, DC_5 and DC_6 respectively, in comparison to that across DC_1. It can be concluded from the results that the static temperature remains almost same across the diverged wall tilted diffuser in comparison to parallel wall straight diffuser.

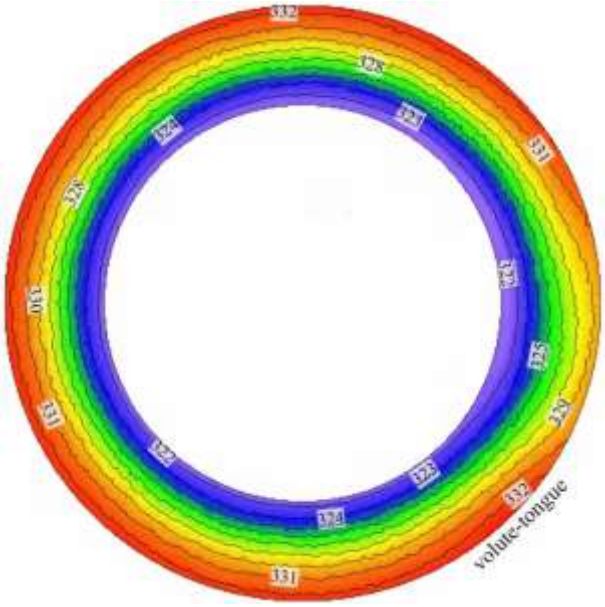

(a)

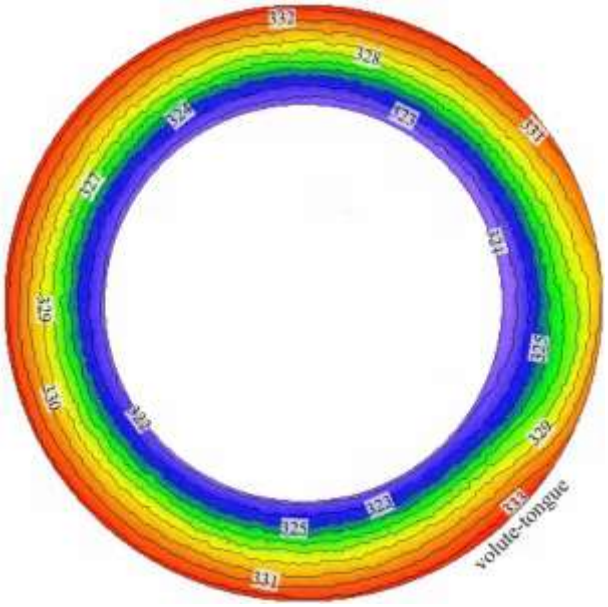

(b)

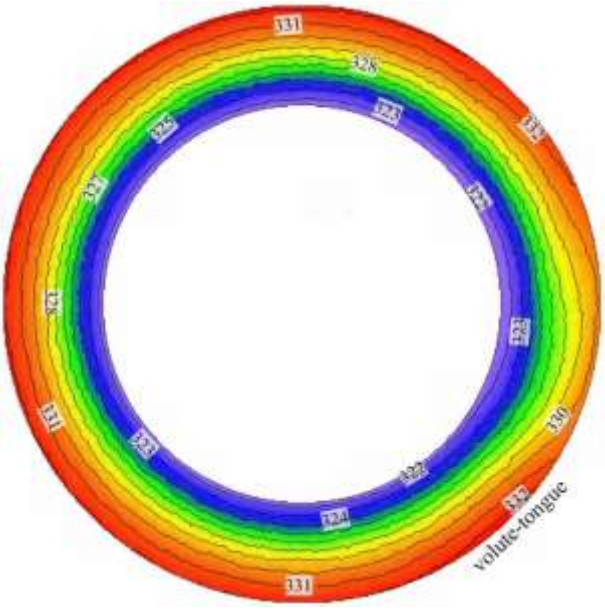

(c)

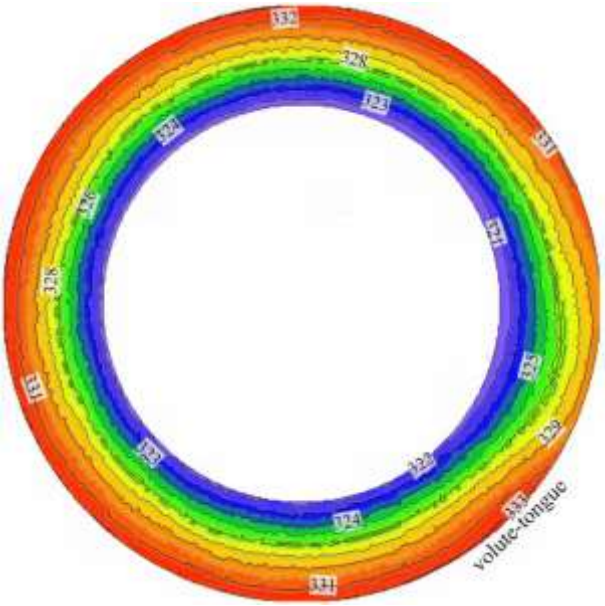

(d)

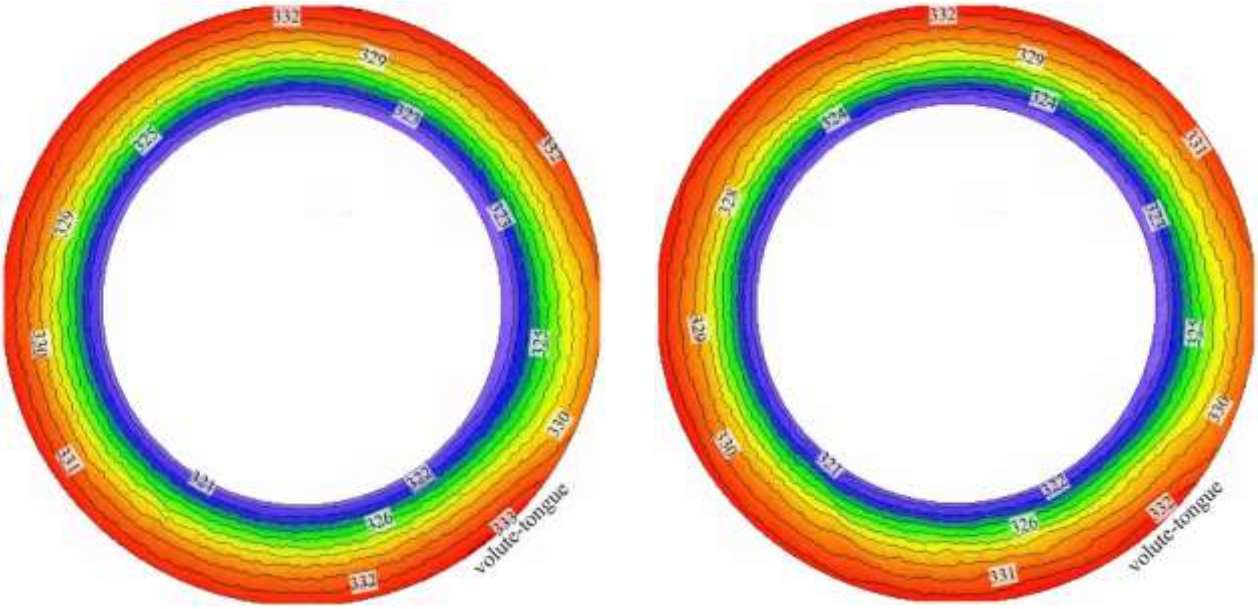

(e) (f)

Figure 5.17: Static temperature (K) variations across the centreline of the diverged wall tilted diffuser (a) DC_1, (b) DC_2, (c) DC_3, (d) DC_4, (e) DC_5 and (f) DC_6 at BEP at an operational speed of 58.9rpsK$^{-1/2}$

5.6.1. Effect of Asymmetric Ratio acroos the Diverged Wall Tilted Diffuser

The behaviour of the flow within the diverged wall tilted diffuser is highly dependent upon the geometrical parameter considered. It has been noticed in the previous section that combined increase of diffuser width ratio, tilt angle and divergence location on the hub wall of the diffuser from the diffuser inlet increases the asymmetry of the flow towards the hub wall of the diverged wall diffuser. A new term is introduced that shows the change in behaviour of the flow across the diverged wall diffusers. The asymmetric ratio of the flow is defined as α, which is the ratio between the flow velocity near the shroud wall and the flow velocity near the hub wall. Equation 4.1 is used again to obtain the global effect of diverged wall diffuser. The major effect of geometrical parameters on the asymmetric flow behaviour and stage performance is described in detail.

Figure 5.18 depicts the global asymmetric ratio for the velocity magnitude across the diverged wall tilted diffuser at BEP at an operational speed of 58.9rpsK$^{-1/2}$. It can be seen that the global asymmetric ratio across the diverged wall tilted diffusers is towards the hub wall of the diffuser. The global asymmetric ratio for the velocity magnitudes is first decreased from 0% to 50% distance from the

diffuser inlet and then increased towards the diffuser outlet across all diverged wall diffuser configurations.

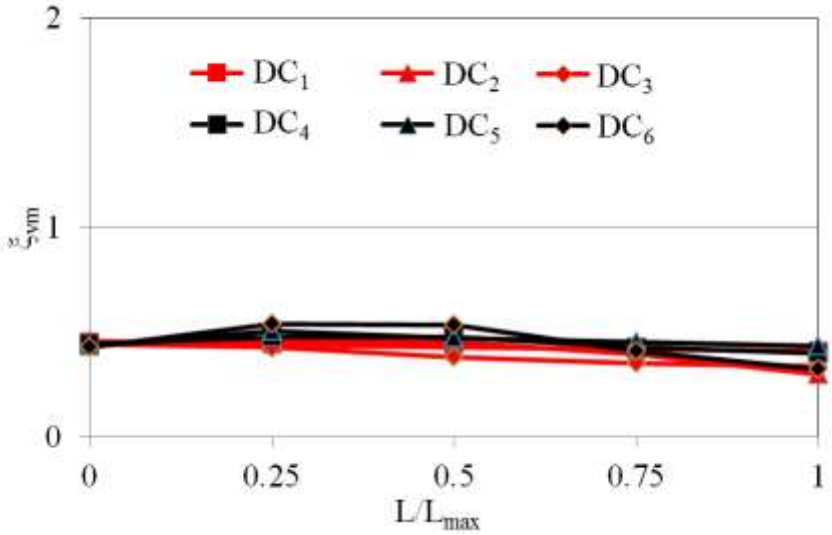

Figure 5.18: Global asymmetric ratio for the velocity magnitude of the diverged wall tilted diffuser at BEP at an operational speed of 58.9rpsK$^{-1/2}$

Figure 5.19 depicts the global asymmetric ratio for the radial velocity across the diverged wall tilted diffuser at BEP at an operational speed of 58.9rpsK$^{-1/2}$. It can be seen that the global asymmetric ratio across the diverged wall tilted diffusers is towards the hub wall of the diffuser. The global asymmetric ratio for the radial velocity is first decreased from 0% to 50% distance from the diffuser inlet and then increased towards the diffuser outlet across all diverged wall diffuser configurations.

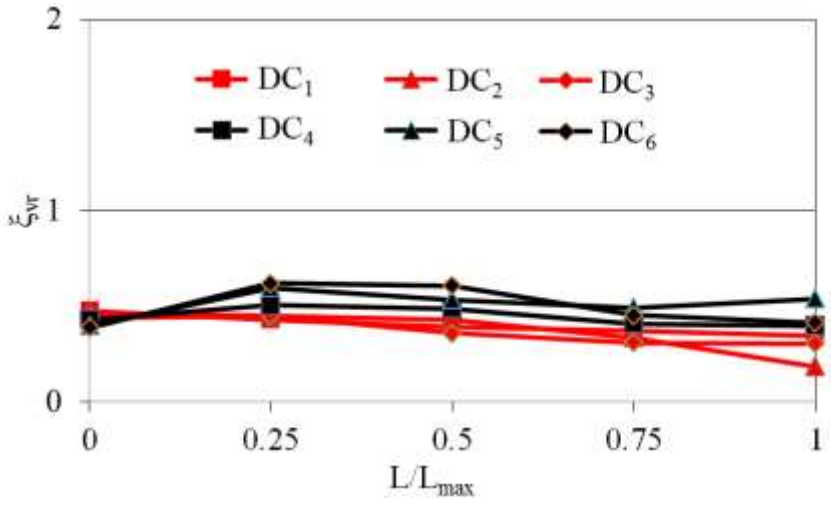

Figure 5.19: Global asymmetric ratio for the radial velocity of the diverged wall tilted diffuser at BEP at an operational speed of 58.9rpsK$^{-1/2}$

Figure 5.20 depicts the global asymmetric ratio for the circumferential velocity across the diverged wall tilted diffuser at BEP at an operational speed of 58.9rpsK$^{-1/2}$. It can be seen that the global asymmetric ratio across the diverged wall tilted diffusers is towards the hub wall of the diffuser. The global asymmetric ratio for the circumferential velocity is first decreased from 0% to 50% distance from the diffuser inlet and then increased towards the diffuser outlet across all diverged wall diffuser configurations.

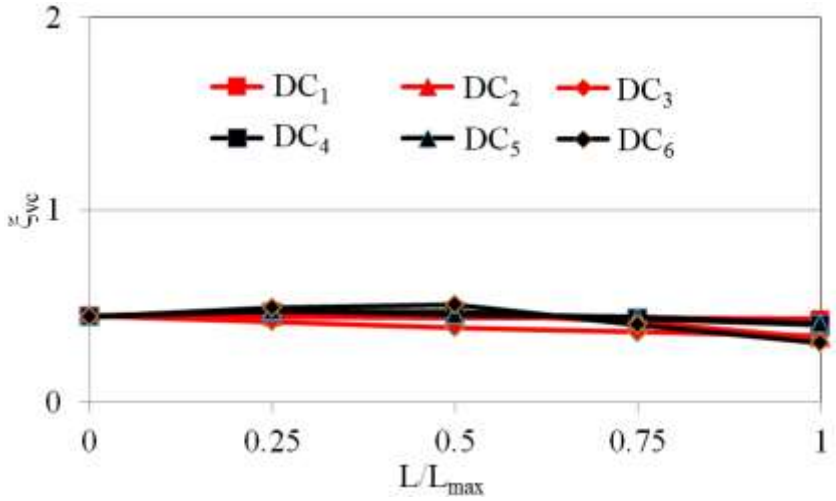

Figure 5.20: Global asymmetric ratio for the circumferential velocity of the diverged wall tilted diffuser at BEP at an operational speed of 58.9rpsK$^{-1/2}$

It is concluded from the above results the flow is asymmetrical across the diverged wall tilted diffusers. It has been noticed that the variations in the asymmetry are due to the outlet-to-inlet width ratio, tilt angle and wall divergence location from the inlet. However, there is not much effect on the flow behaviour if the wall divergence location from the inlet is increased. In order to understand the overall effect of the geometrical effect on the diffuser flow field and stage performance, the equation 4.2 is modified to obtain the effect of tilt angle. Therefore, the new equation is as follows.

$$\zeta = \frac{1}{n}\left[\frac{\xi_1 r_1 + \xi_2 r_2 + \xi_3 r_3 + \xi_4 r_4 + \xi_5 r_5}{r_t}\right]\cos\theta \qquad (5.4)$$

Figure 5.21 depicts the comparison of diffuser asymmetric effect for velocity magnitude across the diverged wall straight diffusers and parallel wall diffuser at BEP at the operational speed of 58.9rpsK$^{-1/2}$. It can be seen the diffuser asymmetric effect is reduced with the increase of outlet-to-inlet width ratio, tilt angle and wall divergence location form the inlet. The asymmetric effect is much less (below 1), which shows the flow asymmetry towards hub wall in comparison to that across the parallel wall

straight diffuser. The stage efficiency increases with the increase of diffuser outlet-to-inlet width ratio and wall divergence location from inlet having maximum stage efficiency across diffuser configuration of DC_2. The stage efficiency decreases with combined increase of all geometrical parameters.

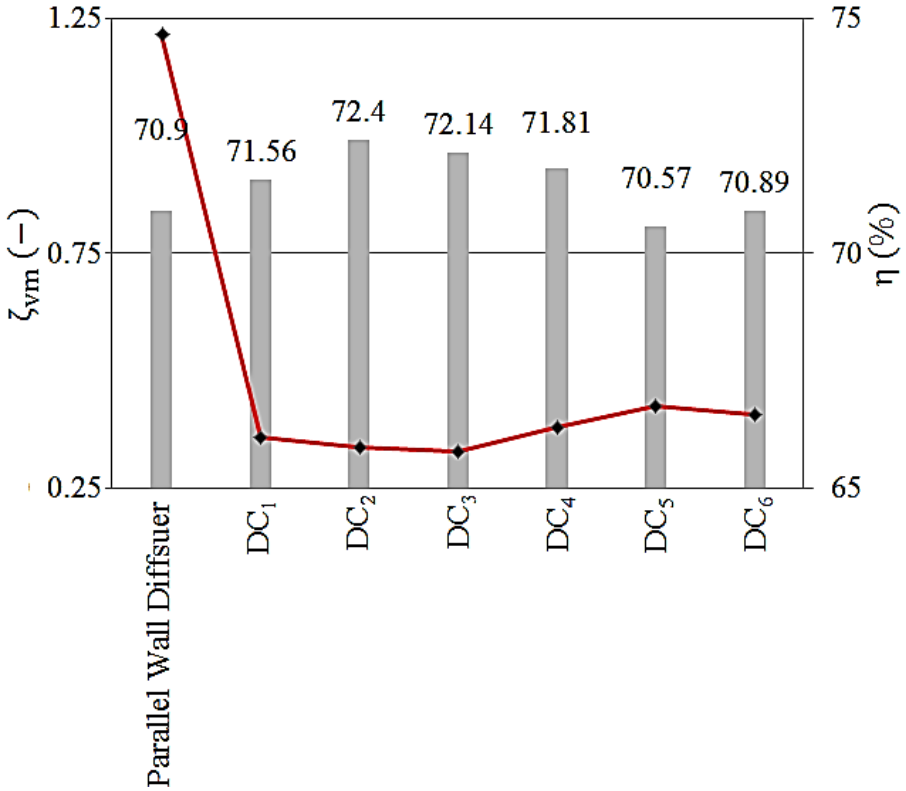

Figure 5.21: Comparison of diffuser asymmetric effect for velocity magnitude across the diverged wall tilted diffusers at BEP at the operational speeds of 58.9rpsK$^{-1/2}$

Figure 5.22 depicts the comparison of diffuser asymmetric effect for radial velocity across the diverged wall straight diffusers and parallel wall diffuser at BEP at the operational speed of 58.9rpsK$^{-1/2}$. It can be seen the diffuser asymmetric effect is reduced with the increase of outlet-to-inlet width ratio, tilt angle and wall divergence location form the inlet. The asymmetric effect is much less (below 1), which shows the flow asymmetry towards hub wall in comparison to that across the parallel wall straight diffuser.

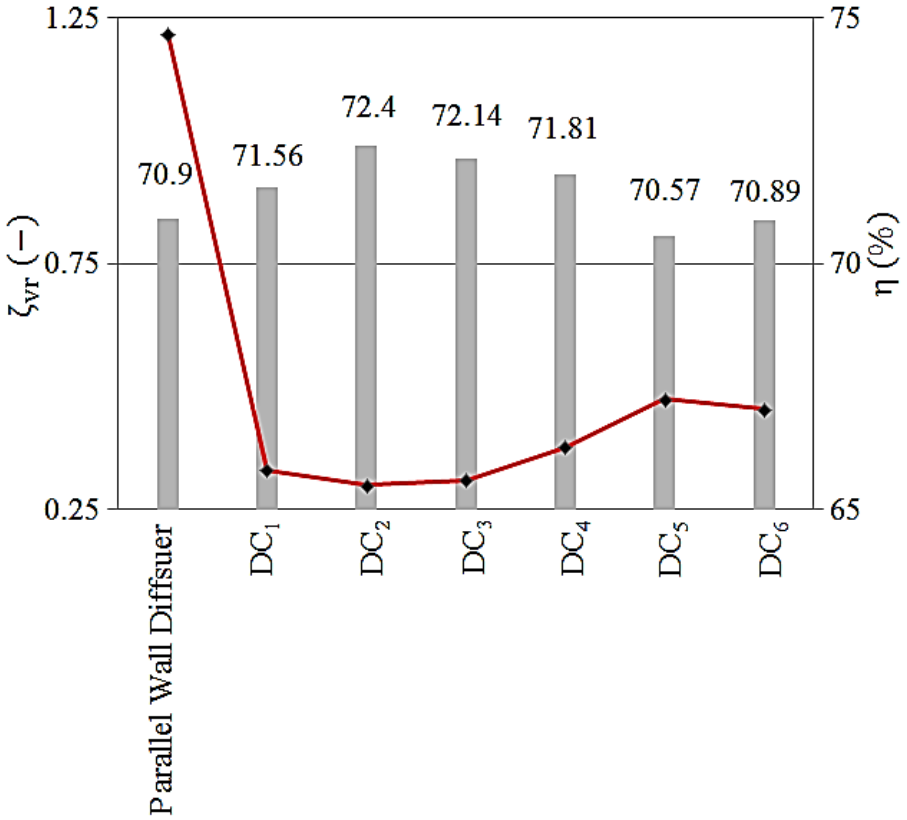

Figure 5.22: Comparison of diffuser asymmetric effect for radial velocity across the diverged wall tilted diffusers at BEP at the operational speeds of 58.9rpsK$^{-1/2}$

Figure 5.23 depicts the comparison of diffuser asymmetric effect for circumferential velocity across the diverged wall straight diffusers and parallel wall diffuser at BEP at the operational speed of 58.9rpsK$^{-1/2}$. It can be seen the diffuser asymmetric effect remains almost similar with the increase of outlet-to-inlet width ratio, tilt angle and wall divergence location form the inlet. The asymmetric effect is much less (below 1), which shows the flow asymmetry towards hub wall in comparison to that across the parallel wall straight diffuser.

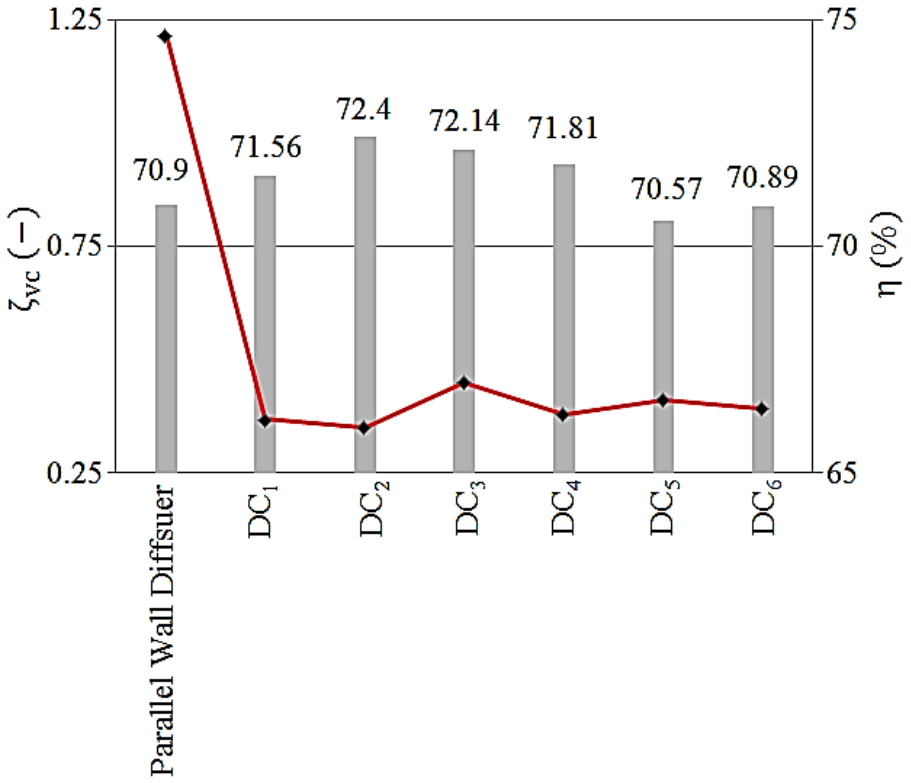

Figure 5.23: Comparison of diffuser asymmetric effect for circumferential velocity across the diverged wall tilted diffusers at BEP at the operational speeds of 58.9rpsK$^{-1/2}$

5.7 Characteristics of Geometrical Parameters

This section investigates the effects of the divergence on the shroud wall of the diffuser and diffuser outlet-to-inlet width ratio on the diffuser local performance. The diffuser performance is dependent upon the recovery of static pressure across the diffuser.

5.7.1. Effects of Geometrical Parameters on Pressure Recovery across the different Diffusers

Three geometrical parameters, tilt angle, the divergence on the hub wall of the diffuser and the diffuser outlet-to-inlet width ratio have used to modify the vaneless diffuser geometry. These configurations have affected the diffuser performance. Figure 5.24 depicts the variation in the coefficient of pressure C_p while changing the diffuser outlet-to-inlet area ratio across the parallel wall diffuser and diverged wall diffuser configurations (DC_1 and DC_2). It can be seen that increase of the diffuser outlet-to-inlet area ratio decreases the pressure recovery within the diffuser in comparison to parallel wall diffuser. The area ratio is a function of the tilt angle, the divergence location on the hub wall of the diffuser and outlet-to-inlet width ratio.

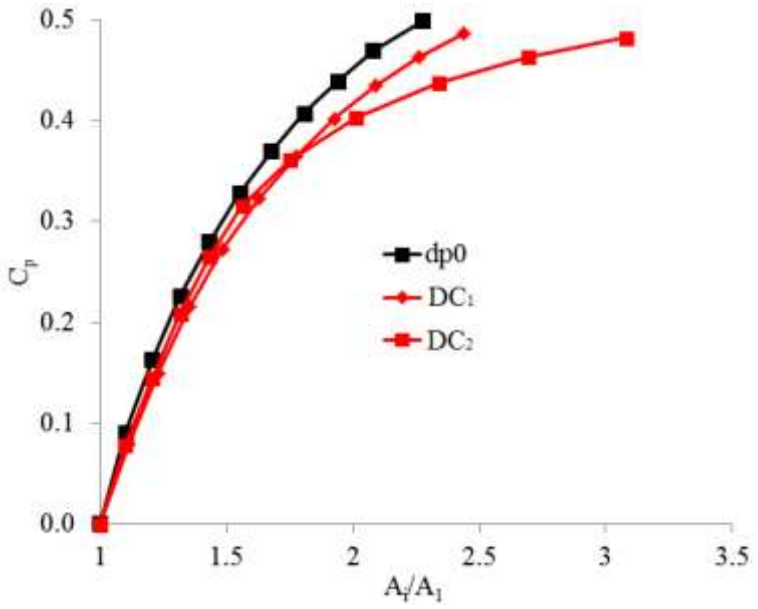

Figure 5.24: Variation in the coefficient of pressure C_p across the parallel wall diffuser and diverged wall diffuser configurations

Figure 5.25 depicts the variation in the coefficient of pressure C_p while changing the diffuser outlet-to-inlet area ratio across the parallel wall diffuser and diverged wall diffuser configurations (DC_3 and DC_4). It can be seen that increase of the diffuser outlet-to-inlet area ratio increases the pressure recovery within DC_3 upto half-length of the diffuser in comparison to parallel wall diffuser. The area ratio is a function of the tilt angle, the divergence location on the hub wall of the diffuser and outlet-to-inlet width ratio. However, increasing diffuser outlet-to-inlet area ratio decreases the pressure recovery as shown in DC_4.

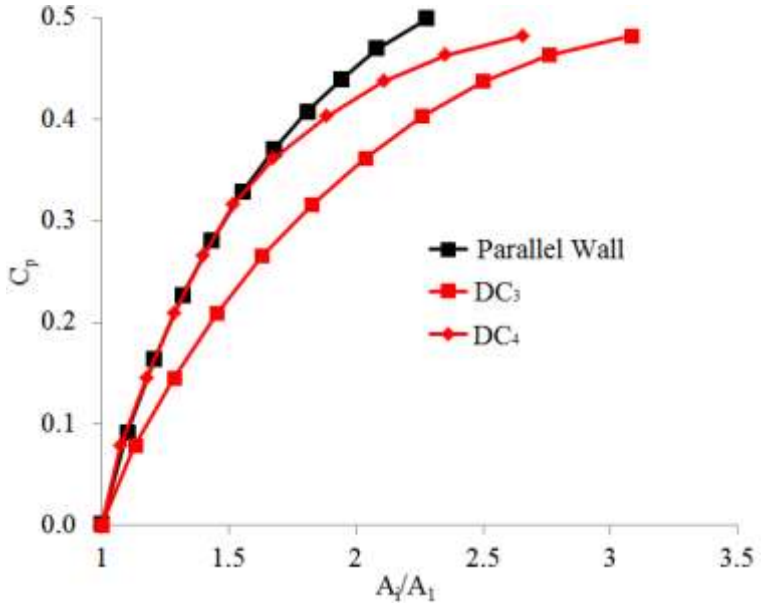

Figure 5.25: Variation in the coefficient of pressure C_p across the parallel wall diffuser and diverged wall diffuser configurations

Figure 5.26 depicts the variation in the coefficient of pressure C_p while changing the diffuser outlet-to-inlet area ratio across the parallel wall diffuser and diverged wall diffuser configurations (DC_5 and DC_6). It can be seen that increase of the diffuser outlet-to-inlet area ratio increases the pressure recovery within DC_3 upto half-length of the diffuser in comparison to parallel wall diffuser. The area ratio is a function of the tilt angle, the divergence location on the hub wall of the diffuser and outlet-to-inlet width ratio. However, increasing diffuser outlet-to-inlet area ratio decreases the pressure recovery as shown in DC_4. Therefore, it can be concluded that increase of tilt angle increases the pressure recovery within the diffuser; however increase outlet-to-inlet width ratio causes decrease on pressure recovery.

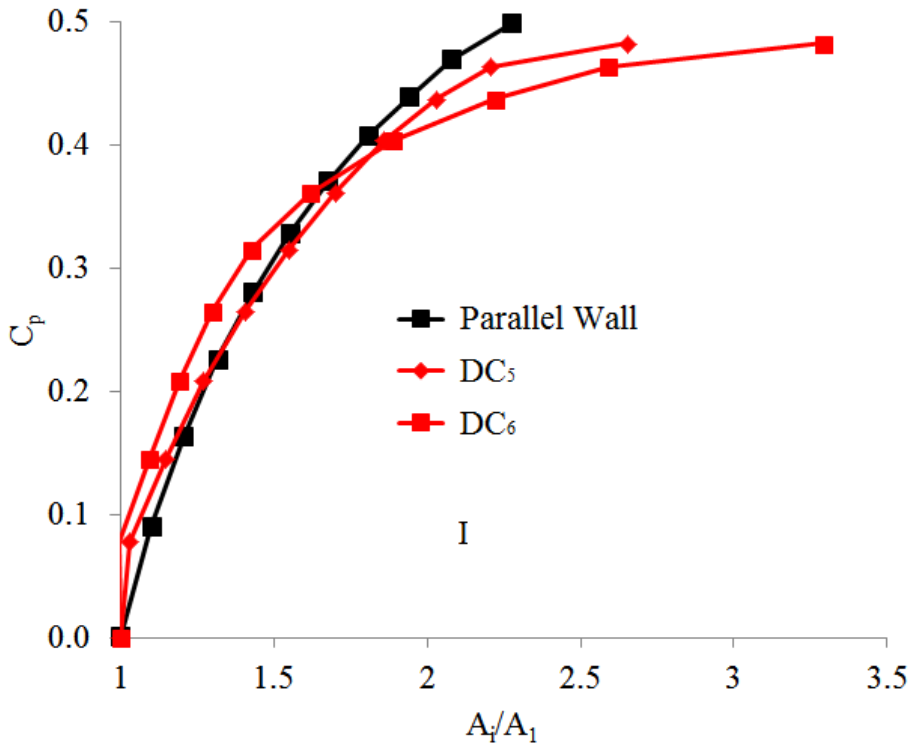

Figure 5.26: Variation in the coefficient of pressure C_p across the parallel wall diffuser and diverged wall diffuser configurations

5.8. Summary

From the result presented in this chapter, it has been concluded that the alteration of diffuser wall causes increase in static pressure. It is important to obtain high isentropic compression efficiency within the compressor stage to decrease losses during operation. Moreover, compacting the compressor stage is a key role. The diffuser is one of the most important components of the turbocharger compressor stage and has a key purpose of partially recovering the static pressure and help in compacting the compressor stage. The local isentropic efficiency has been investigated and a semi-empirical equation has been developed by which the isentropic efficiency can be calculated when different geometrical parameters' values are considered. Various flow phenomena have been noticed during this investigation, which are as follows;

1. Increase in b_2/b_1 causes decrease in pressure recovery.
2. Increase in b_2/b_1 causes decrease in the static temperature, which results in increased isentropic efficiency.
3. Increase of L/L_{max} does not have much effect on the stage performance.
4. Increasing tilt angle increase the pressure recovery.

Furthermore, diffuser asymmetric effect for the diverged wall diffusers has been investigated. It has been noticed that increase θ/θ_{max}, b_2/b_1 and L/L_{max} decreases the diffuser asymmetric effect. No flow reversals are obtained by diverging the wall, which decreases losses within the diverged wall tilted diffuser in comparison to diverged wall straight diffuser.

CHAPTER 6
NOVEL DESIGN OF THE DIVERGED WALL CURVED DIFFUSER

This chapter comprises of the results obtained after performing CFD simulations for the cases discussed in chapter 3, regarding the curved and diverged wall diffusers. Parametric investigations have been carried out to increase the compressor stage performance by modifying the hub wall of the diffuser. A detailed qualitative and quantitative analysis of the results has been carried out in order to understand the complex flow structure in curved and diverged wall diffusers. The effect of geometrical parameters and flow-related parameters on the stage performance has been investigated.

6.1. Description of Compressor Model using Curved Diffuser Model

Many researchers have carried out various investigations to make the compressor stage more compact by curving the diffuser as described in Chapter 2 of the thesis. Similar, approach is used in this chapter to make the compressor stage more compact. However, this causes reduction in the stage performance. Wall divergence technique, which is applied in chapter 2 and chapter 3 on parallel wall straight diffuser and parallel wall tilted respectively, is applied on curved wall diffuser. This technique aids to improve the stage performance. Since, tilting the diffuser generates some losses by dissipating the energy because of sudden tilt after the impeller trailing edges. To provide a smooth flow across the diffuser, the tilted wall has been modified into curved wall. Furthermore, oppositely interfaced volute is again used as been explained in the previous chapter. Furthermore, wall divergence is applied to recover the losses generated within the curved diffuser. Wall divergence increases the outlet-to-inlet width ratio of the curved diffuser. Therefore, these techniques are used in this chapter to identify the effects of curving the diffuser as well as increasing the outlet-to-inlet diffuser width on the stage performance. Furthermore, the effect of diffuser curving and hub wall divergence on the local flow variations is also investigated in this chapter. Parametric investigations have been carried out to analyse the flow field characteristics within the diverged wall curved diffuser. To carry out the parametric investigations a Full Factorial based Design of Experiments (DoE) technique has been employed in the present study to determine the possible practical combinations of the geometrical parameters. Minitab 17 Statistical Software has been used in the present study to carry out Full Factorial based DoE studies, where a practical range of different parameters has been specified. The factors/parameters considered for the diffuser configurations, along with their levels, have been summarised in the Table 6.1. The geometric parameters considered are radius ratio of the curvature r/r_{max}, angle ratio of curvature θ/θ_{max} and ratio of axial distance from diffuser inlet-to-outlet and diffuser inlet x/b_1. Furthermore, a sample design of diverged wall straight diffuser has also been presented in Figure 6.1. It can be seen that a ratio of axial distance from diffuser inlet-to-outlet and diffuser inlet width has been considered that ranges from 1.71 to 4.35 with an interval of 0.66. Moreover, diffuser has been curved with a radius ratio ranging from 0.6 to 1.0 with in interval of 0.1. Similarly, angle of curvature has also been specified to the diffuser with a ratio ranging from 0 to 1.0 with an interval of 0.5. The reason of curving the wall is to guide the flow and hence reduces losses at the diffuser inlet and it increases the streamwise length of the flow.

The resulting numbers of numerical simulations, which are equal to 75, have been performed and total-to-total pressure and efficiency have been recorded for each simulation. Best design model has been chosen based upon the maximum localised and stage isentropic efficiency across the compressor stage, which is the function of various geometrical and flow parameters.

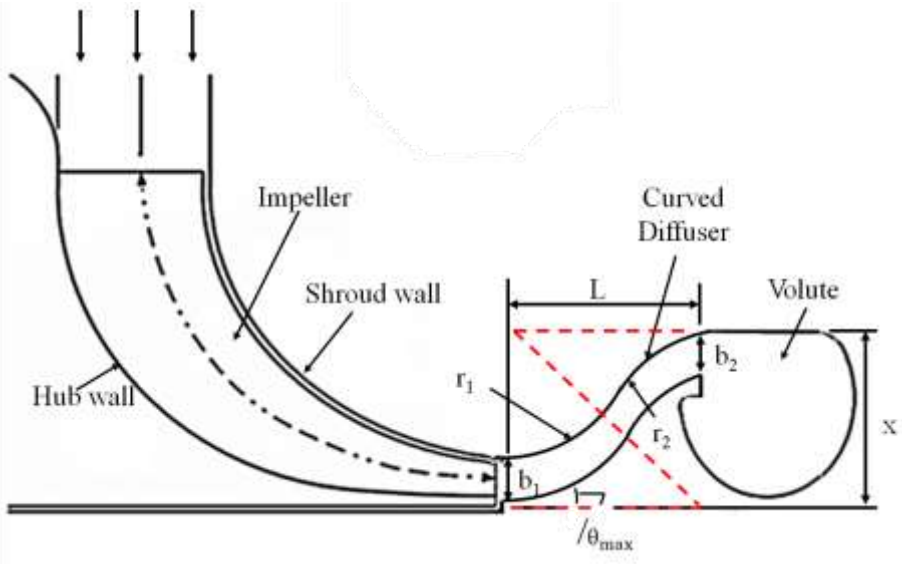

Figure 6.1: Sample configuration of the curved diffuser

Table 6.1: Factors and levels for full factorial design of the curved diffuser

Factors	Level 1	Level 2	Level 3	Level 4	Level 5
x/b_1 (-)	1.71	2.37	3.03	3.69	4.35
θ/θ_{max} (-)	0	0.5	1.0	-	-
r/r_{max} (-)	0.6	0.7	0.8	0.9	1.0

The flow field analysis has been carried out in the curved diffuser geometry. The curved diffuser geometry used in this analysis is constructed using the reverse curves with equal branches ($r_1 = r_2$) and the reverse curves with unequal branches ($r_1 \neq r_2$). Furthermore, these reverse curves are also tilted from the diffuser inlet ($\theta/\theta_{max} > 0$) as shown in Figure 6.1. The construction is based upon the reverse curves whereby x/b_1, θ/θ_{max} and θ/θ_{max} values are used as shown in table 6.1, and the whole diffuser model is constructed. The detailed construction of the diffuser model is presented in appendix A-9.

6.2. Performance Characteristcs of Compressor Stage using Curved Diffuser

Numerical analysis is carried out to obtain the total-to-total stage performance and flow field characteristics across various configurations of the curved diffuser have been analysed. Table 6.2 shows the results obtained from numerical simulations of CFD for the global parameters of all 75

configurations. Three geometrical parameters are considered, radius ratio of the curvature r/r_{max}, angle ratio of curvature θ/θ_{max} and ratio of axial distance from diffuser inlet-to-outlet and diffuser inlet x/b_1 to analyse the effect on the local flow field and on the total-to-total stage performance. Following results are obtained from the Table 6.2.

i. Increasing the radius ratio causes isentropic efficiency and total-to-total stage pressure ratio to reduce up to a value of 0.8 and thereafter the performance parameters are increased.

ii. Increase of angle of curvature causes total-to-total stage pressure ratio to increase, however isentropic efficiency reduces.

iii. Increase of axial distance between the hub wall near the diffuser inlet and the shroud wall near the outlet of the diffuser has caused the total-to-total stage pressure ratio and isentropic efficiency to increase up to $x/b_1 = 3.03$. Thereafter, both the performance parameters decrease.

Table 6.2: CFD results of centrifugal compressor stage using different configurations of curved diffusers

	x/b_1	θ/θ_{max}	r/r_{max}	PR_C	η		x/b_1	θ/θ_{max}	r/r_{max}	PR_C	η
Row No.	(-)	(-)	(-)	(-)	(%)	Row No.	(-)	(-)	(-)	(-)	(%)
1	1.71	0	0.6	1.536	71.68	46	3.69	0	0.6	1.536	71.71
2			0.7	1.536	71.67	47			0.7	1.536	71.73
3			0.8	1.536	71.65	48			0.8	1.536	71.72
4			0.9	1.536	71.70	49			0.9	1.537	71.75
5			1	1.537	71.67	50			1	1.537	71.69
6		0.5	0.6	1.537	71.68	51		0.5	0.6	1.540	71.29
7			0.7	1.536	71.67	52			0.7	1.540	71.38
8			0.8	1.536	71.64	53			0.8	1.541	71.46
9			0.9	1.538	71.67	54			0.9	1.540	71.45
10			1	1.537	71.63	55			1	1.541	71.47
11		1	0.6	1.538	71.65	56		1	0.6	1.546	69.63
12			0.7	1.538	71.68	57			0.7	1.546	69.87
13			0.8	1.539	71.66	58			0.8	1.547	70.08
14			0.9	1.536	71.63	59			0.9	1.548	70.21
15			1	1.539	71.68	60			1	1.549	70.31
16	2.37	0	0.6	1.536	71.73	61	4.35	0	0.6	1.535	71.53
17			0.7	1.537	71.75	62			0.7	1.535	71.54
18			0.8	1.536	71.74	63			0.8	1.535	71.57
19			0.9	1.536	71.72	64			0.9	1.536	71.59
20			1	1.537	71.69	65			1	1.536	71.58

21			0.6	1.538	71.72	66		0.5	0.6	1.538	70.59
22			0.7	1.538	71.72	67			0.7	1.539	70.85
23		0.5	0.8	1.538	71.72	68			0.8	1.540	71.02
24			0.9	1.538	71.70	69			0.9	1.541	71.10
25			1	1.539	71.69	70			1	1.541	71.16
26			0.6	1.542	71.41	71		1	0.6	1.538	67.08
27			0.7	1.542	71.43	72			0.7	1.542	68.05
28		1	0.8	1.542	71.45	73			0.8	1.546	68.55
29			0.9	1.542	71.46	74			0.9	1.548	68.92
30			1	1.543	71.45	75			1	1.549	69.16
31			0.6	1.537	71.79						
32			0.7	1.537	71.76						
33		0	0.8	1.537	71.75						
34			0.9	1.536	71.72						
35			1	1.537	71.71						
36			0.6	1.538	71.79						
37			0.7	1.538	71.76						
38	3.03	0.5	0.8	1.540	71.67						
39			0.9	1.540	71.67						
40			1	1.539	71.69						
41			0.6	1.546	70.87						
42			0.7	1.545	71.02						
43		1	0.8	1.545	71.00						
44			0.9	1.545	71.06						
45			1	1.546	71.09						

6.2.1. Flow Field Characteristics within the Curved Diffusers

This section demonstrates the flow field analyses within the curved diffusers based upon static pressure, velocity magnitude, circumferential velocity, radial velocity and static temperature variations. The analyses have been carried out in such a way that certain combinations of simulated data have been compared to obtain the effect of geometrical parameters on the stage performance. The geometrical parameters considered are θ/θ_{max}, r/r_{max} and x/b_1. The combinations considered to analyse the flow performance within the curved diffuser of the compressor stage are mentioned in Table 6.3 with their names. These names are used in the analysis. Furthermore, the effect of wall divergence on the flow asymmetry within the diffuser has been quantified to establish a relationship of wall divergence with asymmetric effect and isentropic efficiency.

Table 6.3: Practical combinations selected for the flow field analysis

Names	x/b_1	θ/θ_{max}	r/r_{max}
	(-)	(-)	(-)

CDC_1	1.71	0.0	0.6
CDC_2			1.0
CDC_3		1.0	0.6
CDC_4			1.0
CDC_5	16.5	0.0	0.6
CDC_6			1.0
CDC_7		1.0	0.6
CDC_8			1.0

Figure 6.2 depicts the static pressure variations across the centreline of the curved diffuser configurations (CDC_1, CDC_2, CDC_3 and CDC_4) at BEP at an operational speed of 58.9rpsK$^{-1/2}$. The trend of the static pressure across the curved diffusers is similar to that across the straight diffuser. It can be seen that the minimum static pressure is obtained at the diffuser inlet after the volute-tongue region. The static pressure increases radially across the diffuser. Furthermore, the static pressure also increases circumferentially in the direction of impeller rotation (ω). The maximum static pressure is obtained at the diffuser outlet near the volute-tongue region. It can be seen that the static pressure is decreased by 0.75% and 1.34% at the diffuser inlet and diffuser outlet respectively across the diffuser configuration of CDC_1 in comparison to parallel wall straight diffuser. Furthermore, it can also be seen that the static pressure is same at the diffuser inlet of CDC_4 and at the diffuser outlet of CDC_2 in comparison to that for diffuser configuration of CDC_1. It can also be seen that the static pressure is decreased by 0.8% each at the diffuser inlet of CDC_2 and CDC_3 respectively and decreased by 0.7% each at the diffuser outlet of CDC_3 and CDC_4 respectively in comparison to that of CDC_1. It can be concluded from the results that the static pressure decreases by increasing the ratio of θ/θ_{max}. Moreover, increasing the ratio of r/r_{max} does not affect the static pressure variations.

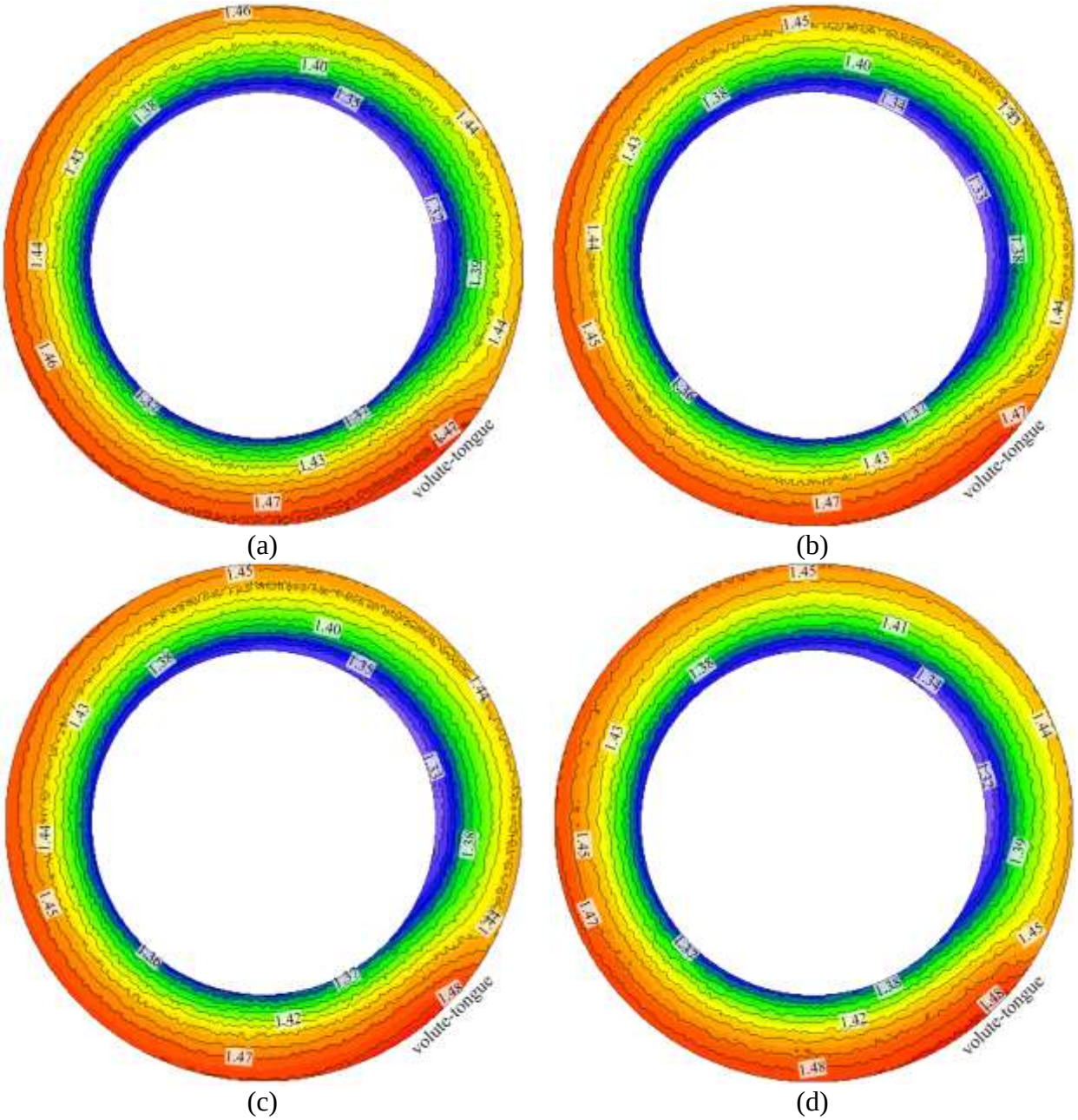

(a) (b)

(c) (d)

Figure 6.2: Static Pressure (atm) variations across the centreline of the curved diffuser configurations (a) CDC_1, (b) CDC_2, (c) CDC_3 and (d) CDC_4 at BEP at an operational speed of $58.9 rpsK^{-1/2}$

Figure 6.3 depicts the static pressure variations across the centreline of the curved diffuser configurations (CDC_1, CDC_2, CDC_3 and CDC_4) at BEP at an operational speed of $58.9 rpsK^{-1/2}$. The trend of the static pressure across the curved diffuser is similar to that across the straight diffuser. It can be seen that the minimum static pressure is obtained at the diffuser inlet after the volute-tongue region. The static pressure increases radially across the diffuser. Furthermore, the static pressure also increases circumferentially in the direction of impeller rotation (ω). The maximum static pressure is

obtained at the diffuser outlet near the volute-tongue region. It can be seen that the static pressure is decreased by 0.75% and 0.67% at the diffuser inlet and diffuser outlet respectively for the diffuser configuration of CDC_5 in comparison to parallel wall straight diffuser. Furthermore, it can also be seen that the static pressure is same at the diffuser inlet of CDC_6 and at the diffuser outlet of CDC_6 and CDC_7 in comparison to that across diffuser configuration of CDC_5. It can also be seen that the static pressure is decreased by 0.8% each at the diffuser inlet of CDC_7 and CDC_8 respectively and decreased by 1.4% at the diffuser outlet of CDC_8 in comparison to that of CDC_5. It can be concluded from the results that the static pressure increases by increasing the ratio of x/b_1. Furthermore, it can also be seen that the static pressure increases by increasing the ratio of θ/θ_{max}. Moreover, increasing the ratio of r/r_{max} decreases the static pressure.

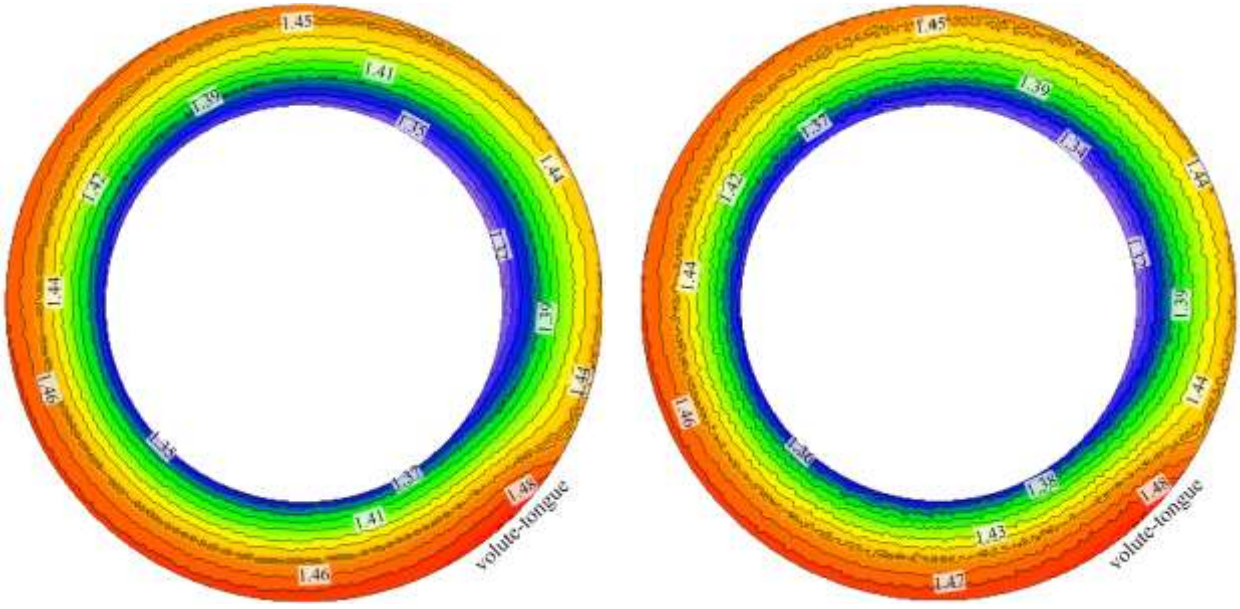

(a) (b)

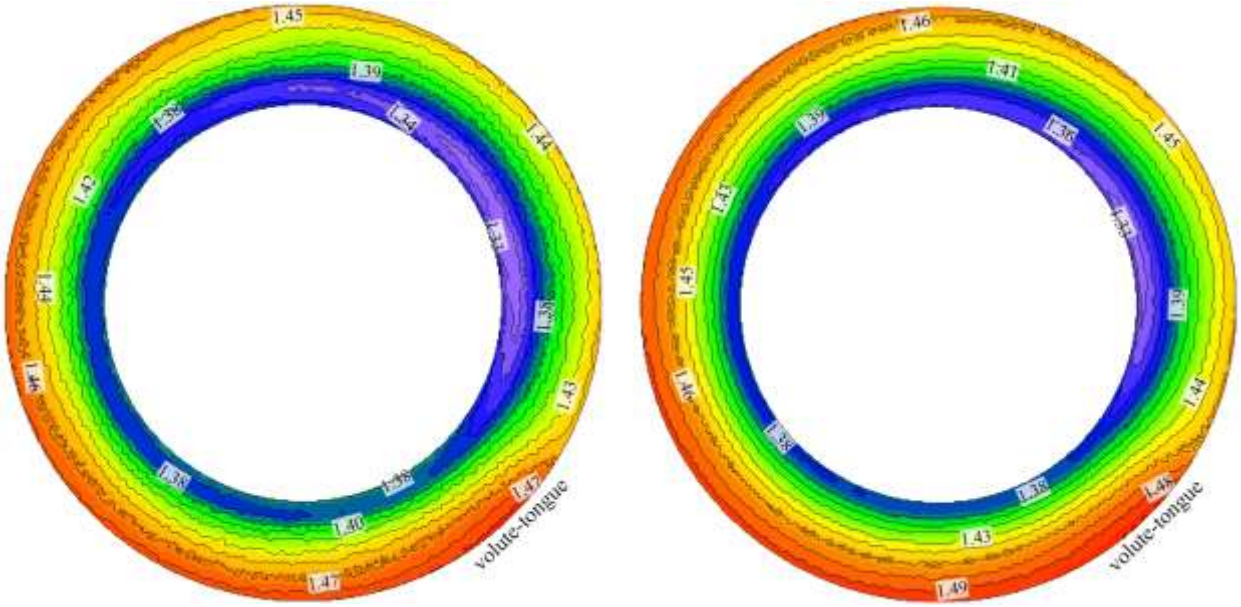

(c) (d)

Figure 6.3: Static Pressure (atm) variations across the centreline of the curved diffuser configurations (a) CDC_5, (b) CDC_6, (c) CDC_7 and (d) CDC_8 at BEP at an operational speed of 58.9rpsK$^{-1/2}$

Figure 6.4 depicts the comparison of velocity magnitude distribution across straight diffuser and curved diffuser configurations (CDC_1, CDC_2, CDC_3 and CDC_4) from the hub wall to the shroud wall at BEP at an operational speed of 58.9rpsK$^{-1/2}$. It can be seen that the velocity magnitude is reduced radially across the diffuser. It can be seen that the velocity magnitude across curved diffusers is higher in comparison to straight diffuser. Furthermore, it has been observed that the velocity magnitude is asymmetric towards hub wall across curved diffusers in comparison to parallel wall diffuser, which has asymmetric velocity magnitude towards the shroud wall. However, the detailed analysis has been carried out by quantifying the asymmetric ratio for the velocity magnitude profile across curved diffuser configurations.

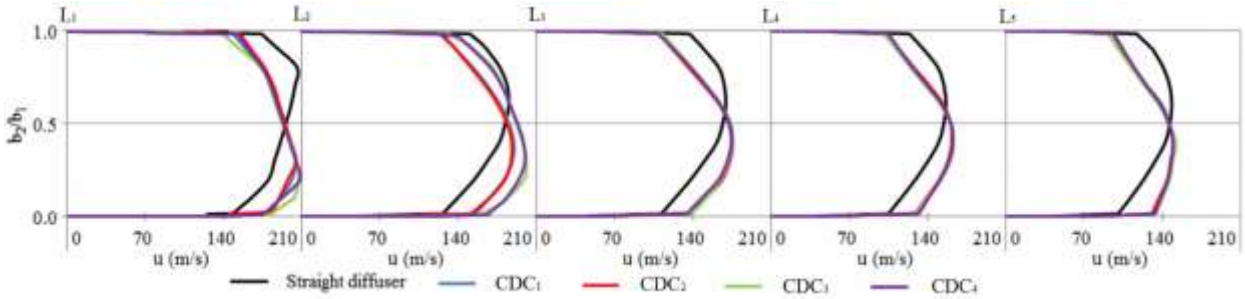

Figure 6.4: Comparison of velocity magnitude (m/s) distribution across the straight diffuser and curved diffuser configurations from the hub wall to the shroud wall at BEP at an operational speed of 58.9rpsK$^{-1/2}$

Figure 6.5 depicts the local asymmetric ratio for the velocity magnitudes, α_{vm} across the curved diffusers (CDC_1, CDC_2, CDC_3 and CDC_4) at BEP at an operational speed of 58.9rpsK$^{-1/2}$. It can be seen that the flow is asymmetric towards the hub wall across the curved diffusers. The asymmetric ratio for the velocity magnitude constantly increases from the centreline of the diffuser towards the wall and from the diffuser inlet to the diffuser outlet across all the diffuser configurations. It has been noticed that the asymmetric ratio for the velocity magnitude constantly increases from the centreline of the diffuser towards the wall and decreases from the diffuser inlet to the diffuser outlet across all the diffuser configurations.

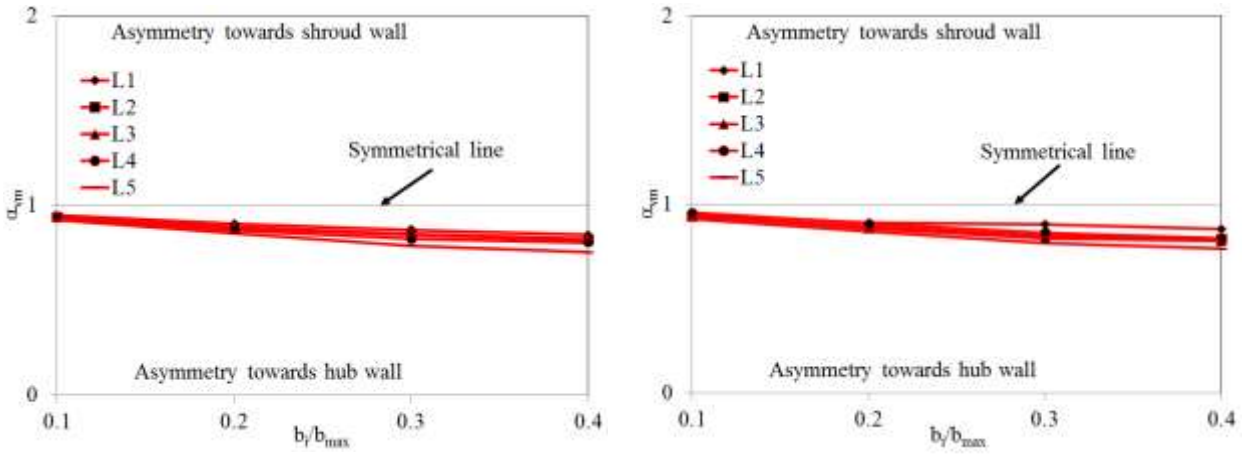

(a) (b)

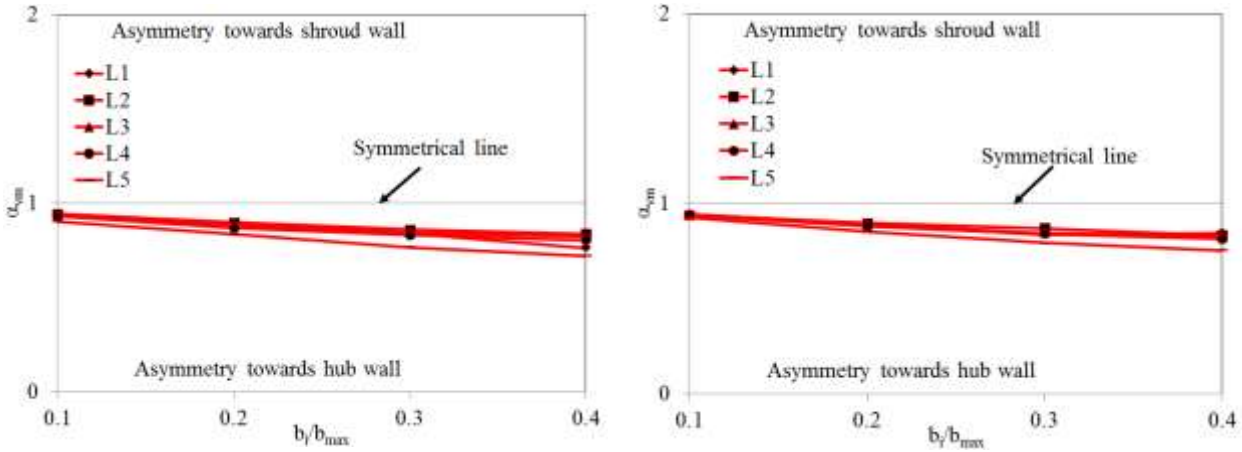

Figure 6.5: Local asymmetric ratio for the velocity magnitude, α_{vm} across the curved diffusers ((a) CDC_1, (b) CDC_2, (c) CDC_3 and (d) CDC_4) at BEP at an operational speed of 58.9rpsK$^{-1/2}$

Figure 6.6 depicts the comparison of velocity magnitude distribution across straight diffuser and curved diffuser configurations (CDC_5, CDC_6, CDC_7 and CDC_8) from the hub wall to the shroud wall at BEP at an operational speed of 58.9rpsK$^{-1/2}$. It can be seen that the velocity magnitude is reduced radially across the diffuser. It can be seen that the velocity magnitude across curved diffusers is higher in comparison to straight diffuser. Furthermore, it has been observed that the velocity magnitude is asymmetric towards hub wall across curved diffuser configurations of CDC_5 and CDC_6 in comparison to parallel wall diffuser, which has asymmetric velocity magnitude towards the shroud wall. Moreover, velocity magnitude is highly asymmetric towards the hub wall at L_1 (diffuser inlet) and then it decreases towards L_2 across CDC_5 and CDC_6. The velocity magnitude becomes symmetric between L_2 and L_3 and then the velocity magnitude becomes asymmetric towards the shroud wall from L_3 to L_5 (diffuser outlet) across CDC_5 and CDC_6. However, the detailed analysis has been carried out by quantifying the asymmetric ratio for the velocity magnitude profile across curved diffuser configurations.

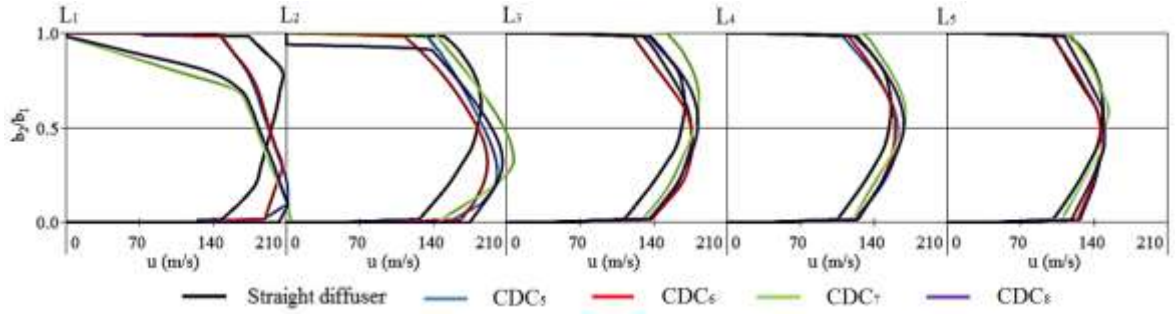

Figure 6.6: Comparison of velocity magnitude (m/s) distribution across the straight diffuser and curved diffuser configurations from the hub wall to the shroud wall at BEP at an operational speed of 58.9rpsK$^{-1/2}$

Figure 6.7 depicts the local asymmetric ratio for the velocity magnitudes, α_{vm} across the curved diffusers (CDC_5, CDC_6, CDC_7 and CDC_8) at BEP at an operational speed of 58.9rpsK$^{-1/2}$. It can be seen that the flow is asymmetric towards the hub wall across CDC_5 and CDC_6. The asymmetric ratio for the velocity magnitude constantly increases from the centreline of the diffuser towards the wall. Furthermore, it decreases from the diffuser inlet to the half-length of the diffuser and it than increases towards the diffuser outlet across CDC_5 and CDC_6. Moreover, it can also be seen that the flow is asymmetric towards the shroud wall across CDC_7 and CDC_8. The asymmetric ratio for the velocity magnitude constantly increases from the centreline of the diffuser towards the wall and diffuser inlet to the diffuser outlet across CDC_7 and CDC_8.

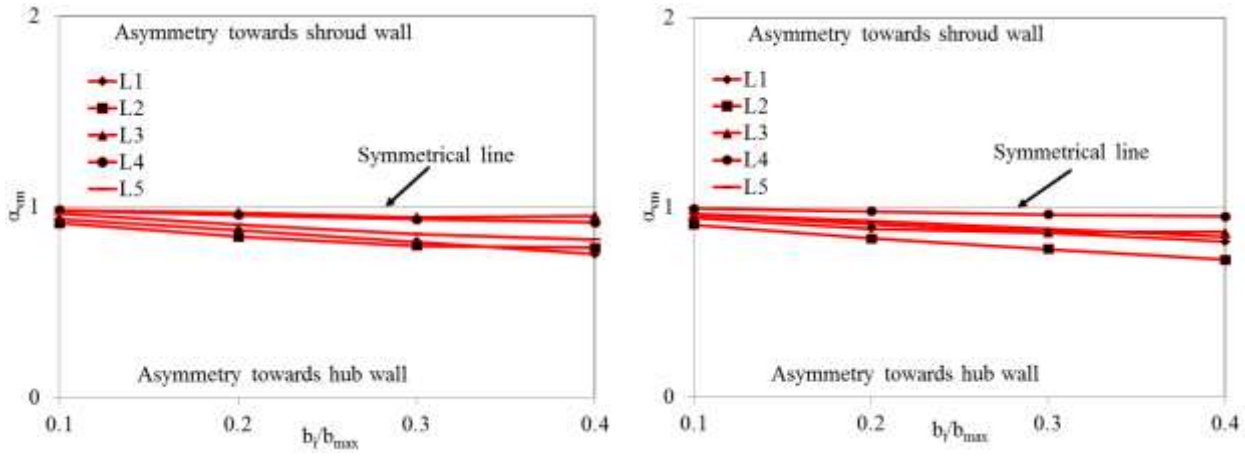

(a) (b)

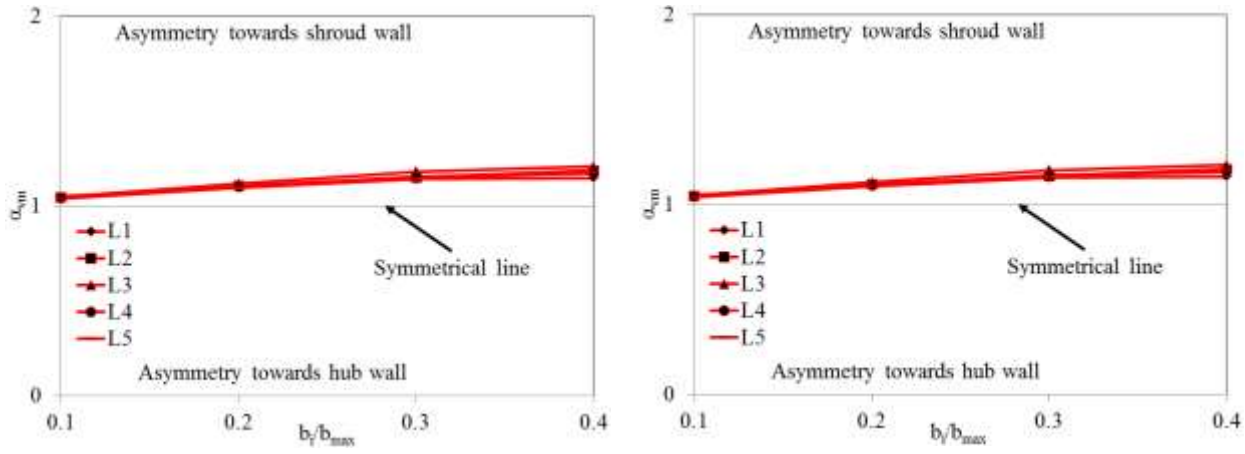

Figure 6.7: Local asymmetric ratio for the velocity magnitude, α_{vm} across the curved diffusers ((a) CDC_5, (b) CDC_6, (c) CDC_7 and (d) CDC_8) at BEP at an operational speed of 58.9rpsK$^{-1/2}$

Figure 6.8 depicts the radial velocity distribution across the centreline of the curved diffuser configurations (CDC_1, CDC_2, CDC_3 and CDC_4) at BEP at an operational speed of 58.9rpsK$^{-1/2}$. The trend of the radial velocity across the curved diffusers is similar to that across the straight diffuser. It can be seen that the maximum radial velocity is obtained at the diffuser inlet after the volute-tongue region. The radial velocity decreases radially across the diffuser. Furthermore, the radial velocity also decreases circumferentially in the direction of impeller rotation (ω). The minimum radial velocity is obtained at the diffuser outlet at near the volute-tongue region. It can be seen that the radial velocity is increased at the diffuser inlet and diffuser outlet by 12% and 1% respectively across the CDC_1 in comparison to that across the straight diffuser. Furthermore, radial velocity is decreased at the diffuser inlet by 1.6% of CDC_2 in comparison to that of CDC_1. Moreover, the radial velocity is increased at the diffuser outlet by 1% and 1.9% of CDC_2 and CDC_4 respectively in comparison to that of CDC_1. Similarly, the radial velocity is same at the diffuser inlet of CDC_3 and CDC_4 respectively and diffuser outlet of CDC_3 in comparison to that of CDC_1. It can be concluded from the results that the radial velocity increases by increasing the ratio of θ/θ_{max} and r/r_{max}.

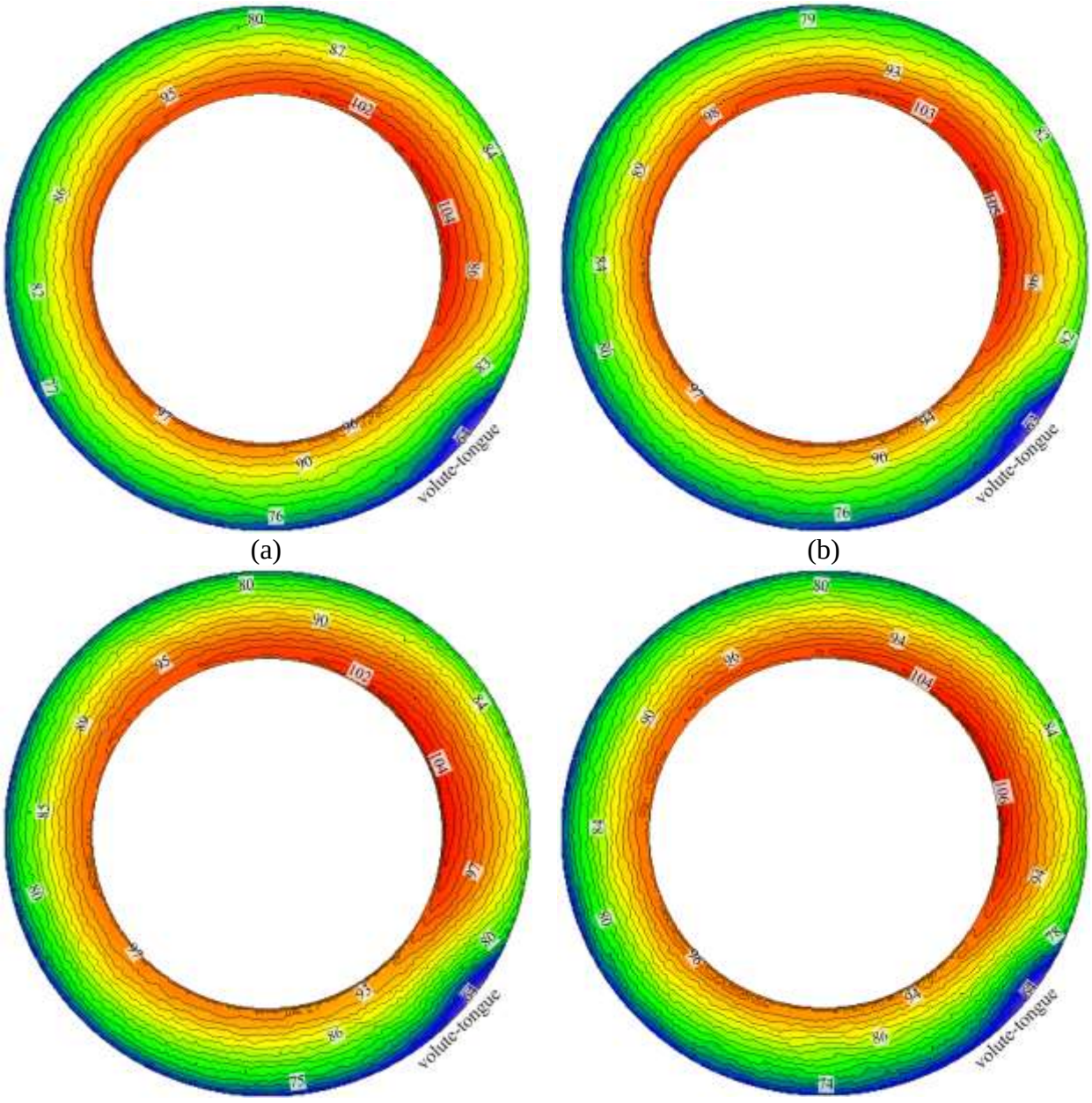

(a) (b) (c) (d)

Figure 6.8: Radial velocity (m/s) distribution across the centreline of the curved diffuser configurations (a) CDC_1, (b) CDC_2, (c) CDC_3 and (d) CDC_4 at BEP at an operational speed of 58.9rpsK$^{-1/2}$

Figure 6.9 depicts the comparison of radial velocity distribution across straight diffuser and curved diffuser configurations (CDC_1, CDC_2, CDC_3 and CDC_4) from the hub wall to the shroud wall at BEP at an operational speed of 58.9rpsK$^{-1/2}$. It can be seen that the radial velocity is reduced radially across the diffuser. It can be seen that the radial velocity across curved diffusers is higher in comparison to straight diffuser. Furthermore, it has been observed that the radial velocity is asymmetric towards hub wall across curved diffusers in comparison to parallel wall diffuser, which has asymmetric radial

velocity towards the shroud wall. However, the detailed analysis has been carried out by quantifying the asymmetric ratio for the radial velocity profile across curved diffuser configurations.

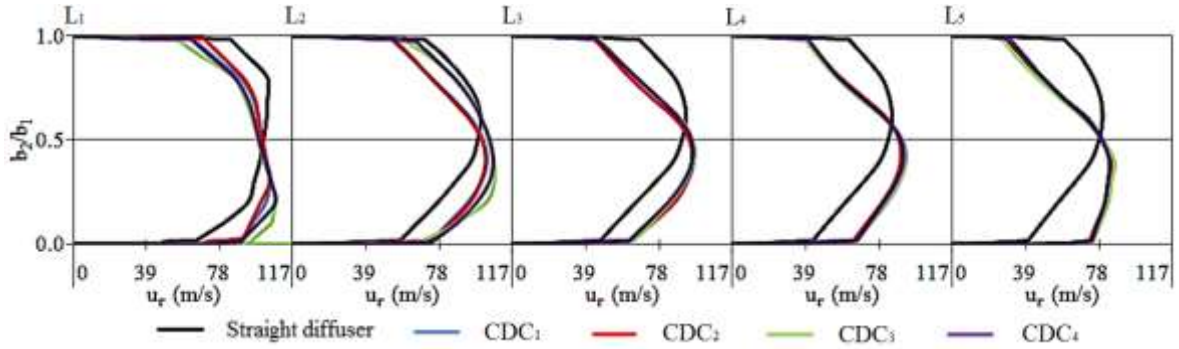

Figure 6.9: Comparison of radial velocity (m/s) distribution across the straight diffuser and curved diffuser configurations from the hub wall to the shroud wall at BEP at an operational speed of 58.9rpsK$^{-1/2}$

Figure 6.10 depicts the local asymmetric ratio for the radial velocity, α_{vr} across the curved diffusers (CDC_1, CDC_2, CDC_3 and CDC_4) at BEP at an operational speed of 58.9rpsK$^{-1/2}$. It can be seen that the flow is asymmetric towards the hub wall across the curved diffusers. The asymmetric ratio for the radial velocity constantly increases from the centreline of the diffuser towards the wall and from the diffuser inlet to the diffuser outlet across all the diffuser configurations. It has been noticed that the asymmetric ratio for the radial velocity constantly increases from the centreline of the diffuser towards the wall and decreases from the diffuser inlet to the diffuser outlet across all the diffuser configurations.

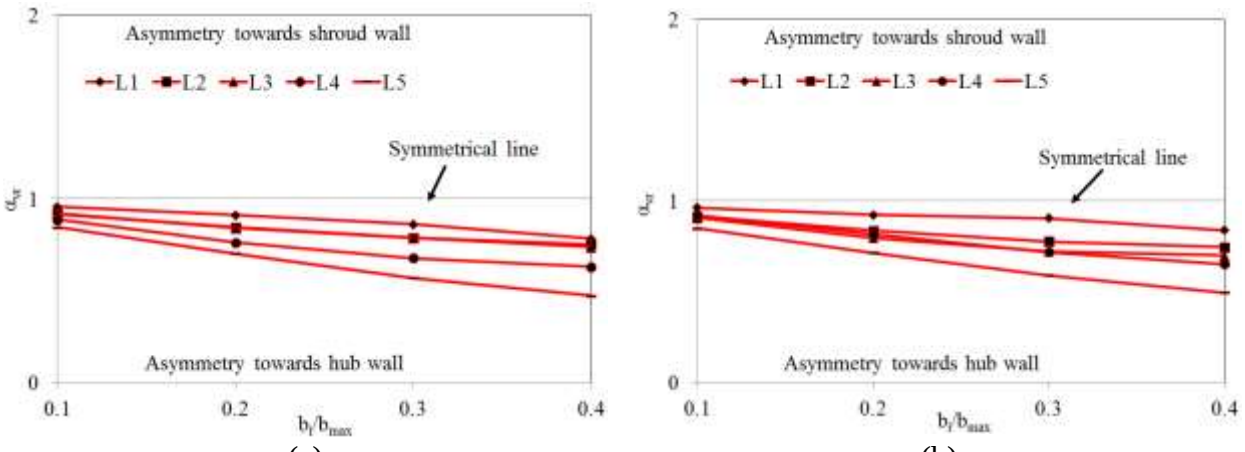

(a) (b)

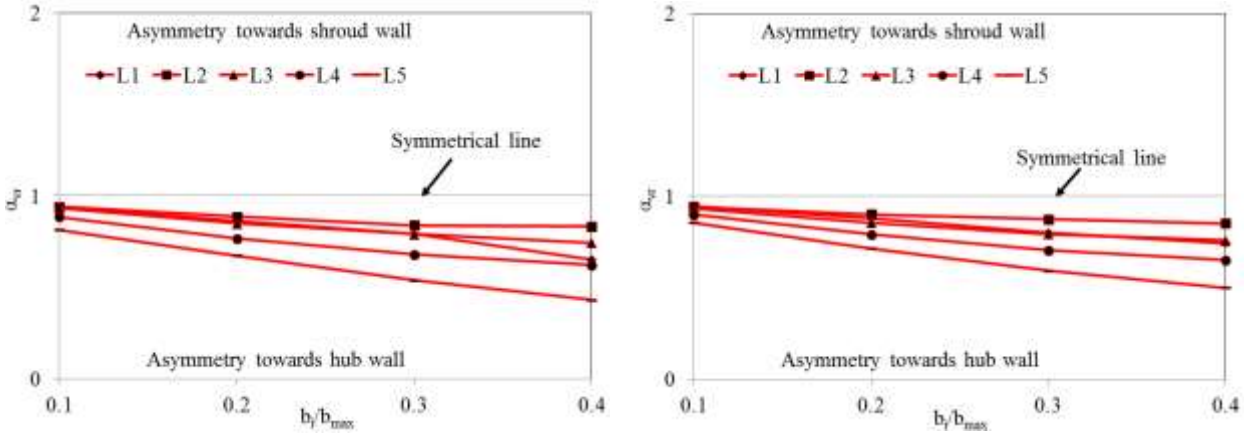

Figure 6.10: Local asymmetric ratio for the radial velocity, α_{vr} across the curved diffusers ((a) CDC_1, (b) CDC_2, (c) CDC_3 and (d) CDC_4) at BEP at an operational speed of 58.9rpsK$^{-1/2}$

Figure 6.11 depicts the radial velocity distribution across the centreline of the curved diffuser configurations (CDC_5, CDC_6, CDC_7 and CDC_8) at BEP at an operational speed of 58.9rpsK$^{-1/2}$. The trend of the radial velocity across the curved diffusers is similar to that across the straight diffuser. It can be seen that the maximum radial velocity is obtained at the diffuser inlet after the volute-tongue region. The radial velocity decreases radially across the diffuser. Furthermore, the radial velocity also decreases circumferentially in the direction of impeller rotation (ω). The minimum radial velocity is obtained at the diffuser outlet at near the volute-tongue region. It can be seen that the radial velocity is increased at the diffuser inlet and diffuser outlet by 12% and decreased at the diffuser outlet by 2.9% respectively across the CDC_5 in comparison to that across the straight diffuser. Furthermore, radial velocity is decreased at the diffuser inlet by 3% of CDC_6 and increased across the diffuser inlet by 3% and 9.4% of CDC_7 and CDC_8 respectively in comparison to that of CDC_5. Moreover, the radial velocity is increased at the diffuser outlet by 2% each of CDC_6 and CDC_8 respectively and decreased at the diffuser outlet by 2% of CDC_7 in comparison to that of CDC_5. It can be concluded from the results that the radial velocity decreases by increasing the ratio of x/b_1. Furthermore, it can also be seen that the radial velocity decreases by increasing the ratio of θ/θ_{max}. Moreover, increasing the ratio of r/r_{max} increases the radial velocity. Moreover, radial flow velocity is highly disturbed across these curved diffuser configurations of CDC_5, CDC_6, CDC_7 and CDC_8 in comparison to that across curved diffuser configurations of CDC_1, CDC_2, CDC_3 and CDC_4.

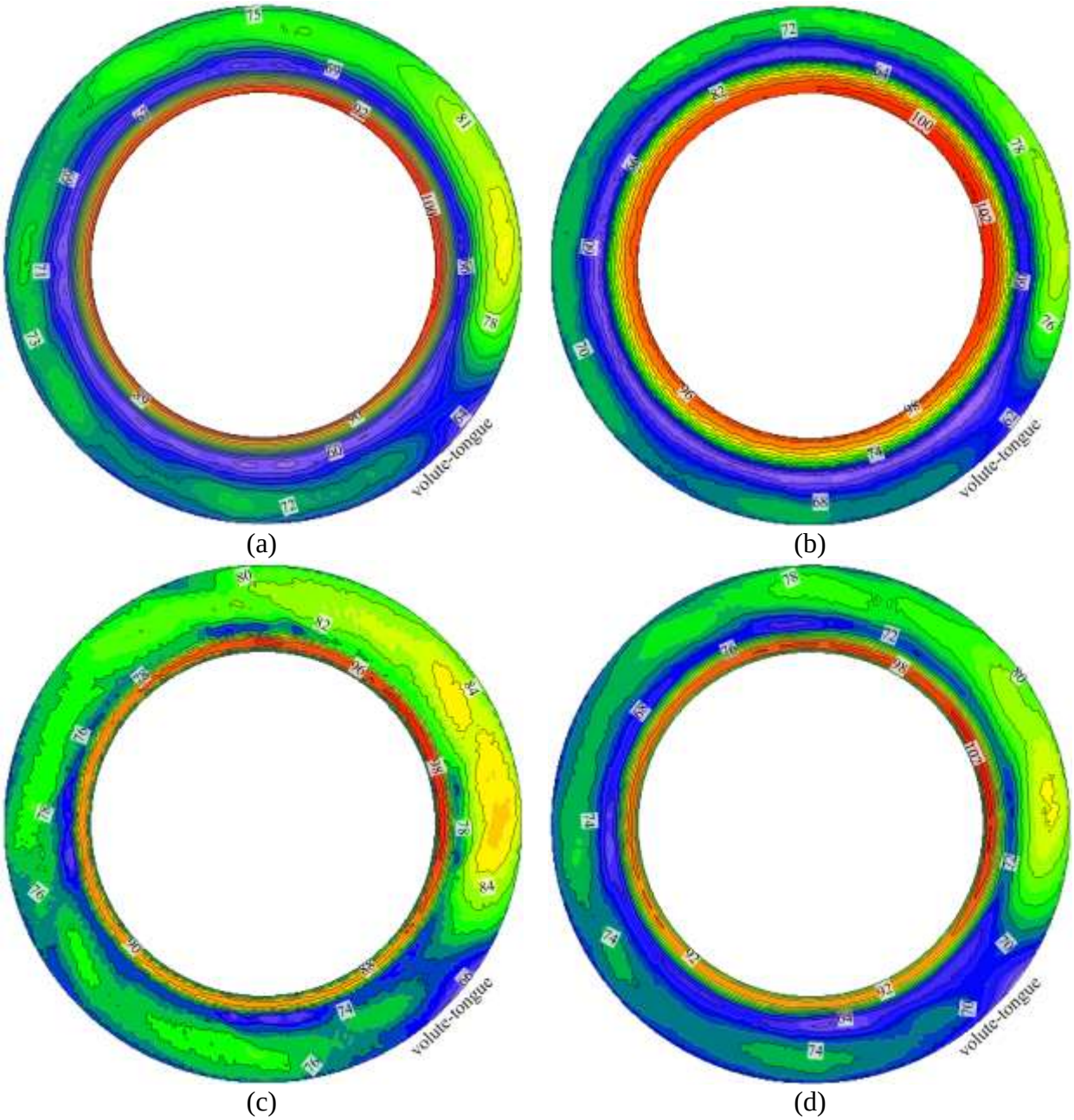

(a) (b) (c) (d)

Figure 6.11: Radial velocity (m/s) distribution across the centreline of the curved diffuser configurations (a) CDC_5, (b) CDC_6, (c) CDC_7 and (d) CDC_8 at BEP at an operational speed of $58.9rpsK^{-1/2}$

Figure 6.12 depicts the comparison of radial velocity distribution across straight diffuser and curved diffuser configurations (CDC_5, CDC_6, CDC_7 and CDC_8) from the hub wall to the shroud wall at BEP at an operational speed of $58.9rpsK^{-1/2}$. It can be seen that the radial velocity is reduced radially across the diffuser. It can be seen that the radial velocity across curved diffusers is higher in comparison to straight diffuser. Furthermore, it has been observed that the radial velocity is asymmetric towards hub

wall across curved diffuser configurations of CDC_5 and CDC_6 in comparison to parallel wall diffuser, which has asymmetric radial velocity towards the shroud wall. Moreover, radial velocity is highly asymmetric towards the hub wall at L_1 (diffuser inlet) and then it decreases towards L_2 across CDC_5 and CDC_6. The radial velocity becomes symmetric between L_2 and L_3 and then the radial velocity becomes asymmetric towards the shroud wall from L_3 to L_5 (diffuser outlet) across CDC_5 and CDC_6. However, the detailed analysis has been carried out by quantifying the asymmetric ratio for the radial velocity profile across curved diffuser configurations.

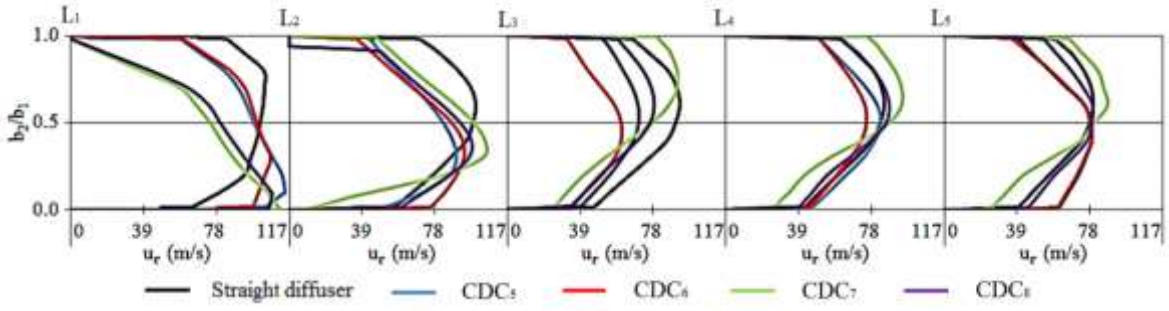

Figure 6.12: Comparison of radial velocity (m/s) distribution across the straight diffuser and curved diffuser configurations from the hub wall to the shroud wall at BEP at an operational speed of $58.9 rpsK^{-1/2}$

Figure 6.13 depicts the local asymmetric ratio for the radial velocity, α_{vr} across the curved diffusers (CDC_5, CDC_6, CDC_7 and CDC_8) at BEP at an operational speed of $58.9 rpsK^{-1/2}$. It can be seen that the radial velocity is highly disturbed across these curved diffuser configurations. The radial flow velocity is asymmetric towards the hub wall from L_1 (diffuser inlet) to L_2 and then the radial flow velocity is asymmetric towards the shroud wall from L_3 to L_4 and finally at L_5 (diffuser outlet) the radial flow velocity is again asymmetric towards the hub wall across CDC_5. Furthermore, the asymmetric ratio for the radial velocity increases from the centreline of the diffuser towards the wall. Moreover, the asymmetric ratio for the radial velocity increases L_1 (diffuser inlet) to L_2 and then decreases from L_3 to L_4 and finally at L_5 (diffuser outlet) the asymmetric ratio for the radial flow velocity again increases across CDC_6. The asymmetric ratio for the radial velocity increases L_1 (diffuser inlet) to L_5 (diffuser outlet) across CDC_7 and the flow asymmetry is towards the shroud wall. The asymmetric ratio for the radial velocity decreases L_1 (diffuser inlet) to L_2 across CDC_7 and the flow is asymmetry towards the hub wall. Thereafter, at L_3 the radial flow velocity became highly asymmetric towards the shroud wall with high values of local asymmetric ratio, and then the local asymmetric ratio decreases from L_3 to L_5 (diffuser outlet).

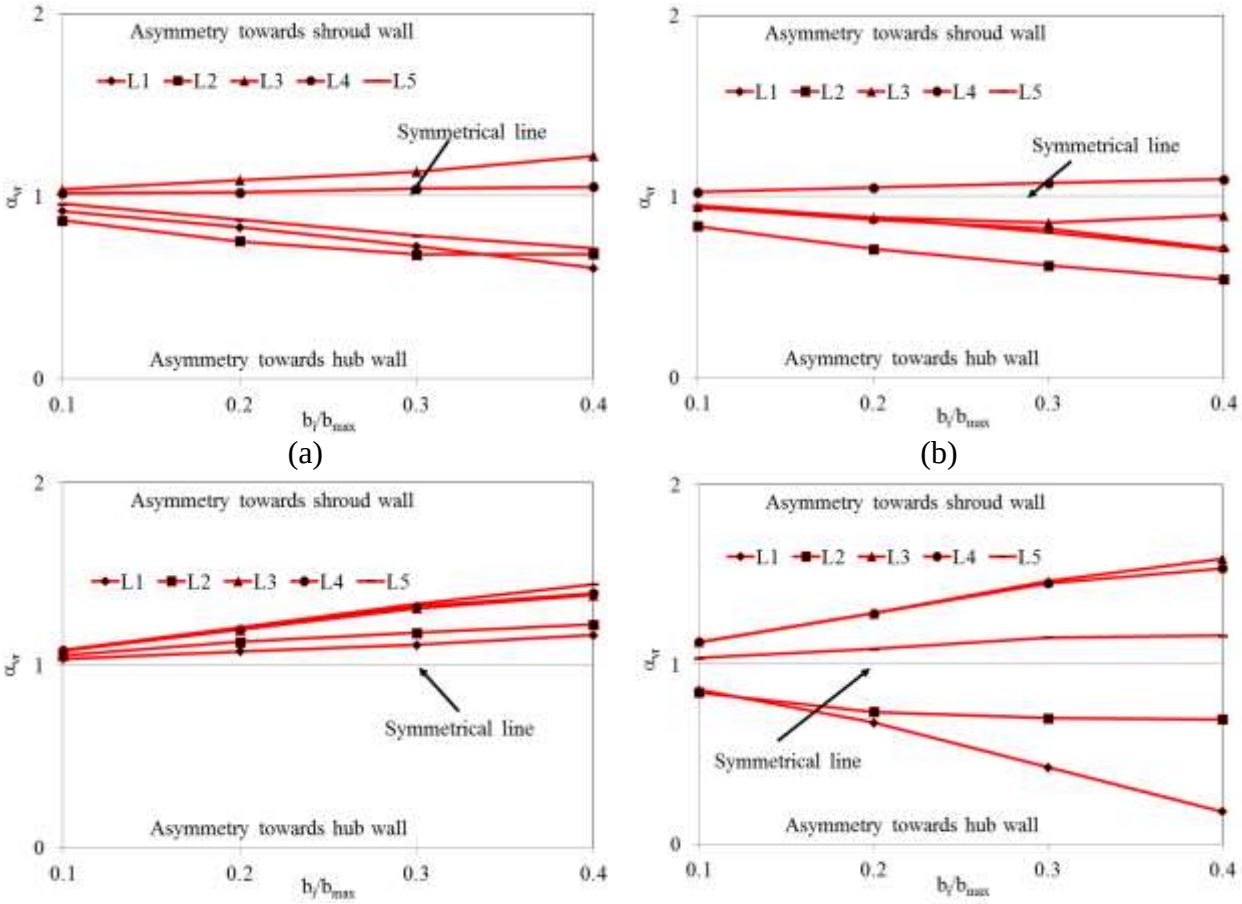

Figure 6.13: Local asymmetric ratio for the radial velocity, α_{vr} across the curved diffusers ((a) CDC_5, (b) CDC_6, (c) CDC_7 and (d) CDC_8) at BEP at an operational speed of 58.9rpsK$^{-1/2}$

Figure 6.14 depicts the circumferential velocity distribution across the centreline of the curved diffuser configurations (CDC_1, CDC_2, CDC_3 and CDC_4) at BEP at an operational speed of 58.9rpsK$^{-1/2}$. The trend of the circumferential velocity across the curved diffusers is similar to that across the straight diffuser. It can be seen that the maximum circumferential velocity is obtained at the diffuser inlet after the volute-tongue region. The circumferential velocity decreases radially across the diffuser. Furthermore, the circumferential velocity also decreases circumferentially in the direction of impeller rotation (ω). The minimum circumferential velocity is obtained at the diffuser outlet at near the volute-tongue region. It can be seen that the circumferential velocity is increased at the diffuser inlet by 8.7% and decreased at the diffuser outlet by 2.4% across the CDC_1 in comparison to that across the straight diffuser. Furthermore, circumferential velocity is same at the diffuser inlet of CDC_2 and CDC_4 respectively in comparison to that of CDC_1. The circumferential velocity is increased at the diffuser inlet by 1.8% CDC_3 in comparison to that of CDC_1. Moreover, the circumferential velocity is increased at the diffuser outlet by 11.8%, 0.6% and 0.6% of CDC_2, CDC_3

and CDC_4 respectively in comparison to that of CDC_1. It can be concluded from the results that increasing the ratio of θ/θ_{max} increases circumferential velocity. Moreover, increasing the ratio of r/r_{max} decreases the circumferential velocity.

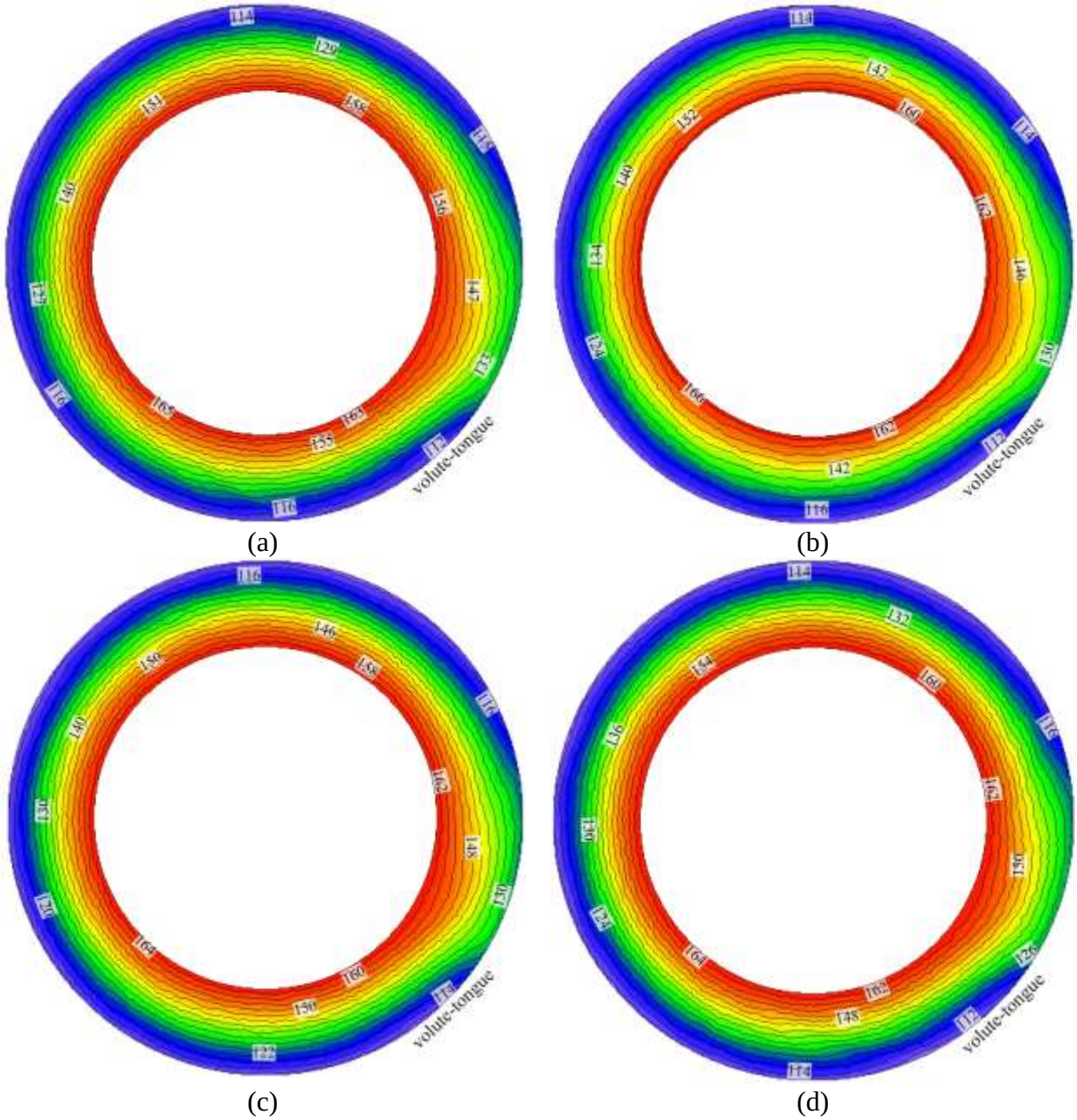

(a) (b)

(c) (d)

Figure 6.14: Circumferential velocity (m/s) distribution across the centreline of the curved diffuser configurations (a) CDC_1, (b) CDC_2, (c) CDC_3 and (d) CDC_4 at BEP at an operational speed of $58.9 rpsK^{-1/2}$

Figure 6.15 depicts the comparison of circumferential velocity distribution across straight diffuser and curved diffuser configurations (CDC_1, CDC_2, CDC_3 and CDC_4) from the hub wall to the shroud wall at BEP at an operational speed of 58.9rpsK$^{-1/2}$. It can be seen that the circumferential velocity is reduced radially across the diffuser. It can be seen that the circumferential velocity across curved diffusers is higher in comparison to straight diffuser. Furthermore, it has been observed that the circumferential velocity is asymmetric towards hub wall across curved diffusers in comparison to parallel wall diffuser, which has asymmetric circumferential velocity towards the shroud wall. However, the detailed analysis has been carried out by quantifying the asymmetric ratio for the circumferential velocity profile across curved diffuser configurations.

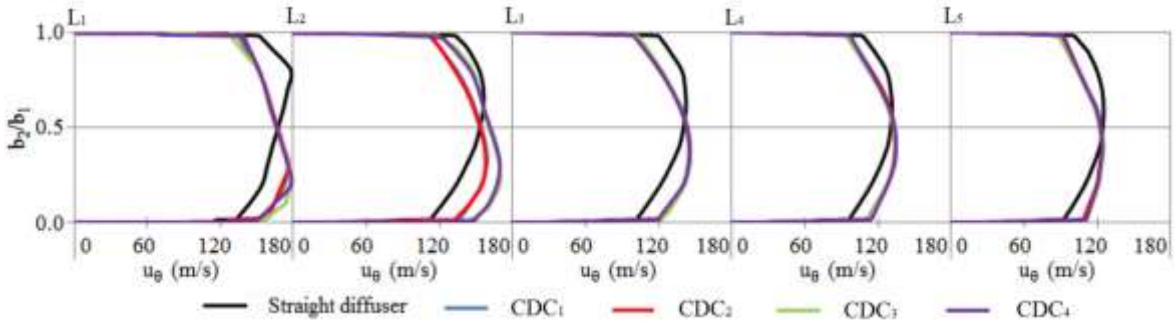

Figure 6.15: Comparison of circumferential velocity (m/s) distribution across the straight diffuser and curved diffuser configurations from the hub wall to the shroud wall at BEP at an operational speed of 58.9rpsK$^{-1/2}$

Figure 6.16 depicts the local asymmetric ratio for circumferential velocity, α_{vc} across the curved diffusers (CDC_1, CDC_2, CDC_3 and CDC_4) at BEP at an operational speed of 58.9rpsK$^{-1/2}$. It can be seen that the flow is asymmetric towards the hub wall across the curved diffusers. The asymmetric ratio for the circumferential velocity constantly increases from the centreline of the diffuser towards the wall and from the diffuser inlet to the diffuser outlet across all the diffuser configurations. It has been noticed that the asymmetric ratio for the circumferential velocity constantly increases from the centreline of the diffuser towards the wall and decreases from the diffuser inlet to the diffuser outlet across all the diffuser configurations. Furthermore, it has only been noticed in CDC_1 that the circumferential velocity is asymmetric towards the shroud wall at L_5 (diffuser outlet) similar to straight diffuser and the local asymmetry increases from the centreline of the diffuser towards the wall.

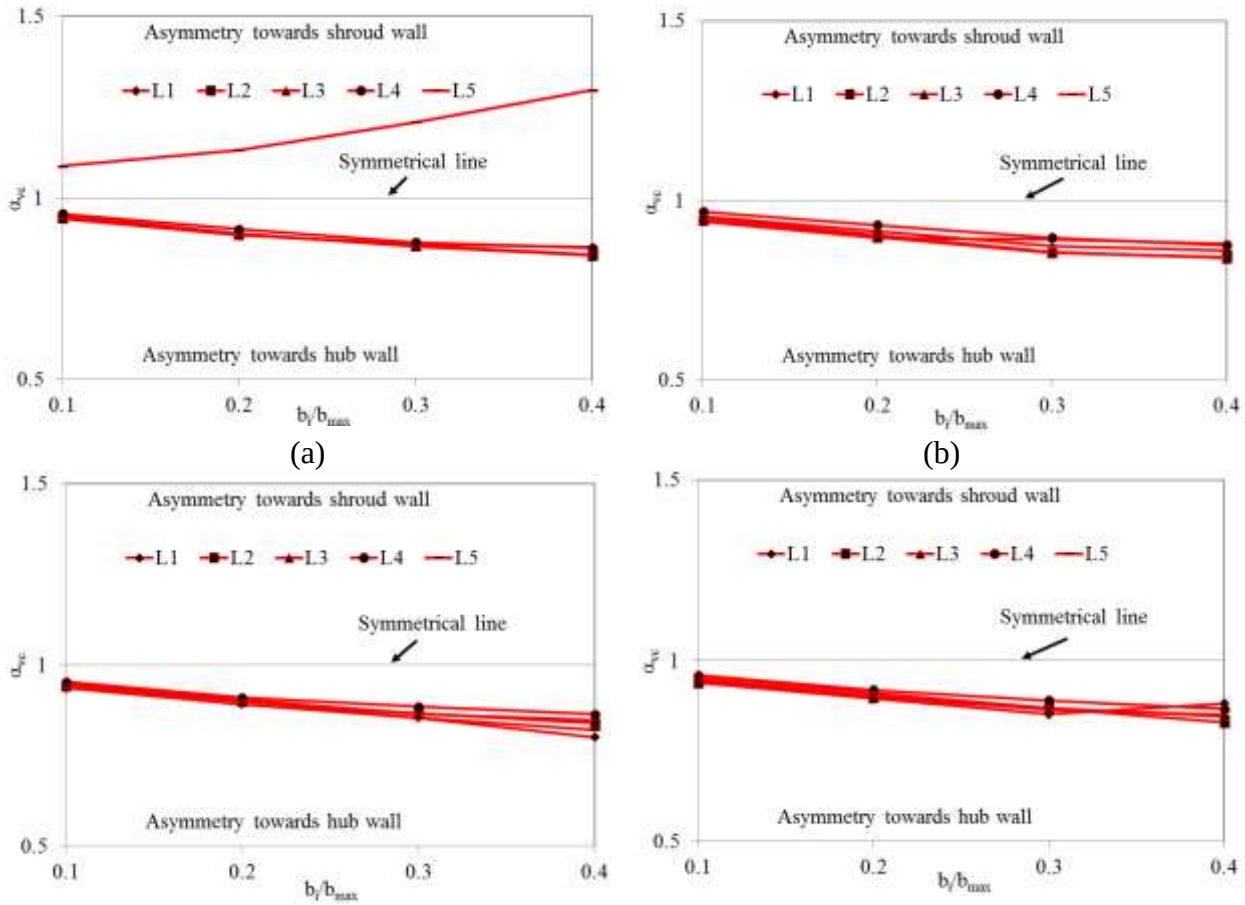

Figure 6.16: Local asymmetric ratio for the circumferential velocity, α_{vc} across the curved diffusers ((a) CDC_1, (b) CDC_2, (c) CDC_3 and (d) CDC_4) at BEP at an operational speed of $58.9 rpsK^{-1/2}$

Figure 6.17 depicts the circumferential velocity distribution across the centreline of the curved diffuser configurations (CDC_5, CDC_6, CDC_7 and CDC_8) at BEP at an operational speed of $58.9 rpsK^{-1/2}$. The trend of the circumferential velocity across the curved diffusers is similar to that across the straight diffuser. It can be seen that the maximum circumferential velocity is obtained at the diffuser inlet after the volute-tongue region. The circumferential velocity decreases radially across the diffuser. Furthermore, the circumferential velocity also decreases circumferentially in the direction of impeller rotation (ω). The minimum circumferential velocity is obtained at the diffuser outlet at near the volute-tongue region. It can be seen that the circumferential velocity is increased at the diffuser inlet by 8.7% and decreased at the diffuser outlet by 1.8% across the CDC_1 in comparison to that across the straight diffuser. Furthermore, circumferential velocity is same at the diffuser inlet of CDC_2 in comparison to that of CDC_1. The circumferential velocity is increased at the diffuser inlet by 2.7% and 4.5% of CDC_3 and CDC_4 respectively in comparison to that of CDC_1. Moreover, the

circumferential velocity is increased at the diffuser outlet by 1.2%, 1.8% and 1.8% of CDC_2, CDC_3 and CDC_4 respectively in comparison to that of CDC_1. It can be concluded from the results that the circumferential velocity increases by increasing the ratio of x/b_1. Furthermore, it can also be seen that the circumferential velocity increases by increasing the ratio of θ/θ_{max}. Moreover, increasing the ratio of r/r_{max} increases the circumferential velocity.

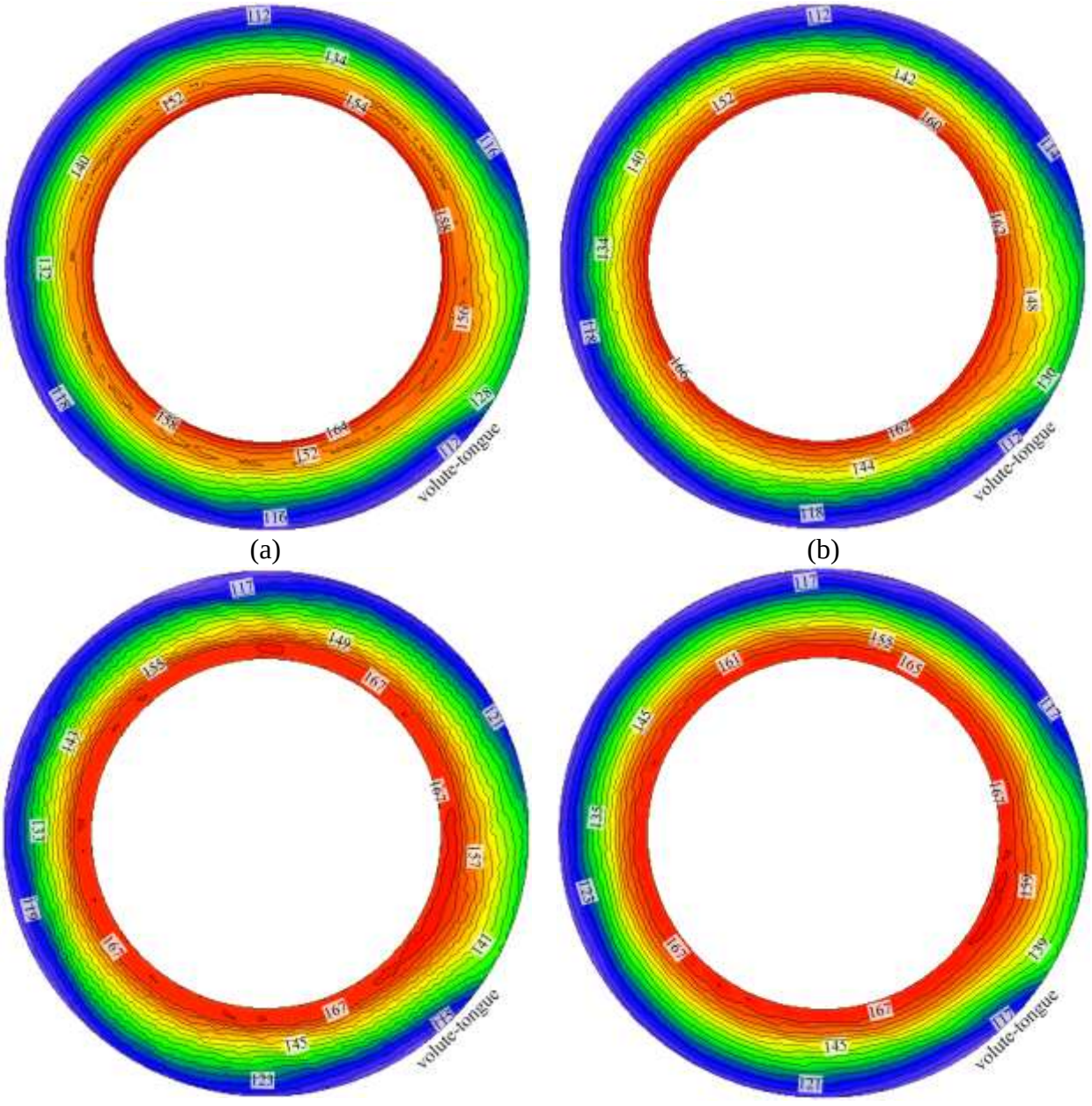

(a) (b)

(c) (d)

Figure 6.17: Circumferential velocity (m/s) distribution across the centreline of the curved diffuser configurations (a) CDC_5, (b) CDC_6, (c) CDC_7 and (d) CDC_8 at BEP at an operational speed of $58.9 rpsK^{-1/2}$

Figure 6.18 depicts the comparison of circumferential velocity distribution across straight diffuser and curved diffuser configurations (CDC_5, CDC_6, CDC_7 and CDC_8) from the hub wall to the shroud wall at BEP at an operational speed of 58.9rpsK$^{-1/2}$. It can be seen that the circumferential velocity is reduced radially across the diffuser. It can be seen that the circumferential velocity across curved diffusers is higher in comparison to straight diffuser. Furthermore, it has been observed that the circumferential velocity is asymmetric towards hub wall across curved diffuser configurations of CDC_5 and CDC_6 in comparison to parallel wall diffuser, which has asymmetric circumferential velocity towards the shroud wall. Moreover, circumferential velocity is highly asymmetric towards the hub wall at L_1 (diffuser inlet) and then it decreases towards L_2 across CDC_5 and CDC_6. The circumferential velocity becomes symmetric between L_2 and L_3 and then the circumferential velocity becomes asymmetric towards the shroud wall from L_3 to L_5 (diffuser outlet) across CDC_5 and CDC_6. However, the detailed analysis has been carried out by quantifying the asymmetric ratio for the circumferential velocity profile across curved diffuser configurations.

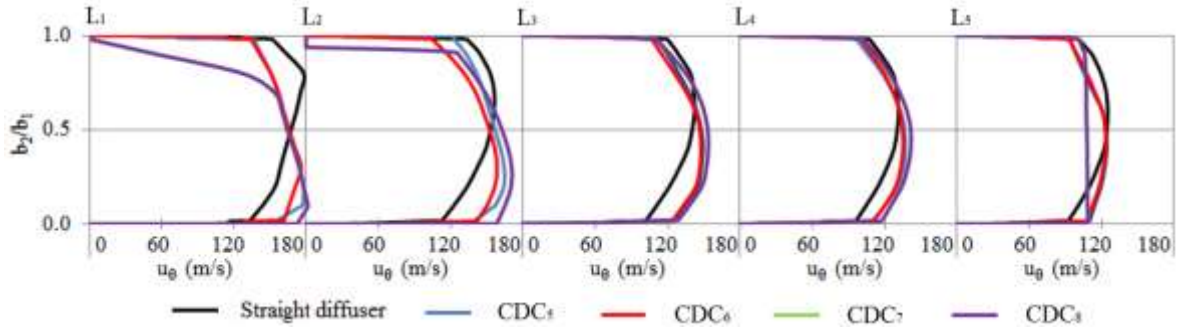

Figure 6.18: Comparison of circumferential velocity (m/s) distribution across the straight diffuser and curved diffuser configurations from the hub wall to the shroud wall at BEP at an operational speed of 58.9rpsK$^{-1/2}$

Figure 6.19 depicts the local asymmetric ratio for the circumferential velocity, α_{vc} across the curved diffusers (CDC_5, CDC_6, CDC_7 and CDC_8) at BEP at an operational speed of 58.9rpsK$^{-1/2}$. It can be seen that the flow is asymmetric towards the hub wall across CDC_5 and CDC_6. The asymmetric ratio for the circumferential velocity constantly increases from the centreline of the diffuser towards the wall. Furthermore, it decreases from the diffuser inlet to the half-length of the diffuser and it than increases towards the diffuser outlet across CDC_5 and CDC_6. Moreover, it can also be seen that the flow is asymmetric towards the shroud wall across CDC_7 and CDC_8. The asymmetric ratio for the circumferential velocity constantly increases from the centreline of the diffuser towards the wall and diffuser inlet to the diffuser outlet across CDC_7 and CDC_8.

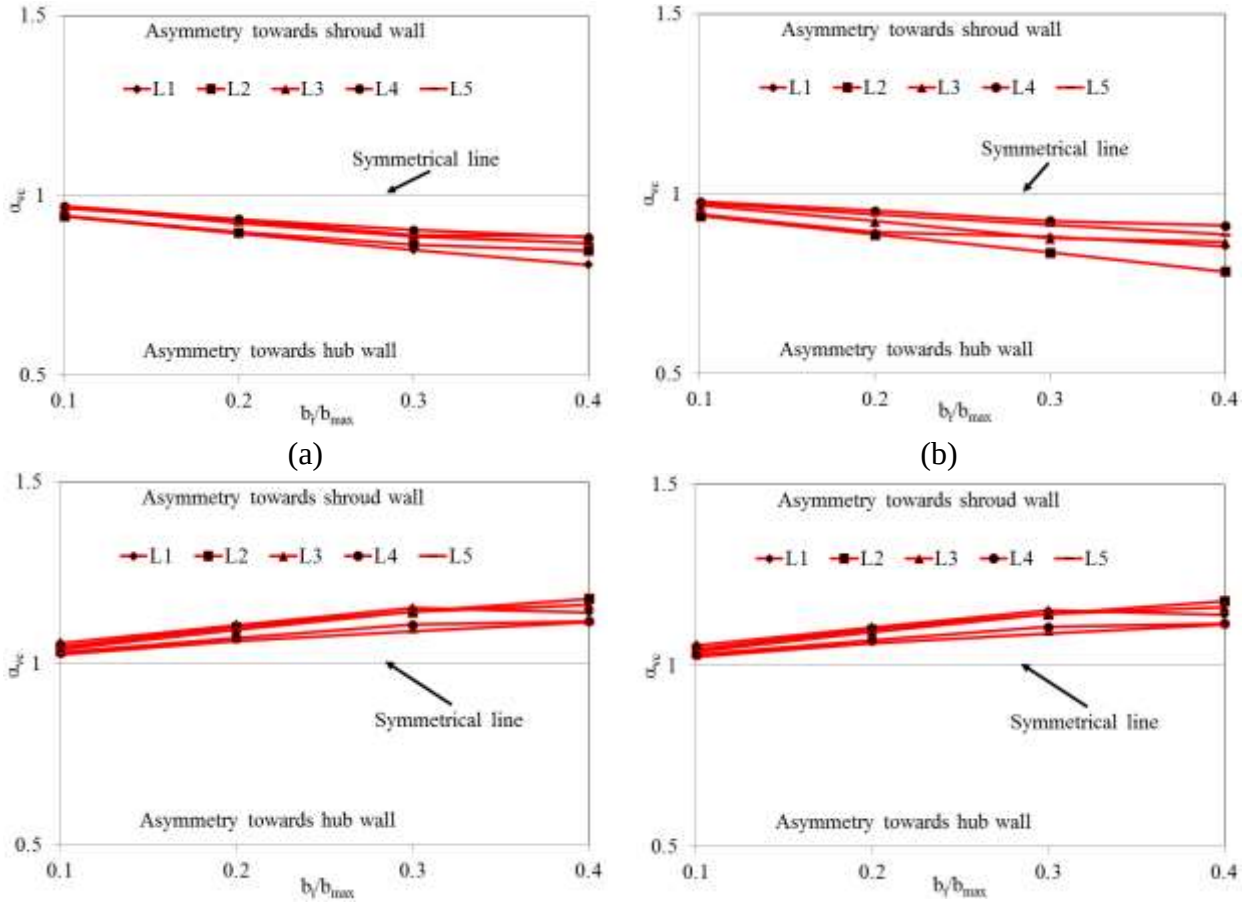

Figure 6.19: Local asymmetric ratio for the circumferential velocity, α_{vc} across the curved diffusers (a) CDC_5, (b) CDC_6, (c) CDC_7 and (d) CDC_8) at BEP at an operational speed of 58.9rpsK$^{-1/2}$

Figure 6.20 depicts the static temperature variations across the centreline of the curved diffuser configurations (CDC_1, CDC_2, CDC_3 and CDC_4) at BEP at an operational speed of 58.9rpsK$^{-1/2}$. The trend of the static temperature across the curved diffusers is similar to that across the parallel wall diffuser. It can be seen that the minimum static temperature is obtained at the diffuser inlet after the volute-tongue region. The static temperature increases radially across the diffuser. Furthermore, the static temperature also increases circumferentially in the direction of impeller rotation (ω). The maximum static temperature is obtained at the diffuser outlet near the volute-tongue region. It can be seen that the static temperature is decreased by 0% and 0.6% at the diffuser inlet and diffuser outlet respectively across the diffuser configuration of CDC_1 in comparison to straight diffuser. Furthermore, it can also be seen that the static temperature is same at the diffuser inlet and diffuse outlet across all diffuser configurations in comparison to that across diffuser configuration of CDC_1.

It can be concluded from the results that the static temperature is not changed by increasing the ratio of θ/θ_{max} or r/r_{max}.

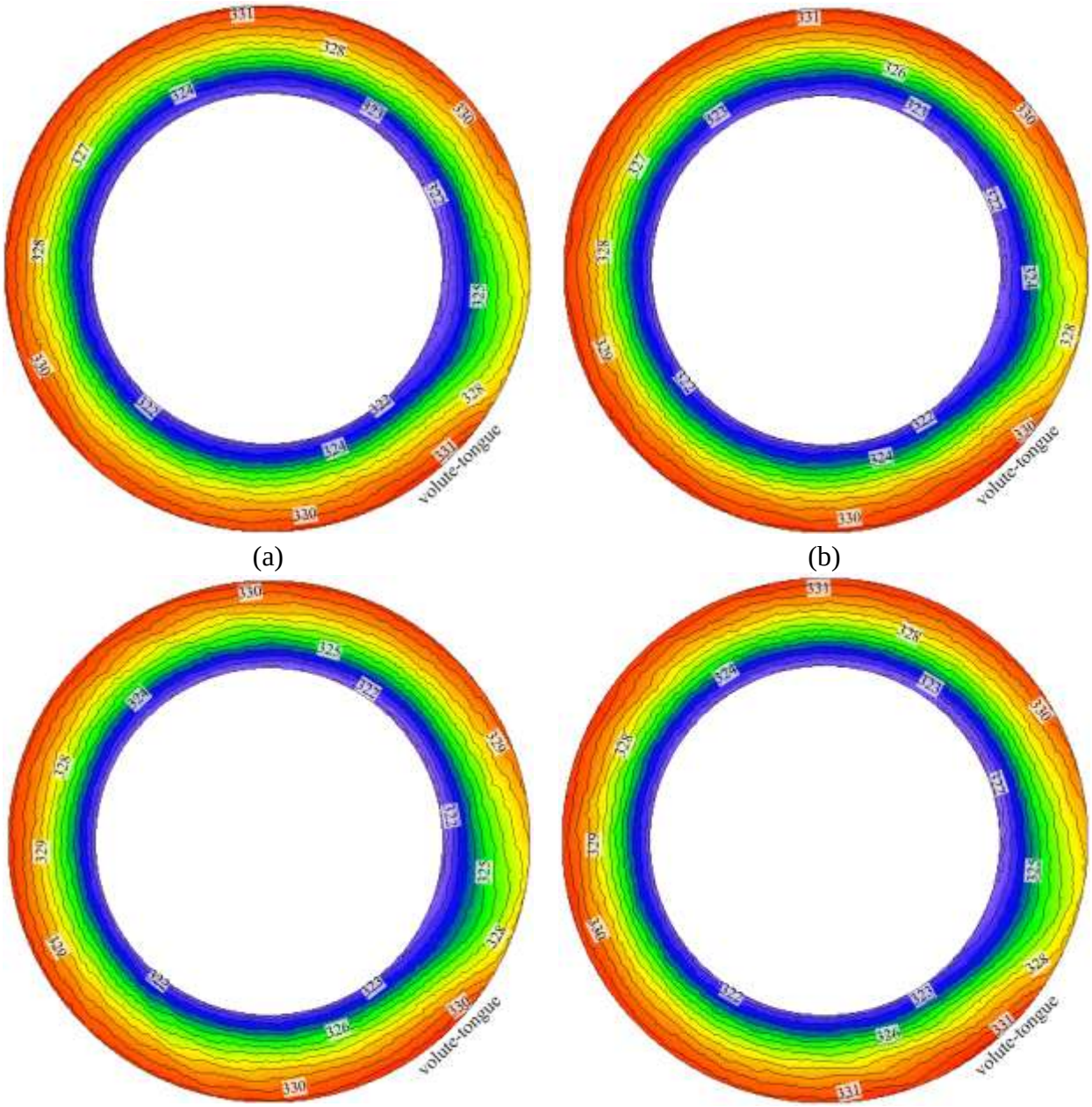

(a) (b)

(c) (d)

Figure 6.20: Static Temperature (atm) variations across the centreline of the curved diffuser configurations (a) CDC_1, (b) CDC_2, (c) CDC_3 and (d) CDC_4 at BEP at an operational speed of 58.9rpsK$^{-1/2}$

Figure 6.21 depicts the static temperature variations across the centreline of the curved diffuser configurations (CDC_5, CDC_6, CDC_6 and CDC_7) at BEP at an operational speed of 58.9rpsK$^{-1/2}$. The trend of the static temperature across the curved diffusers is similar to that across the parallel wall

diffuser. It can be seen that the minimum static temperature is obtained at the diffuser inlet after the volute-tongue region. The static temperature increases radially across the diffuser. Furthermore, the static temperature also increases circumferentially in the direction of impeller rotation (ω). The maximum static temperature is obtained at the diffuser outlet near the volute-tongue region. It can be seen that the static temperature is decreased by 0.3% each at the diffuser inlet and diffuser outlet respectively for the diffuser configuration of CDC_5 in comparison to parallel wall straight diffuser. Furthermore, it can also be seen that the static temperature is same at the diffuser inlet and diffuser outlet of CDC_6 in comparison to that for diffuser configuration of CDC_5. Furthermore, it can also be seen that the static temperature is increased at the diffuser inlet by 0.9% each of CDC_7 and CDC_8 respectively Moreover, the static temperature is increased at the diffuser outlet by 1.2% and 0.9% respectively of CDC_8 in comparison to that of CDC_5. It can be concluded from the results that the static temperature increases by increasing the ratio of x/b_1. Furthermore, it can also be seen that the static temperature increases by increasing the ratio of θ/θ_{max}. Moreover, increasing the ratio of r/r_{max} decreases the static temperature.

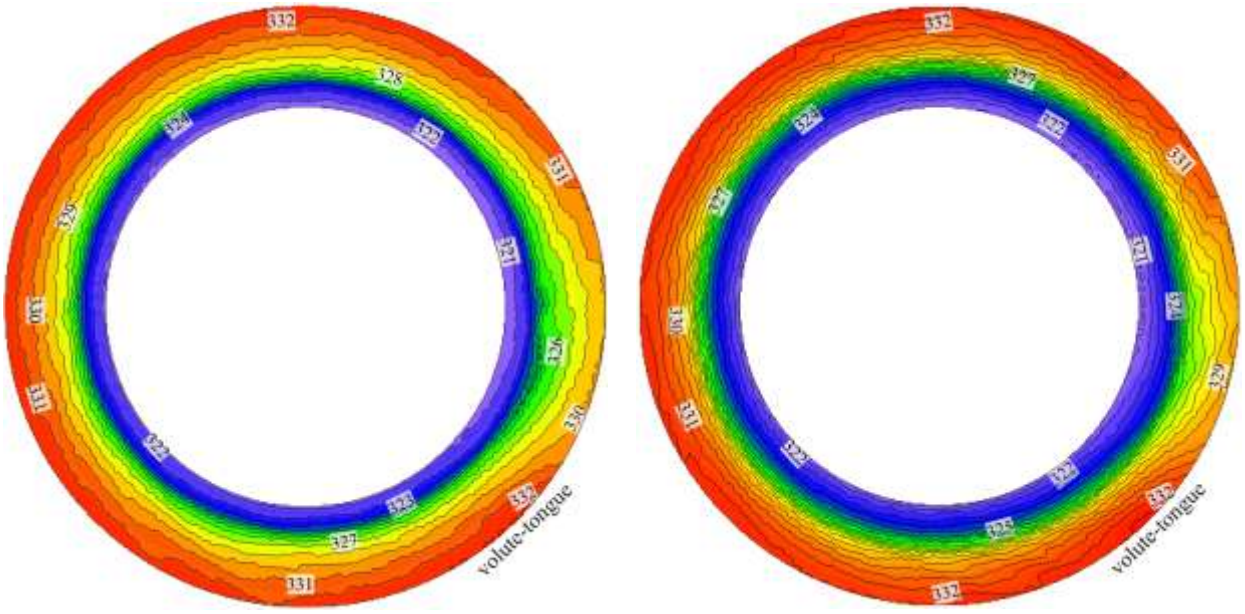

(a) (b)

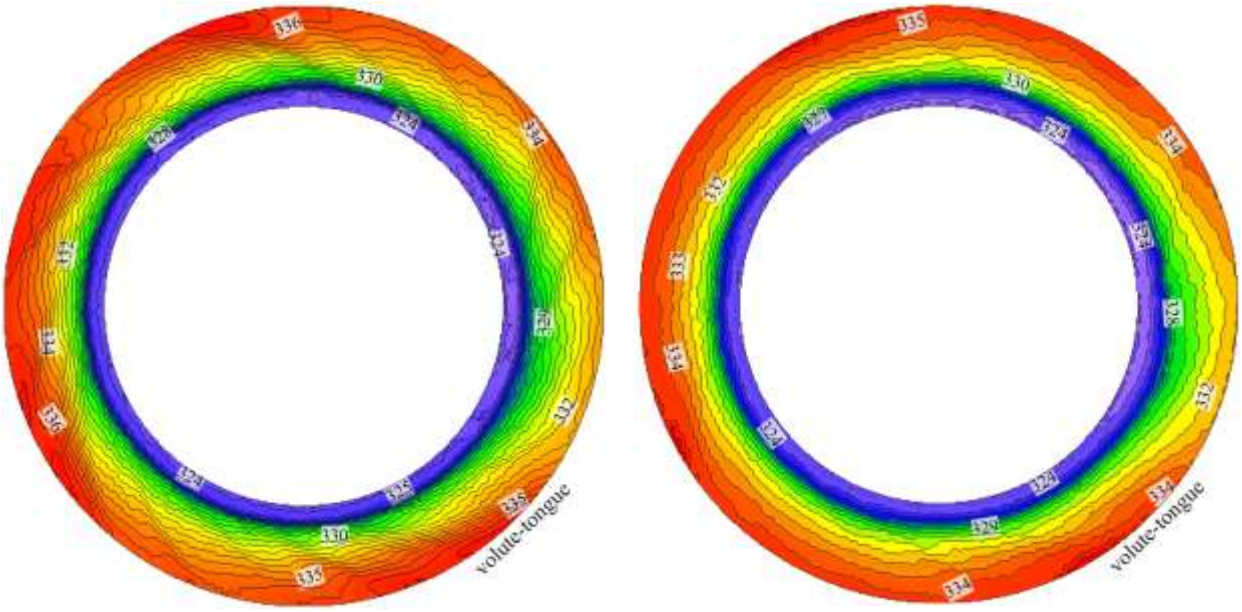

(c) (d)

Figure 6.21: Static Temperature (atm) variations across the centreline of the curved diffuser configurations (a) CDC_5, (b) CDC_6, (c) CDC_7 and (d) CDC_8 at BEP at an operational speed of 58.9rpsK$^{-1/2}$

6.2.2. Effect of Asymmetric Ratio across the Curved Diffusers

The behaviour of the flow within the curved diffusers is highly dependent upon the geometrical parameters considered. It has been noticed in the previous section that increase of ratio of r/r_{max} and θ/θ_{max} increases the asymmetry of the flow towards the hub wall of the diverged wall diffuser. However, increase of ratio of x/b_1 increases the asymmetric ratio, which shifts the flow from hub wall towards the shroud wall. A term Equation 4.1, which is introduced in Chapter 4 for the global asymmetric ratio, has been modified shown Equation 6.1 that shows the change in behaviour of the flow across the curved diffusers and shows the global effect of the asymmetry across the curved diffuser. The major effect of geometrical parameters on the asymmetric flow behaviour and stage performance is described in detail.

$$\xi = \frac{1}{2}\left[\frac{\alpha_1 x_{t1}+\alpha_2 x_{t2}+\alpha_3 x_{t3}+\alpha_4 x_{t4}}{x_t}\right] \tag{6.1}$$

Where, n is the number of diffuser widths considered (shown in Figure 4.19) from the walls and x is the curved diffuser width (Equation for x is presented in Appendix A-9). Furthermore, the subscripts 1, 2, 3 and 4 are width locations from the wall, which are explained earlier in the previous section. Moreover, subscript t stands for total/maximum and ave stands for average. The global asymmetric

ratio for different velocity vectors across the diffuser are described in the following section. Furthermore, the major effect of velocity vectors on the design and off-design conditions is described in detail.

Figure 6.22 depicts the global asymmetric ratio for the velocity magnitude across the curved diffusers of CDC_1, CDC_2, CDC_3 and CDC_4 at BEP at an operational speed of 58.9rpsK$^{-1/2}$. It can be seen that the global asymmetric ratio across these curved diffusers is towards the hub wall of the diffuser. The global asymmetric ratio for the velocity magnitudes is seemed to be same from L_1 (diffuser inlet) to L_4 and then decreased towards at L_5 (diffuser outlet) across the curved diffuser considered.

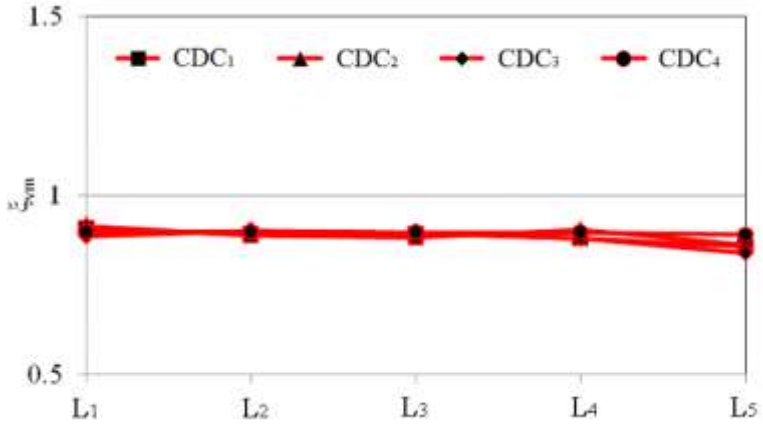

Figure 6.22: Global asymmetric ratio for the velocity magnitude across the curved diffusers (CDC_1, CDC_2, CDC_3 and CDC_4) at BEP at an operational speed of 58.9rpsK$^{-1/2}$

Figure 6.23 depicts the global asymmetric ratio for the velocity magnitude across the curved diffusers of CDC_5, CDC_6, CDC_7 and CDC_8 at BEP at an operational speed of 58.9rpsK$^{-1/2}$. It can be seen that the global asymmetric ratio across CDC_5 and CDC_6 is below 1.0 at L_1 (diffuser inlet) in comparison to that at CDC_7 and CDC_8 showing flow asymmetry towards hub wall. It can be seen that the global asymmetric ratio decreases from L_1 (diffuser inlet) to L_2. Thereafter, the global asymmetric ratio increases from L_2 to L_5 (diffuser outlet). Furthermore, it can also be seen that the global asymmetric ratio across CDC_7 and CDC_8 is mostly above 1.0 showing flow asymmetry towards shroud wall. It can be seen that the global asymmetric ratio is same from the diffuser inlet to diffuser outlet across the curved diffusers considered.

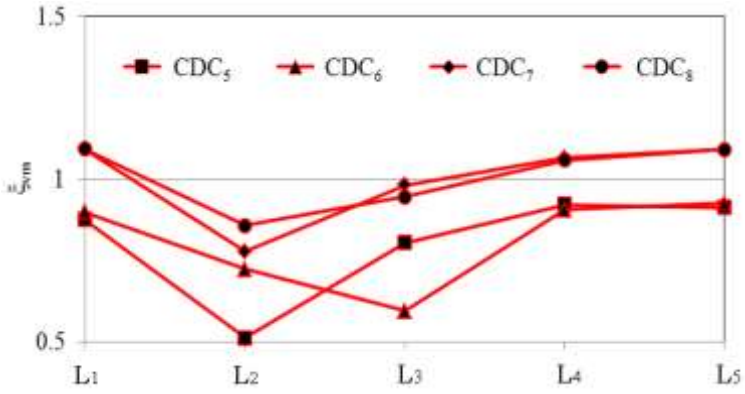

Figure 6.23: Global asymmetric ratio for the velocity magnitude across the curved diffusers (CDC_5, CDC_6, CDC_7 and CDC_8) at BEP at an operational speed of 58.9rpsK$^{-1/2}$

Figure 6.24 depicts the global asymmetric ratio for the radial velocity across the curved diffusers of CDC_1, CDC_2, CDC_3 and CDC_4 at BEP at an operational speed of 58.9rpsK$^{-1/2}$. It can be seen that the global asymmetric ratio across these curved diffusers is towards the hub wall of the diffuser. The global asymmetric ratio is constantly decreasing from L_1 (diffuser inlet) to L_5 (diffuser outlet).

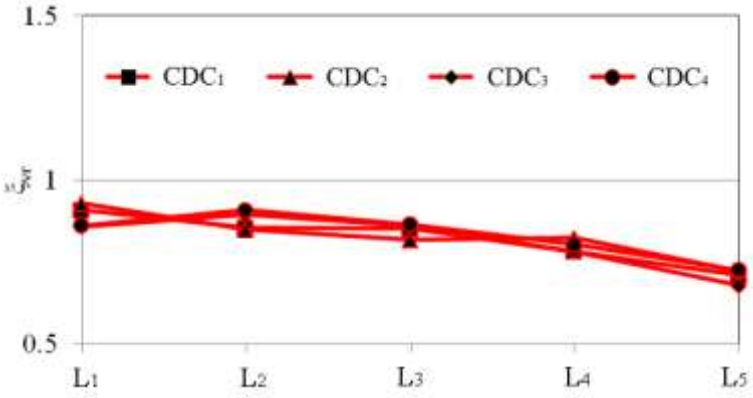

Figure 6.24: Global asymmetric ratio for the radial velocity across the curved diffusers (CDC_1, CDC_2, CDC_3 and CDC_4) at BEP at an operational speed of 58.9rpsK$^{-1/2}$

Figure 6.25 depicts the global asymmetric ratio for the radial velocity across the curved diffuser of CDC_5, CDC_6, CDC_7 and CDC_8 at BEP and at an operational speed of 58.9rpsK$^{-1/2}$. It can be seen that the global asymmetric ratio varies above and below the value of 1.0, showing the radial flow asymmetry is decreasing and increasing across the diffuser configuration of CDC_7 and CDC_8. On the other hand, the global asymmetric ratio is below 1.0 at CDC_5 and CDC_6 showing the radial flow asymmetric towards the hub wall. It can be seen that the global asymmetric ratio decreases from L_1

(diffuser inlet) to L_2. Thereafter, the global asymmetric ratio increases from L_2 to L_4 and then decreases towards L_5 (diffuser outlet).

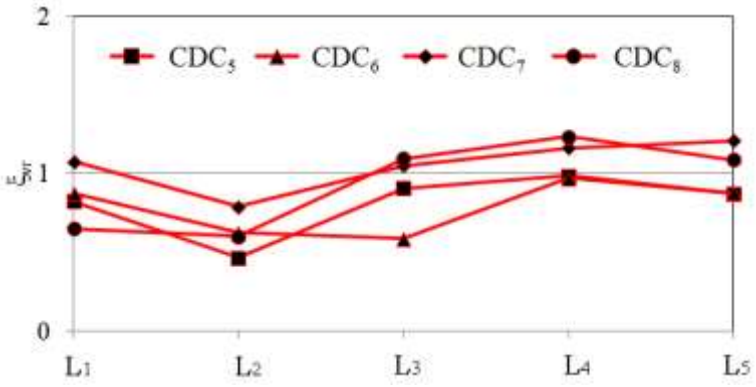

Figure 6.25: Global asymmetric ratio for the radial velocity of the curved diffusers (CDC_5, CDC_6, CDC_7 and CDC_8) at BEP at an operational speed of 58.9rpsK$^{-1/2}$

Figure 6.26 depicts the global asymmetric ratio for the circumferential velocity across the curved diffusers (CDC_1, CDC_2, CDC_3 and CDC_4) at BEP and at an operational speed of 58.9rpsK$^{-1/2}$. It can be seen that the global asymmetric ratio across these curved diffusers is towards the hub wall of the diffuser. The global asymmetric ratio for the circumferential velocity is same across these curved diffusers except at L_5 (diffuser outlet) of CDC_4 whereby the asymmetric ratio is above 1.0 showing flow asymmetry towards the shroud wall.

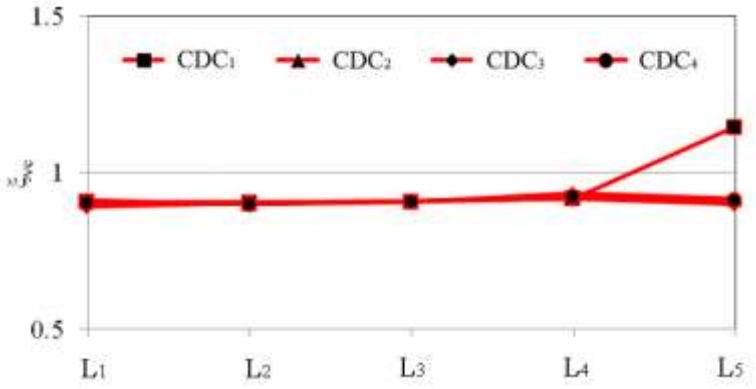

Figure 6.26: Global asymmetric ratio for the circumferential velocity across the curved diffusers (CDC_1, CDC_2, CDC_3 and CDC_4) at BEP at an operational speed of 58.9rpsK$^{-1/2}$

Figure 6.27 depicts the global asymmetric ratio for the circumferential velocity across the curved diffusers (CDC_5, CDC_6, CDC_7 and CDC_8) at BEP at an operational speed of 58.9rpsK$^{-1/2}$. It can be

seen that the global asymmetric ratio across CDC_5 and CDC_6 is below 1.0 at L_1 (diffuser inlet) in comparison to that at CDC_7 and CDC_8 showing flow asymmetry towards hub wall. It can be seen that the global asymmetric ratio decreases from L_1 (diffuser inlet) to L_2. Thereafter, the global asymmetric ratio increases from L_2 to L_5 (diffuser outlet). Furthermore, it can also be seen that the global asymmetric ratio across CDC_7 and CDC_8 is mostly above 1.0 showing flow asymmetry towards shroud wall. It can be seen that the global asymmetric ratio is same from the diffuser inlet to diffuser outlet across the curved diffusers considered.

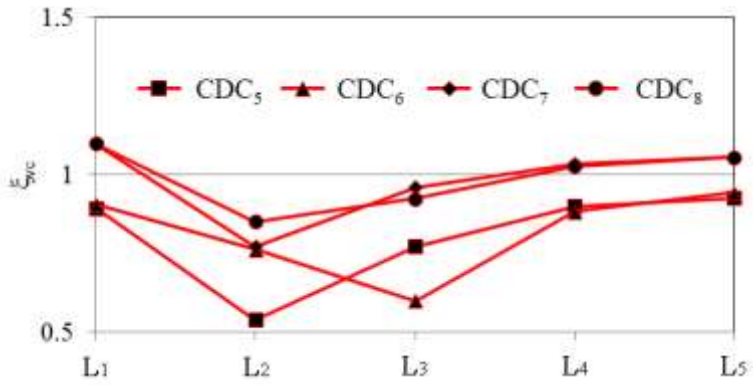

Figure 6.27: Global asymmetric ratio for the circumferential velocity across the curved diffusers (CDC_5, CDC_6, CDC_7 and CDC_8) at BEP at an operational speed of 58.9rpsK$^{-1/2}$

It is concluded from the above results the flow is asymmetrical across the curved diffusers. It has been noticed that the variations in the asymmetry of the flow are due to x/b_1, r/r_{max} and θ/θ_{max}. In order to understand the overall effect of the geometrical changes on the diffuser flow field and stage performance, the equation 4.2 is used.

Figure 6.28 depicts the comparison of diffuser asymmetric effect for velocity magnitude across the curved diffusers and straight diffuser at BEP and at an operational speed of 58.9rpsK$^{-1/2}$. It can be seen there is not much difference in the asymmetric effect with the variations in r/r_{max} and θ/θ_{max} having $x/b_1 = 1.71$. Conversely, the asymmetric effect increases with the variations in r/r_{max} and θ/θ_{max} having $x/b_1 = 4.35$. The asymmetric effect is below 1, which shows the flow asymmetry towards hub wall in comparison to that across the straight diffuser. Furthermore, the stage efficiency remains similar at $x/b_1 = 1.71$ with variations in r/r_{max} and θ/θ_{max}. Conversely, the stage efficiency variations are higher when geometrical parameters of r/r_{max} and θ/θ_{max} are varied having $x/b_1 = 4.35$. The stage efficiency is maximum having a value of 71.68% at CDC_1 and CDC_4. The stage efficiency is minimum having a value of 67.08% at CDC_7.

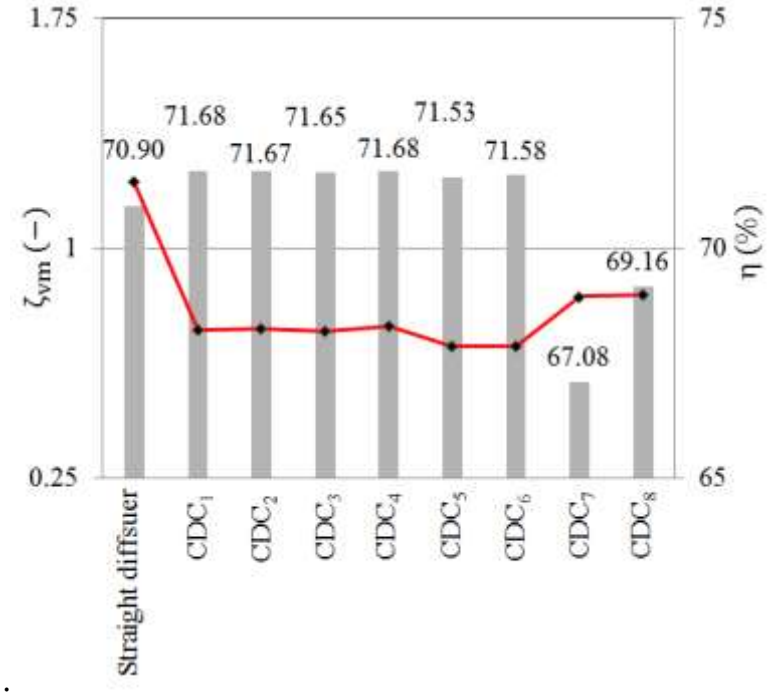

Figure 6.28: Comparison of diffuser asymmetric effect for velocity magnitude across the curved diffusers at BEP and at the operational speed of 58.9rpsK$^{-1/2}$

Figure 6.29 depicts the comparison of diffuser asymmetric effect for radial velocity across the curved diffusers and straight diffuser at BEP and at an operational speed of 58.9rpsK$^{-1/2}$. It can be seen there is not much difference in the asymmetric effect with the variations in r/r_{max} and θ/θ_{max} having x/b_1 = 1.71. Conversely, the asymmetric effect increases with the variations in r/r_{max} and θ/θ_{max} having x/b_1 = 4.35. The asymmetric effect is below 1, which shows the flow asymmetry towards hub wall in comparison to that across the straight diffuser. Furthermore, the stage efficiency is remains similar at x/b_1 = 1.71 with variations in r/r_{max} and θ/θ_{max}. Conversely, the stage efficiency variations are higher when geometrical parameters of r/r_{max} and θ/θ_{max} are varied having x/b_1 = 4.35.

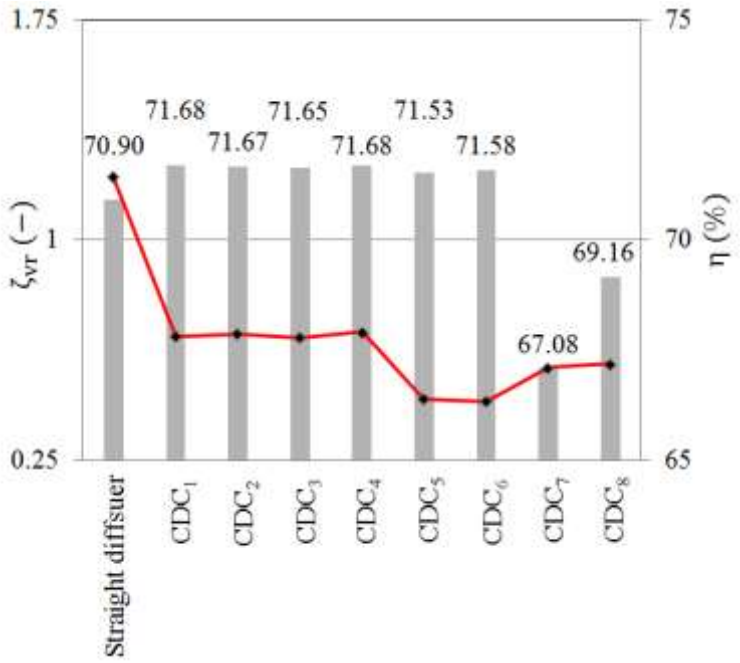

Figure 6.29: Comparison of diffuser asymmetric effect for radial velocity across the curved diffusers at BEP and at the operational speed of 58.9rpsK$^{-1/2}$

Figure 6.30 depicts the comparison of diffuser asymmetric effect for circumferential velocity across the curved diffusers and straight diffuser at BEP and at an operational speed of 58.9rpsK$^{-1/2}$. It can be seen there is not much difference in the asymmetric effect with the variations in r/r_{max} and θ/θ_{max} having x/b_1 = 1.71 and x/b_1 = 4.35. The asymmetric effect is below 1, which shows the flow asymmetry towards hub wall in comparison to that across the straight diffuser. The asymmetric effect only reduces at one diffuser configuration of CDC_6. Furthermore, the stage efficiency remains similar at x/b_1 = 1.71 with variations in r/r_{max} and θ/θ_{max}. Conversely, the stage efficiency variations are higher when geometrical parameters of r/r_{max} and θ/θ_{max} are varied having x/b_1 = 4.35.

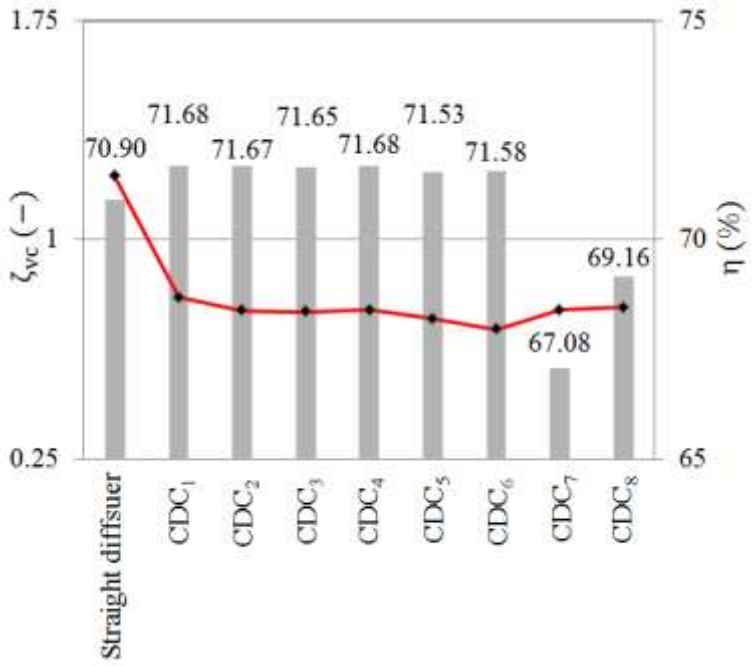

Figure 6.30: Comparison of diffuser asymmetric effect for circumferential velocity across the curved diffusers at BEP and at the operational speed of 58.9rpsK$^{-1/2}$

6.3. Characteristics of Geometrical Parameters

This section investigates the effects of x/b_1, r/r_{max} and θ/θ_{max} on the diffuser local performance. The diffuser performance is dependent upon the recovery of static pressure across the diffuser.

6.3.1. Effects of Geometrical Parameters on Pressure Recovery across the Curved Diffuers

Three geometrical parameters x/b_1, r/r_{max} and θ/θ_{max} have used to modify the vaneless diffuser geometry. These configurations have affected the diffuser performance. Figure 6.31 depicts the variation in the coefficient of pressure C_p while changing r/r_{max} and θ/θ_{max} having $x/b_1 = 1.71$ across the straight diffuser and curved diffusers (CDC_1, CDC_2, CDC_3 and CDC_4) at BEP and at an operational speed of 58.9rpsK$^{-1/2}$. It can be seen that C_p decreases from CDC_1 to CDC_3 and it than increases to CDC_4 across the curved diffusers in comparison to that across the straight diffuser. The area ratio is a function of r/r_{max}, θ/θ_{max} and x/b_1.

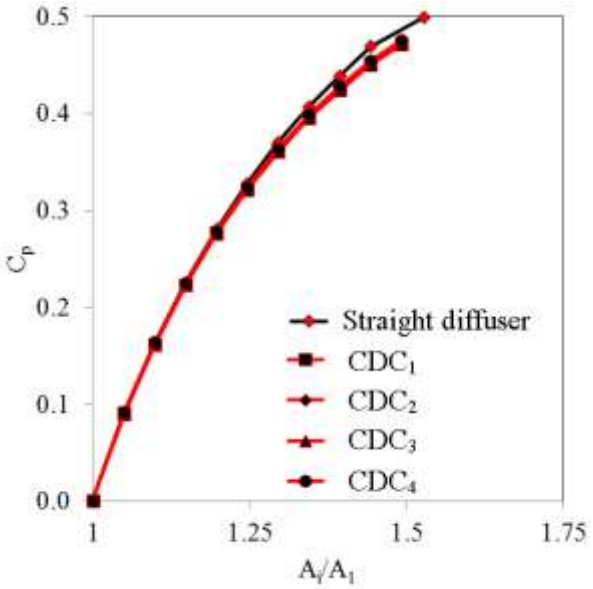

Figure 6.31: Variation in the coefficient of pressure C_p across the straight diffuser and curved diffuser configurations

Figure 6.32 depicts the variation in the coefficient of pressure C_p while changing r/r_{max} and θ/θ_{max} having $x/b_1 = 4.35$ across the straight diffuser and curved diffusers (CDC_5, CDC_6, CDC_7 and CDC_8) at BEP and at an operational speed of 58.9rpsK$^{-1/2}$. It can be seen that C_p increases from CDC_5 to CDC_6 than decreases from CDC_6 to CDC_7 and it than increases from CDC_7 to CDC_8 across the curved diffusers in comparison to that across the straight diffuser. The area ratio is a function of r/r_{max}, θ/θ_{max} and x/b_1.

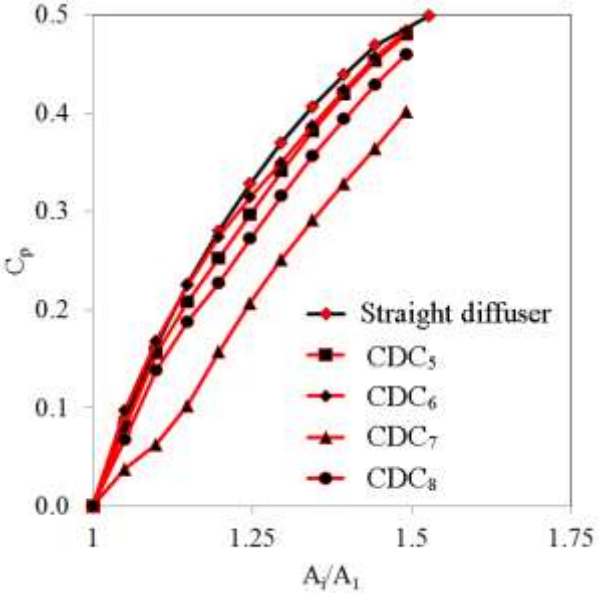

Figure 6.32: Variation in the coefficient of pressure C_p across the straight diffuser and curved diffuser configurations

6.4. Flow Field Characteristics within the Optimal Curved Diffuser

This section investigates the flow field within the optimal curved diffuser configuration without wall divergence based upon the static pressure, velocity magnitude and static temperature variations. These results are compared with straight diffuser (baseline model). The optimisation of a model is dependent upon maximum isentropic efficiency and total-to-total stage pressure ratio. Based upon the analysis carried out in the previous section, it has been observed that maximum stage performance is obtained by the curved diffuser is when geometrical parameters used are $x/b_1 = 3.03$, $\theta/\theta_{max} = 0.0$ and $r/r_{max} = 0.6$. It can be seen that isentropic efficiency of 71.79% and pressure ratio of 1.537 are increased by 1.19% and 0.65% respectively in comparison to that using straight diffuser (shown in Table 6.4). The detailed local flow field inside the compressor stage is presented hereafter.

Table 6.4: Comparison of performance parameters of straight diffuser and optimal curved diffuser

	x/b_1 (-)	θ/θ_{max} (-)	r/r_{max} (-)	PR_C (-)	η (%)	Percentage difference in PR_C (%)	Percentage difference in η (%)
Straight wall diffuser	1.0	0.0	-	1.527	70.93	-	-
Optimal curved diffuser model	3.03	0.0	0.6	1.537	71.79	0.65	1.19

Figure 6.33 depicts the static pressure variations across the centreline of the optimal curved diffuser configuration at BEP at an operational speed of 58.9rpsK$^{-1/2}$. The trend of the static pressure across the curved diffuser passage is similar to that across the straight diffuser. It can be seen that the minimum static pressure is obtained at the diffuser inlet after the volute-tongue region. The static pressure increases radially across the diffuser. Furthermore, the static pressure also increases circumferentially in the direction of impeller rotation (ω). The maximum static pressure is obtained at the diffuser outlet near the volute-tongue region. It can be seen that the static pressure is decreased by 0.75% at the diffuser inlet and same static pressure values are obtained at the diffuser outlet for the optimal curved diffuser in comparison to straight diffuser.

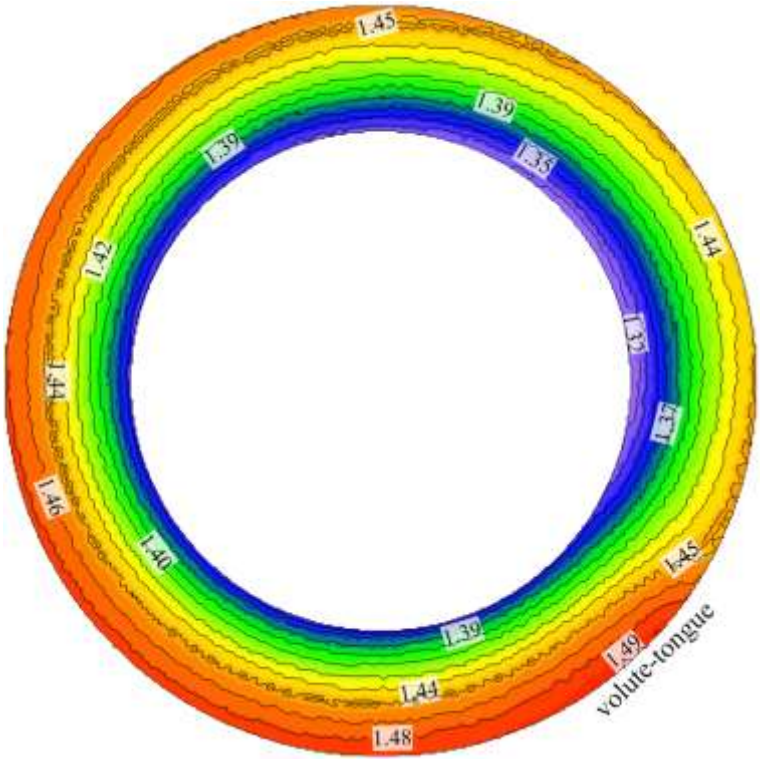

Figure 6.33: Static Pressure (atm) variations across the centreline of the optimal curved diffuser at BEP at an operational speed of 58.9rpsK$^{-1/2}$

Figure 6.34 depicts flow streamlines radially across the cross-section of straight diffuser and volute passage (baseline model) and optimal curved diffuser and oppositely interface volute at BEP and at an operational speed of 58.9rpsK$^{-1/2}$. It can be seen from the figure that no recirculation is found within straight diffuser and optimal curved diffuser and hence, no losses are being generated. The colour inside the passages shows the velocity magnitude within the diffuser and volute passages. The velocity is higher at the diffuser inlet and reduces radially across the diffusers.

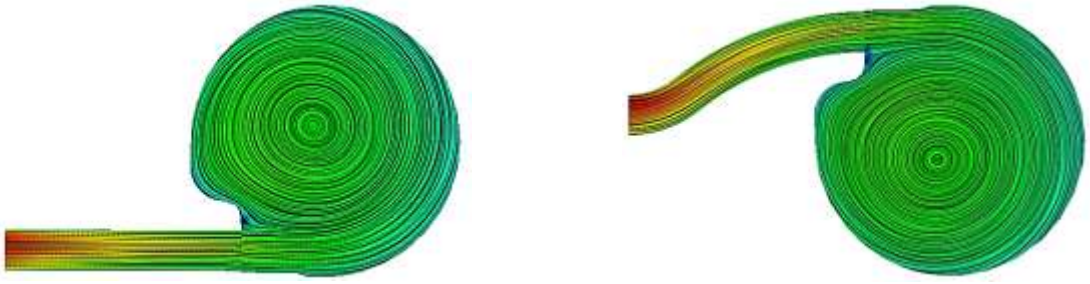

(a) (b)

Figure 6.34: Flow streamlines radially across the (a) straight diffuser and volute (baseline) and (b) optimal curved diffuser and oppositely interfaced volute at BEP and at an operational speed of 58.9rpsK$^{-1/2}$

Figure 6.35 depicts the comparison of velocity magnitude distribution across straight diffuser and the optimal curved diffuser configuration from the hub wall to the shroud wall at BEP and at an operational speed of 58.9rpsK$^{-1/2}$. It can be seen that the velocity magnitude is reduced radially across the optimal curved diffuser. It can also be seen that the velocity magnitude across optimal curved diffuser is higher in comparison to that across the straight diffuser. Furthermore, it has been observed that the velocity magnitude is asymmetric towards hub wall across the optimal curved diffuser in comparison to that across the straight diffuser, which has velocity magnitude asymmetric towards the shroud wall. However, the detailed analysis has been carried out by quantifying the local asymmetric ratio for the velocity magnitude profile across the optimal curved diffuser.

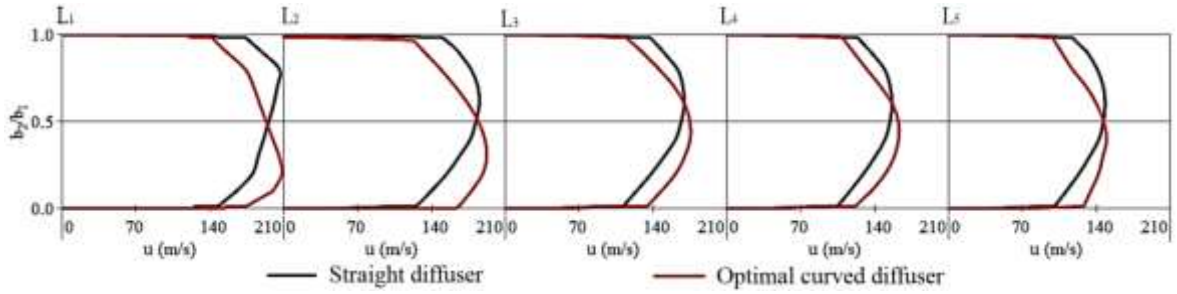

Figure 6.35: Comparison of velocity magnitude (m/s) distribution across the straight diffuser and the optimal curved diffuser from the hub wall to the shroud wall at BEP and at an operational speed of 58.9rpsK$^{-1/2}$

Figure 6.36 depicts the local asymmetric ratio for the velocity magnitudes, α_{vm} across the optimal curved diffuser at BEP and at an operational speed of 58.9rpsK$^{-1/2}$. It can be seen that the flow is asymmetric towards the hub wall across the curved diffusers. The asymmetric ratio for the velocity magnitude constantly increases from the centreline towards the wall of the diffuser. Furthermore, it can also be noticed that the local asymmetric ratio is decreased from L1 (diffuser inlet) to L2, then it is increased from L2 to L3 and then it again has decreased from L3 to L5 (diffuser outlet).

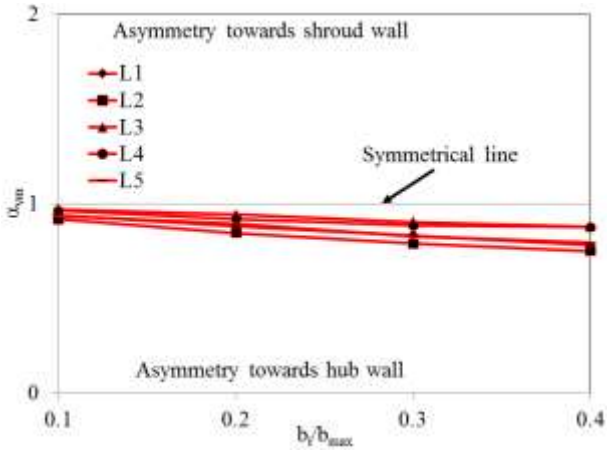

Figure 6.36: Local asymmetric ratio for the velocity magnitude, α_{vm} across the optimal curved diffuser at BEP and at an operational speed of 58.9rpsK$^{-1/2}$

Figure 6.37 depicts the radial velocity distribution across the centreline of the optimal curved diffuser configuration at BEP at an operational speed of 58.9rpsK$^{-1/2}$. The trend of the radial velocity across the optimal curved diffuser is similar to that across the straight diffuser. It can be seen that the maximum radial velocity is obtained at the diffuser inlet after the volute-tongue region. The radial velocity decreases radially across the diffuser. Furthermore, the radial velocity also decreases circumferentially in the direction of impeller rotation (ω). The minimum radial velocity is obtained at the diffuser outlet at near the volute-tongue region. It can be seen that the radial velocity is increased at the diffuser inlet and diffuser outlet by 10.5% and decreased at the diffuser outlet by 3.9% in comparison to that for the straight diffuser.

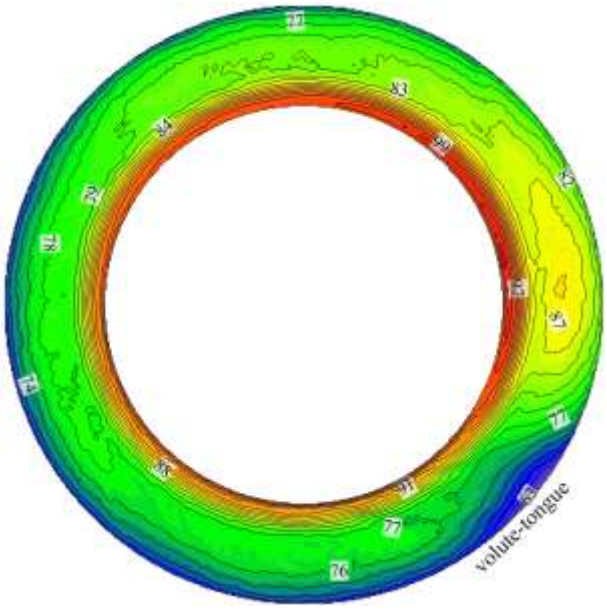

Figure 6.37: Radial velocity (m/s) distribution across the centreline of the optimal curved diffuser at BEP and at an operational speed of 58.9rpsK$^{-1/2}$

Figure 6.38 depicts the comparison of radial velocity distribution across the straight diffuser and the optimal curved diffuser from the hub wall to the shroud wall at BEP and at an operational speed of 58.9rpsK$^{-1/2}$. It can be seen that the radial velocity is reduced radially across the diffuser. It can also be seen that the radial velocity across optimal curved diffuser is higher in comparison to that across the straight diffuser. Furthermore, it has been observed that the radial velocity is asymmetric towards the hub wall across the optimal curved diffuser in comparison to that across the straight diffuser, which has radial velocity asymmetric towards the shroud wall. Moreover, radial velocity is highly

asymmetric towards the hub wall at L_1 (diffuser inlet) and then the asymmetry has reduced, and the flow has become symmetric at L_3. Thereafter, the flow again has become asymmetric after L_3 towards L_5 (diffuser outlet). However, the detailed analysis has been carried out by quantifying the asymmetric ratio for the radial velocity profile across the optimal curved diffuser.

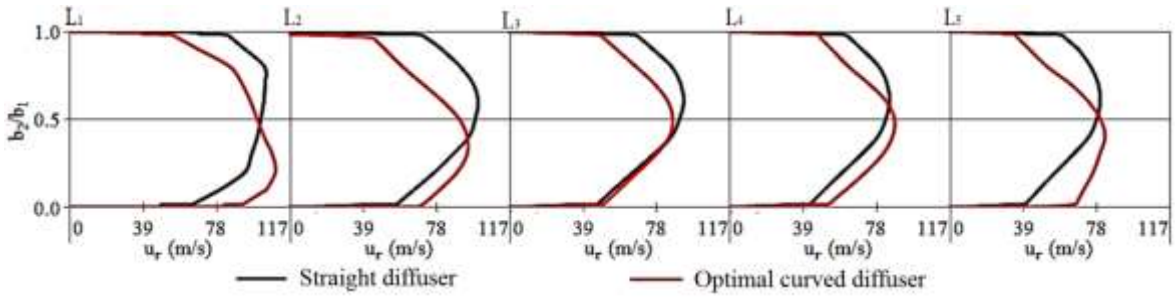

Figure 6.38: Comparison of radial velocity (m/s) distribution across the straight diffuser and the optimal curved diffuser from the hub wall to the shroud wall at BEP and at an operational speed of 58.9rpsK$^{-1/2}$

Figure 6.39 depicts the local asymmetric ratio for the radial velocity, α_{vr} across the optimal curved diffuser at BEP and at an operational speed of 58.9rpsK$^{-1/2}$. The radial flow velocity is asymmetric towards the hub wall from L_1 (diffuser inlet) to L_2, then the flow has become symmetric at L_3 and then the flow has again become asymmetric towards the hub wall from L_4 to L_5 (diffuser outlet).

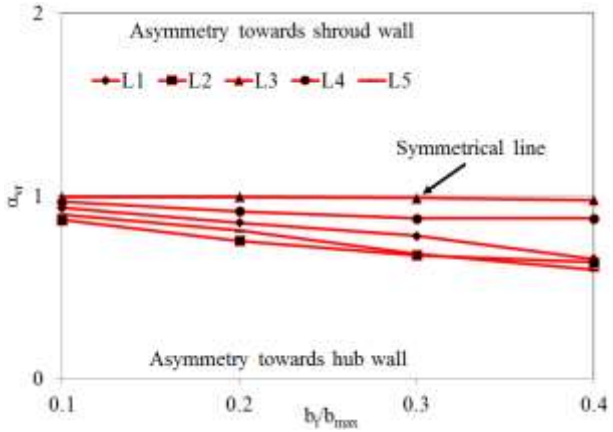

Figure 6.39: Local asymmetric ratio for the radial velocity, α_{vr} across the optimal curved diffuser at BEP and at an operational speed of 58.9rpsK$^{-1/2}$

Figure 6.40 depicts the circumferential velocity distribution across the centreline of the optimal curved diffuser at BEP and at an operational speed of 58.9rpsK$^{-1/2}$. The trend of the circumferential velocity across the optimal curved diffuser is similar to that across the straight diffuser. It can be seen

that the maximum circumferential velocity is obtained at the diffuser inlet after the volute-tongue region. The circumferential velocity decreases radially across the diffuser. Furthermore, the circumferential velocity also decreases circumferentially in the direction of impeller rotation (ω). The minimum circumferential velocity is obtained at the diffuser outlet at near the volute-tongue region. It can be seen that the circumferential velocity is increased at the diffuser inlet by 6.7% and decreased at the diffuser outlet by 4.2% of the optimal curved diffuser in comparison to that across the straight diffuser

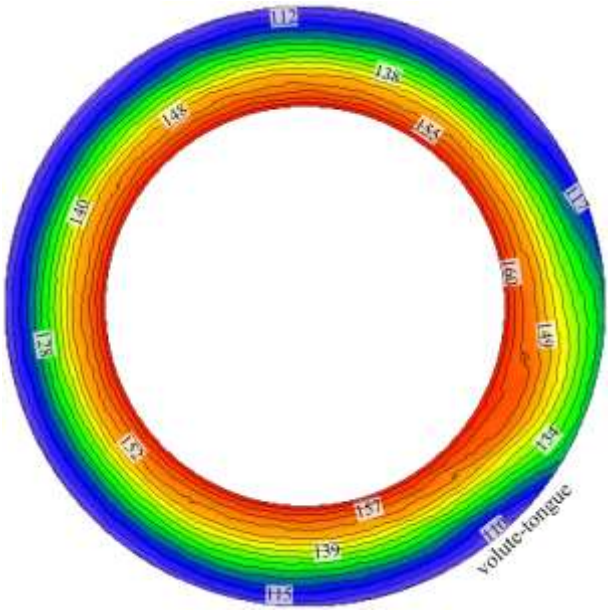

Figure 6.40: Circumferential velocity (m/s) distribution across the centreline of the optimal curved diffuser at BEP and at an operational speed of 58.9rpsK$^{-1/2}$

Figure 6.41 depicts the comparison of circumferential velocity distribution across the straight diffuser and the optimal curved diffuser from the hub wall to the shroud wall at BEP and at an operational speed of 58.9rpsK$^{-1/2}$. It can be seen that the circumferential velocity is reduced radially across the diffuser. It can also be seen that the circumferential velocity across the optimal curved diffuser is higher in comparison to that across the straight diffuser. Furthermore, it has been observed that the circumferential velocity is asymmetric towards hub wall across the optimal curved diffuser in comparison to that across the straight diffuser, which has asymmetric circumferential velocity towards the shroud wall. However, the detailed analysis has been carried out by quantifying the asymmetric ratio for the circumferential velocity profile across curved diffuser configurations.

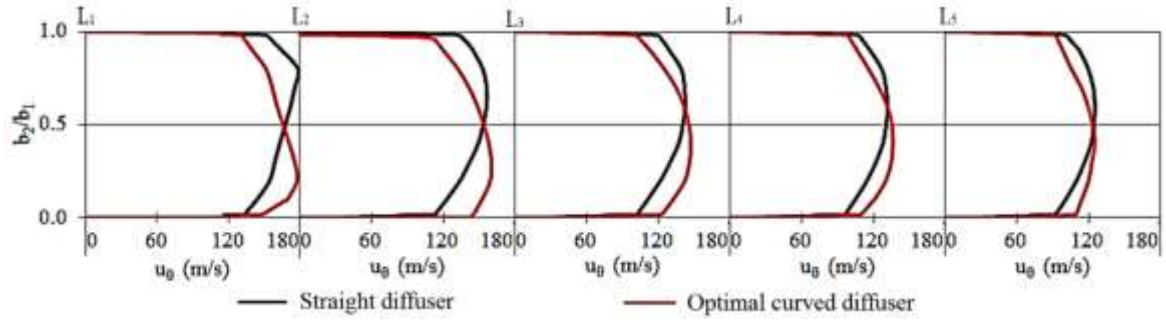

Figure 6.41: Comparison of circumferential velocity (m/s) distribution across the straight diffuser and the optimal curved diffuser from the hub wall to the shroud wall at BEP and at an operational speed of 58.9rpsK$^{-1/2}$

Figure 6.42 depicts the local asymmetric ratio for the circumferential velocity, α_{vc} across the optimal curved diffuser at BEP and at an operational speed of 58.9rpsK$^{-1/2}$. It can be seen that the flow is asymmetric towards the hub wall across optimal curved diffuser. The asymmetric ratio for the circumferential velocity constantly increases from the centreline of the diffuser towards the wall. Furthermore, it can also be seen that the local asymmetric ratio decreases from L_1 to L_2, then it increases from L_2 to L_4 and then it decreases L_4 to L_5.

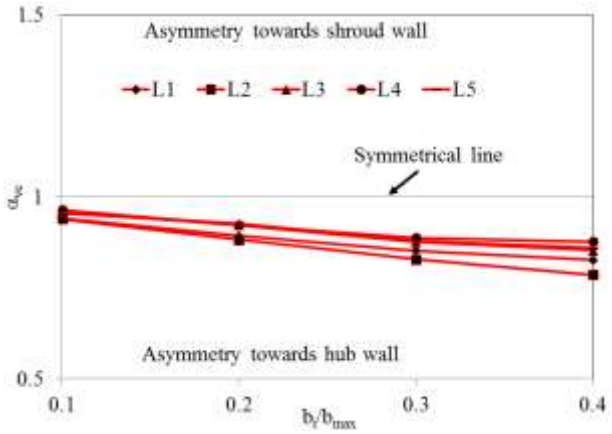

Figure 6.42: Local asymmetric ratio for the circumferential velocity, α_{vr} across the optimal curved diffuser at BEP and at an operational speed of 58.9rpsK$^{-1/2}$

Figure 6.43 depicts the static temperature variations across the centreline of the optimal curved diffuser at BEP and at an operational speed of 58.9rpsK$^{-1/2}$. The trend of the static temperature across the optimal curved diffuser is similar to that across the straight diffuser. It can be seen that the minimum static temperature is obtained at the diffuser inlet after the volute-tongue region. The static temperature increases radially across the diffuser. Furthermore, the static temperature also increases

circumferentially in the direction of impeller rotation (ω). The maximum static temperature is obtained at the diffuser outlet near the volute-tongue region. It can be seen that the static temperature is decreased by 0% and 0.3% at the diffuser inlet and diffuser outlet respectively across the optimal curved diffuser in comparison to that across the straight diffuser.

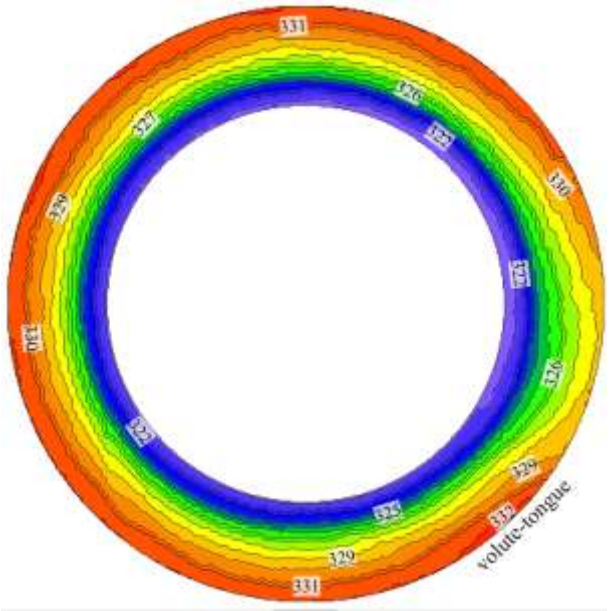

Figure 6.43: Static temperature (K) variations across the centreline of the optimal curved diffuser at BEP at an operational speed of 58.9rpsK$^{-1/2}$

6.4.1. Effect of Flow Assemetry on the Performance of the Optimal Curved Diffuser

The behaviour of the flow within the optimal curved diffuser is highly dependent upon the geometrical parameter considered. It has been noticed in the previous section that increase of ratio of r/r_{max} and θ/θ_{max} increases the asymmetry of the flow towards the hub wall of the curved diffuser. However, increase of ratio of x/b_1 increases the asymmetric ratio, which shifts the flow from hub wall towards the shroud wall. An Equation 4.1 is used to obtain the global asymmetric ratio, which shows the change in behaviour of the flow across the curved diffuser and the global effect of the asymmetry across the curved diffuser. The major effect of geometrical parameters on the asymmetric flow behaviour and stage performance is described in detail.

Figure 6.44 depicts the global asymmetric ratio for the velocity magnitude across the straight diffuser and the optimal curved diffuser at BEP and at an operational speed of 58.9rpsK$^{-1/2}$. It can be seen that the global asymmetric ratio across the optimal curved diffuser is towards the hub wall of the diffuser in comparison to that across the straight diffuser, which has global asymmetric ratio towards the

shroud wall. The global asymmetric ratio for the velocity magnitudes is seemed to be decreased from L_1 (diffuser inlet) to L_2, then increased from L_2 to L_3 and then finally decreased from L_3 to L_5 (diffuser outlet).

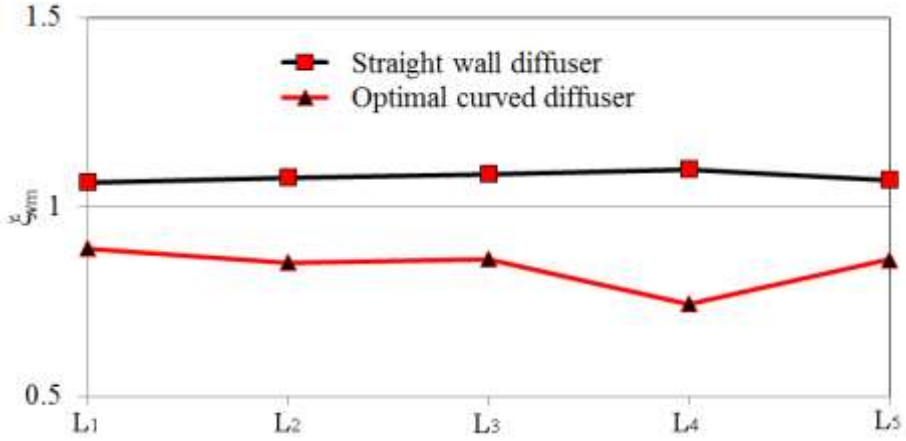

Figure 6.44: Global asymmetric ratio for the velocity magnitude across the straight diffuser and the optimal curved diffuser at BEP and at an operational speed of 58.9rpsK$^{-1/2}$

Figure 6.45 depicts the global asymmetric ratio for the radial velocity across the straight diffuser and the optimal curved diffuser at BEP and at an operational speed of 58.9rpsK$^{-1/2}$. It can be seen that the global asymmetric ratio across the optimal curved diffuser is towards the hub wall in comparison to that across the straight diffuser, which has global asymmetric ratio towards the shroud wall. The global asymmetric ratio for the velocity magnitudes is seemed to be decreased from L_1 (diffuser inlet) to L_2, then increased from L_2 to L_3 and then finally decreased from L_3 to L_5 (diffuser outlet).

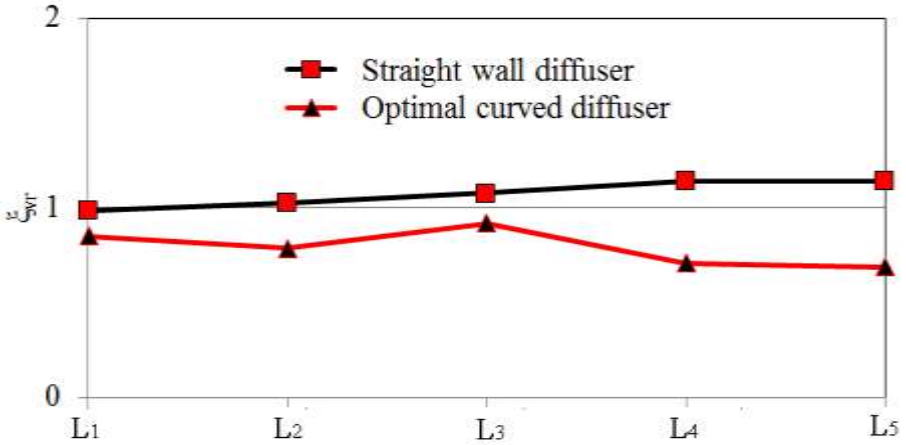

Figure 6.45: Global asymmetric ratio for the radial velocity across the straight diffuser and the optimal curved diffuser at BEP and at an operational speed of 58.9rpsK$^{-1/2}$

Figure 6.46 depicts the global asymmetric ratio for the circumferential velocity across the straight diffuser and the optimal curved diffuser at BEP and at an operational speed of 58.9rpsK$^{-1/2}$. It can be seen that the global asymmetric ratio across the optimal curved diffuser is towards the hub wall in comparison to that across the straight diffuser, which has global asymmetric ratio towards the shroud wall. The global asymmetric ratio for the velocity magnitudes is seemed to be decreased from L_1 (diffuser inlet) to L_2, then increased from L_2 to L_3 and then finally global asymmetric ratio remains same from L_3 to L_5 (diffuser outlet).

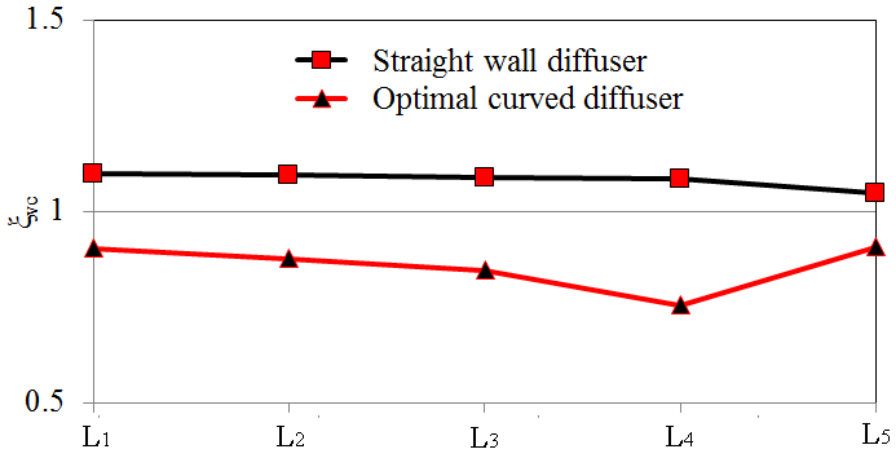

Figure 6.46: Global asymmetric ratio for the circumferential velocity across the straight diffuser and the optimal curved diffuser at BEP and at an operational speed of 58.9rpsK$^{-1/2}$

It is concluded from the above results that the flow is asymmetrical across straight diffuser and optimal curved diffuser. It has been noticed that the variations in the asymmetry are due to r/r_{max}, θ/θ_{max} and x/b_1. In order to understand the overall effect of the geometrical effect on the diffuser flow field and stage performance, the equation 4.2 is used.

Figure 6.47 depicts the comparison of the diffuser asymmetric effect for the velocity magnitude across the straight diffuser and optimal curved diffuser at BEP and at an operational speed of 58.9rpsK$^{-1/2}$. It can be seen that the asymmetric effect for the velocity magnitude is below 1 for optimal curved diffuser showing the flow is asymmetric towards the hub wall in comparison to that of straight diffuser having flow asymmetry towards the shroud wall. Furthermore, it can also be seen that the stage efficiency of optimal curved diffuser is increased to 71.79% in comparison to that across the straight diffuser having stage efficiency of 70.9%.

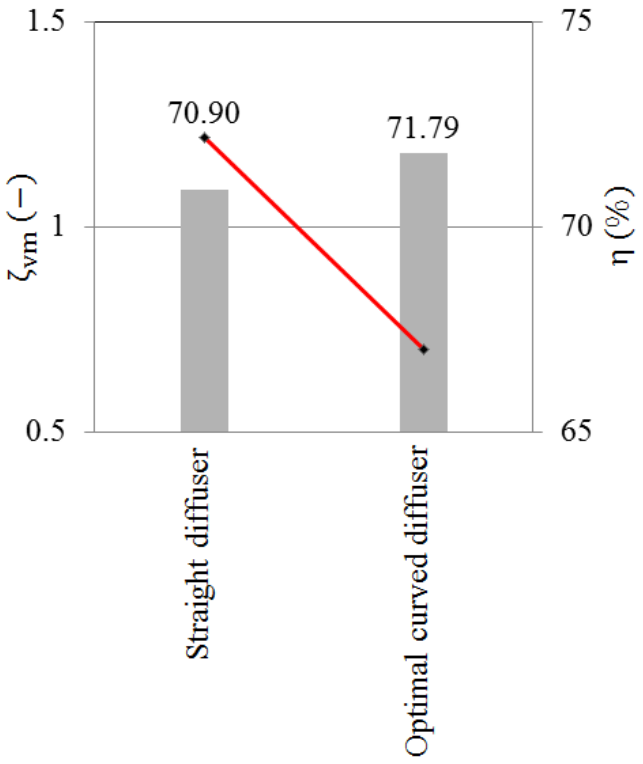

Figure 6.47: Comparison of diffuser asymmetric effect for velocity magnitude across the straight diffuser and optimal curved diffuser at BEP and at the operational speed of 58.9rpsK$^{-1/2}$

Figure 6.48 depicts the comparison of the diffuser asymmetric effect for the radial velocity across the straight diffuser and optimal curved diffuser at BEP and at an operational speed of 58.9rpsK$^{-1/2}$. It can be seen that the asymmetric effect for the radial velocity is below 1 for optimal curved diffuser showing the flow is asymmetric towards the hub wall in comparison to that of straight diffuser having flow asymmetry towards the shroud wall. Furthermore, it can also be seen that the stage efficiency of optimal curved diffuser is increased to 71.79% in comparison to that across the straight diffuser having stage efficiency of 70.9%.

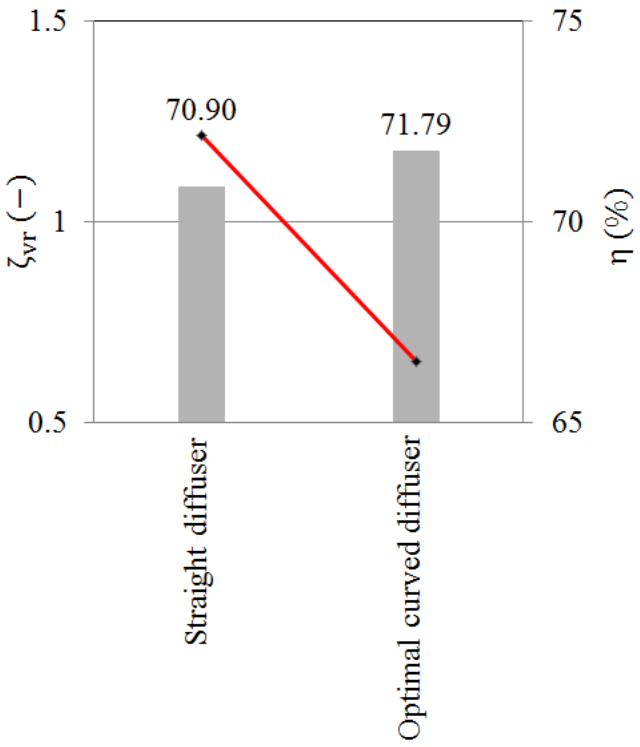

Figure 6.48: Comparison of diffuser asymmetric effect for radial velocity across the straight diffuser and optimal curved diffuser at BEP and at the operational speed of 58.9rpsK$^{-1/2}$

Figure 6.49 depicts the comparison of the diffuser asymmetric effect for the circumferential velocity across the straight diffuser and optimal curved diffuser at BEP and at an operational speed of 58.9rpsK$^{-1/2}$. It can be seen that the asymmetric effect for the circumferential velocity is below 1 for optimal curved diffuser showing the flow is asymmetric towards the hub wall in comparison to that of straight diffuser having flow asymmetry towards the shroud wall. Furthermore, it can also be seen that the stage efficiency of optimal curved diffuser is increased to 71.79% in comparison to that across the straight diffuser having stage efficiency of 70.9%.

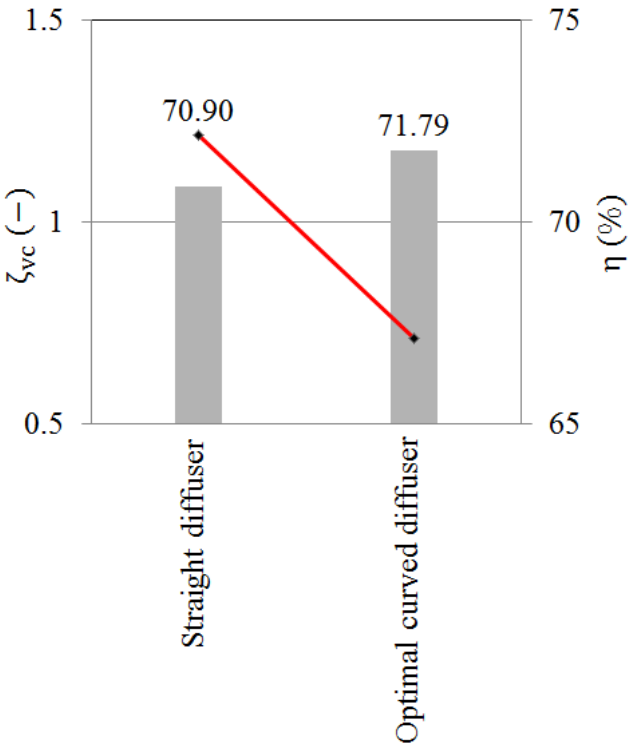

Figure 6.49: Comparison of diffuser asymmetric effect for circumferential velocity across the straight diffuser and optimal curved diffuser at BEP and at the operational speed of 58.9rpsK$^{-1/2}$

This section demonstrates the comparison of optimal curved diffuser and straight diffuser on the basis of diffuser geometries used. The diffuser performance is dependent upon the recovery of static pressure across the diffuser.

Three geometrical parameters x/b_1, r/r_{max} and θ/θ_{max} have used to modify the optimal curved diffuser geometry. This configuration has affected the diffuser performance. Figure 6.50 depicts the variation in the coefficient of pressure C_p having $x/b_1 = 3.03$, $\theta/\theta_{max} = 0.0$ and $r/r_{max} = 0.6$ of the optimal curved diffuser and straight diffuser at BEP and at an operational speed of 58.9rpsK$^{-1/2}$. It can be seen that C_p almost remains similar across the optimal curved diffuser and straight diffuser. The area ratio is a function of r/r_{max}, θ/θ_{max} and x/b_1.

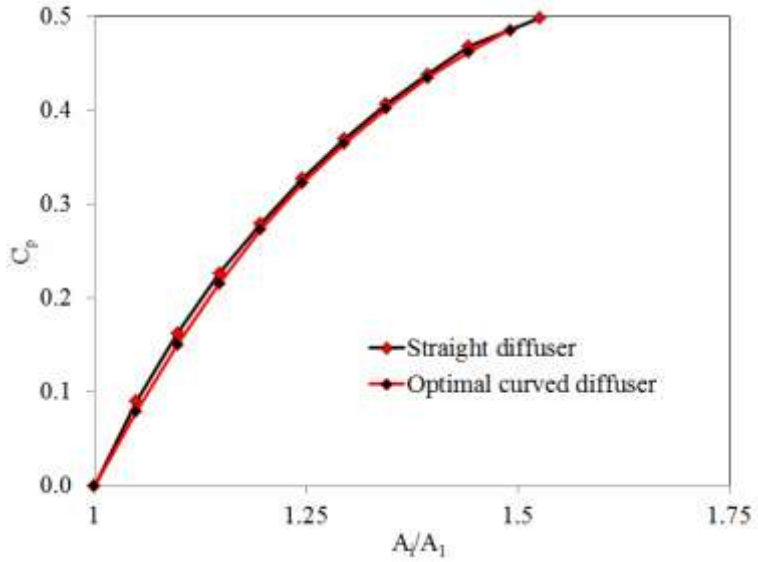

Figure 6.50 Variation in the coefficient of pressure C_p across the straight diffuser and optimal curved diffuser

6.5. Description of Compressor Model using Diverged Wall Curved Diffuser Model

Many researchers have carried out various investigations to improve the compressor stage performance either by pinching, converging or diverging the diffuser walls as described in Chapter 2 of the thesis. Similar approach is used in this section as well to identify the effects of the wall divergence on the curved diffuser to obtain the performance of the compressor stage. Furthermore, in this study the effect of wall divergence on the local flow variations are also investigated. This methodology has helped to enhance the compressor stage performance while compacting the compressor using curved diffuser. Parametric investigations have been carried out to analyse the flow field characteristics within the diverged wall curved diffuser. To carry out the parametric investigations a Full Factorial based Design of Experiments (DoE) technique has been employed in the present study to determine the possible practical combinations of the geometrical parameters. Minitab 17 Statistical Software has been used in the present study to carry out Full Factorial based DoE studies, where a practical range of different parameters has been specified. The factors/parameters considered for the diffuser configurations, along with their levels, have been summarised in the Table 6.5. Furthermore, a sample design of diverged wall curved diffuser has also been presented in Figure 6.51. It can be seen that the hub wall is diverged from the diffuser inlet to one-fifth of the diffuser and is applied on the circumference of the diffuser. Furthermore, the diffuser outlet width has increased up to 1.4 of the diffuser inlet width. The diffuser outlet width cannot be extended more than 1.4 because of the limitation on the volute inlet section. The results obtained from the diverged wall curved diffuser have been compared with the parallel wall diffuser to investigate

the performance improvement within the compressor stage. Based upon the Full Factorial based DoE 24 number of numerical simulations has been required to carry out this parametric investigation. The total-to-total pressure ratio and isentropic efficiency have been recorded for each simulation. Best design model has been chosen based upon the highest localised isentropic efficiency within the compressor stage, which is the function of various geometrical and flow parameters.

Table 6.5: Factors and levels for full factorial design of diffuser configurations

Factors	Level 1	Level 2	Level 3	Level 4	Level 5	Level 6
L/L_{max}	0.0	0.1	0.2	0.3	0.4	0.5
b_2/b_1	1.1	1.2	1.3	1.4	-	-

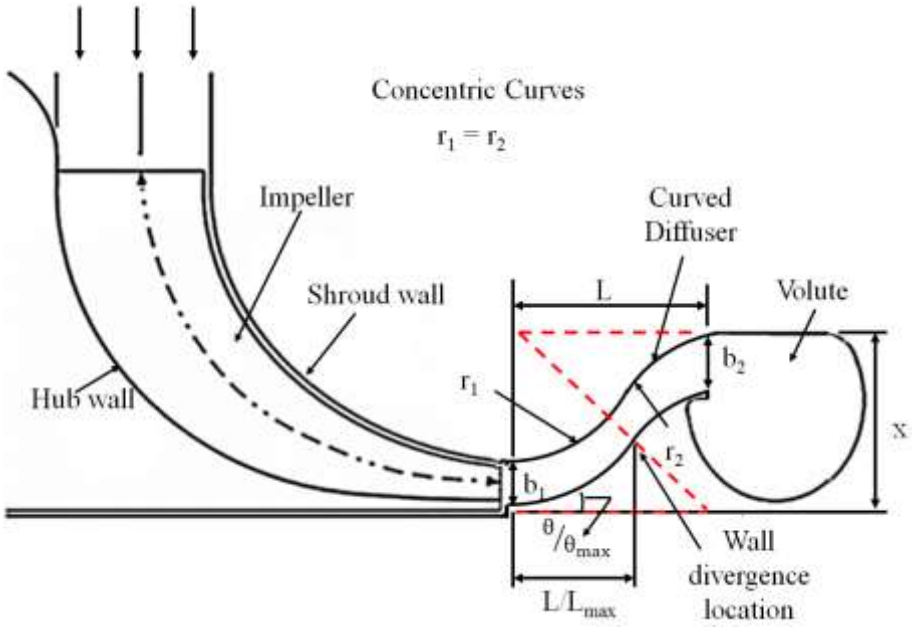

Figure 6.51: Sample configuration of the diverged wall curved diffuser

6.6. Performance Characteristics of Compressor Stage using Diverged Wall Curved Diffuser

Numerical analysis has been carried out to obtain the total-to-total stage performance and flow field characteristics across various configurations of the diverged wall curved diffuser have been analysed. Table 6.6 shows the results obtained from numerical simulations of CFD for the global parameters of all 24 configurations. Two geometrical parameters are considered, divergence location from the inlet on the hub wall and the diffuser outlet-to-inlet width ratio to analyse the effect on the local flow field and on the total-to-total stage performance. It can be seen from the Table 6.6 that a small increase of outlet-to-inlet width ratio causes decrease in the pressure ratio and the isentropic efficiency. Furthermore, change in the location of wall divergence from 0.0 to 0.3 increases the stage

performance and then the performance decreases. Moreover, local flow field analysis has been carried out in the later sections that explain the flow field details within the diffuser to obtain the local effects. It is concluded from the results that the combined effect all two geometrical parameters give maximum stage performance of 72.20% isentropic efficiency and 1.542 total-to-total stage pressure ratio at $L/L_{max} = 0.3$ and $b_2/b_1 = 1.2$.

Table 6.6: CFD results of centrifugal compressor stage using different configurations of diverged wall curved diffuser

Parameters	Divergence location from the inlet on the hub wall, L/L_{max}	Diffuser outlet-to-inlet width ratio, b_2/b_1	Pressure Ratio, PR_C	Isentropic efficiency, η
Configuration No.	(-)	(-)	(-)	(%)
Straight wall diffuser	0.0	0.0	1.527	70.9
Curved wall diffuser	0.0	0.0	1.537	71.8
1	0.0	1.1	1.542	72.2
2		1.2	1.540	71.9
3		1.3	1.539	71.8
4		1.4	1.532	71.0
5	0.1	1.1	1.541	72.1
6		1.2	1.541	72.1
7		1.3	1.535	71.4
8		1.4	1.528	70.6
9	0.2	1.1	1.541	72.1
10		1.2	1.540	72.0
11		1.3	1.540	71.9
12		1.4	1.526	70.3
13	0.3	1.1	1.542	72.1
14		1.2	1.542	72.4
15		1.3	1.539	71.9
16		1.4	1.533	71.2
17	0.4	1.1	1.540	72.0
18		1.2	1.541	72.1
19		1.3	1.536	71.5
20		1.4	1.531	70.9
21	0.5	1.1	1.541	72.2
22		1.2	1.539	71.8
23		1.3	1.536	71.4
24		1.4	1.534	71.4

6.6.1. Flow Field Characteristics within the Diverged Wall Curved Diffuser

This section demonstrates the flow field analyses within the diverged wall curved diffuser based upon static pressure, velocity magnitude, circumferential velocity, radial velocity and static temperature variations. The analyses have been carried out in such a way that firstly the effect of outlet-to-inlet diffuser width ratio has been investigated by considering configurations having same wall divergence from the diffuser inlet. Thereafter, the effect of the wall divergence at different locations on the hub wall from the diffuser inlet has been investigated by considering those configurations' maximum diffuser outlet-to-inlet width ratio. Finally, the combined effects of the wall divergence at different locations on the shroud wall from the diffuser inlet and the diffuser outlet-to-inlet width ratio have been investigated. The combinations considered to analyse the flow performance within the diverged wall curved diffuser of the compressor stage are mentioned in Table 6.7 with their names. These investigations have helped the author to quantify the effects of geometrical parameters on the local flow field within the diverged wall curved diffuser. Furthermore, the effect of wall divergence on the flow asymmetry within the diffuser has been quantified to establish a relationship of wall divergence with asymmetric effect and isentropic efficiency.

Table 6.7: Practical combinations selected for the flow field analysis

Analysis Procedure	Names	L/L_{max} (-)	b_2/b_1 (-)
First Set	$DWCD_1$	0.0	1.1
	$DWCD_2$	0.0	1.4
Second Set	$DWCD_3$	0.5	1.1
	$DWCD_4$	0.5	1.4
Third Set	$DWCD_5$	0.0	1.1
	$DWCD_6$	0.2	1.2
	$DWCD_7$	0.4	1.3
	$DWCD_8$	0.5	1.4

Note:
$DWCD_1 = DWCD_5$
$DWCD_4 = DWCD_8$

Figure 6.52 depicts the static pressure variations across the centreline of the Diverged Wall Curved Diffuser (DWCD) configurations ($DWCD_1$ and $DWCD_2$) at BEP and at an operational speed of $58.9 rpsK^{-1/2}$. The trend of the static pressure across the diverged wall curved diffuser is similar to that across the straight diffuser. It can be seen that the minimum static pressure is obtained at the diffuser

inlet after the volute-tongue region. The static pressure increases radially across the diffuser. Furthermore, the static pressure also increases circumferentially in the direction of impeller rotation (ω). The maximum static pressure is obtained at the diffuser outlet at near the volute-tongue region. It can be seen that the static pressure is increased at the diffuser inlet by 1.5% and is same at the diffuser outlet of $DWCD_1$ in comparison to that of the straight diffuser. Furthermore, it can also be seen that the static pressure is decreased at the diffuser inlet and the diffuser outlet by 1.5% and 1.3% of $DWCD_2$ in comparison to that of $DWCD_1$. This trend explains that the static pressure decreases when outlet-to-inlet width ratio of the diffuser is increased by keeping the divergence location at the diffuser inlet.

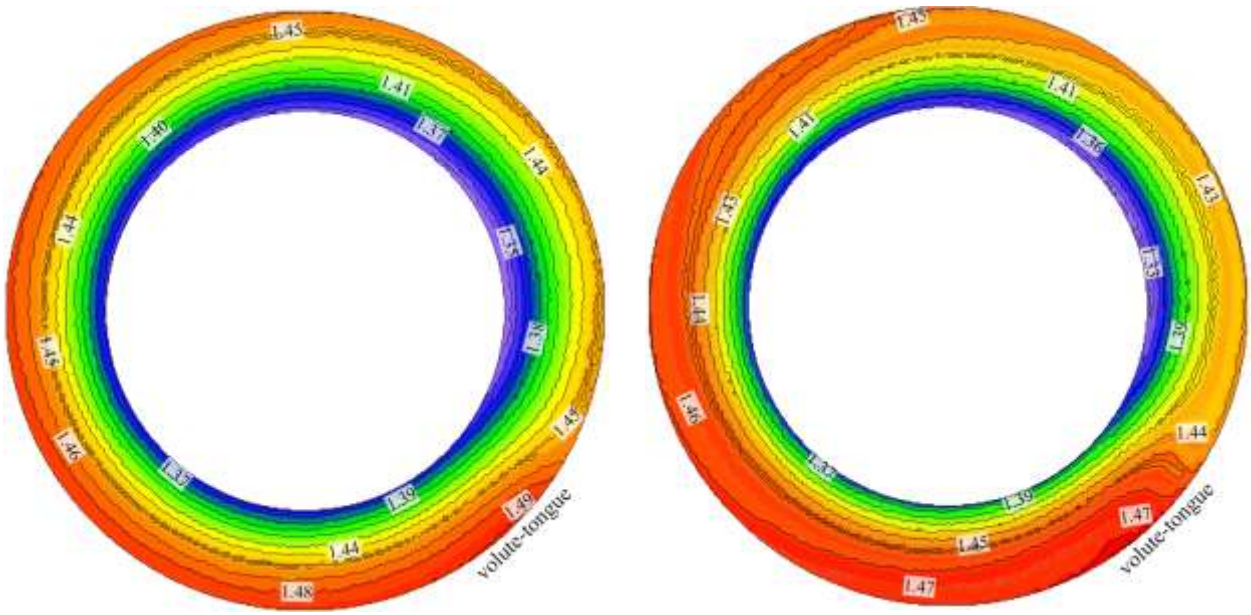

(a) (b)

6.52: Static pressure (atm) variations across the centreline of the diverged wall curved diffusers (a) $DWCD_1$ and (b) $DWCD_2$ at BEP and at an operational speed of 58.9rpsK$^{-1/2}$

Figure 6.53 depicts the static pressure variations across the centreline of the diverged wall curved diffuser configurations ($DWCD_3$ and $DWCD_4$) at BEP and at an operational speed of 58.9rpsK$^{-1/2}$. The trend of the static pressure across the diverged wall curved diffuser configurations is similar to that across the straight diffuser. It can be seen that the minimum static pressure is obtained at the diffuser inlet after the volute-tongue region. The static pressure increases radially across the diffuser. Furthermore, the static pressure also increases circumferentially in the direction of impeller rotation (ω). The maximum static pressure is obtained at the diffuser outlet at near the volute-tongue region. It can be seen that the static pressure is increased at the diffuser inlet by 0.75% and is same at the

diffuser outlet of $DWCD_3$ in comparison to that of the straight diffuser. Furthermore, it can also be seen that the static pressure is decreased at the diffuser inlet and the diffuser outlet by 1.5% and 1.3% respectively of $DWCD_4$ in comparison to that of $DWCD_3$. This trend explains that the static pressure decreases when outlet-to-inlet width ratio of the diffuser is increased by keeping the divergence location at 50% distance of the diffuser length from the diffuser inlet.

(a) (b)

Figure 6.53: Static pressure (atm) variations across the centreline of the diverged wall curved diffuser (a) $DWCD_3$ and (b) $DWCD_4$ at BEP and at an operational speed of 58.9rpsK$^{-1/2}$

Figure 6.54 depicts the static pressure variations across the centreline of the diverged wall curved diffuser configurations ($DWCD_5$, $DWCD_6$, $DWCD_7$ and $DWCD_8$) at BEP and at an operational speed of 58.9rpsK$^{-1/2}$. The trend of the static pressure across the diverged wall curved diffuser configurations is similar to that across the straight diffuser. It can be seen that the minimum static pressure is obtained at the diffuser inlet after the volute-tongue region. The static pressure increases radially across the diffuser. Furthermore, the static pressure also increases circumferentially in the direction of impeller rotation (ω). The maximum static pressure is obtained at the diffuser outlet at near the volute-tongue region. It can be seen that the static pressure is increased at the diffuser inlet by 1.5% and is same at the diffuser outlet of $DWCD_5$ in comparison to that of the straight diffuser. Furthermore, the static pressure is decreased at the diffuser inlet of $DWCD_6$, $DWCD_7$ and $DWCD_8$ by 2.2%, 3% and 2.2% respectively in comparison to that of $DWCD_5$. Similarly, the static pressure is also decreased at the diffuser outlet of $DWCD_6$, $DWCD_7$ and $DWCD_8$ by 0.7%, 2% and 1.3% respectively in comparison

to that of $DWCD_5$. It can be concluded from this trend that combined increase of L/L_{max} and b_2/b_1 decreases the static pressure across the diverged wall curved diffuser configurations.

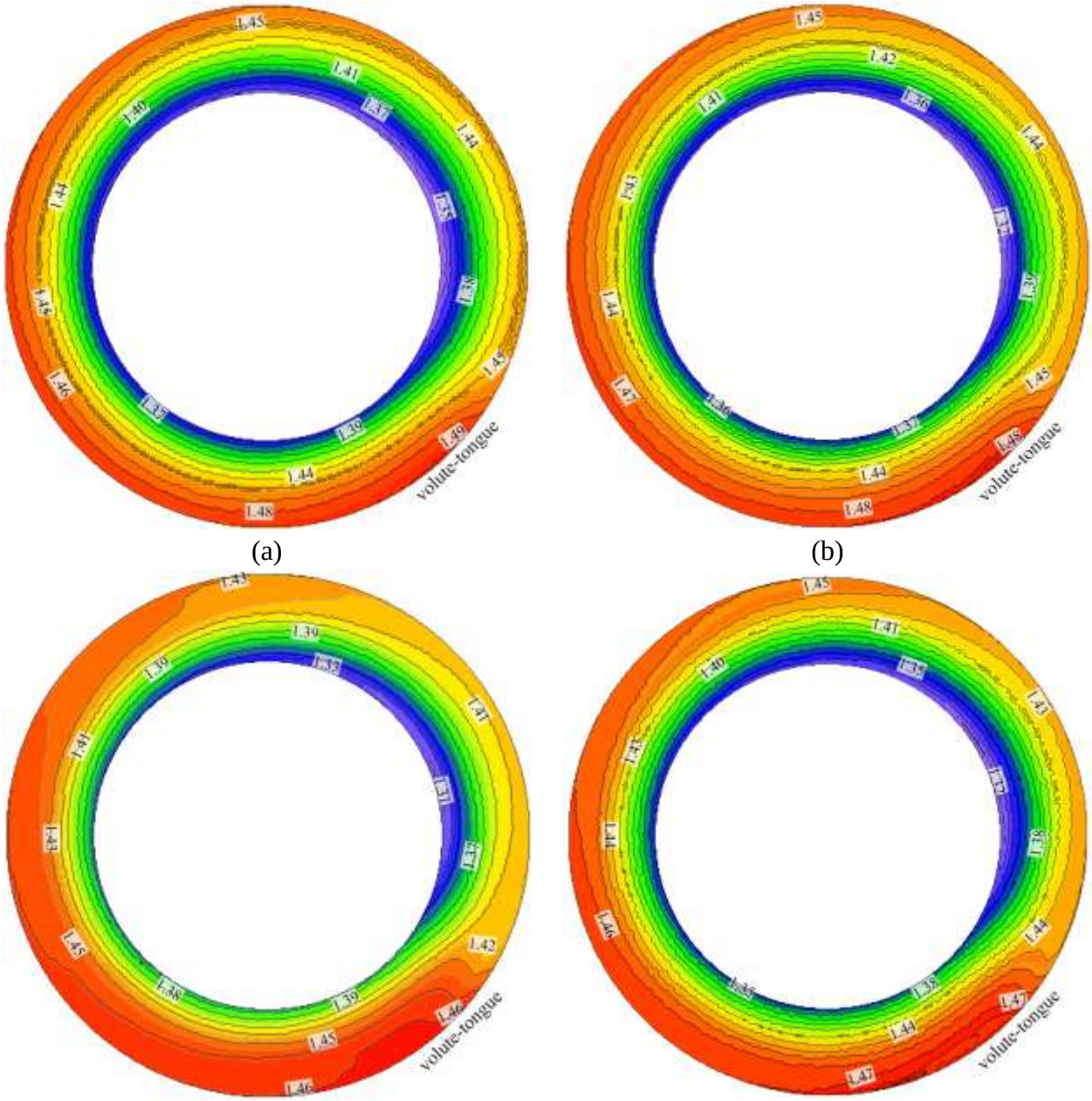

Figure 6.54: Static pressure (atm) variations across the centreline of the diverged wall curved diffuser (a) $DWCD_5$, (b) $DWCD_6$, (c) $DWCD_7$ and (d) $DWCD_8$ at BEP and at an operational speed of $58.9 rpsK^{-1/2}$

Figure 6.55 depicts the flow streamlines radially across straight diffuser, optimal curved diffuser and diverged wall curved diffuser configurations ($DWCD_1$, $DWCD_2$, $DWCD_3$, $DWCD_6$, $DWCD_7$ and $DWCD_8$) at BEP and at an operational speed of $58.9 rpsK^{-1/2}$. It can be seen from the Figure 6.55(a) and Figure 6.55(b) that the flow streamlines within the straight diffuser and the optimal curved diffuser are uniform, with no flow reversals. Similar flow behaviour is obtained across diverged wall curved diffusers of $DWCD_1$, $DWCD_3$ and $DWCD_6$, whereby the maximum outlet-to-inlet width ratio reaches upto 1.2. It can be seen that when the outlet-to-inlet width ratio is either 1.3 or 1.4, there are flow reversals introduced within the diverged wall curved diffuser near the diffuser outlet close to the diffuser hub wall (as shown in Figure 6.55(d), Figure 6.55(g) and Figure 6.55(h)). Furthermore, it has also been noticed that increase of L/L_{max} ratio reduces the size of flow reversals area (as shown in Figure 6.55(g) and Figure 6.55(h). Moreover, it has also been noticed that the size of flow reversals in curved diffuser is much smaller in comparison to that across diverged wall straight diffusers shown in Chapter 4. Since these analyses are qualitative based, which has provided an overview of the flow structure within the diverged wall curved diffusers, however, the detailed quantitative analyses are discussed in the next sections.

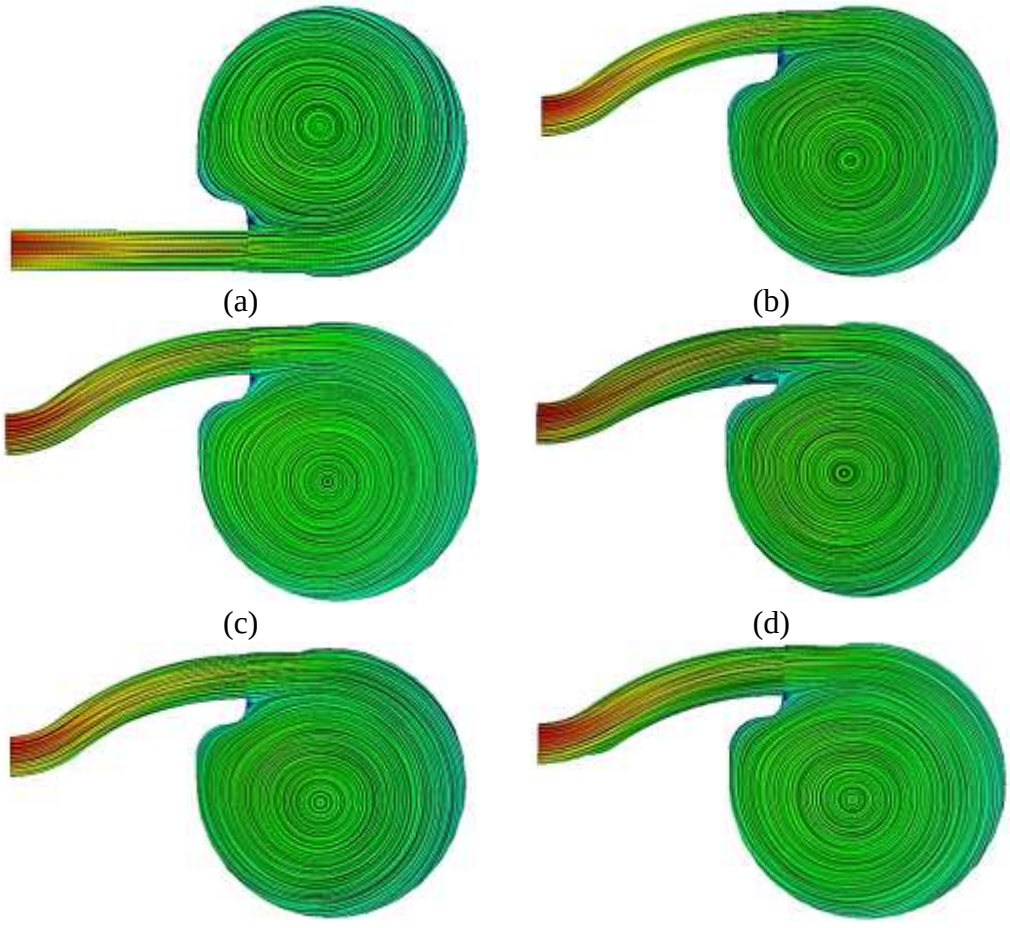

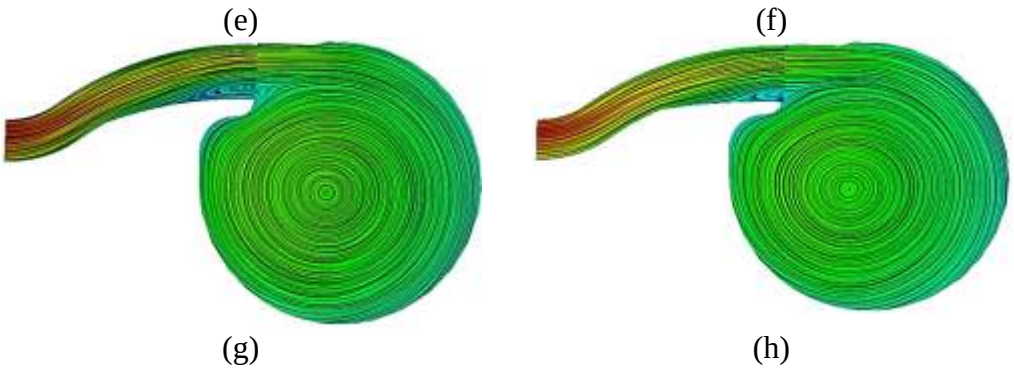

6.55: Flow streamlines radially across the (a) straight diffuser (b) optimal curved diffuser and diverged wall curved diffuser configurations ((c) $DWCD_1$, (d) $DWCD_2$, (e) $DWCD_3$, (f) $DWCD_6$, (g) $DWCD_7$, and (h) $DWCD_8$) interfaced with volute at BEP and at an operational speed of $58.9rpsK^{-1/2}$

Figure 6.56 depicts the comparison of velocity magnitude distribution across straight diffuser and diverged wall curved diffuser configurations ($DWCD_1$ and $DWCD_2$) from the hub wall to the shroud wall at BEP and at an operational speed of $58.9rpsK^{-1/2}$. It can be seen that the velocity magnitude is reduced radially across the diffuser. It can also be seen that the velocity magnitude across diverged wall curved diffusers is higher in comparison to that across the straight diffuser. Furthermore, it has been observed that the velocity magnitude is asymmetric towards the hub wall across diverged wall curved diffusers in comparison to that across straight diffuser, which has asymmetric velocity magnitude towards the shroud wall. However, the detailed analysis has been carried out by quantifying the asymmetric ratio for the velocity magnitude profile across the curved diffuser configurations.

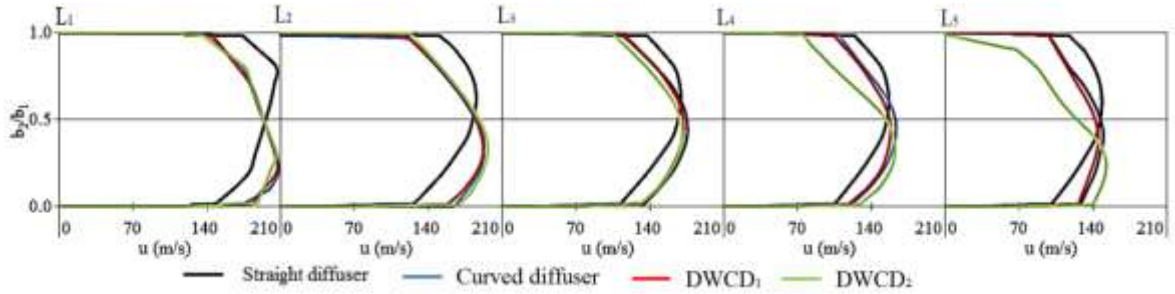

Figure 6.56: Comparison of velocity magnitude (m/s) distribution across the straight diffuser, optimal curved diffuser and diverged wall curved diffuser configurations ($DWCD_1$ and $DWCD_2$) from the hub wall to the shroud wall at BEP and at an operational speed of 58.9rpsK$^{-1/2}$

The behaviour of velocity magnitude across the diverged wall straight diffuser is explained using symmetric and asymmetric behaviour of the velocity field profiles. Figure 6.57 depicts the local asymmetric ratio for the velocity magnitudes, α_{vm} across the diverged wall diffusers ($DWCD_1$ and $DWCD_2$) at BEP and at an operational speed of 58.9rpsK$^{-1/2}$. α_{vm} values of 1.0 shows the flow is symmetric, α_{vm} values below 1.0 shows asymmetric flow towards the hub wall and α_{vm} values above 1.0 shows asymmetric flow towards the shroud wall. It can be seen that the flow is asymmetric towards the hub wall across the diverged wall curved diffuser. The asymmetric ratio for the velocity magnitude decreases from the centreline of the diffuser towards the wall. Moreover, the asymmetric ratio for the velocity magnitude also decreases from L_1 (diffuser inlet) to L_2, then increases from L_2 to L_3 and then it decreases from L_3 to L_5 (diffuser outlet) across both diverged wall curved diffusers considered. However, it has been noticed that increase of outlet-to-inlet width ratio by considering same wall diverged location from the inlet makes the flow highly asymmetrical.

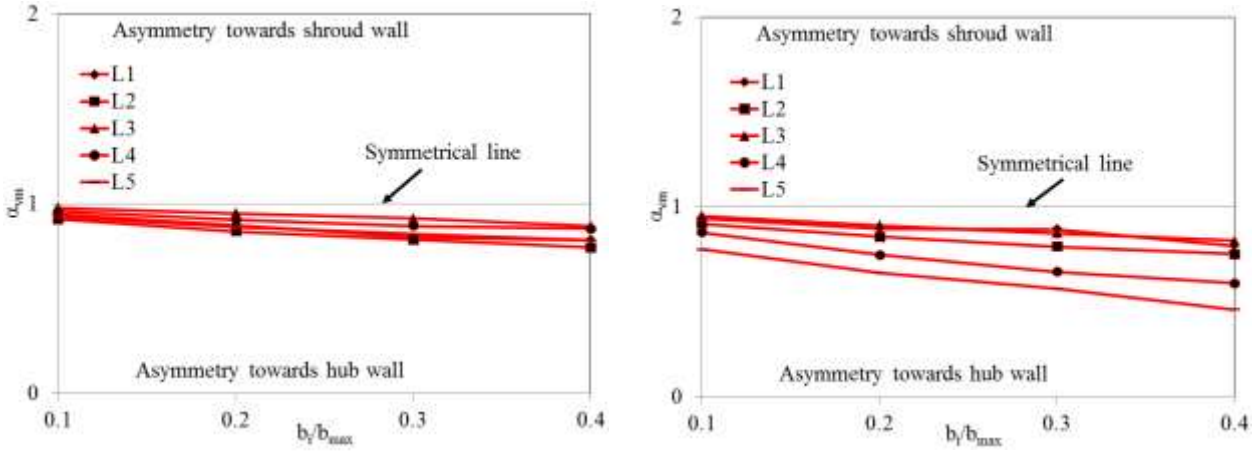

Figure 6.57: Local asymmetric ratio for the velocity magnitude, α_{vm} across the diverged wall diffusers ((a) $DWCD_1$ and (b) $DWCD_2$) at BEP and at an operational speed of 58.9rpsK$^{-1/2}$

Figure 6.58 depicts the comparison of velocity magnitude distribution across straight diffuser and diverged wall curved diffuser configurations ($DWCD_3$ and $DWCD_4$) from the hub wall to the shroud wall at BEP and at an operational speed of 58.9rpsK$^{-1/2}$. It can be seen that the velocity magnitude is reduced radially across the diffuser. It can also be seen that the velocity magnitude across diverged wall curved diffusers is higher in comparison to that across the straight diffuser. Furthermore, it has

been observed that the velocity magnitude is asymmetric towards the hub wall across diverged wall curved diffusers in comparison to that across straight diffuser, which has asymmetric velocity magnitude towards the shroud wall. However, the detailed analysis has been carried out by quantifying the asymmetric ratio for the velocity magnitude profile across the curved diffuser configurations.

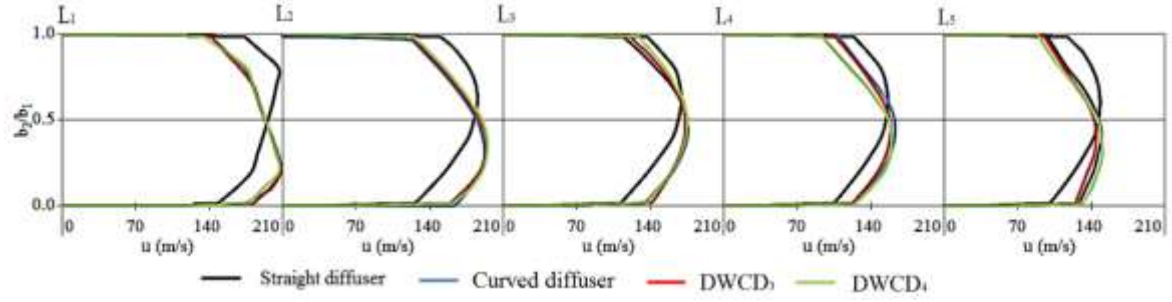

Figure 6.58: Comparison of velocity magnitude (m/s) distribution across the straight diffuser, optimal curved diffuser and diverged wall curved diffuser configurations ($DWCD_3$ and $DWCD_4$) from the hub wall to the shroud wall at BEP and at an operational speed of 58.9rpsK$^{-1/2}$

The behaviour of velocity magnitude across the diverged wall straight diffuser is explained using symmetric and asymmetric behaviour of the velocity field profiles. Figure 6.59 depicts the local asymmetric ratio for the velocity magnitudes, α_{vm} across the diverged wall diffusers ($DWCD_3$ and $DWCD_4$) at BEP and at an operational speed of 58.9rpsK$^{-1/2}$. α_{vm} values of 1.0 shows the flow is symmetric, α_{vm} values below 1.0 shows asymmetric flow towards the hub wall and α_{vm} values above 1.0 shows asymmetric flow towards the shroud wall. It can be seen that the flow is asymmetric towards the hub wall across the diverged wall curved diffuser. The asymmetric ratio for the velocity magnitude decreases from the centreline of the diffuser towards the wall. Moreover, the asymmetric ratio for the velocity magnitude also decreases from L_1 (diffuser inlet) to L_2, then increases from L_2 to L_3 and then it decreases from L_3 to L_5 (diffuser outlet) across both diverged wall curved diffusers considered. It has been noticed that flow is nearly symmetrical at L_3 across $DWCD_4$ in comparison to that across $DWCD_3$. However, it has been noticed that increase of outlet-to-inlet width ratio by keeping the divergence location at 50% distance of the diffuser length from the diffuser inlet makes the flow highly asymmetrical.

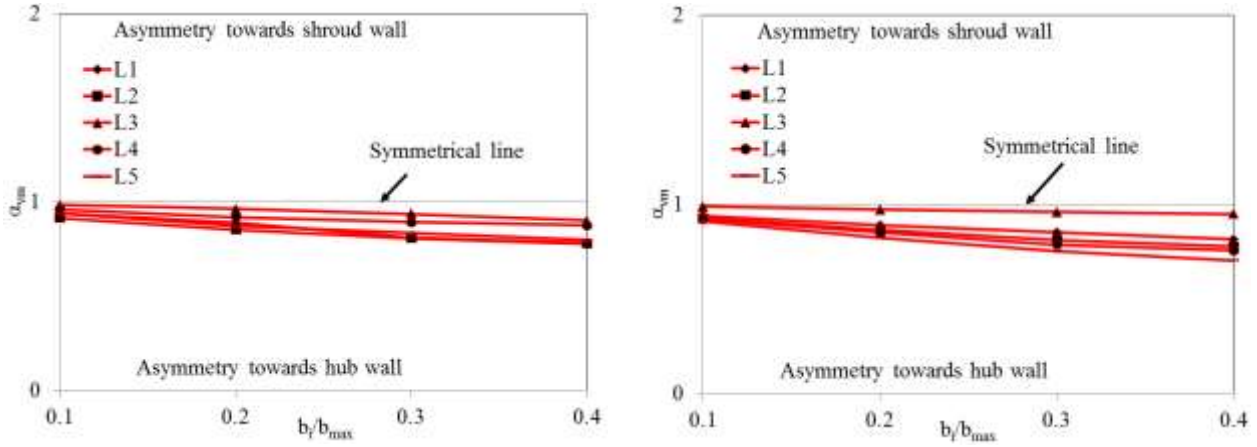

Figure 6.59: Local asymmetric ratio for the velocity magnitude, α_{vm} across the diverged wall diffusers ((a) $DWCD_3$ and (b) $DWCD_4$) at BEP and at an operational speed of 58.9rpsK$^{-1/2}$

Figure 6.60 depicts the comparison of velocity magnitude distribution across straight diffuser and diverged wall curved diffuser configurations ($DWCD_5$, $DWCD_6$, $DWCD_7$ and $DWCD_8$) from the hub wall to the shroud wall at BEP and at an operational speed of 58.9rpsK$^{-1/2}$. It can be seen that the velocity magnitude is reduced radially across the diffuser. It can also be seen that the velocity magnitude across diverged wall curved diffusers is higher in comparison to that across the straight diffuser. Furthermore, it has been observed that the velocity magnitude is asymmetric towards the hub wall across diverged wall curved diffusers in comparison to that across straight diffuser, which has asymmetric velocity magnitude towards the shroud wall. However, the detailed analysis has been carried out by quantifying the asymmetric ratio for the velocity magnitude profile across the curved diffuser configurations.

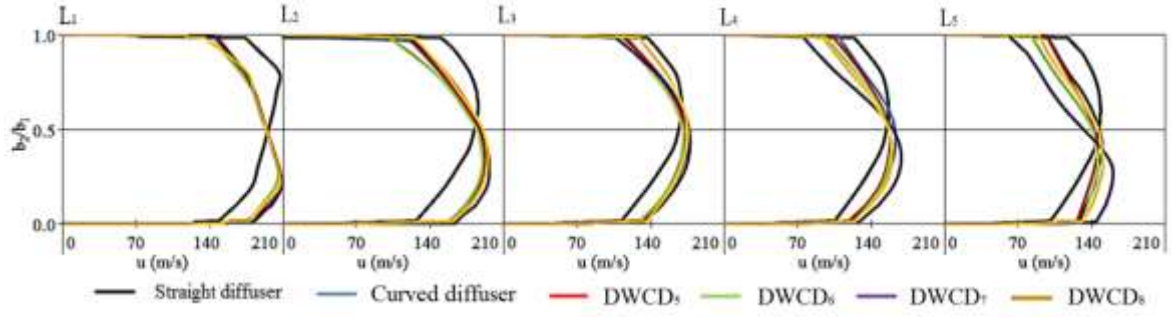

Figure 6.60: Comparison of velocity magnitude (m/s) distribution across the straight diffuser, optimal curved diffuser and diverged wall curved diffuser configurations ($DWCD_5$, $DWCD_6$, $DWCD_7$ and $DWCD_8$) from the hub wall to the shroud wall at BEP and at an operational speed of 58.9rpsK$^{-1/2}$

The behaviour of velocity magnitude across the diverged wall straight diffuser is explained using symmetric and asymmetric behaviour of the velocity field profiles. Figure 6.61 depicts the local asymmetric ratio for the velocity magnitudes, α_{vm} across the diverged wall diffusers ($DWCD_5$, $DWCD_6$, $DWCD_7$ and $DWCD_8$) at BEP and at an operational speed of 58.9rps$K^{-1/2}$. α_{vm} values of 1.0 shows the flow is symmetric, α_{vm} values below 1.0 shows asymmetric flow towards the hub wall and α_{vm} values above 1.0 shows asymmetric flow towards the shroud wall. It can be seen that the flow is asymmetric towards the hub wall across the diverged wall curved diffuser. The asymmetric ratio for the velocity magnitude decreases from the centreline of the diffuser towards the wall. Moreover, the asymmetric ratio for the velocity magnitude also decreases from L_1 (diffuser inlet) to L_2, then increases from L_2 to L_3 and then it decreases from L_3 to L_5 (diffuser outlet) across all diverged wall curved diffusers considered. It has been noticed that flow is nearly symmetrical at L_3 across $DWCD_8$ in comparison to that across $DWCD_4$. However, it has been noticed that increase of outlet-to-inlet width ratio and wall diverged location from the inlet makes the flow more asymmetrical upto diffuser configuration of $DWCD_7$ and then flow local asymmetric ratio for the velocity magnitude increases across $DWCD_8$.

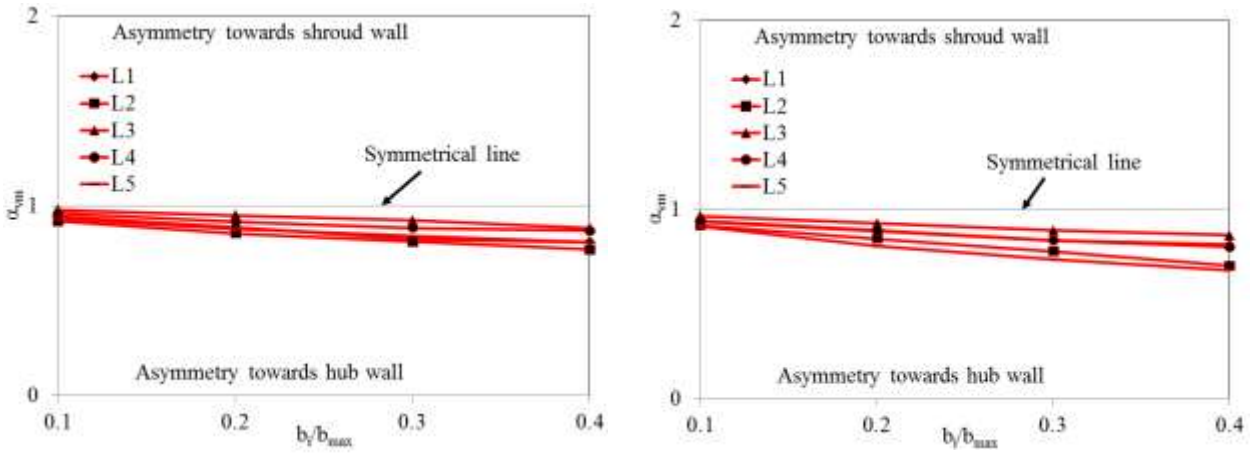

(a) (b)

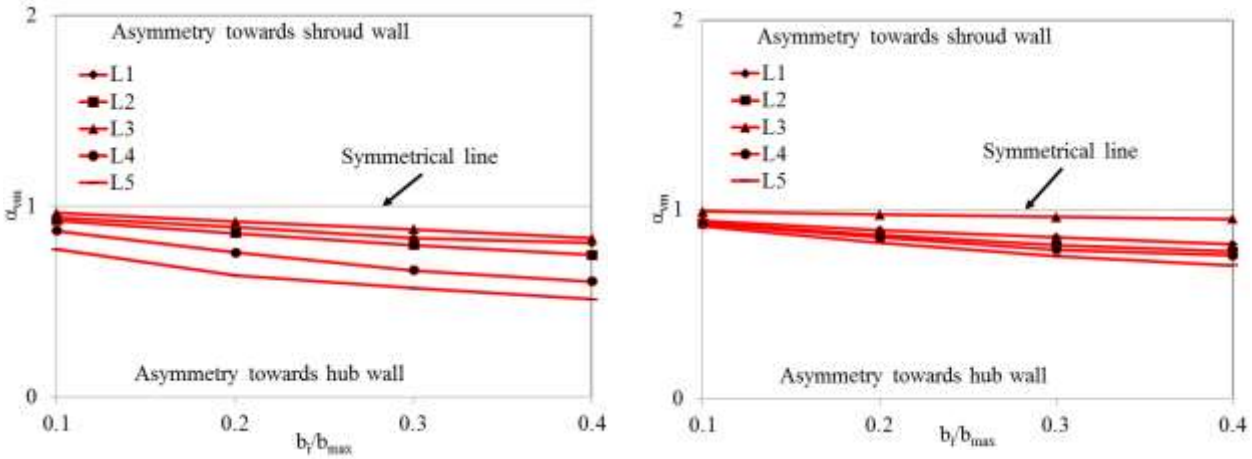

Figure 6.61: Local asymmetric ratio for the velocity magnitude, α_{vm} across the diverged wall diffusers ((a) $DWCD_5$ (b) $DWCD_6$, (c) $DWCD_7$ and (d) $DWCD_8$) at BEP and at an operational speed of 58.9rpsK$^{-1/2}$

Figure 6.62 depicts the radial velocity distribution across the centreline of the diverged wall curved diffuser configurations ($DWCD_1$ and $DWCD_2$) at BEP and at an operational speed of 58.9rpsK$^{-1/2}$. The trend of the radial velocity across the diverged wall diffusers is similar to that across the straight diffuser. It can be seen that the maximum radial velocity is obtained at the diffuser inlet after the volute-tongue region. The radial velocity decreases radially across the diffuser. Furthermore, the radial velocity also decreases circumferentially in the direction of impeller rotation (ω). The minimum radial velocity is obtained at the diffuser outlet at near the volute-tongue region. It can be seen that the radial velocity is same at the diffuser inlet and is decreased by 3.5% at the diffuser outlet of $DWCD_1$ in comparison to that of straight diffuser. Furthermore, the radial velocity is increased by 1% at the diffuser inlet is decreased by 104% at the diffuser outlet of $DWCD_2$ in comparison to that of $DWCD_1$. This trend explains that the radial velocity decreases when outlet-to-inlet width ratio of the diffuser is increased whilst keeping the divergence location at the diffuser inlet. Moreover, negative radial velocity is found near diffuser outlet of $DWCD_2$, which is the sign of flow reversals near the diffuser outlet.

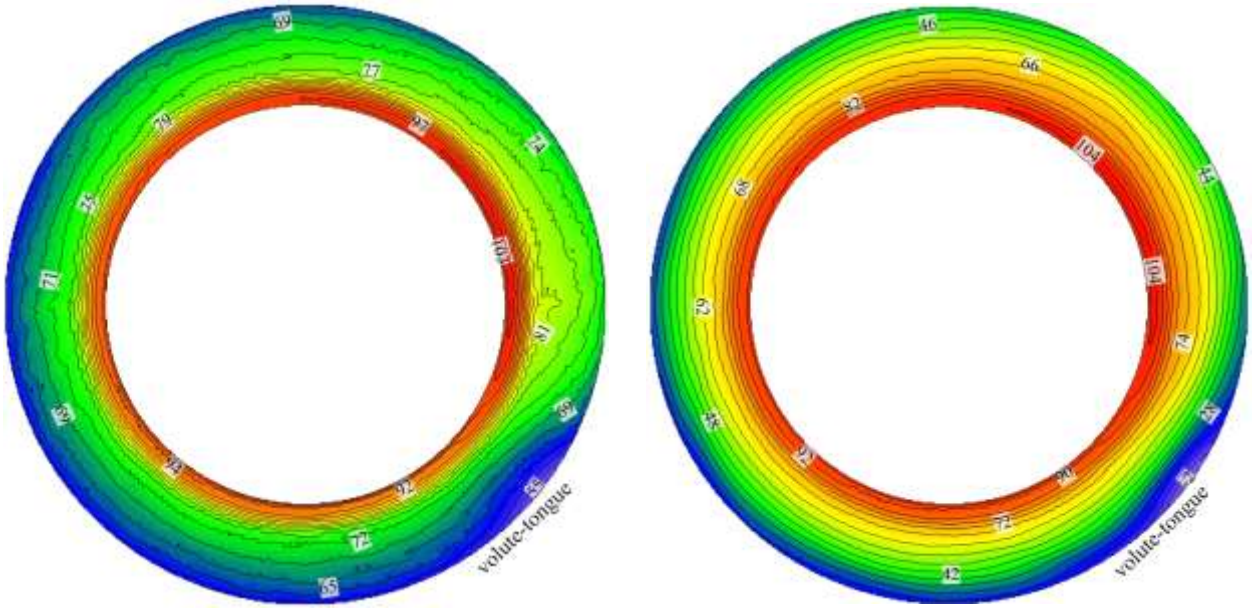

(a) (b)

Figure 6.62: Radial velocity (m/s) distributions across the centreline of the diverged wall curved diffuser (a) $DWCD_1$ and (b) $DWCD_2$ at BEP and at an operational speed of 58.9rpsK$^{-1/2}$

Figure 6.63 depicts the comparison of radial velocity distribution across straight diffuser, optimal curved diffuser and diverged wall curved diffuser configurations ($DWCD_1$ and $DWCD_2$) from the hub wall to the shroud wall at BEP and at an operational speed of 58.9rpsK$^{-1/2}$. It can be seen that the radial velocity is reduced radially across the diffuser. It can also be seen that the radial velocity across diverged wall curved diffusers is higher from L_1 (diffuser inlet) to L_2, then the radial velocity reduces at L_3 and then it again increases from L_4 to L_5 (diffuser outlet) in comparison to that across the straight diffuser in both diverged wall curved diffusers considered. Moreover, negative radial velocity is also found at L_5 (diffuser outlet) near the shroud wall of $DWCD_2$. Furthermore, it has been observed that the radial velocity is asymmetric towards the hub wall across diverged wall curved diffusers in comparison to that across straight diffuser, which has asymmetric radial velocity towards the shroud wall. However, the detailed analysis has been carried out by quantifying the asymmetric ratio for the radial velocity profile across the curved diffuser configurations.

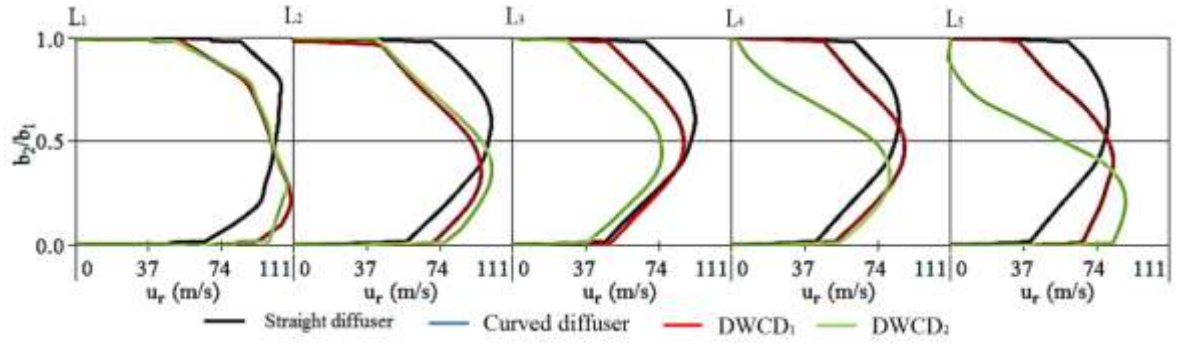

Figure 6.63: Comparison of radial velocity (m/s) distribution across the straight diffuser, optimal curved diffuser and diverged wall curved diffuser configurations ($DWCD_1$ and $DWCD_2$) from the hub wall to the shroud wall at BEP and at an operational speed of 58.9rpsK$^{-1/2}$

The behaviour of radial velocity across the diverged wall straight diffuser is explained using symmetric and asymmetric behaviour of the velocity field profiles. Figure 6.64 depicts the local asymmetric ratio for the of radial velocity, α_{vr} across the diverged wall diffusers ($DWCD_1$ and $DWCD_2$) at BEP and at an operational speed of 58.9rpsK$^{-1/2}$. α_{vr} values of 1.0 shows the flow is symmetric, α_{vr} values below 1.0 shows asymmetric flow towards the hub wall and α_{vr} values above 1.0 shows asymmetric flow towards the shroud wall. It can be seen that the flow is asymmetric towards the hub wall across the diverged wall curved diffuser. The asymmetric ratio for the radial velocity decreases from the centreline of the diffuser towards the wall. Moreover, the asymmetric ratio for the of radial velocity also decreases from L_1 (diffuser inlet) to L_2, then increases from L_2 to L_3 and then it decreases from L_3 to L_5 (diffuser outlet) across both diverged wall curved diffusers considered. However, it has been noticed that increase of outlet-to-inlet width ratio by considering same wall diverged location from the inlet makes the flow highly asymmetrical.

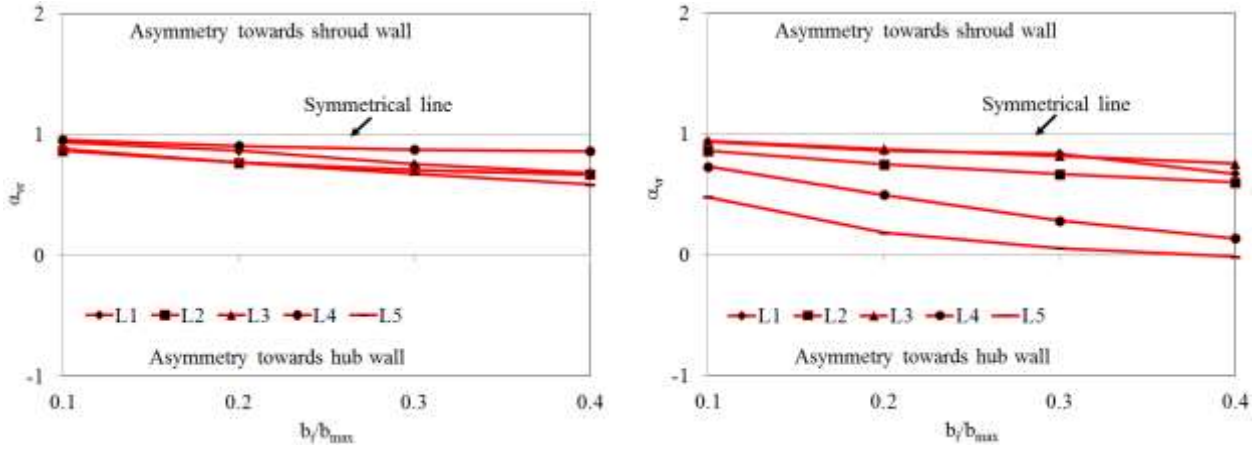

Figure 6.64: Local asymmetric ratio for the radial velocity, α_{vr} across the diverged wall diffusers ((a) $DWCD_1$ and (b) $DWCD_2$) at BEP and at an operational speed of 58.9rpsK$^{-1/2}$

Figure 6.65 depicts the radial velocity distribution across the centreline of the diverged wall curved diffuser configurations ($DWCD_3$ and $DWCD_4$) at BEP and at an operational speed of 58.9rpsK$^{-1/2}$. The trend of the radial velocity across the diverged wall diffuser passages is similar to that across the straight diffuser. It can be seen that the maximum radial velocity is obtained at the diffuser inlet after the volute-tongue region. The radial velocity decreases radially across the diffuser. Furthermore, the radial velocity also decreases circumferentially in the direction of impeller rotation (ω). The minimum radial velocity is obtained at the diffuser outlet at near the volute-tongue region. It can be seen that the radial velocity is increased by 1% at the diffuser inlet and is decreased by 1.8% at the diffuser outlet of $DWCD_3$ in comparison to that of straight diffuser. Furthermore, the radial velocity is decreased by 1% and 95% at the diffuser inlet and diffuser outlet of $DWCD_4$ in comparison to that of $DWCD_3$. This trend explains that the radial velocity decreases when outlet-to-inlet width ratio of the diffuser is increased whilst keeping the divergence location at 50% distance of the diffuser length from the diffuser inlet.

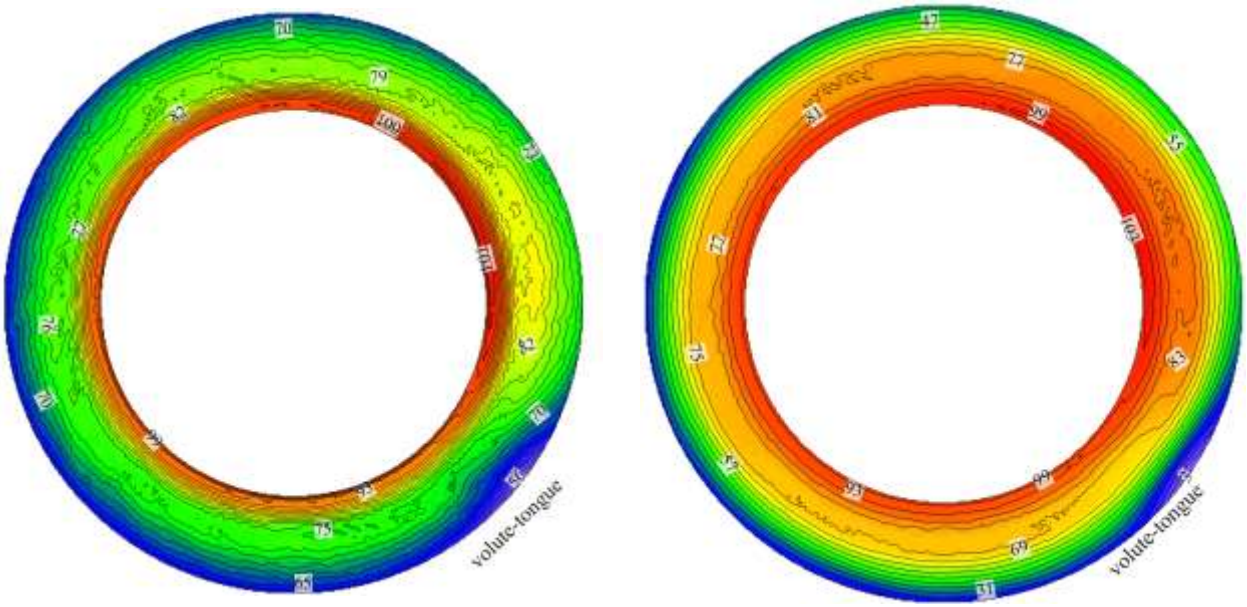

(a) (b)

Figure 6.65: Radial velocity (m/s) distributions across the centreline of the diverged wall curved diffuser (a) $DWCD_3$ and (b) $DWCD_4$ at BEP and at an operational speed of 58.9rpsK$^{-1/2}$

Figure 6.66 depicts the comparison of radial velocity distribution across straight diffuser, optimal curved diffuser and diverged wall curved diffuser configurations ($DWCD_3$ and $DWCD_4$) from the hub wall to the shroud wall at BEP and at an operational speed of 58.9rpsK$^{-1/2}$. It can be seen that the radial velocity is reduced radially across the diffuser. It can also be seen that the radial velocity across diverged wall curved diffusers is higher from L_1 (diffuser inlet) to L_2, then the radial velocity reduces

at L_3 and then it again increases from L_4 to L_5 (diffuser outlet) in comparison to that across the straight diffuser in both diverged wall curved diffusers considered. Moreover, negative radial velocity is also found at L_5 (diffuser outlet) near the shroud wall of $DWCD_4$. Furthermore, it has been observed that the radial velocity is asymmetric towards the hub wall across diverged wall curved diffusers in comparison to that across straight diffuser, which has asymmetric radial velocity towards the shroud wall. However, the detailed analysis has been carried out by quantifying the asymmetric ratio for the radial velocity profile across the curved diffuser configurations.

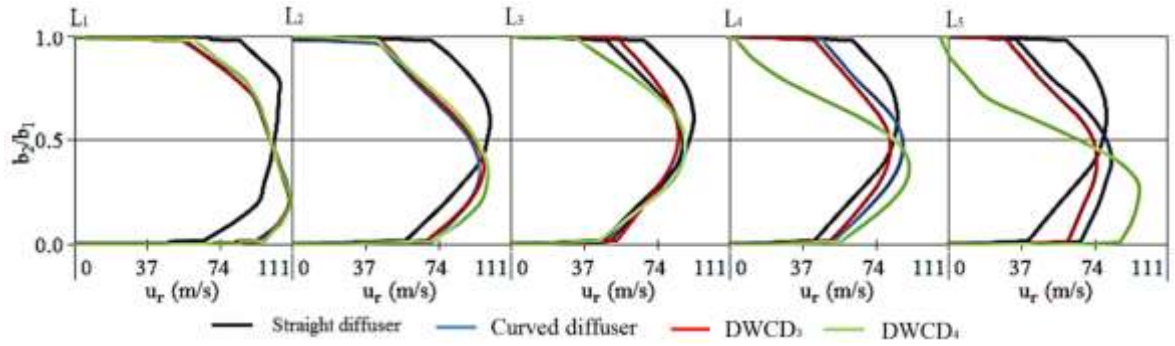

Figure 6.66: Comparison of radial velocity (m/s) distribution across the straight diffuser, optimal curved diffuser and diverged wall curved diffuser configurations ($DWCD_3$ and $DWCD_4$) from the hub wall to the shroud wall at BEP and at an operational speed of 58.9rpsK$^{-1/2}$

The behaviour of radial velocity across the diverged wall straight diffuser is explained using symmetric and asymmetric behaviour of the velocity field profiles. Figure 6.67 depicts the local asymmetric ratio for the radial velocity, α_{vr} across the diverged wall diffusers ($DWCD_3$ and $DWCD_4$) at BEP and at an operational speed of 58.9rpsK$^{-1/2}$. α_{vr} values of 1.0 shows the flow is symmetric, α_{vr} values below 1.0 shows asymmetric flow towards the hub wall and α_{vr} values above 1.0 shows asymmetric flow towards the shroud wall. It can be seen that the flow is deviated around the value of 1.0 showing the flow is asymmetric towards the hub wall from L_1 (diffuser inlet) to L_2 and then the flow is asymmetric towards the shroud wall at L_3 across $DWCD_3$. Thereafter the flow is asymmetric towards the hub wall from L_4 to L_5 (diffuser outlet) across $DWCD_3$. Conversely, the flow is asymmetric towards the hub wall across $DWCD_4$. The asymmetric ratio for the radial velocity decreases from the centreline of the diffuser towards the wall. Moreover, the asymmetric ratio for the of radial velocity also decreases from L_1 (diffuser inlet) to L_2, then increases from L_2 to L_3 and then it decreases from L_3 to L_5 (diffuser outlet) across both diverged wall curved diffusers considered. However, it has been noticed that increase of outlet-to-inlet width ratio by keeping the divergence

location at 50% distance of the diffuser length from the diffuser inlet makes the flow highly asymmetrical towards the hub wall. Moreover, it can also be noticed that increasing the wall divergence location from the inlet makes the flow more symmetrical.

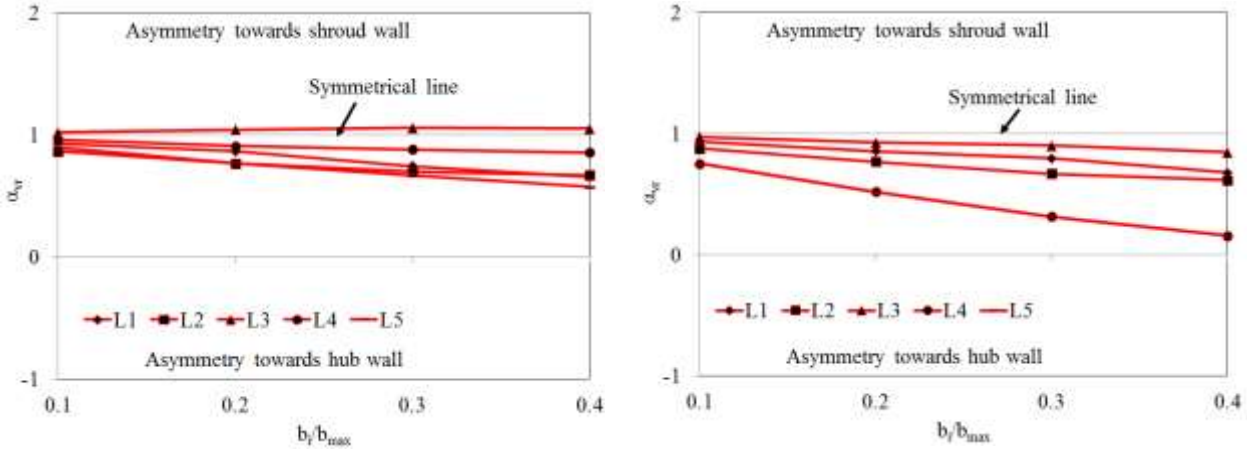

Figure 6.67: Local asymmetric ratio for the radial velocity, α_{vr} across the diverged wall diffusers ((a) $DWCD_3$ and (b) $DWCD_4$) at BEP and at an operational speed of 58.9rpsK$^{-1/2}$

Figure 6.68 depicts the radial velocity distribution across the centreline of the diverged wall curved diffuser configurations ($DWCD_5$, $DWCD_6$, $DWCD_7$ and $DWCD_8$) at BEP and at an operational speed of 58.9rpsK$^{-1/2}$. The trend of the radial velocity across the diverged wall diffuser passages is similar to that across the straight diffuser. It can be seen that the maximum radial velocity is obtained at the diffuser inlet after the volute-tongue region. The radial velocity decreases radially across the diffuser. Furthermore, the radial velocity also decreases circumferentially in the direction of impeller rotation (ω). The minimum radial velocity is obtained at the diffuser outlet at near the volute-tongue region. It can be seen that the radial velocity is same at the diffuser inlet and is decreased by 3.5% at the diffuser outlet of $DWCD_5$ in comparison to that of straight diffuser. Furthermore, the radial velocity is increased by 0%, 2.9% and 0% at the diffuser inlet of $DWCD_6$, $DWCD_7$ and $DWCD_8$ respectively in comparison to that of $DWCD_5$. Similarly, the radial velocity is decreased by 18%, 100% and 95% at the diffuser outlet of $DWCD_6$, $DWCD_7$ and $DWCD_8$ respectively in comparison to that of $DWCD_5$. This trend explains that the radial decreases with the increase of both the distance between the divergence location and the diffuser inlet and outlet-to-inlet width ratio of the diffuser. Moreover, negative radial velocity is found near diffuser outlet of $DWCD_7$ and $DWCD_8$, which is the sign of flow reversals near the diffuser outlet.

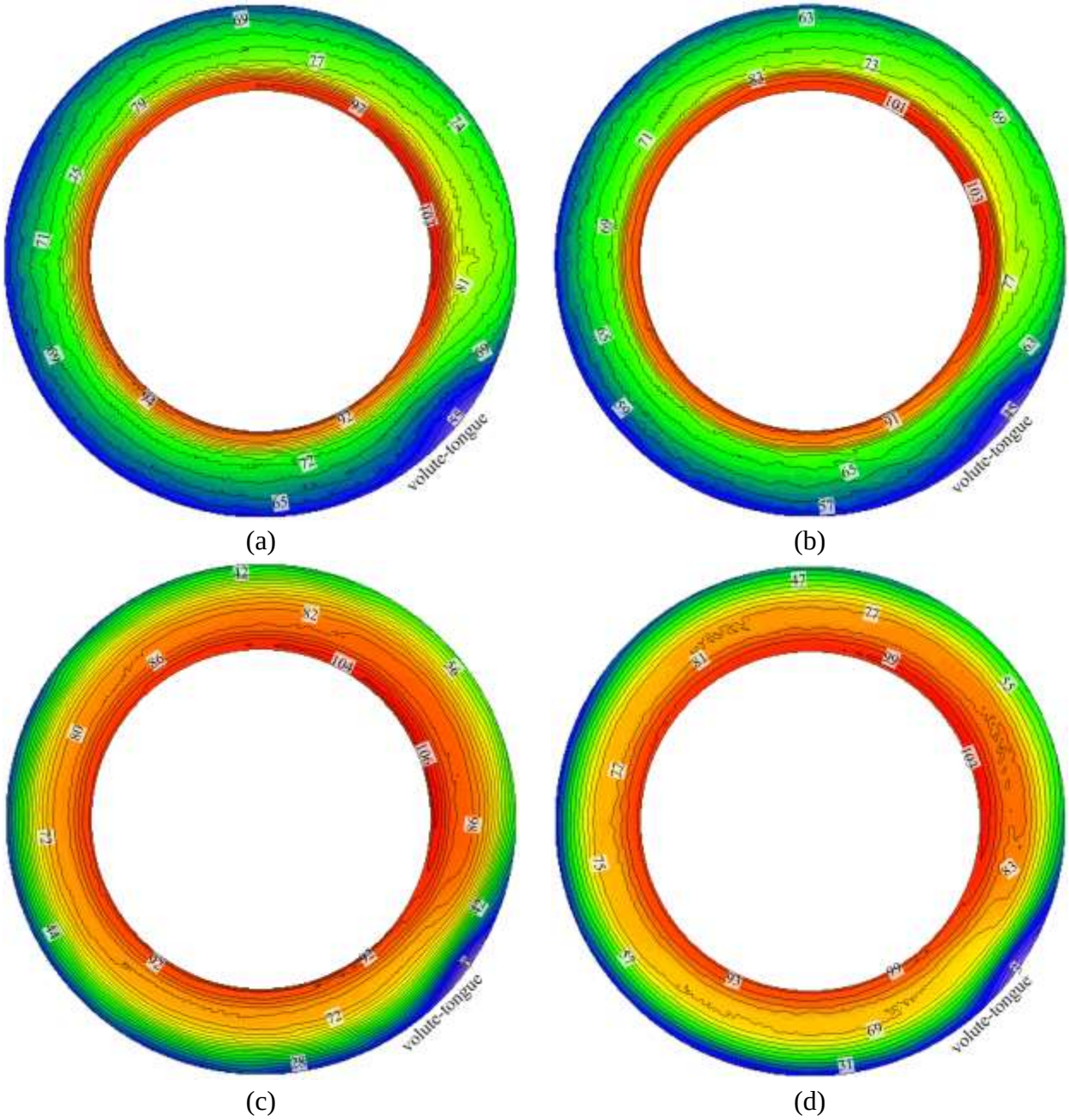

(a) (b)

(c) (d)

Figure 6.68: Radial velocity (m/s) distributions across the centreline of the diverged wall curved diffuser (a) $DWCD_5$, (b) $DWCD_6$, (c) $DWCD_7$ and (d) $DWCD_8$ at BEP and at an operational speed of 58.9rpsK$^{-1/2}$

Figure 6.69 depicts the comparison of radial velocity distribution across straight diffuser, optimal curved diffuser and diverged wall curved diffuser configurations ($DWCD_5$, $DWCD_6$, $DWCD_7$ and $DWCD_8$) from the hub wall to the shroud wall at BEP and at an operational speed of 58.9rpsK$^{-1/2}$. It can be seen that the radial velocity is reduced radially across the diffuser. It can also be seen that the radial velocity across diverged wall curved diffusers is higher from L_1 (diffuser inlet) to L_2, then the

radial velocity reduces at L_3 and then it again increases from L_4 to L_5 (diffuser outlet) in comparison to that across the straight diffuser in all diverged wall curved diffusers considered. Moreover, negative radial velocity is also found at L_5 (diffuser outlet) near the shroud wall of $DWCD_7$ and $DWCD_8$. Furthermore, it has been observed that the radial velocity is asymmetric towards the hub wall across diverged wall curved diffusers in comparison to that across straight diffuser, which has asymmetric radial velocity towards the shroud wall. However, the detailed analysis has been carried out by quantifying the asymmetric ratio for the radial velocity profile across the curved diffuser configurations.

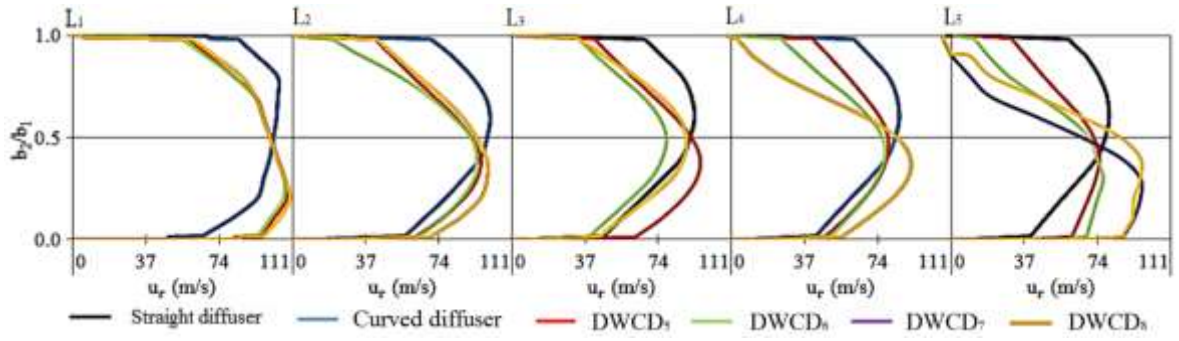

Figure 6.69: Comparison of radial velocity (m/s) distribution across the straight diffuser, optimal curved diffuser and diverged wall curved diffuser configurations ($DWCD_5$, $DWCD_6$, $DWCD_7$ and $DWCD_8$) from the hub wall to the shroud wall at BEP and at an operational speed of $58.9 rpsK^{-1/2}$

The behaviour of radial velocity across the diverged wall straight diffuser is explained using symmetric and asymmetric behaviour of the velocity field profiles. Figure 6.70 depicts the local asymmetric ratio for the of radial velocity, α_{vr} across the diverged wall diffusers ($DWCD_5$, $DWCD_6$, $DWCD_7$ and $DWCD_8$) at BEP and at an operational speed of $58.9 rpsK^{-1/2}$. α_{vr} values of 1.0 shows the flow is symmetric, α_{vr} values below 1.0 shows asymmetric flow towards the hub wall and α_{vr} values above 1.0 shows asymmetric flow towards the shroud wall. It can be seen that the flow is asymmetric towards the hub wall across all the diverged wall curved diffusers considered. The asymmetric ratio for the radial velocity decreases from the centreline of the diffuser towards the wall. Moreover, the asymmetric ratio for the radial velocity also decreases from L_1 (diffuser inlet) to L_2, then increases from L_2 to L_3 and then it decreases from L_3 to L_5 (diffuser outlet) across both diverged wall curved diffusers considered. However, it has been noticed that combined increase of outlet-to-inlet width ratio wall diverged location from the inlet makes the flow highly asymmetrical.

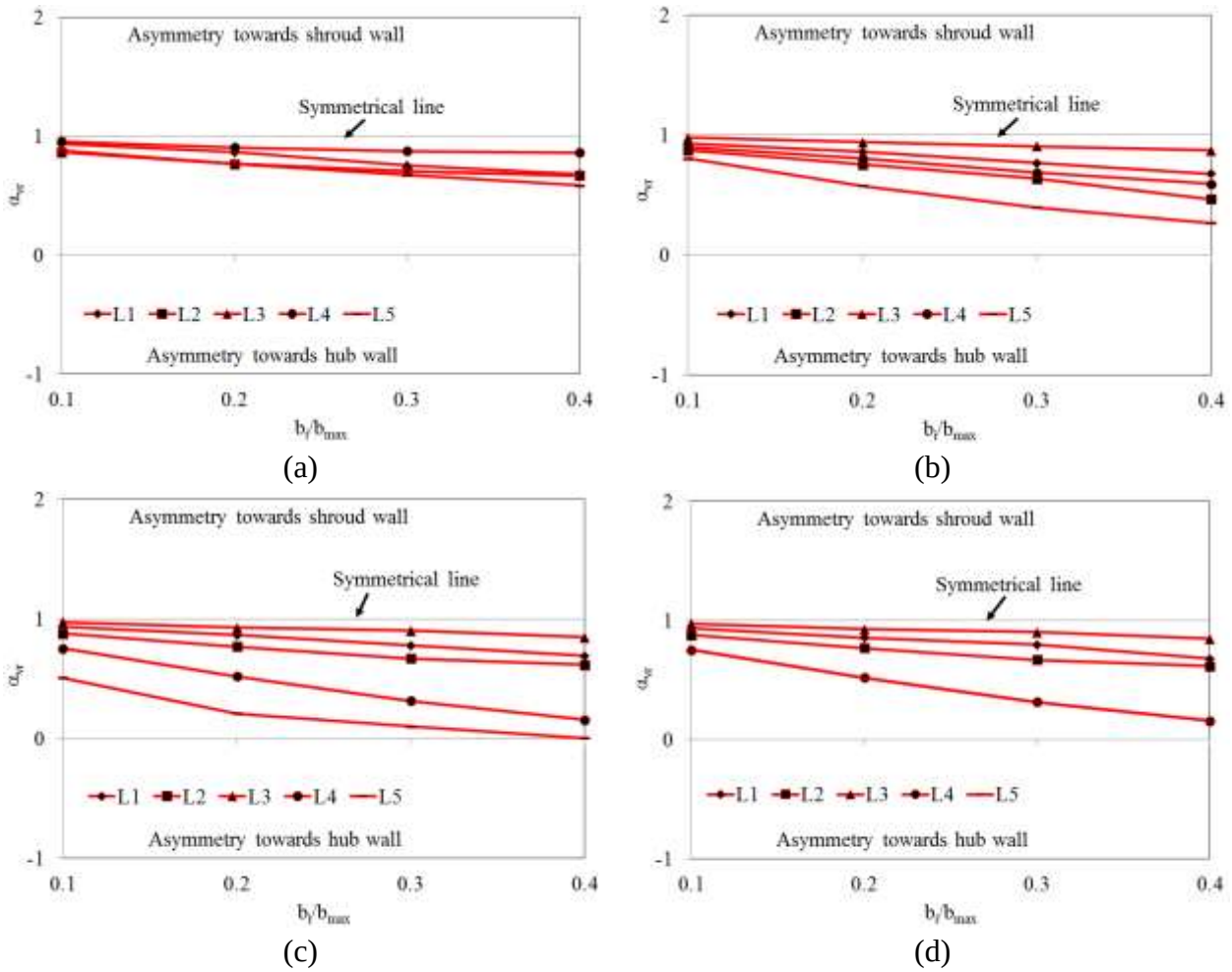

Figure 6.70: Local asymmetric ratio for the radial velocity, α_{vr} across the diverged wall diffusers ((a) $DWCD_5$ (b) $DWCD_6$, (c) $DWCD_7$ and (d) $DWCD_8$) at BEP and at an operational speed of $58.9rpsK^{-1/2}$

Figure 6.71 depicts the circumferential velocity distribution across the centreline of the diverged wall curved diffuser configurations ($DWCD_1$ and $DWCD_2$) at BEP and at an operational speed of $58.9rpsK^{-1/2}$. The trend of the circumferential velocity across the diverged wall diffuser passages is similar to that across the straight diffuser. It can be seen that the maximum circumferential velocity is obtained at the diffuser inlet after the volute-tongue region. The circumferential velocity decreases radially across the diffuser. Furthermore, the circumferential velocity also decreases circumferentially in the direction of impeller rotation (ω). The minimum circumferential velocity is obtained at the diffuser outlet at near the volute-tongue region. It can be seen that the circumferential velocity decreased by 0.6% at the diffuser inlet and is increased by 6.8% at the diffuser outlet of $DWCD_1$ in comparison to that of straight diffuser. Furthermore, the circumferential velocity is decreased by 1.2% and 33% at the diffuser inlet and diffuser outlet respectively of $DWCD_2$ in comparison to that of

$DWCD_1$. This trend explains that the circumferential velocity decreases when outlet-to-inlet width ratio of the diffuser is increased whilst keeping the divergence location at the diffuser inlet.

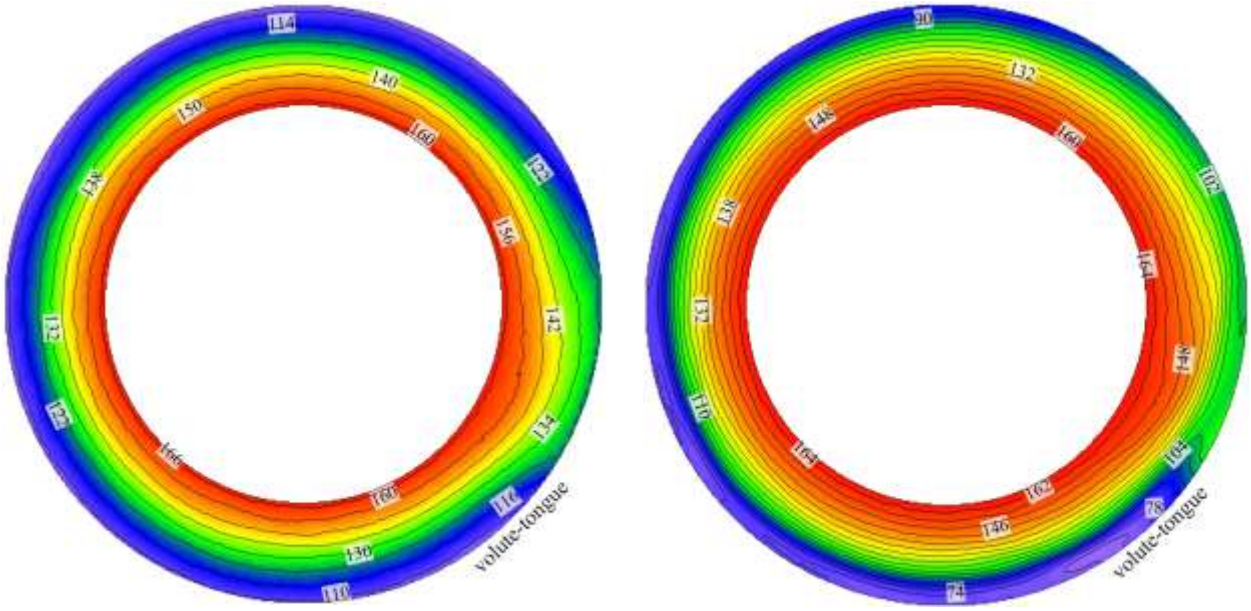

(a) (b)

Figure 6.71: Circumferential velocity (m/s) distributions across the centreline of the diverged wall curved diffuser (a) $DWCD_1$ and (b) $DWCD_2$ at BEP and at an operational speed of 58.9rpsK$^{-1/2}$

Figure 6.72 depicts the comparison of circumferential velocity distribution across straight diffuser, optimal curved diffuser and diverged wall curved diffuser configurations ($DWCD_1$ and $DWCD_2$) from the hub wall to the shroud wall at BEP and at an operational speed of 58.9rpsK$^{-1/2}$. It can be seen that the circumferential velocity is reduced radially across the diffuser. It can also be seen that the circumferential velocity across diverged wall curved diffusers is higher in comparison to that across the straight diffuser. Furthermore, it has been observed that the circumferential velocity is asymmetric towards the hub wall across diverged wall curved diffusers in comparison to that across straight diffuser, which has asymmetric circumferential velocity towards the shroud wall. However, the detailed analysis has been carried out by quantifying the asymmetric ratio for the circumferential velocity profile across the curved diffuser configurations.

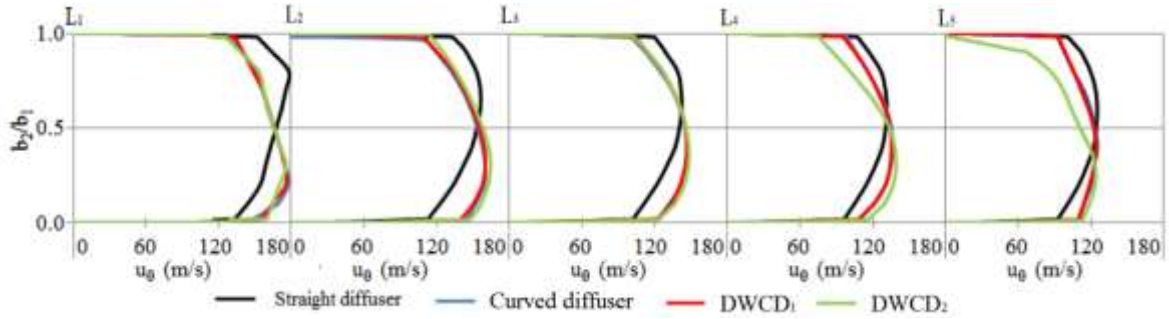

Figure 6.72: Comparison of circumferential velocity (m/s) distribution across the straight diffuser, optimal curved diffuser and diverged wall curved diffuser configurations ($DWCD_1$ and $DWCD_2$) from the hub wall to the shroud wall at BEP and at an operational speed of $58.9 rpsK^{-1/2}$

The behaviour of circumferential velocity across the diverged wall straight diffuser is explained using symmetric and asymmetric behaviour of the velocity field profiles. Figure 6.73 depicts the local asymmetric ratio for the circumferential velocity, α_{vc} across the diverged wall diffusers ($DWCD_1$ and $DWCD_2$) at BEP and at an operational speed of $58.9 rpsK^{-1/2}$. α_{vc} values of 1.0 shows the flow is symmetric, α_{vc} values below 1.0 shows asymmetric flow towards the hub wall and α_{vc} values above 1.0 shows asymmetric flow towards the shroud wall. It can be seen that the flow is asymmetric towards the hub wall across all the diverged wall curved diffusers considered. The asymmetric ratio for the circumferential velocity decreases from the centreline of the diffuser towards the wall. Moreover, the asymmetric ratio for the circumferential velocity also decreases from L_1 (diffuser inlet) to L_2, then increases from L_2 to L_3 and then it decreases from L_3 to L_5 (diffuser outlet) across both diverged wall curved diffusers considered. However, it has been noticed that increase of outlet-to-inlet width ratio by considering same wall diverged location from the inlet makes the flow highly asymmetrical

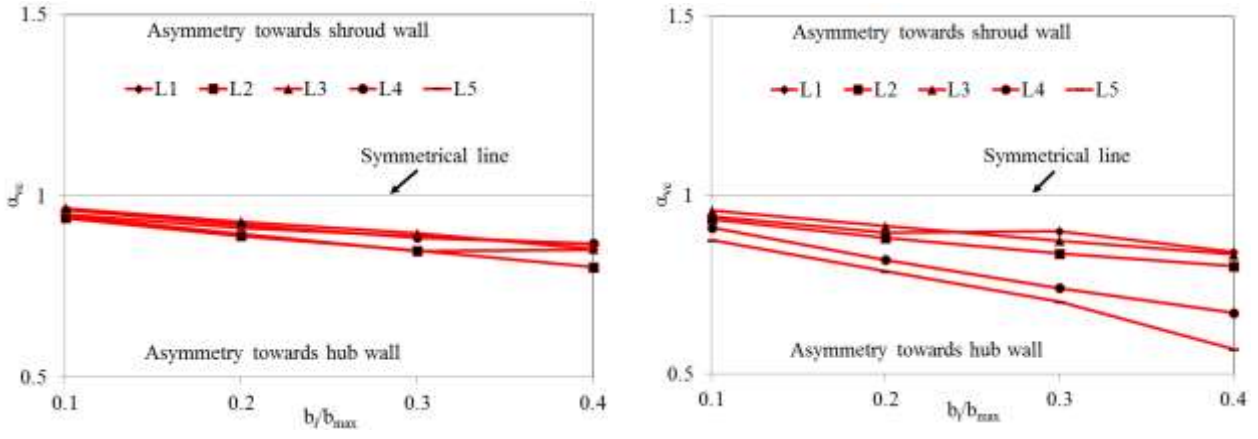

(a) (b)

Figure 6.73: Local asymmetric ratio for the circumferential velocity, α_{vc} across the diverged wall diffusers ((a) $DWCD_1$ and (b) $DWCD_2$) at BEP and at an operational speed of $58.9 rpsK^{-1/2}$

Figure 6.74 depicts the circumferential velocity distribution across the centreline of the diverged wall curved diffuser configurations ($DWCD_3$ and $DWCD_4$) at BEP and at an operational speed of 58.9rpsK$^{-1/2}$. The trend of the circumferential velocity across the diverged wall diffuser passages is similar to that across the straight diffuser. It can be seen that the maximum circumferential velocity is obtained at the diffuser inlet after the volute-tongue region. The circumferential velocity decreases radially across the diffuser. Furthermore, the circumferential velocity also decreases circumferentially in the direction of impeller rotation (ω). The minimum circumferential velocity is obtained at the diffuser outlet at near the volute-tongue region. It can be seen that the circumferential velocity is decreased by 3% at the diffuser inlet and is increased by 5% at the diffuser outlet of $DWCD_3$ in comparison to that of straight diffuser. Furthermore, the circumferential velocity is increased by 2% at the diffuser inlet and decreased by 27% at the diffuser outlet of $DWCD_4$ in comparison to that of $DWCD_3$. This trend explains that the circumferential velocity decreases when outlet-to-inlet width ratio of the diffuser is increased whilst keeping the divergence location at the diffuser inlet.

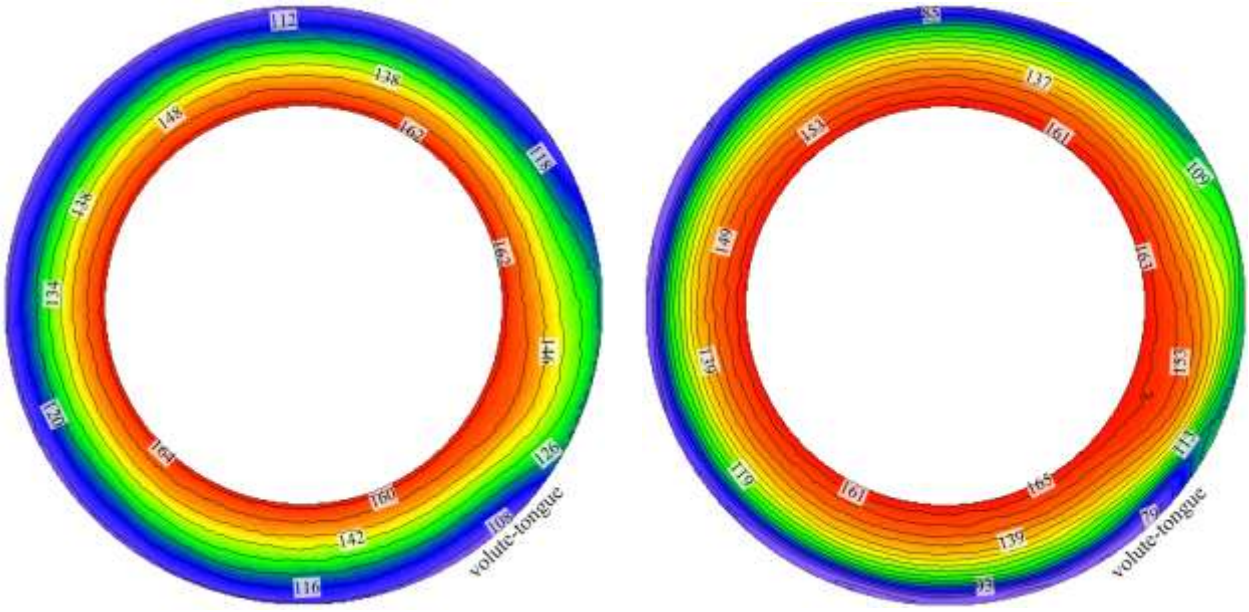

(a) (b)

Figure 6.74: Circumferential velocity (m/s) distributions across the centreline of the diverged wall curved diffuser (a) $DWCD_3$ and (b) $DWCD_4$ at BEP and at an operational speed of 58.9rpsK$^{-1/2}$

Figure 6.75 depicts the comparison of circumferential velocity distribution across straight diffuser, optimal curved diffuser and diverged wall curved diffuser configurations ($DWCD_3$ and $DWCD_4$) from the hub wall to the shroud wall at BEP and at an operational speed of 58.9rpsK$^{-1/2}$. It can be seen

that the circumferential velocity is reduced radially across the diffuser. It can also be seen that the circumferential velocity across diverged wall curved diffusers is higher in comparison to that across the straight diffuser. Furthermore, it has been observed that the circumferential velocity is asymmetric towards the hub wall across diverged wall curved diffusers in comparison to that across straight diffuser, which has asymmetric circumferential velocity towards the shroud wall. However, the detailed analysis has been carried out by quantifying the asymmetric ratio for the circumferential velocity profile across the curved diffuser configurations.

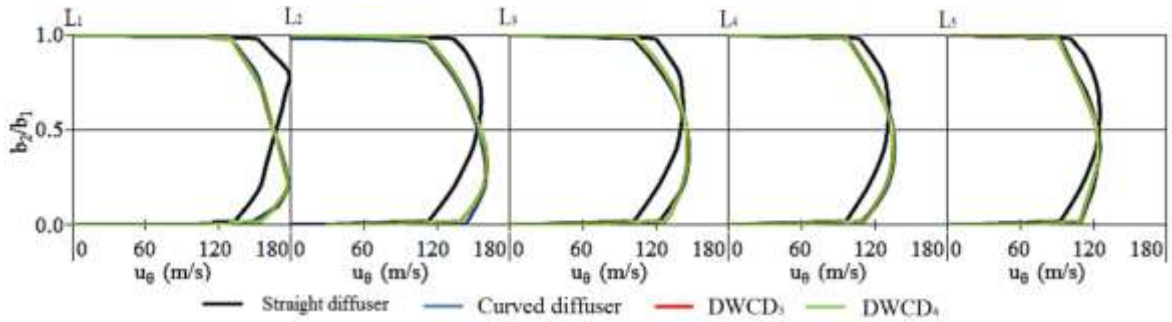

Figure 6.75: Comparison of circumferential velocity (m/s) distribution across the straight diffuser, optimal curved diffuser and diverged wall curved diffuser configurations ($DWCD_3$ and $DWCD_4$) from the hub wall to the shroud wall at BEP and at an operational speed of 58.9rpsK$^{-1/2}$

The behaviour of circumferential velocity across the diverged wall straight diffuser is explained using symmetric and asymmetric behaviour of the velocity field profiles. Figure 6.76 depicts the local asymmetric ratio for the circumferential velocity, α_{vc} across the diverged wall diffusers ($DWCD_3$ and $DWCD_4$) at BEP and at an operational speed of 58.9rpsK$^{-1/2}$. α_{vc} values of 1.0 shows the flow is symmetric, α_{vc} values below 1.0 shows asymmetric flow towards the hub wall and α_{vc} values above 1.0 shows asymmetric flow towards the shroud wall. It can be seen that the flow is asymmetric towards the hub wall across all the diverged wall curved diffusers considered. The asymmetric ratio for the circumferential velocity decreases from the centreline of the diffuser towards the wall. Moreover, the asymmetric ratio for the circumferential velocity also decreases from L_1 (diffuser inlet) to L_2, then increases from L_2 to L_3 and then it decreases from L_3 to L_5 (diffuser outlet) across both diverged wall curved diffusers considered. However, it has been noticed that increase of outlet-to-inlet width ratio by keeping the divergence location at 50% distance of the diffuser length from the diffuser inlet makes the flow highly asymmetrical towards the hub wall

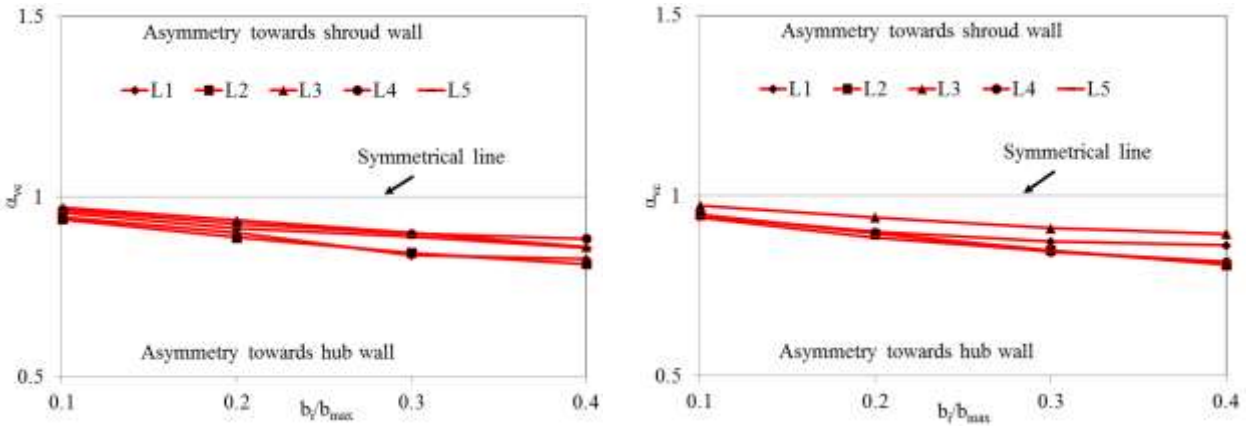

Figure 6.76: Local asymmetric ratio for the circumferential velocity, α_{vc} across the diverged wall diffusers ((a) $DWCD_3$ and (b) $DWCD_4$) at BEP and at an operational speed of 58.9rpsK$^{-1/2}$

Figure 6.77 depicts the circumferential velocity distribution across the centreline of the diverged wall curved diffuser configurations ($DWCD_5$, $DWCD_6$, $DWCD_7$ and $DWCD_8$) at BEP and at an operational speed of 58.9rpsK$^{-1/2}$. The trend of the circumferential velocity across the diverged wall diffuser passages is similar to that across the straight diffuser. It can be seen that the maximum circumferential velocity is obtained at the diffuser inlet after the volute-tongue region. The circumferential velocity decreases radially across the diffuser. Furthermore, the circumferential velocity also decreases circumferentially in the direction of impeller rotation (ω). The minimum circumferential velocity is obtained at the diffuser outlet at near the volute-tongue region. It can be seen that the circumferential velocity decreased by 0.6% at the diffuser inlet and is increased by 6.8% at the diffuser outlet of $DWCD_5$ in comparison to that of straight diffuser. Furthermore, the circumferential velocity is decreased by 0.6%, 1.2% and 0.6% at the diffuser inlet of $DWCD_6$, $DWCD_7$ and $DWCD_8$ respectively in comparison to that of $DWCD_5$. Similarly, the circumferential velocity is decreased by 8%, 29% and 28% at the diffuser outlet of $DWCD_6$, $DWCD_7$ and $DWCD_8$ respectively in comparison to that of $DWCD_5$. This trend explains that the circumferential decreases with the increase of both the distance between the divergence location and the diffuser inlet and outlet-to-inlet width ratio of the diffuser.

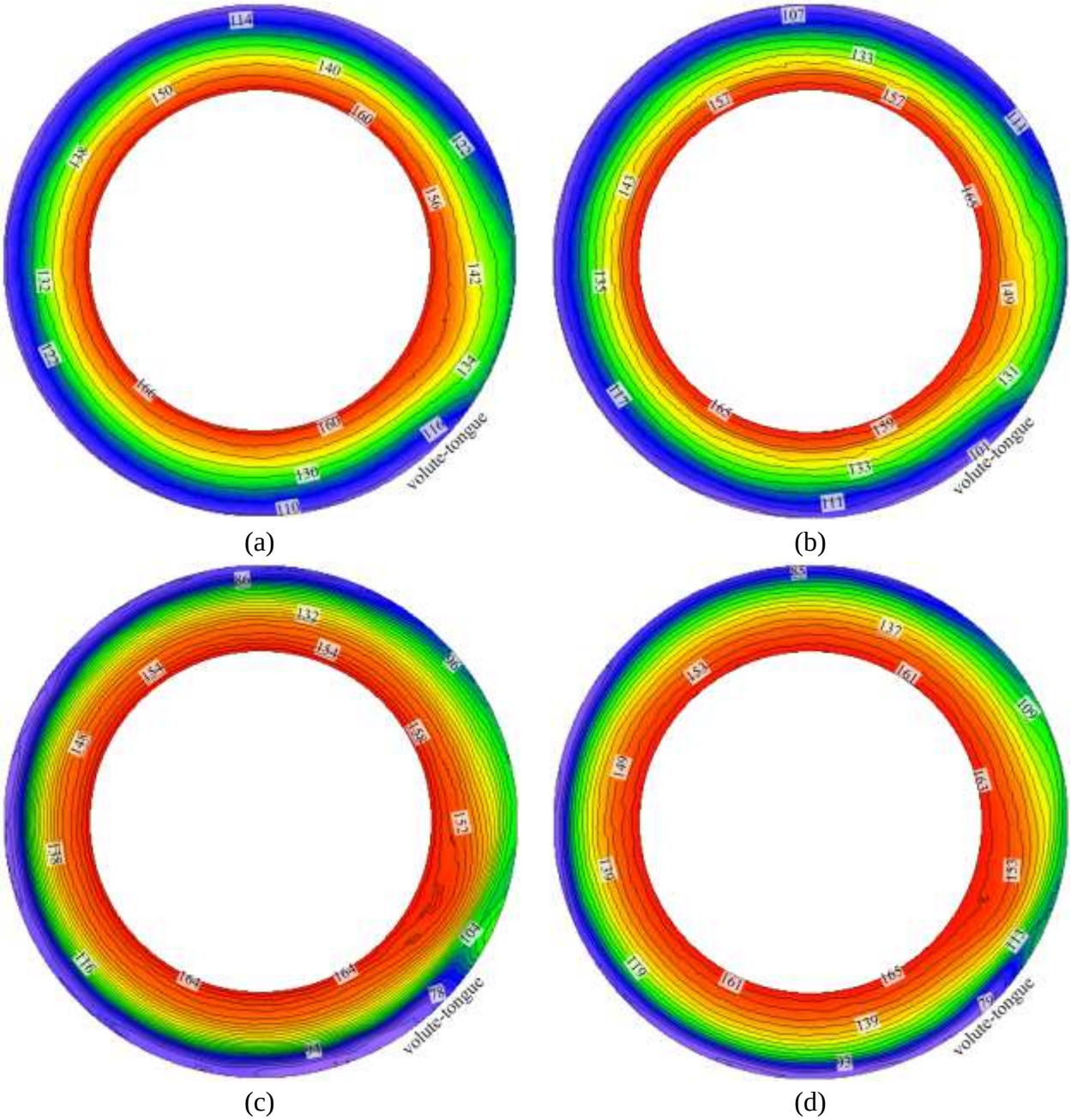

(a) (b)

(c) (d)

Figure 6.77: Circumferential velocity (m/s) distributions across the centreline of the diverged wall curved diffuser (a) $DWCD_5$, (b) $DWCD_6$, (c) $DWCD_7$ and (d) $DWCD_8$ at BEP and at an operational speed of 58.9rpsK$^{-1/2}$

Figure 6.78 depicts the comparison of circumferential velocity distribution across straight diffuser, optimal curved diffuser and diverged wall curved diffuser configurations ($DWCD_5$, $DWCD_6$, $DWCD_7$ and $DWCD_8$) from the hub wall to the shroud wall at BEP and at an operational speed of 58.9rpsK$^{-1/2}$. It can be seen that the circumferential velocity is reduced radially across the diffuser. It can also be seen that the circumferential velocity across diverged wall curved diffusers is higher in comparison to that across the straight diffuser. Furthermore, it has been observed that the

circumferential velocity is asymmetric towards the hub wall across diverged wall curved diffusers in comparison to that across straight diffuser, which has asymmetric circumferential velocity towards the shroud wall. However, the detailed analysis has been carried out by quantifying the asymmetric ratio for the circumferential velocity profile across the curved diffuser configurations.

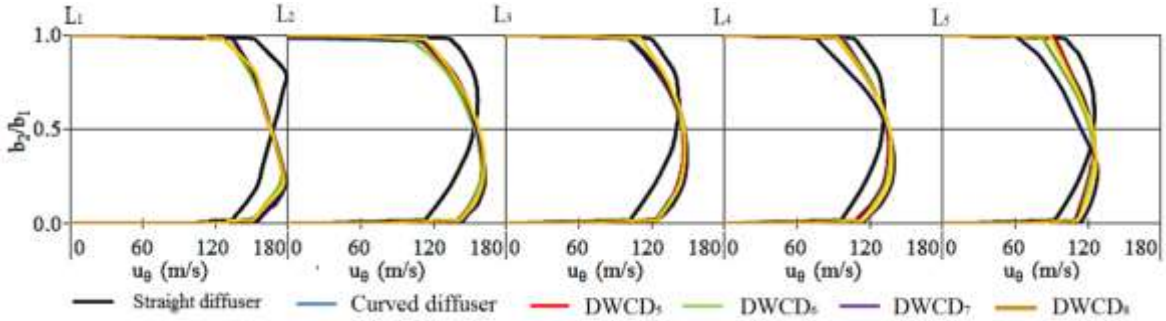

Figure 6.78: Comparison of circumferential velocity (m/s) distribution across the straight diffuser, optimal curved diffuser and diverged wall curved diffuser configurations ($DWCD_5$, $DWCD_6$, $DWCD_7$ and $DWCD_8$) from the hub wall to the shroud wall at BEP and at an operational speed of $58.9 rpsK^{-1/2}$

The behaviour of circumferential velocity across the diverged wall straight diffuser is explained using symmetric and asymmetric behaviour of the velocity field profiles. Figure 6.79 depicts the local asymmetric ratio for the circumferential velocity, α_{vc} across the diverged wall diffusers ($DWCD_5$, $DWCD_6$, $DWCD_7$ and $DWCD_8$) at BEP and at an operational speed of $58.9 rpsK^{-1/2}$. α_{vc} values of 1.0 shows the flow is symmetric, α_{vc} values below 1.0 shows asymmetric flow towards the hub wall and α_{vc} values above 1.0 shows asymmetric flow towards the shroud wall. It can be seen that the flow is asymmetric towards the hub wall across all the diverged wall curved diffusers considered. The asymmetric ratio for the circumferential velocity decreases from the centreline of the diffuser towards the wall. Moreover, the asymmetric ratio for the circumferential velocity also decreases from L_1 (diffuser inlet) to L_2, then increases from L_2 to L_3 and then it decreases from L_3 to L_5 (diffuser outlet) across both diverged wall curved diffusers considered. However, it has been noticed that combined increase of outlet-to-inlet width ratio wall diverged location from the inlet makes the flow highly asymmetrical.

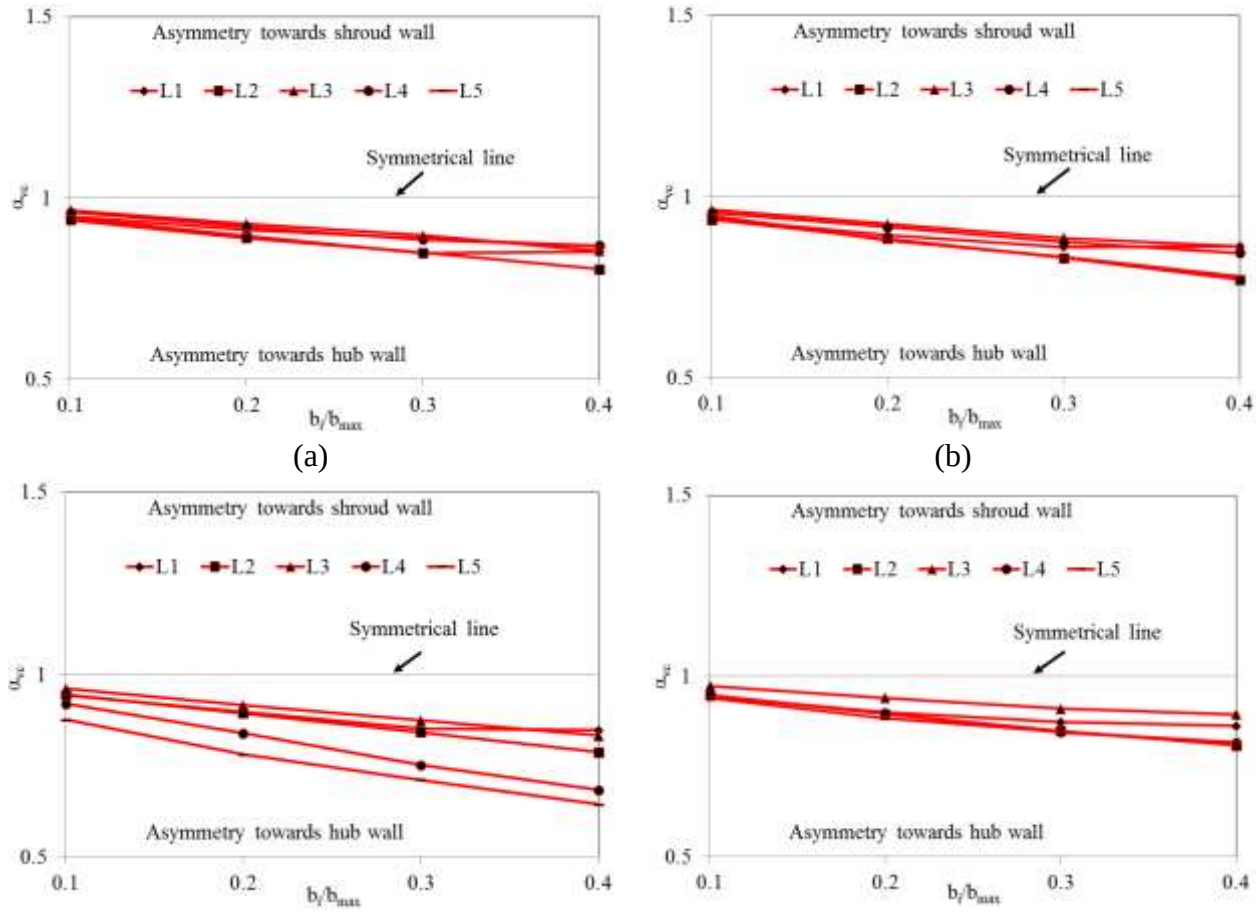

Figure 6.79: Local asymmetric ratio for the circumferential velocity, α_{vc} across the diverged wall diffusers ((a) $DWCD_5$ (b) $DWCD_6$, (c) $DWCD_7$ and (d) $DWCD_8$) at BEP and at an operational speed of 58.9rpsK$^{-1/2}$

Figure 6.80 depicts the static temperature variations across the centreline of the diverged wall curved diffuser configurations ($DWCD_1$ and $DWCD_2$) at BEP and at an operational speed of 58.9rpsK$^{-1/2}$. The trend of the static temperature across the diverged wall curved diffuser is similar to that across the straight diffuser. It can be seen that the minimum static temperature is obtained at the diffuser inlet after the volute-tongue region. The static temperature increases radially across the diffuser. Furthermore, the static temperature also increases circumferentially in the direction of impeller rotation (ω). The maximum static temperature is obtained at the diffuser outlet at near the volute-tongue region. It can be seen that the static temperature is decreased by 0.3% and 0.6% at the diffuser inlet and diffuser outlet respectively of $DWCD_1$ in comparison to that of the straight diffuser. Furthermore, it can also be seen that the static temperature is same at the diffuser inlet and is increased by 1.2% at the diffuser outlet of $DWCD_2$ in comparison to that of $DWCD_1$. This trend explains that

the static temperature decreases when outlet-to-inlet width ratio of the diffuser is increased initially by keeping the divergence location at the diffuser inlet and then increased by increasing more outlet-to-inlet width ratio.

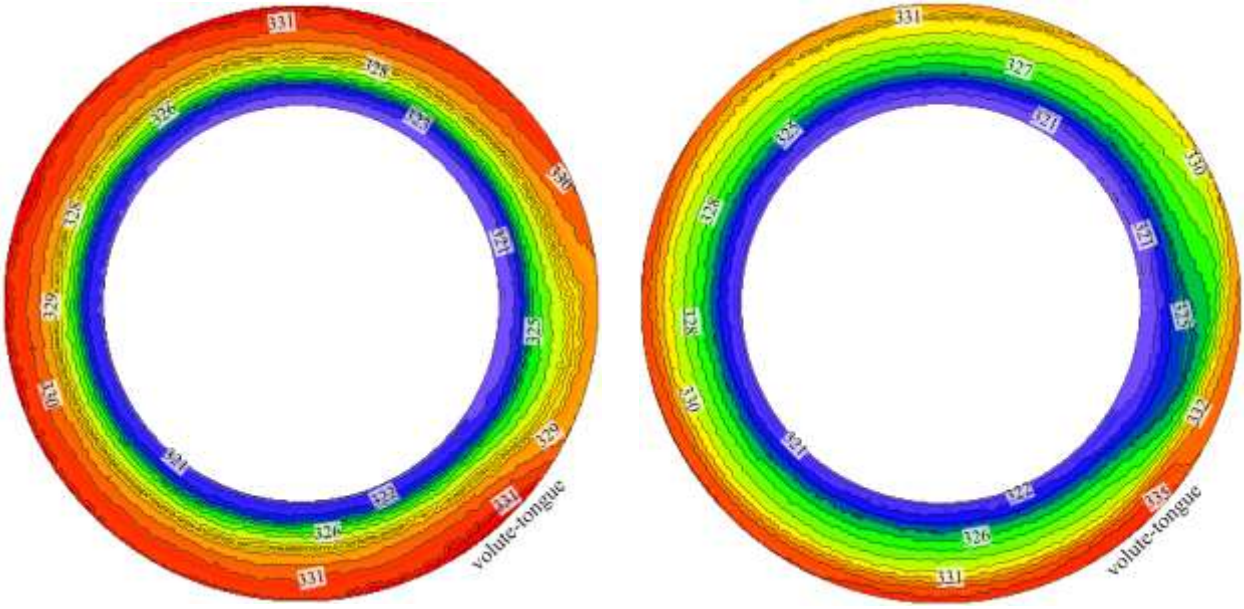

(a) (b)

6.80: Static temperature (K) variations across the centreline of the diverged wall curved diffusers (a) $DWCD_1$ and (b) $DWCD_2$ at BEP and at an operational speed of 58.9rpsK$^{-1/2}$

Figure 6.81 depicts the static temperature variations across the centreline of the diverged wall curved diffuser configurations ($DWCD_3$ and $DWCD_4$) at BEP and at an operational speed of 58.9rpsK$^{-1/2}$. The trend of the static temperature across the diverged wall curved diffuser configurations is similar to that across the straight diffuser. It can be seen that the minimum static temperature is obtained at the diffuser inlet after the volute-tongue region. The static temperature increases radially across the diffuser. Furthermore, the static temperature also increases circumferentially in the direction of impeller rotation (ω). The maximum static temperature is obtained at the diffuser outlet at near the volute-tongue region. It can be seen that the static temperature is decreased by 0.3% each at the diffuser inlet and diffuser outlet respectively of $DWCD_3$ in comparison to that of the straight diffuser. Furthermore, it can also be seen that the static temperature is same at the diffuser inlet and is increased by 0.6% at the diffuser outlet of $DWCD_2$ in comparison to that of $DWCD_1$. This trend explains that the static temperature decreases when outlet-to-inlet width ratio of the diffuser is increased initially by keeping the divergence location at the diffuser inlet and then increased by increasing more outlet-to-inlet width ratio.

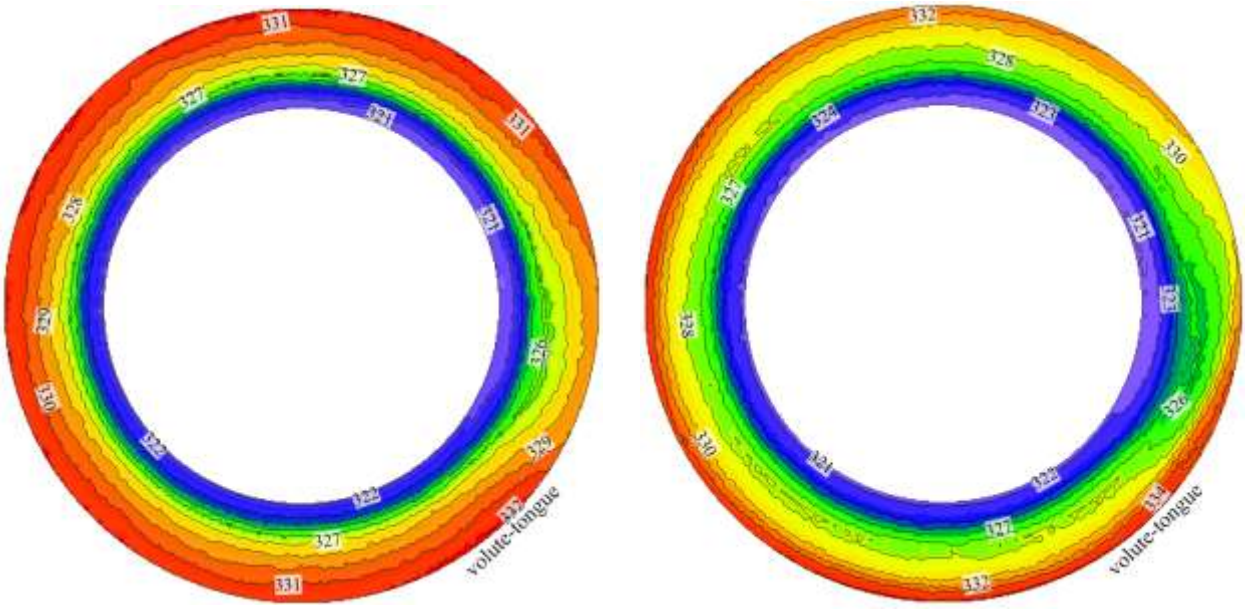

(a) (b)

Figure 6.81: Static temperature (K) variations across the centreline of the diverged wall curved diffuser (a) $DWCD_3$ and (b) $DWCD_4$ at BEP and at an operational speed of 58.9rpsK$^{-1/2}$

Figure 6.82 depicts the static temperature variations across the centreline of the diverged wall curved diffuser configurations ($DWCD_5$, $DWCD_6$, $DWCD_7$ and $DWCD_8$) at BEP and at an operational speed of 58.9rpsK$^{-1/2}$. The trend of the static temperature across the diverged wall curved diffuser configurations is similar to that across the straight diffuser. It can be seen that the minimum static temperature is obtained at the diffuser inlet after the volute-tongue region. The static temperature increases radially across the diffuser. Furthermore, the static temperature also increases circumferentially in the direction of impeller rotation (ω). The maximum static temperature is obtained at the diffuser outlet at near the volute-tongue region. It can be seen that the static temperature is decreased by 0.3% and 0.6% at the diffuser inlet and diffuser outlet respectively of $DWCD_5$ in comparison to that of the straight diffuser. Furthermore, the static temperature remains same at the diffuser inlet of $DWCD_6$, $DWCD_7$ and $DWCD_8$ in comparison to that of $DWCD_5$. Moreover, the static temperature is increased at the diffuser outlet of $DWCD_6$, $DWCD_7$ and $DWCD_8$ by 0.3%, 1.2% and 0.9% respectively in comparison to that of $DWCD_5$. It can be concluded from this trend that combined increase of L/L_{max} and b_2/b_1 increases the static temperature across the diverged wall curved diffuser configurations.

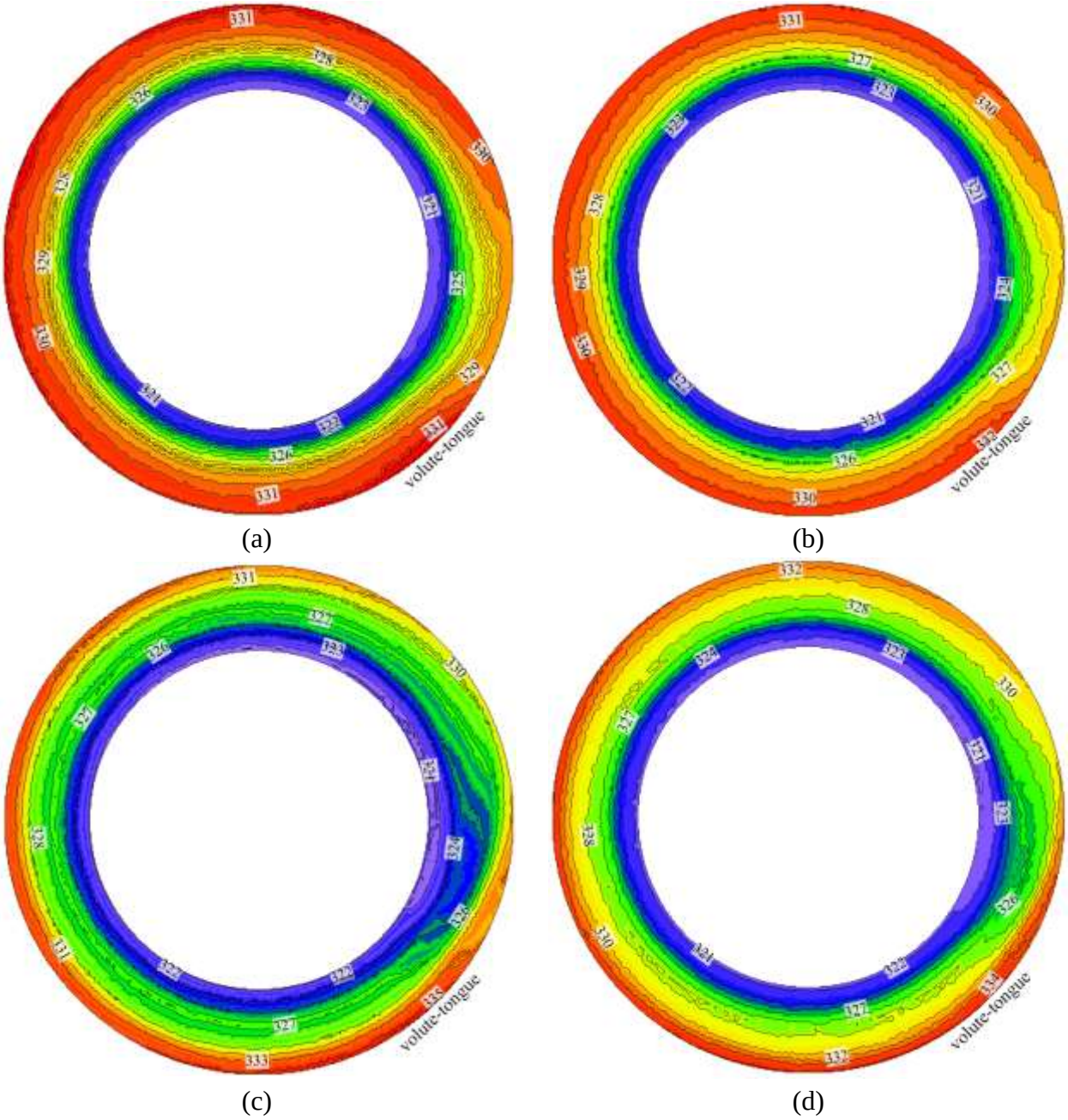

(a) (b)

(c) (d)

Figure 6.82: Static temperature (K) variations across the centreline of the diverged wall curved diffuser (a) $DWCD_5$, (b) $DWCD_6$, (c) $DWCD_7$ and (d) $DWCD_8$ at BEP and at an operational speed of 58.9rpsK$^{-1/2}$

6.6.2. Effect of Asymmetric Ratio across the Curved Diffusers

The behaviour of the flow within the curved diffusers is highly dependent upon the geometrical parameters considered. It has been noticed in the previous section that increase of diffuser width ratio increases the asymmetry of the flow towards the hub wall of the diverged wall curved diffuser. Furthermore, increase of divergence location on the hub wall of the diffuser from the diffuser inlet

makes the flow symmetric. A term Equation 6.1, which is introduced earlier in this chapter for the global asymmetric ratio, has been used that shows the change in behaviour of the flow across the diverged wall curved diffusers and shows the global effect of the asymmetry across the diverged wall curved diffusers. The geometrical parameters used in this equation must be for diverged wall curved diffuser. The major effect of geometrical parameters on the asymmetric flow behaviour and stage performance is described in detail.

Figure 6.83 depicts the global asymmetric ratio for the velocity magnitude across the diverged wall curved diffusers of $DWCD_1$ and $DWCD_2$ at BEP and at an operational speed of 58.9rpsK$^{-1/2}$. It can be seen that the global asymmetric ratio across these diverged wall curved diffusers is towards the hub wall of the diffuser. The global asymmetric ratio for the velocity magnitudes is decreased from L_1 (diffuser inlet) to L_2, then it is increased from L_2 to L_3 and then decreased towards L_5 (diffuser outlet). Furthermore, the global asymmetric ratio is lower for $DWCD_2$ in comparison to that for $DWCD_1$, which means the increase of outlet-to-inlet width ratio increases the flow asymmetry towards the hub wall for diverged wall curved diffusers.

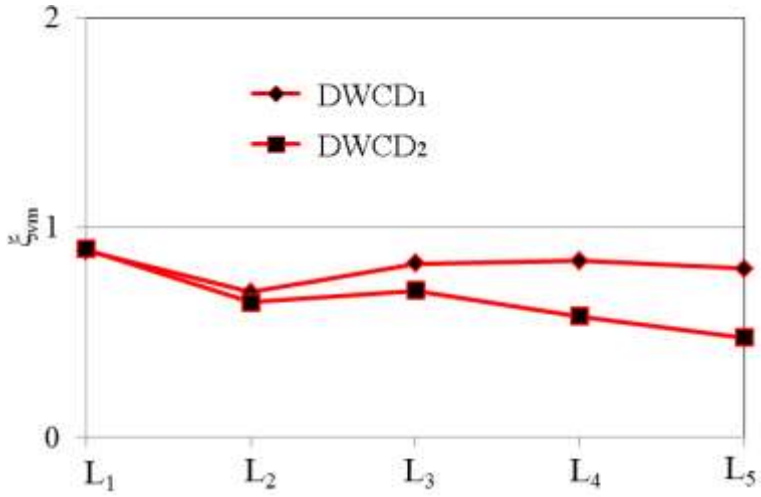

Figure 6.83: Global asymmetric ratio for the velocity magnitude across the curved diffusers ($DWCD_1$ and $DWCD_2$) at BEP at an operational speed of 58.9rpsK$^{-1/2}$

Figure 6.84 depicts the global asymmetric ratio for the velocity magnitude across the diverged wall curved diffusers of $DWCD_3$ and $DWCD_4$ at BEP and at an operational speed of 58.9rpsK$^{-1/2}$. It can be seen that the global asymmetric ratio across these diverged wall curved diffusers is towards the hub wall of the diffuser. The global asymmetric ratio for the velocity magnitudes is decreased from L_1 (diffuser inlet) to L_2, then it is increased from L_2 to L_3 and then decreased towards L_5 (diffuser

outlet). Furthermore, the global asymmetric ratio is same $DWCD_3$ and $DWCD_4$ until L_3 (50% distance from the diffuser inlet) and then decreased for $DWCD_4$ in comparison to that for $DWCD_3$.

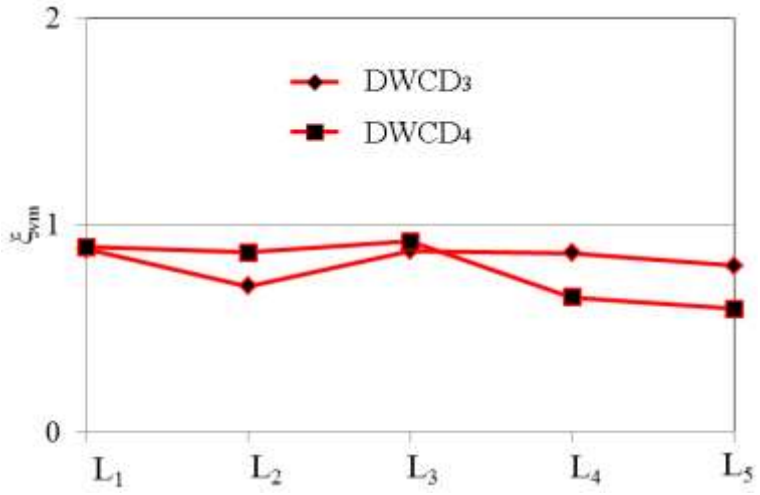

Figure 6.84: Global asymmetric ratio for the velocity magnitude across the curved diffusers ($DWCD_3$ and $DWCD_4$) at BEP at an operational speed of 58.9rpsK$^{-1/2}$

Figure 6.85 depicts the global asymmetric ratio for the velocity magnitude across the diverged wall curved diffusers of $DWCD_5$, $DWCD_6$, $DWCD_7$ and $DWCD_8$ at BEP and at an operational speed of 58.9rpsK$^{-1/2}$. It can be seen that the global asymmetric ratio across these diverged wall curved diffusers is towards the hub wall of the diffuser. The global asymmetric ratio for the velocity magnitudes is decreased from L_1 (diffuser inlet) to L_2, then it is increased from L_2 to L_3 and then decreased towards L_5 (diffuser outlet).

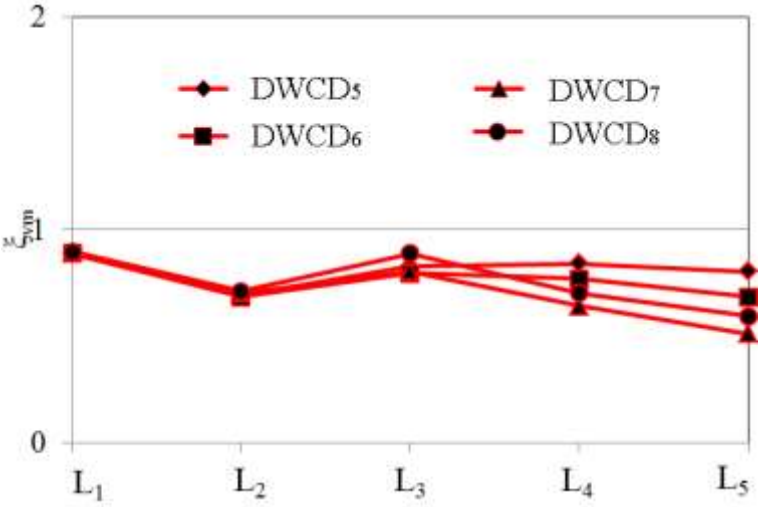

Figure 6.85: Global asymmetric ratio for the velocity magnitude across the curved diffusers ($DWCD_5$, $DWCD_6$, $DWCD_7$ and $DWCD_8$) at BEP at an operational speed of 58.9rpsK$^{-1/2}$

Figure 6.86 depicts the global asymmetric ratio for the radial velocity across the diverged wall curved diffusers of $DWCD_1$ and $DWCD_2$ at BEP and at an operational speed of $58.9rpsK^{-1/2}$. It can be seen that the global asymmetric ratio across these diverged wall curved diffusers is towards the hub wall of the diffuser. The global asymmetric ratio for the radial velocity is decreased from L_1 (diffuser inlet) to L_2, then it is increased from L_2 to L_4 and then decreased towards L_5 (diffuser outlet) across $DWCD_1$. Conversely, the global asymmetric ratio for the radial velocity is decreased from L_1 (diffuser inlet) to L_2, then it is increased from L_2 to L_3 and then decreased towards L_5 (diffuser outlet) across $DWCD_2$.

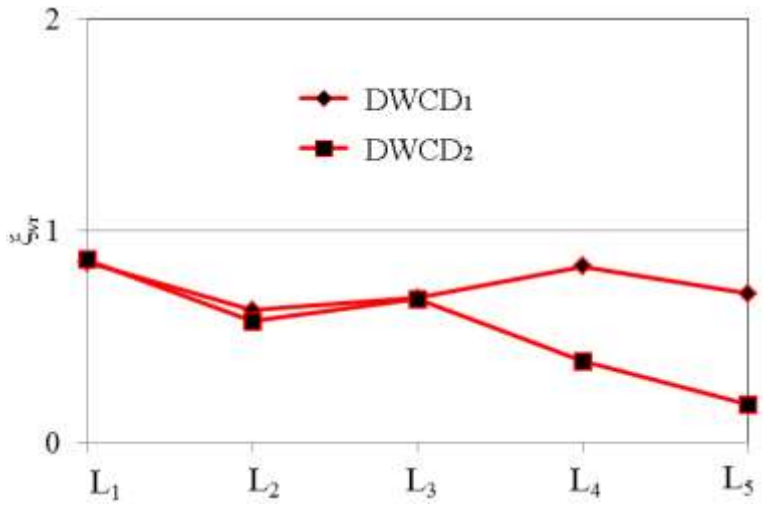

Figure 6.86: Global asymmetric ratio for the radial velocity across the curved diffusers ($DWCD_1$ and $DWCD_2$) at BEP and at an operational speed of $58.9rpsK^{-1/2}$

Figure 6.87 depicts the global asymmetric ratio for the radial velocity across the diverged wall curved diffusers of $DWCD_3$ and $DWCD_4$ at BEP and at an operational speed of $58.9rpsK^{-1/2}$. It can be seen that the global asymmetric ratio across these diverged wall curved diffusers is towards the hub wall of the diffuser. The global asymmetric ratio for the radial velocity is decreased from L_1 (diffuser inlet) to L_2, then it is increased from L_2 to L_3 and then decreased towards L_5 (diffuser outlet) across both diverged wall curved diffusers.

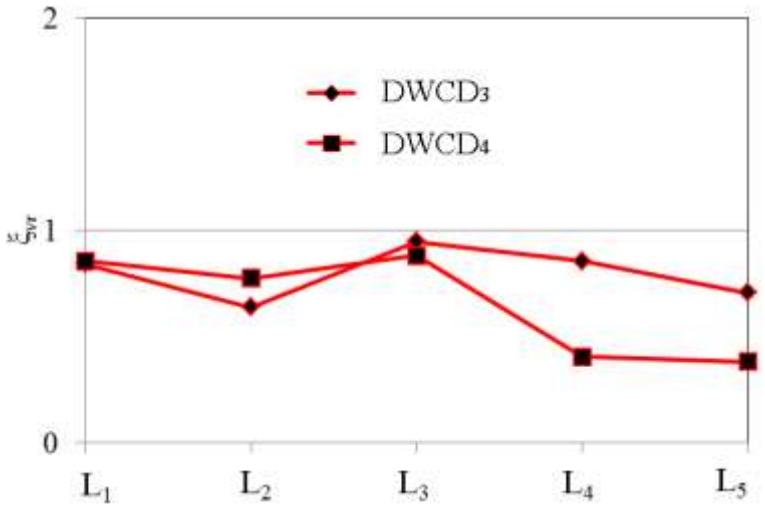

Figure 6.87: Global asymmetric ratio for the radial velocity of the curved diffusers ($DWCD_3$ and $DWCD_4$) at BEP at an operational speed of 58.9rpsK$^{-1/2}$

Figure 6.88 depicts the global asymmetric ratio for the radial velocity across the diverged wall curved diffusers of $DWCD_5$, $DWCD_6$, $DWCD_7$ and $DWCD_8$ at BEP and at an operational speed of 58.9rpsK$^{-1/2}$. It can also be seen that the global asymmetric ratio across these diverged wall curved diffusers is towards the hub wall of the diffuser. The global asymmetric ratio for the radial velocity is decreased from L_1 (diffuser inlet) to L_2, then it is increased from L_2 to L_4 and then decreased towards L_5 (diffuser outlet) across $DWCD_5$. Furthermore, the global asymmetric ratio for the radial velocity is decreased from L_1 (diffuser inlet) to L_2, then it is increased from L_2 to L_3 and then decreased towards L_5 (diffuser outlet) across $DWCD_6$, $DWCD_7$ and $DWCD_8$.

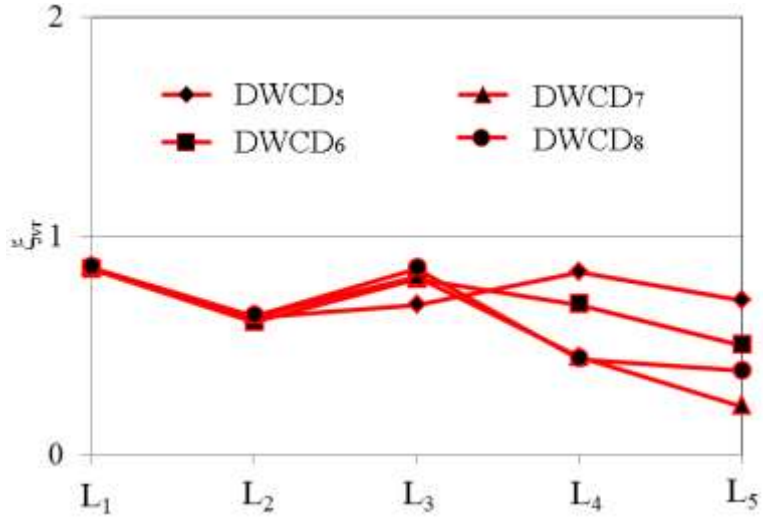

Figure 6.88: Global asymmetric ratio for the radial velocity of the curved diffusers ($DWCD_5$, $DWCD_6$, $DWCD_7$ and $DWCD_8$) at BEP at an operational speed of 58.9rpsK$^{-1/2}$

Figure 6.89 depicts the global asymmetric ratio for the circumferential velocity across the diverged wall curved diffusers of $DWCD_1$ and $DWCD_2$ at BEP and at an operational speed of $58.9rpsK^{-1/2}$. It can be seen that the global asymmetric ratio across these diverged wall curved diffusers is towards the hub wall of the diffuser. The global asymmetric ratio for the circumferential velocity is decreased from L_1 (diffuser inlet) to L_2, then it is increased from L_2 to L_3 and then decreased towards L_5 (diffuser outlet).

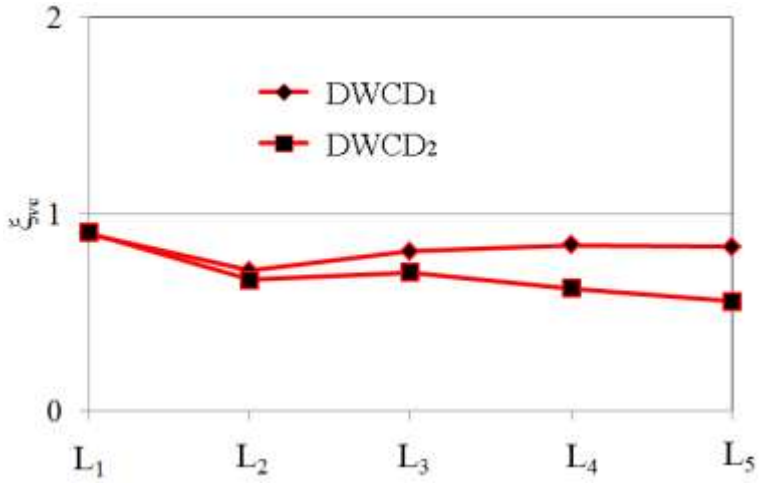

Figure 6.89: Global asymmetric ratio for the circumferential velocity across the curved diffusers ($DWCD_1$ and $DWCD_2$) at BEP at an operational speed of $58.9rpsK^{-1/2}$

Figure 6.90 depicts the global asymmetric ratio for the circumferential velocity across the diverged wall curved diffusers of $DWCD_3$ and $DWCD_4$ at BEP and at an operational speed of $58.9rpsK^{-1/2}$. It can be seen that the global asymmetric ratio across these diverged wall curved diffusers is towards the hub wall of the diffuser. The global asymmetric ratio for the circumferential velocity is decreased from L_1 (diffuser inlet) to L_2, then it is increased from L_2 to L_3 and then decreased towards L_5 (diffuser outlet). Furthermore, the global asymmetric ratio is same $DWCD_3$ and $DWCD_4$ until L_3 (50% distance from the diffuser inlet) and then decreased for $DWCD_4$ in comparison to that for $DWCD_3$.

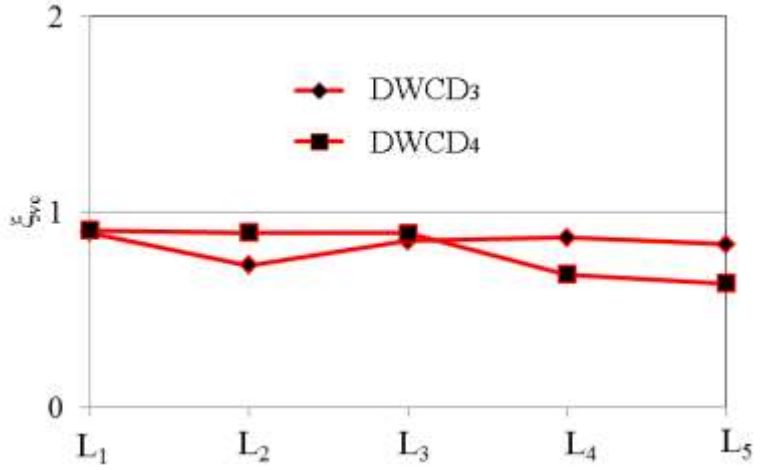

Figure 6.90: Global asymmetric ratio for the circumferential velocity across the curved diffusers ($DWCD_3$ and $DWCD_4$) at BEP at an operational speed of 58.9rpsK$^{-1/2}$

Figure 6.91 depicts the global asymmetric ratio for the circumferential velocity across the diverged wall curved diffusers of $DWCD_5$, $DWCD_6$, $DWCD_7$ and $DWCD_8$ at BEP and at an operational speed of 58.9rpsK$^{-1/2}$. It can be seen that the global asymmetric ratio across these diverged wall curved diffusers is towards the hub wall of the diffuser. The global asymmetric ratio for the circumferential velocity is decreased from L_1 (diffuser inlet) to L_2, then it is increased from L_2 to L_3 and then decreased towards L_5 (diffuser outlet).

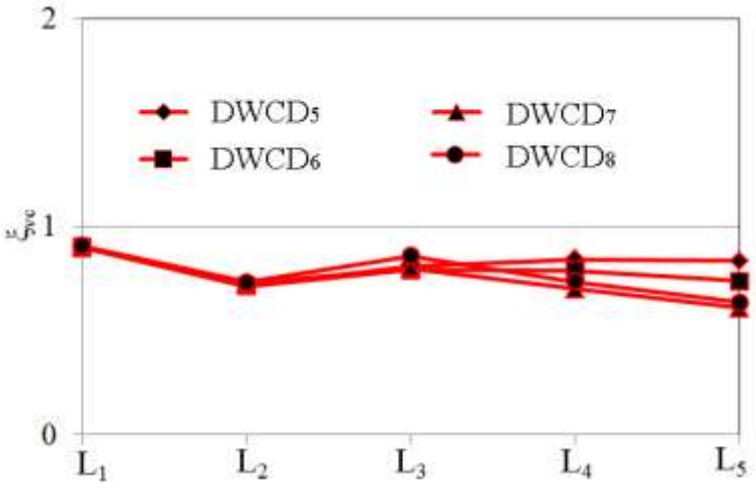

Figure 6.91: Global asymmetric ratio for the circumferential velocity across the curved diffusers ($DWCD_5$, $DWCD_6$, $DWCD_7$ and $DWCD_8$) at BEP at an operational speed of 58.9rpsK$^{-1/2}$

It is concluded from the above results that the flow is asymmetrical across the diverged wall curved diffusers. It has been noticed that the variations in the asymmetry of the flow are due to outlet-to-inlet width ratio and divergence location on the hub wall of the diffuser from the diffuser inlet. In order to

understand the overall effect of the geometrical changes on the diffuser flow field and stage performance, the equation 4.2 is used.

Figure 6.92 depicts the comparison of diffuser asymmetric effect for velocity magnitude across the diverged wall curved diffusers and straight diffuser at BEP and at an operational speed of 58.9rpsK$^{-1/2}$. It can be seen the asymmetric effect is fluctuated with the variations in b_2/b_1 and L/L_{max}. The asymmetric effect is below 1, which shows the flow asymmetry towards hub wall in comparison to that across the straight diffuser. Furthermore, the stage efficiency is fluctuated as well. It can be seen that the fluctuations for the diffuser asymmetric effect and stage efficiency remains consistent but the overall performance and asymmetric effect is increased. The stage efficiency is maximum having a value of 72% at $DWCD_1$ and $DWCD_3$. The stage efficiency is minimum having a value of 71% at $DWCD_2$.

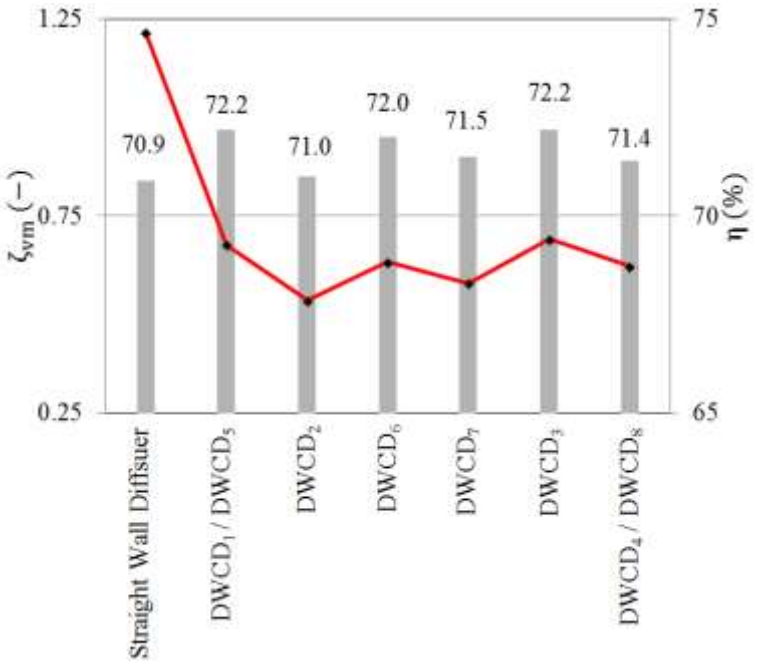

Figure 6.92: Comparison of diffuser asymmetric effect for velocity magnitude across the straight diffuse and the diverged wall curved diffusers at BEP and at the operational speed of 58.9rpsK$^{-1/2}$

Figure 6.93 depicts the comparison of diffuser asymmetric effect for radial velocity across the diverged wall curved diffusers and straight diffuser at BEP and at an operational speed of 58.9rpsK$^{-1/2}$. It can be seen the asymmetric effect is fluctuated with the variations in b_2/b_1 and L/L_{max}. The asymmetric effect is below 1, which shows the flow asymmetry towards hub wall in comparison to that across the straight diffuser. Furthermore, the stage efficiency is fluctuated as well. It can be seen that the fluctuations for the diffuser asymmetric effect and stage efficiency remains consistent but the

overall performance and asymmetric effect is increased. The stage efficiency is maximum having a value of 72% at $DWCD_1$ and $DWCD_3$. The stage efficiency is minimum having a value of 71% at $DWCD_2$.

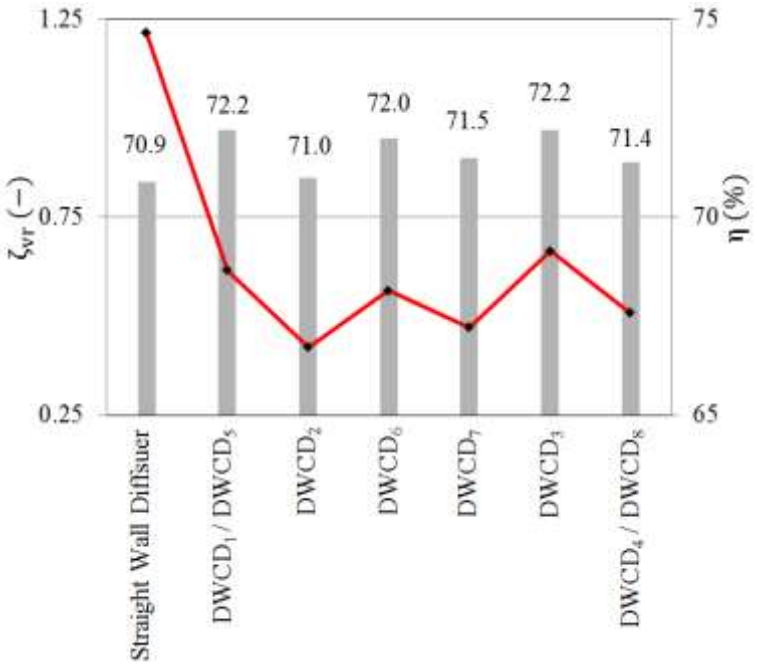

Figure 6.93: Comparison of diffuser asymmetric effect for radial velocity across the diverged wall tilted diffusers at BEP at the operational speeds of 58.9rpsK$^{-1/2}$

Figure 6.94 depicts the comparison of diffuser asymmetric effect for circumferential velocity across the diverged wall curved diffusers and straight diffuser at BEP and at an operational speed of 58.9rpsK$^{-1/2}$. It can be seen the asymmetric effect is fluctuated with the variations in b_2/b_1 and L/L_{max}. The asymmetric effect is below 1, which shows the flow asymmetry towards hub wall in comparison to that across the straight diffuser. Furthermore, the stage efficiency is fluctuated as well. It can be seen that the fluctuations for the diffuser asymmetric effect and stage efficiency remains consistent but the overall performance and asymmetric effect is increased. The stage efficiency is maximum having a value of 72% at $DWCD_1$ and $DWCD_3$. The stage efficiency is minimum having a value of 71% at $DWCD_2$.

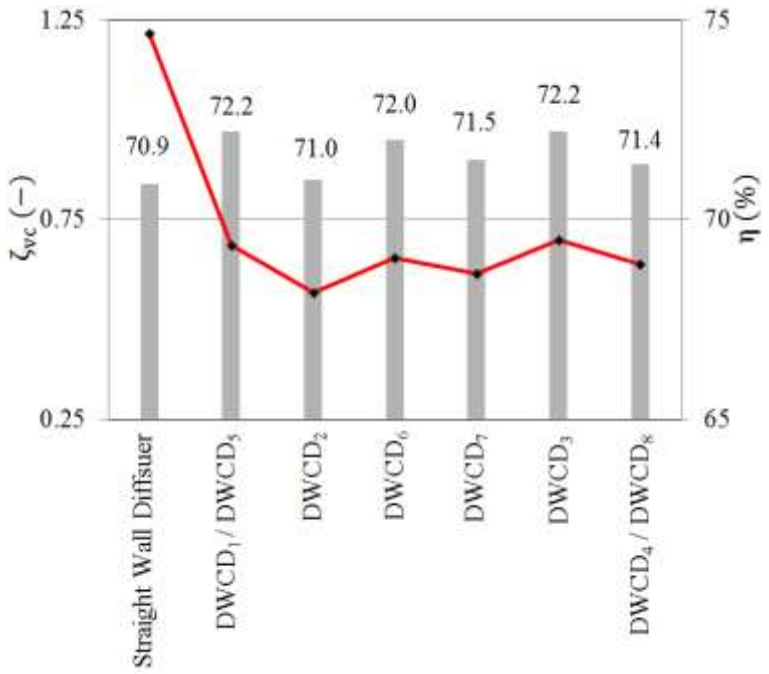

Figure 6.94: Comparison of diffuser asymmetric effect for circumferential velocity across the diverged wall tilted diffusers at BEP at the operational speeds of 58.9rpsK$^{-1/2}$

6.7. Characteristics of Geometrical Parameters

This section investigates the effects of the divergence on the hub wall of the curved diffuser and diffuser outlet-to-inlet width ratio on the curved diffuser local performance. The curved diffuser performance is dependent upon the recovery of static pressure across the diffuser.

6.7.1. Effects of Geometrical Parameters on Pressure Recovery across the Curved Diffuers

Two geometrical parameters b_2/b_1 and L/L_{max} have used to modify the curved diffuser geometry. These configurations have affected the diffuser performance. Figure 6.95 depicts the variation in the coefficient of pressure C_p while changing b_2/b_1 and L/L_{max} across and diverged wall curved diffusers ($DWCD_1$ and $DWCD_2$) and the straight diffuser at BEP and at an operational speed of 58.9rpsK$^{-1/2}$. It can be seen that increase of the diffuser outlet-to-inlet width ratio increases the pressure recovery within the diverged wall curved diffuser in comparison to that of straight diffuser. However, increasing large number of the diffuser outlet-to-inlet width ratio decreases the pressure recovery, C_p. The area ratio is a function of r/r_{max}, θ/θ_{max} and x/b_1.

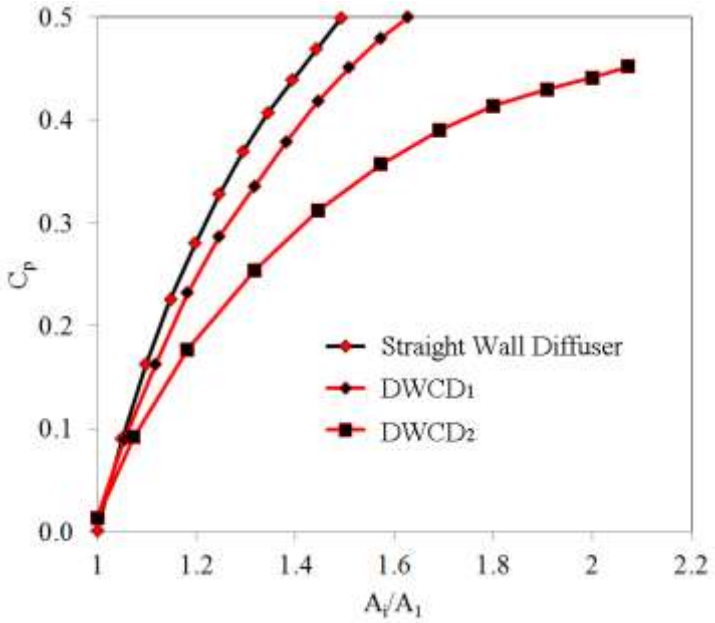

Figure 6.95: Variation in the coefficient of pressure C_p across the straight diffuser and diverged wall curved diffuser configurations

Figure 6.96 depicts the variation in the coefficient of pressure C_p while changing b_2/b_1 and L/L_{max} across and diverged wall curved diffusers ($DWCD_3$ and $DWCD_4$) and the straight diffuser at BEP and at an operational speed of 58.9rpsK$^{-1/2}$. It can be seen that C_p remains similar across the diverged wall curved diffuser and straight up to a wall divergence location and it is higher after wall divergence location of diverged wall curved diffusers. However, C_p reduces when the area ratio is very high (higher b_2/b_1).

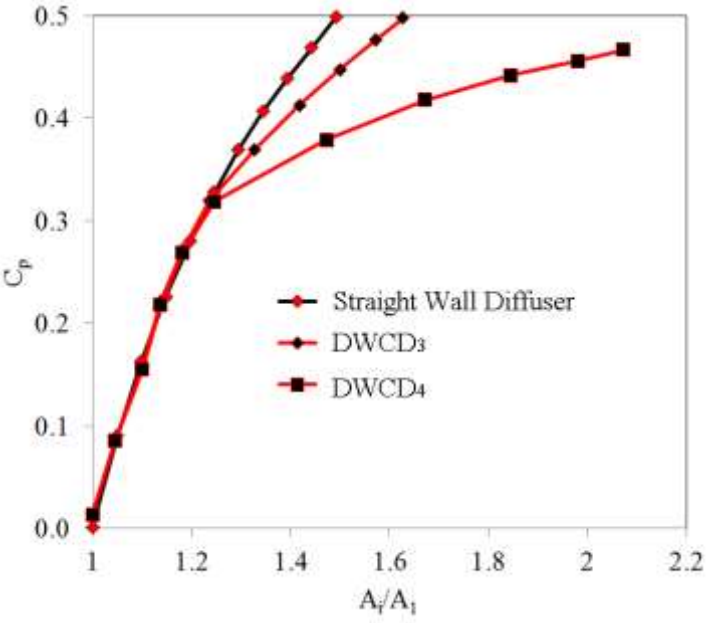

Figure 6.96: Variation in the coefficient of pressure C_p across the parallel wall diffuser and diverged wall diffuser configurations

Figure 6.97 depicts the variation in the coefficient of pressure C_p while changing b_2/b_1 and L/L_{max} across and diverged wall curved diffusers ($DWCD_5$, $DWCD_6$, $DWCD_7$ and $DWCD_8$) and the straight diffuser at BEP and at an operational speed of 58.9rpsK$^{-1/2}$. It can be seen that C_p remains similar across the diverged wall curved diffuser and straight up to a wall divergence location and it is higher after wall divergence location of diverged wall curved diffusers. However, C_p reduces when the area ratio is very high (higher b_2/b_1).

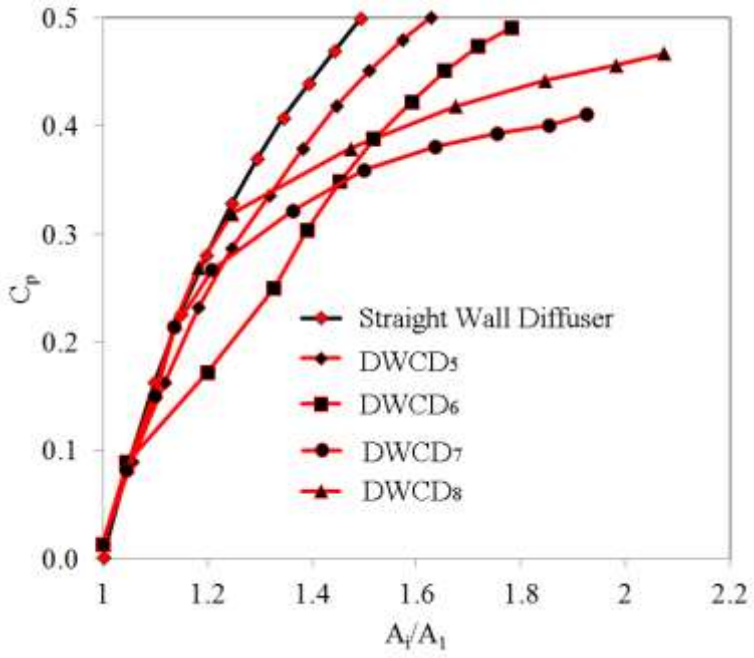

6.97: Variation in the coefficient of pressure C_p across the parallel wall diffuser and diverged wall diffuser configurations

6.8. Flow Field Characterisitics within Optimal Diverged Wall Curved Diffuser

This section investigates the flow field inside the optimal curved diffuser model with wall divergence based upon the static pressure, velocity magnitude and static temperature variations. These results are compared with straight diffuser (baseline model) and optimal curved diffuser. The optimisation of a model is dependent upon maximum isentropic efficiency and total-to-total stage pressure ratio. Based upon the analysis carried out in the previous section, it has been observed that maximum stage performance is obtained by the diverged wall curved diffuser is when geometrical parameters used are L/L_{max} = 0.3 and b_2/b_1 = 1.2. It can be seen that isentropic efficiency of 72.4% and pressure ratio

of 1.542 are increased by 2.07% and 0.93% respectively in comparison to that using straight diffuser (shown in Table 6.4). The detailed local flow field inside the compressor stage is presented hereafter.

Table 6.8: Comparison of performance parameters of straight diffuser, optimal curved diffuser and optimal diverged wall curved diffuser

	L/L_{max} (-)	b_2/b_1 (-)	PR_C (-)	η (%)	Percentage difference in PR_C (%)	Percentage difference in η (%)
Straight diffuser	0.0	0.0	1.527	70.9	-	-
Optimal curved diffuser	0.0	0.0	1.537	71.8	0.65	1.19
Optimal diverged wall curved diffuser	0.3	1.2	1.542	72.4	0.93	2.07

Figure 6.98 depicts the static pressure variations across the centreline of the optimal diverged wall curved diffuser at BEP and at an operational speed of 58.9rpsK$^{-1/2}$. The trend of the static pressure across the optimal diverged wall curved diffuser is similar to that across the straight diffuser. It can be seen that the minimum static pressure is obtained at the diffuser inlet after the volute-tongue region. The static pressure increases radially across the diffuser. Furthermore, the static pressure also increases circumferentially in the direction of impeller rotation (ω). The maximum static pressure is obtained at the diffuser outlet near the volute-tongue region. It can be seen that the static pressure is increased by 0.75% at the diffuser inlet and decreased by 0.67% at the diffuser outlet of the optimal diverged wall curved diffuser in comparison to that of straight diffuser.

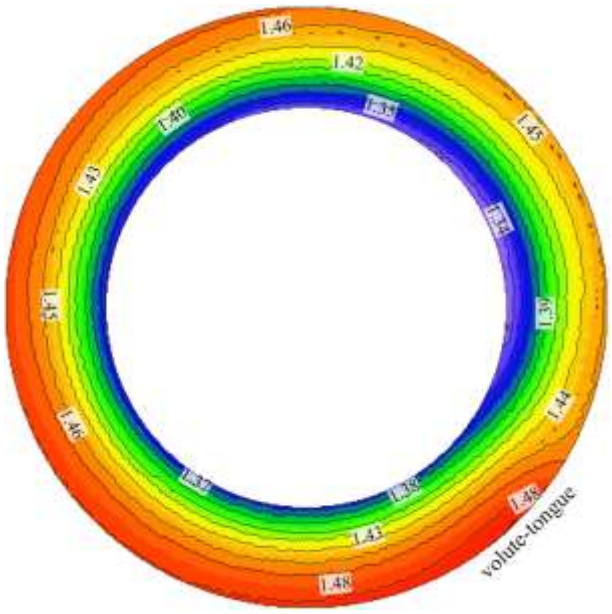

Figure 6.98: Static Pressure (atm) variations across the centreline of the optimal diverged wall curved diffuser at BEP at an operational speed of 58.9rpsK$^{-1/2}$

Figure 6.99 depicts flow streamlines radially across the cross-section of optimal diverged wall curved diffuser and oppositely interface volute at BEP and at an operational speed of 58.9rpsK$^{-1/2}$. It can be seen from the figure that no recirculation is found within the optimal diverged wall curved diffuser and hence, no losses are being generated. The colour inside the passages shows the velocity magnitude within the diffuser and volute passage. The velocity is higher at the diffuser inlet and reduces radially across the diffuser.

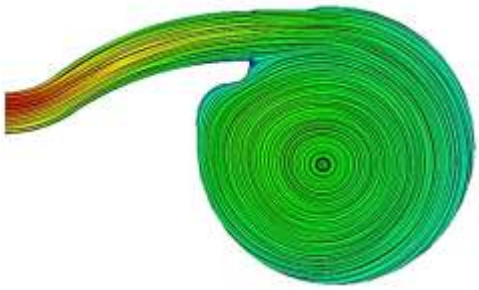

Figure 6.99: Flow streamlines radially across the (a) straight diffuser and volute (baseline) and (b) optimal diverged wall curved diffuser and oppositely interfaced volute at BEP and at an operational speed of 58.9rpsK$^{-1/2}$

Figure 6.100 depicts the comparison of velocity magnitude distribution across straight diffuser, optimal curved diffuser and optimal diverged wall curved diffuser from the hub wall to the shroud wall at BEP and at an operational speed of 58.9rpsK$^{-1/2}$. It can be seen that the velocity magnitude is reduced radially across the optimal diverged wall curved diffuser. It can also be seen that the velocity magnitude across optimal diverged wall curved diffuser is higher in comparison to that across the straight diffuser and similar to optimal curved diffuser. Furthermore, it has been observed that the velocity magnitude is asymmetric towards hub wall across the optimal diverged wall curved diffuser in comparison to that across the straight diffuser, which has velocity magnitude asymmetric towards the shroud wall. However, the detailed analysis has been carried out by quantifying the local asymmetric ratio for the velocity magnitude profile across the optimal diverged wall curved diffuser.

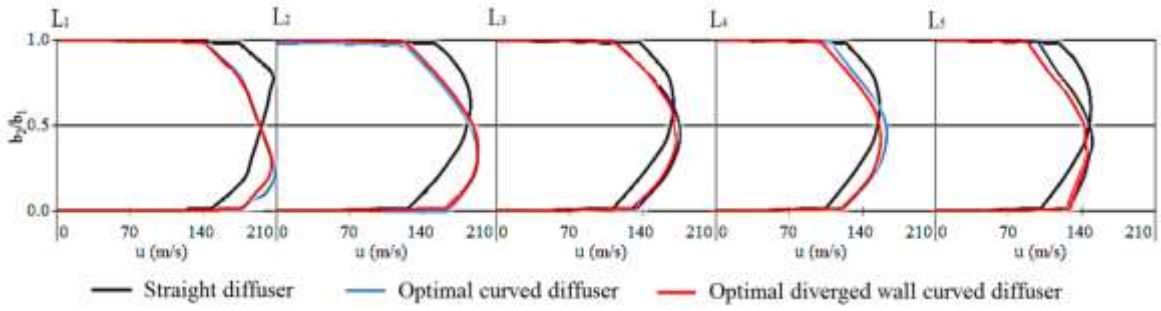

Figure 6.100: Comparison of velocity magnitude (m/s) distribution across the straight diffuser, optimal curved diffuser and the optimal diverged wall curved diffuser from the hub wall to the shroud wall at BEP and at an operational speed of 58.9rpsK$^{-1/2}$

Figure 6.101 depicts the local asymmetric ratio for the velocity magnitudes, α_{vm} across the optimal diverged wall curved diffuser at BEP and at an operational speed of 58.9rpsK$^{-1/2}$. It can be seen that the flow is asymmetric towards the hub wall across the optimal diverged wall curved diffuser. The asymmetric ratio for the velocity magnitude constantly increases from the centreline towards the wall of the diffuser. Furthermore, it can also be noticed that the local asymmetric ratio is decreased from L_1 (diffuser inlet) to L_2, then it is increased from L_2 to L_3 and then it again has decreased from L_3 to L_5 (diffuser outlet).

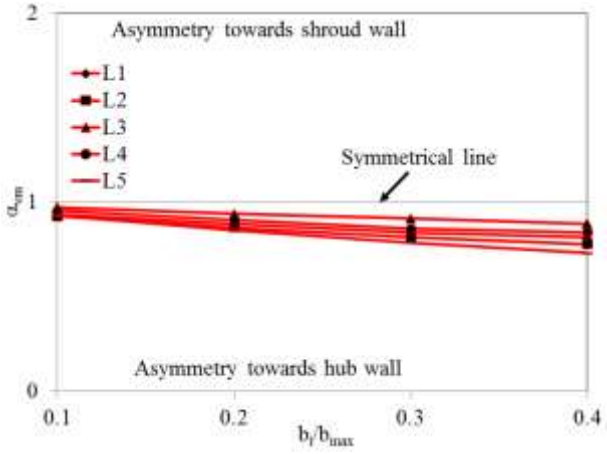

Figure 6.101: Local asymmetric ratio for the velocity magnitude, α_{vm} across the optimal diverged wall curved diffuser at BEP and at an operational speed of 58.9rpsK$^{-1/2}$

Figure 6.102 depicts the radial velocity distribution across the centreline of the optimal diverged wall curved diffuser at BEP and at an operational speed of 58.9rpsK$^{-1/2}$. The trend of the radial velocity across the optimal diverged wall curved diffuser is similar to that across the straight diffuser. It can

be seen that the maximum radial velocity is obtained at the diffuser inlet after the volute-tongue region. The radial velocity decreases radially across the diffuser. Furthermore, the radial velocity also decreases circumferentially in the direction of impeller rotation (ω). The minimum radial velocity is obtained at the diffuser outlet at near the volute-tongue region. It can be seen that the radial velocity is decreased by 1% and 19% at the diffuser inlet and the diffuser outlet respectively of optimal diverged wall curved diffuser in comparison to that of the straight diffuser.

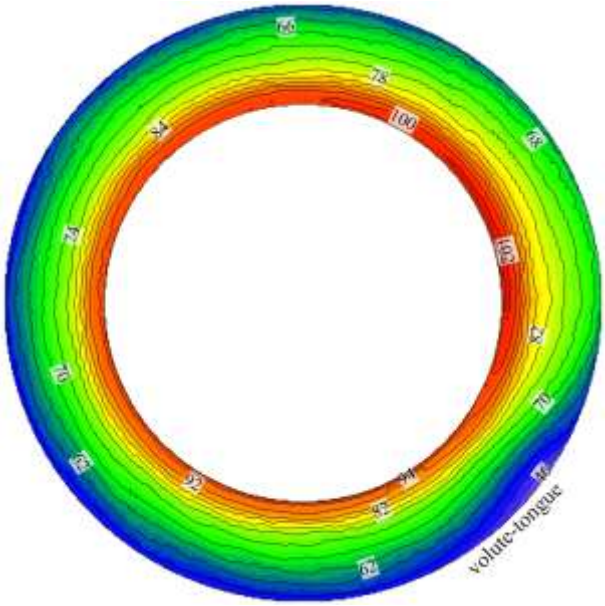

Figure 6.102: Radial velocity (m/s) distribution across the centreline of the optimal diverged wall curved diffuser at BEP and at an operational speed of 58.9rpsK$^{-1/2}$

Figure 6.103 depicts the comparison of radial velocity distribution across straight diffuser, optimal curved diffuser and optimal diverged wall curved diffuser from the hub wall to the shroud wall at BEP and at an operational speed of 58.9rpsK$^{-1/2}$. It can be seen that the radial velocity is reduced radially across the diffuser. It can also be seen that the radial velocity across optimal diverged wall curved diffuser is higher in comparison to that across the straight diffuser. Furthermore, it has been observed that the radial velocity is asymmetric towards the hub wall across the optimal diverged wall curved diffuser in comparison to that across the straight diffuser, which has radial velocity asymmetric towards the shroud wall. Moreover, radial velocity is highly asymmetric towards the hub wall at L_1 (diffuser inlet) and then the asymmetry has reduced, and the flow has become symmetric at L_3. Thereafter, the flow again has become asymmetric after L_3 towards L_5 (diffuser outlet).

However, the detailed analysis has been carried out by quantifying the asymmetric ratio for the radial velocity profile across the optimal diverged wall curved diffuser.

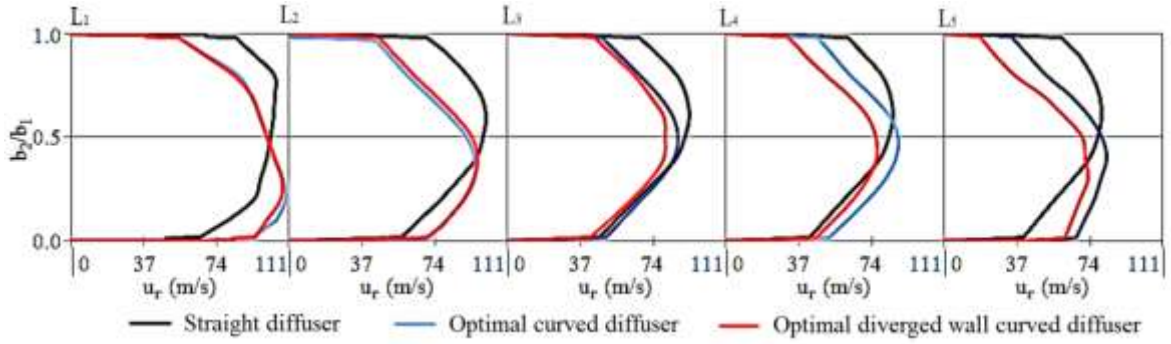

Figure 6.103: Comparison of radial velocity (m/s) distribution across the straight diffuser, optimal curved diffuser and the optimal diverged wall curved diffuser from the hub wall to the shroud wall at BEP and at an operational speed of 58.9rpsK$^{-1/2}$

Figure 6.104 depicts the local asymmetric ratio for the radial velocity, α_{vr} across the optimal diverged wall curved diffuser at BEP and at an operational speed of 58.9rpsK$^{-1/2}$. The radial flow velocity is asymmetric towards the hub wall from L_1 (diffuser inlet) to L_2, then the flow has become symmetric at L_3 and then the flow has again become asymmetric towards the hub wall from L_4 to L_5 (diffuser outlet).

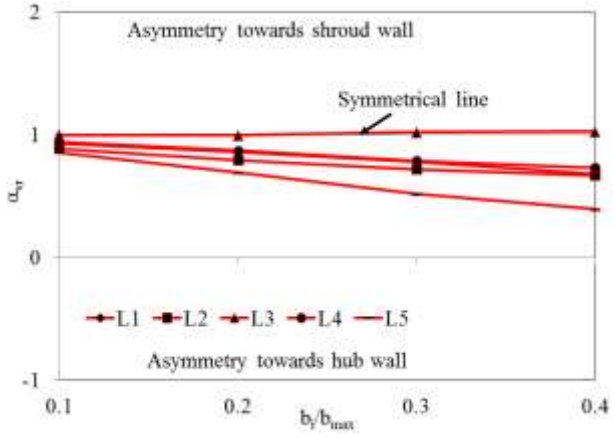

Figure 6.104: Local asymmetric ratio for the radial velocity, α_{vr} across the optimal diverged wall curved diffuser at BEP and at an operational speed of 58.9rpsK$^{-1/2}$

Figure 6.105 depicts the circumferential velocity distribution across the centreline of the optimal diverged wall curved diffuser at BEP and at an operational speed of 58.9rpsK$^{-1/2}$. The trend of the

circumferential velocity across the optimal diverged wall curved diffuser is similar to that across the straight diffuser. It can be seen that the maximum circumferential velocity is obtained at the diffuser inlet after the volute-tongue region. The circumferential velocity decreases radially across the diffuser. Furthermore, the circumferential velocity also decreases circumferentially in the direction of impeller rotation (ω). The minimum circumferential velocity is obtained at the diffuser outlet at near the volute-tongue region. It can be seen that the circumferential velocity is decreased at the diffuser inlet by 1.2% and increased at the diffuser outlet by 3.9% of the optimal diverged wall curved diffuser in comparison to that of the straight diffuser.

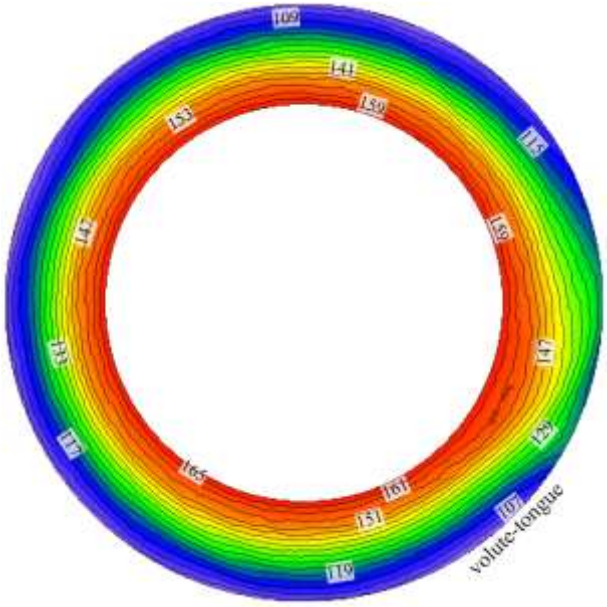

Figure 6.105: Circumferential velocity (m/s) distribution across the centreline of the optimal diverged wall curved diffuser at BEP and at an operational speed of 58.9rpsK$^{-1/2}$

Figure 6.106 depicts the comparison of circumferential velocity distribution across straight diffuser, optimal curved diffuser and optimal diverged wall curved diffuser from the hub wall to the shroud wall at BEP and at an operational speed of 58.9rpsK$^{-1/2}$. It can be seen that the circumferential velocity is reduced radially across the diffuser. It can also be seen that the circumferential velocity across the optimal diverged wall curved diffuser is higher in comparison to that across the straight diffuser. Furthermore, it has been observed that the circumferential velocity is asymmetric towards hub wall across the optimal curved diffuser in comparison to that across the straight diffuser, which has asymmetric circumferential velocity towards the shroud wall. However, the detailed analysis has been

carried out by quantifying the asymmetric ratio for the circumferential velocity profile across curved diffuser configurations.

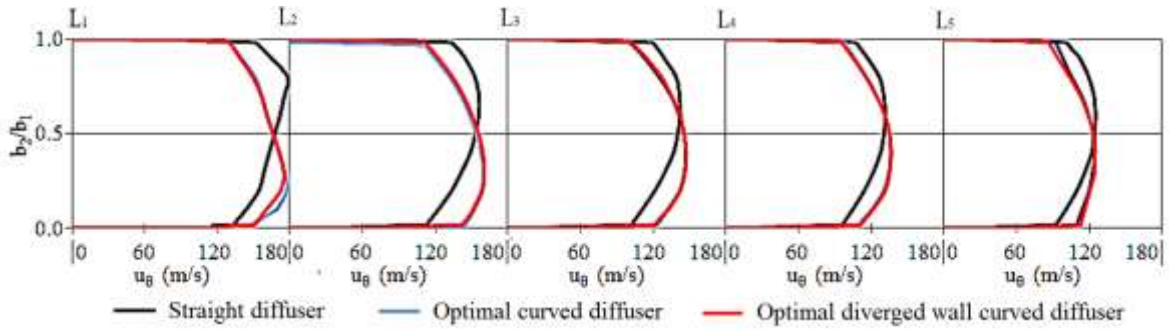

Figure 6.106: Comparison of circumferential velocity (m/s) distribution across the straight diffuser, optimal curved diffuser and the optimal diverged wall curved diffuser from the hub wall to the shroud wall at BEP and at an operational speed of 58.9rpsK$^{-1/2}$

Figure 6.107 depicts the local asymmetric ratio for the circumferential velocity, α_{vc} across the optimal diverged wall curved diffuser at BEP and at an operational speed of 58.9rpsK$^{-1/2}$. It can be seen that the flow is asymmetric towards the hub wall across optimal diverged wall curved diffuser. The asymmetric ratio for the circumferential velocity constantly increases from the centreline of the diffuser towards the wall. Furthermore, it can also be seen that the local asymmetric ratio decreases from L_1 to L_2, then it increases from L_2 to L_4 and then it decreases L_4 to L_5.

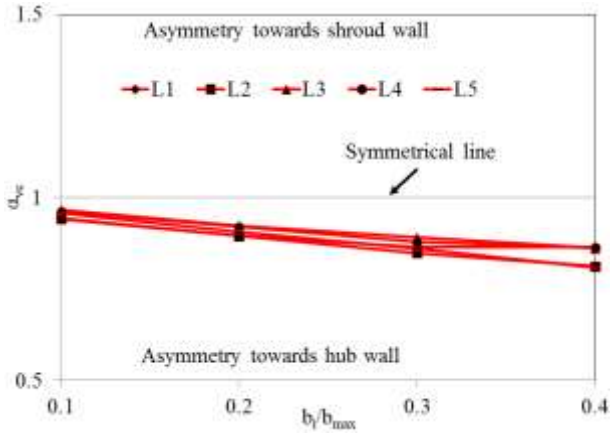

Figure 6.107: Local asymmetric ratio for the circumferential velocity, α_{vr} across the optimal diverged wall curved diffuser at BEP and at an operational speed of 58.9rpsK$^{-1/2}$

Figure 6.108 depicts the static temperature variations across the centreline of the optimal diverged wall curved diffuser at BEP and at an operational speed of 58.9rpsK$^{-1/2}$. The trend of the static

temperature across the optimal diverged wall curved diffuser is similar to that across the straight diffuser. It can be seen that the minimum static temperature is obtained at the diffuser inlet after the volute-tongue region. The static temperature increases radially across the diffuser. Furthermore, the static temperature also increases circumferentially in the direction of impeller rotation (ω). The maximum static temperature is obtained at the diffuser outlet near the volute-tongue region. It can be seen that the static temperature is decreased by 0.3% and 0.6% at the diffuser inlet and diffuser outlet respectively of the optimal diverged wall curved diffuser in comparison to that of the straight diffuser.

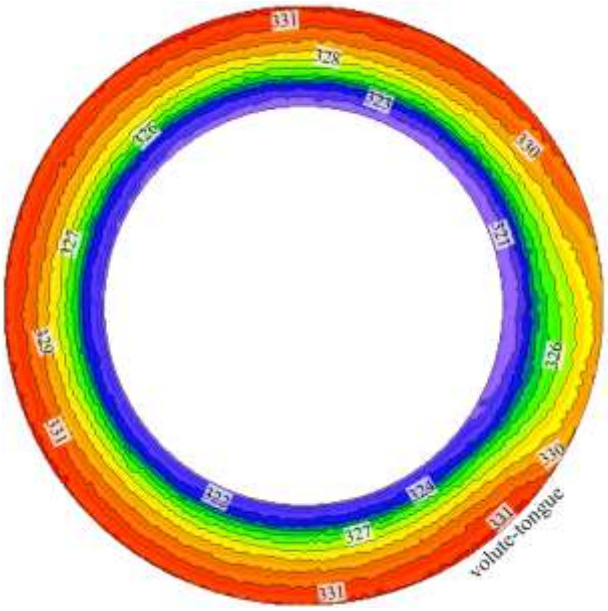

Figure 6.108: Static temperature (K) variations across the centreline of the optimal diverged wall curved diffuser at BEP at an operational speed of 58.9rpsK$^{-1/2}$

6.8.1. Effect of Flow Assemetry on the Performance of the Optimal Curved Diffuser

The behaviour of the flow within the optimal diverged wall curved diffuser is highly dependent upon the geometrical parameter considered. It has been noticed in the previous section that increase of ratio of b_2/b_1 and L/L_{max} increases the asymmetry of the flow towards the hub wall of the diverged wall curved diffuser. An Equation 4.1 is used to obtain the global asymmetric ratio, which shows the change in behaviour of the flow across the curved diffuser and the global effect of the asymmetry across the curved diffuser. The major effect of geometrical parameters on the asymmetric flow behaviour and stage performance is described in detail.

Figure 6.109 depicts the global asymmetric ratio for the velocity magnitude across the straight diffuser and the optimal diverged wall curved diffuser at BEP and at an operational speed of 58.9rpsK^{-}

$^{1/2}$. It can be seen that the global asymmetric ratio across the optimal diverged wall curved diffuser is towards the hub wall of the diffuser in comparison to that across the straight diffuser, which has global asymmetric ratio towards the shroud wall. The global asymmetric ratio for the velocity magnitudes is seemed to be decreased from L_1 (diffuser inlet) to L_2, then increased from L_2 to L_3 and then finally decreased from L_3 to L_5 (diffuser outlet).

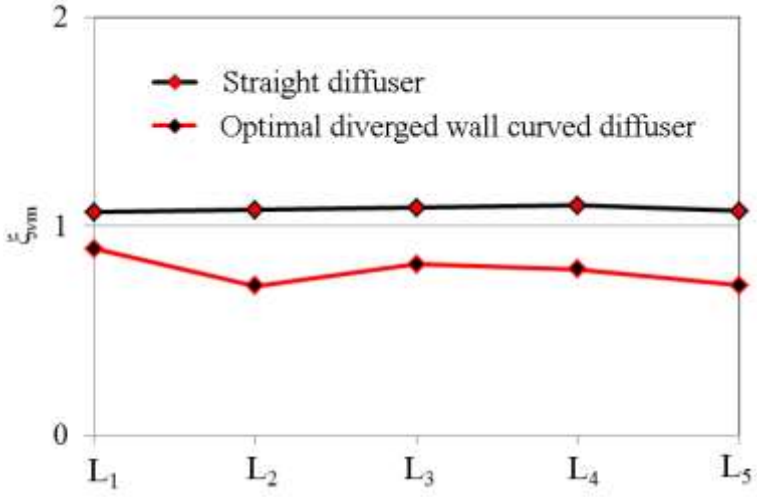

Figure 6.109: Global asymmetric ratio for the velocity magnitude across the straight diffuser and the optimal diverged wall curved diffuser at BEP and at an operational speed of 58.9rpsK$^{-1/2}$

Figure 6.110 depicts the global asymmetric ratio for the radial velocity across the straight diffuser and the optimal diverged wall curved diffuser at BEP and at an operational speed of 58.9rpsK$^{-1/2}$. It can be seen that the global asymmetric ratio across the optimal diverged wall curved diffuser is towards the hub wall in comparison to that across the straight diffuser, which has global asymmetric ratio towards the shroud wall. The global asymmetric ratio for the velocity magnitudes is seemed to be decreased from L_1 (diffuser inlet) to L_2, then increased from L_2 to L_3 and then finally decreased from L_3 to L_5 (diffuser outlet).

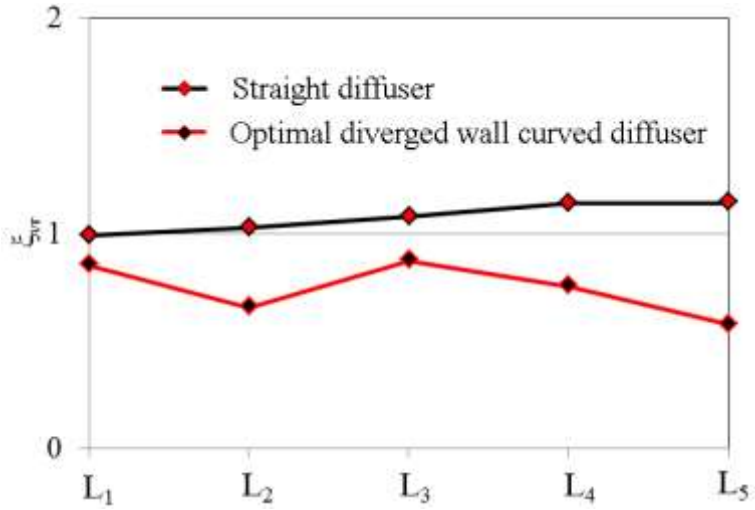

Figure 6.110: Global asymmetric ratio for the radial velocity across the straight diffuser and the optimal diverged wall curved diffuser at BEP and at an operational speed of 58.9rpsK$^{-1/2}$

Figure 6.111 depicts the global asymmetric ratio for the circumferential velocity across the straight diffuser and the optimal diverged wall curved diffuser at BEP and at an operational speed of 58.9rpsK$^{-1/2}$. It can be seen that the global asymmetric ratio across the optimal diverged wall curved diffuser is towards the hub wall in comparison to that across the straight diffuser, which has global asymmetric ratio towards the shroud wall. The global asymmetric ratio for the velocity magnitudes is seemed to be decreased from L_1 (diffuser inlet) to L_2, then increased from L_2 to L_3 and then finally global asymmetric ratio remains same from L_3 to L_5 (diffuser outlet).

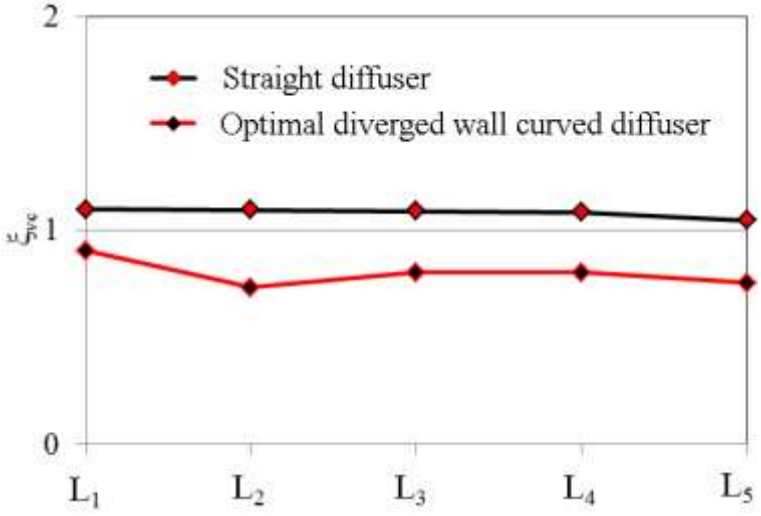

Figure 6.111: Global asymmetric ratio for the circumferential velocity across the straight diffuser and the optimal diverged wall curved diffuser at BEP and at an operational speed of 58.9rpsK$^{-1/2}$

It is concluded from the above results that the flow is asymmetrical across straight diffuser and optimal diverged wall curved diffuser. It has been noticed that the variations in the asymmetry are due to b_2/b_1 and L/L_{max}. In order to understand the overall effect of the geometrical changes on the diffuser flow field and stage performance, the equation 4.2 is used.

Figure 6.112 depicts the comparison of the diffuser asymmetric effect for the velocity magnitude across the straight diffuser and optimal curved diffuser at BEP and at an operational speed of 58.9rpsK$^{-1/2}$. It can be seen that the asymmetric effect for the velocity magnitude is below 1 for optimal diverged wall curved diffuser showing the flow is asymmetric towards the hub wall in comparison to that of straight diffuser having flow asymmetry towards the shroud wall. Furthermore, it can also be seen that the stage efficiency of optimal curved diffuser and optimal diverged wall curved diffuser is increased to 71.79% and 72.2% respectively in comparison to that across the straight diffuser having stage efficiency of 70.9%.

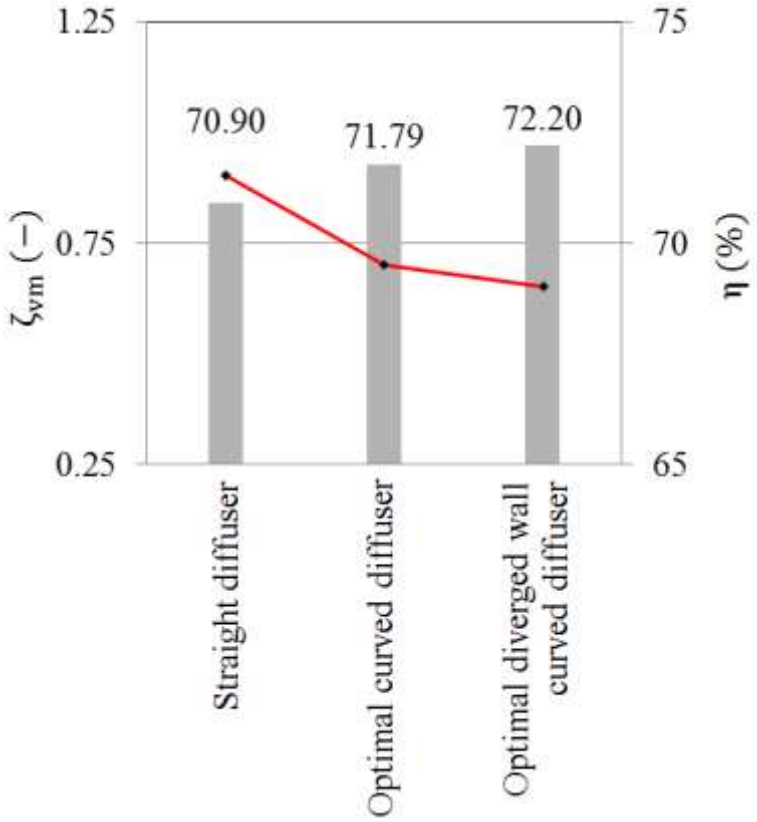

Figure 6.112: Comparison of diffuser asymmetric effect for velocity magnitude across the straight diffuser, optimal curved diffuser and optimal diverged wall curved diffuser at BEP and at the operational speed of 58.9rpsK$^{-1/2}$

Figure 6.113 depicts the comparison of the diffuser asymmetric effect for the radial velocity across the straight diffuser and optimal curved diffuser at BEP and at an operational speed of 58.9rpsK$^{-1/2}$. It can be seen that the asymmetric effect for the radial velocity is below 1 for optimal diverged wall curved diffuser showing the flow is asymmetric towards the hub wall in comparison to that of straight diffuser having flow asymmetry towards the shroud wall. Furthermore, it can also be seen that the stage efficiency of optimal curved diffuser and optimal diverged wall curved diffuser is increased to 71.79% and 72.2% respectively in comparison to that across the straight diffuser having stage efficiency of 70.9%.

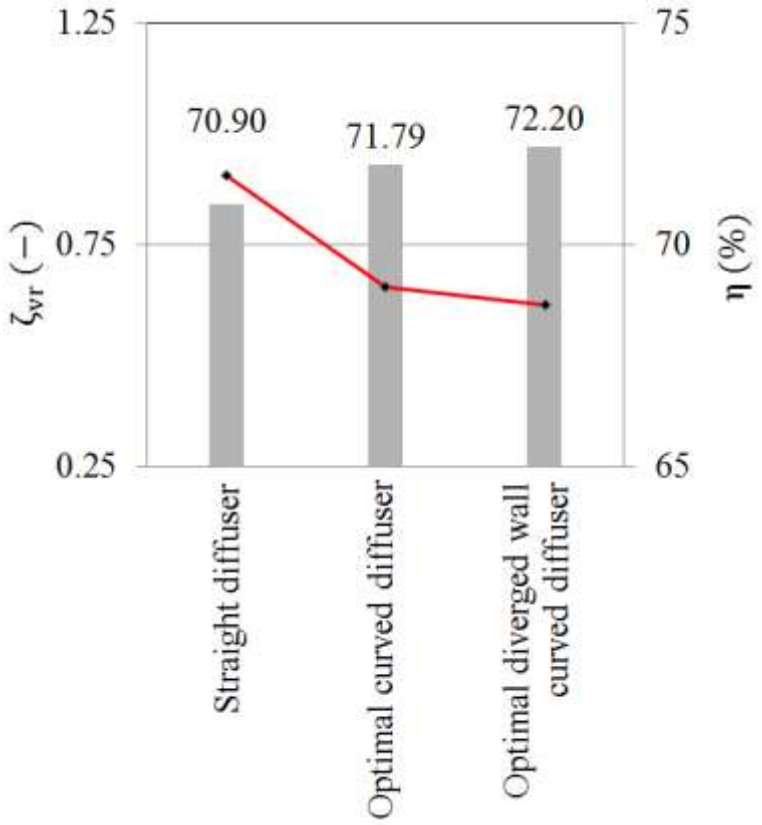

Figure 6.113: Comparison of diffuser asymmetric effect for radial velocity across the straight diffuser, optimal curved diffuser and optimal diverged wall curved diffuser at BEP and at the operational speed of 58.9rpsK$^{-1/2}$

Figure 6.114 depicts the comparison of the diffuser asymmetric effect for the circumferential velocity across the straight diffuser and optimal curved diffuser at BEP and at an operational speed of 58.9rpsK$^{-1/2}$. It can be seen that the asymmetric effect for the circumferential velocity is below 1 for optimal diverged wall curved diffuser showing the flow is asymmetric towards the hub wall in comparison to that of straight diffuser having flow asymmetry towards the shroud wall. Furthermore, it can also be seen that the stage efficiency of optimal curved diffuser and optimal diverged wall

curved diffuser is increased to 71.79% and 72.2% respectively in comparison to that across the straight diffuser having stage efficiency of 70.9%.

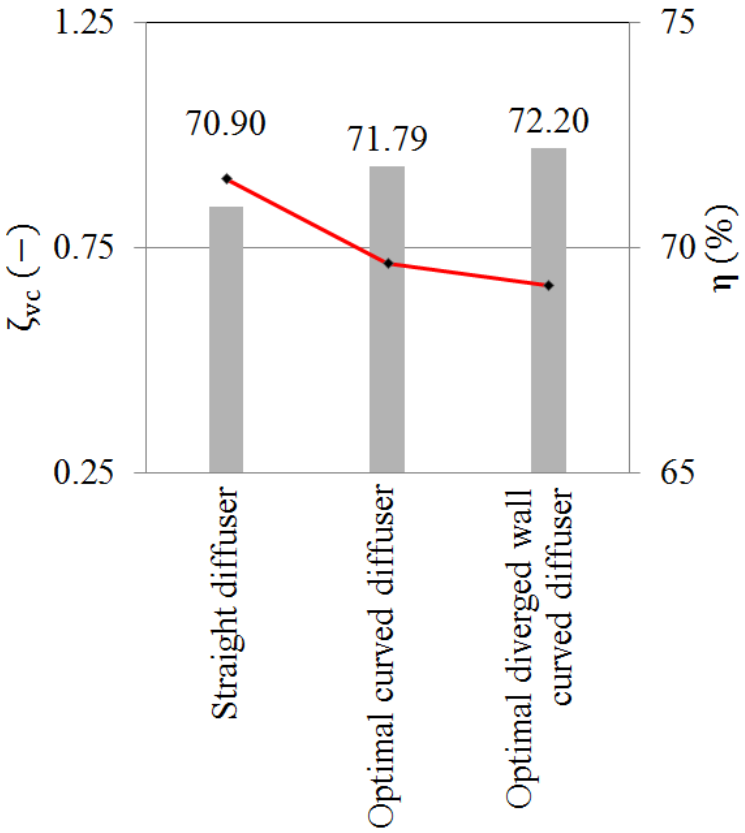

Figure 6.114: Comparison of diffuser asymmetric effect for circumferential velocity across the straight diffuser, optimal curved diffuser and optimal diverged wall curved diffuser at BEP and at the operational speed of 58.9rpsK$^{-1/2}$

This section demonstrates the comparison of optimal diverged wall curved diffuser, optimal curved diffuser and straight diffuser on the basis of diffuser geometries used. The diffuser performance is dependent upon the recovery of static pressure across the diffuser.

Two geometrical parameters b_2/b_1 and L/L_{max} have used to modify the optimal diverged wall curved diffuser geometry. This configuration has affected the diffuser performance. Figure 6.115 depicts the variation in the coefficient of pressure C_p having $L/L_{max} = 0.3$ and $b_2/b_1 = 1.2$ of the optimal diverged wall curved diffuser, optimal curved diffuser and straight diffuser at BEP and at an operational speed of 58.9rpsK$^{-1/2}$. It can be seen that C_p almost remains similar across the optimal curved diffuser and straight diffuser. However, C_p and area ratio increases across optimal diverged wall curved diffuser in comparison to that across straight and optimal curved diffuser.

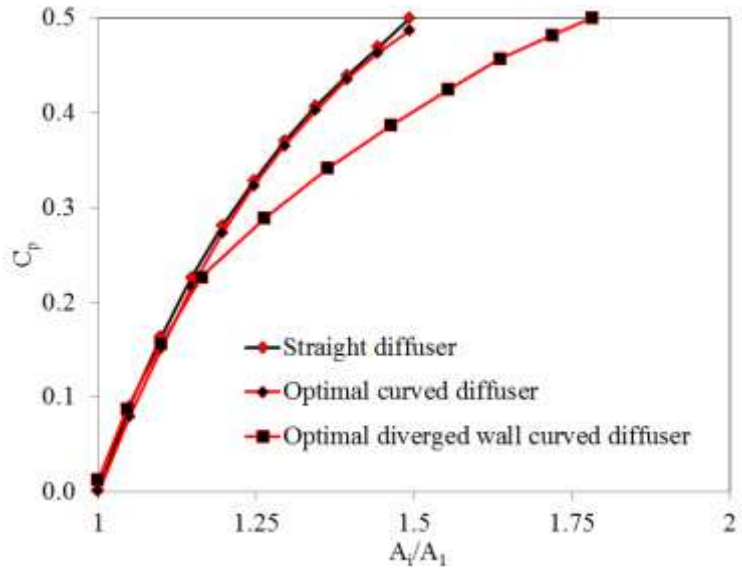

Figure 6.115 Variation in the coefficient of pressure C_p across the straight diffuser, optimal curved diffuser and optimal diverged wall curved diffuser at BEP and at the operational speed of 58.9rpsK$^{-1/2}$

6.9. Summary

From the result presented in this chapter, it can be concluded that the curving the diffuser wall causes an increase in static pressure and allows to make the compressor stage more compact. It is important to obtain high isentropic compression efficiency within the compressor stage to decrease losses during operation. The diffuser is one of the most important components of the turbocharger compressor stage and has a key purpose of partially recovering the static pressure. The local isentropic efficiency has been investigated. Various flow phenomena have been noticed during this investigation, which are as follows;

1. Increasing the radius ratio causes isentropic efficiency and total-to-total stage pressure ratio to reduce up to a value of 0.8 and thereafter the performance parameters are increased.

2. Increase of angle of curvature causes total-to-total stage pressure ratio to increase, however isentropic efficiency reduces.

3. Increase of axial distance between the hub wall near the diffuser inlet and the shroud wall near the outlet of the diffuser has caused the total-to-total stage pressure ratio and isentropic efficiency to increase up to $x/b_1 = 3.03$. Thereafter, both the performance parameters decrease.

4. Increase of outlet-to-inlet width ratio causes decrease in the pressure ratio and the isentropic efficiency.
5. Change in the location of wall divergence from 0.0 to 0.3 increases the stage performance and then the performance decreases.

Furthermore, diffuser asymmetric effect for the curved wall diffusers and diverged wall curved diffusers has been investigated. It has been noticed that increase of ratio of r/r_{max} and θ/θ_{max} increases the asymmetry of the flow towards the hub wall of the curved diffuser. However, increase of ratio of x/b_1 increases the asymmetric ratio, which shifts the flow from hub wall towards the shroud wall. Furthermore, it also been noticed that increase of divergence location on the hub wall of the curved wall diverged diffuser from the diffuser inlet makes the flow symmetric.

CHAPTER 7
CONCLUSIONS

From the results obtained in the previous chapters regarding the flow inside parallel, diverged, tilted and curved diffuser passages and based upon their critical analysis, detailed conclusions have been drawn in this chapter. The major achievements and contributions to the existing knowledge base are summarised and wherever possible referenced back to the initial aims of this study. Finally, the works carried out in this study are evaluated and requirements for future work in the area of vaneless diffusers for the centrifugal compressors are defined.

7.1. Research Problem Synopsis

Engine downsizing is potentially one of the most effective strategies being explored to improve fuel economy. Turbochargers are used to provide extra boost to the engine in terms of high pressure of fluid flow. A main problem of downsizing using a turbocharger is the small range of stable functioning of the turbocharger centrifugal compressor at high boost pressures. Several techniques were studied to increase the compressor operating range without sacrificing the compressor efficiency and the technique used in this study is modifying the shape of vaneless diffuser inside the compressor stage. With the advent of powerful computing machines and sophisticated software to analyse the flow fields, it has now become possible to computationally model a turbocharger compressor stage and map the flow within the centrifugal compressor stage under varying geometric and flow conditions.

From a comprehensive review of the published literature, a number of limitations have been identified which are concerned with the aforementioned points. In order to accurately predict the flow behaviour in vaneless diffuser of the centrifugal compressor stage, a set of aims and objectives have been formulated which define the scope of this research study. A summary of the primary aims of the thesis is provided in the following sections of this chapter along with the major achievements and contributions. For reference, the detailed objectives within each of these aims are given in Chapter 2.

7.2. Research Aims and Major Achievements

The main aims of the thesis defined from an extensive literature review in this area are as follows:

Research Aim # 1: An improved understanding of the flow behaviour within diverged wall vaneless diffusers

Achievement # 1: This study provides a detailed CFD based investigation on the local flow field within the straight diffuser of the centrifugal compressor stage, presented in Chapter 4. It also identifies its effect on the total-to-total stage performance parameters and proposes a prediction diffuser model, which increases the stage performance. A numerical study on the flow across the straight diffuser with wall divergence, having flow rate ranging from design conditions to off-design conditions at lower rotating speeds, has been presented. Experimental data is used to verify the data

with the numerically obtained CFD results and treated the model as the baseline model. In order to cover a wide range of geometrical parameters for a vaneless diffuser (only limited geometrical parameters are available in literature for which local flow fields have been analysed), flow at lower rotating speeds in centrifugal compressor stage has been numerically simulated for various (a) outlet-to-inlet width ratios and (b) divergence locations.

Based on the detailed numerical investigation of the flow structure and behaviour, the pressure, temperature and velocity fields in vaneless diffusers have been critically analysed both qualitatively and quantitatively. Qualitative analysis makes use of the pressure, temperature and velocity contours in the vaneless diffusers whereas, the quantitative analysis makes use of the coefficient of pressure and normalised local flow velocity for the analysis of pressure, velocity distribution and asymmetric behaviour of the flow within the diffusers respectively. The results presented give a clear picture of the flow behaviour within the diffusers and the effect of the outlet-to-inlet width ratios and wall divergence locations on the flow structure and the static pressure rise within the diffusers locally and on the total-to-total compressor stage performance.

Research Aim # 2: Development of novel diffuser configurations having tilted and diverged walls

Achievement # 2: This study provides a detailed CFD based investigation on the local flow field inside the tilted vaneless diffuser passage of the centrifugal compressor stage, presented in Chapter 5. It also identifies its effect on the total-to-total stage performance parameters and proposes a prediction diffuser model, which increases the stage performance. A numerical study on the flow across the tilted wall vaneless diffuser passage with wall divergence, having flow rate ranging at design conditions and lower rotating speeds, has been presented. The results are compared with the baseline model. Design of experiments using Taguchi method is used to reduce the number of simulations and an optimisation technique based upon analysis of variances has been applied to obtain the best model. In order to cover a wide range of geometrical parameters for a tilted vaneless diffuser (only limited geometrical parameters are available in literature for which local flow fields have been analysed), flow at lower rotating speeds in centrifugal compressor stage has been numerically simulated for various (a) tilted angle positions, (b) outlet-to-inlet width ratios and (c) divergence locations.

Based on the detailed numerical investigation of the flow structure and behaviour, the pressure, temperature and velocity fields in vaneless diffusers have been critically analysed both qualitatively and quantitatively. Qualitative analysis makes use of the pressure, temperature and velocity contours in the vaneless diffusers whereas, the quantitative analysis makes use of the coefficient of pressure and normalised local flow velocity for the analysis of pressure and velocity distribution and asymmetric behaviour of the flow within the diffusers respectively. The results presented give a clear picture of the flow behaviour within the diffusers and the effect of the tilted angle positions, outlet-to-inlet width ratios and wall divergence locations on the flow structure and the static pressure rise within the diffusers locally and on the total-to-total compressor stage performance.

Research Aim # 3: Development of novel diffuser configurations having curved and diverged walls

Achievement # 3: This study provides a detailed CFD based investigation on the local flow field inside the curved vaneless diffuser passage of the centrifugal compressor stage, presented in Chapter 6. It also identifies its effect on the total-to-total stage performance parameters and proposes a prediction diffuser model, which increases the stage performance. A numerical study on the flow across the curved wall vaneless diffuser passage with wall divergence, having flow rate ranging at design conditions and lower rotating speeds, has been presented. The results are compared with the baseline model. A full factorial method is employed to obtain the effect of each geometrical parameter on the flow phenomena. In order to cover a wide range of geometrical parameters for a curved vaneless diffuser (only limited geometrical parameters are available in literature for which local flow fields have been analysed), flow at lower rotating speeds in centrifugal compressor stage has been numerically simulated for various (a) curved angle positions, (b) radius of curve (c) diffuser inlet-to-outlet axial position (d) outlet-to-inlet width ratios and (e) divergence locations.

Based on the detailed numerical investigation of the flow structure and behaviour, the pressure, temperature and velocity fields in vaneless diffusers have been critically analysed both qualitatively and quantitatively. Qualitative analysis makes use of the pressure, temperature and velocity contours in the vaneless diffusers whereas, the quantitative analysis makes use of the coefficient of pressure and normalised local flow velocity for the analysis of pressure and velocity distribution and asymmetric behaviour of the flow within the diffusers respectively. The results presented give a clear

picture of the flow behaviour within the diffusers and the effect of the curved angle positions, radius of curve diffuser inlet-to-outlet axial position, outlet-to-inlet width ratios and wall divergence locations on the flow structure and the static pressure rise within the diffusers locally and on the total-to-total compressor stage performance.

7.3. Thesis Conclusions

A comprehensive study has been carried out to support the existing literature regarding the flow within the vaneless diffusers of the centrifugal compressor stage and to provide novel additions to improve the current understanding of the design process, operational characteristics, geometry related effects and optimization methodology for the vaneless diffusers of the centrifugal compressor stage. The major conclusions from each facet of this research study are summarized as follows:

Research Objective # 1: To determine the effect of diffuser wall on the flow variations within the diffuser and on the compressor stage performance

Conclusion # 1: From the investigations regarding the effect of outlet-to-inlet width ratio of the straight diffuser and diffuser length, carried out in this study, it can be concluded that small increase of outlet-to-inlet width ratio near outlet helps in increasing total-to-total stage performance. Moreover, increase of diffuser length helps in recovering the static pressure across the straight diffuser. Furthermore, straight diffuser helps to increase the total-to-total pressure ratio and isentropic efficiency of the compressor stage. Moreover, asymmetric ratio has been calculated across the straight diffuser and it has been concluded that flow is near the hub wall which is asymmetric flow and the flow tends to be symmetric near the outlet. Moreover, due to stage interface applied between the rotor and stator jets and wakes cannot be detected however an average effect from the blades can be obtained. Furthermore, a small effect can also be obtained from the volute tongue region, which changes the flow structure in the circumference of the diffuser. However, the radial flow change is higher in comparison to circumferential flow change.

Research Objective # 2: To determine the effect of diffuser wall divergence on the flow variations within the diffuser and on the compressor stage performance

Conclusion # 2: From the investigations regarding the effect of outlet-to-inlet width ratio of the straight diffuser and location of the wall divergence, carried out in this study, it can be concluded that increase of outlet-to-inlet width ratio helps in increasing total-to-total stage performance and location of wall divergence does not have significant effect on the stage performance. As far as the flow structure is concerned, slight increase of outlet-to-inlet width ratio causes increase in static pressure across the diffuser. However, excessive increase of outlet-to-inlet width ratio causes flow reversals near the hub wall at the diffuser outlet due to adverse pressure gradient at the downstream. This causes increase in total pressure loss inside the boundary layers. Furthermore, a small effect can also be obtained from the volute tongue region, which changes the flow structure in the circumference of the diffuser. However, the radial flow change is higher in comparison to circumferential flow change.

Research Objective # 3: To formulate the effect of tilted diffuser wall on the flow variations within the diffuser and on the compressor stage performance

Conclusion # 3: From the investigations regarding the effect of tilt angle for the straight diffuser carried out in this study, it can be concluded that tilting of the diffuser aids in increasing the stage performance because the streamwise length has been increased and flow reversals have reduced to minimum. Furthermore, tilt angle also helps in compacting the compressor stage. Moreover, this investigation is carried out based upon the DOE using Taguchi method. Therefore, certain numerical simulations have been carried out. In order to obtain the best model, optimisation technique based upon Analysis of Variances has been carried out. This helps to choose the best model and hence it has shown great improvement in the stage performance.

Research Objective # 4: To formulate the effect of tilted diffuser wall divergence on the flow variations within the diffuser and on the compressor stage performance

Conclusion # 4: From the investigations regarding the effect of outlet-to-inlet width ratio of the vaneless diffuser passage, tilt angle and location of the wall divergence, carried out in this study, it can be concluded that increase of outlet-to-inlet width ratio helps in increasing total-to-total stage performance and location of wall divergence does not have significant effect on the stage performance. As far as the flow structure is concerned, slight increase of outlet-to-inlet width ratio causes increase in static pressure across the diffuser. However, excessive increase of outlet-to-inlet width ratio decreases the stage performance. Furthermore, a small effect can also be obtained from the volute tongue region, which changes the flow structure in the circumference of the diffuser. However, the radial flow change is higher in comparison to circumferential flow change. Moreover, this investigation is carried out based upon the DOE using Taguchi method. Therefore, certain numerical simulations have been carried out. In order to obtain the best model, optimisation technique based upon Analysis of Variances has been carried out. This helps to choose the best model and hence it has shown great improvement in the stage performance.

Research Objective # 5: To analyse the effect of curved diffuser wall on the flow variations within the diffuser and on the compressor stage performance

Conclusion # 5: From the investigations regarding the effect of curvature of the diffuser, angle of curvature, radius of the curve and axial distance between inlet to outlet of the diffuser, carried out in this study, it can be concluded that the curvature of the wall helps in reducing the losses generated within the compressor stage and increase total-to-total stage performance. The axial distance between inlet-to-outlet of the diffuser passage helps to increase the radial streamwise length of the diffuser passage. This helps in increasing static pressure. Furthermore, angle of curvature helps to reduce the tip leakage flow and aids to increase the stage performance.

Research Objective # 6: To analyse the effect of curved diffuser wall divergence on the flow variations within the diffuser and on the compressor stage performance

Conclusion # 6: From the investigations regarding the effect of outlet-to-inlet width ratio of the curved diffuser and location of the wall divergence, carried out in this study, it can be concluded that increase of outlet-to-inlet width ratio helps in increasing total-to-total stage performance and location of wall divergence helps in making the flow structure symmetrical. As far as the flow structure is concerned, slight increase of outlet-to-inlet width ratio causes increase in static pressure across the curved wall diffuser. However, excessive increase of outlet-to-inlet width ratio causes flow reversals near the hub wall across the diffuser passage due to adverse pressure gradient at the downstream.

Research Objective # 7: Development of semi-empirical relations for the isentropic efficiency and the geometrical configurations

Conclusion # 7: From the investigations regarding the outlet-to-inlet width ratio and wall divergence location from the diffuser inlet, a semi-empirical equation has been developed, which helps in obtained the local isentropic efficiency across the straight diffuser and diverged wall straight diffuser. It can be concluded from the results that the maximum effect is obtained on the isentropic efficiency is due to Mach number of the flow entering the diffuser.

Research Objective # 8: Development of a compact diffuser used within the compressor stage based on the isentropic efficiency to volume ratio

Conclusion # 8: The major objective of this research is to make the compressor stage more compact whilst either maintain the stage performance or increase the stage performance. It has been concluded from the study that tilting and curving approach help in compacting the compressor stage. Moreover, wall divergence on the tilted diffuser and curved diffuser helps in improving the stage performance. Furthermore, it has been noticed that tilted diffuser has more impact on the rise in stage performance

in comparison to curved diffuser. Conversely curved diffuser has more impact on compacting the compressor stage in comparison to tilted diffuser.

7.4. Thesis Contribution

The major contributions of this research are summarised below in which novelties of this research are described:

Contribution # 1:

One of the major contributions of this study is detailed investigations on local and global flow characteristics within the straight diffuser and diverged wall straight diffusers of the compressor stage. The available literature does not provide detailed information on asymmetric ratio effect of the flow within such diffusers on the stage performance. The availability of computational fluid dynamics tools along with the experimental data has enabled the author to carry out this investigation. The pressure, velocity and temperature variations within the straight diffuser and diverged wall straight diffusers have been investigated over a wide operating range of the flow conditions. Effects of geometrical parameters such as diffuser outlet-to-inlet width ratio and wall divergence location on the flow parameters have clearly been enumerated. Furthermore, asymmetric ratio of the flow has been computed within the diffuser and the effect of asymmetry on the stage efficiency has been investigated. Moreover, semi-empirical equation has been developed that has helped to obtain the local diffuser efficiency of the compressor stage.

Contribution # 2:

Another major contribution of this study is reducing the size of the compressor model by changing the diffuser shape and detailed investigations on local and global flow characteristics within the tilted diffuser and diverged wall tilted diffusers of the compressor stage. The available literature does not provide detailed information on asymmetric ratio effect of the flow within such diffusers on the stage performance. The availability of computational fluid dynamics tools along with the experimental data has enabled the author to carry out this investigation. The pressure, velocity and temperature variations within the tilted diffuser and diverged wall tilted diffusers have been investigated over a

wide operating range of the flow conditions. Effects of geometrical parameters such as diffuser outlet-to-inlet width ratio, tilt angle and wall divergence location on the flow parameters have clearly been enumerated. Furthermore, asymmetric ratio of the flow has been computed within the tilted diffuser and the effect of asymmetry on the stage efficiency has been investigated. Moreover, statistical methods have been incorporated of to optimise the tilted diffuser model and semi-empirical equation for the stage efficiency has been generated, which is a factor of each geometrical parameter of the tilted diffuser considered.

Contribution # 3:

Another major contribution of this study is detailed investigations on local and global flow characteristics within the curved diffuser and diverged wall curved diffusers of the compressor stage. The diffuser model is curved to provide a smooth flow and reduce the size of the compressor model to make it more compact. The available literature does not provide detailed information on asymmetric ratio effect of the flow within such diffusers on the stage performance. The availability of computational fluid dynamics tools along with the experimental data has enabled the author to carry out this investigation. The pressure, velocity and temperature variations within the curved diffuser and diverged wall curved diffusers have been investigated over a wide operating range of the flow conditions. Effects of geometrical parameters such as curve radius, tilt angle of the curve, axial distance from diffuser inlet-to-outlet, outlet-to-inlet width ratio and wall divergence location on the flow parameters have clearly been enumerated. Furthermore, asymmetric ratio of the flow has been computed within the curved diffuser and the effect of asymmetry on the stage efficiency has been investigated. The geometry of the curved diffuser and diverged wall curved diffusers has been created using mathematical procedure, which helps to develop all such type of geometries. The asymmetric ratio effect within the straight, tilted and curved diffusers with or without wall divergence is a novel contribution to the knowledge base that can be used to analyse the asymmetric effect on the stage performance. Until now no models were developed to make the compressor model more compact along with increasing the stage performance. The development of these compact size compressor models is a step forward in automotive industry.

7.5. Recommendations for Future Work

The design, operation and optimisation of diffusers of the turbocharger compressor stage have presented in the present study such that gaps identified in literature could be bridged. In light of the

concluded remarks provided in the previous sections, a vast potential of further research in this particular area of automotive industry has been unlocked. The main area identified for further work are described below, which are associated to further performance-related analysis, design and optimisation of diffusers of the turbocharger compressor stage.

Recommendation # 1:

Flow phenomena within the compressor stage is a transient phenomenon where impeller is rotating, and flow trajectories varies under the influence of impeller rotation. In order to accommodate these unsteady effects within the compressor stage and most importantly within the diffuser, a numerical study on the transient behaviour of the flow using sliding mesh technique needs to be carried out. Such a study will provide precious information regarding the generation of complex flow structures within the compressor stage using different diffuser configurations in both space and time. This task requires additional computational power as the tangential velocities form the impeller blades will computed that are introduced within the diffuser area. Furthermore, transient analysis of compressor stage provides the information of the vortical structures within the compressor stage and most importantly within the various diffusers considered in the present study.

Recommendation # 2:

More advanced modelling techniques have now become available such as dynamic mesh, immersed boundary method etc. Using such models helps to analyse the flow behaviour within the compressor stage more accurately and diffuser design can be optimised. Furthermore, large eddy simulation turbulence model can be used to compute the turbulence intensity and eddies within the compressors stage. Combined use of modelling techniques and turbulence model can help in analysing the flow within the diffuser in more detail and optimise the diffuser. These advanced modelling techniques are indeed computationally very expensive and requires massive computational power. Furthermore, these tools require extra computational skills in terms of writing complex scripts to define the changing mesh structure and extraction of the data.

Recommendation # 3:

Inverse design approach is a best method to create the diffuser model for the compressor stage. Since inverse design approach is used for straight diffusers by restricting the constraints of diffuser. If the geometrical parameters of tilted and curved diffusers along with diffuser outlet-to-inlet width ratio

used in the present study are added, the diffuser model can be optimised the stage performance can be drastically increased. Furthermore, different algorithms such genetic algorithm, response surface methodology etc. can be used to optimise the diffuser geometry and proper orthogonal decomposition method can be introduced to reduce large number of simulations and gives high accuracy.

REFERENCES

[1] Aungier, R. H. (2000). Centrifugal compressors: a strategy for aerodynamic design and analysis. American Society of Mechanical Engineers.

[2] Sheng, F., Chen, H., Zhu, X. C., & Du, Z. H. (2012). A three-dimensional compressible flow model for rotating waves in vaneless diffusers with unparallel walls. *Proceedings of the Institution of Mechanical Engineers, Part C: Journal of Mechanical Engineering Science*, *226*(9), 2230-2249.

[3] Japikse, D. (1996). *Centrifugal compressor design and performance* (Vol. 2). White River Junction, VT: Concepts Eti.

[4] Fluent, I. N. C. (2006). FLUENT 6.3 user's guide. *Fluent documentation*.

[5] Robinson, C., Casey, M., Hutchinson, B., & Steed, R. (2012, June). Impeller-diffuser interaction in centrifugal compressors. In *ASME Turbo Expo 2012: Turbine Technical Conference and Exposition* (pp. 767-777). American Society of Mechanical Engineers.

[6] Achilleos, P. (2014). *Design optimisation of a diffuser for a turbocharger compressor stage* (Doctoral dissertation, University of Huddersfield).

[7] Shaaban, S. (2015). Design optimization of a centrifugal compressor vaneless diffuser. *International Journal of Refrigeration*, *60*, 142-154.

[8] Sweetland, P., Grabowska, D. G., Sekularac, A., & Roby, S. I. (2014). *U.S. Patent No. 8,632,304*. Washington, DC: U.S. Patent and Trademark Office.

[9] Boehm, B. P. (2013). Performance optimization of a subsonic Diffuser-Collector subsystem using interchangeable geometries (Doctoral dissertation, Virginia Tech).

[10] Thenambika, V., Ponsankar, S., & Prabhu, M. K. (2016). Design and flow analysis of S duct diffuser with submerged vortex Generators. *International Journal of Engineering Research and Applications*, *6*(2), 79-84.

[11] Japikse, D., & Baines, N. (1994). *Introduction to turbomachinery*.

[12] Whitfield, A. (1989, June). The preliminary design of radial inflow turbines. In *ASME 1989 International Gas Turbine and Aeroengine Congress and Exposition* (pp. V001T01A049-V001T01A049). American Society of Mechanical Engineers.

[13] De Wet, A. L., von Backström, T. W., & Van der Spuy, S. J. (2012, June). Performance investigation of a turbocharger compressor. In *ASME Turbo Expo 2012: Turbine Technical Conference and Exposition* (pp. 939-953). American Society of Mechanical Engineers.

[14] Biba, Y., & Menegay, P. (2004). Inverse design of centrifugal compressor stages using a meanline approach. *International Journal of Rotating Machinery*, *10*(1), 75-84.

[15] Pampreen, R. C. (1993). *Compressor surge and stall*. Concepts Eti.

[16] Kammer, N., & Rautenberg, M. (1986). A distinction between different types of stall in a centrifugal compressor stage. *Journal of Engineering for Gas Turbines and Power*, *108*(1), 83-92.

[17] Maskell, E. C. (1955). *Flow separation in three dimensions*. Ministry of Supply, Royal Aircraft Establishment, RAE Farnborough.

[18] Japikse, D., & Osborne, C. Optimization of Industrial Centrifugal Compressors. *Part 6a and b: Studies in Component Performance-Eight Design Cases from 1972 to 1982*, 8-12.

[19] Aungier, R. H. (1993, May). Aerodynamic design and analysis of vaneless diffusers and return channels. In *ASME 1993 International Gas Turbine and Aeroengine Congress and Exposition* (pp. V001T03A042-V001T03A042). American Society of Mechanical Engineers.

[20] Aungier, R. H. (1988). A performance analysis for the vaneless components of centrifugal compressors. *Flows In Non-Rotating Turbomachinery Components, ASME*, *69*, 35-42.

[21] Reneau, L. R., Johnston, J. P., & Kline, S. J. (1967). Performance and design of straight, two-dimensional diffusers. *Journal of Basic Engineering*, *89*(1), 141-150.

[22] Schlichting, H., & Gersten, K. (2016). *Boundary-layer theory*. Springer.

[23] Japikse, D., & Goebel, J. (1979). Turbocharger compressor performance evaluation and critical flow field measurements(No. 790315). SAE Technical Paper.

[24] Adachi, Y., Otsuki, A., Bantle, K., & Miyake, Y. (1992). Performance Improvement of a Vaneless Diffuser of Centrifugal Compressor.

[25] Lee, Y. T., & Bein, T. W. (2002). *U.S. Patent No. 6,382,912*. Washington, DC: U.S. Patent and Trademark Office.

[26] Turunen-Saaresti, T., Reunanen, A., & Larjola, J. (2006). Computational and experimental study of pinch on the performance of a vaneless diffuser in a centrifugal compressor. *Journal of Thermal Science*, *15*(4), 306-313.

[27] Jaatinen, A., Grönman, A., Turunen-Saaresti, T., & Röyttä, P. (2011). Effect of vaneless diffuser width on the overall performance of a centrifugal compressor. *Proceedings of the Institution of Mechanical Engineers, Part A: Journal of Power and Energy*, *225*(5), 665-673.

[28] Mohtar, H., Chesse, P., & Chalet, D. (2011). Effect of a map width enhancement system on turbocharger centrifugal compressor performance and surge margin. *Proceedings of the Institution of Mechanical Engineers, Part D: Journal of Automobile Engineering*, *225*(3), 395-405.

[29] Robinson, C., Casey, M., Hutchinson, B., & Steed, R. (2012, June). Impeller-diffuser interaction in centrifugal compressors. In *ASME Turbo Expo 2012: Turbine Technical Conference and Exposition* (pp. 767-777). American Society of Mechanical Engineers.

[30] Jaatinen-Värri, A., Turunen-Saaresti, T., Röyttä, P., Grönman, A., & Backman, J. (2013). Experimental study of centrifugal compressor tip clearance and vaneless

diffuser flow fields. *Proceedings of the Institution of Mechanical Engineers, Part A: Journal of Power and Energy*, *227*(8), 885-895.

[31] Sheng, F., Chen, H., Zhu, X. C., & Du, Z. H. (2012). A three-dimensional compressible flow model for rotating waves in vaneless diffusers with unparallel walls. *Proceedings of the Institution of Mechanical Engineers, Part C: Journal of Mechanical Engineering Science*, *226*(9), 2230-2249.

[32] Schiff, J. (2013). A Preliminary Design Tool for Radial Compressors. *ISRN LUTMDN/TMHP--13/5287--SE*.

[33] Jaatinen-Värri, A., Grönman, A., Turunen-Saaresti, T., & Backman, J. (2014). Investigation of the stage performance and flow fields in a centrifugal compressor with a vaneless diffuser. *International Journal of Rotating Machinery*, *2014*.

[34] Karpinska, A. M., & Bridgeman, J. (2017). CFD as a Tool to Optimize Aeration Tank Design and Operation. *Journal of Environmental Engineering*, *144*(2), 05017008.

[35] Yunus, A. C., & Cimbala, J. M. (2006). Fluid mechanics fundamentals and applications. *International Edition, McGraw Hill Publication, 185201*.

[36] Cox. G. D., (2007). Recent CFD techniques applied during turbomachinery design. International Aerospace CFD Conference

[37] Cox, G., Wu, J., & Finnigan, B. (2007, January). A study on the flow around the scallops of a mixed-flow turbine and its effect on efficiency. In *ASME Turbo Expo 2007: Power for Land, Sea, and Air* (pp. 1017-1028). American Society of Mechanical Engineers.

[38] Sbardella, L. S. A. and Imregun, M.(2000)“Semi-structured meshes for axial turbomachinery blades”. International Journal for Numerical Methods in Fluids, 32(5), 569-584.

[39] Sayma, A. I., Vahdati, M., Sbardella, L., & Imregun, M. (2000). Modeling of three-dimensional viscous compressible turbomachinery flows using unstructured hybrid grids. *AIAA journal*, *38*(6), 945-954.

[40] ANSYS, I., (2013). CFD User's Manual. Ansys Inc.

[41] Jaatinen, A., Gronman, A., & Turunen-Saaresti, T. (2012, May). Effect of diffuser width and tip clearance on the static pressure distributions in a vaneless diffuser of a high-speed centrifugal compressor'. In *10th International Conference on Turbochargers and Turbocharging* (p. 319). Elsevier.

[42] Liu, Zand Hill, D. L. (2000). Issues Surrounding Multiple Frames of Reference Models for Turbo Compressor Applications, International Compressor Engineering Conference, Purdue University Purdue e-Pubs

[43] JAATINEN, A. Performance improvement of centrifugal compressor stage with pinched geometry or vaned diffuser. 2009.

[44] Venkatakrishnan, V. (1993, January). On the accuracy of limiters and convergence to steady state solutions. In *31st Aerospace Sciences Meeting* (p. 880).

[45] Sitaram, N., Govardhan, M., & Murali, K. V. (2012, December). Effects of Inlet Pressure Distortion on the Performance and Flow Field of a Centrifugal Compressor at Off-Design Conditions. In *ASME 2012 Gas Turbine India Conference* (pp. 35-50). American Society of Mechanical Engineers.

[46] Roy, R. K. (2010). *A primer on the Taguchi method*. Society of Manufacturing Engineers.

[47] Torng, C. C., Chou, C. Y., & Liu, H. R. (1999). Applying quality engineering technique to improve wastewater treatment. *J. Ind. Technol*, *15*, 1-7.

[48] Date, A. W. (2005). *Introduction to computational fluid dynamics*. Cambridge University Press.

[49] Versteeg, H. K., & Malalasekera, W. (2007). An introduction to computational fluid dynamics: the finite volume method. Pearson Education.

[50] Munson, B. R., Okiishi, T. H., Rothmayer, A. P., & Huebsch, W. W. (2014). *Fundamentals of fluid mechanics*. John Wiley & Sons.

[51] Hirsch, C. (2007). Numerical computation of internal and external flows: The fundamentals of computational fluid dynamics. Butterworth-Heinemann.

[52] Jaatinen-Värri, A., Grönman, A., Turunen-Saaresti, T., & Backman, J. (2014). Investigation of the stage performance and flow fields in a centrifugal compressor with a vaneless diffuser. *International Journal of Rotating Machinery*, *2014*.

[53] White, F. M. (2017). Fluid Mechanics Fourth Edition.

[54] Schobeiri, M. (2005). *Turbomachinery flow physics and dynamic performance* (p. 153). Heidelberg: Springer.

[55] Menter, F. R. (1994). Two-equation eddy-viscosity turbulence models for engineering applications. *AIAA journal*, *32*(8), 1598-1605.

[56] Ansys, C. F. X. (2009). ANSYS CFX-solver modeling guide. *Southpointe, Canonsburg, USA*.

[57] Kays, W. M. (2012). *Convective heat and mass transfer*. Tata McGraw-Hill Education.

[58] White, F. M., & Corfield, I. (2006). *Viscous fluid flow* (Vol. 3). New York: McGraw-Hill.

[59] Coleman, H. W., Hodge, B. K., & Taylor, R. P. (1984). A re-evaluation of Schlichting's surface roughness experiment. *Journal of Fluids Engineering*, *106*(1), 60-65.

[60] Taguchi, G., & Jugulum, R. (2002). The Mahalanobis-Taguchi strategy: A pattern technology system. John Wiley & Sons.

[61] Kacker, R. N., Lagergren, E. S., & Filliben, J. J. (1991). Taguchi's orthogonal arrays are classical designs of experiments. *Journal of research of the National Institute of Standards and Technology*, *96*(5), 577.

[62] Christensen, C., Betz, K. M., & Stein, M. S. (2013). *The certified quality process analyst handbook*. ASQ Quality Press.

[63] Hathaway, M. D. (2002, January). Self-recirculating casing treatment concept for enhanced compressor performance. In *ASME Turbo Expo 2002: Power for Land, Sea, and Air* (pp. 411-420). American Society of Mechanical Engineers.

[64] Jaatinen, A., Grönman, A., Turunen-Saaresti, T., & Röyttä, P. (2011). Effect of vaneless diffuser width on the overall performance of a centrifugal compressor. *Proceedings of the Institution of Mechanical Engineers, Part A: Journal of Power and Energy*, *225*(5), 665-673.

[65] Berge Djebedjian (2003) 'Diffuser Optimization using Computational Fluid Dynamics and Micro-Genetic Algorithms', Mansoura Engineering Journal, Vol. (28)

[66] Kalinkevych, M., & Shcherbakov, O. (2013). Numerical modeling of the flow in a vaneless diffuser of centrifugal compressor stage. *ISRN Mechanical Engineering*, *2013*.

[67] Sherstyuk, A. N. (1974). The Turbulent Boundary Layer. *Moscow: Energy*.

[68] Turbo, C., Turbocharger Components Poster, Holset Turbochargers. Retrieved March, 2014, from http://www.cumminsturbotechnologies.com

[69] Cummins Turbo Technologies, How a Turbocharger Works. Retrieved January 2014, from http://cumminsturbotechnologies.com

[70] Cummins Turbo Technologies Reveals Fuel-Saving Technology. (March 20, 2013). Work Truck Megazine, Retrieved from http://www.worktruckonline.com.

[71] Cummins Turbo Technologies, Compressor Map. Retrieved February 11, 2013.

[72] Fluent, A. (2009). 12.0 Theory Guide. *Ansys Inc*, *5*(5).

[73] Cummins Turbo Technologies, Holset Turbocharger – HE400VG (3D Animation) http://www.cumminsturbotechnologies.com

[74] Eynon, P. A. (1996). Application of low solidity vaned diffusers for broad operating range turbocharger compressors (Doctoral dissertation, University of Bath).

[75] Grissom, T. (2013). Turbocharging for improved engine performance and reduced CO_2 emissions. *Borg Warner Turbo Systems at Automotive Megatrends. USA: SAE*.

[76] Lee, C. S., Lee, K. H., Whang, D. H., Choi, S. W., & Cho, H. M. (1997). Supercharging performance of a gasoline engine with a supercharger. *KSME International Journal*, *11*(5), 556-564.

[77] Peters, E. (September 1999). Turbos and Superchargers. Automotive Consumer, 33, 35.

[78] Wheeler, W. R. (201). Entropy: Second Law Characteristics [PowerPoint slides]. Retrieved from http://web.clark.edu/bwheeler/

[79] Dolton, M., Sharp, N., McMath, D., Lancaster, C., Zhang, K.,yau, R., Ryder, O., (2014, May 15, 16). The Application of Turbo-machinery to Reciprocating Engines. Lecture conducted from Cummins Turbo Technologies CTT, Huddersfield, UK.

[80] Hathaway, M. D. (2002, January). Self-recirculating casing treatment concept for enhanced compressor performance. In *ASME Turbo Expo 2002: Power for Land, Sea, and Air* (pp. 411-420). American Society of Mechanical Engineers.

[81] Yahya, S. M. (2010). *Turbines compressors and fans*. Tata McGraw-Hill Education.

[82] Vijaykumar, A. (2007). Design methodology for aerodynamic design of centrifugal compressor (Doctoral dissertation, VIT UNIVERSITY).

[83] Abdelhamid, A. N., & Bertrand, J. (1979, March). Distinctions between two types of self excited gas oscillations in vaneless radial diffusers. In *ASME 1979 International Gas Turbine Conference and Exhibit and Solar Energy Conference* (pp. V01AT01A058-V01AT01A058). American Society of Mechanical Engineers.

[84] Jaatinen, A. (2009). Performance improvement of centrifugal compressor stage with pinched geometry or vaned diffuser. Lappeenranta University of Technology.

[85] Tseng, K. H., Shiao, Y. F., Chang, R. F., & Yeh, Y. T. (2013). Optimization of microwave-based heating of cellulosic biomass using Taguchi method. *Materials*, *6*(8), 3404-3419.

[86] Sivagnanasundaram, S., Spence, S., Early, J., & Nikpour, B. (2010, October). An investigation of compressor map width enhancement and the inducer flow field using various configurations of shroud bleed slot. In *ASME Turbo Expo 2010: Power for Land, Sea, and Air* (pp. 1701-1710). American Society of Mechanical Engineers.

[87] Khalfallah, S., & Ghenaiet, A. (2010). Analyses of impeller—vaneless-diffuser—scroll interactions in a radial compressor. *Proceedings of the Institution of Mechanical Engineers, Part A: Journal of Power and Energy*, *224*(6), 851-867.

[88] Bhatti, M. S. (1987). Turbulent and transition flow convective heat transfer in ducts. *Handbook of single-phase convective heat transfer*.

[89] Kays, W. M. (2012). *Convective heat and mass transfer*. Tata McGraw-Hill Education.

[90] Kurz, R., Marechale, R. K., Fowler, E. J., Ji, M., & Cave, M. J. (2011). Operation of Centrifugal Compressors in Choke Conditions. In *Proceedings of the 40th Turbomachinery Symposium*. Texas A&M University. Turbomachinery Laboratories.

[91] Larry Dixon, S. (2013). Fluid Mechanics, Thermodynamics of Turbomachinery.

[92] Rodgers, C. (1964). Typical performance characteristics of gas turbine radial compressors. *Journal of Engineering for Power*, *86*(2), 161-170.

[93] Harada, H. (1986, June). Performance characteristics of two-and three-dimensional impellers in centrifugal compressors. In *ASME 1986 International Gas Turbine*

Conference and Exhibit(pp. V001T01A060-V001T01A060). American Society of Mechanical Engineers.

[94] Bangalore, A. V. V. Numerical Flow Analysis of Axial Flow Compressor for Steady and Unsteady Flow Cases.

[95] Khalfallah, S., & Ghenaiet, A. (2010). Analyses of impeller—vaneless-diffuser—scroll interactions in a radial compressor. *Proceedings of the Institution of Mechanical Engineers, Part A: Journal of Power and Energy*, *224*(6), 851-867.

[96] Abir, A., & Whitfield, A. (1989). Stability of Conical and Curved Annular Diffusers for Mixed-Flow Compressors. *International Journal of Turbo and Jet Engines*, *6*(1), 27-36.

[97] Analysis of the improvement in performance characteristics of S-shaped rectangular diffuser

[98] Gopaliya, M. K., Goel, P., Prashar, S., & Dutt, A. (2011). CFD analysis of performance characteristics of S-shaped diffusers with combined horizontal and vertical offsets. *Computers & fluids*, *40*(1), 280-290.

[99] Gopaliya, M. K., Jain, P., Kumar, S., Yadav, V., & Singh, S. (2014). Performance improvement of s-shaped diffuser using momentum imparting technique. *IOSR Journal of Mechanical and Civil Engineering*, *11*, 23-31.

[100] Sinha, P. K., & Majumdar, B. (2011). Numerical investigation of flow through annular curved diffusing duct. *International Journal of Engineering & Technology IJET-IJENS*, *3*(03), 190-196.

[101] Sinha, P. K., Mullick, A. N., Halder, B., & Majumdar, B. (2012). Computational investigation of performance characteristics in a C-shape diffusing duct. *International journal of advances in engineering & technology*, *3*(1), 129.

[102] Elliott, K. J. (2012). Numerical investigation of highly curved turbulent flows in centrifugal compressors and in a simplified geometry.

[103] Nordin, N., Karim, A., Ambri, Z., Othman, S., & R Raghavan, V. (2015). Numerical investigation of turning diffuser performance: validation and verification-model II.

[104] Nordin, N., Karim, A., Ambri, Z., Othman, S., & R Raghavan, V. (2015). Simulation and development of performance correlations of 3-D turning diffuser via ACFD.

[105] Gopaliya, M.K., Singla, A., & Saini, A. (2015). Performance Improvement of S-Shaped Diffuser Using Suction and Blowing Methods. IOSR Journal of Mechanical and Civil Engineering (IOSR-JMCE). 12 (3), 23-28.

[106] Sovran, G. (1967). Fluid mechanics of internal flow: proceedings of the Symposium ... General Motors Research Laboratories, Warren, Mich., 1965. Amsterdam: Elsevier.

[107] Ackeret, J. (1958). Boundary layers in straight and curved diffusers. In boundary layer research/Boundary Layer Research (pp. 22-40). Springer Berlin Heidelberg.

[108] Sprenger, H (1955), Measurements on diffusers. VDI-Ber. 3, 10-110.

[109] Sprenger, H. (1962). *Experimental Investigations of Straight and Curved Diffusers*. Technical Information and Library Services, Ministry of Aviation.

[110] Fox, R. W., & Kline, S. J. (1962). Flow regimes in curved subsonic diffusers. *Journal of Basic Engineering*, *84*(3), 303-312.

[111] Kline, S. J. (1954). Optimum design of straight-walled diffusers. *Trans. ASME Ser. D J. Basic Eng.*, *81*, 321-331.

[112] Moore Jr, C. A., & Kline, S. J. (1958). Some effects of vanes and of turbulence in two-dimensional wide-angle subsonic diffusers.

[113] Goulas A. K., Fluid Mechanics, Aristotle University of Thessaloniki, Department of Mechanical Engineering.

[114] Bakken, L. E., Jordal, K., Syverud, E., & Veer, T. (2004, January). Centenary of the First Gas Turbine to Give Net Power Output: A Tribute to Ægidius Elling.

In *ASME Turbo Expo 2004: Power for Land, Sea, and Air* (pp. 83-88). American Society of Mechanical Engineers.

APPENDICES

A-1. Computational Fluid Dynamics

Computational Fluid Dynamics (CFD) is a commercial code and a powerful tool that is based on numerical solutions governed predominantly by the mass, momentum and energy equations of a moving fluid. This advanced technique is utilised across a wide spectrum of sectors, such as the aerodynamics of aircraft and vehicles, flow phenomena inside rotating and stationary passages of turbo-machines, combustion process in internal combustion engines, and many more. CFD is used extensively in basic and applied research with respect to designing equipment, and in calculating the geophysical phenomena that occur in the environment, such as ocean currents, weather and so forth [48].

The use of CFD has many unique advantages over experimental based approaches to fluid system designs. The implementation of CFD allows investigations of systems that experience extreme conditions further than their average operating limits to be carried out. It essentially provides unlimited level of detailed predicted results to be produced for large volumes of investigations, in a cheap manner. This in turn, assists in determining optimal solutions for various engineering problems [49].

A-1.1. Cfd Codes And Their Working

CFD codes are developed using robust numerical algorithms that enable fluid flow problems to be solved. Graphical User Interface (GUI) applications are used as problem parameters so that the computed results can be examined and analysed. The codes embedded within the software provides a complete CFD analysis, comprising of three main elements, (i) a pre-processor, (ii) a solver and (iii) a post-processor, whereby a framework of these interconnecting with respect to each other is depicted in Figure A-1. The operational processes of these elements are briefly explained in the next paragraphs.

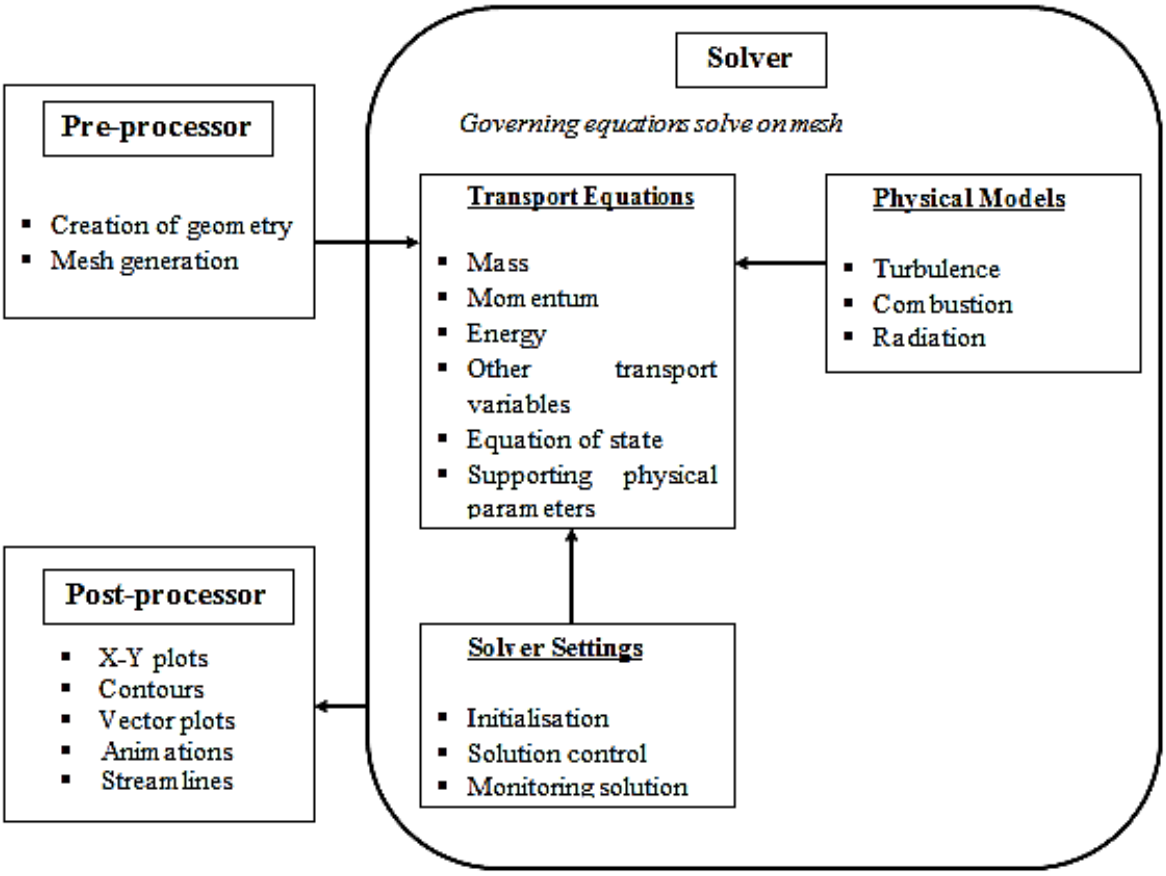

Figure A-1: The interconnectivity operational processes framework of the three main elements within a CFD analysis

The 'pre-processing' element inputs the flow problem into a CFD program by defining the system geometry; grid generation that divides the domain into a number of smaller, non-overlapping sub-domains (grid or mesh of cells); and selection of physical and chemical phenomena that requires modelling. Additionally, this stage also requires the fluid properties and appropriate boundary conditions to be specified [49].

The solver primarily consists of setting up the numerical model and the computation/monitoring of the solution. The setting up of the numerical model includes the following:

- Selection of appropriate physical models - turbulence, combustion, multiphase or radiation etc.
- Defining material properties like the fluid, solid, mixture etc.
- Prescribing operating conditions
- Prescribing boundary conditions

- Prescribing solver setting
- Prescribing initial solution
- Setting up convergence monitors

The computation of the solution includes:

- The discretised conservation equations are solved iteratively. Numbers of iterations are required to achieve a converged solution.
- The convergence is achieved when the solution variables that are altered from the first iteration to the next is negligible. The residuals are a tool to help monitor this trend.
- The accuracy of the converged solution is dependent on the setup, grid resolution, grid independence, and the appropriateness of the physical model.

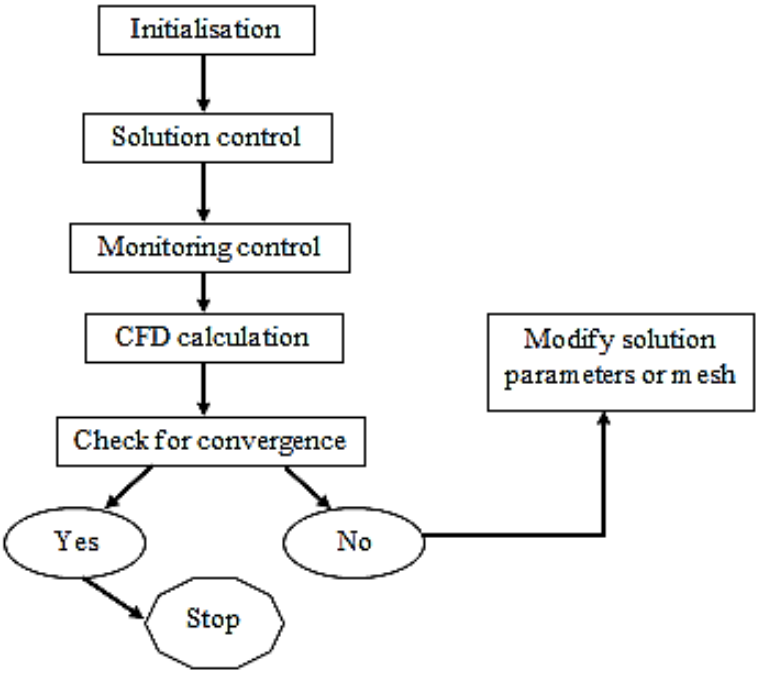

Figure A-2: An overview of the solution procedure

Post processing comprises the examination of the results obtained, and revision of the model based on these results. The results can be viewed as contours, vector plots or specific values at specific region.

A-2. Governing the equations of fluid flow in a turbocharger

CFD utilises governing equations of fluid dynamics, namely: continuity, momentum and energy equations. These equations mathematically state three fundamental physical principles whereby fluid dynamics is established:

- Mass is conserved.
- Newton's second law, F = ma → momentum is conserved.
- Energy is conserved.

Since this research is based on the fluid flow inside the turbocharger compressor, all of the above principles are explained by taking fluid as a model. The principles mentioned previously can be applied onto the fluid in many different ways, such as the system approach, which is a collection of matter with the same fluid particles that can move, flow, and interact with its surroundings; or the control volume approach being a volume in space independent of mass through which fluid may flow [50].

A-2.1. Conservation of Mass

The law for mass conservation is a general statement of kinematic nature, which illuminates the empirical fact that the variation of mass flow of a fluid system equals to the mass flow passed through the boundary of the system. The mass conservation equation, also called the Continuity Equation on a fluid element is established as:

Rate of increase of mass in fluid element	=	Net rate of flow of mass into fluid element

$$\frac{\partial \rho}{\partial t} = \boldsymbol{\nabla} \cdot (\rho \mathbf{u}) = 0 \qquad \text{A-1}$$

where ρ is the mass density, t is time and u is the velocity vector. **(∇·)** denotes the divergence operator, then the expansion of the second item in the above equation is

$$\nabla \cdot (\rho u) = \frac{\partial (\rho u_x)}{\partial x} + \frac{\partial (\rho u_y)}{\partial y} + \frac{\partial (\rho u_z)}{\partial z} \qquad \text{A-2}$$

where u_x, u_y, u_z are the components of **u** in *x*, *y*, *z* direction, respectively. For incompressible flow, ρ is constant in the whole field then eq. 3.1 can be reduced to the divergence free condition for the velocity:

$$\boldsymbol{\nabla} \cdot \mathbf{u} = 0 \qquad \text{A-3}$$

This equation defines the net flow of mass that exits the element across its boundaries. The above equation can be expanded as:

$$\frac{\partial u}{\partial x} + \frac{\partial v}{\partial y} + \frac{\partial w}{\partial z} = 0 \qquad \text{A-4}$$

The expanded equation above characterises the steady state of mass-conserved in three-dimensional form at a point in an incompressible fluid. If the flow is steady, then ρ will not change with time, then eq. 3.1 can be replaced by

$$\boldsymbol{\nabla} \cdot (\rho \mathbf{u}) = 0 \qquad \text{A-5}$$

A-2.2. Conservation of Momentum

The momentum conservation law is the expression of the generalized Newton's second law, defining the equation of a fluid, which means the momentum variation of a fluid system equals to the total external forces imposed on it. In Newton's second law of motion, it is stated that:

Rate of increase of momentum of the fluid element	=	Sum of forces acting on the fluid particle

There are two types of forces acting on fluid particles, namely surface forces and the body forces. The surface forces comprise of;

- Pressure forces
- Viscous forces

Whilst body forces comprise of;

- Gravitational forces
- Centrifugal forces
- Coriolis forces

- Electromagnetic forces

The momentum conservation equation involves three components. For the x – component of the fluid element, the momentum equation can be determined by establishing the rate of change of x – momentum to be equal to the total force in the x – direction. This is due to surface stresses, as well as the rate of increase of x – momentum due to sources. The momentum equation for the x, y and z – component are therefore as follows:

$$\frac{\partial(\rho u_x)}{\partial t} + \boldsymbol{\nabla} \cdot (\rho u_x \mathbf{u}) = -\frac{\partial p}{\partial x} + \frac{\partial \tau_{xx}}{\partial x} + \frac{\partial \tau_{yx}}{\partial y} + \frac{\partial \tau_{zx}}{\partial z} + f_x$$

$$\frac{\partial(\rho u_y)}{\partial t} + \boldsymbol{\nabla} \cdot (\rho u_y \mathbf{u}) = -\frac{\partial p}{\partial y} + \frac{\partial \tau_{xy}}{\partial x} + \frac{\partial \tau_{yy}}{\partial y} + \frac{\partial \tau_{zy}}{\partial z} + f_y \qquad \text{A-6}$$

$$\frac{\partial(\rho u_z)}{\partial t} + \boldsymbol{\nabla} \cdot (\rho u_z \mathbf{u}) = -\frac{\partial p}{\partial z} + \frac{\partial \tau_{xz}}{\partial x} + \frac{\partial \tau_{yz}}{\partial y} + \frac{\partial \tau_{zz}}{\partial z} + f_z$$

where p donates the static gauge pressure, τ_{ii} and f_i ($i = x, y, z$) are the components of viscous stress shear tensor, $\boldsymbol{\tau}$ and body force, f. this equation is valid for both Newtonian fluid and non-Newtonian fluid. For Newtonian fluid, the components of $\boldsymbol{\tau}$ are defined by

$$\tau_{xx} = 2\mu \frac{\partial u_x}{\partial x} + \lambda \boldsymbol{\nabla} \cdot \mathbf{u}$$

$$\tau_{yy} = 2\mu \frac{\partial u_y}{\partial y} + \lambda \boldsymbol{\nabla} \cdot \mathbf{u} \qquad \text{A-7}$$

$$\tau_{zz} = 2\mu \frac{\partial u_z}{\partial z} + \lambda \boldsymbol{\nabla} \cdot \mathbf{u}$$

and

$$\tau_{xy} = \tau_{yx} = \mu \left(\frac{\partial u_x}{\partial y} + \frac{\partial u_y}{\partial x} \right)$$

$$\tau_{xz} = \tau_{zx} = \mu \left(\frac{\partial u_x}{\partial z} + \frac{\partial u_z}{\partial x} \right) \qquad \text{A-8}$$

$$\tau_{yz} = \tau_{zy} = \mu \left(\frac{\partial u_y}{\partial z} + \frac{\partial u_z}{\partial y} \right)$$

where μ is the *dynamic viscosity coefficient* of fluid and λ is the *second viscosity coefficient*. The latter is related to a viscous stress caused by the change of the volume, thus it is also called *volume viscosity* or *bulk viscosity*. For most fluids, the *Stoke's hypothesis* is satisfied [51]

$$2\mu + 3\lambda = 0 \tag{A-9}$$

Another viscosity coefficient *v*, called Kinematic Viscosity, is often used which defined as $v=\mu/\rho$. Substituting eq. 3.7 and eq. 3.8 into eq. 3.6 and utilizing eq. 3.9, the N-S equations of motion is obtained:

$$\frac{\partial(\rho u_x)}{\partial t} + \boldsymbol{\nabla} \cdot (\rho u_x \mathbf{u}) = \mu \Delta u_x - \frac{\partial p}{\partial x} + Q_x$$

$$\frac{\partial(\rho u_x)}{\partial t} + \boldsymbol{\nabla} \cdot (\rho u_x \mathbf{u}) = \mu \Delta u_x - \frac{\partial p}{\partial x} + Q_x \tag{A-10}$$

$$\frac{\partial(\rho u_x)}{\partial t} + \boldsymbol{\nabla} \cdot (\rho u_x \mathbf{u}) = \mu \Delta u_x - \frac{\partial p}{\partial x} + Q_x$$

where (∇) is the Laplace operator. Q_i (i = x, y, z) denotes the generalized source item which can be expanded as

$$Q_x = f_x + \frac{\partial}{\partial x}\left(\mu \frac{\partial u_x}{\partial x}\right) + \frac{\partial}{\partial y}\left(\mu \frac{\partial u_y}{\partial x}\right) + \frac{\partial}{\partial z}\left(\mu \frac{\partial u_z}{\partial x}\right) + \frac{\partial}{\partial x}\left(\lambda \boldsymbol{\nabla}(\mathbf{u})\right)$$

$$Q_y = f_y + \frac{\partial}{\partial x}\left(\mu \frac{\partial u_x}{\partial y}\right) + \frac{\partial}{\partial y}\left(\mu \frac{\partial u_y}{\partial y}\right) + \frac{\partial}{\partial z}\left(\mu \frac{\partial u_z}{\partial y}\right) + \frac{\partial}{\partial y}\left(\lambda \boldsymbol{\nabla}(\mathbf{u})\right) \tag{A-11}$$

$$Q_z = f_z + \frac{\partial}{\partial x}\left(\mu \frac{\partial u_x}{\partial z}\right) + \frac{\partial}{\partial y}\left(\mu \frac{\partial u_y}{\partial z}\right) + \frac{\partial}{\partial z}\left(\mu \frac{\partial u_z}{\partial z}\right) + \frac{\partial}{\partial z}\left(\lambda \boldsymbol{\nabla}(\mathbf{u})\right)$$

[52] The shear stress from the volume viscosity can be neglected for the majority of fluid flows. For incompressible fluids, the sources items can be reduced to the body force **F**. Therefore, eq. 3.10 can be rewritten in a vector format:

$$\frac{\partial(\rho \mathbf{u})}{\partial t} + \mathbf{u} \cdot \boldsymbol{\nabla}(\rho \mathbf{u}) = \mu \Delta(\mathbf{u}) - \boldsymbol{\nabla} p + \mathbf{F} \tag{A-12}$$

The second item on the left-hand side of the eq. 3.12 is called *convective item*, while the first item on the right-hand side is called *diffusive item*. The ratio between momentum of the convection item and the diffusive item gives an important dimensionless number *Re*, the so-called *Reynolds number*:

$$Re = \frac{\rho|\mathbf{u}|L}{\mu} \quad \text{A-13}$$

Substituting the dynamic viscosity with the kinematic viscosity, *v*, then gives

$$Re = \frac{L|\mathbf{u}|}{\upsilon} \quad \text{A-14}$$

A-2.3. Energy Equation

The energy conservation law is also referred to as the expression of the first principle of thermodynamics, which states that the variation of total energy in a fluid system is the work of the forces acting on the system plus the heat transmitted into the system.

Rate of change of energy inside fluid element	=	Net flux of heat into element	+	The rate of work done on element due to body and surface forces

The conservation of energy is given by:

$$\frac{\partial(\rho E)}{\partial t} + \mathbf{\nabla} \cdot (\rho E \mathbf{u}) = \mathbf{\nabla} \cdot (k \nabla T) + \nabla \cdot (-p\mathbf{u} + \tau \cdot \mathbf{u}) + W_f + q_H \quad \text{A-15}$$

where, *E* denotes the specific total energy, *k* is the thermal conductivity coefficient, T is the absolute temperature, W_F and q_H denote the work of body forces and the heat source item, respectively. Usually, the specific total energy *E* is related to the specific internal energy *e* and the kinetic energy by

$$E = e + \frac{|\mathbf{u}|^2}{2} \quad \text{A-16}$$

Another useful state variable is the total internal enthalpy H which is defined as

$$H = E + \frac{p}{\rho} = e + \frac{p}{\rho} + \frac{|\mathbf{u}|^2}{2} \quad \text{A-17}$$

The related specific internal enthalpy is

$$h = e + \frac{p}{\rho} = c_p \nabla T \quad \text{A-18}$$

where, c_p is the specific heat, which is can be related to v and k by a dimensionless number Pr = $\mu c_p/k$, namely *Prandtl Number*, which indicates the ratio of momentum diffusivity (kinematic viscosity) and thermal diffusivity. Introducing Eq. A-16 and Eq. A-18 into Eq. A-19 leads to the conservation equation for enthalpy:

$$\frac{\partial(\rho h)}{\partial \mathrm{t}} + \boldsymbol{\nabla} \cdot (\rho h \boldsymbol{u}) = \boldsymbol{\nabla} \cdot (k \boldsymbol{\nabla} T) + \boldsymbol{\nabla} \cdot (\tau \cdot \mathbf{u}) + q_H \qquad \text{A-19}$$

Usually, an additional correlative equation between p and ρ is needed, which is called *state equation*. For perfect gas, the state equation is

$$p = \rho R T \qquad \text{A-20}$$

where R is the *Molar gas constant*, which is about 287 J/kgK for air. Then, a closed system of six unknowns (p, T, ρ, u_x, u_y, u_z) with five nonlinear partial differential equations and a state equation is obtained.

A compact general format of N-S equation can be expressed in:

$$\frac{\partial \mathbf{U}}{\partial t} + \boldsymbol{\nabla} \cdot \mathbf{F}_{\mathrm{C}} = \boldsymbol{\nabla} \cdot \mathbf{F}_{\mathrm{V}} + \mathbf{Q} \qquad \text{A-21}$$

The items of eq. 3.21 in sequence are *transient term*, *convective term*, *diffusive term* and *source term*. The expansion of the transient term U is:

$$\mathbf{U} = \begin{bmatrix} \rho \\ \rho u_x \\ \rho u_y \\ \rho u_z \\ \rho E \end{bmatrix} \qquad \text{A-22}$$

The convection term FC and the diffusive term FV denote the vector as below, respectively:

$$\mathbf{F}_C = \begin{bmatrix} \rho \mathbf{u} \\ \rho u_x \mathbf{u} + p_x \\ \rho u_y \mathbf{u} + p_y \\ \rho u_z \mathbf{u} + p_z \\ (\rho E + p)\mathbf{u} \end{bmatrix} \qquad \text{A-22}$$

and

$$\mathbf{F}_V = \begin{bmatrix} 0 \\ \tau_x \\ \tau_y \\ \tau_z \\ \tau\mathbf{u} + k\nabla T \end{bmatrix} \quad \text{A-22}$$

The last term Q is:

$$Q = \begin{bmatrix} 0 \\ S_x \\ S_y \\ S_z \\ W_F + q_H \end{bmatrix} \quad \text{A-23}$$

More details about the governing equations of fluid dynamics and more comprehensive discussions can be found in Hirsch [51] and White [53].

A-3. Multiple Reference Frame Model (MRF)

Multiple reference frame approach is a steady-state approximation method, which takes into account the motion of the moving frame with respect to the stationary zones. This approach can provide a reasonable model of the flow for many applications such as turbo-machinery applications. This approach assists in assigning different rotational and translational speeds to the individual cell zones.

The multiple reference fames although considered as the simplest, can provide the ability of modelling multiple rotating reference frames in a single domain. The opposing cell zones do not require to be interfaced when only one rotating component exists. Moreover, the nodes must be identical at the boundary where the two zones meet. MRF approach is a steady-state approximation method, which does not take into account the motion of the moving frame with respect to the stationary zones; hence the grid is fixed for the computational procedure. MRF method is observing the instantaneous flow field with a fix rotor also called as frozen rotor approach. It approximates the flow field, which cannot take consider the transient effects into account, but it can provide a reasonable model of the flow within the compressor stage, where the stator (guide) blades are absent or generally for problems with weak transient effects. The flow domains are divided into sub-domains that can be rotating and/or translating with respect to the internal frame. The governing equations in each sub-domain are written with respect to that sub-domains reference frame.

Accounting for the particular flow situation in turbomachinery, it is necessary to be able to describe the flow behaviour relatively to a rotating frame of reference that is attached to the rotor. Without loss of generality, it is assumed that the moving part of turbomachinery is rotating steadily with angular velocity, ω around the machine axis along which a coordinate z is aligned.

Define **w** as a velocity field relative to a rotating system and $\mathbf{v} = \omega \times \mathbf{r}$ as the circumferential velocity. Thus, an observer located outside the rotating frame observes the velocity

$$\mathbf{u} = \mathbf{w} + \mathbf{v} = \mathbf{w} + \omega \times \mathbf{r} \qquad \text{A-24}$$

Introducing eq. 3.24 into eq. 3.1 gives the mass conservation equation in a rotating frame of reference:

$$\frac{\partial \rho}{\partial t} + \boldsymbol{\nabla} \cdot [\rho(\mathbf{w} + \mathbf{v})] = 0 \qquad \text{A-25}$$

Expanding the above equation gives:

$$\frac{\partial \rho}{\partial t} + \rho \boldsymbol{v} + \mathbf{w} \cdot \boldsymbol{\nabla}\rho + \rho \boldsymbol{\nabla} \cdot \mathbf{w} + \rho \boldsymbol{\nabla} \cdot \mathbf{v} = 0 \qquad \text{A-26}$$

The first term in eq. 3.26 indicates the time rate of change of density at a fixed station in an absolute frame of reference. The second term involves the spatial change of density registered by a stationary observer. Combining of these two terms expresses the time rate of change of the velocity within the rotating frame of reference. Since the last term is zero [54], eq. 3.24 is reduced to.

$$\frac{\partial \rho}{\partial t} + \boldsymbol{\nabla} \cdot (\rho \mathbf{w}) = 0 \qquad \text{A-27}$$

where, the subscript *r* refers to the rotating frame of reference. Comparing eq. 3.27 with eq. 3.1, it is found that the mass conservation equation keeps the same expression in both stationary and rotating frames of reference. Without causing confusion, the subscript *r* can be omitted in general.

Using eq. 3.24, the acceleration is also can be redefined as

$$\frac{du}{dt} = \frac{\partial(\mathbf{w}+\omega\times\mathbf{r})}{\partial t} + (\mathbf{w} + \mathbf{v}).\boldsymbol{\nabla}(\mathbf{w} + \mathbf{v}) \qquad \text{A-28}$$

Expanding eq. 3.28 and rearranging the items result in

$$\frac{\mathrm{d}\mathbf{u}}{\mathrm{dt}} = \frac{\partial \mathbf{w}}{\partial t} + \frac{\partial \mathbf{v}}{\partial t} + \mathbf{w} \cdot \boldsymbol{\nabla}(\mathbf{w}) + 2\mathbf{w} \times \omega + \omega \times \mathbf{v} \qquad \text{A-29}$$

The first item on right-hand side expresses the local acceleration of the velocity field within the rotating frame of reference. The second term and third item denote the angular velocity acceleration and the convective term within the rotating frame of reference, respectively.

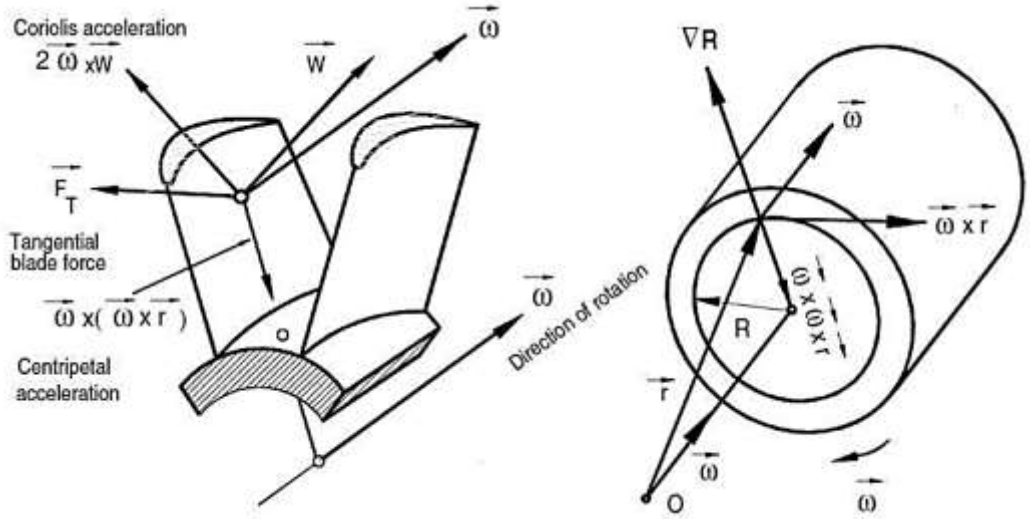

Figure A-3: Coriolis and centripetal forces created by the rotating frame of reference (Schobeiri, 2005 [51])

While, the fourth item and last item are the *Coriolis acceleration* and the centrifugal acceleration, respectively, which are fictitious forces produced as a result of transformation from stationary frame to rotating frame of reference. Figure A-3 shows the directions of the velocity and the acceleration, and relationship between the absolute velocity, relative velocity and rotation. Substituting the acceleration in eq. 3.12 and eq. 3.15 separately, equations of motion and energy in rotating frame of reference can be obtained:

$$\frac{\partial(\rho\mathbf{w})}{\partial t}+\frac{\partial(\rho\mathbf{v})}{\partial t}+\mathbf{w}.\boldsymbol{\nabla}(\mathbf{w})+\omega\times\mathbf{v}+2\omega\times\mathbf{w}=\mu\Delta(\mathbf{w})-\boldsymbol{\nabla}p+\mathbf{F} \qquad \text{A-30}$$

$$\frac{d\left[\rho\left(h+\frac{|\mathbf{w}|^2}{2}-\frac{|\mathbf{v}|^2}{2}\right)\right]}{\mathrm{d}t}=\frac{\partial p}{\partial t}+\boldsymbol{\nabla}\cdot(k\boldsymbol{\nabla}T)+\boldsymbol{\nabla}\cdot(\tau\cdot\mathbf{w})+W_F+q_H \qquad \text{A-31}$$

It should be noted that W_F is the work of body forces in rotating frame of reference, while the subscript *r* is omitted here. The detailed derivation process of governing equations in rotating frame of reference can be found in Schobeiri [54].

A-4. Finite Volume Method

A-4.1. Discretization Method

Three families of numerical methods are available for discretization of N-S equations: Finite Difference Method (FDM), Finite Element Method (FEM) and Finite Volume Method (FVM). The most traditional method is FDM, which is based on the properties of Taylor Expansions. In FDM, the derivative is estimated straightforward by the ratio of two differences according to the theoretical definition of the derivative. Hence, FDM is probably the simplest method to apply, but it requires that the mesh must be structured, and the nodes have to be located on the parallel lines of coordinate, which results in some limitations in application. The second method FEM originates from the field of structural analysis, which is based on the Weighted Residual Method. In FEM, a computational domain is divided into many small sub-domains, called elements, and reassembled after each element had been analyzed. In fact, it is seldom used in fluid dynamic analysis due to the large computational cost. By far the most widely applied method in CFD today is FVM which was developed in 1970s. The strength of FVM is in its direct connection to the physical flow properties. The basis of this method relies on the direct discretization of the integral form of the conservation law, which distinguishes FVM significantly from FDM. FVM is employed by the solver used in the present thesis, named Ansys CFX. Therefore, a detailed description of FVM is given below. More complete descriptions about the other two methods can be found in Hirsch [51].

A-4.2. Mesh Generation

In order to solve the N-S equations numerically, the space, also called domain, has to be discretized into a set of time-invariant, non-overlapping volumes (also called cells), which could be polygons, like triangles and quadrilaterals in 2D, and polyhedra, like tetrahedra, pyramids, prisms and hexahedra in 3D. The space discretization formed is called the mesh or grid. The mesh can be built in a structured way or an unstructured way. Unstructured mesh is more flexible for complicated geometries, and the generation process is easier than that of structured mesh. Moreover, to specify the structured mesh onto turbomachinery high amount of experience is required, whereas unstructured mesh is very simply applied to turbomachinery components by a solver called ICEM. Furthermore, in order to obtain the boundary layer effects prism layers could be added which than merge with unstructured mesh. Combination of both unstructured mesh and prism mesh (hexahedral mesh) is called hybrid mesh. Hence, unstructured hybrid meshes are adopted in simulations of this thesis.

A-5. Turbulence Modelling

The flow phenomenon inside the turbocharger compressor stage is very complex because the stall characteristics of compressor stage are controlled by the flow separation from the rotor blades and diffuser vanes. Therefore, many turbulence models have been developed by aerodynamic community to work with this type of complicated projects. k-ε model and k-ω models are widely used to investigate the flow phenomena inside the turbomachines. [55] Two equation-based models, Shear Stress Transport (SST), have developed to overcome the deficiencies in the k- ω and BSL (baseline) k-ω models, which has been used in this research study. This model is designed to give highly accurate predictions of the onset and the amount of flow separation under adverse pressure gradient by the inclusion of transport effects into the formulation of the eddy-viscosity. [56] This model is highly recommended for high accuracy boundary layer simulations. To benefit from this model a resolution of the boundary layer of more than 10 points is required.

A-6. Interface Type and Model

Domain interfaces provide a way of connecting meshes or domains together. Domains can be connected together with a domain interface. This is often useful for connecting static domains together with non-matching grids. For example, hex meshes can be connected to tetrahedral or hybrid meshes. This is a useful strategy for reducing meshing effort. Domains that have a change in the reference frame (such as rotor-stator) can be connected together. A domain may contain multiple mesh blocks than non-matching interfaces can be connected together using a domain interface. There are two methods of connecting meshes that exist in Ansys CFX so called as one-to-one (direct) and general grid interface (GGI).

The one-to-one (direct) connection is available if, after any applicable rotational or translational transformation (such as for a periodic interface), all of the nodes on one side of the interface correspond in location with all of the nodes on the other side of the interface, to within a spatial tolerance governed by the Mesh Match Tolerance parameter. Henceforth, it is suitable for conformal type of mesh, whereby the nodes location of either domain interface is matched within the defined tolerance.

General Grid Interface (GGI) connections refer to the class of grid connections where the grid on either side of the two connected surfaces does not match as shown in Figure A-4. In general, GGI connections permit non-matching of node location, element type, surface extent, surface shape and

even non-matching of the flow physics across the connection. The regions that are on each side of a GGI connection are allowed to be of different size and are allowed to have non-overlap regions.

Furthermore, General connection interface model is used in this numerical work. The General Connection interface model is a powerful way to connect regions together. A general connection can be used to apply a frame change at the interface between a rotor and stator, connect non-matching grids and apply fully transient sliding interfaces between domains.

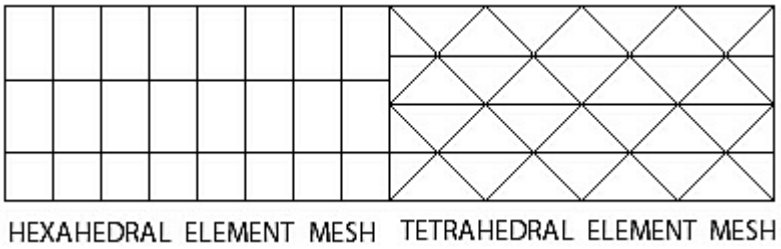

Figure A-4: General connection with no frame change

The General Connection option is necessary when the frame of reference or pitch changes across the interface, such as one side is in a stationary frame of reference and the other side is in a rotating frame of reference. When a general connection is selected, the Frame change or a mixing model needs to be selected. There are three types of frame change or mixing models available in Ansys CFX:

- Frozen rotor
- Stage (Mixing - plane)
- Transient rotor-stator

Each side of the interface must be a surface of revolution and both sides must sweep out the same surface of revolution.

A-6.1. Frozen Rotor

The frame of reference and/or pitch is changed but the relative orientation of the components across the interface is fixed in frozen rotor approach. The two frames of reference connect in such a way that they each have a fixed relative position throughout the calculation. In this approach if the frame changes the appropriate equation transformations are made and if the pitch changes, the fluxes are scaled by the pitch change.

This model produces a steady-state solution to the multiple frame of reference problem, with some account of the interaction between the two frames. The quasi-steady approximation involved becomes

small when the through flow speed is large relative to the machine speed at the interface. Frozen Rotor analysis is most useful when the circumferential variation of the flow is large relative to the component pitch. Furthermore, if the point of interest is to obtain the wake effect on the downstream component performance then frozen rotor method must be employed. This model requires the least amount of computational effort of the three-frame change/mixing models.

The disadvantages of this model are that the transient effects at the frame change interface are not modelled. Modelling errors are incurred when the quasi-steady assumption does not apply. Also, the losses incurred in the real (transient) situation as the flow is mixed between stationary and rotating components is not modelled. Moreover, this model also overestimates the performance parameters as it gives the information from upstream to the downstream via interface for every node of the cell, which over predicts the results.

A-6.2. Stage (Mixing Plane)

The Stage model (also known as the Mixing-Plane model) is an alternative to the Frozen Rotor model for modelling frame and/or pitch change. Instead of assuming a fixed relative position of the components, the Stage model performs a circumferential averaging of the fluxes through bands on the interface. Steady-state solutions are then obtained in each reference frame. This model enables steady-state predictions to be obtained for multi-stage machines. The stage averaging at the frame change interface incurs a one-time mixing loss. This loss is equivalent to assuming that the physical mixing supplied by the relative motion between components is sufficiently large to cause any upstream velocity profile to mix out prior to entering the downstream machine component. Stage analysis is most appropriate when the circumferential variation of the flow is of the order of the component pitch.

Stage averaging between blade passages accounts for time average interaction effects, but it neglects transient interaction effects. Stage analysis is not appropriate when the circumferential variation of the flow is significant relative to the component pitch (for example, a pump and volute combination at off-design conditions).

The Stage model usually requires more computational effort than the Frozen Rotor model to converge, but not as much as the transient rotor-stator model. An approximate solution using a Frozen Rotor interface needs to be obtained and then Stage interface is carried to obtain the best results. Implicit stage averaging option is used as this option helps to improve the convergence of the Stage

(Mixing-Plane) model and minimizes reflection on the upstream side of the interface due to locally supersonic flow that is subsonic in the direction normal to the interface.

A-6.3. Transient Rotor-Stator

This model should be used when it is important to account for transient interaction effects at a sliding (frame change) interface. It predicts the true transient interaction of the flow between a stator and rotor passage. In this approach the transient relative motion between the components on each side of the GGI connection is simulated. It ultimately accounts for all interaction effects between components that are in relative motion to each other. The interface position is updated each timestep, as the relative position of the grids on each side of the interface changes. It is possible to use a transient sliding interface anywhere a Stage or Frozen Rotor sliding interface could be used. The principle disadvantage of this method is that the computer resources required may be large, in terms of simulation time, disk space and quantitative post processing of the data.

A-7. Rough Walls and Sand Grain Roughness

The near wall treatment that was discussed above (Scalable Wall Functions, Automatic Wall Treatment) is appropriate when walls can be considered as hydraulically smooth. Surface roughness can have a significant effect on flows of engineering interest. Surface roughness typically leads to an increase in turbulence production near the wall. This in turn can result in significant increase in the wall shear stress and the wall heat transfer coefficients. For the accurate prediction of near wall flows, particularly with heat transfer, the proper modelling of surface roughness effects is essential for a good agreement with experimental data.

Wall roughness increases the wall shear stress and breaks up the viscous sublayer in turbulent flows. Figure A-5 depicts the downward shift of the Logarithmic velocity profile shows the downward shift in the logarithmic velocity profile:

$$u^+ = \frac{1}{\kappa}\ln(y^+) + B - \Delta B \qquad \text{A-32}$$

where B=5.2. The shift ΔB is a function of the dimensionless roughness height, h^+, defined as.

$$h^+ = \frac{hu_\tau}{\upsilon} \qquad \text{A-33}$$

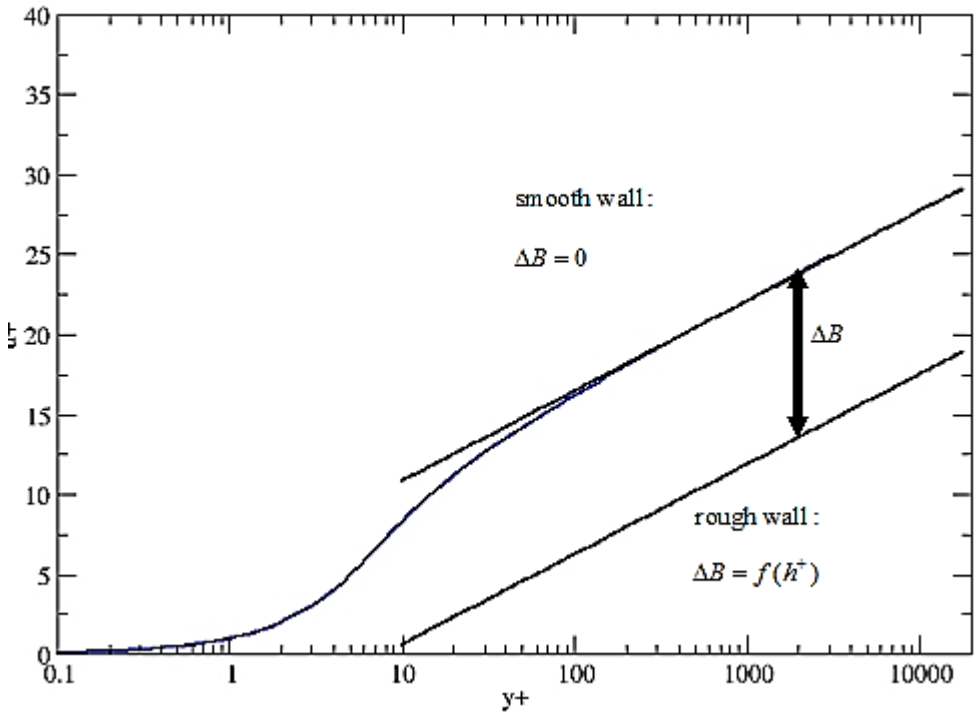

Figure A-5: Downward Shift of the Logarithmic Velocity Profile

For sand-grain roughness, the downward shift can be expressed as:

$$\Delta B = \frac{1}{\kappa}\ln(1 + 0.3h_s^+) \qquad \text{A-34}$$

It has been shown that a technical roughness, which has peaks and valleys of different shape and size, can be described by an equivalent sand-grain roughness [22], [57]. The corresponding picture is a wall with a layer of closely packed spheres, which have an average roughness height as depicted in Figure A-6

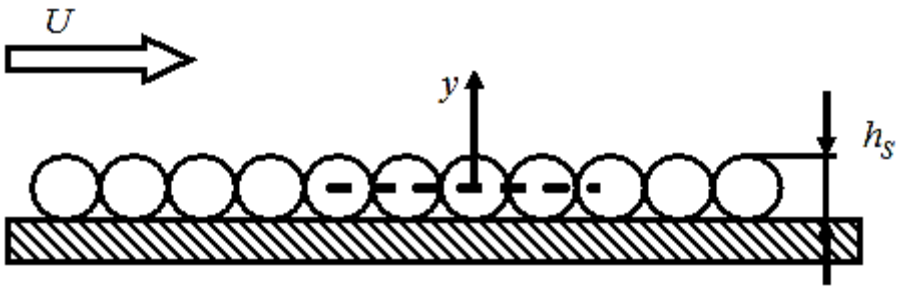

Figure A-6: Equivalent Sand-Grain Roughness

Guidance to determine the appropriate equivalent sand-grain roughness height can be obtained from Schlichting [22], White [58] and Coleman et al. [59].

Depending on the dimensionless sand-grain roughness h_s^+, three roughness regimes can be distinguished:

- hydraulically smooth wall: $0 \leq h_s^+ \leq 5$
- transitional-roughness regime: $5 \leq h_s^+ \leq 70$
- fully rough flow: $h_s^+ \geq 70$

The viscous sublayer is fully established near hydraulically smooth walls. In the transitional roughness regime, the roughness elements are slightly thicker than the viscous sublayer and start to disturb it, so that in fully rough flows the sublayer is destroyed, and viscous effects become negligible.

From the picture of the sand-grain roughness, it can be assumed that the roughness has a blockage effect, which is about 50% of its height. The idea is to place the wall physically at 50% height of the roughness elements:

$$y = \max(y, h_s/2) \qquad \text{A-35}$$

This gives about the correct displacement caused by the surface roughness.

A-8. Construction of Orthogonal Arrays

Taguchi's catalogue of orthogonal array derived by Taguchi [60] has been widely used in many industries to perform experiments. [46] However, the Taguchi himself has provided either no

information or insufficient information on the construction of the orthogonal arrays. Therefore, [61] Kacker has described the structure and constructions of Taguchi's orthogonal arrays with the illustration of their fractional factorial nature. [62] Fractional factorial is an experimental design consisting of a subset (fraction) of the factorial design. Typically, the fraction is a simple proportion of the full set of possible treatment combinations. Fractional factorial designs require fewer runs, some degree of confounding (often called degree of freedom –give a relative result rather than absolute) occurs. [61] Furthermore, the author also pointed out that his catalogue can be expanded to include orthogonal arrays developed since 1960. An orthogonal array is a type of experiment, whereby the columns for the independent variables are orthogonal (means statistically independent) to one another. An orthogonal array of s elements, denoted by $OA_N(s^m)$, is an $N \times m$ matrix. Each column consists of a pair of columns where each of the possible ordered pairs of elements appears the same number of times. In this study, three control factors with five set of levels have been chosen, which come under $OA_{25}(5^3)$ orthogonal array. This orthogonal array has been obtained from $OA_{25}(5^6)$ orthogonal array. The specification and construction of the aforementioned array has been discussed in the next sub-section.

A-8.1. Five-Element Orthogonal Array, $OA_{25}(5^6)$

[61] The nature of fractional factorial design of five-element (levels) orthogonal arrays has been dependent upon the construction of these orthogonal arrays. Therefore, the method of constructing these arrays has been explained in this section and then, the nature of these arrays will be explained. A complete five-element orthogonal array with 5^r rows has $(5^r–1)/(5–1)$ columns, whereby r is a factor, and it is constructed column by column in the following three steps.

Step 1: Write in the r column numbers columns specified by 1, 2, 7, 32, ..., $((5^r–1)/(5–1)+1)$. It is a complete factorial plan in r factors each having five test levels represented by 0, 1, 2, 3, 4 and 5 respectively. In order to match Taguchi's display format, write this plan in such a way that the entries of the left most columns change less frequently than the entries of the right most columns. The entries of these r columns are used to calculate and define the entries of the remaining columns. Therefore, these r columns are referred to as the basic columns and marked as $x_1, x_2, ..., x_r$, respectively.

Table A-1: Coefficient of the generators of the five-element orthogonal array of 5^r rows for r = 2, 3, …

Coefficients of $x_1, x_2, x_3, \ldots, x_r$

Column No.	a_1	a_2	a_{r-1}	a_r
1	1	0	First $(5^{r-2}-1)/(5-1)$	First $(5^{r-1}-1)/(5-1)$
2	0	1	entries are 0	entries are 0
3	1	1	Next (5^{r-2})	Last (5^{r-1})
4	2	1	entries are 1	entries are 1
5	3	1	Next (5^{r-2})	
6	4	1	entries are 0	
.			Next (5^{r-2})	
.			entries are 1	
.			Next (5^{r-2})	
.			entries are 2	
.	Repeat (0, 1, 2, 3, 4)		Next (5^{r-2})	
.			entries are 3	
.			Next (5^{r-2})	
.			entries are 4	
.				
$(5^r-1)/(5-1)$	3	3		

The explanation of the first step is presented the Table A-1, which is a construction of an $OA_{25}(5^6)$, whereby $N = 25 = 5^2$, hence r = 2. Therefore, Table A-2 has the description of the first step when $r = 2$.

Table A-2: Basic column when r = 2

Column No.	1	2	3	4	5	6
Row No.						
1	0	0				
2	0	1				
3	0	2				
4	0	3				
5	0	4				
6	1	0				
7	1	1				
8	1	2				
9	1	3				
10	1	4				
11	2	0				
12	2	1				
13	2	2				
14	2	3				
15	2	4				

16	3	0
17	3	1
18	3	2
19	3	3
20	3	4
21	4	0
22	4	1
23	4	2
24	4	3
25	4	4
Generator	x_1	x_2

Step 2: These basic columns are used to generate the other columns. The generator of a particular column is a rule of the form $a_1x_l + a_2x_2 + ... + a_rx_r$, where $x_1, x_2, ..., x_r$ denote the r basic columns and the coefficients $a_1, a_2, ..., a_r$ for a particular column are given in appropriate row of Table . List the generators in the order of column numbers. [61] Kacker has built these generators mentioned in Table A-3 that are used to create the five-element orthogonal array introduced by Taguchi [60].

Table A-3: List of the generators required for all elements

Column No.	Generator
1	x_1
2	x_2
3	$x_2+ x_1$
4	$x_2+ 2x_1$
5	$x_2+ 3x_1$
6	$x_2+ 4x_1$

Step 3: Compute the entries of the remaining columns by using the entries of the r basic columns and the appropriate generators. The required calculations are performed in modulo 6 arithmetic, which are finite additions and multiplications by Galois field defined in Table A-4 and Table A-5.

Table A-4: Addition table for a Galois field of five-elements

+	0	1	2	3	4
0	0	1	2	3	4
1	1	2	3	4	0
2	2	3	4	0	1
3	3	4	0	1	2
4	4	0	1	2	3

Table A-5: Multiplication table for a Galois field of five-elements

*	0	1	2	3	4
0	0	0	0	0	0
1	0	1	2	3	4
2	0	2	4	1	3
3	0	3	1	4	2
4	0	4	3	2	1

Henceforth, the combination of step 2, whereby the generators for five-elements have been identified and finite additions and multiplication defined by Galois presented in tables earlier has helped to generate a five-element orthogonal array that has been presented in the Table A-6.

Table A-6: A complete five-element orthogonal array $OA_{25}(5^6)$

Column No.	1	2	3	4	5	6
Row No.						
1	0	0	0	0	0	0
2	0	1	1	1	1	1
3	0	2	2	2	2	2
4	0	3	3	3	3	3
5	0	4	4	4	4	4
6	1	0	1	2	3	4
7	1	1	2	3	4	0
8	1	2	3	4	0	1
9	1	3	4	0	1	2
10	1	4	0	1	2	3
11	2	0	2	4	1	3
12	2	1	3	0	2	4
13	2	2	4	1	3	0
14	2	3	0	2	4	1
15	2	4	1	3	0	2
16	3	0	3	1	4	2
17	3	1	4	2	0	3
18	3	2	0	3	1	4
19	3	3	1	4	2	0
20	3	4	2	0	3	1
21	4	0	4	3	2	1
22	4	1	0	4	3	2
23	4	2	1	0	4	3
24	4	3	2	1	0	4
25	4	4	3	2	1	0

Generator	x_1	x_2	x_2+x_1	x_2+2x_1	x_2+3x_1	x_2+4x_1

[62] This analogous construction methods of constructing three, four, and five-element orthogonal arrays are based on the mathematical theory of fractional factorials developed by Bose [63]. The entries of the *r* basic columns identified by column numbers 1, 2, 7, 32, ..., $((5^r-1)/(5-1)+1)$ form a complete factorial plan and the other columns correspond to the interaction effects. Since each column contains five distinct elements, four degrees of freedom are associated with each column. An interaction effect involving *k* factors carries $(5-1)^k = 4^k$ degrees of freedom. Therefore, 4^{k-1} columns correspond to each interaction effect involving *k* factors. In particular, four columns correspond to each pairwise interaction effect. When all $(5^r-1)/(5-1)$ columns are associated with factors, a five-element (five-level) array $OA_N(5^m)$ where $N = 5^r$ and $m = (5^r-1)/(5-1)$ represents a $N/5^m = (1/5)^{m-r}$ fraction of a complete 5^m factorial plan. For example, $OA_{25}(5^6)$ represents a $(1/5)^4$ fraction of a complete 5^6 factorial plan.

A-9. Construction of Curved Diffuser Geometry

The curved diffuser geometry is composed of reverse curves. The construction of the curved diffuser is started from the centerline of the diffuser geometry. Three geometrical parameters are only given (x/b_1, θ/θ_{max} and r/r_{max}), and the rest of the geometry is composed using the procedure provided later in the section. This procedure is applicable to reverse curves with equal and unequal branches. Figure A-7 depicts the reverse curve ABC consists of two simple curves AB and BC that turn in opposite directions and meet at the point B where they have a common tangent. This point is called the Point of Reverse Curvature (P.R.C). The center of the branch AB is at D, and the center of the branch BC is at E. The tangent AF through the Point of Curvature (P.C.) and the tangent CG through the Point of Tangency (P.T.) are parallel, and the line HBJ is tangent to both branches of the curve at the P.R.C. Whether the two branches AB and BC have equal radii or unequal radii, each curve must have the same central angle; in other words, the angles ADB and BEC must be equal. In Figure A-7, the branches AB and BC of the reverse curve have unequal radii, and the P.R.C. at B is not midway between the parallel tangents AF and CG through the P.C. and P.T., respectively. However, since the central angles ADB and BEC of the two branches are wqual, the deflection angles FAB and GCB are also equal, and the chords AB and BC must lie in the same straight line, as for equal branches. Usually, the distance x between the tangents is fixed, and the degree of curve of one branch and the length *l* of the straight line from the P.C. to the P.T. are selected to meet the requirements of the

particular case. It is then required to determine the radius or degree of the other branch and the central angle for each branch. The formulas to be used in this case may be derived as follows.

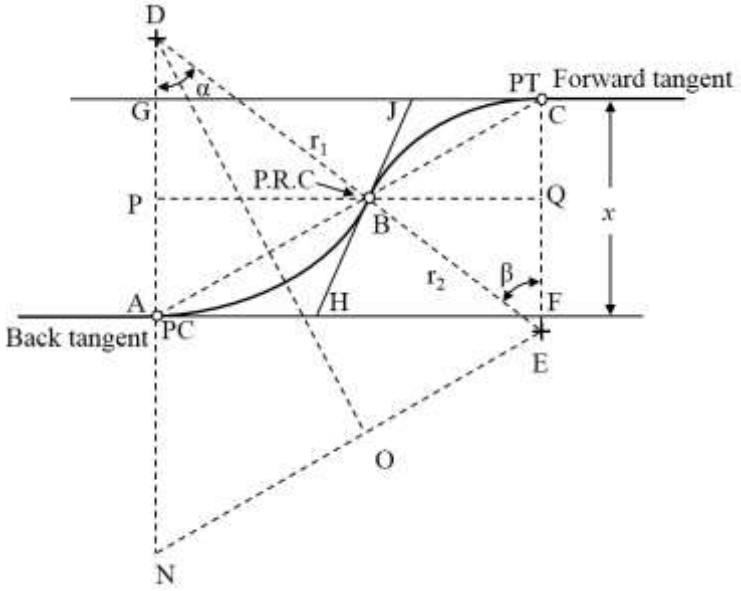

Figure A-7: Reverse curve having unequal radii

If the line EN is drawn parallel to the chord AC, and the radius DA is extended to meet the line EN at N, then the figure ACEN is a parallelogram. Hence, EN = AC = *l* and AN = CE. Also, if the line DO is drawn perpendicular to EN it will bisect EN at O, or NO = ½EN = ½*l*. Since the angles NDO and FAC are equal, the right triangles NDO and FAC are similar and DN : NO = AC : CF. If the radius of the branch AB is denoted by r_1 and the radius of the branch BC by r_2, DN = $r_1 + r_2$ and ($r_1 + r_2$) : ½*l* = *l* : x. Hence,

$$r_1 + r_2 = \frac{l^2}{2x} \tag{A-36}$$

When the radius of either branch is known, the radius of the other branch can be readily found by using equation A-36. Also $\sin(FAC) = \frac{FC}{AC}$; or if α represents the central angle of either branch of the curve, as angle NDE, angle FAC is ½α and

$$\sin\left({}^{1}/_{2}\,\alpha\right) = \frac{x}{l} \tag{A-37}$$

The above equations are suitable for reverse curves with no tilt angle, θ (as shown in Figure A-8). If the reverse curves are tilted than equations are modified. The variable p will be used instead of x in the equation A-36 and equation A-37, where p is defined as follows:

$$p = x - r_1(1 + 2cos\theta) \tag{A-38}$$

where θ is a tilt angle. Hence equation A-36 and equation A-37 are modified for the tilt angle are as follows:

$$r_1 + r_2 = \frac{l^2}{2p} \tag{A-39}$$

$$\sin\left({}^{1}/_{2}\,\alpha\right) = \frac{p}{l} \tag{A-40}$$

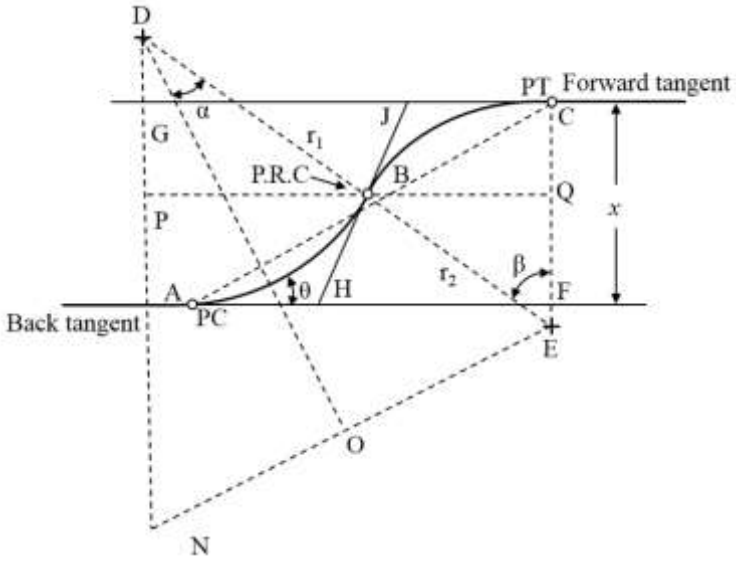

Figure A-8: Reverse curve having unequal radii and tilted at back tangent region

The above procedure only helps to create a centerline for the cured diffuser model. Since, diffuser width varies hence a method is introduced, which helps in obtaining diffuser widths.

In this section curved diffuser widths needs to be computed. The width is from the centerline towards the shroud wall, x_s and from the centerline towards the hub wall, x_h. Generic equations have been developed. The curved diffuser geometry is divided into four regions. This is because different methods are used to compute the diffuser widths. The equations are written as follows:

Region 1 – (Condition 1: $y_1 < L_1$ and $y_1 < r_{sy1}$)

$$x_s = \sqrt{{r_1}^2 - {y_1}^2} - \sqrt{\left(r_1 - {b}/{2}\right)^2 - {y_1}^2} \quad \text{(A-41)}$$

$$x_h = \sqrt{\left(r_1 + {b}/{2}\right)^2 - {y_1}^2} - \sqrt{{r_1}^2 - {y_1}^2} \quad \text{(A-42)}$$

$$x_{t1} = x_s + x_h \quad \text{(A-43)}$$

Region 2 – (Condition 2: $y_1 > L_1$, $y_1 > r_{sy1}$ and $y_1 > r_{hy1}$)

$$x_s = \sqrt{\left(r_2 + {b}/{2}\right)^2 - (L - y_1)^2} - \sqrt{{r_2}^2 - (L - y_1)^2} \quad \text{(A-44)}$$

$$x_h = \sqrt{{r_2}^2 - (L - y_1)^2} - \sqrt{\left(r_2 - {b}/{2}\right)^2 - (L - y_1)^2} \quad \text{(A-45)}$$

$$x_{t4} = x_s + x_h \quad \text{(A-46)}$$

Region 3 – (Condition 3: $y_1 < L_1$, $y_1 > r_{sy1}$ and $y_1 < r_{hy1}$)

$$x_s = \sqrt{\left(r_2 + {b}/{2}\right)^2 - (L - y_1)^2} - \sqrt{{r_2}^2 - (L - y_1)^2} \quad \text{(A-47)}$$

$$x_h = \sqrt{\left(r_1 + {b}/{2}\right)^2 - {y_1}^2} - \sqrt{{r_1}^2 - {y_1}^2} \quad \text{(A-48)}$$

$$x_{t4} = x_s + x_h \quad \text{(A-49)}$$

Region 4 – (Condition 4: $y_1 > L_1$, $y_1 > r_{sy1}$ and $y_1 < r_{hy1}$)

$$x_s = \sqrt{\left(r_2 + {b}/{2}\right)^2 - (L - y_1)^2} - \sqrt{{r_2}^2 - (L - y_1)^2} \quad \text{(A-50)}$$

$$x_h = \sqrt{\left(r_1 + {b}/{2}\right)^2 - {y_1}^2} - r_1 - r_2 + r_2 \cos\left(sin^{-1}\left(\frac{L-y}{r_2}\right)\right) \quad \text{(A-51)}$$

$$x_{t4} = x_s + x_h \quad \text{(A-52)}$$

Generic equation for curved diffuser width is defined in equation A-53. The diffuser width is dependent upon the location of y_1.

$$x_t = x_s + x_h \tag{A-53}$$

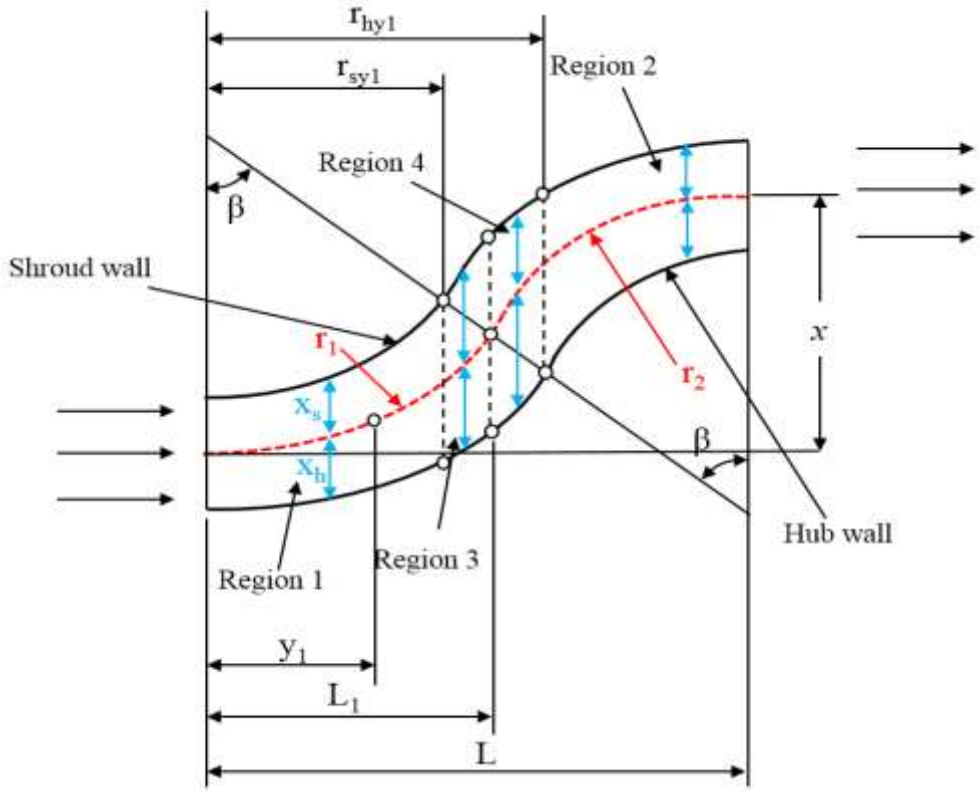

Figure A-9: Reverse curves having unequal radii (curved diffuser)

If the hub wall of the curved diffuser model is diverged at some location than the curved diffuser width equations for all four conditions are modified as shown below. A new term is introduced, which is conditional equation.

$$a = if(y_1 < L_d)$$

$$Than\ a = 0$$

$$Else\ a = 1$$

Where L_d is same as L/L_{max}, which is a geometrical parameter considered in Chapter 6 (Section 6.5).

Region 1 – (Condition 1: $y_1 < L_1$ and $y_1 < r_{sy1}$)

$$x_s = \sqrt{{r_1}^2 - {y_1}^2} - \sqrt{\left(r_1 - {b}/{2}\right)^2 - {y_1}^2} \quad \text{(A-41)}$$

$$x_h = \sqrt{\left(r_1 + {b}/{2}\right)^2 - {y_1}^2} - \sqrt{{r_1}^2 - {y_1}^2} + a\left(\frac{(b_2-b)\times s(L-L_d)}{L-L_d}\right) \quad \text{(A-42)}$$

$$x_{t1} = x_s + x_h \quad \text{(A-43)}$$

Region 2 – (Condition 2: $y_1 > L_1$, $y_1 > r_{sy1}$ and $y_1 > r_{hy1}$)

$$x_s = \sqrt{\left(r_2 + {b}/{2}\right)^2 - (L-y_1)^2} - \sqrt{{r_2}^2 - (L-y_1)^2} \quad \text{(A-44)}$$

$$x_h = \sqrt{{r_2}^2 - (L-y_1)^2} - \sqrt{\left(r_2 - {b}/{2}\right)^2 - (L-y_1)^2} + a\left(\frac{(b_2-b)\times s(L-L_d)}{L-L_d}\right) \quad \text{(A-45)}$$

$$x_{t4} = x_s + x_h \quad \text{(A-46)}$$

Region 3 – (Condition 3: $y_1 < L_1$, $y_1 > r_{sy1}$ and $y_1 < r_{hy1}$)

$$x_s = \sqrt{\left(r_2 + {b}/{2}\right)^2 - (L-y_1)^2} - \sqrt{{r_2}^2 - (L-y_1)^2} \quad \text{(A-47)}$$

$$x_h = \sqrt{\left(r_1 + {b}/{2}\right)^2 - {y_1}^2} - \sqrt{{r_1}^2 - {y_1}^2} + a\left(\frac{(b_2-b)\times s(L-L_d)}{L-L_d}\right) \quad \text{(A-48)}$$

$$x_{t4} = x_s + x_h \quad \text{(A-49)}$$

Region 4 – (Condition 4: $y_1 > L_1$, $y_1 > r_{sy1}$ and $y_1 < r_{hy1}$)

$$x_s = \sqrt{\left(r_2 + {b}/{2}\right)^2 - (L-y_1)^2} - \sqrt{{r_2}^2 - (L-y_1)^2} \quad \text{(A-50)}$$

$$x_h = \sqrt{\left(r_1 + {b}/{2}\right)^2 - {y_1}^2} - r_1 - r_2 + r_2\cos\left(sin^{-1}\left(\frac{L-y}{r_2}\right)\right) + a\left(\frac{(b_2-b)\times s(L-L_d)}{L-L_d}\right) \quad \text{(A-51)}$$

$$x_{t4} = x_s + x_h \quad \text{(A-52)}$$

where b2 is outlet-to-inlet width ratio, a geometrical parameter considered in Chapter 6 (Section 6.5) and s is non-dimensional variable used for locating y, which ranges from 0 to 1.

LIST OF PUBLICATIONS

1. Ahmed, N., Asim, T., Mishra, R., Sivagnanasundaram, S., & Eynon, P. (2015). Optimal Vaneless Diffuser Design for a High-End Centrifugal Compressor.